

INTERNATIONAL CONFERENCE
ON ENGINEERING TECHNOLOGIES

ICENTE'24

November 21-23, 2024

Konya/TURKEY

PROCEEDINGS BOOK

Editors:

Prof. Dr. Şakir TAŞDEMİR

Prof. Dr. Nurettin DOĞAN



icente.selcuk.edu.tr



E-ISBN: 978-625-95385-8-7





**8th International Conference on
Engineering Technologies
ICENTE 2024**

November 21-23, 2024, Konya, Turkey

PROCEEDINGS BOOK

Editors

**ŞAKİR TAŞDEMİR
NURETTİN DOĞAN**

International Conference on Engineering Technologies, ICENTE'24

Konya, Turkey, November 21-23, 2024

8th International Conference on Engineering Technologies ICENTE 2024

21-23 November 2024

PROCEEDINGS BOOK

EDITORS:

Prof. Dr. Şakir TAŞDEMİR

Rector of Sinop University, Turkey
15 Temmuz Campus, 57000, Sinop, TURKEY
sakirtasdemir@sinop.edu.tr

Prof. Dr. Nurettin DOĞAN

Selçuk University, Turkey
Department of Computer Engineering, Faculty of Technology
Alaeddin Keykubat Campus, 42130, Konya, TURKEY
nurettin.dogan@selcuk.edu.tr

All rights of this book are reserved. All or any part of this book cannot be published, stored, printed, filmed or used indirectly without the permission of the authors. It cannot be reproduced by photocopy or any other technique. All responsibility of all texts and visuals published in the book belongs to the author(s).

EBOOK ISBN: 978-625-95385-8-7



PREFACE

International Conference on Engineering Technologies (ICENTE'24) was organized in Konya, Turkey on 21-23 November 2024 by Selçuk University Faculty of Technology and cooperation with Sinop University Faculty of Engineering and Architecture.

The main objective of ICENTE'24 is to present the latest research and results of scientists related to Biomedical, Computer, Electrical & Electronics, Mechanical, Mechatronic, Metallurgical & Materials, Civil, Chemical, Industrial, Environmental, Geological and Mining Engineering fields. This conference provides opportunities for the delegates from different areas in order to exchange new ideas and application experiences, to establish business or research relations and to find global partners for future collaborations.

All paper submissions have been double blind and peer reviewed and evaluated based on originality, technical and/or research content/depth, correctness, relevance to conference, contributions, and readability. Papers presented in the conference that match with the topics of the journals will be published in the following journals:

- Artificial Intelligence Studies (AIS)
- Gazi Journal of Engineering Sciences (GJES)
- International Journal of Automotive Engineering and Technologies (IJAET)
- International Journal of Energy Applications and Technology (IJEAT)
- Selçuk University Journal of Engineering Sciences (SUJES)
- Intelligent Methods In Engineering Sciences (IMIENS)
- Turkish Journal of Mathematics and Computer Science (TJMCS)
- Positive Science International

At this conference, there are 172 paper submissions. Each paper proposal was evaluated by two reviewers, and finally, 117 papers were presented at the conference from 4 different countries with 69 local and foreign universities and organizations participating.

In particular, we would like to thank Prof. Dr. Hüseyin YILMAZ, Rector of Selçuk University, conference scientific committee, session chairs, invited speakers, reviewers, technical team, participants, and all our colleagues who have contributed. They have made a crucial contribution to the success of this conference. Our thanks also go to our colleagues in our conference office.



Prof. Dr. Şakir TAŞDEMİR
Prof. Dr. Nurettin DOĞAN
Editors

PROGRAMME COMMITTEES**Honorary and Advisory Board:**

Hüseyin YILMAZ, Rector of Selçuk University, Turkey

Şakir TAŞDEMİR, Rector of Sinop University, Turkey

General Chairs:

Şakir Taşdemir, Sinop University, Turkey

Nurettin Doğan, Selçuk University, Turkey

Vice Chairs:

Selahattin ALAN, Selçuk University, Turkey

Sema SERVİ, Selçuk University, Turkey

Hakan TERZİOĞLU, Selçuk University, Turkey

Sabri BİLGİN, Sinop University, Turkey

Scientific Committee:

Abdullah Erdal TÜMER, Kirgizistan Turkiye Manas University - KG

Ahmet Afsin KULAKSIZ, Konya Technical University - TR

Ahmet KARAOĞLU, Sinop University- TR

Ahmet TIĞLI, Sinop University- TR

Ahmet YÖNETKEN, Afyon Kocatepe University- TR

Ali ATEŞ, Sinop University- TR

Ali TİFTİKÇİ, Sinop University- TR

Ali YAŞAR, Selçuk University- TR

Alina Ivan Dramogir, Gheorghe Asachitechnical University of Iasi - RO

Almoataz Youssef Abdelaziz, Ain Shams University - EG

Amar Ramdane Cherif, University of Versailles - FR

Anca Loana Andreescu, Academy of Economic Studies - BG

Alexander Sudnitson, Tallinn University of Technology - EE

Anne Villems, University of Tartu - EE

Antonella Reitano, University of Calabria - IT

Antonio Mendes, Universidade De Coimbra - PT

Aristomenis Antoniadis, Technical University of Crete - GR

Artan Luma, South East European University - MK

Aytaç ÇELİK, Sinop University- TR

Biagio Lenzitti, University of Palermo - IT

Binod Kumar, Jspm Jayawant Institute of Computer Applications Pune - IN

Boris Akanaev, Kazak National University - KZ

Dilek GÜMÜŞ, Sinop University- TR

Domenico Tegolo, Università Degli Studi Di Palermo - IT

Ekrem GÜLSEVİNÇLER, Sinop University- TR

Eisha Akanksha, Mvj College of Engineering - IN

Elinda Kajo Mece, Polytechnic University of Tirana - RO

Engin Ozdemir, Kocaeli University - TR

Fatih BAŞÇİFTÇİ, Selçuk University - TR

Gabriel Luna Sandoval, Sonora State University - MX

Hakan US, Sinop University- TR

Hamit Saruhan, Düzce University - TR

Hamza Bensouilah, Laboratoire de Mecanique et Structures - DZ

Hasan Erdiñ KOÇER, Selçuk University – TR
Hasan OĞUL, Sinop University- TR
Howard Duncan, Dublin City University - IE
Humar KAHRAMANLI ÖRNEK, Selçuk University – TR
Hüseyin Turan ARAT, Sinop University- TR
Huse Fatkic, University of Sarajevo - BA
İlker Ali ÖZKAN, Selçuk University- TR
İsmail SARITAŞ, Selçuk University- TR
Ivan Jelinek, Czech Technical University - CZ
Jaharah A Ghani, National University of Malaysia - MY
Jan Vom Brocke, University of Liechtenstein - LI
Janis Grundspenkis, Riga Technical University - LV
Janusz Jablonowski, Warsaw University - PL
Jiri Srba, Aalborg University - DK
Karl Jones, Liverpool John Moores University - GB
Laurentiu Cristian Deaconu, University of Pitesti - RO
Levent ÖNCEL, Sinop University- TR
M. Kemal BALKI, Sinop University- TR
Mahdi Shahbakhti, Michigan Technology University - US
Majida Ali Abed Meshari, Tikrit University - IQ
Marco Porta, University of Pavia - IT
Mehmet Turan Demirci, Selçuk University - TR
Mirjana Ivanovic, University of Novi Sad - RS
Miroslav Neslusan, University of Zilina - SK
Muhammet ÇAKMAK, Sinop University- TR
Mustafa ACARER, Selçuk University- TR
Mustafa ACAROĞLU, Selçuk University- TR
Mustafa Altin, Konya Technical University - TR
Mustafa Can CANOĞLU, Sinop University- TR
Mustafa KARAKAYA, Sinop University- TR
Natasia Hoic Bozic, University of Rijeka - HR
Necaattin BARIŞCI, Gazi University – TR
Nihat Yildirim, Gaziantep University - TR
Nikolaos Blasis, Technical University of Crete - GR
Olçay Ilcasu, Rowan University – USA
Osman Ayhan ERDEM, Gazi University – TR
Pantha Ghosal, University of Technology Sydney - AU
Pino Caballero Gil, University of La Laguna - ES
Polyxeni Arapi, Technical University of Greece - GR
Recai KUŞ, Selçuk University- TR
Rita Ismailova, Kyrgyz Turkish Manas University - KG
Salih DAĞLI, Sinop University- TR
Semet Celik, Ataturk University - TR
Silyan Sibinov Arsov, Rousse University - BG
Spiridon Cretu, Gheorghe Asachitechnical University of Iasi - RO
Stavros Christodoulakis, Technical University of Crete - GR
Stavros Nikolopoulos, University of Ioannina - GR
Suleyman NEŞELI, Selçuk University- TR
Şakir TAŞDEMİR, Sinop University- TR
Tatjana Dulinskiene, Kaunas University of Technology - LT
Tayfun Findik, Gazi University - TR

Temel Kayikcioglu, Karadeniz Technical University - TR
Tuba Gökhan, Mohamed bin Zayed University of Artificial Intelligence - UAE
Thomas Engel, University of Luxembourg - LU
Tugce Demirdelen, Adana Science Technology University - TR
Turgay KORKUT, Sinop University- TR
Ulku Sultan Keskin, Konya Technical University - TR
Ulvi Seker, Gazi University - TR
Yuri Pavlov, Bulgarian Academy of Sciences - BG
Zarifa Jabrayilova, Institute of Information Technology Anas – AZ
Zarife Sibel ŞAHİN, Sinop University- TR

Organizing Committee:

Abdullah Engin ÖZÇELİK, Selçuk University- TR
Ali YAŞAR, Selçuk University- TR
Angel Smrikarov, Rouse University - BG
Hasan Erdiñç KOÇER, Selçuk University- TR
İlker Ali ÖZKAN, Selçuk University- TR
İsmail SARITAŞ, Selçuk University- TR
Kinyas POLAT, Sinop University – TR
Lilia Georgieva, Heriot Watt University - GB
Meryem SEFERİNOĞLU, Sinop University – TR
Muhammet Serdar BAŞÇIL, Selçuk University- TR
Murat SARIKAYA, Sinop University – TR
Nurcan AKDURAN, Selçuk University- TR
Oylum GÖKKURT BAKİ, Sinop University – TR
Polyxeni Arapi, Technical University of Greece - GR
Selahattin ALAN, Selçuk University- TR
Selahattin BARDAK, Sinop University – TR
Sema SERVİ, Selçuk University- TR
Silyan Sibinov Arsov, Rouse University – BG
Suleyman NEŞELİ, Selçuk University- TR
Şükrü ÇELİK, Sinop University – TR

Local Organizing Committee

Burak TEZCAN, Selçuk University – TR
Gülnihal UYKUN, Selçuk University – TR
İlkay ÇINAR, Selçuk University- TR
İrem Nur YOLDAŞ, Selçuk University – TR
Musa DOĞAN, Selçuk University - TR
Sümeyra Büşra ŞENGÜL, Selçuk University – TR
Yusuf ERYESİL, Selçuk University – TR

TABLE OF CONTENTS

OPTIMIZING POWER DISTRIBUTION SYSTEMS WITH INTEGRATED SOLAR PLANTS, DSTATCOM, AND EV CHARGING STATIONS USING RUNGE-KUTTA ALGORITHM	1
<i>MURAT ÇIKAN</i>	
OPTIMIZATION OF A 69-BUS POWER DISTRIBUTION SYSTEM USING RECONFIGURATION AND THE RUNGEKUTTA ALGORITHM FOR MULTI-OBJECTIVE POWER LOSS AND VOLTAGE DEVIATION MINIMIZATION	6
<i>NİSA NACAR ÇIKAN</i>	
SIMULTANEOUS WIND TURBINE AND EV CHARGING STATION ALLOCATION IN A 33-BUS SYSTEM USING THE SLIME MOULD ALGORITHM FOR POWER LOSS MINIMIZATION AND VOLTAGE PROFILE IMPROVEMENT	9
<i>NİSA NACAR ÇIKAN</i>	
THERMAL BUCKLING RISK IN RAILWAYS: AN ANSYS-BASED ANALYSIS FOR TÜRKİYE	12
<i>FERHAT ÇEÇEN, MEHMET SALTAN</i>	
NUMERICAL INVESTIGATION OF THE EFFECT OF STEEL BRACES ON MULTI-STORY REINFORCED CONCRETE FRAME BEHAVIOR	16
<i>HÜRMET KÜÇÜKGÖNCÜ</i>	
SKIP-GRAM ADAPTED FOR SESSION-BASED RECOMMENDATION SYSTEMS	22
<i>ENES ÇELİK, SEVİNÇ İLHAN OMURCA</i>	
INVESTIGATION OF RECOVERY OF VALUABLE FOOD COMPONENTS BY USING SUPERCRITICAL CARBON DIOXIDE EXTRACTION METHOD	27
<i>SEVİL YILDIZ, SÜHEYLÂ TONGUR, RABİA SERPİL GÜNHAN</i>	
PREDICTING STUDENT DROPOUT IN HIGHER EDUCATION USING MACHINE LEARNING TECHNIQUES: A PREDICTIVE MODEL USING XGBOOST ALGORITHM	31
<i>ANAS ALHARDI, SELAHATTİN ALAN</i>	
RECONFIGURATION OF BUCK TOPOLOGY INTO BUCKBOOST CONVERTER WITH THE SAME CONTROL UNIT FOR NEGATIVE VOLTAGE GENERATION	37
<i>CAĞFER YANARATEŞ</i>	
MEASUREMENT OF AMPLITUDE PRODUCED BY VARIOUS SIZED PARTICLES IN PIEZOELECTRIC ELEMENT	42
<i>NİHAT ÇANKAYA</i>	
NEUROLOGICAL DISORDERS: TYPES, DIAGNOSIS, AND MACHINE LEARNING AND DEEP LEARNING APPROACHES	45
<i>MEHR ALİ QASİMİ, ZÜLEYHA YILMAZ ACAR</i>	
DEVELOPMENT OF A SKULL PHANTOM FOR ARTIFICIAL EEG WAVE GENERATION AND ANALYSIS	52
<i>ELİF NUR SELÇUK, EKREM GÜLSEVİNÇLER, GÖKÇENUR ÇAKMAK KEÇELİOĞLU, HATİCE AKMAN, MUSTAFA REŞİT USAL</i>	

DETECTION OF SURFACE DEFECTS ON COLD-ROLLED GALVANIZED STEEL USING AI-DRIVEN IMAGE FILTERING TECHNIQUES <i>YASİN BIYIKLI, YUSUF BAHRİ ÖZÇELİK, AYTAÇ ALTAN</i>	61
SILENT MODE APPLICATION FOR MOBILE DEVICES WITH WIRELESS BROADCAST TECHNOLOGY <i>MUHAMMED ABDÜL VAHAP İSTER, AHMET CEVAHİR ÇINAR</i>	67
A STUDY ON SOLAR-ASSISTED HYDROGEN PRODUCTION AND REUTILIZATION IN RURAL AREAS <i>S. Z. SHEKARDASHT, ALİ ATEŞ</i>	72
INVESTIGATION OF SUPERSTRATE EFFECTS ON SELJUK STAR MICROSTRIP ANTENNA <i>AYŞE ÖZGE ÇINAR AK, DİLEK UZER</i>	78
DYNAMIC ANALYSIS OF 3D-PRINTED ABS, PET-G AND PLA STRAIGHT BEAM <i>SİNAN MARAŞ</i>	83
PAN-SHARPENING IN SATELLITE IMAGERY <i>DAMLANUR ALKAN, LÜTFİYE KARASAKA</i>	89
GOOGLE EARTH ENGINE AND ITS USAGE IN REMOTE SENSING: THE CASE STUDY OF SAPANCA LAKE, TÜRKİYE <i>DAMLANUR ALKAN, LÜTFİYE KARASAKA</i>	94
RADIOLOGICAL EVALUATION WITH POSSIBLE ACCIDENT SCENARIO OF SINOP NUCLEAR POWER PLANT <i>ABDULLAH ZENGİN, HÜSEYİN ŞAHİNER, EKREM GÜLSEVİNÇLER</i>	99
MALWARE AND THEIR REMOTE CONTROL IN THE CONTEXT OF DETECTION AND PREVENTION OF GLOBAL THREATS <i>NURETTİN DOĞAN, ZEYNEP BAKIRTEMİZLER AYDIN</i>	105
DESIGN OF A MAXIMUM POWER POINT TRACKING SYSTEM USING A SWITCHED-CAPACITOR WITH A CLASS E RESONANT INVERTER <i>KENAN ÜNAL, SALİH NACAR</i>	108
INTERFACE OPTIMIZATION OF MASNI3/FASNI3 BASED PEROVSKITE SOLAR CELLS <i>KENAN ÖZEL, ABDULLAH YILDIZ</i>	112
IMPORTANCE OF ARTIFICIAL INTELLIGENCE APPLICATIONS IN FOOD INDUSTRY <i>RABİA SERPİL GÜNHAN</i>	116
DEVELOPMENT OF A DEEP LEARNING METHOD USING MAGNETIC RESONANCE IMAGES FOR THE DIAGNOSIS OF MULTIPLE SCLEROSIS <i>FATMA AKSU, AHMET CEVAHİR ÇINAR</i>	121
A FOUR-WAY STRIPLINE POWER DIVIDER DESIGN WITH INCREASED ISOLATION IN THE 500-1000 MHZ FREQUENCY BAND <i>BETÜL ÖZEN GÜLER, MESUT KARTAL</i>	125
ENHANCING AUTOMATED AND EARLY DETECTION OF ALZHEIMER'S DISEASE USING IMAGE PROCESSING AND MACHINE LEARNING <i>FURKAN ŞENOL, HÜSEYİN ESAD ÖNER, MAHMUT BÜYÜKBAŞ</i>	131

INDUSTRY 4.0 BASED CUSTOMER-ORIENTED UNMANNED PRODUCTION SYSTEM	137
<i>AHMET SAİT MÜLAYİM, YUSUF KEREM TÜRKMEN, MERAL ÖZARSLAN YATAK</i>	
FOUR YEARS UPDATE OF LPG CONVERSION FIELD STATUS OF A SPARK IGNITION INTERNAL COMBUSTION ENGINE PASSENGER VEHICLE	143
<i>EYÜB CANLI</i>	
AN EXPERIMENTAL STUDY ON THE EFFECT OF COLEMANITE CONCENTRATOR WASTE ON GAMMA-RAY BEAMS, SETTING TIME, AND COMPRESSIVE STRENGTH PROPERTIES IN CEMENT-BASED MORTARS	147
<i>ŞEVKİ EREN, DOĞAN YAŞAR, SELAHATTİN GÜZELKÜÇÜK, GÖKHAN EKİNCİOĞLU, YUNUS KARATAŞ</i>	
DETECTION OF PLANT DISEASES WITH DEEP LEARNING FOR PRODUCTIVITY AND SUSTAINABILITY IN AGRICULTURE	154
<i>ŞEYMA TAŞ, AHMET GÜREL, MEHMET EREN, ÖZLEM DİLEK ACAR, SEMA SERVİ, ONUR İNAN</i>	
CHARACTERIZATION OF AA2024/CNT NANOCOMPOSITES AS A FUNCTION OF MILLING TIME AND CNT CONTENT	159
<i>HAYRUNNİSA ÖZER, ÖZLEM CANPOLAT, TEMEL VAROL</i>	
AGRIVOLTAIC TECHNOLOGY IMPLEMENTATION ON SOYBEAN FARMS IN NIGERIA	163
<i>HAMZE MOHAMED ABDULLAHI, ÖMER ÖNDER ERAT, BÜLENT YEŞİLATA</i>	
LYAPUNOV-BASED DEEP NEURAL NETWORK ROBUST TRAJECTORY CONTROL FOR ROBOTIC SYSTEM	168
<i>FIRAT CAN YILMAZ, RECEP ÖNLER</i>	
CONTROLLED MORPHOLOGY TRANSFORMATION IN NICO2O4 VIA HYDROTHERMAL SYNTHESIS	171
<i>BURAK KIVRAK, İ. BALCI, İ.C. KAYA, M. AKYOL, H. AKYILDIZ</i>	
OFFLINE SIGNATURE VERIFICATION OF GENUINE SIGNATURES: A SIAMESE CNN-BASED MAJORITY VOTING METHOD	174
<i>ERCE ÖZTÜRK, ÖNSEN TOYGAR</i>	
A LIE DETECTION: VIA SPECTRAL FEATURES USING “BAG OF LIES”	179
<i>SEMİYE DEMİRCAN, S. KUMRU</i>	
APPLICATION OF DEEP LEARNING-BASED TRANSFER LEARNING MODELS IN MONKEYPOX DIAGNOSIS	183
<i>MUSTAFA KEMAL TOPÇU, ONUR İNAN</i>	
A PERFORMANCE COMPARISON OF DIFFERENT MACHINE LEARNING ALGORITHMS TO FORECAST WIND ENERGY IN TÜRKİYE	187
<i>SEMA SERVİ, ONUR İNAN, FATİH YILMAZ, İSMAİL ARSEL, AHMET PEKGÖR, AŞIR GENÇ, GALİP OTURANÇ</i>	
EXPERIMENTAL INVESTIGATION OF THRUST AND FLOW CHARACTERISTICS IN TERMS OF GROUND-BODY INTERACTION OF REUSABLE VERTICAL TAKE-OFF/LANDING ROCKET	193
<i>MAİDENUR YÜKSEL, ÜMMÜ SELEME ÖZLEN, HÜRREM AKBIYIK</i>	

MODELING AND SOC ESTIMATION OF LITHIUM-ION BATTERIES USED IN ELECTRIC VEHICLES	200
<i>BERFİN YAĞCI, MURAT ÜNLÜ</i>	
<hr/>	
LOCAL ANOMALY DETECTION WITH MACHINE LEARNING IN EMBEDDED SYSTEMS: HIGH FREQUENCY DATA PROCESSING	205
<i>ABDULKADİR SADAY, SÜLEYMAN CANAN, ENES ERDOĞAN</i>	
<hr/>	
DIGITAL TWIN IMPLEMENTATION OPPORTUNITIES FOR CIVIL ENGINEERING APPLICATIONS	210
<i>MERVE KAYA, ÖNDER HALİS BETTEMİR, MEHMET FATİH ACAR</i>	
<hr/>	
DEVELOPMENT OF A BATTERY MANAGEMENT SYSTEM WITH IOT-ENABLED DATA TRACKING FOR AUTONOMOUS LOAD ROBOT	217
<i>İBRAHİM ETHEM DERE, DAVUT ERTEKİN, TALHA TELLİ, SÜLEYMAN CANAN</i>	
<hr/>	
ANDROID PERMISSION ANALYSIS AND MALWARE DETECTION USING MACHINE LEARNING METHODS	223
<i>MUHAMMED TALHA ÇALIŞ, ZÜLEYHA YILMAZ ACAR</i>	
<hr/>	
SELECTION AND APPLICATION OF ROBOTICS PROCESS AUTOMATION IN A MEDIUM SIZED MANUFACTURING COMPANY	227
<i>MEHMET TEVFİK ÇOBANOĞLU</i>	

Optimizing Power Distribution Systems with Integrated Solar Plants, DSTATCOM, and EV Charging Stations using Runge-Kutta Algorithm

MURAT ÇIKAN

Cukurova University, Adana/Turkey, mcikan@cu.edu.tr

Abstract - This study presents an innovative approach to power distribution system optimization utilizing the state-of-the-art Runge-Kutta Algorithm (RKO). The research addresses the complex challenge of simultaneously allocating and sizing solar power plants and DSTATCOM within the distribution network. Additionally, it incorporates the strategic placement of 5 MW electric vehicle (EV) charging station, acknowledging the growing importance of electric mobility in modern power systems. The optimization process is guided by a dual objective function that aims to minimize both power losses and voltage deviations, thus enhancing overall system efficiency and stability. By leveraging the RKO's advanced meta-heuristic capabilities, this study offers a sophisticated solution to the multifaceted problem of integrating renewable energy sources, improving power quality, and accommodating emerging load patterns. The results demonstrate the effectiveness of the proposed methodology in achieving a balanced and optimized power distribution system. This research contributes significantly to the evolving field of smart grid management, providing valuable insights for power system planners and operators in the context of increasing renewable penetration and electrification of transportation.

Keywords – Power Distribution Network (PDN), DG Allocation, Electric Vehicle (EV) Charging Stations, Allocation and Sizing, Meta-heuristic Algorithm.

I. INTRODUCTION

The paradigm of modern power distribution networks has undergone a fundamental transformation, driven by the unprecedented integration of renewable energy sources, electric vehicle (EV) charging infrastructure, and sophisticated power electronics. This evolution has positioned Distributed Generation (DG) systems, Distribution Static Synchronous Compensators (DSTATCOMs), and EV charging facilities as pivotal elements in the pursuit of enhanced grid reliability, operational efficiency, and environmental sustainability. The optimization of these components' placement and dimensioning has emerged as a critical challenge in achieving multifaceted operational objectives, including power loss minimization, voltage stability enhancement, and the effective management of stochastic load profiles and intermittent renewable generation [1], [2], [3].

The proliferation of DG installations, particularly photovoltaic (PV) systems, represents a paradigmatic shift in energy generation paradigms, offering substantial potential for reducing carbon footprint and fostering energy independence [3], [4]. Strategic deployment and sizing of PV units within

distribution networks not only augments energy efficiency but also facilitates improved voltage profiles through localized active and reactive power injection. However, the inherent variability of PV generation necessitates sophisticated control mechanisms, exemplified by DSTATCOMs, to maintain robust voltage stability and manage reactive power equilibrium.

DSTATCOMs have emerged as indispensable power quality enhancement devices in contemporary distribution systems, offering dynamic reactive power compensation capabilities crucial for voltage stabilization under varying operational conditions. These devices demonstrate exceptional efficacy in addressing multiple power quality challenges, including voltage fluctuations, phase imbalances, and harmonic distortions. Their significance is particularly pronounced in modern grid architectures characterized by high renewable energy penetration and substantial EV charging demands.

The integration of EV charging infrastructure introduces additional layers of complexity to distribution network operations. These facilities present substantial and variable power demands that can significantly impact network congestion patterns, power loss profiles, and voltage stability metrics. The strategic positioning and capacity optimization of EV charging stations thus becomes paramount in ensuring their seamless integration while maintaining optimal system performance parameters [5], [6].

The concurrent optimization of these diverse system components necessitates sophisticated methodological frameworks capable of addressing multiple, often conflicting, objectives spanning power loss minimization, voltage stability maximization, and economic viability. Advanced optimization techniques, particularly those leveraging the Runge-Kutta Algorithm (RKA) [7], have demonstrated remarkable efficacy in navigating these complex solution spaces. These methodologies incorporate comprehensive consideration of network constraints, power boundaries, and spatial limitations to derive solutions that optimize both technical performance and economic feasibility [4].

This research presents a comprehensive optimization framework for the concurrent placement and sizing of DG systems (specifically PV units), DSTATCOMs, and EV charging facilities within a 136-bus distribution network. The proposed methodology emphasizes efficient resource utilization while enhancing overall network operational efficiency. The results demonstrate the effectiveness of this

integrated optimization approach in achieving significant reductions in power losses, enhanced voltage stability profiles, and seamless integration of renewable energy sources and EV charging infrastructure into distribution networks. This work contributes to the growing body of knowledge addressing the challenges of modern power distribution system optimization and provides valuable insights for system planners and operators.

II. FORMULAS

A. Constraints

The proposed optimization model incorporates key constraints to ensure the technical feasibility and reliability of the power distribution network [8]. These constraints are described in Eq.'s (1)-(3)

$$I_{ij} \leq I_{ij,max} \quad (1)$$

$$V_{min} \leq V_i \leq V_{max} \quad (2)$$

$$\sum_i P_i = \sum_j P_j + \sum_j P_{L,j} \quad (3)$$

The voltage current at each phase for every bus 'i' in the power distribution network must remain within specified upper and lower limits.

B. Fitness Function

The optimization framework developed in this study incorporates two primary objective functions: power loss minimization and voltage stability index (VSI) improvement. These objectives are critical for enhancing the operational efficiency and reliability of the power distribution system. One of the key goals of the optimization process is to minimize active losses across the distribution network. Power loss minimization directly contributes to reducing energy wastage and improving the overall efficiency of the system [9].

$$P_{Loss}^{min} = \sum_{i,k=1}^{N_{br}} r_{(i,k)} \cdot \left(\frac{P_k^2 + Q_k^2}{V_k^2} \right) \quad (4)$$

$$VSI = \frac{4 |V_S|^2 |C||D||S_R| \cos(\phi_R + \delta_S) \sin(\delta_S)}{|S_S|^2 \cdot \cos^2(\phi_S + \delta_R)} \leq 1 \quad (5)$$

Voltage stability is a critical measure of the system's ability to maintain acceptable voltage levels under varying load and generation conditions. The Voltage Stability Index (VSI) is used as a metric to evaluate and improve the stability of the network.

C. 136-Bus Power Distribution Test System

The 136-Bus Test System [10], representing a complex power distribution network, was employed to evaluate the effectiveness of the optimization algorithm. This system presents a network structure reflective of real-world scenarios, enabling a rigorous assessment of algorithmic performance [11]. The 136-bus system includes 156 branches, with 21 left de-energized to maintain a radial configuration suitable for distribution network operations, as shown in the circuit diagram. The network comprises 107 spot loads, all modelled as PQ loads, distributed across the buses. The total active and reactive loads for the distribution line are 18.3 MW and 7.9 MVAR, respectively. Additionally, the system experiences

total active and reactive power losses of 0.32037 MW and 0.70295 MVAR, respectively, across the distribution line. This test setup provides a robust framework for examining optimization solutions in power distribution contexts. The 136-bus test distribution power system is given in Figure 1.

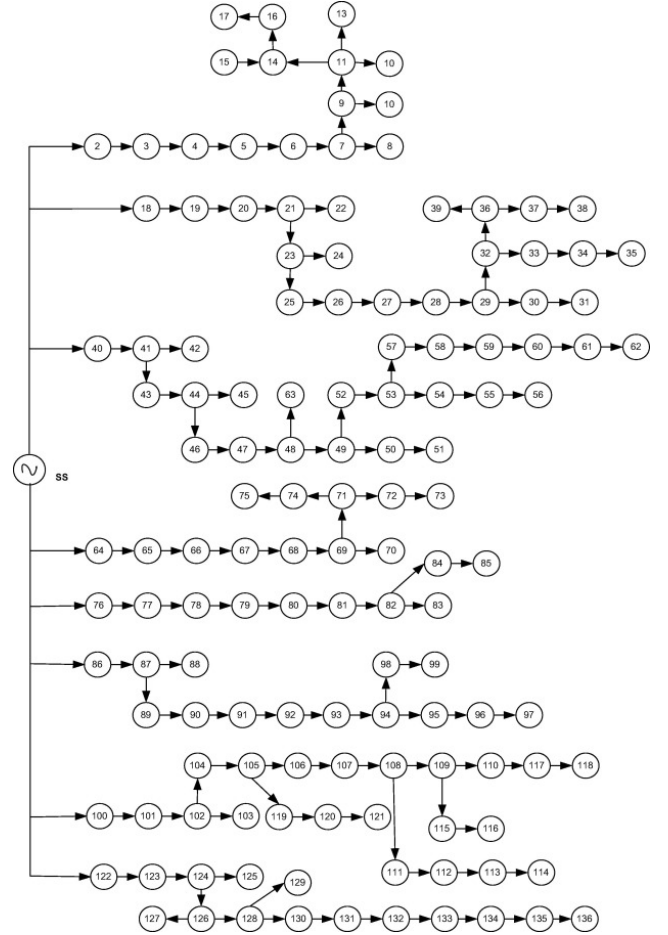


Figure 1: 136-Bus Power Distribution Network [10]

III. RUNGE-KUTTA ALGORITHM (RKA)

The Runge-Kutta optimizer (RUN) is a swarm-based algorithm inspired by the mathematical principles of the Runge-Kutta (RK4) method [7]. RUN employs RK4 slope calculations to guide its population-based exploration and exploitation of the decision space. The optimization process initializes a random set of solutions within defined bounds, then iteratively evolves these solutions using RK-based rules. RUN balances global and local search strategies to efficiently identify promising areas and converge toward the optimal solution, making it a robust and mathematically-grounded optimization technique. Eq.'s are given in (7) and (8).

$$k_1 = \frac{1}{2\Delta_x} (\text{rand}_{no} \cdot (x_{worst} - u \cdot x_{best})) \quad (6)$$

$$k_{i+1} = \frac{1}{2\Delta_x} \left(\text{rand}_{no} \cdot (x_{worst} - k_i \cdot \Delta_x \cdot \text{rand}_{no,i}) - (u \cdot x_{best} + k_i \cdot \Delta_x \cdot \text{rand}_{no,i+1}) \right) \quad (7)$$

IV. RESULTS

In this study, the optimal placement and sizing of Electric Vehicle Charging Stations (EVCS) and renewable energy sources (Photovoltaic) were performed using the Runge-Kutta Algorithm (RKA). The lower and upper boundary values for the optimized equipment are presented in Table 1. The reactive power component of the equipment was designed as a DSTATCOM. Throughout the study, the instantaneous demand power of the EVCS was determined based on 30% of the peak load power of the network. The installed power generation capacity of the PV panels is approximately 4 MW.

Table 1: Upper and Lower Boundary of Obj. Func. Variables

Variab.	WT	Active Power Size	Reactive Power Size	EV Location	Demand Power
Lb	2	0	-4	1	0
Ub	136	4	4	136	5

Table 2 provides a comprehensive summary of the allocation and sizing of distributed generation (DG), DSTATCOM units, and electric vehicle charging stations (EV) for the three scenarios (Case-1, Case-2, and Case-3) considered in the study. The table also includes the power losses (active and reactive) for the 136-bus power distribution system before and after optimization.

Table 2: Allocation and Sizing

Case	DG Type	Location (Bus No)	DG (MW) Dstatcom (Mvar) EV (MW)	Losses (MW+ j.MVA)
Initial	w/o PV	-----	-----	0.3204 + 0.70293.i
Case 1	1 st PV	106	2.85303915	0.2143 + 0.45891.i
	1 st Dstatcom	106	1.2100853.i	
	1 st EV	100	5.00000000	
Case 2	1 st PV	106	2.84072266	0.1825 + 0.38642.i
	1 st Dstatcom	29	1.0583489.i	
	1 st EV	2	2.50000000	
	2 nd PV	9	3.21369353	
	2 nd Dstatcom	106	1.2100323.i	
	2 nd EV	100	2.50000000	
Case 3	1 st PV	106	2.82841181	0.1492 + 0.30991.i
	1 st Dstatcom	11	0.9440457.i	
	1 st EV	64	2.00000000	
	2 nd PV	7	3.14030043	
	2 nd Dstatcom	29	1.0583487.i	
	2 nd EV	2	2.00000000	
	3 rd PV	52	3.20690336	
	3 rd Dstatcom	106	1.2099932.i	
3 rd EV	52	1.00000000		

In Case-1, a single PV unit, DSTATCOM, and EV charging station were optimally located and sized. For instance, the PV unit was placed at Bus 106 with a capacity of 2.853 MW, while the DSTATCOM, also at Bus 106, contributed 1.21 MVAR of reactive power. The EV charging station was allocated at Bus 100 with a demand of 5.0 MW. The optimization process led to a reduction in power losses, with active and reactive losses minimized to 0.2143 MVA and 0.45891 MVA, respectively.

In Case-2, two PV units, two DSTATCOMs, and two EV charging stations were optimally allocated. The PV units were

placed at Buses 106 and 9, with capacities of 2.841 MW and 3.214 MW, respectively. DSTATCOMs were installed at Buses 29 and 106, contributing 1.058 MVAR and 1.21 MVAR, respectively. The EV charging stations were positioned at Buses 2 and 100, each with a demand of 2.5 MW. This configuration further reduced power losses to 0.1825 MVA (active) and 0.38642 MVA (reactive).

In Case-3, three PV units, three DSTATCOMs, and three EV charging stations were strategically located and sized. The PV units were assigned to Buses 106, 7, and 52, with capacities of 2.828 MW, 3.140 MW, and 3.207 MW, respectively. The DSTATCOMs were installed at Buses 11, 29, and 106, with contributions of 0.944 MVAR, 1.058 MVAR, and 1.21 MVAR, respectively. The EV charging stations were placed at Buses 64, 2, and 52, with respective demands of 2.0 MW, 2.0 MW, and 1.0 MW. This scenario achieved the lowest power losses, reducing active and reactive losses to 0.1492 MVA and 0.30991 MVA, respectively.

Table 3 illustrates the improvements in voltage stability, minimum voltage, and power loss reduction achieved by optimizing the allocation of DG equipment in the system. It provides a comparative analysis of the Voltage Stability Index (VSI), the minimum voltage (in p.u.), and the percentage reduction in active and reactive power losses across different cases.

Table 3: Voltage stability index

Case	Voltage Stability Index	Minimum Voltage [p.u.]	Loss Reduction (%)
Initial	3.182e-1	0.931 p.u. Bus-117	-----
Case 1	2.61e-1	0.9711 pu Bus-85	33.11% 34.71%
Case 2	1.49e-1	0.971 p.u. Bus-85	43.04% 45.03%
Case 3	1.374e-1	0.971 p.u. Bus-85	53.43% 55.91%

In Case-1, the VSI improved to 0.261, highlighting enhanced network stability. The minimum voltage increased significantly to 0.9711 p.u., measured at Bus 85. Moreover, the optimization process reduced active and reactive power losses by 33.11% and 34.71%, respectively.

In Case-2, further enhancements were observed, with the VSI reaching a positive value of 0.149, demonstrating a significant improvement in system stability. The minimum voltage remained stable at 0.971 p.u., still at Bus 85. The reductions in active and reactive power losses were recorded as 43.04% and 45.03%, respectively.

In Case-3, the VSI showed maximum improvement, reaching 0.1374, reflecting a highly stable network. The minimum voltage remained consistent at 0.971 p.u. at Bus 85. This scenario achieved the highest reduction in power losses, with active and reactive losses minimized by 53.43% and 55.91%, respectively.

These results confirm the effectiveness of the proposed optimization methodology in improving voltage stability, minimizing power losses, and enhancing the overall performance of the 136-bus distribution system.

V. CONCLUSION

This research presents a sophisticated optimization framework for the strategic deployment and dimensioning of multiple grid components—Distributed Generation (DG) units, Distribution Static Synchronous Compensators (DSTATCOMs), and Electric Vehicle Charging Stations (EVCS)—within a 136-bus distribution infrastructure. The methodology demonstrates exceptional efficacy in achieving multifaceted objectives: power loss minimization, voltage stability enhancement, and overall system efficiency optimization across diverse operational scenarios.

The empirical results validate the robustness of the proposed optimization strategy through a progressive analysis of three distinct configurations. In the initial configuration (Case-1), the integration of singular units of PV, DSTATCOM, and EVCS yielded substantial improvements in system performance metrics. Notably, active and reactive power losses were significantly curtailed to 0.2143 MVA and 0.45891 MVA, respectively. The enhancement in voltage profiles was particularly remarkable, with the minimum voltage elevated to 0.9711 p.u., demonstrating the effectiveness of strategic component placement in maintaining voltage stability.

The intermediate configuration (Case-2) further exemplified the scalability of the proposed methodology through the integration of additional component sets. This enhanced configuration achieved more pronounced reductions in system losses, with active and reactive components diminishing to 0.1825 MVA and 0.38642 MVA, respectively. A notable improvement in the Voltage Stability Index (VSI) to 0.149 was observed, while maintaining the minimum voltage at 0.971 p.u., thereby ensuring robust voltage support across the network infrastructure.

The optimal configuration (Case-3), incorporating three units each of PVs, DSTATCOMs, and EVCSs, demonstrated superior performance metrics across all evaluation criteria. This configuration achieved unprecedented reductions in active and reactive power losses to 0.1492 MVA and 0.30991 MVA, respectively, while further enhancing the VSI to 0.1374. These results underscore the methodology's capability in managing complex power distribution systems while maintaining optimal performance parameters.

The comprehensive analysis of these results illuminates several critical insights regarding modern power distribution network optimization:

- 1- The strategic placement and sizing of grid components significantly influence system performance metrics
- 2- Progressive integration of multiple units demonstrates consistent improvements in system efficiency
- 3- The optimization framework exhibits robust scalability and adaptability across varying system configurations
- 4- Voltage stability and power loss reduction objectives can be simultaneously achieved through strategic component placement

These findings carry substantial implications for the evolution of smart grid infrastructures, particularly in contexts characterized by increasing renewable energy integration and growing electric vehicle adoption. The proposed methodology, leveraging advanced optimization techniques including the Runge-Kutta Algorithm, establishes a robust framework for addressing contemporary challenges in power distribution systems.

This research contributes significantly to the evolving body of knowledge in power distribution system optimization, providing both theoretical insights and practical methodologies for enhancing grid performance in the context of increasing renewable energy penetration and electrified transportation infrastructure.

ACKNOWLEDGMENT

This work was supported by the Scientific and Technological Research Council of Turkey (TÜBİTAK) under Grant No. 124E002 (1001-Project). The author gratefully acknowledges TÜBİTAK for their valuable support.

During the preparation of this work the author(s) used ChatGPT 4.0-mini in order to refine the English wording of certain phrases. After using this tool/service, the author reviewed and edited the content as needed and take(s) full responsibility for the content of the publication.

REFERENCES

- [1] M. Cikan and N. N. Cikan, "Optimum allocation of multiple type and number of DG units based on IEEE 123-bus unbalanced multi-phase power distribution system," *International Journal of Electrical Power & Energy Systems*, vol. 144, p. 108564, 2023, doi: <https://doi.org/10.1016/j.ijepes.2022.108564>.
- [2] N. Nacar Cikan and M. Cikan, "Reconfiguration of 123-bus unbalanced power distribution network analysis by considering minimization of current & voltage unbalanced indexes and power loss," *International Journal of Electrical Power & Energy Systems*, vol. 157, p. 109796, 2024, doi: <https://doi.org/10.1016/j.ijepes.2024.109796>.
- [3] M. Çıkan, "Çıta optimizasyon algoritması kullanarak kısmi gölgelenme altındaki fotovoltaik sistemlerde maksimum güç noktası izleyicisinin tasarlanması," *Gazi Üniversitesi Mühendislik Mimarlık Fakültesi Dergisi*, vol. 40, no. 1, pp. 555–572, 2024, doi: 10.17341/gazimmf.1183267.
- [4] M. Cikan and K. Dogansahin, "A Comprehensive Evaluation of Up-to-Date Optimization Algorithms on MPPT Application for Photovoltaic Systems," *Energy Sources, Part A: Recovery, Utilization, and Environmental Effects*, vol. 45, no. 4, pp. 10381–10407, Oct. 2023, doi: 10.1080/15567036.2023.2245771.
- [5] M. Çıkan and N. Nacar Çıkan, "Elektrikli Araç Şarj İstasyonlarının Enerji Dağıtım Hatlarına Optimum Şekilde Konumlandırılması" *Kahramanmaraş Sütçü İmam Üniversitesi Mühendislik Bilimleri Dergisi*, vol. 27, no. 2, pp. 340–363, 2024, doi: 10.17780/ksujes.1365209.
- [6] K. Aygül, M. Cikan, T. Demirdelen, and M. Tümay, "Butterfly optimization algorithm based maximum power point tracking of photovoltaic systems under partial shading condition," *Energy Sources, Part A: Recovery, Utilization,*

and Environmental Effects, pp. 1–19, Oct. 2019, doi: 10.1080/15567036.2019.1677818.

- [7] I. Ahmadianfar, A. A. Heidari, A. H. Gandomi, X. Chu, and H. Chen, “RUN beyond the metaphor: An efficient optimization algorithm based on Runge Kutta method,” *Expert Syst Appl*, vol. 181, p. 115079, 2021, doi: <https://doi.org/10.1016/j.eswa.2021.115079>.
- [8] M. Cikan and B. Kekezoglu, “Comparison of metaheuristic optimization techniques including Equilibrium optimizer algorithm in power distribution network reconfiguration,” *Alexandria Engineering Journal*, vol. 61, no. 2, pp. 991–1031, 2022, doi: <https://doi.org/10.1016/j.aej.2021.06.079>.
- [9] K. Doğanşahin and M. Çıkan, “A new line stability index for voltage stability analysis based on line loading,” vol. 1, no. 1, pp. 23–30, 2023, doi: 10.14744/cetj.2023.000.
- [10] J. R. S. Mantovani, F. Casari, and R. A. Romero, “Reconfiguração De Sistemas De Distribuição Radiais Utilizando O Critério De Queda De Tensão,” 2000.
- [11] F. Akın, M. Çıkan, O. Arıkan, and B. Kekezoğlu, “Optimizing Distribution Network Reconfiguration for Power Loss and Fault Current Management,” *Mühendislik Bilimleri ve Araştırmaları Dergisi*, vol. 6, no. 2, pp. 188–197, 2024, doi: 10.46387/bjesr.1501986.

Optimization of a 69-Bus Power Distribution System Using Reconfiguration and the Runge-Kutta Algorithm for Multi-Objective Power Loss and Voltage Deviation Minimization

NİSA NACAR ÇIKAN¹

¹ Cukurova University, Electrical and Electronics Engineering Department, Adana/Türkiye, ncikan@cu.edu.tr

Abstract - This paper presents the optimization of a 69-bus power distribution system utilizing a reconfiguration technique. Two key objective functions are considered: the minimization of active power loss and the reduction of voltage deviation index. The optimization process leverages the Runge-Kutta algorithm, applied as a state-of-the-art metaheuristic approach. Both single and multi-objective optimization scenarios are examined, allowing for a comprehensive evaluation of the system's performance. The results demonstrate significant improvements in both power loss and voltage deviation, highlighting the effectiveness of the proposed method for enhancing distribution system efficiency and stability.

Keywords - Reconfiguration, Power distribution network, Metaheuristic search algorithm, Power loss minimization.

I. INTRODUCTION

POWER distribution networks (PDN) connect load centers and generation centers through transmission lines. The goal of PDN is to deliver the generated energy to consumers at a specific voltage level while minimizing losses. This is achieved through reconfiguration by switching switches so that energy is delivered to consumers at a given voltage ratio and with minimum losses. The state of these switches is switched by normally closed sectionalized switches (SS) and normally open tie switches (TS) [1,2].

The reconfiguration study has been performed using different methods in the literature. For example, Baran and Wu [3] used the branch exchange method, while Ventagesh et al [4] used the evolutionary programming method. Subsequently, many researchers have tried to solve the reconfiguration problem in PDNs by developing different methods [1,2]. In this paper, a metaheuristic algorithm, Runge-Kutta algorithm, is used to solve the reconfiguration problem in a 69-bus PDN. The objective is to improve the voltage profile by minimizing the active power loss.

The paper is organized as follows: In Section II, technical details of the 69-bus test system are provided, and the problem formulation is presented. Section III explains the Runge-Kutta algorithm. Section IV presents the obtained results, and finally, the conclusion is given.

II. 69-BUS POWER DISTRIBUTION NETWORK

The 69-bus power distribution network is a commonly used test system that provides power transmission with 69 bus nodes as shown in Figure 1. IEEE 69-bus test system consists of 5 TSs, 68 SSs, 73 branches. Total substation load is 3802.2 kW and 2694.6 kVAR [1].

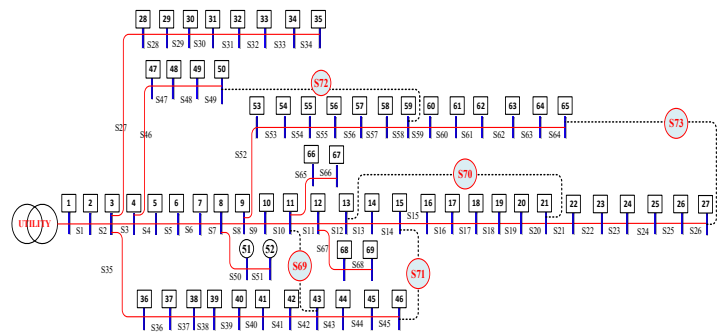


Figure 1. IEEE 69-bus test system [1]

A. Problem Formalization

The power loss minimization formula is presented in Equation 1 [1].

$$P_{\text{Loss}}^{\min} = \left(\sum_{i,k=1}^{N_{\text{br}}} r_{(i,k)} \cdot \left(\frac{P_k^2 + Q_k^2}{V_k^2} \right) \cdot Sw_{(i,k)} \right) \quad (1)$$

Voltage stability index calculation formula is given in Equation 2 [1].

$$VSI = \frac{4|V_i|^2|C||D||S_k| \cos(\varphi_k + \delta_s) \cdot \sin(\delta_i)}{|S_i|^2 \cdot \cos^2(\varphi_i + \delta_k)} \leq 1 \quad (2)$$

There are many different voltage stability index calculation methods in the literature. However, most of these calculations neglect various parameters or are based on assumptions. In this study, an index based on line loading and taking into account many characteristics of the line is used [5]. This index produced consistent results under all loading scenarios [5].

The current limit formula is shown in Equation 3 [1].

$$I_{i,\phi} \leq I_{i,\phi}^{\max} \quad \forall \phi \in \{a, b, c\}, \quad \forall i \in \text{Branches} \quad (3)$$

The voltage fluctuation formula is given in Equation 4 [1].

$$V_{i,\phi}^{\min} \leq V_{i,\phi} \leq V_{i,\phi}^{\max}, \quad \forall \phi \in \{a, b, c\}, \quad \forall i \in \text{Buses} \quad (4)$$

The calculation of the power in the system is presented in Equation 5 [1].

$$\sum_{i=1}^{N_{\text{Gen}}} P_{i,\text{Gen}}^{\phi} = \sum_{i=1}^{N_{\text{Load}}} P_{i,\text{Load}}^{\phi} + \sum_{i=1}^{N_{\text{Branch}}} P_{i,\text{Loss}}^{\phi} + \sum P_{i,\text{Loss}}^{\text{equipment}}, \quad \forall \phi \in \{a, b, c\} \quad (5)$$

The formula for transformer is shown in Equation 6 [1].

$$X_{i,\theta}^{\text{trfmin}} \leq X_{i,\theta,\text{trf}} \leq X_{i,\theta}^{\text{trfmax}} \quad \forall \phi \in \{a, b, c\} \quad (6)$$

The total power formula is given in Equation 7 [1].

$$S_{i,\theta,\text{line}} \leq S_{i,\theta,\text{line}}^{\max}, \quad \forall \phi \in \{a, b, c\}, \quad \forall i \in \text{Lines} \quad (7)$$

III. RUNGA-KUTTA ALGORITHM

The Runge-Kutta method is a widely used method, especially for numerical solutions of differential equations [6]. This method estimates the solution of the equation step by step, calculating the slope of the curve at each step from several different points. The most widely used fourth order Runge-Kutta method (RK4) provides high accuracy by taking slope values at four different points at each step and combining them with specific weights. One of the major advantages of the Runge-Kutta method is that it uses only function values while providing high accuracy; therefore, it does not require more complex higher-order derivative calculations [6]. Thus, in this study, the RK method was preferred to achieve precise results in solving the reconfiguration problem in the 69-bus PDN.

IV. RESULTS AND DISCUSSIONS

The power flow results before and after reconfiguration is shown in Figure 2. Before reconfiguration, the active power loss is 224.9 kW and the reactive power loss is 102.2 kVAR, respectively. After the optimization and reconfiguration process, the active power loss is reduced to 98.5 kW and the reactive power loss is decreased to 92 kVAR. This resulted in a significant improvement in the power loss in the PDN.

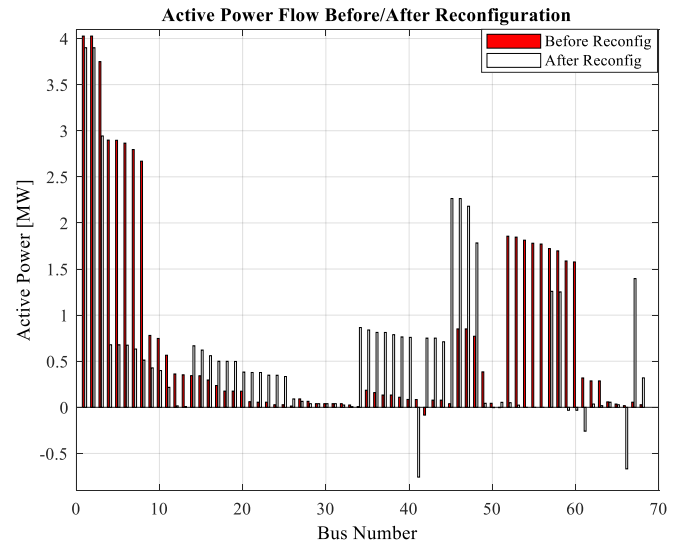


Figure 2. Active power results before/after reconfiguration

Figure 3 shows the bus voltage values before and after the optimization process. The reconfiguration process was performed using the Runge Kutta Algorithm.

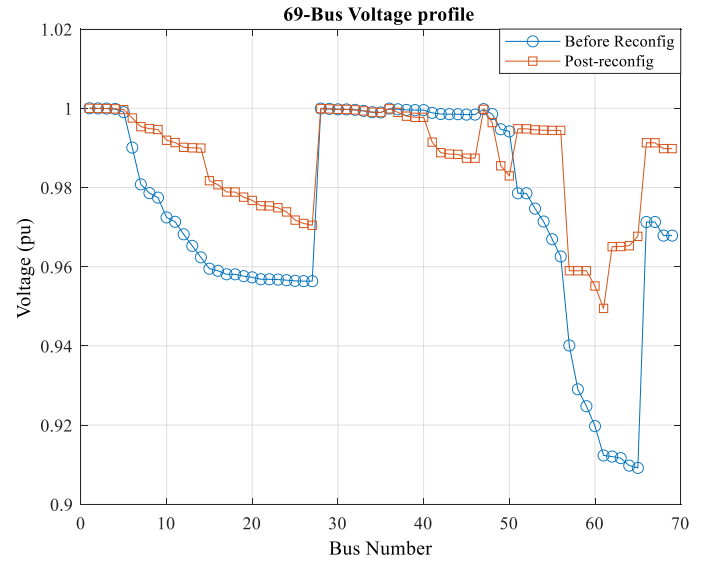


Figure 3. Voltage profile before and after reconfiguration

By analyzing Figure 3, it becomes clear that voltage levels have improved across all buses, except for buses between 40 and 49. Notably, the voltage has risen from 0.91 p.u. to 0.95 p.u., showing a positive impact on the network's overall voltage stability, with the majority of buses experiencing benefits from the optimization process.

V. CONCLUSION

In conclusion, this study emphasizes the effectiveness of the Runge Kutta Algorithm in optimizing a 69-bus Power Distribution Network, with a focus on two main goals: improving the VSI and reducing active power loss. The results reveal significant improvements in the system's performance

through network reconfiguration, highlighting the benefits of optimized network topologies in power systems. The Pareto front produced by the multi-objective optimization clearly illustrates the trade-off between minimizing power loss and boosting voltage stability, making it an essential tool for decision-making by system operators.

REFERENCES

- [1] M. Çıkan and B. Kekezoglu, "Comparison of metaheuristic optimization techniques including Equilibrium optimizer algorithm in power distribution network reconfiguration," *Alexandria Engineering Journal.*, vol.61, pp.991-1031, 2022.
- [2] N. Nacar Çıkan and M. Çıkan, "Reconfiguration of 123-bus unbalanced power distribution network analysis by considering minimization of current & voltage unbalanced indexes and power loss," *International Journal of Electrical Power & Energy Systems*, vol.157, pp.109796, 2024.
- [3] M. E. Baran and F. Wu, "Network reconfiguration in distribution system for loss reduction and load balancing," *IEEE Trans. Power Del.*, vol.4, pp. 1401–1407, 1989.
- [4] B. Venkatesh and R. Rajan, "Optimal radial distribution system reconfiguration using the fuzzy adoption of evolutionary programming," *Energy power and Energy systems*, vol. 25 pp.775-780, 2003.
- [5] M. Çıkan and K. Dogansahin, "A Comprehensive Evaluation of Up-to-Date Optimization Algorithms on MPPT Application for Photovoltaic Systems," *Energy Sources, Part A: Recovery, Utilization, and Environmental Effects*, vol. 45, pp.10381-10407, 2023.
- [6] I. Ahmadianfar, AA. Heidari, AH. Gandomi, X. Chu, and H. Chen, "An efficient optimization algorithm based on Runge Kutta method. *Expert Syst Appl*, vol. 181, pp. 115079, 2021.
- [7] H. Poor, *An Introduction to Signal Detection and Estimation*. New York: Springer-Verlag, 1985.

Simultaneous Wind Turbine and EV Charging Station Allocation in a 33-Bus System Using the Slime Mould Algorithm for Power Loss Minimization and Voltage Profile Improvement

NİSA NACAR ÇIKAN¹

¹ Cukurova University, Electrical and Electronics Engineering Department, Adana/Türkiye, ncikan@cu.edu.tr

Abstract - This study presents an advanced optimization approach for the simultaneous allocation and sizing of wind turbines and electric vehicle (EV) charging stations in a 33-bus distribution system. The primary objective is to minimize active power losses while improving the voltage profile, ensuring optimal integration of renewable energy sources and EV infrastructure. To solve this complex multi-objective problem, the Slime Mould Algorithm (SMA), a state-of-the-art metaheuristic, is employed due to its robust performance in distributed generation (DG) allocation. The proposed method demonstrates superior results in enhancing system efficiency and voltage stability, offering a promising solution for sustainable energy integration into modern power grids.

Keywords - DG allocation, Power distribution network, Electrical vehicle charge stations, Optimization.

I. INTRODUCTION

THE integration of renewable energy sources and electric vehicle (EV) infrastructure in modern power systems is crucial for meeting rising energy demands while promoting environmental sustainability. However, adding these resources to distribution systems requires complex planning; the correct placement and sizing of distributed generation (DG) resources are essential factors directly influencing system performance [1-5]. Improper allocation can lead to unwanted power losses in distribution networks, whereas optimal DG placement minimizes active power losses and strengthens voltage stability. Thus, the simultaneous allocation of wind turbines and EV charging stations presents a complex optimization problem that plays a key role in achieving sustainability objectives.

This study aims to minimize active power losses and improve the voltage profile in an IEEE 33-bus distribution system by optimally placing and sizing wind turbines and EV charging stations. To address this challenge, the Slime Mould Algorithm (SMA) [6], an advanced metaheuristic method, is employed. SMA is chosen for its robust ability to explore large solution spaces effectively, providing superior performance in DG allocation. The algorithm offers significant advantages in improving the voltage stability and reducing power losses, thus supporting the efficiency and reliability of distribution systems.

The rest of this paper is structured as follows: Section 2 presents the 33-bus distribution system model and outlines the constraints considered in this study. Section 3 provides a detailed overview of the Slime Mould Algorithm (SMA) and its application to this optimization problem. Section 4 presents the simulation results and analyzes their implications for system performance. Section 5 wraps up the paper by summarizing the findings and their potential impact on future power distribution systems.

II. 33-BUS POWER DISTRIBUTION NETWORK

The IEEE 33-bus distribution system functions as a critical benchmark for analyzing the performance of power distribution networks. It consists of 33 buses, 37 branches, one feeder, five tie switches (T.S.), and 32 sectionalizing switches (S.S.), making it a typical configuration for simulating real-world distribution systems. The total active power demand of the system is 3.72 MW, while the reactive power demand stands at 2.3 MVAR. Under this configuration, the network experiences active power losses of 202.6771 kW and reactive power losses of 135.14 kW. The Figure 1 shows the 33-bus PDN.

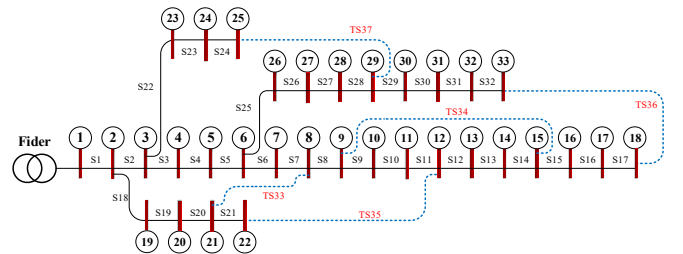


Figure 1: 33-bus power distribution network [1].

III. PROBLEM FORMULAZATION

The purpose of this study is to enhance power loss and to enhance the voltage stability index after DG allocation in a 33-bus PDN. Thus, the power loss calculation formula is given in Equation 1 [1].

$$P_{\text{Loss}}^{\min} = \left(\sum_{i,k=1}^{N_{br}} r_{(i,k)} \cdot \left(\frac{P_k^2 + Q_k^2}{V_k^2} \right) \cdot Sw_{(i,k)} \right) \quad (1)$$

Voltage stability index calculation formula is provided in

Equation 2 [1].

$$VSI = \frac{4|V_i|^2|C||D||S_k|\cos(\varphi_k+\delta_S)\sin(\delta_i)}{|S_i|^2\cos^2(\varphi_i+\delta_k)} \leq 1 \quad (2)$$

Other constraints, such as voltage limits, current limits, transformer operator limits, etc., can be found in detail in references [1] and [2].

IV. SLIME MOULD ALGORITHM

The Slime Mould Algorithm (SMA), proposed by Li et al. in 2020 [6], is a recent swarm intelligence algorithm that has garnered significant attention from the research community. It draws inspiration from the food-capturing behavior of pharyngodon polycephalum, a species of slime mould. This organism expands in a fan-shaped pattern, covering multiple points to search for food, and forms a venous network to connect these points. The venous network demonstrates a unique ability to contract, guided by rhythmic feedback from individual slime bacteria. This mechanism allows it to dynamically modify its spread and enhance the efficiency of the network. Slime moulds tend to concentrate in areas with higher food densities, which is why the algorithm simulates this behavior. In the mathematical model, the optimization problem's decision space reflects the environment in which the slime moulds survive. The objective function assesses the food concentration at different points within this environment, with the globally optimal solution representing the location of the highest food concentration. SMA is a swarm intelligence approach where each solution candidate corresponds to an individual slime mold. These molds interact through a feedback system, both positive and negative, forming a venous network that supports cooperation and competition among them. Through repeated iterations, the population continuously seeks the optimal food source within its environment, and this search process is mapped to the optimization problem as the algorithm pursues the best solution.

In this study, SMA was chosen for its high performance in complex optimization problems such as DG allocation, due to its ability to effectively explore the solution space and provide optimal results.

V. RESULTS AND DISCUSSION

Table 1 shows the different cases that are applied in this work.

Table 1.

Case	DG Type	Location (Bus No)	Size of DG/ EV (kW)	Power Factor
Initial	w/o PV	---	---	---
Case 1	1 st WT	6	3510.797	0.867238
	1 st EV	6	500	1.00
Case 2	1 st WT	13	1400.383	0.959451
	1 st EV	2	500	1.00

Case 3	2 nd WT	30	1530.990	0.750952
	2 nd EV	13	500	1.00
	1 st WT	30	1849.176	0.836318
	1 st EV	30	500	1.00
	2 nd WT	24	1229.8028	0.906893
	2 nd EV	2	500	1.00
	3 rd WT	13	866.3456	0.906739
	3 rd EV	2	500	1.00

Table 2.

Case	P_{Loss}^{Active} (kW)	Q_{Loss}^{Active} (kVar)	Minimum Voltage (p.u.)	Bus No at V_{min}	Loss Reduction (%)
Initial	202.68	135.14	0.9131∠ − 0.50°	18	0.00
Case 1	61.363	48.365	0.967∠ − 0.52°	18	69.724 % 64.211 %
Case 2	29.762	21.028	0.980∠ − 0.17°	25	85.315 % 84.439 %
Case 3	13.192	10.542	0.992∠ − 0.21°	8	93.491% 92.199 %

According to the data in the table, the strategic placement of distributed generation (DG) and electric vehicle (EV) charging stations significantly reduces power losses in the power system and improves voltage stability. In the initial scenario (Initial), there is no DG or EV connection in the system. In this case, the active power loss is 202.68 kW, reactive power loss is 135.14 kVar, voltage stability index is 37.9e-3, and the minimum voltage is 0.9131 p.u. This scenario serves as a reference for comparison with other cases.

In Case 1, a wind turbine and an EV charging station are added to the system. A wind turbine with a power rating of 3510.797 kW and a power factor of 0.867238, along with a 500 kW EV charging station with a power factor of 1.00, are connected to bus 6. Consequently, the active power loss drops to 61.363 kW, and the reactive power loss reduces to 48.365 kVar. This configuration provides a 69.724% reduction in active power losses and a 64.211% reduction in reactive power losses. Furthermore, the minimum voltage level rises to 0.967 p.u.

In Case 2, two wind turbines and one EV charging station are added. A 1400.383 kW wind turbine with a power factor of 0.959451 is linked to bus 13, a 500 kW EV charging station with a power factor of 1.00 is linked to bus 2, and another 1530.990 kW wind turbine with a power factor of 0.750952 is added to bus 30. This setup decreases the active power loss to 29.762 kW and the reactive power loss to 21.028 kVar. In this case, there is an 85.315% reduction in active power losses and an 84.439% reduction in reactive power losses. The minimum voltage level also increases to 0.980 p.u., indicating improved voltage stability in the system.

Finally, in Case 3, three wind turbines and three EV charging stations are integrated into the system. A 1849.176 kW wind turbine with a power factor of 0.836318 and a 500 kW EV

charging station with a power factor of 1.00 are linked to bus 30; a 1229.8028 kW wind turbine with a power factor of 0.906893 is linked to bus 24; an 866.3456 kW wind turbine with a power factor of 0.906739 is linked to bus 13; and two EV charging stations, each with a power rating of 500 kW and a power factor of 1.00, are linked to bus 2. With this configuration, the active power loss decreases to 13.192 kW, and the reactive power loss drops to 10.542 kVar. The active power losses are reduced by 93.491%, while the reactive power losses decrease by 92.199%. The minimum voltage level is recorded at 0.992 p.u., showing a substantial improvement in system voltage stability.

Overall, the results in the table indicate that the placement of DG and EV units significantly reduces system losses and enhances voltage stability. Strategically positioning DG and EV sources is an effective method for minimizing losses and ensuring voltage stability in power systems.

VI. CONCLUSION

This study proposed a comprehensive optimization approach for the simultaneous allocation and sizing of wind turbines and electric vehicle (EV) charging stations in a 33-bus distribution system. Employing the Slime Mould Algorithm (SMA), a cutting-edge metaheuristic, the research successfully addressed the complex multi-objective challenge of reducing active power losses while enhancing voltage stability. The results demonstrate that strategic placement and sizing of distributed generation (DG) resources, specifically wind turbines and EV charging stations, significantly improve the efficiency and stability of the distribution network.

The findings reveal that optimal DG and EV integration leads to considerable reductions in power losses and improvements in the voltage profile, confirming the effectiveness of SMA in handling complex DG allocation problems. The scenarios examined in this study show substantial improvements in system performance, with notable reductions in active and reactive power losses and enhancements in minimum voltage levels across various cases. These results highlight the potential of SMA as a powerful tool for achieving sustainable energy integration in modern power grids, paving the way for more resilient and efficient distribution systems.

The methodology and outcomes of this research provide valuable insights for the optimal planning of renewable energy and EV infrastructure in power systems. By demonstrating the advantages of SMA in a real-world distribution network model, this study establishes a promising framework for future studies and real-world applications focused on improving sustainability and reliability of power distribution networks.

ACKNOWLEDGMENT

This work was supported by the Scientific and Technological

Research Council of Turkey (TÜBİTAK) under Grant No. 124E002 (1001-Project). The author gratefully acknowledges TÜBİTAK for their valuable support.

REFERENCES

- [1] M. Çıkan and B. Kekezoglu, "Comparison of metaheuristic optimization techniques including Equilibrium optimizer algorithm in power distribution network reconfiguration," *Alexandria Engineering Journal*, vol.61, pp.991-1031.
- [2] M. Çıkan and N. Nacar Çıkan, "Optimum allocation of multiple type and number of DG units based on IEEE 123-bus unbalanced multi-phase power distribution system," *International Journal of Electrical Power & Energy Systems*, vol.144, pp.108564.
- [3] M. Çıkan and K. Dogansahin, "A Comprehensive Evaluation of Up-to-Date Optimization Algorithms on MPPT Application for Photovoltaic Systems," *Energy Sources, Part A: Recovery, Utilization, and Environmental Effects*, vol. 45, pp.10381-10407.
- [4] M. Çıkan, "Çıta optimizasyon algoritması kullanarak kısmi gölgelenme altındaki fotovoltaik sistemlerde maksimum güç noktası izleyicisinin tasarlanması," *Gazi Üniversitesi Mühendislik Mimarlık Fakültesi Dergisi*, vol.40, pp.555-572.
- [5] M. Çıkan and N. Nacar Çıkan, "Elektrikli araç şarj istasyonlarının enerji dağıtım hatlarına optimum şekilde konumlandırılması," *Kahramanmaraş Sütçü İmam Üniversitesi Mühendislik Bilimleri Dergisi*, vol.27, pp.340-363, Jun. 2024.
- [6] S. Li, H. Chen, M. Wang, A.A. Heidari, and S. Mirjalili, "Slime mould algorithm: A new method for stochastic optimization," *Future Generation Computer Systems*, vol.111, pp.300-323.

Thermal Buckling Risk in Railways: An ANSYS-Based Analysis for Türkiye

FERHAT ÇEÇEN¹, MEHMET SALTAN²

¹ Süleyman Demirel University, Isparta/Türkiye, cecenferhat@sdu.edu.tr

² Süleyman Demirel University, Isparta/Türkiye, mehmetsaltan@sdu.edu.tr

Abstract - The impact of climate change on transportation systems is becoming increasingly significant, with railways being particularly susceptible. In this context, rail thermal buckling (RTB) is a critical issue that can lead to track deformation, heightening the risk of train derailments and accidents. High-speed railway systems are especially vulnerable due to their strict geometric tolerances. As global temperatures rise, RTB incidents are expected to become more frequent, necessitating engineering solutions to mitigate these risks. Despite its importance, academic studies on RTB remain limited, particularly regarding regional variations. This study employs ANSYS finite element modeling to assess the technical factors contributing to RTB across various regions of Türkiye. By calculating the difference between Stress-Free Temperature (SFT) and predicted maximum rail temperatures, the study identifies the cities with the highest risks. A 36-meter rail model was developed, and rail stress and buckling risk factors were analyzed using ANSYS static structural, steady-state thermal, and eigenvalue buckling modules. Results show a clear correlation between SFT and maximum rail temperature differences and RTB risk. Cities like Sivas, where this difference exceeds 42°C, are at the highest risk. In contrast, cities with higher rail temperatures but smaller differences between SFT and predicted minimum rail temperatures, such as İzmir, exhibit lower RTB potential.

Keywords - Railway, Sun Kink, Climate Change, Finite Element Analysis, Eigenvalue Thermal Buckling.

I. INTRODUCTION

CLIMATE change is adversely affecting railways, just as it impacts other modes of transportation. In this context, rail temperature plays a critical role in railway safety, and one of the major issues associated with it is Rail Thermal Buckling (RTB), also known as "sun kink" in the U.S. [1-3].

RTB incidents, generally defined as 'the warping of rails under thermal stress,' have historically been observed mainly in desert or extreme continental climates. However, with the impact of *global warming* and *climate change*, reports of these incidents have increased in a wider geographical area [2, 3]. Recent statistics show that rail buckling incidents have risen in proportion to global warming over the years [4-8]. In the U.S. alone, more than 2,100 rail buckling events have been recorded in the past 40 years [8]. The risk is expected to grow, with predictions indicating that these incidents will double every 30 years based on meteorological data [9]. This problem is especially dangerous for high-speed railway systems, where strict geometric tolerances are mandatory.



Figure 1: RTB-related accident in Pazarcık, Kahramanmaraş [10].

Another significant factor contributing to the rise in RTB incidents is the use of continuously welded rails (CWR) and long welded rails (LWR) in modern railway systems [3, 11]. Previously, bolted rail joints, which allowed rails to expand and contract with temperature changes, were commonly used. In contrast, modern rail systems utilize CWR and LWR, which offer benefits like high speeds, low maintenance, and improved comfort [11]. However, when rail temperature exceeds the Stress-Free Temperature (SFT) and reaches the Critical Rail Temperature (CRT), RTB incidents may occur, potentially leading to derailments if safety measures like speed restrictions are not implemented in time [2, 3]. Additionally, improper SFT calibration and inadequate rail stress management during construction or maintenance can result in excessive compressive forces causing buckling in hot weather or tensile forces leading to rail breaks in cold conditions [3].

In essence, RTB incidents lead to increased maintenance needs, higher costs, derailments, and severe accidents.

Furthermore, this challenge is anticipated to intensify in the future as climate change continues to amplify its effects. The rise in these incidents has prompted engineers to seek solutions for mitigating RTB risks. However, despite the urgency of this issue, research on the topic remains limited, particularly regarding regional variations. This study calculates SFT values for various cities in Türkiye and compares RTB risks using finite element analysis. The aim of this research is to raise awareness and provide guidance for industry professionals facing this issue, as well as for potential researchers seeking effective solutions.

II. METHOD

In this study, ANSYS finite element analyses were used to investigate the technical background of RTB. The analysis utilized the highest and lowest air temperatures recorded in various Turkish cities over the past 50 years (Table 1), along with the estimated maximum and minimum rail temperatures and SFT values from [11]. We also calculated the difference between the maximum rail temperature and the SFT, which is added to the last column of Table 1. The following sections will present finite element analyses and interpretations based on the significance of this difference.

Table 1: Thermal parameters in various cities in Türkiye (°C) [11].

City	Max. air temp.	Min. air / rail temp.	Max. rail temp.	SFT	Difference
Samsun	38.3	-8.1	57.5	29.7	27.8
İzmir	42.7	-6.4	64.1	33.8	30.2
İstanbul	40.5	-13.9	60.8	28.4	32.3
K.Maraş	44.3	-9.6	66.5	33.4	33.0
Adana	45.6	-8.1	68.4	35.2	33.3
Eskişehir	40.6	-23.8	60.9	23.6	37.4
Ankara	40.8	-24.4	61.2	23.4	37.8
Konya	40.6	-26.5	60.9	22.2	38.7
Erzurum	35.6	-37.0	53.4	13.2	40.2
Sivas	40.0	-34.6	60.0	17.7	42.3

As shown in Fig. 1, a finite element model (FEM) was developed for a railway line with two parallel 36-meter rails and 60 sleepers. The rails have elasticity modulus of 200 GPa, a Poisson's ratio of 0.3, and a density of 7.85 kg/mm³, while the sleepers have elasticity modulus of 37 GPa, a Poisson's ratio of 0.18, and a density of 2.4 kg/mm³, respectively. The thermal expansion coefficient for both is $1.2 \times 10^{-5} \text{ } ^\circ\text{C}^{-1}$. The 36-meter

length was chosen to reduce computational time. As these parameters will remain constant in subsequent analyses, they are sufficient for reasonably comparable results.

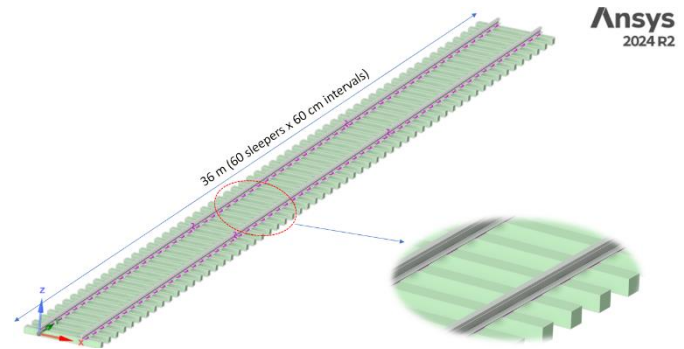


Figure 1: Prepared FEM for a 36-meter rail superstructure.

Subsequently, as shown in Fig. 2, ballast modeling was conducted in the ANSYS Static Structural Module, utilizing elastic supports of 0.15 N/mm³ for the bottom surfaces and 0.015 N/mm³ for the lateral surfaces of sleepers [12]. Finally, both ends of the 36-meter rails were modeled as fixed supports to restrict thermal expansion, simulating rail weld joints.

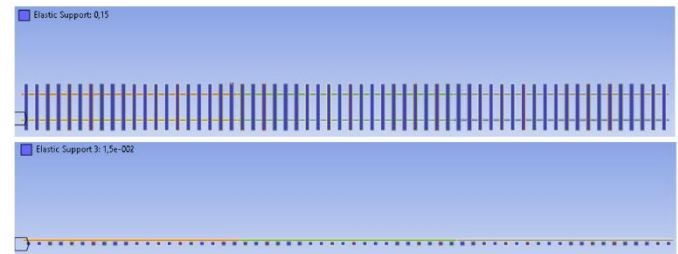


Figure 2: Ballast modeling.

The project schematic of the prepared ANSYS model is shown in Fig. 3. As seen, thermal modeling of the track was conducted at the SFT values from Table 1 using the Steady-State Thermal module (Fig. 3, Column A). Next, boundary conditions were modeled with the Static Structural module (Fig. 3, Column B). After confirming that the stress in the rails at the SFT is approximately zero, temperatures above the SFT were modeled again using the Steady-State Thermal module (Fig. 3, Column C). Rail thermal stress values were then determined with the Static Structural module (Fig. 3, Column D). Finally, the RTB risk factor was calculated using the Eigenvalue Buckling module (Fig. 3, Column E).

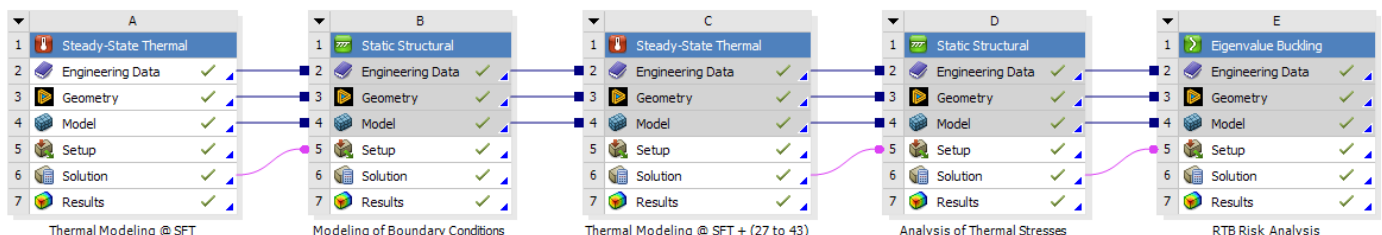


Figure 3: Project schematic of the ANSYS finite element model.

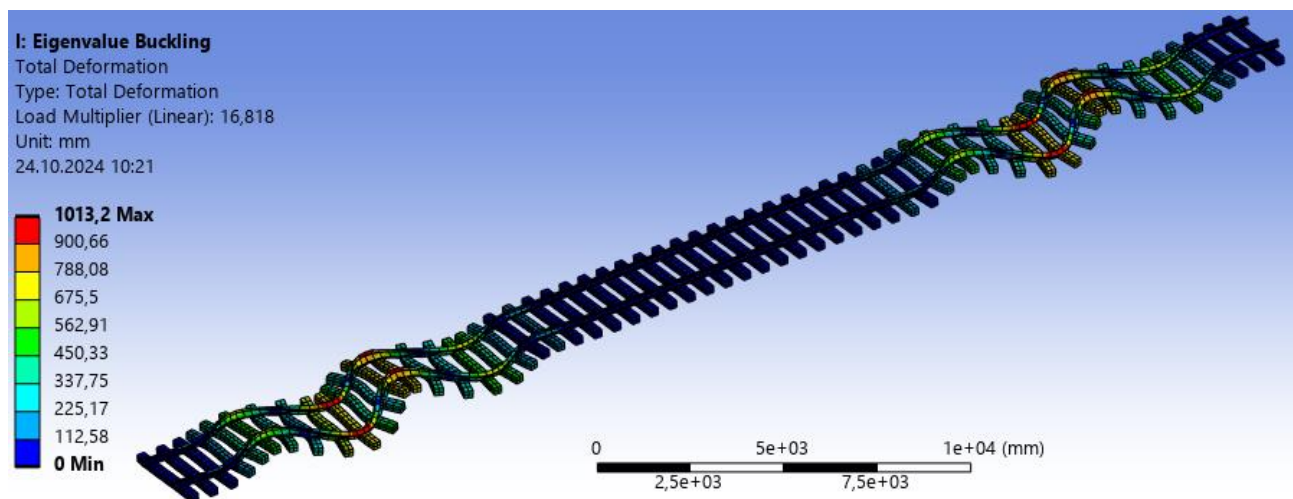


Figure 4: The first buckling mode shape of the railway in Sivas at the expected maximum temperature (60 °C).

III. RESULTS

Using the finite element method (FEM) detailed in the previous section, analyses have been conducted based on the potential maximum rail temperatures in the cities listed in Table 1, and RTB risks have been compared. In Sivas, which has the highest 'difference' value among the cities in Table 1, the Eigenvalue Buckling analysis for the expected maximum rail temperature of 60 °C has revealed the first buckling mode shape shown in Fig. 4. These analyses have been performed for all cities in Table 1, and the aggregated results related to stresses in the rails and RTB risk factors are illustrated in Fig. 5. In this study, the parameter referred to as the RTB factor corresponds to the Linear Load Multiplier in ANSYS, indicating that as this value decreases, the risk of buckling increases. Indeed, a review of the graphs in Fig. 5 shows that as the RTB factor decreases, the equivalent stress in the rails increases inversely.

IV. CONCLUSION

Rail Thermal Buckling (RTB) incidents are becoming increasingly prevalent as climate change continues to amplify its effects. This study employs ANSYS finite element analyses to calculate RTB risk factors and rail thermal stress values

across various Turkish cities. The main conclusions of this study are as follows:

- The analysis of maximum rail temperatures and Stress-Free Temperature (SFT) values reveals that as the difference between these two values increases, the RTB risk also rises (indicated by a decrease in ANSYS linear load multiplier values).
- There is a correlation between RTB risk and equivalent stresses in the rails. Thus, an increase in the difference between maximum rail temperatures and SFT values results in a higher RTB risk.
- Reducing the difference between SFT and maximum rail temperatures will decrease thermal stresses in the rails and mitigate the risk of RTB. A newly emerging solution to reduce this risk is painting the rails white.
- Cities like Sivas, Erzurum, Konya, Ankara, and Eskişehir have more pronounced continental climates, leading to lower minimum rail temperatures and lower SFT values, which increase the risk of Rail Thermal Buckling (RTB) compared to cities like Adana, Kahramanmaraş, and İzmir, where rail temperatures are higher but show smaller maximum-minimum differences.

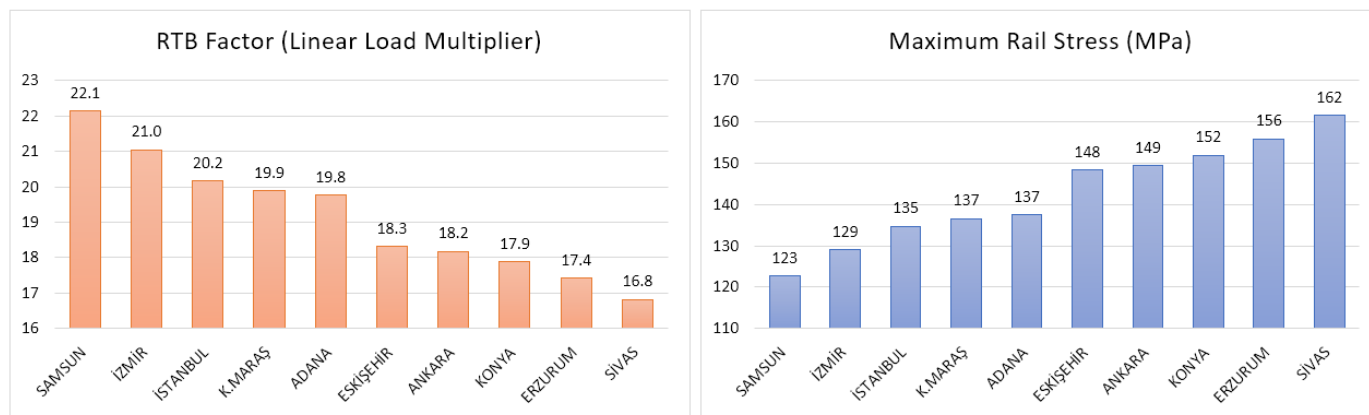


Figure 5: RTB Factor and Maximum Rail Stress values determined by ANSYS analyses for the 10 cities listed in Table 1.

- In coastal cities like Samsun, İzmir, and İstanbul, which have relatively milder climates compared to inland regions of Türkiye, the difference between the SFT temperature and the maximum and minimum rail

temperatures is smaller, leading to a lower risk of RTB.

It is important to note that all of the above-mentioned assessments apply only to an ideal and uniform railway infrastructure. Several other factors, such as ballast contamination, weakened shoulder support, weld joint damages, the use of lighter sleepers like wooden ones, and various ballastless track models, are excluded from the scope of our research, representing a limitation of the investigation. In the future, the authors plan to analyze RTB risk across all cities in Türkiye and develop a customized solution for determining SFT.

REFERENCES

- [1] N T. C. Milli Eğitim Bakanlığı, Ankara, Türkiye. Raylı Sistemler Teknolojisi: Demiryolu İnşaatı. (2011). Accessed: 10.01.2024. [Online]. Available: https://megep.meb.gov.tr/mte_program_modul/moduller_pdf/Demir%20Yolu%20%C4%B0n%C5%9Faat%C4%B1.pdf
- [2] E. Ferranti, L. Chapman, C. Lowe, S. McCulloch, D. Jaroszowski, A. Quinn, "Heat-related failures on southeast England's railway network: Insights and implications for heat risk management," *Wea. Climate Soc.*, vol. 8, pp. 177–191, 2016, doi: <https://doi.org/10.1175/WCAS-D-15-0068.1>
- [3] F. Çeçen, B. Aktaş, "Ray Sıcaklığı Takip Sistemleri (RSTS) İçin En Uygun Yerlerin Belirlenmesinde Termal Kameralardan Yararlanılması: Hızlı Analiz Metotları Geliştirilmesi," *Demiryolu Mühendisliği*, vol. 20, pp. 141-154, 2024, doi: <https://doi.org/10.47072/demiryolu.1474099>
- [4] PEBS News Hour, "Heat Wave Causes Kinks in Rail Tracks," 2010. [Online]. Available: <https://www.pbs.org/newshour/world/heat-wave-causes-kinks-in-rail-tracks>
- [5] K. Dobney, "Quantifying the effects of an increasingly warmer climate with a view to improving the resilience of Great Britain's railway network: Is a new stressing regime the answer?," PhD Thesis, University of Birmingham, Department of Engineering, School of Civil Engineering, 2010
- [6] Transportation Safety Board of Canada, "Railway Investigation Report R02M0050," 2002. [Online]. Available: <https://www.bst.gc.ca/eng/rapports-reports/rail/2002/r02m0050/r02m0050.html>
- [7] I. V. Sanchis, R. I. Franco, P. M. Fernandez, P. S. Zuriaga, J. B. F. Torres, "Risk of increasing temperature due to climate change on highspeed rail network in Spain," *Transportation Research Part D*, vol. 82, ID: 102312, 2020, doi: <https://doi.org/10.1016/j.trd.2020.102312>
- [8] Climate Central, "Derailments May Increase as 'Sun Kinks' Buckle Tracks," 2014. [Online]. Available: <https://www.climatecentral.org/news/climate-change-warp-railroad-tracks-sun-kinks-17470>
- [9] K. Dobney, C. J. Baker, L. Chapman, A. D. Quinn, "The future cost to the United Kingdom's railway network of heat-related delays and buckles caused by the predicted increase in high summer temperatures owing to climate change," *Journal of Rail and Rapid Transit*, vol. 224 (1), pp. 25-34, 2009, doi: <https://doi.org/10.1243/09544097JRRT292>
- [10] CNN Türk, "Sıcaktan tren rayları bile genleşti!," 2010. [Online]. Available: <https://www.cnntrk.com/turkiye/sicaktan-tren-raylari-bile-genlesti-11-12-2018?page=1>
- [11] T. C. Milli Eğitim Bakanlığı, Ankara, Türkiye. Raylı Sistemler Teknolojisi: UKR (Uzun Kaynaklı Ray). (2013). Accessed: 10.01.2024. [Online]. Available: [https://www.megep.meb.gov.tr/mte_program_modul/moduller_pdf/UKR%20\(Uzun%20Kaynaklı%C4%B1%20Ray\).pdf](https://www.megep.meb.gov.tr/mte_program_modul/moduller_pdf/UKR%20(Uzun%20Kaynaklı%C4%B1%20Ray).pdf)
- [12] F. Çeçen, "6 Şubat 2023 Kahramanmaraş Depremlerinin Demiryolu Üst yapısına Etkilerinin Saha Gözlemleri ve Sonlu Eleman Analizleriyle İncelenmesi," *Demiryolu Mühendisliği*, vol. 18, pp. 59-72, 2023, doi: <https://doi.org/10.47072/demiryolu.1294730>

Numerical Investigation of the Effect of Steel Braces on Multi-Story Reinforced Concrete Frame Behavior

HURMET KUCUKGONCU¹

¹ Abdullah Gül University, Civil Engineering Department, Kayseri/Turkey, hurmet.kucukgoncu@agu.edu.tr

Abstract - Nowadays, the architecture of cities develops vertically instead of horizontally due to increasing population and urbanization. Especially in cities defined as metropolises, the number of multi-story buildings increases day by day. However, the design of multi-story buildings is quite important under unpredictable loads such as earthquakes. For this reason, steel braces are used to increase the existing strength and rigidity of structures built in earthquake zones. Steel braces allow the structure to carry more load and displace less under horizontal loads. Thus, they increase the strength and rigidity of structures. In this study, reinforced concrete frames were modeled by SAP 2000 finite element software, and then concentric steel braces were added to these structures. As a result of the analysis, the period, frequency, top displacement, base shear force and story drift values of the structures were obtained. Thus, the structural behavior of the frames designed and analyzed under vertical load and earthquake effects was compared.

Keywords - Reinforced concrete structure, earthquake, concentric steel brace, numerical analysis, structural behavior

I. INTRODUCTION

INCREASES in population and urbanization lead to the emergence of a rapidly growing irregular and uncontrolled building stock. Many of these structures develop in the form of vertical architecture, rather than horizontal architecture, due to factors such as increasing needs, the unavailability of suitable lands and soils, high costs, etc. In particular, medium and high-rise structures constitute the majority of this building stock. The behavior of these structures against earthquakes is even more important since our country is located in an earthquake zone. In order to prevent possible loss of life and property after an earthquake, structures must be designed with enough strength, stiffness, and energy consumption capacity. Therefore, steel braces are used for strengthening purposes to both improve the structural behavior of newly constructed structures and to improve the earthquake performance of structures in the existing building stock. Steel braces are used to increase the strength and stiffness of structures against horizontal loads and are classified as concentric and eccentric steel braces. In bearing systems where steel braces are used, horizontal loads are resisted by diagonal members. For this reason, diagonal members are exposed to high axial forces and limit the lateral displacement of the structure. In concentric braced systems, the braces are connected to the connection points of the main frame

in a way that does not create eccentricity. These systems have high horizontal stiffness and carry horizontal loads such as earthquakes and wind [1].

There are some studies in the literature on concentric steel braces. Öztürk et al. used steel braces to strengthen reinforced concrete structures constructed in different soil classes. As a result of the study, the performance analysis of steel braced structures was performed by comparing the base shear force, peak displacement, story displacements, and interstory drift curves of the bearing systems [2]. Özkaynak et al. conducted a study on strengthening a reinforced concrete structure with specially designed steel braces as metal dampers. Nonlinear dynamic analyses of both the existing structure and the reinforced structure with steel braces were performed in the study. As a result, it is shown that steel braces limit the interstory drift and shear force demands of structures and improve their seismic performance [3]. A study was conducted on the structural performance and damage detection of a reinforced concrete frame strengthened with lateral-buckling restrained steel braces at different stages [4]. In addition, Karalis et al. conducted an experimental and numerical study on a single-story and single-span reinforced concrete reference frame and a steel braced frame and investigated the strengthening of the existing structure with steel braces. They demonstrated both experimentally and numerically that steel braces increase the strength, stiffness and energy consumption capacity of the frame system at the end of the study [5]. On the other hand, steel braces are used not only to improve the structural behavior of reinforced concrete structures but also to increase the seismic performance of steel structures. In his study, Şeker modeled 22 steel structures with different brace types and common brace types according to the Turkish Building Earthquake Code 2018 (TBEC 2018) and Principles on Design, Calculation, and Construction of Steel Structures (ÇYTHYE 2018) regulations and compared their behaviors under horizontal load. Accordingly, the structural weights, seismic forces, the base shear force of the steel braced frames, and the overturning safety ratios, period, and displacement values were compared, and it was seen that the models were sufficient in terms of both horizontal displacement limit and rigidity [6]. Aribaş et al. designed a building consisting of moment-resisting steel frames and a building consisting of eccentric steel braced frames under vertical load and earthquake and compared the structural analysis results. After the analysis,

it was observed that the top floor drift of the building with eccentric V braces was less under the earthquake, and the section dimensions were reduced accordingly [7].

Unlike most studies in the literature, in this study, the changing structural performance due to the concentric X steel braced elements added to multi-story reinforced concrete frame bearing systems at different heights was investigated numerically by considering the building height classes. Concentric steel X braces were added to symmetrical structures designed with 5 spans in the x and y directions in different building height classes of 8-story, 12-story, and 18-story in the study. 3 reference and 3 X steel braced were modeled using SAP 2000 [8] software and analyzed according to the mode superposition method. The top story displacement, period, interstory drifts, story shear forces, and base shear forces of each structure were obtained and compared at the end of the analyses. Thus, the performances of the structures in terms of strength and stiffness were evaluated, and the effect of building heights on the performance of steel braces was investigated.

II. MATERIAL AND METHOD

Three 3-D reference frames and three frame systems with concentric X steel braces were modeled and analyzed using SAP 2000 finite element software in the study. While creating the building models, different height classes were taken into consideration as $BYS = 3$, $BYS = 4$, and $BYS = 5$ according to Turkish Building Earthquake Code 2018 (TBEC 2018) [9]. In this way, the effects of different building heights and building height classes on the structural behavior of buildings modeled with steel braces were investigated. The views of the reference and steel braced structural models are illustrated in Figure 1.

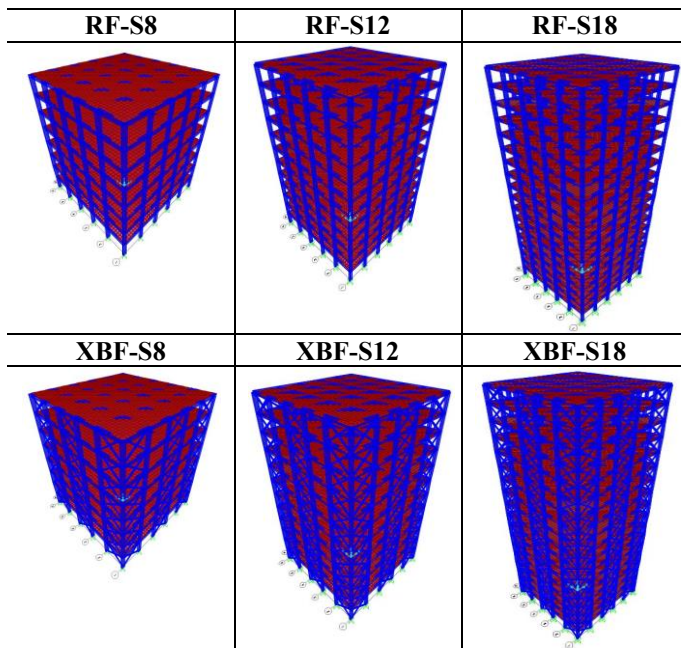


Figure 1: Structural models of reference and steel braced bearing systems.

Structures with a reference bearing system are denoted as RF, representing the reinforced concrete reference frame model, and structures with a concentric X steel braced bearing system are denoted as XBF, representing the reinforced concrete X braces frame model in the study. S8, S12 and S18 show the number of story of the structural models.

Structural analyses were performed using the mode superposition method. Spectral acceleration coefficients and design spectrum values were obtained from the AFAD application [10] for the earthquake ground motion level DD2 and ZC soil class. The models were analyzed in the x and y directions using the reduced design acceleration spectrum curve in accordance with the obtained design spectrum values with the mode superposition method. Accordingly, the top story displacement, building period, interstory drifts, story shear forces, and base shear forces for each model were obtained and compared.

III. NUMERICAL STUDY

The structural models were created as frame systems consisting of only columns and beams with 5 spans in the x and y directions with 8-story, 12-story and 18-story, respectively. The concrete compressive strength was defined as 35 MPa, and the reinforcement yield strength was entered as 420 MPa for the columns and beams of the frame system. The length of each span in both x and y directions is 4 m, and the total length in both directions is 20 m. The story height is 3 m in all models, and the total building height is 24 m for 8-story buildings, 36 m for 12-story buildings, and 54 m for 18-story buildings. The dimensions of all beams used in the carrier system are 400x500 mm, and the column dimensions are 500x600 mm. The concrete cover in both column and beam members is 30 mm. The longitudinal reinforcement ratio in columns is 0.0186 and in beams 0.00535. The diameter and arrangement of longitudinal reinforcement in columns is 10 \varnothing 26, while it is 5 \varnothing 16 at the bottom and 3 \varnothing 12 at the top of beams. The diameter and space of transverse reinforcement in columns are \varnothing 10/100, and in beams are \varnothing 8/100. The slab thickness is designed as 150 mm. The dead load acting on the story is 2.5 kN/m² and the live load is 2.0 kN/m², the snow load acting on the last floor is 0.75 kN/m². The load-bearing system building importance coefficient is considered as $I=1$. The dimensions and reinforcement arrangements of the structural members of the load-bearing system models are given in Figure 2. The models analyzed as references were created and reanalyzed by adding concentric X steel braces to the outer and middle axes in both x and y directions. For both the reference and steel-braced structures, a symmetrical architecture was preferred on both axes and does not arrange with any irregularities. The location of the diagonals on the structure is arranged symmetrically. SAP 2000 software was used for both modeling and structural analysis.

Column: 500x600 mm	Beam: 400x500 mm	X-Brace
Longitudinal Rebars: 10Ø26	Longitudinal Rebars: 5Ø16 (bottom) 3Ø12 (top)	Tube 140x140x8
Transverse Rebars: Ø10/100	Transverse Rebars: Ø8/100	

Figure 2: Dimension and reinforcement of structural members.

Since it is assumed that the designed buildings will be constructed in the Kadıköy district of Istanbul, the spectral acceleration coefficients and design spectrum values were obtained through the AFAD application [10], taking this location into account. After calculating the horizontal elastic design spectral acceleration and reduced design spectral acceleration, spectrum curves were obtained. The data required to obtain the reduced design spectrum curve to be used for the mode superposition method is presented in Table 1.

Table 1: Data information used for earthquake load.

Earthquake Ground Motion Level	DD2
Local Soil Class	ZC
S _{DS}	1.182
S _{D1}	0.402
Building Usage Class (BKS)	3
Building Importance Coefficient (I)	1
Earthquake Design Class (DTS)	1
Building Height Class (BYS)	3,4,5
Bearing System Behavior Coefficient (R)	8
Excess Strength Coefficient (D)	3

The horizontal elastic design spectrum curve and the reduced design acceleration spectrum curve obtained using the above data are given in Figure 3. Using these curves, the analyses of the reference and concentric X steel braced frame models were analyzed in accordance with the mode superposition method. Earthquake loadings were subjected to both x and y directions via SAP 2000 software.

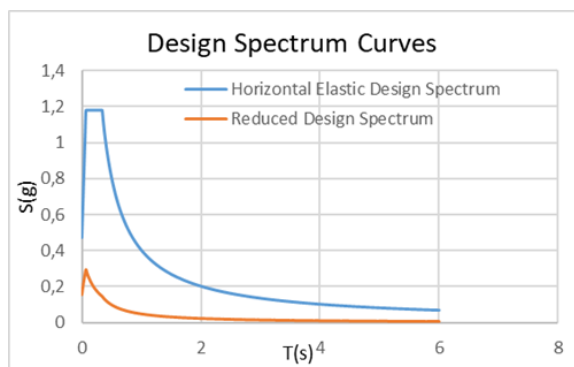


Figure 3: Design spectrum curves.

IV. RESULTS AND DISCUSSION

After the dynamic analyses of the reference and steel braced frame systems were performed, the structure period, frequency, top displacement, interstory drifts, story shear forces, and base shear forces were obtained and compared for all models.

A. Structure Period and Frequency

As a result of the analysis, the building periods of both the reference frame and the concentric X steel braced models were obtained and presented in Table 2.

Table 2: Periods and frequencies of reference and steel braced structure models.

Models	T(s)	f (1/s)	T%	f%
RF-S8	0.650	1.538	-	-
RF-S12	1.579	0.633	-	-
RF-S18	2.421	0.413	-	-
XBF-S8	0.504	1.984	22.496	29.030
XBF-S12	1.055	0.948	33.197	49.693
XBF-S18	1.724	0.580	28.793	40.434

As seen in Table 2, the dominant periods of the reference models are larger and their frequencies are smaller than the periods of the steel braced models. As the coefficient increases, the periods of both the reference models and the braced structures increase, and their frequencies decrease as expected. By adding steel braces to the structural models, the periods of the building increased while their frequencies decreased. This shows that the braces provided additional stiffness and stability to the structure.

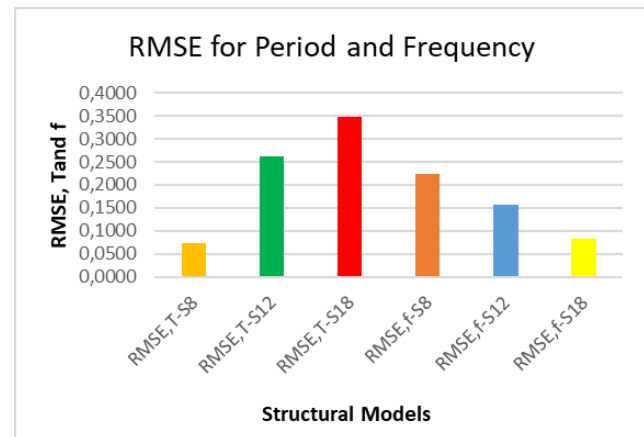


Figure 4: RMSE values of period and frequency values.

Root Mean Square Error (RMSE) values between the reference structure and the steel braced structure are calculated and presented in Figure 4. Here, the values obtained from the reference model are considered as the real observation series x_i , and the values obtained from the braced frames are considered as the estimated data series \hat{x}_i . N is the number of data points. RMSE values are calculated by Equation (1).

$$\sqrt{\frac{\sum_{i=1}^N (x_i - \hat{x}_i)^2}{N}} \quad (1)$$

Accordingly, the biggest difference for period values was obtained from 18-story building models, while for frequency values it was obtained from 8-story models. Thus, as the number of story increases, the effect of steel braces on the dominant period of the structure increases.

B. Story Displacement and Interstory Drift

By analyzing the frame structures under Ex and Ey earthquake loads, the top displacements were obtained from both x and y directions. These top displacements also correspond to the maximum displacements of the reference and braced frame structures. Table 3 shows the maximum story drifts for all models. Accordingly, as the number of stories in frame structures increases, the top story displacements also increase. There is no different situation in steel braced structures. As the number of stories and the building height increased, the maximum story drifts of the steel braced structures increased. Thanks to the concentric X steel braced structures added to the frame structure, the top displacements were reduced.

Table 3: Maximum story drifts of reference and steel braced structure models.

Models	dxmax (m)	dymax (m)	dxmax %	dymax %
RF-S8	0.009517	0.010469	-	-
RF-S12	0.024606	0.02558	-	-
RF-S18	0.038163	0.039518	-	-
XBF-S8	0.007845	0.008321	17.569	20.518
XBF-S12	0.017929	0.018272	27.136	28.569
XBF-S18	0.029601	0.030162	22.435	23.675

In Figure 5, the story displacement obtained from the 8, 12, and 18-story reference frames and steel braced frames along the stories are given for the x and y earthquake directions. According to this, the lowest story displacement among both the reference and braced frames belong to the RF-S8 and XBF-S8 samples. It was observed that the story displacement decreased with the addition of X steel braces, while the displacements of RF-S18 and RF-S12 frames were the highest, respectively.

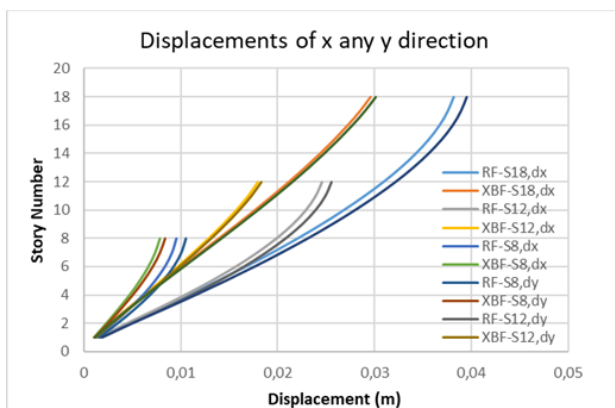


Figure 5: Story displacement of frame models in x and y earthquake directions.

Interstory drifts are an important indicator of structural damage in relation to the structural performance level and are given for both earthquake directions in Figure 6. The highest values of interstory drifts were obtained from models RF-S18 and RF-S12, respectively. The interstory drifts of the RF-S8 and XBF-S8 models are the lowest. It was observed that the interstory drift values decrease for all samples by adding steel braces to the reference samples. In this way, it was observed that the concentric X steel braces limited the interstory drifts of the frame structures.

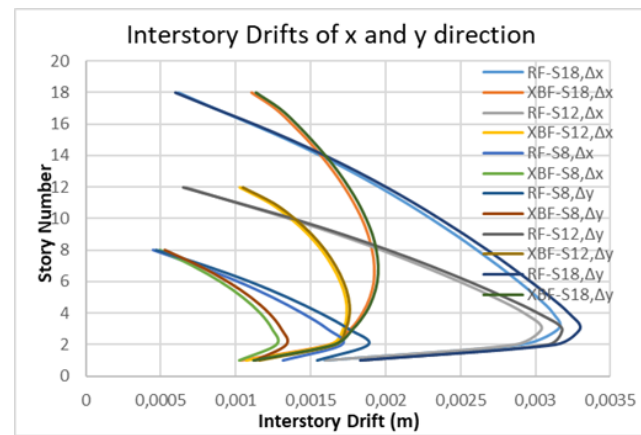


Figure 6: Interstory drifts of frame models in x and y earthquake directions.

As the number of stories and the building height increase, the interstory drift values increase in both RF and XBF models. Accordingly, the interstory drift difference between the reference frames and the braced frames was determined by the RMSE value (Figure 7). This difference was obtained from 12-story frames for both directions. It was followed by 18-story and 8-story models, respectively. The difference between the 8-story frame models is quite low compared to other multi-story frames.

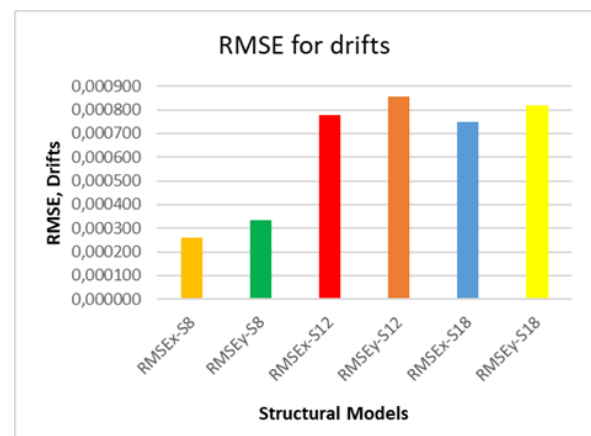


Figure 7: RMSEs of interstory drifts in x and y earthquake directions.

C. Shear Force

After the analyses, the maximum base shear force values to which the columns were exposed in both earthquake directions in the reference and X steel braced frames are given in Table 4.

According to this, the base shear force decreased as the number of stories increased in both RF and XBF frames. By adding steel braces to the structure, the base shear forces acting on the columns were significantly reduced. This decrease, ranging between 25% and 32%, is most noticeable in the 18-story frame system. As the number of stories decreased, this ratio decreased slightly, although not very high. However, even for an 8-story building, this decrease is around 20%. In this way, the forces acting on the vertical bearing members of the frame system under horizontal loads are reduced, and the steel braces members provide this.

Table 4: Base shear forces of reference and steel braced structure models.

Models	V _x (KN)	V _y (KN)	V _x %	V _y %
RF-S8	2805.212	2568.154	-	-
RF-S12	1699.911	1632.043	-	-
RF-S18	1662.296	1610.228	-	-
XBF-S8	2192.628	1877.434	21.837	26.896
XBF-S12	1302.518	1149.698	23.377	29.555
XBF-S18	1234.384	1089.75	25.742	32.323

In Figure 8, the story shear forces acting on the stories for each model are given for the x and y earthquake directions. The shear forces acting on the stories are reduced for both earthquake directions with the addition of steel braces to the bearing system. This indicates that some of the horizontal forces are resisted by the steel brace members.

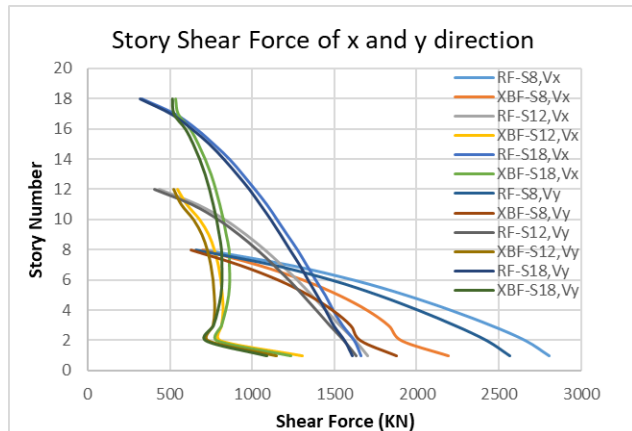


Figure 8: Story shear forces of frame models in x and y earthquake directions.

The RMSE values of the story shear forces in the x and y earthquake directions are given in Figure 9. Although the difference between the RMSE values is low, the highest value in terms of story shear forces acting on the stories of the reference models and braced models was calculated for the 8-story model, while the lowest value was calculated from the 18-story model. This situation is different from that obtained from the base shear force, and in particular, the difference between the shear forces acting on the columns at each story is lower in the 12, and 18-story models than in the 8-story models. It is thought that the reason for its low value is that steel braces carry higher horizontal forces, especially in multi-story framed structures.

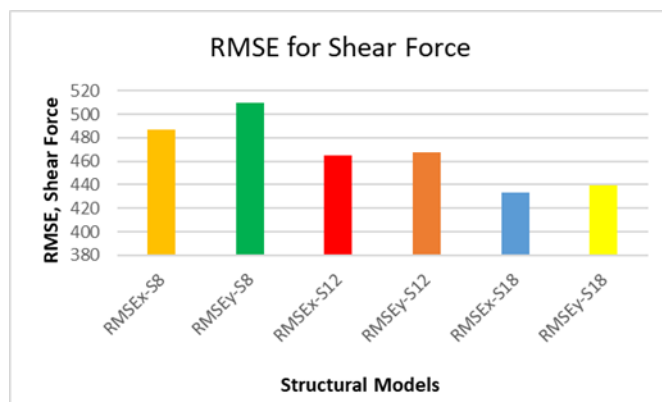


Figure 9: RMSEs of story shear forces in x and y earthquake directions.

V. CONCLUSION

The results were obtained in the study conducted on the reference and concentric X steel braced frame bearing system with different building height classes as follows:

- By adding steel braces to the bearing system, the period of the structure increases while its frequency decreases. As the number of stories and the height of the building increase, the effect of X steel braces on the dominant period of the structure increases.
- The addition of X steel braces to the frame bearing system structures reduced the displacement demand of the bearing system and the interstory drift values. However, when the story height is low, the difference between the interstory drift values of frame and steel braced structures is less, while this difference increases significantly as the story height increases.
- The base shear forces acting on the columns in the concentric X steel braced frame system decrease significantly. As the story height increases, this difference increases in terms of base shear force. Similarly, story shear forces are lower in steel braced systems than in frame-only systems.

In light of the above results, it was observed that concentric X steel braces provide additional stiffness and stability to multi-story buildings whose bearing system consists of only frames. In addition, it was revealed that some of the horizontal forces are resisted by these members. Thus, it was concluded that concentric X steel braces improve earthquake performance by providing additional strength, stiffness, and stability to multi-story buildings under horizontal loads.

REFERENCES

- [1] O. Akagündüz, "Investigation of the effect of steel bracing used in reinforced concrete structures on structural behavior," MSc Thesis, Dept. Civ. Eng., Uşak Univ., Uşak, 2019.
- [2] H. Öztürk, G. Dok, A. Demir, and N. Çağlar, "Performance evaluation of reinforced concrete frames strengthened with steel braces in different soil class," in Conf. Rec. 2016 International Natural Disaster and Disaster Management Symposium, pp.260-263.
- [3] H. Özkaynak, B. Adak, B. M. Ağca. (2018). The effect of specially designed braces on the earthquake behaviour reinforced concrete

- structures. Eskişehir Technical University Journal of Science and Technology B- Theoretical Sciences. Vol.4, pp.163—174. Available: DOI: 10.20290/aubtdb.489450
- [4] B. Yavaş, “The determination of dynamic properties of RC structures retrofitted with buckling restrained braces by using health monitoring procedures,” MSc Thesis, Dept. Civ. Eng., Akdeniz Univ., Antalya, 2017.
- [5] A. Karalis, K.A. Georgiadi-Stefanidi, T.N. Salonikios, K.C. Stylianidis, E.S. Mistakidis, “*Experimental and Numerical Study of the Behaviour of high Dissipation Metallic Devices for the Strengthening of Existing Structures*,” in *Conf. Rec.2011. Proceedings of the III ECCOMAS Thematic Conference on Computational Methods in Structural Dynamics and Earthquake Engineering*.
- [6] M.T. Şeker, “Theoretical investigation of behaviour of multi-storey steel structures having different steel bracing types,” MSc Thesis, Dept. Civ. Eng., Konya Teknik Univ., Konya, 2022.
- [7] S. Arıbaş, S. Sancioğlu, S. Çarbaş. (2019). Investigation of Eccentric V Braces on a Steel Structure. *KMU Journal of Engineering and Natural Sciences*. 1(1). pp. 79—97.
- [8] SAP2000, Linear and nonlinear static and dynamic analysis of three-dimensional structures, Computer and Structures, Berkeley, CA, 2017.
- [9] Ministry of Interior, Disaster and Emergency Management Presidency. TBEC 2018, Turkish Building Earthquake Code. Ankara: Government of Republic of Turkey, 2018.
- [10] Ministry of Interior Disaster and Emergency Management Presidency, (AFAD). 06 16, 2020. AFAD Turkish Earthquake Hazard Maps Interactive Web Application. Available: <https://tdth.afad.gov.tr/TDTH/main.xhtml>.

Skip-Gram Adapted for Session-Based Recommendation Systems

ENES ÇELİK^{1,2}, SEVİNÇ İLHAN OMURCA¹

¹ Kocaeli University, Kocaeli/Türkiye, silhan@kocaeli.edu.tr

² Kırklareli University, Kırklareli/Türkiye, enes.celik@klu.edu.tr

Abstract - A session-based recommendation system predicts the next click or the sequence of items the user will interact with by considering their previous clicks and interactions. Modeling users' future behavior probabilistically in online transactions is challenging because most behavioral information is not available. Sequence-based recurrent neural networks, which encode a user's past behavior sequence, and graph-based neural models, which encode item relationships, may overlook different time periods in previous sessions. In this study, we propose an adapted skip-gram model to address these challenges in session-based recommendation systems. Our proposed method, skip-gram, not only captures sequential user interest through item-specific subsequences within the session but also learns complex interaction patterns between items. By employing the adapted skip-gram approach, our model can address many issues found in sequence-based models and better learn accurate transition patterns between items. Extensive experiments on two large real-world datasets demonstrate that our method outperforms state-of-the-art solutions in terms of the mean reciprocal rank score based on the skip-gram model.

Keywords - Skip-gram, session-based recommendation systems, item-specific subdirectories, contextual connections, recommender system.

I. INTRODUCTION

WITH the abundance of information available today, recommendation systems have become essential tools for filtering and customizing content. Driven by an array of state-of-the-art machine learning techniques, these systems seek to predict the behavior of a user and generate recommendations for items like products, movies, or news articles. These systems effectively eliminate the cognitive load of decision-making by analyzing large volumes of user data and therefore enhance user experience [1].

Most of the traditional recommendation systems are collaborative filtering based which have its own uses and shortcomings that they decide prediction based on similarity between users or items. But this method may have the cold-start problem that it is hard to provide recommendations for any new user or item without any previous interaction records. To counter this limitation, one approach is hybrid: it collects collaborative filtering and content-based filtering of item attributes [2].

Session-based recommendation systems have emerged as a powerful tool for predicting user preferences within a single session, particularly in scenarios where long-term user profiles

are unavailable or insufficient. These systems aim to capture short-term user interests and dynamics, enabling more accurate and timely recommendations. Unlike traditional recommendation systems that rely on historical user behavior, session-based approaches focus on the current user session, leveraging the sequence of items interacted with to predict the next item of interest [3].

Session-based recommendation systems aim to predict the next item a user is likely to interact with within a given session, leveraging only the user's current interaction history [4]. While traditional recommendation systems often rely on long-term user profiles, session-based approaches are particularly valuable for anonymous users or those with limited interaction history [5]. The Skip-Gram model, a neural network architecture introduced as part of the Word2Vec framework, has proven instrumental in learning distributed representations of words by predicting the context in which words appear. Leveraging the Skip-Gram model's ability to capture semantic relationships, recent research has adapted its architecture to session-based recommendation systems, where user interactions are temporally constrained and lack long-term user profiles [6]. This paper proposes a novel approach that adapts the Skip-Gram model, originally developed for natural language processing, to the context of session-based recommendations [7]. By leveraging the Skip-Gram model's ability to capture semantic and syntactic relationships between words, the proposed method aims to learn meaningful representations of items within a session, thereby improving the accuracy of next-item predictions [8].

Rendle et al. including matrix factorization (MF) and adaptive k-nearest-neighbor (kNN), these approaches are not inherently designed to optimize for personalized ranking tasks. To address this, they introduce a general optimization criterion, BPR-Opt (Bayesian Personalized Ranking Optimization), which serves as a maximum posterior estimator rooted in a Bayesian framework for ranking [9].

Sarwar et al. unlike user-based methods, which analyze user similarities to predict preferences, item-based collaborative filtering emphasizes similarities between items to make recommendations. By constructing item-item similarity matrices, the algorithm predicts a user's interest in a particular item based on their previous interactions with similar items [10].

Rendle et al. introduce a novel method that synergizes both matrix factorization and Markov Chains approaches by

employing personalized transition graphs constructed over individual Markov chains. Specifically, the method learns a unique transition matrix for each user, resulting in a three-dimensional "transition cube." Since data for estimating transitions is often sparse, the method utilizes a pairwise interaction model, a variant of the Tucker Decomposition, to factorize the transition cube effectively [11].

Hidasi et al. explores the application of recurrent neural networks (RNNs) within the domain of recommender systems, focusing on session-based recommendations. The authors argue that a more accurate recommendation can be achieved by modeling the entirety of the session's interactions. Consequently, they propose an RNN-based method tailored for session-based recommendations, incorporating practical adaptations such as a ranking loss function to enhance the model's suitability for the task [12].

Li et al. introduce a novel neural network framework called the Neural Attentive Recommendation Machine (NARM). This framework utilizes a hybrid encoder with an attention mechanism to jointly model the user's sequential behavior and the primary purpose of their current session, resulting in a unified session representation. Recommendation scores for candidate items are then computed using a bi-linear matching scheme based on this unified representation [13].

Liu et al. contend that long-term memory models alone may be inadequate for handling long sessions, where user interests can shift due to unintended or unrelated clicks. To address this limitation, a novel short-term attention/memory priority model is introduced. This model effectively captures users' overarching interests through long-term session memory while simultaneously incorporating their most recent interests by leveraging short-term memory focused on last-click behaviors [14].

Wang et al. introduce the Collaborative Session-based Recommendation Machine (CSRSM), a novel hybrid framework designed to enhance session-based recommendations by incorporating collaborative neighborhood information. CSRSM operates through two parallel modules: the Inner Memory Encoder (IME) and the Outer Memory Encoder (OME). The IME uses Recurrent Neural Networks (RNNs) combined with an attention mechanism to model a user's behavior and information within the current session. In contrast, the OME leverages collaborative information by examining neighborhood sessions to more accurately predict the intent of the current session [15].

Wu et al. introduce Session-based Recommendation with Graph Neural Networks (SR-GNN). This approach models session sequences as graph-structured data, allowing Graph Neural Networks (GNNs) to capture intricate item transitions that previous sequential methods cannot effectively reveal. By representing each session as a composition of global preferences and current interests through an attention network, SR-GNN achieves more accurate and contextually aware item embeddings [16].

Xu et al. introduce the Graph Contextualized Self-Attention Model (GC-SAN). GC-SAN combines the strengths of graph neural networks (GNNs) and self-attention mechanisms to

enhance session-based recommendations. The model dynamically constructs a graph structure for session sequences to capture rich local dependencies through GNNs, while the self-attention mechanism learns long-range dependencies [17].

Hu et al. propose a novel framework called Preference Evolution Networks for Session-based Recommendation (PEN4Rec). This model captures the evolution of user preferences through a two-stage retrieval process from historical contexts. The first stage integrates relevant behaviors based on recent items, while the second stage models the dynamic trajectory of preference evolution over time to infer more nuanced and rich preferences [18].

Finally, for each session, we predict the probability of each item to be the next click. Extensive experiments conducted on real-world representative datasets demonstrate the effectiveness of the proposed method over the state-of-the-art. The main contributions of this work are summarized as follows:

- We investigate item-item dependencies for session-based recommendations and propose a method that generates embedding vectors with an adapted skip-gram model to discover item-item context.
- We conduct extensive experiments on two real-world benchmark datasets. The results demonstrate the proposed model's effectiveness and superiority compared to the state-of-the-art.

II. MATERIALS AND METHODS

A. Problem Definition

User preferences and behaviors are complex and dynamic, making traditional recommendation systems' assumption that all historical interactions carry equal weight increasingly questionable. While long-term historical preferences play a role, a user's current choices are often heavily influenced by their short-term and recent interactions. The time-sensitive nature of user behavior means that recently viewed or purchased items may carry more relevance than older interactions, even though these recent activities might represent only a small fraction of the user's total interaction history. Additionally, user preferences evolve, requiring a more nuanced approach to recommendations. This recognition has led to the development of session-based recommendation algorithms, prioritizing recent user interactions over historical preferences. This approach not only better captures the temporal nature of user preferences but also offers a practical advantage: it can effectively serve anonymous users who might be browsing without logging in or in incognito mode, making it more versatile in real-world applications. A new user is navigating an online shopping platform, exploring categories such as clothing, stationery, and accessories. We conceptualize the user's recent browsing activity as a "session." A session encapsulates multiple interactions by the user that occur continuously within a defined period. These interactions may include, but are not limited to, products purchased during a transaction, items viewed but not bought, and misclicks on unintended items. Sessions may unfold within a single day or span several days, weeks, or even months. The fundamental

question arises: What recommendations should we make to the user during their next session? High-quality recommendations can enhance the likelihood that the user will engage further, potentially leading to clicks and purchases of products that align with their preferences. Conversely, suboptimal suggestions could at best result in no additional revenue for the company, and at worst, lead to a negative user experience. Our objective is to accurately predict the product that the user will find appealing enough to click on during their next session. This predictive task is commonly referred to as Next Event Prediction. Specifically, given a sequence of prior events, the aim is to forecast the user's subsequent interaction (e.g., click, product, or item). Figure 1 provides an overview of the session-based recommendation system.

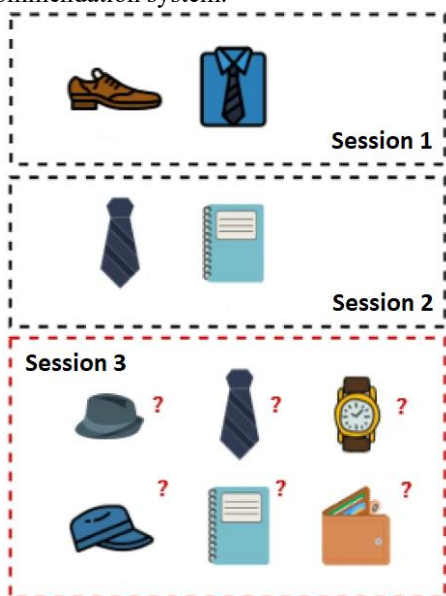


Figure 1: Structure of the session-based recommendation system.

B. Proposed Approach

A flowchart showing the Skip-gram process adapted for session-based recommendations consists of three main parts. The proposed model is shown in Figure 2.

Preprocessing: Collect session data (user interactions and behaviors). Cleans and segments the data. Convert sessions into sequences of items (e.g., products, articles). Filter short sessions or irrelevant data (sessions with less than three items are removed).

Skip-gram Training: Skip-gram sets the window size to 5. Create context-target pairs within sessions using a sliding window approach. For example, in a sequence of items [A, B, C, D], generate pairs (A, B), (A, C), (A, D), etc. Train the Skip-gram model to predict context items given a target item. Obtain vector embeddings for items based on training results. The model aims to predict context item given a target item. Once the Skip-gram model is trained, it generates vector representations (embeddings) for each item in the session. These embeddings capture contextual similarities between items. For a given user session, create a session representation by concatenating the embeddings of the items in the session. Store the trained item embeddings for future use. Negative sampling (out-of-context items) is not used in the adapted Skip-gram.

Recommendation: Retrieve the embeddings for items that interacted within the session. Calculate cosine similarity scores between session context embeddings and candidate items. Rank the candidate items based on their cosine similarity to the session representation. Present the ranked list of items as personalized recommendations for the user (Top N=20).

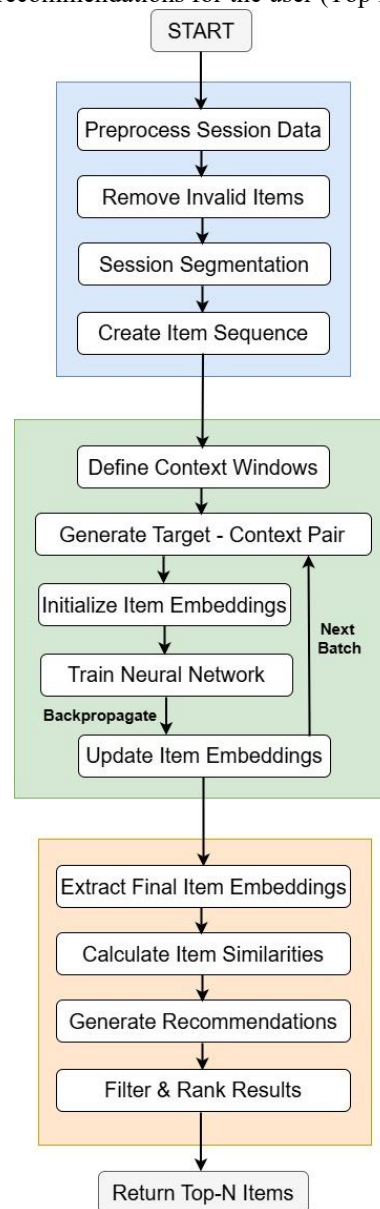


Figure 2: Architecture of the proposed model.

C. Datasets

The Last.fm dataset is a publicly available collection of music listening data from the Last.fm streaming service, commonly used in academic research, particularly in recommender systems, music information retrieval, data mining, and user behavior analysis. It contains anonymized user listening habits, enabling studies on user recommendation algorithms, music consumption behaviors, and user-item interactions in session-based systems. As a valuable resource, it aids in exploring machine learning and user modeling challenges, especially in music recommendations and social network analysis, advancing modern recommendation

techniques, and enhancing user engagement in digital music platforms [19].

The Retailrocket dataset is a publicly available collection of anonymized user interaction data from a real-world e-commerce platform, provided by Retail Rocket. Its structure and content make it well-suited for research focused on modeling short-term user interactions within a session context on an e-commerce platform. Researchers can use this data to model user behavior, predict future interactions, and personalize recommendations. The Retailrocket dataset is indeed used for developing and testing session-based recommendation systems [20]. The statistical properties of the datasets are given in Table 1.

Table 1: A summary of the dataset's key statistics.

Datasets	Last.FM	RetailRocket
Items	39,168	48,759
Clicks	3,804,922	1,684,820
Training Sets	26,984	1,351,148
Testing Sets	5,771	333,672
Avg. Length	13.52	3.55

D. Evaluation Metrics

When analyzing sequences of user interactions with items, we divide each sequence into two sets: training, and test. For a sequence with n interactions, we use the first $(n-1)$ interactions as the training data. From the remaining interactions, we randomly select the $(n-1)$ th and n th interactions to use as the test sets. For making predictions, we take the last interaction in the training sequence (*the $(n-1)$ th interaction*) as the query item. We then find the K items that are most similar to the query item, based on the cosine similarity of their vector representations [21]. Evaluate the performance of the model using the following metrics:

Recall at K (Recall@ K) is defined as the ratio of instances where the true relevant item appears within the top K recommendations for all test cases.

$$\text{Recall@}K = \frac{\text{Number of relevant items retrieved in the top } K}{\text{Total number of relevant items}} \quad (1)$$

Mean Reciprocal Rank at K (MRR@ K), takes the average of the reciprocal ranks of the ground truth items within the top K recommendations for all test cases. This metric emphasizes and rewards higher positions within the ranked list of recommendations.

$$\text{MRR@}K = \frac{1}{Q} \sum_{i=1}^Q \frac{1}{\text{rank}_i} \quad (2)$$

Where, Q is the set of all queries or test cases, rank_i is the position of the first relevant item in the ordered list of recommendations for the i th query. This formula computes the average of the reciprocal ranks of the first relevant item found for each query.

E. Comparison Methods

We compare our proposed model with several baseline

models. The POP and SPOP baselines consistently recommend the most popular items, either from the entire training set (POP) or the current session (S-POP). BPR-MF [9] employs matrix factorization for recommendation. Item-KNN [10] recommends items similar to those already present in the session, with similarity determined based on the co-occurrence frequency of item pairs. FPMC [11] is a hybrid model designed for next-basket recommendation; to adapt it for session-based recommendation, we omit user latent representations when computing recommendation scores. GRU4Rec [12] leverages a recurrent neural network (RNN) with gated recurrent units (GRUs) and a session-parallel mini-batch training strategy. NARM [13] extends GRU4Rec by incorporating a neural attention mechanism to capture users' primary intents and sequential behaviors. STAMP [14] utilizes an attention mechanism to capture both general preferences and recent focuses. CSRM [15] employs key-value memory networks to integrate information from the current session and neighboring sessions. SR-GNN [16] encodes session graphs using gated graph neural networks (GGNN) and applies an attention layer to represent preferences. GC-SAN [17] builds on this approach by incorporating self-attention layers after GGNN to capture long-range dependencies. PEN4Rec [18] models the evolution of user preferences through a two-stage retrieval process based on historical contexts.

F. Implementation Details

When starting with skip-gram adapted, a few key hyperparameters should be considered [22]. These include the embedding dimension (commonly set to 100, or 300 dimensions depending on the complexity of the dataset), and the context window size (often chosen as 5 items on either side of the target). The learning rate for optimization is also critical; initial values typically range between 0.001 and 0.01, decaying over time as training progresses. Batch size is another hyperparameter to tune, with smaller batches often improving generalization but at a cost to computational efficiency. 16-512 is a common range. Larger batch sizes can speed up training, but they may require more memory. Commonly, 5-15 epochs may be sufficient, but for larger or more complex datasets, 100 epochs or more might be necessary. Monitor the validation loss to determine when to stop training. The tests were performed using the Adam optimizer, with the most appropriate hyperparameters determined through a parameter scan.

III. EXPERIMENTAL RESULTS

To demonstrate the proposed model's overall performance, we compare it with other baseline session-based recommendation methods. In the existing literature, recommendation lists typically consist of 5, 10, or 20 suggestions. In this study, a recommendation list of 20 items was utilized to align with standard practices. The overall performance in terms of R@20 and MRR@20 is shown in Table 2, with the best results highlighted in bold.

Table 2: Experimental results (%) on two datasets.

Methods	LastFM		RetailRocket	
	R@20	MRR@20	R@20	MRR@20
POP	4.43	1.15	1.59	0.44
S-POP	22.38	8.73	13.58	6.85
BPR-MF	13.38	5.73	27.19	14.07
Item-KNN	11.59	4.19	25.56	10.68
FPMC	24.08	8.23	32.37	13.82
GRU4Rec	21.42	8.21	45.59	15.77
NARM	25.64	9.18	50.22	24.59
STAMP	---	---	50.96	25.17
CSRM	27.55	9.71	47.21	27.14
SR-GNN	26.20	10.43	50.63	26.95
GC-SAN	26.61	10.62	50.32	26.04
PEN4Rec	28.82	11.33	---	---
Our Model	29.68	11.78	44.38	19.73

The proposed model achieves the best performance on the LastFM dataset, which shows that the Skip-gram model is effective in discovering the contexts between items. Including our model, all deep learning-based methods outperform traditional methods (POP, S-POP, BPR-MF, Item-KNN, FPMC) that cannot effectively use temporal order. The proposed model outperforms traditional methods when observed on the RetailRocket dataset. The reason why the measurements made with the RetailRocket dataset fall behind the latest methods may be that the sufficient training process has not been carried out. Although the proposed model achieved poor results with RetailRocket, it achieved successful results on the LastFM dataset.

IV. CONCLUSION

This study addresses the challenges of predicting user behavior in session-based recommendation systems, which aim to forecast the next click or sequence of user interactions based on prior activity. Traditional models, such as sequence-based recurrent neural networks and graph-based neural models, may fail to capture varying temporal patterns across sessions. To overcome these limitations, the study proposes an adapted skip-gram model that effectively captures user interest through item-specific sub-sequences and complex interaction patterns. By leveraging this approach, the model demonstrates superior learning of accurate item transition patterns. Extensive experiments on two large-scale datasets validate the proposed method's effectiveness, outperforming state-of-the-art models based on mean reciprocal rank scores.

In future work, other natural language processing algorithms will be integrated into session-based recommendation systems. Additionally, it would be useful to make the model more efficient in real-time recommendation scenarios and to examine its adaptation to dynamic user behavior.

REFERENCES

[1] Zuo, Y., Zeng, J., Gong, M., & Jiao, L. Tag-aware recommender systems based on deep neural networks. *Neurocomputing*, 204, 51-60. 2016.

[2] Gupta, M., Thakkar, A., Gupta, V., & Rathore, D. P. S. Movie recommender system using collaborative filtering. In *2020 international*

conference on electronics and sustainable communication systems, ICESc, 2020, pp. 415-420.

[3] Wang, S., Cao, L., Wang, Y., Sheng, Q. Z., Orgun, M. A., & Lian, D. A survey on session-based recommender systems. *ACM Computing Surveys (CSUR)*, 2021, 54(7), 1-38.

[4] Salamapasi, M., Katsalis, A., Siomos, T., Delianidi, M., Tektonidis, D., Christantonis, K., et. al. A Flexible Session-Based Recommender System for e-Commerce. *Applied Sciences*, 13(5), 3347. 2023.

[5] Zhang, X., Xu, B., Li, C., Zhou, Y., Li, L., & Lin, H. Side Information-Driven Session-based Recommendation: A Survey. *arXiv preprint arXiv:2402.17129*, 2024.

[6] Mikolov, T., Sutskever, I., Chen, K., Corrado, G. S., & Dean, J. Distributed representations of words and phrases and their compositionality. *Advances in neural information processing systems*, 26. 2013.

[7] Celik, E., & Ilhan Omurca, S. Skip-Gram and Transformer Model for Session-Based Recommendation. *Applied Sciences*, 14(14), 2024, 6353.

[8] Kang, W. C., & McAuley, J. Self-attentive sequential recommendation. In *2018 IEEE international conference on data mining, ICDM*, pp. 197-206. 2018.

[9] Rendle, S., Freudenthaler, C., Gantner, Z., & Schmidt-Thieme, L. BPR: Bayesian personalized ranking from implicit feedback. *arXiv preprint arXiv:1205.2618*. 2012.

[10] Sarwar, B., Karypis, G., Konstan, J., & Riedl, J. Item-based collaborative filtering recommendation algorithms. In *Proceedings of the 10th international conference on World Wide Web*, 2001, pp. 285-295.

[11] Rendle, S., Freudenthaler, C., & Schmidt-Thieme, L. Factorizing personalized markov chains for next-basket recommendation. In *Proceedings of the 19th international conference on World wide web*, 2010, pp. 811-820.

[12] Hidasi, B, K. A. Session-based recommendations with recurrent neural networks. *arXiv preprint arXiv:1511.06939*. 2015.

[13] Li, J., Ren, P., Chen, Z., Ren, Z., Lian, T., & Ma, J. Neural attentive session-based recommendation. In *Proceedings of the 2017 ACM on Conference on Information and Knowledge Management*, 2017, pp. 1419-1428.

[14] Liu, Q., Zeng, Y., Mokhosi, R., & Zhang, H. STAMP: short-term attention/memory priority model for session-based recommendation. In *Proceedings of the 24th ACM SIGKDD international conference on knowledge discovery & data mining 2018*, pp. 1831-1839.

[15] Wang, M., Ren, P., Mei, L., Chen, Z., Ma, J., & De Rijke, M. A collaborative session-based recommendation approach with parallel memory modules. In *Proceedings of the 42nd international ACM SIGIR conference on research and development in information retrieval*, 2019, pp. 345-354.

[16] Wu, S., Tang, Y., Zhu, Y., Wang, L., Xie, X., & Tan, T. Session-based recommendation with graph neural networks. In *Proceedings of the AAAI conference on artificial intelligence*, Vol. 33, No. 01, 2019, pp. 346-353.

[17] Xu, C., Zhao, P., Liu, Y., Sheng, V. S., Xu, J., Zhuang, F., & Zhou, X. Graph contextualized self-attention network for session-based recommendation. In *IJCAI*, 2019, Vol. 19, pp. 3940-3946.

[18] Hu, D., Wei, L., Zhou, W., Huai, X., Fang, Z., & Hu, S. Pen4rec: Preference evolution networks for session-based recommendation. In *International Conference on Knowledge Science, Engineering and Management*, 2021, pp. 504-516.

[19] Available: <http://ocelma.net/MusicRecommendationDataset/lastfm-1K.html>

[20] Available: <https://www.kaggle.com/datasets/retailrocket/ecommerce-dataset>

[21] Ludewig, M., & Jannach, D. Evaluation of session-based recommendation algorithms. *User Modeling and User-Adapted Interaction*, 28, 2018, pp. 331-390.

[22] Khattak, F. K., Jebblee, S., Pou-Prom, C., Abdalla, M., Meaney, C., & Rudzicz, F. A survey of word embeddings for clinical text. *Journal of Biomedical Informatics*, 100, 100057. 2019.

Investigation of Recovery of Valuable Food Components by Using Supercritical Carbon Dioxide Extraction Method

SEVİL YILDIZ¹, SÜHEYLÂ TONGUR¹, RABİA SERPİL GÜNHAN¹

¹Konya Technical University, Konya/Turkey, e248128001002@ktun.edu.tr

¹Konya Technical University, Konya/Turkey, stongur@ktun.edu.tr

¹Konya Technical University, Konya/Turkey, rsgunhan@ktun.edu.tr

Abstract - Many studies have been conducted to determine the physical and chemical properties of some foodstuffs. As a result of these analyses, it has been determined that some foodstuffs such as walnuts have nutritionally important components. Essential fatty acids and proteins are the basic nutrients in these foods. Walnuts, which are rich in antioxidant phenolic components. Within the scope of the study, it was aimed to evaluate the extracts obtained from walnut shells and walnut testan (walnut membrane) of the walnut plant with supercritical extraction, a green and innovative extraction, in terms of phenolic substance, flavonoid and antioxidant capacity contents. Supercritical carbon dioxide extraction (SC - CO₂) will be used due to its advantages such as shorter extraction time compared to classical extraction methods, not leaving toxic residues, obtaining extracts without damaging their natural structure and obtaining value-added products. As a result, the study aims to obtain findings on the recovery of functional components from walnut plant waste and their inclusion in the circular economy. Thus, it is aimed to evaluate walnuts and walnut products with high antioxidant capacity and bioavailability potential in accordance with the zero waste principle and to contribute to the country's economy.

Keywords - Food components, Super critical extraction, Zero waste, Walnut testan, Phenolic substance.

I. INTRODUCTION

WALNUT (*Juglans regia* L.) is a food that draws attention with its rich nutritional content and positive effects on health. Many studies conducted to determine the physical and chemical properties of walnuts have revealed that walnuts are rich in essential fatty acids, proteins and antioxidant phenolic compounds. Walnuts are a rich source of polyunsaturated fatty acids in particular. The main fatty acids are: Palmitic acid; is one of the saturated fatty acids found in walnuts. Stearic acid; is another of the saturated fatty acids. Oleic acid; is a monounsaturated fatty acid and is abundant in walnuts. Linoleic acid; is known as omega - 6 fatty acid and is found in significant amounts in walnuts. Linolenic acid; is known as omega - 3 fatty acid and supports cardiovascular health. Polyunsaturated fatty acids play an important role in preventing cardiovascular diseases and vascular occlusions. Walnuts are also a rich source of antioxidant phenolic compounds. These compounds prevent cell damage by fighting free radicals and thus help prevent many diseases. Juglone is a compound found in walnuts and is

known for its high antioxidant content. The green outer shell of the walnut is also used in the production of traditional walnut liqueur and contains the juglone compound. Epidemiological studies have detailed the positive effects of walnuts on health. Walnuts, which are especially rich in omega-3 fatty acids, are effective in reducing heart disease, diabetes, high blood pressure and clinical depression.

Polyphenols are a large group of molecules that include compounds such as phenolic acids and phenolic alcohols. They are among the most desired phytochemicals due to their antioxidant activity and have antimicrobial, antiviral and anti-inflammatory properties in addition to their antioxidant capacity). Fruit seeds are rich in insoluble phenol compounds [1]. Although the composition and biological activities of different parts of the walnut tree have been investigated in many studies, they stated that the inner septum of the walnut kernel has been evaluated less. They stated that the components of the walnut septum are safe, as well as having a wide range of biological properties, and that this has convinced them to shift the focus from the useless by-product of the walnut septum to a natural plant material with valuable properties. The aim of their review study is to summarize the current research on the chemical composition and biological activities of the walnut septum. Various phytochemical studies have shown that walnut septum is a rich source of secondary metabolites such as polyphenols with high antioxidant properties [2].

Food waste is a source of many important compounds that are beneficial to health, such as polyphenols, fatty acids and carotenoids, which have antioxidant, anticancer, anti-inflammatory, antiviral and neuro-sedative activities. Functional foods contain bioactive components that contribute positively to health in addition to their nutritional value, and the recovery of these components from food waste is of great importance. Supercritical carbon dioxide (SC-CO₂) extraction offers great advantages for the recovery of phenolic molecules without damaging their activities due to operating conditions [3]. SC-CO₂ extraction is usually carried out in inert atmospheres, at low temperatures and without light. Thus, all these factors contribute to the prevention of oxidation, thermal degradation and other chemical and biochemical changes common to phenolic compounds.

The fruit of the walnut tree consists of three main parts: green

shell, walnut shell and walnut kernel. The other parts are male and female flowers and leaves. The leaves of the walnut tree have high antioxidant capacity. However, there is not enough research in the literature on the walnut inner membrane and flowers. Therefore, studies to be carried out in these areas can further shed light on the potential effects of walnut on health. Evaluation of walnut waste offers important opportunities in economic and environmental terms. Effective recovery of these bioactive compounds by methods such as SK-CO₂ extraction is important in terms of evaluating the by-products of walnut production and contributing to the national economy [4].

The main subject of this study focuses on walnut waste (*Juglans regia* L.) containing valuable bioactive substances and that these substances can be economically evaluated by recovering them by supercritical carbon dioxide (SC-CO₂) extraction. This process has the potential to contribute to the country's economy in accordance with the zero waste principle.

II. MATERIAL AND METHODS

In this study, samples will be obtained from walnuts that grow abundantly in the Ermenek region and are easy to obtain. In the preparation of walnut wastes; the samples will first be dried in an oven at below 35 °C and then they will be ground into powder with a grinder (800Y, Boou co., LTD, Yongkang, Zhejiang, China) and stored in a dry environment at 25 °C until analysis. Moisture contents of walnut samples will be determined by gravimetric total solids method. Low temperature oven drying or freeze drying will be used for drying process. Valuable components will be recovered from the extracts obtained by supercritical CO₂ extraction (SC-CO₂). Total Phenolic Substance, Total Flavonoid and Antioxidant Capacity Analyses will be performed. Optimization of the experimental results will be done and they will be evaluated in terms of statistics and economy.

A flowchart for the recovery of valuable compounds from food waste is summarized Figure 1. This process contributes to the effective utilization of food waste and ensures the obtainment of high-value products that can be used in various industries.

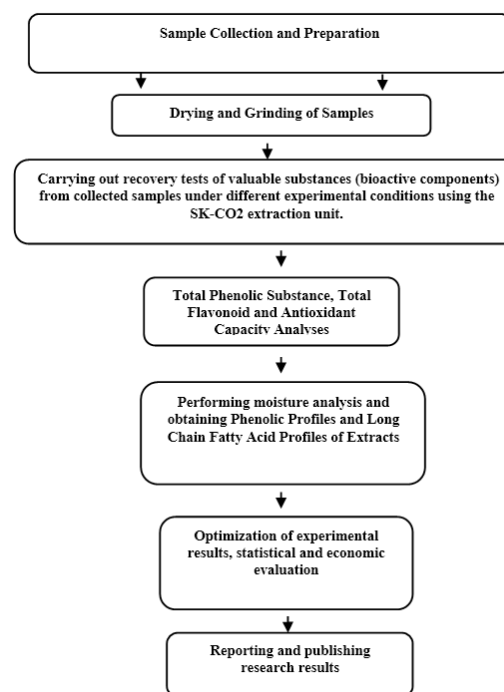


Figure 1: Flow Diagram

III. RESULTS

SC-CO₂ extraction is widely used in the recovery of valuable compounds from fruit and vegetable wastes. For example, many studies have proven the effectiveness of this method such as resveratrol and anthocyanins from grape pomace, β -carotene from apricot, (carotenoids from carrots [5], flavonoids and essential oils from citrus components [6]. SK-CO₂ extraction conditions provide efficient recovery of different phenolic compounds by optimizing parameters such as extraction pressure, temperature and time [7, 8]. The results obtained from literature studies on the subject will be evaluated in this section.

In some similar literature studies on the subject, they evaluated the process of oil extraction from walnut seeds by pressing followed by supercritical CO₂ extraction. In the pressing experiments, a factorial arrangement was made to examine the combined effects of seed moisture content (2.5%, 4.5% and 7.5%) and pressing temperature (25, 50 and 70 °C) on oil recovery and quality parameters. The quality of the oil for all tested conditions was compared with cold pressed walnut oil. It was found that oil recovery increased significantly as moisture content increased. The highest oil recovery (89.3%) was obtained at 7.5% moisture content and 50 °C temperature. The cake resulting from pressing under these conditions was extracted with CO₂ in a high-pressure pilot plant with single-stage separation and solvent recycling. The effect of two different pressures (200 and 400 bar) and temperature (50 and 70 °C) on oil yield, quality and time required for extraction was analyzed. In each condition, the extraction rate was determined to vary with the mass of the solvent and the extraction time. First, the mass of the extracted oil was determined by the solubility of the oil in CO₂ and a linear relationship was observed. The color changed from a whitish clear product to a

yellow product during extraction. The extraction conditions did not significantly affect the fatty acid composition [9].

Walnut (*Juglans regia* L.) is a very important tree nut rich in biologically active molecules, but its septum has been little investigated. In another study, experimental data showed the hypoglycemic effect of septum extracts with almost no details about its phytochemical composition. The main objectives of this study were: (1) obtaining walnut septum (WS) extracts with high content of bioactive compounds and antioxidant activity based on an original experimental design; (2) characterization of phytochemical profile of WS extracts using HPLC - MS/MS; (3) evaluation of the biological potential of the most polyphenolic WS extract. In conclusion, the phytochemical profile of the analyzed plant species extracts proves that WS could be a valuable source of biologically active compounds (polyphenols) for the food and/or pharmaceutical industry and warrants the continuation of current research for further evaluation of its bioactive potential [10].

In this study, walnut shell, which is an abundant agricultural industrial residue/waste rich in various bioactive phytochemicals, was subjected to two-stage high-pressure solvent extraction methodology using supercritical CO₂ (step 1) and subcritical homogeneous liquid CO₂/ethanol/H₂O (0.69:0.28:0.3 M) mixture (step 2). Extractions were carried out at 35 °C and 45 °C and approximately from 10 MPa to 30 MPa. GC-MS analysis revealed that the most abundant compounds in CO₂ extracts were alkanes, terpenes, oxygenated terpenes and alkaloids. The amounts of juglone and 1,4-naphthoquinone in the 1st and 2nd stage extracts were found to be in the range of 0.33 - 0.88 mg/g and 0.65 - 2.77 mg/g, respectively, while the total phenol amounts in the 2nd stage extracts were found to be in the range of 71.5 mg/g - 116.8 mg /g. As an experimental procedure, two-stage high-pressure solvent extraction (HPSE) experiments were carried out using an apparatus previously described in the literature. A 20×10–6 m³ extraction cell (2 cm in diameter and 10 cm in length) was filled with crushed dried walnut shells and glass beads (3 mm in diameter) were placed at the solvent inlet to increase raw material distribution. A porous stainless steel filter was placed at the cell outlet to prevent raw material particles from being dragged out by the solvent flow. The extraction temperature was kept constant with a controlled-temperature water bath (±0.1 °C, Thermo Haake, Germany). The pressure was maintained using a backpressure regulator. High-pressure liquid pumps were used to deliver liquefied CO₂ and liquid EtOH/water solvent mixture (L-6200A, Hitachi, Merck, Germany). The high antioxidant activities obtained with this applied method, independent of juglone and 1,4-naphthoquinone contents, demonstrate the potential of the applied high-pressure methodology to obtain selective extracts for valuable pharmaceutical, agricultural and food applications [11]. The extraction methodology and experimental procedure steps applied in this study are important for the evaluation of the thesis study to be conducted.

This study showed that various phytochemicals, walnut septum, are a rich source of secondary metabolites such as polyphenols with high antioxidant properties. Further experimental studies confirmed many biological activities of

this by-product such as radical scavenging, food preservative, antibacterial, hypoglycemic, hypolipidemic and hepatorenal protective properties. In the study, it was determined that there were 14 compounds isolated from walnut septum [2]. Accordingly, it is important for comparison for the study to be applied.

In this literature study, phenols in *Diaphragma juglandis* fructus (DJF), walnut skin (WP) and *Juglans regia* (FJR) flowers were extracted from walnut using three methods (methanolic condensation extraction, ultrasonic wave extraction and enzyme-assisted extraction). The capacities of phenolics and antioxidants were compared according to different extraction methods. In general, 50 phenolics were identified by HPLC-MS/MS; 41 of them were determined in DJF, 32 in WP and 29 in FJR. It was observed that tannins in WP were higher than in DJF and FJR. Phenolics in walnut were found to have significant antioxidant effect, and the highest effect was observed in WP [12]. This study shows that the analysis and comparison of phenols can be further expanded for the development of functional walnut ready-made foods.

In this study, supercritical CO₂ extraction of Juglone from walnut green husk (WGH) using ethanol as a co-solvent was investigated. The effects of pressure (90–150 bar), temperature (35–50 °C) and particle size (375–1500 µm) on Juglone extraction were investigated by Taguchi method. Gas chromatography–mass spectroscopy (GC-MS) revealed that an increase in pressure from 90 to 150 bar increased the extraction efficiency up to 38.24%, while increasing the temperature and particle size had a negative effect on the value of extracted Juglone. The highest extracted Juglone was 37.26 mg, which was obtained at the optimum conditions of 150 bar, 35°C and 375 µm. The results of variance analysis (VA) showed that pressure was the most important factor with 56.46% contribution on the amount of Juglone extracted, while temperature had the least effect with 6.88% contribution [13]. The method applied in the study constitutes an example for the experimental method to be applied.

Various studies have been published on the extraction of bioactive compounds from walnut waste. The extraction method should allow the extraction of the main compounds of interest and prevent their chemical modification. In this context, it is anticipated that the application of the extraction method with Supercritical technology will be effective on the efficiency of bioactive compounds.

IV. CONCLUSION

The evaluation of walnut waste with SC-CO₂ extraction is an application that complies with the zero waste principle and ensures that waste is added to the economy. The bioactive compounds obtained can be used in the food, cosmetics and pharmaceutical industries. This contributes to both environmental sustainability and enables the production of products with high economic value. The recovery of bioactive compounds from walnut waste with SC-CO₂ extraction has a great potential in terms of both environmental sustainability and

economic gain. This method is important in terms of evaluating the by-products of walnut production and contributing to the country's economy. In conclusion, modern extraction methods used for the recovery of valuable compounds from walnut wastes offer many advantages over classical methods. Optimizing these methods with the right parameters increases the potential for use in various industries by ensuring the recovery of bioactive compounds with high yield and purity. The fact that Turkey ranks fourth in walnut production indicates that this potential should be evaluated. The use of valuable compounds obtained from walnut waste in various industries will make significant contributions to economic growth and environmental protection.

Extraction of bioactive compounds from food-based waste has great potential in terms of sustainability and economic value creation. This utilization of food waste both reduces the environmental burden and allows the recovery of value-added compounds. These compounds can have various applications in the food, pharmaceutical and cosmetic industries and offer significant benefits for human health. Therefore, optimizing and disseminating extraction methods will contribute to the effective utilization of food waste.

REFERENCES

- Gulsunoglu, Z., et al., *Enhancement of phenolic antioxidants in industrial apple waste by fermentation with Aspergillus spp.* Biocatalysis and Agricultural Biotechnology, 2020. **25**: p. 101562.
- Ghiravani, Z., et al., *Internal Septum of Walnut Kernel: a Neglected Functional Food.* Research Journal of Pharmacognosy, 2020. **7**: p. 81-92.
- Argun, M.E., et al., *Recovery of valuable compounds from orange processing wastes using supercritical carbon dioxide extraction.* Journal of Cleaner Production, 2022. **375**: p. 134169.
- ESEN, Ö.B., *HEALTH RELATED PROPERTIES OF DIFFERENT PARTS OF WALNUT (JUGLANS REGIA L.) AND A WALNUT DRINK.* 2013.
- de Andrade Lima, M., D. Charalampopoulos, and A. Chatzifragkou, *Optimisation and modelling of supercritical CO₂ extraction process of carotenoids from carrot peels.* The Journal of Supercritical Fluids, 2018. **133**: p. 94-102.
- Espinosa-Pardo, F.A., et al., *Extraction of phenolic compounds from dry and fermented orange pomace using supercritical CO₂ and cosolvents.* Food and Bioproducts Processing, 2017. **101**: p. 1-10.
- Özkal, S.G. and M.E. Yener, *Supercritical carbon dioxide extraction of flaxseed oil: Effect of extraction parameters and mass transfer modeling.* The Journal of Supercritical Fluids, 2016. **112**: p. 76-80.
- Toews, K.L., et al., *pH-defining equilibrium between water and supercritical CO₂. Influence on SFE of organics and metal chelates.* Analytical Chemistry, 1995. **67**(22): p. 4040-4043.
- Martínez-Huitle, C.A. and E. Brillas, *Decontamination of wastewaters containing synthetic organic dyes by electrochemical methods: A general review.* Applied Catalysis B: Environmental, 2009. **87**(3): p. 105-145.
- Rusu, M., et al., *Process Optimization for Improved Phenolic Compounds Recovery from Walnut (Juglans regia L.) Septum: Phytochemical Profile and Biological Activities.* Molecules, 2018. **23**: p. 1-28.
- Seabra, I.J., et al., *Two-step high pressure solvent extraction of walnut (Juglans regia L.) husks: scCO₂ + CO₂/ethanol/H₂O.* Journal of CO₂ Utilization, 2019. **34**: p. 375-385.
- Zhang, Y.-G., et al., *Comparison of phenolic compounds extracted from Diaphragma juglandis fructus, walnut pellicle, and flowers of Juglans regia using methanol, ultrasonic wave, and enzyme assisted-extraction.* Food Chemistry, 2020. **321**: p. 126672.
- Ramezani, N., et al., *Juglone extraction from walnut (Juglans regia L.) green husk by supercritical CO₂: Process optimization using Taguchi method.* Journal of Environmental Chemical Engineering, 2020. **8**(3): p. 103776.
- Thai, L.Q., et al., *Supercritical carbon dioxide and ethanol-assisted extraction of bioactive compounds from Bourbon, Catimor, and Caturra coffee pulp for maximized antioxidant and therapeutic properties.* Future Foods, 2024. **9**: p. 100381.
- Arumugham, T., et al., *Supercritical carbon dioxide extraction of plant phytochemicals for biological and environmental applications – A review.* Chemosphere, 2021. **271**: p. 129525.
- Cruz-Sánchez, E., et al., *Supercritical CO₂ extraction of lavender flower with antioxidant activity: Laboratory to a large scale optimization process.* Journal of the Taiwan Institute of Chemical Engineers, 2024. **157**: p. 105404.
- De Zordi, N., et al., *The Supercritical carbon dioxide extraction of ω-3, ω-6 lipids and β-sitosterol from Italian walnuts: a central composite design approach.* The Journal of Supercritical Fluids, 2017. **127**: p. 223-228
- Montañés, F., et al., *Extraction of apple seed oil by supercritical carbon dioxide at pressures up to 1300 bar.* The Journal of Supercritical Fluids, 2018. **141**: p. 128-136.
- Mehdizadeh, T., et al., *Effect of walnut kernel septum membranes hydroalcoholic extract on the shelf life of traditional butter.* Heliyon, 2019. **5**(3): p. e01296

Predicting Student Dropout in Higher Education Using Machine Learning Techniques: A Predictive Model Using XGBoost Algorithm

ANAS ALHARDI¹, SELAHATTİN ALAN²

¹Selcuk University, Konya/Turkey, anas.rajahl@gmail.com

²Selcuk University, Konya/Turkey, salan@selcuk.edu.tr

Abstract - One of the biggest challenges facing higher education institutions is student dropout. In this study, we developed a predictive model for students at the risk of dropping out using machine learning technologies. We used an open-source database from one of the higher education institutions in Portugal, containing the data of 4424 students and 35 variables including demographic characteristics, socio-economic factors and academic performance. We used the XGBoost algorithm to build the model due to its high efficiency in processing large and complex data, and its high accuracy in forecasting. The model was able to achieve a high accuracy of 90.3% in identifying students at risk of dropping out. The results confirm the effectiveness of the application of machine learning models in education to identify risk factors, which allows educational institutions to develop an early and effective intervention strategy to support students, reduce dropout rates, enhance academic success, then improving the therapy of education outcomes at the individual and institutional levels.

Keywords - Student Dropout, Machine Learning, Prediction, XGBoost.

I. INTRODUCTION

EDUCATION is a major part of an individual's life because of the close relationship between quality education and an individual's future employment in terms of wages and available job opportunities. This relationship implies that a student's completion of their studies contributes to the overall improvement of society [1].

Considering rapid economic and technological changes, the need for qualified labor is increasing, making higher education more important than ever. Universities play an essential role in preparing cadres with advanced skills, but they face increasing challenges because of the lack of student enrollment and the dropout phenomenon. Therefore, reducing this phenomenon and encouraging students to enroll in higher education is a fundamental necessity to meet the evolving labor market requirements and ensure the quality of education [2]. However, educational institutions face a challenge in explaining the phenomenon of student dropout. It is a complex phenomenon in which economic, social, academic, and other personal factors are intertwined [3]. This complexity makes identifying students at risk of dropout a difficult task, and here the importance of machine learning techniques appears, which have become an effective tool in predicting student dropout. In recent years,

machine learning has become a powerful tool in analyzing and predicting educational data [4]. By training algorithms to learn patterns from data, machine learning can detect insights that may not be obvious using traditional methods. These algorithms enable the identification of factors that affect academic excellence or dropout risk [5]. These technologies allow decision-makers to take early and effective action to reduce this phenomenon [6]. The methods of predicting student dropout vary based on the research objectives and the type of data available. Some studies focus on analyzing the impact of specific factors on dropout using pre-designed questionnaires [7], while other studies rely on data from management information systems in educational institutions [8]. The results vary according to the type of data used, the type of educational institution, and the variables available for analysis [9].

The aim of this study is to develop an approach based on machine learning techniques for early detection of student dropout risks using the XGBoost algorithm. By leveraging these advanced techniques, we aim to accurately identify students at risk of dropping out. In the following sections, we review related works, describe our methodology, present the results, and provide conclusions.

II. RELATED WORK

Many researchers have sought to predict school dropouts through different methodologies and diverse data. Recent years have seen many studies aiming to improve the accuracy of these predictions using different algorithms.

There have been several studies conducted on the same dataset. In one study, Sulak [10] used multiple machine learning algorithms, with the Artificial Neural Network (ANN) achieving the highest accuracy at 77.3%. Another study by Novianidy [11] developed a stacked classifier that combined LightGBM, Random Forest, and Logistic Regression, reaching a final accuracy of 80.23%. Finally, Pratapa [12] employed the Support Vector Machine (SVM) algorithm with SMOTE, achieving an accuracy of 85.35%. In our study, we applied the XGBoost algorithm and achieved an accuracy of 90.3%. This demonstrates the effectiveness of XGBoost algorithm in identifying students at risk of dropping out and contributes to the growing field of machine learning applications in education.

III. MATH

The methodology of this research consists of five main phases: dataset description, data preprocessing, feature selection, implementation of six machine learning algorithms (Decision Trees, SVM, Logistic Regression, Random Forests, Naïve-Bayes, and XGBoost), and definition of model evaluation metrics.

A. Dataset

The dataset used in this research is a free public dataset available to researchers collected from one of the higher education institutions in Portugal during the academic years 2008/2009 to 2018/2019 [13]. The dataset contains 17 university programs in different disciplines and includes 4424 records, each with 35 features. The data set consists of variables related to demographic characteristics, in addition to socioeconomic and academic data. The dataset is available in csv format. The database can be accessed via the following link: <https://zenodo.org/records/5777340>

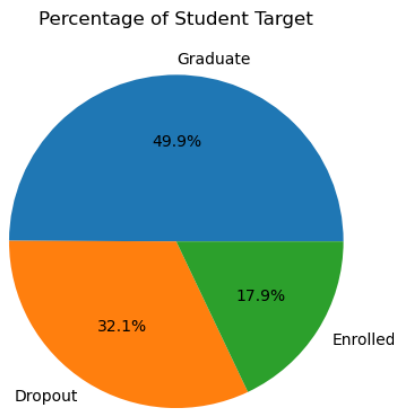


Figure 1: Percentage of Student Target.

Figure 1 shows the distribution of students, with the graduate category accounting for 50% of the data (2209 out of 4424). This is followed by dropouts at 32% (1,421 out of 4,424), while the enrolled category constitutes the lowest percentage at 18% (794 out of 4,424).

B. Data Preprocessing

- Data Cleaning:** To maintain the quality and accuracy of the model, we checked and cleaned the data from missing values during the preprocessing stage, which is essential to avoid bias and ensure the reliability of the results.
- Sample Distribution:** The dataset contained three student categories: graduates, dropouts, and enrolled students. To effectively apply binary classification models, we will exclude the enrolled student category from the analysis, allowing the model to focus solely on distinguishing between graduation and dropout cases.

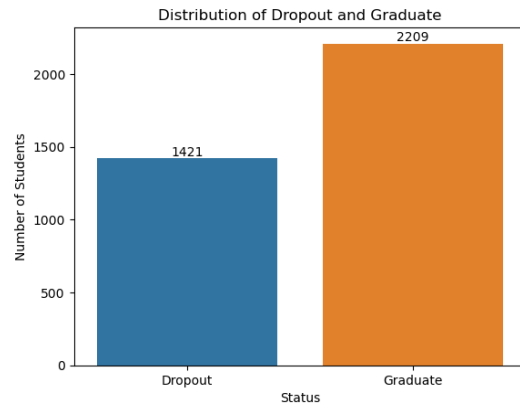


Figure 2: Distribution of Dropout and Graduate.

- Feature Encoding:** Since machine learning algorithms require numeric data for processing, we checked the dataset and found that all columns were numeric except for the Target column. This column contained two text values: “Graduate” and “Dropout”, which were digitally coded using binary coding technology, where the value was assigned 1 for graduating students and 0 for dropouts.

C. Feature Selection

We conducted an exploratory data analysis to understand the information embedded within the dataset. The primary goal was to identify patterns and insights that could directly impact the prediction of whether a student will graduate or drop out. A Cramér's V correlation plot was created to examine the strength and direction of relationships between categorical variables. With the help of a correlation matrix, we identified the most significant features. Out of 35 available features, we've selected the following features that we think are the most impactful: Marital Status, Gender, Age at Enrollment, Scholarship Holder, Previous Qualification, Mother's Qualification, Course, Curricular Units 1st Semester (approved), and Curricular Units 2nd Semester (approved).

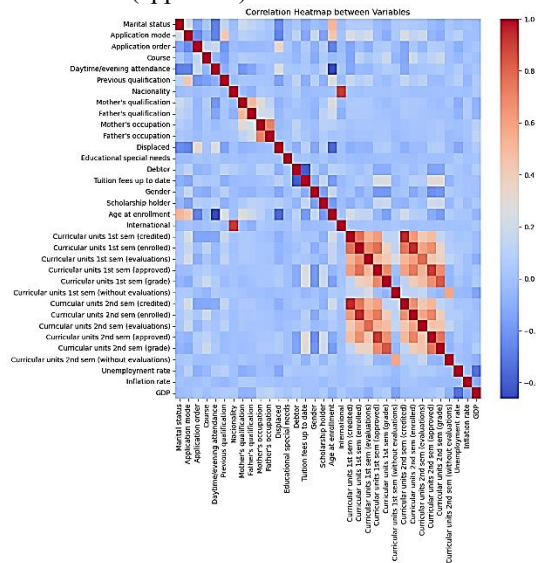


Figure 3: Correlation Heatmap between Variables.

D. Prediction Using Machine Learning Algorithms

- 1) **Decision Trees (DT):** A hierarchical classification model that systematically splits data using input variables to form a tree-like structure. The decision nodes evaluate key characteristics of the data, with branches showing different possible outcomes [14]. The algorithm continues dividing until it reaches leaf nodes containing the final classification results, offering an easy-to-follow decision process [15].
- 2) **Support Vector Machines (SVM):** A supervised learning algorithm that creates optimal boundaries to classify data points in multidimensional space. SVMs employ mathematical functions to convert complex data patterns into simpler forms where separation is achievable. The method finds the best possible separation line by maximizing the space between different groups of data, ensuring the most effective classification of new samples [16].
- 3) **Logistic Regression (LR):** A statistical method that analyzes how different factors influence group membership outcomes. The method calculates the likelihood of belonging to specific groups using a special mathematical formula, making it especially useful for predicting two or more possible outcomes. It works by converting multiple input measurements into probability values, helping to make clear distinctions between different groups [17, 18].
- 4) **Random Forests (RF):** A collective learning approach that unites several decision trees to produce more accurate and robust classifications. The algorithm creates diverse trees by training each one using selected characteristics and portions of the learning dataset. Final classifications are determined through majority voting among all trees, effectively minimizing prediction errors and enhancing model performance compared to single decision trees [19].
- 5) **Naïve-Bayes (NB):** A probabilistic classification algorithm based on Bayes' theorem that operates under the fundamental assumption of feature independence. The algorithm determines the likelihood of various results by analyzing the frequency of feature combinations in historical data. For any given input, Naïve Bayes computes the probability distribution across all possible classes and selects the most probable classification [20].
- 6) **Extreme gradient boosting (XGBoost):** XGBoost, developed by Chen and Guestrin in 2016, is an advanced version of the Gradient Boosting Decision Tree (GBDT) algorithm [21]. It enhances GBDT by utilizing a second-order mathematical approximation of the error measurement and introducing a regularization term into the cost function. This inclusion helps simplify the algorithm's complexity, speeds up convergence, and reduces the risk of overfitting. Additionally, XGBoost automatically handles real-valued features, making the modeling process more efficient.

$$L(f_m) \approx \sum_{i=1}^n \left[g_m(x_i) f_m(x_i) + \frac{1}{2} h_m(x_i) f_m(x_i)^2 \right] + \text{const.} \quad (1)$$

$$\propto \sum_{j=1}^m \sum_{i \in R_{j,m}} \left[g_m(x_i) w_{j,m} + \frac{1}{2} h_m(x_i) w_{j,m}^2 \right] \quad (2)$$

The algorithm sequentially builds decision trees, where each subsequent tree aims to improve the prediction weaknesses of previous trees. XGBoost includes regularization components to minimize model errors and employs a unique system of parallel processing and tree pruning to achieve superior computational performance and predictive accuracy [22].

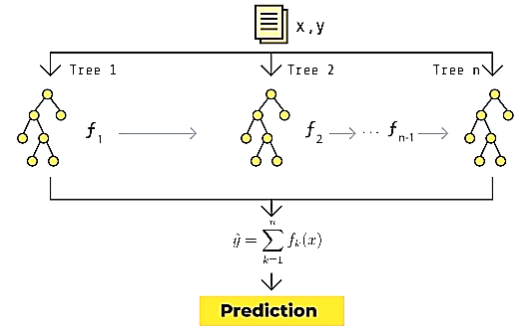


Figure 4: Extreme gradient boosting (XGBoost) [23].

By leveraging the computational power of modern hardware, XGBoost creates a learning system that stands out for its accurate results, fast performance, and smart use of resources. This makes it a valuable tool for solving data science problems, as it gradually builds better predictions by turning simple learning rules into a powerful combined system [24].

E. Model Evaluation Metrics

This study employs the Confusion Matrix, Classification Report, and ROC-AUC metric to evaluate model performance. The evaluation metrics include Accuracy, Precision, Recall, F1-Score, and ROC-AUC, which are calculated for each algorithm to assess their predictive capabilities and determine the most effective model.

IV. RESULTS

The initial dataset underwent a preprocessing phase where the "Enrolled" category, comprising 794 students, was excluded as it did not contribute to our prediction objectives. The final dataset used in this study consisted of 3630 students, who were classified into two distinct categories: Graduate and Dropout. To ensure robust model development and reliable evaluation, the dataset was strategically divided into two portions: 80% was allocated for model training purposes, while the remaining 20% was reserved for testing and validation. This division allowed us to effectively train our models while maintaining a sufficient portion of data for evaluating their predictive performance.

A. Application of Machine Learning Algorithms

The performance metrics for different machine learning models used in this study were evaluated to assess their predictive capabilities. The analysis included six machine

learning algorithms: Decision Trees, Support Vector Machines (SVM), Logistic Regression, Random Forest, Naïve-Bayes (NB), and XGBoost. Each model's performance was assessed using standard evaluation metrics including accuracy, precision, recall, and F1-score. The detailed results for each algorithm are presented as follows:

- 1) **Decision Trees (DT):** The Decision Tree algorithm's performance was assessed through a comparative analysis of training and testing accuracy. The model achieved 100% accuracy on training data and 86.64% on testing data.

Table 1: Classification Report Metrics for Decision Trees.

	Precision	Recall	F1-score	Support
Dropout	0.84	0.82	0.83	290
Graduate	0.88	0.89	0.89	436
Accuracy			0.87	726
Macro ang	0.86	0.86	0.86	726
Weighted avg	0.87	0.87	0.87	726

- 2) **Logistic Regression (LR):** The Logistic Regression algorithm's performance was assessed through a comparative analysis of training and testing accuracy. The model achieved 90.74% accuracy on training data and 89.39% on testing data.

Table 2: Classification Report Metrics for Logistic Regression.

	Precision	Recall	F1-score	Support
Dropout	0.92	0.82	0.87	290
Graduate	0.89	0.95	0.92	436
Accuracy			0.89	726
Macro ang	0.90	0.89	0.89	726
Weighted avg	0.90	0.90	0.90	726

- 3) **Support Vector Machine (SVM):** The SVM algorithm's performance was assessed through a comparative analysis of training and testing accuracy. The algorithm achieved 89.67% accuracy on training data and 88.29% on testing data.

Table 3: Classification Report Metrics for (SVM).

	Precision	Recall	F1-score	Support
Dropout	0.94	0.76	0.84	290
Graduate	0.86	0.97	0.91	436
Accuracy			0.88	726
Macro ang	0.90	0.86	0.87	726
Weighted avg	0.89	0.88	0.88	726

- 4) **Random Forests (RF):** The Random Forest algorithm's performance was assessed through a comparative analysis of training and testing accuracy. The algorithm achieved 92.05% accuracy on training data and 89.81% on testing data.

Table 4: Classification Report Metrics for Random Forests.

	Precision	Recall	F1-score	Support
Dropout	0.91	0.83	0.87	290

Graduate	0.89	0.94	0.92	436
Accuracy			0.89	726
Macro ang	0.90	0.89	0.89	726
Weighted avg	0.90	0.90	0.90	726

- 5) **Naïve-Bayes (NB):** The Naive Bayes algorithm's performance was assessed through a comparative analysis of training and testing accuracy. The algorithm achieved 84.44% accuracy on training data and 83.88% on testing data.

Table 5: Classification Report Metrics for Naïve-Bayes.

	Precision	Recall	F1-score	Support
Dropout	0.83	0.76	0.79	290
Graduate	0.85	0.89	0.87	436
Accuracy			0.84	726
Macro ang	0.84	0.82	0.83	726
Weighted avg	0.84	0.84	0.84	726

- 6) **Extreme gradient boosting (XGBoost):** The XGBoost algorithm's performance was assessed through a comparative analysis of training and testing accuracy. The algorithm achieved 98.90% accuracy on training data and 90.36% on testing data, achieving the highest testing accuracy among all algorithms in this study. The following tables present the evaluation metrics and Confusion Matrix.

Table 6: Classification Report Metrics for XGBoost.

	Precision	Recall	F1-score	Support
Dropout	0.90	0.84	0.87	290
Graduate	0.90	0.94	0.92	436
Accuracy			0.90	726
Macro ang	0.90	0.89	0.90	726
Weighted avg	0.90	0.90	0.90	726

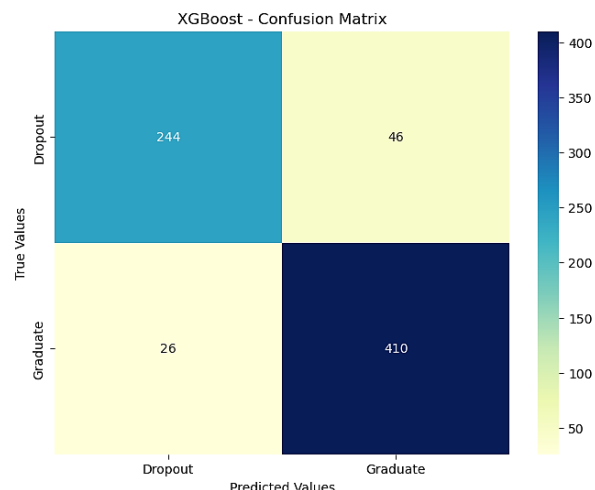


Figure 5: Accuracy of XGBoost algorithm model.

B. Comparison of Results

To facilitate a comprehensive comparison of the algorithms' performance, Table 7 and Figure 6 presents a summary of the

key evaluation metrics for each:

Table 7: Comparison of Results

Algorithm	Accuracy	Precision	Recall	F1-score
XGBoost	90.36	0.90	0.90	0.90
RF	89.81	0.90	0.90	0.90
LR	89.39	0.90	0.90	0.90
SVM	88.29	0.89	0.88	0.88
Decision Tree	86.64	0.87	0.87	0.87
Naive Bayes	83.88	0.84	0.84	0.84

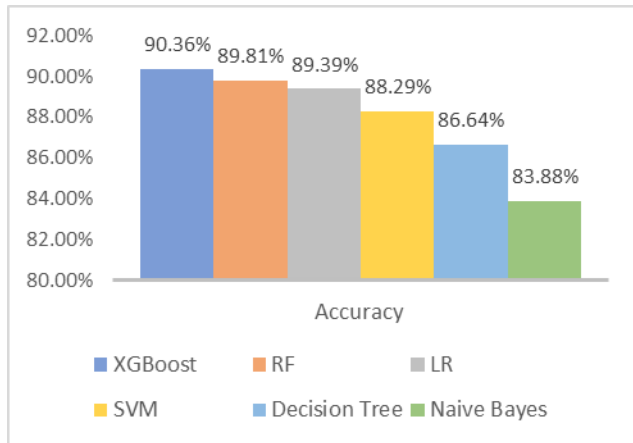


Figure 6: Comparison of results.

As shown in Figure 6, XGBoost achieved the highest accuracy of 90.36%, followed by Random Forest at 89.81%, Logistic Regression at 89.39%, and SVM at 88.29%. The lower accuracy scores were recorded by Decision Tree with 86.64% and Naive Bayes with 83.88%. This demonstrates that XGBoost has the best performance.

The ROC-AUC metric was calculated for the six implemented algorithms. Figure 7 illustrates the ROC-AUC scores for each algorithm:

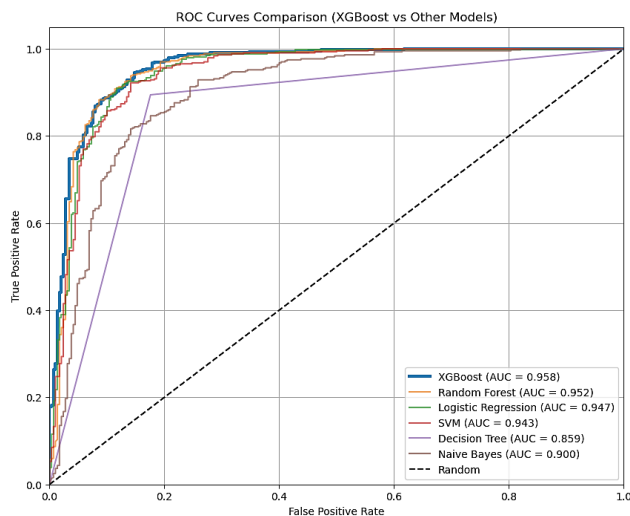


Figure 7: ROC Curves Comparison.

As shown in Figure 7, XGBoost achieved the highest AUC score of 95.80%, followed by Random Forest at 95.22%,

Logistic Regression at 94.71%, and SVM at 94.33%. The lower scores were recorded by Naive Bayes with 89.96% and Decision Tree with 85.93%. This demonstrates that XGBoost has the best performance.

C. Prediction Using XGBoost Model

After selecting XGBoost as the best performing algorithm, it was employed to predict student outcomes for the enrolled category that was previously separated during preprocessing. From a total of 794 enrolled students, the model predicted 417 students (52.5%) as likely to complete their studies successfully, while 377 students (47.5%) were identified as at risk of dropping out. The distribution of these predictions is illustrated in Figure 8.

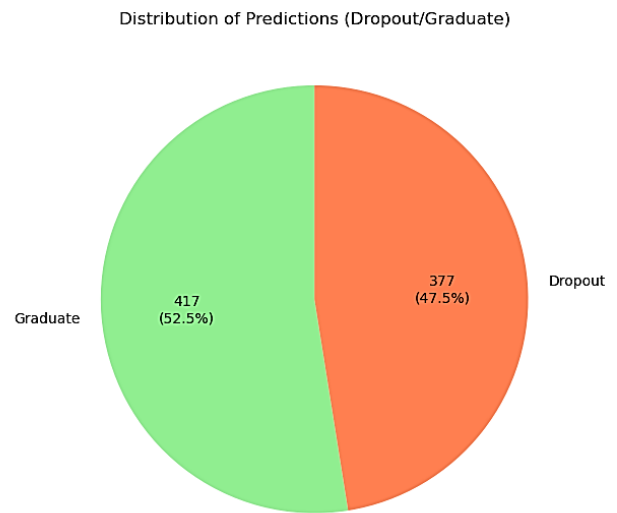


Figure 8: Distribution of Predictions (Dropout/Graduate).

V. CONCLUSION

This study presents an analysis of student dropout prediction using machine learning algorithms, analyzing 4,424 student records from a Portuguese higher education institution. In our comparison of six machine learning algorithms (XGBoost, Random Forest, Logistic Regression, SVM, Decision Tree, and Naive Bayes), XGBoost showed the best performance across multiple metrics. Our results demonstrate that XGBoost performed better than other tested algorithms, achieving the highest ROC-AUC score (95.80%) and classification accuracy (90.36%).

When applied to 794 enrolled students, the model successfully identified 377 students (47.5%) at risk of dropping out and 417 students (52.5%) likely to complete their studies. These results confirm our selection of XGBoost for this prediction task, particularly due to its effectiveness in processing complex educational data.

The model provides educational institutions with an effective tool for early identification of at-risk students, enabling timely intervention strategies. Future work will focus on developing

user-friendly interfaces for academic institutions to implement and interpret predictive models in their decision-making processes, and integrating automated reporting systems to facilitate proactive student support measures.

REFERENCES

- [1] R. W. Rumberger, "The economics of high school dropouts," *The economics of education*, pp. 149-158, 2020.
- [2] I. E. Isphording and T. Raabe, "Early Identification of College Dropouts Using Machine-Learning: Conceptual Considerations and an Empirical Example," Institute of Labor Economics (IZA), 2019.
- [3] Y. Yao *et al.*, "Exploring dropout rates and causes of dropout in upper-secondary vocational schools," *Available at SSRN 2938383*, 2017.
- [4] A. Maulana *et al.*, "Optimizing University Admissions: A Machine Learning Perspective," *Journal of Educational Management and Learning*, vol. 1, no. 1, pp. 1-7, 2023.
- [5] T. R. Noviandy, S. I. Nainggolan, R. Raihan, I. Firmansyah, and R. Idroes, "Maternal Health Risk Detection Using Light Gradient Boosting Machine Approach," *Infolitika Journal of Data Science*, vol. 1, no. 2, pp. 48-55, 2023.
- [6] K. Oqaidi, S. Aouhassi, and K. Mansouri, "Generating Global Model to Predict Students' Dropout in Moroccan Higher Educational Institutions Using Clustering," *International Association for Development of the Information Society*, 2022.
- [7] I. Lykourantzou, I. Giannoukos, V. Nikolopoulos, G. Mparadis, and V. Loumos, "Dropout prediction in e-learning courses through the combination of machine learning techniques," *Computers & Education*, vol. 53, no. 3, pp. 950-965, 2009.
- [8] A. Sales, L. Balby, and A. Cajueiro, "Predicting student dropout: A case study in brazilian higher education," in *Proc. of the 3rd Symposium on Knowledge Discovery, Mining and Learning*, 2015.
- [9] M. Adelman, F. Haimovich, A. Ham, and E. Vazquez, "Predicting school dropout with administrative data: new evidence from Guatemala and Honduras," *Education Economics*, vol. 26, no. 4, pp. 356-372, 2018.
- [10] S. A. SULAK and N. KOKLU, "Predicting Student Dropout Using Machine Learning Algorithms," *Intelligent Methods In Engineering Sciences*, vol. 3, no. 3, pp. 91-98, 2024.
- [11] T. R. Noviandy *et al.*, "Machine Learning for Early Detection of Dropout Risks and Academic Excellence: A Stacked Classifier Approach," *Journal of Educational Management and Learning*, vol. 2, no. 1, pp. 28-34, 2024.
- [12] G. Pratape, K. R. Meesala, S. Panda, and P. Goyal, "Predicting Graduation and Dropout Rates: A Machine Learning Approach," in *2023 International Conference on Advanced Computing & Communication Technologies (ICACCTech)*, 2023: IEEE, pp. 603-609.
- [13] V. Realinho, J. Machado, L. Baptista, and M. V. Martins, "Predicting student dropout and academic success," *Data*, vol. 7, no. 11, p. 146, 2022.
- [14] K. K. Rana, "A survey on decision tree algorithm for classification," *International journal of Engineering development and research*, vol. 2, no. 1, pp. 1-5-1-5, 2014.
- [15] N. KOKLU and S. A. SULAK, "Classification of Environmental Attitudes with Artificial Intelligence Algorithms," *Intelligent Methods In Engineering Sciences*, vol. 3, no. 2, pp. 54-62, 2024.
- [16] M. Tanveer, T. Rajani, R. Rastogi, Y.-H. Shao, and M. Ganaie, "Comprehensive review on twin support vector machines," *Annals of Operations Research*, vol. 339, no. 3, pp. 1223-1268, 2024.
- [17] D. R. Cox, "Regression models and life-tables," *Journal of the Royal Statistical Society: Series B (Methodological)*, vol. 34, no. 2, pp. 187-202, 1972.
- [18] D. W. Hosmer Jr, S. Lemeshow, and R. X. Sturdivant, *Applied logistic regression*. John Wiley & Sons, 2013.
- [19] T. R. Noviandy *et al.*, "Ensemble machine learning approach for quantitative structure activity relationship based drug discovery: A Review," *Infolitika Journal of Data Science*, vol. 1, no. 1, pp. 32-41, 2023.
- [20] H. Zhang, "The optimality of naive Bayes," *Aa*, vol. 1, no. 2, p. 3, 2004.
- [21] T. Chen and C. Guestrin, "Xgboost: A scalable tree boosting system," in *Proceedings of the 22nd acm sigkdd international conference on knowledge discovery and data mining*, 2016, pp. 785-794.
- [22] M. Amjad, I. Ahmad, M. Ahmad, P. Wróblewski, P. Kamiński, and U. Amjad, "Prediction of pile bearing capacity using XGBoost algorithm: modeling and performance evaluation," *Applied Sciences*, vol. 12, no. 4, p. 2126, 2022.
- [23] Y. Gao. "Federated XGBoost with bagging aggregation." <https://flower.ai/blog/2023-11-29-federated-xgboost-with-bagging-aggregation/> (accessed 10 November 2024).
- [24] M. Li, X. Fu, and D. Li, "Diabetes prediction based on XGBoost algorithm," in *IOP conference series: materials science and engineering*, 2020, vol. 768, no. 7: IOP Publishing, p. 072093.

Reconfiguration of Buck Topology into Buck-boost Converter with the Same Control Unit for Negative Voltage Generation

CAĞFER YANARATEŞ¹

¹ Department of Electrical and Energy, Kelkit Aydın Doğan Vocational School, Gümüşhane University, 29600, Gümüşhane/Turkey, cagferyanarates@gumushane.edu.tr

Abstract - This paper presents a novel approach for reconfiguring a conventional buck converter into a buck-boost converter to generate negative voltage, using the same control unit. The proposed transformation is achieved by strategically relocating the DC voltage source and adjusting the grounding, enabling the converter to operate in a buck-boost mode without requiring additional components or significant modifications to the existing control structure. This method leverages the inherent flexibility of the buck converter topology, ensuring compatibility with both positive and negative voltage generation, which is crucial in applications such as operational amplifiers, sensor circuits, and communication systems that require dual or negative voltage rails. A key advantage of the approach is its ability to maintain the same control system, avoiding complex redesigns and reducing cost while enhancing the converter's versatility. Simulations of the reconfigured converter reveal that switching frequency and resistive load variations have a significant impact on output voltage ripples. Additionally, a critical observation is that the total voltage stress on the controller and switching components is dictated by the circuit configuration, rather than solely the input voltage. This finding highlights the necessity of integrating an input capacitor to ensure stable operation and minimize voltage ripples. The study underscores the importance of these factors in designing reliable reconfigurable converters and provides practical insights for optimizing performance in systems requiring negative voltage generation.

Keywords - Buck converter, buck-boost converter, continuous conduction mode, power stage calculations, pulse width modulation.

I. INTRODUCTION

NEGATIVE voltage generation is essential in a variety of electronic and power system applications, such as analogue signal processing, operational amplifier circuits and systems requiring bipolar power supplies [1-3]. It is crucial for powering specific components that require a negative supply to operate correctly, or to provide a stable reference voltage for accurate measurement and control [4,5]. However, despite its importance, achieving negative voltage efficiently and cost-effectively can be challenging, particularly when considering factors such as power efficiency, control complexity and adaptability [6,7].

Conventional methods of generating negative voltage include the use of linear regulators, charge pump circuits and

specialized DC-DC converters [8]. Linear regulators offer simplicity, but suffer from low efficiency, especially when high power levels are required [9]. Charge pump circuits are efficient but may not be suitable for high power applications or systems requiring tight voltage regulation due to their reliance on capacitor switching [10,11]. In contrast, DC-DC converters, such as the inverting buck-boost converter, offer a more versatile and efficient solution [12,13]. However, these converters often require additional control circuitry and special configurations, which can increase complexity and cost [14].

This paper proposes a novel method of generating negative voltage by transforming a standard buck converter into a buck-boost converter using the same control unit. The transformation is achieved by simply shifting the DC input voltage and grounding, minimizing additional hardware requirements. By utilizing the existing control scheme, the proposed method maintains system simplicity and efficiency while allowing negative voltage generation. This approach demonstrates the flexibility and adaptability of buck converters in power electronics systems, highlighting their potential for reconfiguration to meet different power requirements without significant design changes.

The study focuses on the theoretical analysis of the proposed configuration. The performance and stability characteristics of the transformed converter are evaluated through detailed circuit analysis and simulations, with emphasis on how changes in input voltage and grounding affect operation. The paper also discusses the effect of key parameters such as switching frequency and load variations on voltage ripple and system performance.

By examining the effects of this reconfiguration, the paper provides insight into the feasibility and practical application of using a buck-boost converter for negative voltage generation. This study serves as a basis for further research and provides a theoretical framework for the development of more efficient and adaptable power conversion systems.

II. DETAILED RECONFIGURATION PROCESS AND TOPOLOGY TRANSFORMATION

A DC-to-DC converter that increases current from its input (supply) to its output (load) while decreasing voltage is known as a buck converter or step-down converter. In the buck

converter topology, both input (V_{IN}) and output V_{OUT} voltages are positive, and the gain of the system is achieved up to one. DC-to-DC converters with an output voltage magnitude that can be either more or less than the input voltage magnitude is known as buck-boost converters. In the buck-boost topology, the output voltage is negative, and the gain of the system is achieved either lower or higher than one. The generic representation of synchronous buck and buck-boost converters is given in Figure 1.

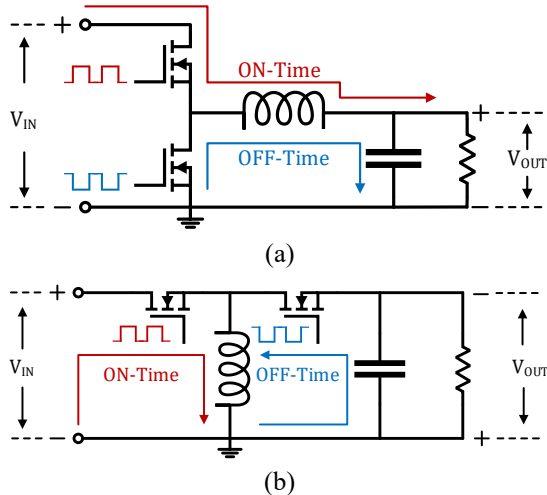


Figure 1: The generic representation of the converters (a) buck (b) buck-boost.

The basis of this study is to obtain a dc-dc buck-boost configuration without changing the control unit of the dc-dc buck converter and to produce negative voltage efficiently with pulse width modulation (PWM) control technique. In this context, the main structure of the intended configuration with the integrated control unit is shown in Figure 2.

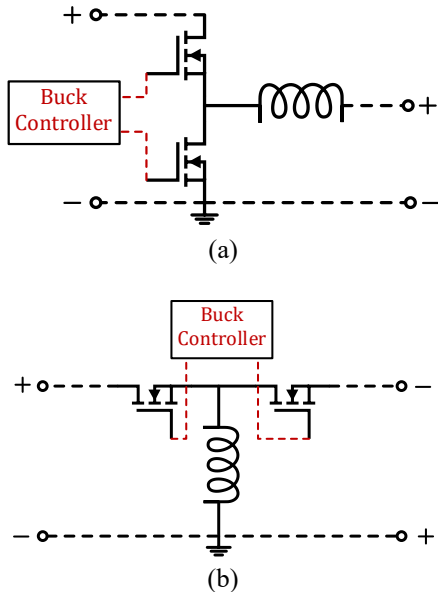


Figure 2: The main structure of the intended configurations with integrated control unit (a) buck (b) buck-boost.

The advantage of generating negative voltage with the proposed topology is using built-in drivers, while two floating

drivers are required in original buck-boost implementations. This application reveals the grounding problem. Reconfiguration of the buck topology obtained by replacing the grounding is given in Figure 3. In the new topology, the output with respect to the relocated ground will be negative voltage.

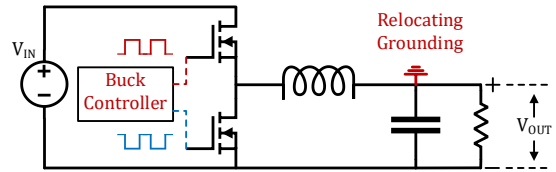


Figure 3: Relocation of the grounding.

It must be noted that the new circuit is not a buck-boost converter at this stage due to the floating power supply V_{IN} as shown in Figure 4.

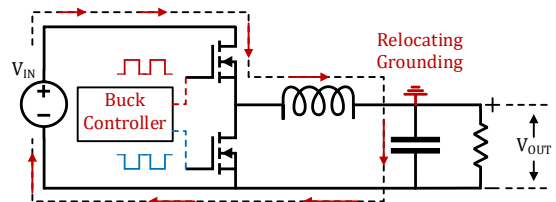


Figure 4: Floating power supply.

The solution to the floating power supply problem is possible by changing its location, as seen in Figure 5.

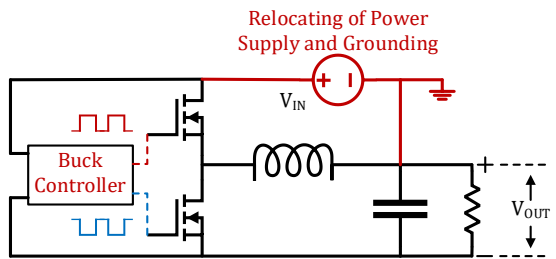


Figure 5: Relocation of the power supply.

In this new configuration, the total voltage across the controller and transistors changes. In the original buck structure, this is just the input voltage, while in the new configuration it is the sum of the input voltage and absolute value of the output voltage.

III. BUCK CONVERTER POWER STAGE

The control circuit and the power stage constitute a switching power supply. With switches and an output filter, the power stage handles the fundamental power conversion from the input voltage to the output voltage. A diode functions as the bottom switch in an asynchronous buck converter, turning on automatically when the higher switch—which is implemented with an IGBT or MOSFET—is turned off. The diode is kept forward biased during this operation in continuous conduction mode (CCM), in which the inductor current stays positive. The equations controlling the behavior of the buck converter will change if this requirement is not satisfied.

As seen in Figure 6, the switched architecture of an

asynchronous buck converter in CCM functions in two different states.

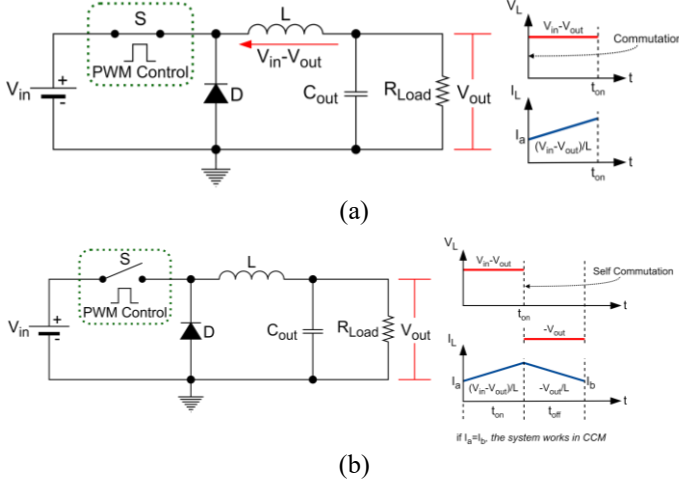


Figure 6: The switched architecture of an asynchronous buck converter in CCM.

The controllable switch S is activated in the high state when the control signal is high, connecting the input voltage to the LC circuit and allowing the inductor current to flow. This condition, referred to as the on-time t_{on} , is upheld for a predetermined amount of time. The control signal then moves to the low state, turning off the controlled switch and redirecting the current through the diode. This state, referred to as the off-time t_{off} , lasts for a predetermined amount of time.

IV. BUCK CONVERTER DESIGN EQUATIONS

In this paper, the buck converter is specifically designed to accept a 50-volt input voltage and convert it to a 25-volt output voltage. The converter functions at a switching frequency of 10 kHz. Under maximum load conditions, the minimum load resistance (R_{min}) is determined to be 5 ohms. During CCM operation, the inductor is permitted to have a maximum ripple equivalent to 20% of the average inductor current and the maximum load. Similarly, the capacitor is allowed to exhibit a maximum ripple of $\pm 2\%$ of the average output voltage.

The plant's steady-state duty cycle is presented as follows:

$$D = \frac{V_{out}}{V_{in}} \quad (1)$$

The following indicates the average inductor current's upper limit:

$$I_{L,avg,max} = \frac{V_{out}}{R_{min}} \quad (2)$$

The maximum ripple current in the inductor, which is 20% of the average current, is as follows:

$$\Delta I_L = 0.2 \times I_{L,avg,max} \quad (3)$$

The following yields the inductance value, denoted by L :

$$L = \frac{V_{in}(1-D)D}{f_{sw}\Delta I_L} \quad (4)$$

As it is $\pm 2\%$ of the average output voltage, the ripple voltage of the capacitor (ΔV_C) or output voltage (ΔV_{out}) is represented as follows:

$$\Delta V_C = \Delta V_{out} = 0.04 \times V_{out} \quad (5)$$

The capacitance value, represented by C , is given by:

$$C = \frac{V_{in}(1-D)D}{8Lf_{sw}^2\Delta V_C} \quad (6)$$

When the diode current drops to zero, the discontinuous conduction mode (DCM) emerges in the second-order elementary PWM converters (buck, boost, and buck-boost). This occurs at a particular operating point based on duty ratio and load resistance. Boundary condition current of the inductor $I_{L(B)}$ is calculated as:

$$I_{L(B)} = \frac{\Delta I_L}{2} \quad (7)$$

Boundary condition load resistance R_B is calculated as:

$$R_B = \frac{V_{out}}{I_{L(B)}} \quad (8)$$

The computed values for the components and parameters of the proposed buck converter are shown in Table 1.

Table 1: Calculated values for the proposed buck converter.

Variables and Constituents	Values
Duty cycle in steady state	0.5
Minimum load inductor current in average (A)	5
Minimum load inductor current ripple in average (A)	1
Inductance (mH)	1.3
Output voltage fluctuation (V)	1
Capacitance (μ F)	12.5
Boundary condition inductor current (A)	0.5
Boundary condition load resistance (Ω)	50

V. RESULTS AND DISCUSSIONS

Using calculated values ignoring parasitic resistances the proposed buck converter is simulated by utilizing MATLAB/Simulink® software. The internal resistance R_{on} and diode resistance R_d of the MOSFET, in ohms (Ω), are chosen as 0.001. Similarly, the diode internal resistance $R_{d(on)}$, in ohms (Ω), is implemented as the default value of 0.001. Additionally, instead of using constant load, a load step of 2 A is applied to the output resistance.

Inductor current and output voltage waveforms of the designed buck converter during the step change of the load is given in Figure 7.

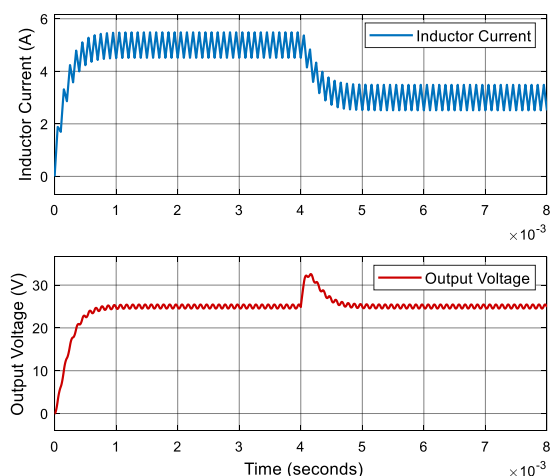


Figure 7: Inductor current and output voltage waveforms.

Total voltage across the controller & the switches and output voltage waveforms of the buck-boost converter reconfigured from the designed buck topology in the presence of load step change is given in Figure 8.

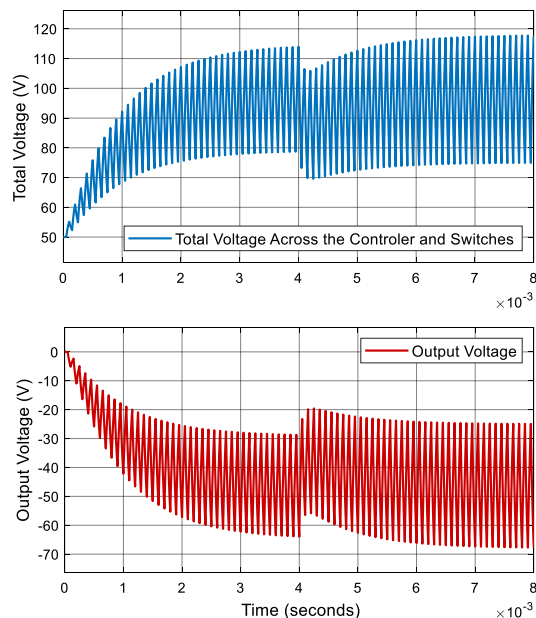


Figure 8: Total voltage across the controller and switches and output voltage waveforms.

It has been noticed that the voltage waveforms in the new configuration exhibit extremely big ripples. Signal statistics of the waveforms obtained in Figure 8 are given in Table 2.

Table 2: Signal statistics of the new configuration.

Signal Statistics	Total Voltage (V)	Output Voltage (V)
Maximum	117.8	0
Minimum	50	-67.76
Peak-to-peak	67.76	67.76
Mean	87.77	-37.77
Median	85.77	-35.77
RMS	89.31	41.23

A. Output Voltage Ripple Cancellation in the New Configuration

A crucial PWM converter parameter that could have a significant impact on system application is output voltage ripple, so it is important to pay particular attention to ripple cancellation. The output voltage ripple is influenced by the value of the inductor and output capacitor while the converter is operating in power skip mode (PSM) under light load conditions. In PSM mode, the voltage ripples are reduced by using a bigger output capacitor and inductor values. The device runs in PWM mode under high load circumstances. Output voltage ripple V_{ripple} is calculated with the following equation:

$$V_{ripple} = \frac{I_{ripple}}{8Cf_{sw}} + \frac{I_{ripple}R_{ESR}^2C}{2} \times \frac{f_{sw}}{D(1-D)} \quad (9)$$

Inductor current ripple calculation is performed with the following equation:

$$I_{ripple} = V_{out} \times \frac{1-D}{L \times f_{sw}} \quad (10)$$

where I_{ripple} , f_{sw} and R_{ESR} are inductor current ripple, switching frequency and equivalent series resistance of the output capacitor, respectively. The Figure 9 demonstrates how various switching frequencies affect output voltage ripples.

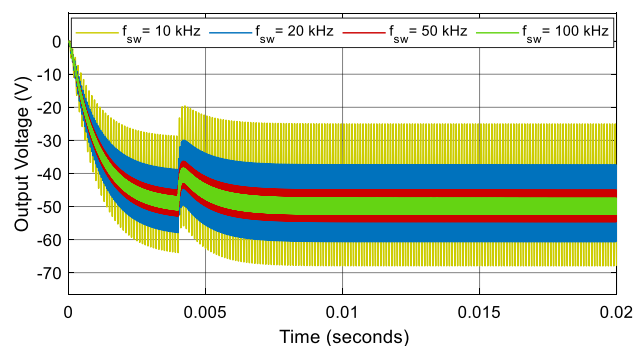


Figure 9: Output voltage ripple under various switching frequencies.

For easier computation, a more basic output voltage ripple model is assumed. The voltage ripple resulting from the capacitor alone and the voltage ripple resulting from the resistor alone add up to the total output ripple with the following equation:

$$V_{ripple} = \frac{I_{ripple}}{8Cf_{sw}} + I_{ripple}R_{ESR} \quad (11)$$

As seen in the simplified calculation in Equation 11, ripple attenuation in the output voltage requires choosing a proper $R_{ESR}C$ regime determined by implementation of a suitable capacitor as well as appropriately selected switching frequency, inductor and load values. Figure 10 illustrates the impact of different resistive output loads on output voltage ripples.

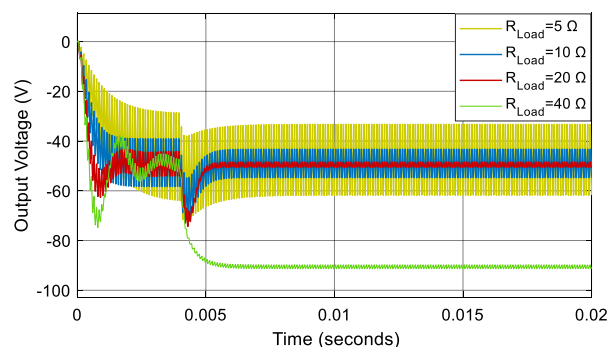


Figure 10: Output voltage ripple under various loads.

VI. CONCLUSION

This study demonstrates a novel and efficient method for transforming a conventional buck converter into a buck-boost converter capable of generating negative voltage while utilizing the same control unit. By strategically relocating the DC voltage source and adjusting the grounding configuration, the converter is reconfigured to operate in a buck-boost mode without the need for additional components or significant modifications to the existing control system. This approach takes advantage of the inherent flexibility of the buck converter topology, making it suitable for generating both positive and negative voltage rails, which is particularly important for applications such as operational amplifiers, sensor circuits, and communication systems that require dual or negative voltage supplies.

The findings reveal that the switching frequency and output resistive load significantly influence the output voltage ripples. Proper selection of these parameters is essential for minimizing ripples and achieving stable converter performance. Additionally, the study highlights that the total voltage stress on the controller and switching components depends on the circuit configuration rather than solely the input voltage, emphasizing the necessity of incorporating an input capacitor to stabilize operation and reduce voltage fluctuations.

Overall, this study provides valuable insights into the design and optimization of reconfigurable converters for applications requiring negative voltage generation. The proposed method enhances the versatility and cost-effectiveness of the converter by maintaining the original control unit, offering a practical and efficient solution for modern electronic systems that demand flexible and reliable power conversion capabilities.

REFERENCES

- [1] H. Qin, W. Wang, S. Xie, X. Han, Z. Xu, and L. Wang, "Characterization and optimization of active negative voltage driving circuit for CoolGaN HEMTs in a phase-leg configuration," *Energy Reports*, vol. 8, pp. 780–788, 2022, doi: 10.1016/j.egy.2022.08.037.
- [2] M. Mansour and I. Mansour, "Compact high-efficiency energy harvesting positive and negative DC supplies voltage for battery-less CMOS receiver," *Sci. Rep.*, vol. 13, no. 1, pp. 1–12, 2023, doi: 10.1038/s41598-023-41236-9.
- [3] H. Y. Tsai, K. H. Chen, K. L. Zheng, Y. H. Lin, S. R. Lin, and T. Y. Tsai, "A GaN-on-Si Gate Driver With Self-Pumped Drive Enhance and Short-Period Negative Voltage Techniques for Reduction of 14.7× Tailing Power Loss and 37% Reverse Conduction Loss," *IEEE J. Solid-State*

- Circuits*, vol. 59, no. 3, pp. 784–793, 2024, doi: 10.1109/JSSC.2023.3331153.
- [4] M. Xiang, T. Li, Y. Zhao, and M. Chen, "The Influence of Negative Voltage on Corrosion Behavior of Ceramic Coatings Prepared by MAO Treatment on Steel," *Coatings*, vol. 12, no. 5, 2022, doi: 10.3390/coatings12050710.
- [5] Y. Liu, H. Cai, and B. Zhao, "A Wide-Range Negative Output DC-DC Converter with Adaptive Drive Technique for Active-Matrix OLED Microdisplays," *Electron.*, vol. 13, no. 3, 2024, doi: 10.3390/electronics13030564.
- [6] C. C. Wang, L. K. S. Tolentino, H. C. Wu, R. G. B. Sangalang, O. L. J. A. Jose, and T. H. Lin, "A negative voltage generator with 4-stage configurable parallel switching for smart window film applications," *Int. J. Electron. Lett.*, vol. 11, no. 3, pp. 361–379, 2023, doi: 10.1080/21681724.2023.2224067.
- [7] S. P. Lin and M. D. Ker, "Design of Stage-Selective Negative Voltage Generator to Improve On-Chip Power Conversion Efficiency for Neuron Stimulation," *IEEE Trans. Circuits Syst. I Regul. Pap.*, vol. 67, no. 11, pp. 4122–4131, 2020, doi: 10.1109/TCSI.2020.3012086.
- [8] J. Beaucour, T. Carrière, A. Gach, D. Laxague, and P. Poirot, "Total dose effects on negative voltage regulator," *IEEE Trans. Nucl. Sci.*, vol. 41, no. 6, pp. 2420–2426, 1994, doi: 10.1109/23.340597.
- [9] Earnest Yan Lei, "CASCADED LINEAR REGULATOR WITH NEGATIVE VOLTAGE TRACKING SWITCHING REGULATOR," Faculty of California Polytechnic State University, 2020.
- [10] M. Bloch, C. Lauterbach, and W. Weber, "High efficiency charge pump circuit for negative high voltage generation at 2 v supply voltage," *Eur. Solid-State Circuits Conf.*, pp. 100–103, 1998, doi: 10.1109/ESSCIR.1998.186218.
- [11] T. Yamazoe, H. Ishida, and Y. Nihongi, "A charge pump that generates positive and negative high voltages with low power-supply voltage and low power consumption for non-volatile memories," *Proc. - IEEE Int. Symp. Circuits Syst.*, pp. 988–991, 2009, doi: 10.1109/ISCAS.2009.5117924.
- [12] J. Zhao, K. K. Kim, and Y. Bin Kim, "Negative high voltage DC-DC converter using a new cross-coupled structure," *J. Integr. Circuits Syst.*, vol. 10, no. 3, pp. 158–165, 2015, doi: 10.29292/jics.v10i3.418.
- [13] Z. Zhang and O. Semiconductor, "How to Generate a Negative Voltage Using Buck Converters?," 475 Oakmead Pkwy Sunnyvale, CA 94085, 2008.[Online].Available: https://www.aosmd.com/res/application_notes/power-ics/PIC-002.pdf.
- [14] N. Rezaei and M. Mirhassani, "Ultra low-power negative DC voltage generator based on a proposed level shifter and voltage reference," *Microelectronics J.*, vol. 113, no. December 2020, p. 105087, 2021, doi: 10.1016/j.mejo.2021.105087.

Measurement of Amplitude Produced by Various Sized Particles in Piezoelectric Element

NIHAT ÇANKAYA¹

¹ Necmettin Erbakan University, Konya/Turkey, ncankaya@erbakan.edu.tr

Abstract – Piezoelectric elements produce electric voltage when subjected to vibration. As the vibration intensity increases, the electric amplitudes produced increase. The amplitude of the electrical signals generated by particles of various sizes hitting a piezoelectric element was measured. The piezoelectric element with a resonance frequency of 2.4 MHz was placed in the flow tube of a vacuum cleaner. The same amount of semolina particles, the sizes of which were 180-212 μ , 212-355 μ , 355-500 μ , collided with the piezoelectric element at a speed of approximately 10 m/s by operating the vacuum cleaner. The electrical signals produced by the piezoelectric element were amplified with an amplifier circuit and then recorded for half a second at a rate of 1 million samples per second. A program was written to calculate the voltage level and the number of amplitudes in the signals. The highest amplitude values in the signals were measured as 1.08 V, 1.21 V and 1.65 V for 180-212 μ , 212-355 μ , 355-500 μ semolina mixtures, respectively. The total number of amplitudes exceeding the 0.6 V threshold in the signals was measured as 21, 184 and 7905, respectively. The results obtained showed that the material size ranges changed proportionally with the amplitude values and could be used as a scale in material size estimation.

Keywords - Acoustic emission, piezoelectric, particle size distribution, signal processing

I. INTRODUCTION

PIEZOELECTRIC materials have a chemical structure that produces electrical energy when pressure is applied to them or when particles are impacted. When particles of different sizes and densities hit piezoelectric elements, information about the impacting particles can be obtained by analyzing the properties of the electrical signals produced by the piezoelectric element. Many studies have been conducted on this subject using different types of materials and piezo elements with different properties. A piezoelectric sensor was placed in a conveying pipe where coal dust was carried. Impact experiments were carried out with glass and coal particles of sizes 64 μ m, 74 μ m, 103 μ m and 133 μ m and it was observed that the impact amplitudes and durations increased as the particle size increased [1]. Experiments were conducted using iron, steel and aluminum particles of sizes ranging from 0.15 to 1.1 mm. It was observed that particle sizes could be measured by analyzing the electrical signals generated by particles dropped by free fall onto a plate to which a piezoelectric-based sensor was attached [2]. Particles ranging in size from 4 to 16 mm were dropped by free fall onto a surface to which the

piezoelectric element was attached and the electrical signals generated were analyzed. As a result of the analysis, it was observed that small particles had higher amplitudes at high frequencies and large particles had higher amplitudes at low frequencies [3]. The particles of willow and miscanthus plants with sizes ranging from 400 to 5000 μ m were collided with a piezoelectric sensor at different speeds and mass flow rates to measure the size distribution of the particles in the mixture [4]. The proportions of glass powders with sizes ranging from 20 to 250 μ m in the mixture were measured. It was observed that as the sizes of the particles increased, the signal amplitudes they produced also increased [5]. The impact effects of small dust particles were investigated using the piezo ceramic element in lead zirconium titanate chemistry [6]. The impact effects of granules of various sizes were investigated using the piezoelectric element in polyvinyl difluoride chemistry [7]. As a result of the experiments carried out at different impact speeds using glass powders with diameters ranging from 0.4 to 1.2 mm, it was concluded that the Stronge theory models the impact effect better than the Hertz theory [8]. It has been observed that particle sizes can be measured with an error of 10% with a particle sizing algorithm in which the acoustic emission signals generated because of experiments using glass bubbles are analyzed [9]. It has been shown that particle sizes can be calculated with a thresholding algorithm because of experiments in which glass and polyethylene particles with sizes ranging from 150-212 and 150-250 μ m are dropped onto the surface to which an acoustic emission sensor is attached by free fall [10], [11].

In this study, semolina particles with sizes ranging from 180-212 μ m, 212-355 μ m, 355-500 μ m were used. The signals created by these particles, which collided with a piezoelectric element placed in the flow pipe of a vacuum cleaner at a speed of approximately 10 m/s while the vacuum cleaner was running, were recorded. A thresholding algorithm was developed to find and count peak amplitudes for the analysis of the signals. The amplitude levels and numbers in the electrical signals produced by the piezoelectric element because of the collisions of particles of different sizes were examined.

II. MATERIALS AND METHODS

The experimental setup shown in Figure 1 was set up to measure the effects of semolina particles of various sizes hitting the piezoelectric element. The setup consists of a vacuum cleaner, a flow pipe with a length of 1 m and a diameter of 5 cm, and a piezoelectric element fixed inside the flow pipe to

create the impact effect. The resonance frequency of the piezoelectric element used is 2.4 MHz, its diameter is 16 mm and its thickness is 1 mm. The piezoelectric element is seen in Figure 1. This element is fixed inside the flow pipe of the vacuum cleaner in the experimental setup shown in Figure 2. The vacuum cleaner was operated by placing 20-25 grams of semolina particles at the end of the vacuum cleaner in each experiment. The particles hitting the piezoelectric element placed inside the flow pipe caused the element to produce electrical signals. These signals were amplified using a circuit that increases voltage by 10 times. Then, 523260 samples were taken and recorded at a rate of 1 million samples per second using a USB type oscilloscope. A software was developed in the MATLAB program to measure the amplitude levels and numbers in the recorded signals. The envelope function was used to find the envelopes of the signals formed in the software and the FINDPEAKS function was used to find the peak amplitudes and numbers.



Figure 1: Piezoelectric Element

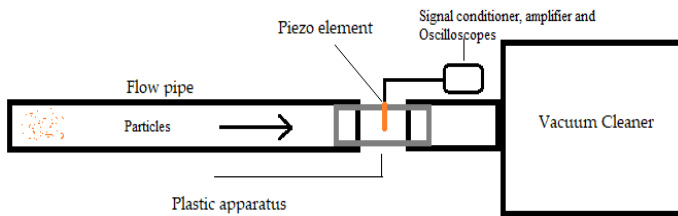


Figure 2: Experimental Setup

III. RESULTS

The appearances of the signals created by semolina particles with sizes ranging from 180-212 μm , 212-355 μm , 355-500 μm in the algorithm interface are given in Figure 3, from top to bottom, respectively. The images of these signal samples can be seen in more detail by zooming in, and their states containing 10000 samples are given in Figure 4 and 1000 samples are given in Figure 5. The vertical axes define the voltage amplitude values, and the horizontal axis defines the sample numbers. Signal envelopes are seen in Figure 5. It is clearly seen in the figures that the amplitudes of the semolina increase with the increase in their size. The peak amplitudes and widths calculated with the FINDPEAKS function according to the signal envelopes are seen in Figure 6. The number of peak amplitudes falling into the voltage amplitude ranges in the signals with the developed thresholding and counting software is given in Table 1. The total peak amplitude numbers and the highest peak amplitude values in the signals were given in Table 2.

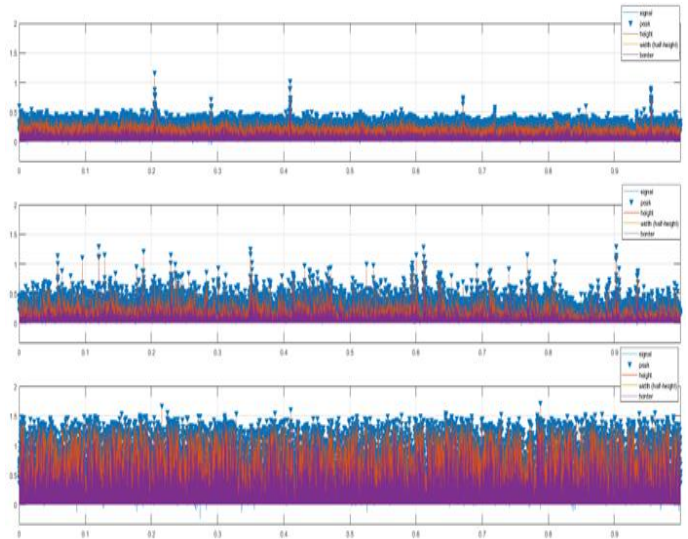


Figure 3: View of all signals in the software interface

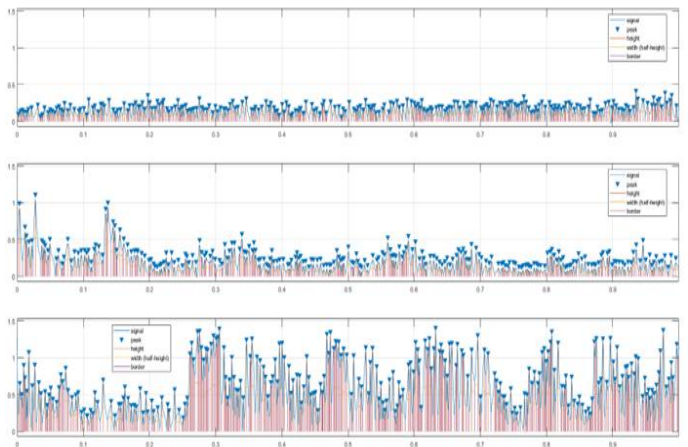


Figure 4: Signal views of 10000 samples

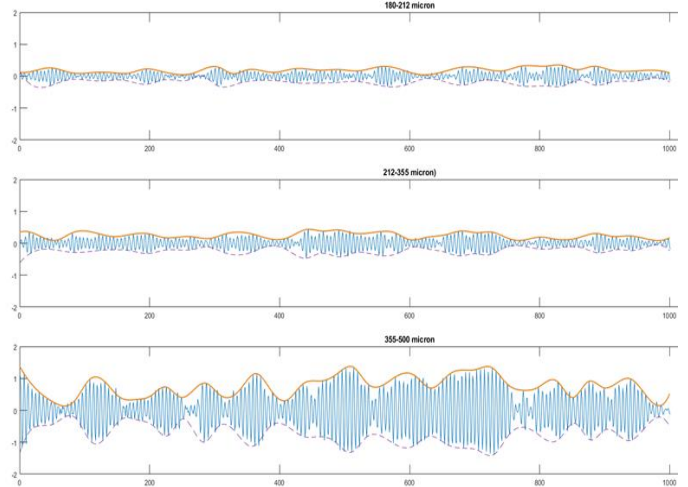


Figure 5: Signal views of 1000 samples

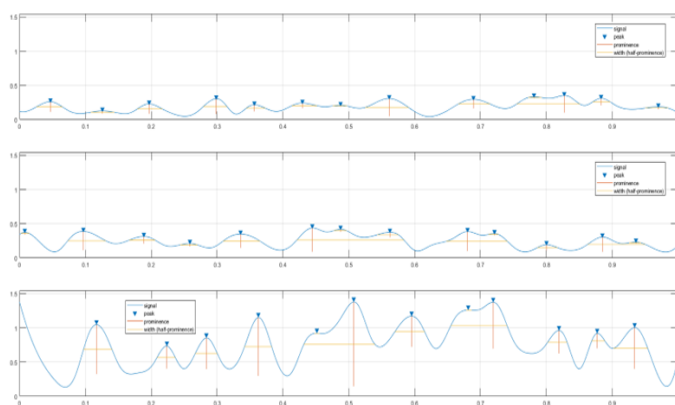


Figure 6: Signal envelopes and peak amplitudes

Table 1: Peak values counted because of thresholding

Signal	Lower threshold	Upper threshold	Total number of peaks
Signal 1 (180-212)	0	0.3	12035
Signal 1 (180-212)	0.3	0.6	858
Signal 1 (180-212)	0.6	0.9	19
Signal 1 (180-212)	0.9	1.2	3
Signal 1 (180-212)	1.2	-	0
Signal 2 (212-355)	0	0.3	10259
Signal 2 (212-355)	0.3	0.6	2133
Signal 2 (212-355)	0.6	0.9	156
Signal 2 (212-355)	0.9	1.2	25
Signal 2 (212-355)	1.2	-	3
Signal 3 (355-500)	0	0.3	724
Signal 3 (355-500)	0.3	0.6	3938
Signal 3 (355-500)	0.6	0.9	4001
Signal 3 (355-500)	0.9	1.2	2943
Signal 3 (355-500)	1.2	-	961

Table 2: Calculated peak numbers and highest peak values

	Semolina sizes	Sample number	Total number of peaks	Max peak value
Signal 1	180-212 micron	523260	12915	1.0861
Signal 2	212-355 micron	523260	12576	1.2135
Signal 3	355-500 micron	523260	12567	1.6519

As the size of the semolina particles increases, the amplitudes produced when they hit the piezoelectric element also increases. The highest amplitudes for semolina particles with sizes between 180-212 μm , 212-355 μm , 355-500 μm were measured as 1.08, 1.21 and 1.65 V, respectively. In the amplitude counts, the amplitude numbers exceeding the 0.6V threshold were measured as 21, 184 and 7095, respectively. As a result, it was seen that the amplitude and numbers produced by the particles hitting the piezoelectric element and the sizes of the particles could be measured. Consistent with previous studies, it was

observed that the amplitudes produced increased with the size of the impacting particles.

ACKNOWLEDGEMENTS

The author would like to thank Mr. Muhammet Emre Irmak for his contributions to the study.

REFERENCES

- [1] P. J. Coghil, "Particle Size of Pneumatically Conveyed Powders Measured Using Impact Duration," *Particle & Particle Systems Characterization*, vol. 24, no. 6, pp. 464–469, Dec. 2007, doi: <https://doi.org/10.1002/ppsc.200601080>.
- [2] A. Boschetto and F. Quadri, "Powder size measurement by acoustic emission," *Measurement*, vol. 44, no. 1, pp. 290–297, Jan. 2011, doi: <https://doi.org/10.1016/j.measurement.2010.10.005>.
- [3] M. Uher and P. Benes, "Measurement of particle size distribution by the use of acoustic emission method," May 2012, doi: <https://doi.org/10.1109/i2mtc.2012.6229375>.
- [4] L. Gao, Y. Yan, R. M. Carter, D. Sun, P. Lee, and C. Xu, "On-line particle sizing of pneumatically conveyed biomass particles using piezoelectric sensors," *Fuel*, vol. 113, pp. 810–816, Nov. 2013, doi: <https://doi.org/10.1016/j.fuel.2012.12.029>.
- [5] Y. Hu, X. Huang, X. Qian, L. Gao, and Y. Yan, "Online particle size measurement through acoustic emission detection and signal analysis," May 2014, doi: <https://doi.org/10.1109/i2mtc.2014.6860883>.
- [6] M. Kobayashi, T. Miyachi, M. Hattori, S. Sugita, S. Takechi, and N. Okada, "Dust detector using piezoelectric lead zirconate titanate with current-to-voltage converting amplifier for functional advancement," *Earth, Planets and Space*, vol. 65, no. 3, pp. 167–173, Mar. 2013, doi: <https://doi.org/10.5047/eps.2012.08.011>.
- [7] James Robert Coombes and Y. Yan, "Experimental investigations into the use of piezoelectric film transducers to determine particle size through impact analysis," *Kent Academic Repository (University of Kent)*, May 2016, doi: <https://doi.org/10.1109/i2mtc.2016.7520464>.
- [8] G. Zhang, Y. Yan, Y. Hu, and G. Zheng, "On-line size measurement of pneumatically conveyed particles through acoustic emission sensing," *Powder Technology*, vol. 353, pp. 195–201, Jul. 2019, doi: <https://doi.org/10.1016/j.powtec.2019.05.023>.
- [9] G. Zhang, Y. Yan, Y. Hu, and G. Zheng, "Investigations into the sensing mechanism of acoustic emission sensors for particle size measurement in a particular case: normal incidence," *Measurement science & technology*, vol. 32, no. 7, pp. 075107–075107, May 2021, doi: <https://doi.org/10.1088/1361-6501/abe338>.
- [10] E. Nsugbe, A. Starr, I. Jennions, and C. R. Carcel, "Particle Size Distribution Estimation of A Mixture of Regular and Irregular Sized Particles Using Acoustic Emissions," *Procedia Manufacturing*, vol. 11, pp. 2252–2259, 2017, doi: <https://doi.org/10.1016/j.promfg.2017.07.373>.
- [11] N. Çankaya, "In-Line Measurement of Particle Weight of Pulses Such as Chickpea by Piezoelectric Sensor," *IEEE Access*, 2024, DOI: 10.1109/ACCESS.2024.3484489

Neurological Disorders: Types, Diagnosis, and Machine Learning and Deep Learning Approaches

MEHR ALİ QASİMİ¹, ZÜLEYHA YILMAZ ACAR²

¹Selcuk University, Institute of Science, Department of Computer Engineering, Konya/Türkiye,
q1.mehrali@gmail.com

²Selcuk University, Faculty of Technology, Department of Computer Engineering, Konya/Türkiye,
zuleyhayilmaz@selcuk.edu.tr

Abstract - Brain tumors, Alzheimer's disease, stroke, and multiple sclerosis are categorized as neurological disorders. These conditions are among the most challenging diseases in medicine and affect more than one billion people worldwide. In addition to having a detrimental impact on the patient's life and the lives of their family members, in certain cases, these diseases can lead to the patient's death. Therefore, it is critical to detect these issues as early as possible in order to slow down or even halt the progression of the disease.

Artificial intelligence (AI), a field of computer science, has demonstrated great capability in analyzing complex healthcare data and identifying key patterns within large datasets in today's modern world. Advances in AI applications in the medical field have shown promising potential in diagnosing and identifying diseases. The subfields of AI, including machine learning (ML) and deep learning (DL), have garnered significant attention from the medical industry. ML and DL are increasingly being employed in medicine to achieve precision treatment and enhance patients' quality of life. Due to their ability to identify complex and abstract patterns, ML and DL methods have proven beneficial in neuroimaging studies of neurological disorders, which are characterized by subtle and scattered changes. These methods are particularly useful for detecting and predicting neurological disorders.

This study provides an overview of the types and diagnostic methods of neurological disorders. It also includes an examination of the applications and techniques of ML and DL, which are among the most impactful fields in computer science, as applied to neurological disorders.

Keywords - Deep Learning, Machine Learning, Neuroimaging, Neurological Disorders, Prediction, Artificial Intelligence.

I. INTRODUCTION

DUE to population growth and an aging demographic, the prevalence of long-term neurological diseases (NDs) is increasing [1]. It is estimated that one in five individuals worldwide suffers from neurological issues, with the prevalence of neurological disorders rising more significantly among younger populations than adults [2]. These conditions are often accompanied by symptoms such as pain, disorientation, muscle weakness, loss of consciousness, depression, and other issues. In modern medicine, diagnosing these diseases presents a major challenge [3]. According to a

study conducted by the World Health Organization, conditions such as epilepsy, Alzheimer's disease, and stroke affect over one billion people globally [1].

Diseases affecting the nervous system are known as neurological disorders, with over 600 distinct diseases estimated to affect the nervous system, including Alzheimer's disease, epilepsy, stroke, Parkinson's disease, dementia, migraine, multiple sclerosis, brain tumors, and others [4]. Neurological disorders, commonly identified by behavioral, cognitive, or brain-related issues, typically impair an individual's ability to walk, speak, learn, or move. These conditions directly affect the human spine and brain and are extremely serious. Significant impairments associated with certain brain diseases can lead to an increased risk of mortality [5].

The variability in brain responses exhibited by each individual makes the treatment of neurological disorders highly challenging. Neurological issues need to be identified as quickly as possible, and currently, the primary criterion for diagnosing neurological diseases is the expertise of medical professionals, requiring neurologists to spend hours diagnosing a single patient [3]. This highlights the need for a reliable and advanced diagnostic system that can assist in the identification and assessment of such disorders. There are several stages in identifying neurological disorders, and technological advancements that enhance the accuracy and effectiveness of clinical assessments can improve traditional clinical practices and enable more affordable and personalized treatment options [6]. To achieve this goal, various neuroimaging techniques and analytical approaches based on deep learning (DL) and machine learning have been developed for the early detection and appropriate treatment of these diseases [7].

This study provides insights into subtypes and diagnostic methods for neurological diseases, including brain tumors, Alzheimer's, stroke, and multiple sclerosis, while also summarizing proposed diagnostic approaches from the literature. It aims to support researchers focused on diagnosing neurological diseases by highlighting areas where artificial intelligence can contribute to understanding these diseases and enhancing diagnostic methods.

II. NEUROLOGICAL DISORDER: TYPES AND DIAGNOSIS METHODS

A. Brain Tumor

The brain, the most complex organ in the human body, controls all of our mental and physical functions [8]. A brain tumor is a mass formed by abnormal cells in the brain. Early diagnosis of brain tumors is crucial for saving lives [5]. Symptoms of brain tumors include headaches, seizures, speech and vision problems, memory loss, and loss of balance [8]. In the early stages of the disease, brain cancer is at a treatable and potentially curable stage. A brain tumor example is shown as Figure 1.



Figure 1: A brain tumor example [9].

1) Types of Brain Tumor:

Primary brain tumors are classified into two categories: benign and malignant. Benign tumors do not spread to other parts of the body. However, they can become problematic if they compress normal brain tissue or press on nerves. Malignant tumors, on the other hand, have the ability to invade nearby tissues and may even spread to other parts of the body, posing a life-threatening risk.

According to the World Health Organization (WHO), brain tumors are classified into four grades [5]:

- Pilocytic Astrocytomas or Grade I: These tumors grow slowly and do not spread rapidly. They are often almost entirely removable through surgery and are associated with increased long-term survival rates.
- Low-Grade Astrocytomas or Grade II: These tumors grow slowly but have the potential to spread to other tissues and transform into higher-grade tumors. They may recur even after surgical removal.
- Anaplastic Astrocytomas or Grade III: These tumors can infiltrate nearby tissues and grow more quickly than Grade II tumors. Surgery may be supplemented with chemotherapy or radiation therapy for this type.
- Glioblastoma Multiforme or Grade IV: Known as the most aggressive and invasive tumors, these can even utilize blood vessels to support their rapid growth.

2) Diagnosis of Brain Tumor:

A neurologist specialist typically makes the diagnosis of brain cancer. MRI and/or CT scans are two common imaging methods used in this process, while a biopsy, in which a sample of brain tissue or cells is taken during brain surgery, represents another diagnostic procedure. Completing a thorough neurological and physical examination is also a critical step in the diagnostic process [10]. The most frequently used

techniques for investigating brain cancers include positron emission tomography (PET), magnetic resonance imaging (MRI), computed tomography (CT), angiography, and X-rays [5].

Magnetic resonance imaging (MRI) is a widely used tool for understanding tumors and tracking their progression. Segmenting brain tissue and tumors through MRI imaging has garnered significant attention. As part of standard diagnostic procedures, MRI images are examined to detect abnormalities and diagnose brain tumors. Manual tumor segmentation from MRI images by experts is time-consuming, subjective, and prone to inter-observer variability. Consequently, automated segmentation offers a solution to these challenges, reducing the need for manual segmentation. Other imaging methods used in brain tumor analysis, such as CT and PET scans, have limitations; the radioactive tracers employed can pose health risks [11].

Additionally, compared to standard X-ray images, CT scans provide more detailed information [12]. Furthermore, brain tumors smaller than 3 mm, which may not be detectable through CT or MRI, can be identified using near-infrared imaging technology, which transmits temperature data via wireless sensor networks (WSNs). Figure 2 shows the positive and negative tumor images.

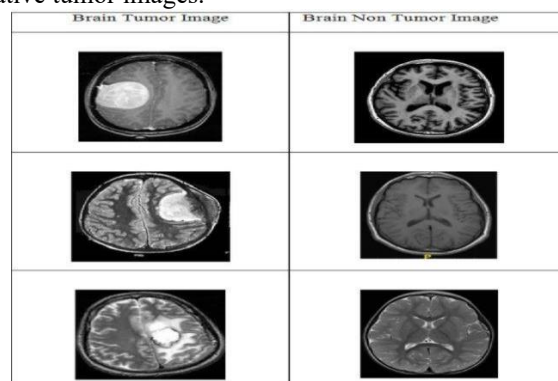


Figure 2: Positive and negative tumor images [13].

B. Alzheimer's Disease

Alzheimer's disease (AD) is the most severe and common neurodegenerative disorder. It begins with the death of brain cells in regions associated with language and memory, leading to memory loss and impairments in daily functioning [14]. In developed countries, AD is one of the leading causes of death, affecting not only psychological functions but also having a profound impact on daily life.

1) Types of AD:

Alzheimer's disease manifests in three primary forms:

- Familial Alzheimer's Disease (FAD): Genetic mutations cause this rare form of Alzheimer's, typically affecting individuals in their 30s, 40s, and 50s.
- Early-Onset Alzheimer's Disease: Individuals under the age of 65 are susceptible to this type of Alzheimer's. It is relatively rare compared to late-onset Alzheimer's and progresses more rapidly.
- Late-Onset Alzheimer's Disease: This most common form usually affects individuals over 65. It does not

appear to be caused by genetic mutations and progresses slowly. A progression of AD is illustrated as Figure 3.

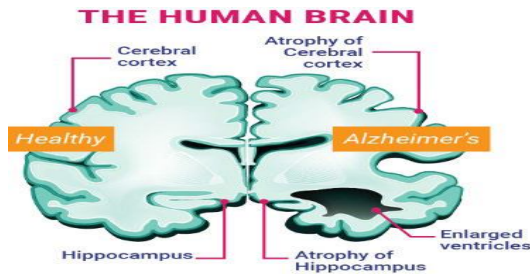


Figure 3: Progression of AD from mild to severe [15].

2) Diagnosis of AD:

In the past, experts used manual detection systems to diagnose the progression of various stages of Alzheimer's disease (AD). However, errors made by these manual systems could lead to adverse outcomes for patients. Early stages of AD can now be automatically detected using the latest machine learning (ML) and deep learning (DL) methods [14].

Early detection of the disease is crucial to slow its progression and delay Alzheimer's. Cognitive domains affected by AD, such as language, memory, and orientation, are assessed using neuropsychological tests. Cerebrospinal fluid (CSF) analysis is among the most reliable diagnostic methods due to its ability to reveal biomarkers, but the procedure to obtain this fluid is an expensive medical intervention that not all patients can afford [16].

Imaging techniques like PET and MRI provide essential biomarker information by showing early structural and molecular changes in the brain. Recent advances also allow doctors to use PET scans to visualize tau and A β proteins associated with AD [17].

C. Stroke

Stroke is a medical emergency caused by an interruption in blood flow, leading to the sudden death of brain cells in a specific area. This condition can result in outcomes such as paralysis, speech impairment, memory loss, coma, and permanent brain damage.

The sooner a stroke victim receives medical intervention, the greater their chances of achieving a full recovery.

1) Types of Stroke:

The two most common types of stroke are hemorrhagic and ischemic [18]:

- Hemorrhagic stroke: Caused by bleeding or leaking blood from arteries.
- Ischemic stroke: Results from insufficient blood and oxygen reaching the brain.

Depending on the cause of reduced blood flow to the brain, ischemic stroke can be further classified as thrombotic or embolic.

2) Diagnosis of Stroke:

Neurological physiological techniques such as blood tests and evoked potential tests, along with brain imaging techniques like CT, MRI, X-rays, EKG, and EEG, can be used to diagnose stroke [4]. Despite the potential risks associated with these

procedures, such as radiation exposure or allergic reactions to contrast agents, CT and MRI are the most commonly used for stroke diagnosis.

Additionally, EEG data can be collected and analyzed in real-time, at a low cost, and with fewer adverse effects. It is considered a practical and cost-effective method for monitoring stroke patients, particularly those with high recurrence rates in daily life, through 24-hour EEG readings [19].

D. Multiple Sclerosis

One of the most common causes of acquired neurological disorders in young adults is multiple sclerosis (MS). The disease progression is characterized by autoimmune and inflammatory central nervous system demyelination and unpredictable relapses [20-21].

1) Types of MS:

The most common types of multiple sclerosis (MS) are: Asymptomatic MS, Relapsing-Remitting MS, Secondary Progressive MS, Primary Progressive MS, and Progressive-Relapsing MS [22]:

In the majority of MS patients, the disease follows a relapsing-remitting form, either partially or fully. The initial attack is typically classified as a clinically isolated syndrome. Most of these patients will transition to a progressive phase, known as secondary progressive MS, with or without relapses. In some individuals who do not experience relapses, a slow-progressing course, known as primary progressive MS, is observed. When some individuals experience relapses in the later stages, this condition is referred to as progressive-relapsing MS. In some cases of relapsing-remitting MS, the disease progresses with minimal disability and a mild course over the years; this form is known as benign MS.

2) Diagnosis of MS:

MS diagnosis requires both spatially and temporally dispersed lesions in the central nervous system to be observed. Typically, a combination of imaging, blood tests, clinical evaluation of symptoms, cerebrospinal fluid examination, and assessment of evoked potentials is used to rule out other diseases with similar symptoms.

Currently, MRI is the most useful method for diagnosing MS. Diffusion MRI scanning is a type of detection technique that uses magnetic fields and radio waves to measure the relative water content of body tissues and distinguish between healthy and diseased tissues [5].

III. MACHINE LEARNING AND DEEP LEARNING APPROACHES FOR DIAGNOSIS

A. The Studies on Brain Tumor Diagnosis

The study focusing on developing brain tumor classification models presents an approach that combines deep learning methods with Generative Adversarial Networks (GAN)-based data augmentation. It investigates improvements in MRI processing for brain tumor classification, concentrating on the use of contemporary deep learning models and enhancing model performance through GANs [23]. The study demonstrates significant increases in tumor classification accuracy and robustness with the proposed data augmentation

method.

In another study on brain tumor classification [24], a novel ensemble model combining the advantages of existing deep learning models such as VGG16, InceptionV3, and Xception achieves an accuracy of 96.94%. This approach has proven to be useful for classifying four categories: pituitary cancers, glioma tumors, meningioma tumors, and no tumor, with varying performance metric values.

The study introduces a deep learning approach for brain tumor diagnosis based on MRI images and CNNs. A dataset divided into four categories—glioma tumors, meningioma tumors, no tumor, and pituitary tumors—was used [25]. The performance of InceptionV3, ResNet50, and VGG16 was compared by automatically extracting features from MR images.

A study employing Dense-Net and Dark-Net classifiers for 3D MR image-based brain tumor diagnosis presents an advanced method. By efficiently segmenting and classifying tumors, it achieves a dice similarity coefficient of 97.91% and an accuracy of 98.67% [26]. These findings demonstrate the strong performance of deep learning models in accurately identifying and categorizing brain tumors from medical images and how such models can improve diagnostic precision.

Another study [27] focuses on how image augmentation techniques perform when applied to deep transfer learning models for brain tumor detection. Evaluations were carried out on three well-known models both before and after data augmentation: InceptionV3, VGG16, and DenseNet169. The results show that image augmentation significantly enhances the accuracy and robustness of these models. This highlights the importance of developing medical datasets to provide reliable frameworks for brain tumor classification.

The study [28] aims to apply deep learning approaches for classifying brain cancers in MRI images, specifically investigating spatiotemporal models. By using advanced neural network designs like ResNet (2+1)D and ResNet Mix, it improves the classification accuracy of low- and high-grade gliomas. These models, initially developed for video recognition, were adapted to 3D MRI data, ensuring more accurate tumor identification and classification. Furthermore, the study concludes that the application of transfer learning techniques strengthens model performance and results in significant improvements in computational efficiency.

B. The Studies on Alzheimer's Disease Diagnosis

This study [29] presents a technique for Alzheimer's Disease (AD) diagnosis using spectrogram features extracted from speech data, enabling families to recognize the early onset of the disease and take preventive actions. The study utilizes machine learning algorithms in combination with Internet of Things (IoT) devices to distinguish between AD patients and healthy controls based on voice data obtained from 23 elderly adults. The ability of artificial intelligence to analyze subtle changes in speech that human listeners might miss is emphasized in this work.

The study [15] examines relevant studies that use MRI data along with various ML and DL methods to investigate

Alzheimer's disease. One of the methods in the study involves assessing cognitive function and protein levels in cerebrospinal fluid (CSF). MRI biomarkers, especially for early detection of mild cognitive impairment (MCI), are noted to hold great promise for distinguishing dementia and control groups. The study also mentions that diffusion tensor imaging (DTI) and functional MRI contribute information about the connections in AD, though regulatory approval for clinical use is still needed.

In this study [30], an automated method using sagittal MRI is developed to define AD. Transfer Learning (TL) approaches are applied to enhance accuracy by using sagittal MRIs from the ADNI and OASIS datasets. The study emphasizes the need for TL to develop deep learning models and reduce the costs associated with dataset collection, especially when data samples are scarce. The proposed method includes a support vector machine (SVM) classifier for model evaluation and a ResNet artificial neural network (ANN) for feature extraction, showing good performance on both datasets. To improve detection accuracy, the developed method integrates MRI data with patient demographics.

This research [31] distinguishes between typical ML and DL methodologies in AD diagnosis. It highlights the necessity of image preprocessing to enhance learning quality, using popular deep learning techniques such as CNNs, RNNs, DNNs, Autoencoders (AEs), and Deep Belief Networks (DBNs) for classification. The study also examines the challenges related to managing datasets in deep learning applications, offering suggestions for potential corrections based on existing research.

The study [32] combines multimodal data such as MRI imaging, electronic health records (EHR), and genetic information (SNP) to build a DL architecture for differentiating between AD, MCI, and control groups. 3D CNNs are used for analyzing MRI data, while stacked denoising autoencoders are employed to extract features from clinical and genetic data. The results show that the deep models outperform traditional models like decision trees (DT) and SVM. Additionally, the research proposes an approach to feature interpretation using degradation and clustering analysis, emphasizing the potential of DL to improve prediction accuracy in AD staging.

This study [33] provides a hybrid DL technique for early AD diagnosis by integrating neuropsychological test scores and multimodal imaging data using CNN and Long Short-Term Memory (LSTM) algorithms. The approach uses two datasets consisting of PET and MRI images. Ant Colony Optimization (ACO) is applied to reduce noise, modified fuzzy C-means is used to segment images, and DNN is used for final classification.

C. The Studies on Stroke Diagnosis

The proposed study [34] uses a variety of DL and ML algorithms to predict stroke probability at an early stage. Extreme Gradient Boosting (XGBoost), AdaBoost, LightGBM, Random Forest, Decision Tree, Logistic Regression, K-Nearest Neighbors, SVM, Naive Bayes, and ANN models were utilized. Random Forest achieved a maximum accuracy of 99%, followed by a four-layer ANN with 92.39% accuracy. The study concludes that ML techniques outperform deep neural

networks in stroke prediction. Principal Component Analysis (PCA) was used to minimize the dimensionality of the dataset and retain the most important features for classification.

This paper [19] presents a stroke prediction algorithm based on DL applied directly to raw EEG data, regardless of frequency features. Real-time EEG data were used to create and compare various models such as LSTM, Bidirectional LSTM, CNN-LSTM, and CNN-Bidirectional LSTM. The CNN-Bidirectional LSTM model achieved 94.0% accuracy. The findings indicate that stroke risk can be predicted in real time, providing a non-invasive, low-cost technique for early stroke diagnosis. The study emphasizes the potential for real-time monitoring, especially for those at high risk of recurrent strokes.

This study [35] used three deep learning object detection networks—Faster R-CNN, YOLOv3, and SSD—to autonomously identify ischemic stroke lesions in brain MRI images, achieving an accuracy rate of 89.77%. Important information for the diagnosis and management of ischemic stroke was obtained from statistical analysis of the lesion areas, shapes, and associated impairments. For small object detection, Faster R-CNN was combined with SSD and YOLOv3, with YOLOv3 incorporating multi-scale feature layers to improve speed. The results support both stroke prevention and smart-assisted diagnosis.

This study [36] focuses on improving the quality of CT scan images of stroke patients using image optimization and noise reduction preprocessing approaches. Eight machine learning algorithms were used to classify stroke images into ischemic and hemorrhagic subtypes: KNN, Naive Bayes, Logistic Regression, Decision Tree, Random Forest, Multi-Layer Perceptron (MLP-NN), DL, and SVM. The Random Forest model produced the best results with the highest accuracy (95.97%), precision (94.39%), recall (96.12%), and F1 score (95.39%).

In this study [37] diffusion-weighted MRI (DWI) and MRI images of patients who suffered an acute ischemic stroke within 24 hours of symptom onset were analyzed using automated image processing. From each image, 89 vector features were extracted using infarct segmentation, image registration, and feature extraction processes. Three ML models—RO, SVM, and LR—were created to categorize the onset of the stroke within 4.5 hours. All ML models demonstrated high specificity (>0.85) and superior sensitivity (>0.70) when compared to human readings of DWI and MRI mismatches. The results suggest that ML methods enhance the process of identifying potential candidates for acute intervention.

This paper [38] proposes an automated method for defining and segmenting CT scans using deep learning networks. The model achieved 100% accuracy in classifying images as either hemorrhagic stroke or non-stroke. A combination of Mask R-CNN and KNN achieved 99.93% specificity and 99.73% accuracy for stroke segmentation within four seconds. The effectiveness and robustness of the proposed strategy were highlighted while addressing segmentation and classification challenges.

D. The Studies on Multiple Sclerosis Diagnosis

The study based on optical coherence tomography (OCT) and clinical data [39] demonstrates that ML methods can improve early diagnosis and predict the long-term course of MS. According to the research, the thickness of the retinal nerve fiber layer (RNFL) is considered a valid biomarker for MS, which can lead to personalized treatment plans for patients. The study, using a five-layer architecture consisting of a bidirectional LSTM layer and several input layers, highlighted the effectiveness of OCT in providing fast, affordable, and non-invasive evaluation of RNFL thickness. By training LSTM models through backpropagation over a 10-year follow-up period, the study emphasized its effectiveness in predicting MS diagnosis and disability progression.

This study [40] evaluates the use of deep learning algorithms to differentiate between neuromyelitis optica spectrum disorder (NMOSD) and MS. A 3D-CNN model trained on MRI images and clinical data achieved an accuracy of 71.1%. Neurologists showed moderate reliability ($k = 0.47\text{--}0.50$), but the model provided faster results and greater consistency (inter-rater reliability, $k = 1.0$).

This paper [41] assesses the practical use of a Deep Back Projection Network (DBPN) model in improving the image quality of accelerated routine brain MRI scans in MS patients. The study focuses on T1-weighted volumetric measurements (thalamus, total brain, gray matter, and white matter), which are associated with neurological outcomes in MS patients. The DL model successfully improved accelerated T1-weighted image quality while maintaining the relationship between volumetric measurements and neurological outcomes, making the images similar to traditional MRI scans. According to the study, improved imaging can provide clinically meaningful insights into the progression of MS.

This study [42] develops a DL model based on a single hidden layer for MS diagnosis prediction. The model includes a regularization term to prevent overfitting and reduce complexity. Compared to four traditional ML methods, the model showed better prediction accuracy (0.8965) and reduced loss (3.573). From a 74-gene expression profile associated with MS etiology, 35 significant features were selected for model training using dimensionality reduction techniques. The YSA model offers two benefits: improving prediction accuracy and providing insights into genetic variations affecting MS sensitivity. The findings suggest that the model could assist in clinical decision-making and the development of preventive medications.

In this study [43] lesions in the MRI images of RRMS patients were classified using DL. The segmentation classification was performed, and performance was evaluated using five-fold cross-validation on predictions combined through a fully connected network. The study indicates that DL detected healing lesions without the need for gadolinium-based contrast agents, which would improve patient safety and reduce costs.

This study [44] used brain MRI data to create a DL model based on a modified ResNet18 to differentiate between

NMOSD and MS. After training with 5-channel images from 3D MRI scans, the model achieved 76.1% accuracy, 0.85 AUC, 77.3% sensitivity, and 74.8% specificity. The study indicates that white matter lesions are significant classifiers. This model provides a strong tool for clinical differentiation between MS and NMOSD, supporting the use of ML in neurology.

IV. CONCLUSION

The growing number of people affected by neurological disorders and the difficulty in diagnosing these conditions highlight the need for early detection and better treatment options. Recent developments in artificial intelligence (AI), particularly in machine learning (ML) and deep learning (DL), offer promising solutions for the diagnosis and prediction of these diseases. ML and DL techniques, when applied to neuroimaging, have shown great potential in identifying subtle patterns and improving the accuracy of diagnoses. This study highlights the significance of AI-driven diagnostic approaches in managing neurological disorders, facilitating early disease detection, providing personalized treatment plans, and improving patient care. As AI technology keeps advancing, it has the potential to greatly improve how we diagnose and treat these complex conditions.

REFERENCES

- [1] A. K. Tripathi and A. K. Tiwari, "Prediction of Neurological Disorders using Deep Learning: A Review," no. Icacse 2021, pp. 135–139, 2022, doi: 10.5220/0010564100003161.
- [2] R. G and L. P.V.S, "Prediction of Neurological Disorders among Children Using Machine Learning Techniques," *Helix*, vol. 9, no. 1, pp. 4775–4780, 2019, doi: 10.29042/2019-4775-4780.
- [3] S. Paul, J. K. Verma, A. Datta, R. N. Shaw, and A. Saikia, "Deep learning and its importance for early signature of neuronal disorders," *2018 4th Int. Conf. Comput. Commun. Autom. ICCCA 2018*, pp. 1–5, 2018, doi: 10.1109/CCAA.2018.8777527.
- [4] S. Siuly and Y. Zhang, "Medical Big Data: Neurological Diseases Diagnosis Through Medical Data Analysis," *Data Sci. Eng.*, vol. 1, no. 2, pp. 54–64, 2016, doi: 10.1007/s41019-016-0011-3.
- [5] M. F. Mridha *et al.*, "A Comprehensive Survey on the Progress, Process, and Challenges of Lung Cancer Detection and Classification," *J. Healthc. Eng.*, vol. 2022, pp. 1–45, 2022, doi: 10.1155/2022/5905230.
- [6] G. Bouallegue, R. Djemal, S. A. Alshebeili, and H. Aldhalaan, "A Dynamic filtering df-rnn deep-learning-based approach for eeg-based neurological disorders diagnosis," *IEEE Access*, vol. 8, pp. 206992–207007, 2020, doi: 10.1109/ACCESS.2020.3037995.
- [7] M. B. T. Noor, N. Z. Zenia, M. S. Kaiser, S. Al Mamun, and M. Mahmud, "Application of deep learning in detecting neurological disorders from magnetic resonance images: a survey on the detection of Alzheimer's disease, Parkinson's disease and schizophrenia," *Brain Informatics*, vol. 7, no. 1, 2020, doi: 10.1186/s40708-020-00112-2.
- [8] H. Kaur and A. K. Gill, "Review of Brain Tumor Detection Using Various Techniques," *Int. J. Adv. Res. Comput. Sci. Softw. Eng.*, vol. 7, no. 5, pp. 867–870, 2017, doi: 10.23956/ijarcsse/v7i4/0221.
- [9] P. G. Rajan and C. Sundar, "Brain Tumor Detection and Segmentation by Intensity Adjustment," *J. Med. Syst.*, vol. 43, no. 8, pp. 1–13, 2019, doi: 10.1007/s10916-019-1368-4.
- [10] G. Kumar, P. Kumar, and D. Kumar, "Brain Tumor Detection Using Convolutional Neural Network," *2021 IEEE Int. Conf. Mob. Networks Wirel. Commun. ICMNWC 2021*, no. 9, pp. 83–88, 2021, doi: 10.1109/ICMNWC52512.2021.9688460.
- [11] G. Raut, A. Raut, J. Bhagade, J. Bhagade, and S. Gavhane, "Deep learning approach for brain tumor detection and segmentation," *2020 Int. Conf. Conver. to Digit. World - Quo Vadis, ICCDW 2020*, no. Iccdw, 2020, doi: 10.1109/ICCDW45521.2020.9318681.
- [12] J. Amin, M. Sharif, A. Haldorai, M. Yasmin, and R. S. Nayak, "Brain tumor detection and classification using machine learning: a comprehensive survey," *Complex Intell. Syst.*, vol. 8, no. 4, pp. 3161–3183, 2022, doi: 10.1007/s40747-021-00563-y.
- [13] A. Miglani, H. Madan, S. Kumar, and S. Kumar, "A literature review on brain tumor detection and segmentation," *Proc. - 5th Int. Conf. Intell. Comput. Control Syst. ICICCS 2021*, no. Iccics, pp. 1513–1519, 2021, doi: 10.1109/ICICCS51141.2021.9432342.
- [14] P. Khan *et al.*, "Machine Learning and Deep Learning Approaches for Brain Disease Diagnosis: Principles and Recent Advances," *IEEE Access*, vol. 9, pp. 37622–37655, 2021, doi: 10.1109/ACCESS.2021.3062484.
- [15] S. Al-Shoukry, T. H. Rassem, and N. M. Makbol, "Alzheimer's diseases detection by using deep learning algorithms: A mini-review," *IEEE Access*, vol. 8, pp. 77131–77141, 2020, doi: 10.1109/ACCESS.2020.2989396.
- [16] E. Perez-Valero, M. Á. Lopez-Gordo, C. M. Gutiérrez, I. Carrera-Muñoz, and R. M. Vilchez-Carrillo, "A self-driven approach for multi-class discrimination in Alzheimer's disease based on wearable EEG," *Comput. Methods Programs Biomed.*, vol. 220, p. 106841, 2022, doi: 10.1016/j.cmpb.2022.106841.
- [17] A. P. Porsteinsson, R. S. Isaacson, S. Knox, M. N. Sabbagh, and I. Rubino, "Diagnosis of Early Alzheimer's Disease: Clinical Practice in 2021," *J. Prev. Alzheimer's Dis.*, vol. 8, no. 3, pp. 371–386, 2021, doi: 10.14283/jpad.2021.23.
- [18] D. Kuriakose and Z. Xiao, "Pathophysiology and treatment of stroke: Present status and future perspectives," *Int. J. Mol. Sci.*, vol. 21, no. 20, pp. 1–24, 2020, doi: 10.3390/ijms21207609.
- [19] Y. A. Choi *et al.*, "Deep learning-based stroke disease prediction system using real-time bio signals," *Sensors*, vol. 21, no. 13, 2021, doi: 10.3390/s21134269.
- [20] F. Moazami, A. Lefevre-Utile, C. Papaloukas, and V. Soumelis, "Machine Learning Approaches in Study of Multiple Sclerosis Disease Through Magnetic Resonance Images," *Front. Immunol.*, vol. 12, no. August, pp. 1–8, 2021, doi: 10.3389/fimmu.2021.700582.
- [21] Z. Y. Acar, F. Başçıftı, and A. H. Ekmekci, "A Convolutional Neural Network model for identifying Multiple Sclerosis on brain FLAIR MRI," *Sustain. Comput. Informatics Syst.*, vol. 35, p. 100706, 2022.
- [22] I. A. Zavalishin *et al.*, "Diagnosis and treatment of multiple sclerosis," *Zhurnal Nevrol. i Psihiatr. Im. S.S. Korsakova*, vol. 111, no. 6, pp. 89–96, 2011, doi: 10.2169/naika.110.2021.
- [23] M. M. E. Yurtsever, Y. Atay, B. Arslan, and S. Sagiroglu, "Development of brain tumor radiogenomic classification using GAN - based augmentation of MRI slices in the newly released gazi brains dataset," *BMC Med. Inform. Decis. Mak.*, vol. 6, 2024, doi: 10.1186/s12911-024-02699-6.
- [24] S. Hossain, A. Chakrabarty, T. R. Gadekallu, M. Alazab, and M. J. Piran, "Vision Transformers, Ensemble Model, and Transfer Learning Leveraging Explainable AI for Brain Tumor Detection and Classification," *IEEE J. Biomed. Heal. Informatics*, vol. 28, no. 3, pp. 1261–1272, 2024, doi: 10.1109/JBHI.2023.3266614.
- [25] M. I. Mahmud, M. Mamun, and A. Abdelgawad, "A Deep Analysis of Brain Tumor Detection from MR Images Using Deep Learning Networks," *Algorithms*, vol. 16, no. 4, pp. 1–19, 2023, doi: 10.3390/a16040176.
- [26] S. Solanki, U. P. Singh, S. S. Chouhan, and S. Jain, "Brain Tumor Detection and Classification Using Intelligence Techniques: An Overview," *IEEE Access*, vol. 11, no. January, pp. 12870–12886, 2023, doi: 10.1109/ACCESS.2023.3242666.
- [27] A. H. Nizamani, Z. Chen, A. A. Nizamani, and U. A. Bhatti, "Advance brain tumor segmentation using feature fusion methods with deep U-Net model with CNN for MRI data," *J. King Saud Univ. - Comput. Inf. Sci.*, vol. 35, no. 9, p. 101793, 2023, doi: 10.1016/j.jksuci.2023.101793.
- [28] S. Chatterjee, F. A. Nizamani, A. Nürnberger, and O. Speck, "Classification of brain tumours in MR images using deep spatiotemporal models," *Sci. Rep.*, vol. 12, no. 1, pp. 1–11, 2022, doi: 10.1038/s41598-022-05572-6.
- [29] L. Liu, S. Zhao, H. Chen, and A. Wang, "A new machine learning method for identifying Alzheimer's disease," *Simul. Model. Pract. Theory*, vol. 99, p. 102023, 2020, doi: 10.1016/j.simpat.2019.102023.
- [30] A. Puente-Castro, E. Fernandez-Blanco, A. Pazos, and C. R. Munteanu, "Automatic assessment of Alzheimer's disease diagnosis

- based on deep learning techniques,” *Comput. Biol. Med.*, vol. 120, no. February, p. 103764, 2020, doi: 10.1016/j.compbimed.2020.103764.
- [31] D. A. Arafa, H. E. D. Moustafa, A. M. T. Ali-Eldin, and H. A. Ali, *Early detection of Alzheimer's disease based on the state-of-the-art deep learning approach: a comprehensive survey*, vol. 81, no. 17. Multimedia Tools and Applications, 2022. doi: 10.1007/s11042-022-11925-0.
- [32] J. Venugopalan, L. Tong, H. R. Hassanzadeh, and M. D. Wang, “Multimodal deep learning models for early detection of Alzheimer's disease stage,” *Sci. Rep.*, vol. 11, no. 1, pp. 1–13, 2021, doi: 10.1038/s41598-020-74399-w.
- [33] P. Balaji, M. A. Chaurasia, S. M. Bilfaqih, A. Muniyasamy, and L. E. G. Alsid, “Hybridized Deep Learning Approach for Detecting Alzheimer's Disease,” *Biomedicines*, vol. 11, no. 1, 2023, doi: 10.3390/biomedicines11010149.
- [34] S. Rahman, M. Hasan, A. K. Sarkar, and F. Khan, “Classification of Parkinson's Disease using Speech Signal with Machine Learning and Deep Learning Approaches,” *Eur. J. Electr. Eng. Comput. Sci.*, vol. 7, no. 2, pp. 20–27, 2023, doi: 10.24018/ejece.2023.7.2.488.
- [35] S. Zhang, S. Xu, L. Tan, H. Wang, and J. Meng, “Stroke Lesion Detection and Analysis in MRI Images Based on Deep Learning,” *J. Healthc. Eng.*, vol. 2021, 2021, doi: 10.1155/2021/5524769.
- [36] T. Badriyah, N. Sakinah, I. Syarif, and D. R. Syarif, “Machine Learning Algorithm for Stroke Disease Classification,” *2nd Int. Conf. Electr. Commun. Comput. Eng. ICECCE 2020*, no. June, pp. 12–13, 2020, doi: 10.1109/ICECCE49384.2020.9179307.
- [37] H. Lee *et al.*, “Machine Learning Approach to Identify Stroke Within 4.5 Hours,” *Stroke*, vol. 51, no. 3, pp. 860–866, 2020, doi: 10.1161/STROKEAHA.119.027611.
- [38] Y. Xu *et al.*, “Deep Learning-Enhanced Internet of Medical Things to Analyze Brain CT Scans of Hemorrhagic Stroke Patients: A New Approach,” *IEEE Sens. J.*, vol. 21, no. 22, pp. 24941–24951, 2021, doi: 10.1109/JSEN.2020.3032897.
- [39] A. Montolio *et al.*, “Machine learning in diagnosis and disability prediction of multiple sclerosis using optical coherence tomography,” *Comput. Biol. Med.*, vol. 133, 2021, doi: 10.1016/j.compbimed.2021.104416.
- [40] H. Kim *et al.*, “Deep Learning-Based Method to Differentiate Neuromyelitis Optica Spectrum Disorder From Multiple Sclerosis,” *Front. Neurol.*, vol. 11, no. November, pp. 1–8, 2020, doi: 10.3389/fneur.2020.599042.
- [41] A. Mani *et al.*, “Applying Deep Learning to Accelerated Clinical Brain Magnetic Resonance Imaging for Multiple Sclerosis,” *Front. Neurol.*, vol. 12, no. September, pp. 1–9, 2021, doi: 10.3389/fneur.2021.685276.
- [42] E. R. Ponce de Leon-Sanchez, O. A. Dominguez-Ramirez, A. M. Herrera-Navarro, J. Rodriguez-Resendiz, C. Paredes-Orta, and J. D. Mendiola-Santibañez, “A Deep Learning Approach for Predicting Multiple Sclerosis,” *Micromachines*, vol. 14, no. 4, pp. 1–12, 2023, doi: 10.3390/mi14040749.
- [43] P. A. Narayana, I. Coronado, S. J. Sujit, J. S. Wolinsky, F. D. Lublin, and R. E. Gabr, “Deep learning for predicting enhancing lesions in multiple sclerosis from noncontrast MRI,” *Radiology*, vol. 294, no. 2, pp. 398–404, 2020, doi: 10.1148/radiol.2019191061.
- [44] J. M. Seok *et al.*, “Differentiation between multiple sclerosis and neuromyelitis optica spectrum disorder using a deep learning model,” *Sci. Rep.*, vol. 13, no. 1, pp. 1–9, 2023, doi: 10.1038/s41598-023-38271-x.

Development of a Skull Phantom for Artificial EEG Wave Generation and Analysis

ELİF NUR SELÇUK¹, EKREM GÜLSEVİNÇLER², GÖKÇENUR ÇAKMAK KEÇELİOĞLU¹,
HATİCE AKMAN³, MUSTAFA REŞİT USAL¹

¹Süleyman Demirel University, Isparta/Turkey, elifnurselcuk99@gmail.com

²Sinop University, Sinop/Turkey, egulsevinctler@sinop.edu.tr

¹Süleyman Demirel University, Isparta/Turkey, gokcenurcakmak@sdu.edu.tr

³Applied Sciences University of Isparta, Isparta/Turkey, haticeakman@isparta.edu.tr

¹Süleyman Demirel University, Isparta/Turkey, resitusal@sdu.edu.tr

Abstract - Electroencephalography (EEG) electrodes are special sensors used to measure the electrical activity of the brain. These electrodes are placed on the scalp and provide information about neural activity by recording brain waves. EEG electrodes are usually small metal disks that are attached to the scalp with a conductive gel or adhesive. The development of biomedical devices, such as EEG electrodes, often requires human trials, which are complicated by the variability of EEG signals, their dependence on movement, and ethical concerns. To address these challenges, artificial tissues (phantoms) are used as substitutes for human organs. This study involved the creation of a skull phantom designed to generate artificial EEG waves. Using Fused Deposition Modeling (FDM) with polylactic acid (PLA) and A366/CQ black steel, beams were placed at three locations on the PLA skull phantom. The phantom was tested at motor speeds ranging from 10 to 100 rpm, and EEG waves were recorded using a piezo sensor connected to an Open BCI board. The collected data were simulated using the Low Resolution Electromagnetic Tomography (LORETA) program, followed by filtering and classification using Python. For the classification process, the Root Mean Square method, a machine learning algorithm, was utilized. In conclusion, the gamma frequency band is dominant across most channels, indicating a high intensity of high-frequency brain activity (above 30 Hz) in the EEG data. Gamma waves are typically associated with intense cognitive processing, perceptual tasks, and conscious awareness. These waves help us understand the complex and integrated functions of the brain and provide important information about neurological health. Analysis of gamma waves can also be used to diagnose and treat neurological disorders.

Keywords – skull phantom, EEG, artificial brain waves, piezo sensor, 3D printing.

I. INTRODUCTION

THE electrical signals produced by the brain are attenuated by the highly resistive skull and reflected onto the scalp. The signal patterns obtained through measurements using non-invasive electrodes placed on the scalp are referred to as electroencephalography (EEG) [1], [2]. A potential difference is generated between two electrodes due to the natural and periodic electrical stimuli produced by neural cell clusters in the brain. This potential difference varies with the distance of the

electrodes from the center of the skull. Additionally, each individual has unique brain activity patterns, which change throughout the day. Electrical signal measurements of brain activity are utilized in the identification of various neurological disorders (such as epilepsy and schizophrenia), in brain-computer interfaces (BCI), and in the investigation of cognitive processes such as perception, attention, memory, and sleep [3], [4]. The diagnosis of these disorders or emotional disturbances is made using EEG brain waves. These waves include alpha (8-12 Hz), beta (12-35 Hz), gamma (>35 Hz), theta (4-8 Hz), delta (0.5-4 Hz), and mu (8-13 Hz) waves [5], [6], [7]. These waves, which arise depending on an individual's mental and emotional state, include delta waves, which are observed during the deep stages of sleep and relaxation. Theta waves, which occur during light sleep, are active when daydreaming or engaging in creative thinking. Alpha waves emerge when the eyes are closed. Beta waves become dominant during attention, focus, wakefulness, and anxiety. Gamma waves are observed during intense concentration and complex problem-solving, when the brain is actively engaged. Although they share the same frequency as alpha waves, mu waves are seen in situations of physical stillness, rest, and the absence of motor activity [8], [9], [10], [11]. These emotional states can change at any moment in an individual, and as a result, the characteristics of brain waves may vary from person to person [12].

In the development of EEG equipment, it is necessary to conduct experiments on humans or animals to assess the detectability of brain signals. However, testing on living organisms presents various challenges due to ethical concerns and the variability of the signals. Therefore, artificial organs and tissues (phantoms) that can mimic the responses of biological organs or systems to external stimuli have been developed [13], [14], [15].

Depending on the application, phantoms are produced either as single-layered or multi-layered, both numerically and physically [16], [17]. In addition, liquid phantoms are commonly used in specific absorption rate (SAR) calculations for the development of wireless devices [18], [19]. Currently, phantoms have been developed for a variety of tissues/organs. Skull [20], brain [21], breast [22], [23], liver [24] are some of the types of phantoms. The materials and number of layers of phantoms are determined based on their application. For

example, conductivity ratios are prioritized for the development and testing of EEG electrodes, and single-layer phantoms are used, while in ultrasound imaging, the viscosity value of the materials is important, and multi-layer phantoms are more suitable [25], [26], [27]. In addition, EEG skull phantoms are produced as multi-layered structures consisting of scalp, skull, cerebrospinal fluid (CSF), and brain, due to the anisotropic nature of the brain, in order to accurately represent the source location arrangement [28], [29], [30], [31]. A variety of materials, such as polydimethylsiloxane (PDMS)-carbon fiber [31], gelatin [32], polypropylene [33], silicone [34], polylactic acid (PLA) [20], agar [35], agarose gel (graphite powder, carbon black, and salt) [36] and clay [37] are used to produce EEG skull phantoms. Phantoms produced using gelatin and molded through casting methods are generally heavy, and the lifespan of gelatin phantoms is also relatively short [38], [39]. Phantoms produced using PLA material through 3D printing have a mass and electron density equivalent to water and soft tissues, and they also have the capacity to replicate the radiological properties of bone tissue. Using Fused Deposition Modeling (FDM) 3D printers, anatomically realistic phantoms are successfully produced using PLA filament [38], [40].

To generate artificial EEG brain waves, signal generators or signal generators are used to apply sinusoidal waves with the desired frequency and amplitude to the phantom, thus producing artificial EEG signals [41], [42]. In this study, a skull phantom was produced using PLA filament with an FDM printer. To generate artificial EEG brain signals, instead of using a signal generator, a motor operating at different rotational speeds (rpm) was employed to drive PLA and A366/CQ black steel beams. A piezo sensor detected vibration or voltage changes and converted the mechanical changes into electrical signals, thus generating artificial signals. The obtained signals were visualized using OpenBCI. The collected signal data were transferred to a Python program, and bandpass and low-pass filtering operations were applied. Frequency-based classification was performed on the filtered signals to determine the dominant channel and waves. The signals were also transferred to the Low Resolution Electromagnetic Tomography (LORETA) program for brain simulations.

II. MATERIALS AND METHODS

A. Materials

The PLA filament was sourced from Porima Polymer Technologies Inc. in Turkey. The skull phantom and beams were printed using a Creality CR-10 Smart FDM printer, with the printing temperature set to 210 °C, a bed temperature of 60 °C, and a speed of 100 mm/s. The 15 mm diameter piezo disc sensor was purchased from Robotistan (Turkey). The 16-channel biosensing board used for acquiring artificial EEG brain waves was purchased from OpenBCI [43]. Brain simulations of the artificially generated signals were performed using the LORETA program [44]. The beams have dimensions of 180*30*1.5 mm, with a total length of 70 mm allocated for the motor and the fixed beam placement.

B. Preparation of Phantom System

In this study, the design of the skull phantom was carried out using Fusion 360 student version. The designed model was exported in .stl format, and then a gcode file was generated for production using an FDM printer. As shown in Figure 1a, three distinct regions located at the back of the skull phantom were driven with a PLA beam and an A366/CQ black steel beam. The three regions were named lower, middle, and upper according to the names of the PLA and A366/CQ black steel beams and the rpm speeds (e.g., PLA_lower_10rpm). To simulate the brain, thermogel molds were placed inside the phantom, with piezo sensors integrated into these molds. The piezo sensors were connected to an oscilloscope to ensure signal stabilization. The mechanical vibrations obtained through motor actuation aim to simulate brain signals via the piezo sensors. The cerebrospinal fluid (CSF), skull, and scalp were modeled using PLA and thermogel layers, which act to attenuate the incoming vibrations. The stabilized piezo sensors were connected to the OpenBCI board to acquire EEG data. The obtained data were visualized using the OpenBCI GUI and exported to Excel.

The collected data were transferred to a Python program for signal processing. In the first step, band-pass and low-pass filtering were applied to suppress high-frequency noise. In these filtering processes, the sampling frequency was set to 256 Hz, and the filter order was set to 4. The signals were classified according to frequency bands. The artificial EEG brain signals measured with OpenBCI were classified based on which of the alpha, beta, theta, delta, or gamma waves were dominant across 8 channels.

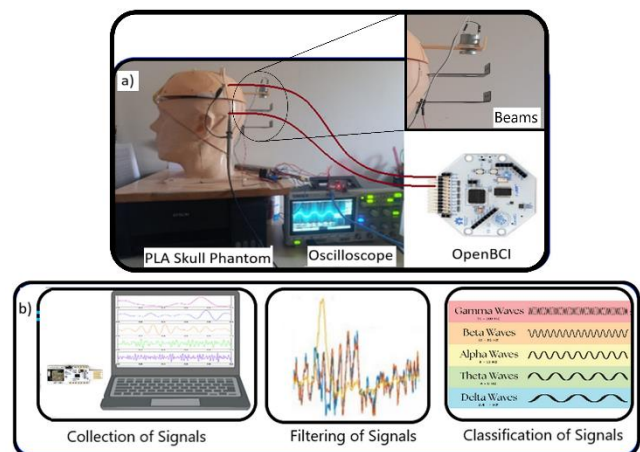


Figure 1: a) Artificial signal generation setup b) Signal processing steps.

III. RESULTS

A. Artificial Brain Waves on OpenBCI board

In this study, the piezo sensor serves as a means to convert mechanical energy into electrical signals. The responses of the piezo sensor, connected to the OpenBCI board, are presented separately for the lower, middle, and upper regions, based on the different rpm speeds applied to the A366/CQ black steel and PLA beams.

When the motor was operated at 10 rpm speed on the A366/CQ black steel beam in the lower region, slight fluctuations were observed on all eight channels, even though the piezo sensor was connected to only two channels. However, when the same speed and position were applied to the PLA beam, no fluctuations were observed on the other channels. This suggests that the steel beam caused noise, while the PLA beam attenuated it. When the motor was operated at 100 rpm, high amplitude fluctuations occurred on both beams, but the fluctuations on the PLA beam were less frequent compared to the steel beam. In the fast Fourier transform (FFT) graph of the OpenBCI GUI board, 8 sharp peaks were detected on the steel beam in the 0-10 Hz frequency range, while 6 sharp peaks were observed on the PLA beam. At the 10 rpm motor speed, the amplitude of the steel beam was higher than that of the PLA beam. These findings indicate that the PLA beam exhibits damping properties at all rpm speeds (Figure 2).

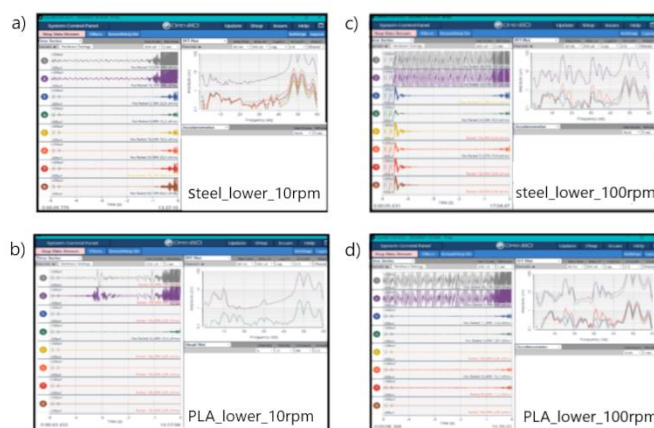


Figure 2: OpenBCI GUI visuals of the steel and PLA beams at 10 and 100 rpm speeds in the lower region.

In the middle region, when the motor was operated at 10 rpm on both beams, slight fluctuations were observed on all eight channels, even though the piezo sensor was connected to only two channels. Similarly, when the motor was operated at 100 rpm in the same region, noise was observed on the other six channels. In this region as well, the PLA beam exhibited some damping properties compared to the steel beam (Figure 3).

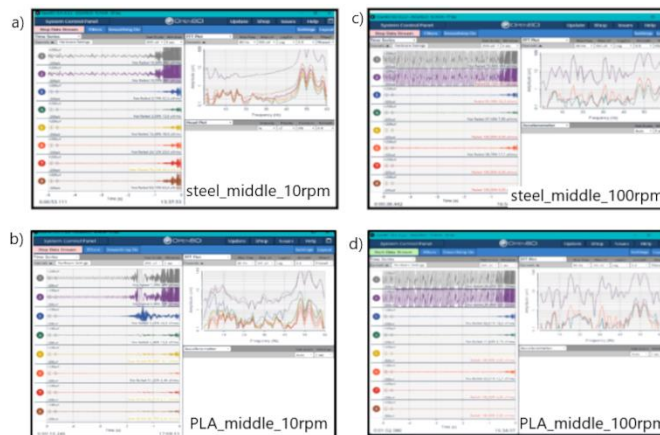


Figure 3: OpenBCI GUI visuals of the steel and PLA beams at 10 and 100 rpm speeds in the middle region.

When the motor was operated at 10 rpm speed in the upper region, more noise was observed on both beams compared to the lower and middle regions. In the FFT graph of the OpenBCI board, 9 sharp peaks were detected for the steel beam, while 6 sharp peaks were observed for the PLA beam (Figure 4). Additionally, it was determined that the amplitude values were higher in the steel beam. At all rpm speeds and in all three regions, the PLA beam was observed to attenuate noise more effectively.

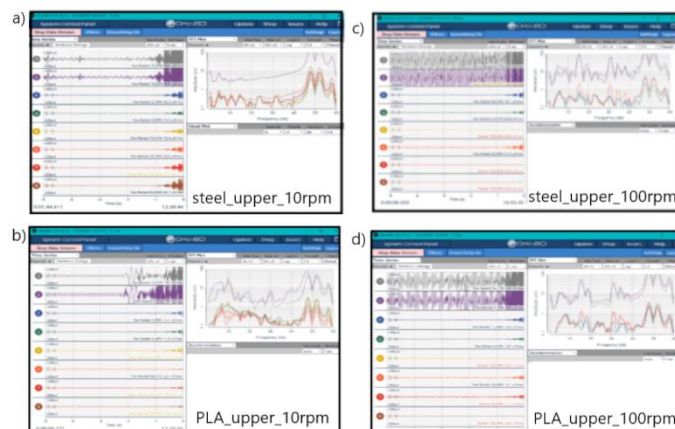


Figure 4: OpenBCI GUI visuals of the steel and PLA beams at 10 and 100 rpm speeds in the upper region.

B. Signal processing

The raw data obtained from the OpenBCI GUI was transferred to the Python environment. After the data was recorded at a 256 Hz sampling frequency, it was processed first with a bandpass filter and then a low-pass filter with a cutoff frequency of 50 Hz. Subsequently, the signal power for each channel was calculated, and classification based on band power was performed at the dominant frequency values.

As shown in Table 1, when the motor was operated at 10 rpm in the lower region, the theta wave was dominant, while at speeds of 20 rpm and above, the dominant wave shifted to the Gamma band. The dominance of the theta band at low speeds indicates that the vibrations in the steel beam occurred at low frequencies. As the speed increased, the higher-frequency, more energetic Gamma waves became dominant, indicating that the beam responded to rapidly increasing frequencies.

In the middle region, the Gamma wave was dominant at all speeds, showing that this region was continuously sensitive to high-frequency vibrations, regardless of the motor speed. The continuous dominance of the Gamma band in the middle region indicates that this region exhibits a more stable and high-frequency response compared to the motor speed.

In the upper region, the Gamma wave was dominant at motor speeds of 10-50 rpm and 70-90 rpm, while the Beta wave was dominant at 60 rpm and 80 rpm. This shift suggests that the

upper region responds with a more sensitive frequency reaction to speed increases. The fact that the Beta band is at a lower frequency compared to the Gamma band and becomes dominant at 60 rpm and 80 rpm speeds indicates that, at these speeds, the upper region transitions to low-frequency waves. This behavior observed in the upper region shows that, at certain speeds, the energy density is concentrated at lower frequencies, with frequency increasing rapidly as speed increases.

Table 1: Artificial Brain Waves for A366/CQ black stell Based on Position and Speed

Location and rpm	Artificial Brain Waves
steel_lower_10rpm	Theta
steel_lower_20rpm	Gamma
steel_lower_30rpm	Gamma
steel_lower_40rpm	Gamma
steel_lower_50rpm	Gamma
steel_lower_60rpm	Gamma
steel_lower_70rpm	Gamma
steel_lower_80rpm	Gamma
steel_lower_90rpm	Gamma
steel_lower_100rpm	Gamma
steel_middle_10rpm	Gamma
steel_middle_20rpm	Gamma
steel_middle_30rpm	Gamma
steel_middle_40rpm	Gamma
steel_middle_50rpm	Gamma
steel_middle_60rpm	Gamma
steel_middle_70rpm	Gamma
steel_middle_80rpm	Gamma
steel_middle_90rpm	Gamma
steel_middle_100rpm	Gamma
steel_upper_10rpm	Gamma
steel_upper_20rpm	Gamma
steel_upper_30rpm	Gamma
steel_upper_40rpm	Gamma
steel_upper_50rpm	Gamma
steel_upper_60rpm	Beta
steel_upper_70rpm	Gamma
steel_upper_80rpm	Beta
steel_upper_90rpm	Gamma
steel_upper_100rpm	Gamma

As a result of all the steel beam experiments, it was observed that the dominant wave band quickly changed between the lower, middle, and upper regions. Especially in the middle region, where the Gamma waves were dominant regardless of speed, this suggests that the frequency response of this region is more stable compared to the other regions. In contrast, in the lower and upper regions, as the speed increased, the frequency band shifted upwards (e.g., from Theta to Gamma), indicating that the beam in these regions vibrates at higher energy frequencies.

In Table 2, artificial brain waves for the PLA beam are shown based on rpm and position (location). In the lower region, Beta waves were observed to be dominant at speeds of 10 rpm, 20 rpm, 40 rpm, and 60 rpm. At other speeds (30 rpm, 50 rpm, 70

rpm, 80 rpm, 90 rpm, and 100 rpm), the Gamma wave became dominant. This indicates that at lower speeds (particularly 10 rpm, 20 rpm, 40 rpm, and 60 rpm), the PLA beam produced lower-frequency vibrations (Beta waves). As the speed increased beyond 30 rpm, the dominant wave shifted to the Gamma band, and the beam exhibited vibrations at higher frequencies. In the lower region, as the speed increased, a transition to higher-frequency (Gamma) waves was observed, showing that with the increase in speed, the energy density in the lower region shifted towards higher frequencies.

In the middle region, Beta waves were dominant at speeds of 10 rpm and 30 rpm, while in all other speeds (20 rpm, 40 rpm, and above), Gamma waves were dominant. This shows that the middle region is generally sensitive to high-frequency waves (Gamma) and only exhibits lower-frequency vibrations at specific low speeds (10 rpm and 30 rpm). The dominance of the Gamma band in the middle region suggests that this region is more independent of speed and more sensitive to high-frequency vibrations compared to other regions.

In the upper region, Beta waves were dominant at 10 rpm, 30 rpm, and 50 rpm speeds, while at other speeds (20 rpm, 40 rpm, and above 60 rpm), Gamma waves became dominant. These findings show that at lower speeds (10 rpm, 30 rpm, and 50 rpm), the upper region exhibited lower-frequency vibrations (Beta), and as speed increased, it transitioned to higher-frequency (Gamma) waves. Although the upper region predominantly exhibited Gamma waves at speeds of 20 rpm and above, the dominance of the Beta wave again at 50 rpm indicates that the upper region is sensitive to speed changes and that at certain speeds, the dominant wave frequency decreases.

Table 2: Artificial Brain Waves for PLA Based on Position and Speed

Location and rpm	Artificial Brain Waves
PLA_lower_10rpm	Beta
PLA_lower_20rpm	Beta
PLA_lower_30rpm	Gamma
PLA_lower_40rpm	Beta
PLA_lower_50rpm	Gamma
PLA_lower_60rpm	Beta
PLA_lower_70rpm	Gamma
PLA_lower_80rpm	Gamma
PLA_lower_90rpm	Gamma
PLA_lower_100rpm	Gamma
PLA_middle_10rpm	Beta
PLA_middle_20rpm	Gamma
PLA_middle_30rpm	Beta
PLA_middle_40rpm	Gamma
PLA_middle_50rpm	Gamma
PLA_middle_60rpm	Gamma
PLA_middle_70rpm	Gamma
PLA_middle_80rpm	Gamma
PLA_middle_90rpm	Gamma
PLA_middle_100rpm	Gamma
PLA_upper_10rpm	Beta
PLA_upper_20rpm	Gamma
PLA_upper_30rpm	Beta
PLA_upper_40rpm	Gamma

PLA_upper_50rpm	Beta
PLA_upper_60rpm	Gamma
PLA_upper_70rpm	Gamma
PLA_upper_80rpm	Gamma
PLA_upper_90rpm	Gamma
PLA_upper_100rpm	Gamma

As a result of the experiments conducted with the PLA beam, it was observed that in all three regions, the Gamma wave became dominant as the speed increased. This finding suggests that with the increase in speed, the beam generally exhibits higher-frequency vibrations. In the lower and upper regions, a transition from Beta to Gamma waves was observed with an increase in speed, while in the middle region, Gamma waves were predominantly dominant. This indicates that the middle region responds with high-frequency vibrations more independently of speed changes and is less variable compared to the other regions. Overall, the PLA beam shows dominance of Beta waves at lower speeds (10-30 rpm), while at higher speeds (40 rpm and above), more energetic Gamma waves become dominant. These results demonstrate that the PLA beam transitions to higher-frequency vibrations (Gamma) as speed increases. Gamma waves (30-70 Hz) are observed as fast (80-200 Hz) and very fast (400-800 Hz). Very fast gamma waves are seen before and at the onset of epileptic seizures, and the amplitudes of these signals also increase. In addition, an increase in gamma waves is also observed in cases of depression [45]. Based on these findings, the phantom system developed in this study could be used in neurological applications such as epilepsy and depression.

A power spectral analysis was performed on the data collected from all experiments (Figure 5). Power Spectral Density (PSD) analysis is used to measure the power density of the frequency components of a signal [46]. In the graph, a high power spectral density is observed in the 0-20 Hz frequency range. This frequency band is typically dominated by low-frequency waves, which are commonly seen in EEG or other biological signals. Low-frequency components such as delta, theta, and alpha waves are associated with brain states such as rest, sleep, awareness, and relaxation.

Beyond 20 Hz, a noticeable decrease in power density is observed, although some significant peaks are still present in this range. This suggests that the signal contains energy at specific mid-range frequencies. A distinct increase in power was observed around 50 Hz; this rise typically indicates

interference from environmental factors or power lines.

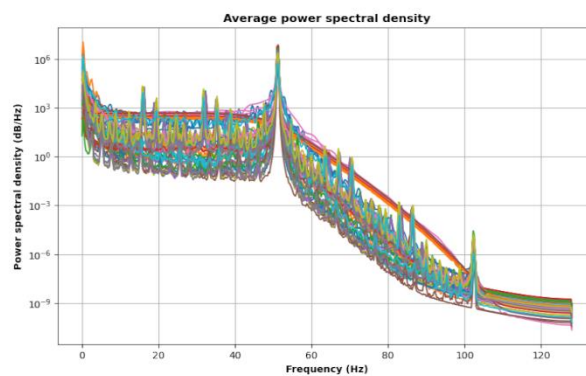


Figure 5: PSD analyses of steel and PLA beams in all regions.

Above 50 Hz, a sharp decrease in PSD values is observed. This indicates that the signal contains less energy in the higher frequency components, and consequently, these frequencies are relatively less dominant in the signal. The decrease in power density at higher frequencies reflects the fact that biological signals tend to be more concentrated in the lower frequency ranges. The graph is plotted on a logarithmic scale, with the power spectral density axis presented in dB/Hz units and shown with logarithmic increments. Notably, after 50 Hz, PSD values rapidly decreased from approximately 10^3 levels to 10^{-6} levels. This suggests that the signal energy at higher frequencies is nearly negligible.

The low energy levels observed for high-frequency components like gamma waves in the PSD analysis are due to certain factors in the data processing and analysis during classification. One of these factors is the normalization of each feature to ensure it is on the same scale and range during the classification process. This adjustment can cause gamma waves, which appear to have low energy in the PSD analysis, to become more dominant in the classification. Another contributing factor is the use of frequency band power-based classification algorithms, which tend to highlight the distinctive characteristics of a frequency band, even if it has low energy. In this case, gamma waves, which may appear low in the PSD, can become more prominent in the classification process.

C. Artificial Brain Waves on LORETA

The EEG data obtained from the OpenBCI board were transferred to the LORETA software, through which artificial brain visualizations were created. The purpose of this program was to visually demonstrate which regions of the brain become active based on the motor speed of the skull phantom's three different regions in the rear part.

Figure 6 presents the visualizations generated using LORETA from the data collected from the lower region. According to the results, when the steel beam was operated at a 10 rpm motor speed, signals were predominantly observed in the frontal lobe, despite being driven from the rear lower region. In contrast, for the same motor speed and position with the PLA beam, the signal intensity became more prominent in the parietal lobe. At a 100 rpm motor speed, signals from both beams were dominant in the parietal lobe of the lower region.

The parietal lobe plays an important role in processing sensory information, spatial awareness, and motor skills. The dominance of the 10 and 100 Hz frequencies in this area suggests that these frequencies influence the electrical activity in the parietal lobe, indicating a more intense brain function or activity in this region [47], [48].

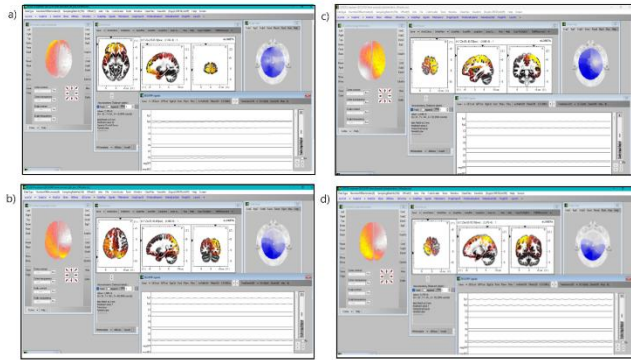


Figure 6: In the lower section, (a) Steel 10 rpm; (b) PLA 10 rpm; (c) Steel 100 rpm; (d) PLA 100 rpm LORETA visualizations.

Figure 7 presents the visualizations generated from the data collected from the middle region using the LORETA program. When the PLA beam was driven at a speed of 10 rpm from the middle region, the signals were observed in the temporal lobe. The temporal lobe is a crucial part of the brain, particularly playing a critical role in auditory functions, language processing, memory, and emotional response regulation. Located on both sides of the brain, the temporal lobes are specifically involved in the processing of sound, meaningful language production, and memory storage. The hippocampus within the temporal lobe acts as a central structure in memory-related processes, while the amygdala plays a role in regulating emotional responses. Additionally, the temporal lobe is linked to visual perception and recognition functions, thus playing a vital role in helping individuals make sense of the world around them. The temporal lobe of the brain is particularly involved in cognitive processes such as sound and language processing, memory consolidation, and emotional response management. The electrical activity in the temporal lobe is often intensified by auditory stimuli or linguistic information. Furthermore, any disruption or damage to this region can have serious effects on language disorders, memory loss, and emotional responses. In this context, studying the temporal lobe holds significant importance for understanding neurological diseases and psychiatric disorders [49], [50]. The signals became concentrated in the parietal lobe as a result of the driving of the steel beam at 10 and 100 rpm in the middle region and the PLA beam at 100 rpm.

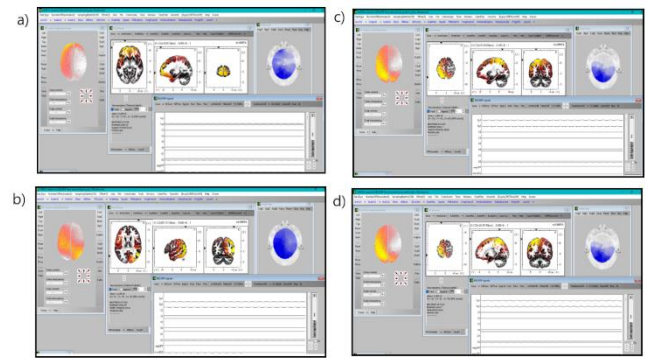


Figure 7: In the middle section, (a) Steel 10 rpm; (b) PLA 10 rpm; (c) Steel 100 rpm; (d) PLA 100 rpm LORETA visualizations.

In Figure 7, it is observed that, as a result of the steel and PLA beams being driven at 10 and 100 rpm motor speeds from the upper region, both beams and speeds show concentration in the frontal lobe.

The frontal lobe is located at the front of the brain and is a crucial region associated with high-level cognitive functions. As the largest lobe in the brain, the frontal lobe is responsible for fundamental tasks such as thinking, planning, decision-making, problem-solving, and motor control. It also plays a key role in managing complex processes such as personality, emotional regulation, and social interaction. The frontal lobe is connected to executive functions and encompasses abilities such as strategy development, planning, and action monitoring to help individuals achieve their goals. Additionally, the frontal lobe is responsible for motor control and coordinates voluntary movements of the body. Specifically, the prefrontal cortex is related to cognitive and emotional processes such as attention, memory, language, and empathy. Therefore, damage or disorders in the frontal lobe can lead to significant changes in decision-making, attention management, and social behavior [46], [51], [52].

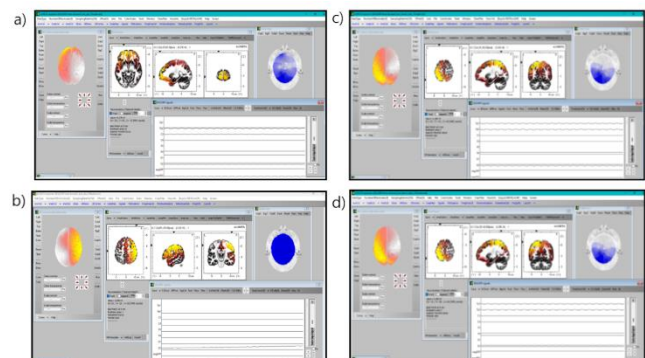


Figure 8: In the upper section, (a) Steel 10 rpm; (b) PLA 10 rpm; (c) Steel 100 rpm; (d) PLA 100 rpm LORETA visualizations.

CONCLUSIONS

In this study, a skull phantom was created using PLA material to obtain artificial EEG brain waves. The responses of

A366/CQ black steel and PLA material beams, placed at the rear of this phantom, to different motor speeds were analyzed separately for the lower, middle, and upper regions. The results of the study showed that, at each speed and in each region, the PLA beam demonstrated greater noise-damping properties compared to the steel beam. This indicates that PLA material has the capacity to reduce vibrations and generates signals with less interference than steel. All findings suggest that the PLA beam could be used as a vibration-damping alternative in biomechanical applications. Additionally, the vibrations of the steel beam were examined through signal power and frequency spectra obtained at different motor speeds. After processing the raw data with bandpass and low-pass filters, the signal power was calculated using PSD analysis, and frequency band classification was performed.

In the lower region, theta waves were observed to be dominant when the motor speed was 10 rpm. However, as the speed increased, especially at speeds of 20 rpm and above, artificial gamma waves became dominant. This indicates that the steel beam vibrates at lower frequencies at low speeds but exhibits higher frequency vibrations as the speed increases. In the middle region, artificial gamma waves were dominant across all speed ranges, indicating that this region is sensitive to high-frequency vibrations regardless of motor speed and provides a more stable response. In the upper region, frequency band fluctuations were observed as the speed increased. Artificial gamma waves were dominant at speeds of 10-50 rpm and 70-90 rpm, while artificial beta waves became more pronounced at speeds of 60 rpm and 80 rpm. This shows that the upper region exhibits a more sensitive frequency response to speed changes and shifts to lower frequency vibrations at certain speeds. In the experiments conducted with the PLA beam, artificial beta waves were found to be dominant at low speeds in the lower region, with a transition to gamma waves observed as speed increased. In the middle region, artificial gamma waves were dominant regardless of speed, while in the upper region, artificial beta waves were observed to become dominant at certain speeds. These findings indicate that the PLA beam shifts to higher frequency vibrations as speed increases, and that the frequency response of each region changes rapidly with speed.

An increase in the amplitude of very fast gamma waves is observed before and at the onset of epilepsy seizures, and gamma waves also increase in cases of depression. These findings suggest that the phantom system developed in this study could be used in neurological applications, such as epilepsy and depression. In the next study, wireless EEG electrodes will be produced and tested on this phantom using the artificial waves obtained from the phantom.

Appendix

EEG	Electroencephalography
FDM	Fused deposition modeling
PLA	Polylactic acid
BCI	Brain computer interface
CSF	Cerebrospinal fluid

SAR	Specific absorption rate
PDMS	Polidimetilsiloksan
FFT	Fast fourier transform
PSD	Power spectral density
LORETA	Low resolution electromagnetic tomography

ACKNOWLEDGMENT

This research is funded by the Scientific Research Projects Coordination Unit of Süleyman Demirel University under project number FDK-2022-8789.

REFERENCES

- [1] C. M. Michel and D. Brunet, "EEG source imaging: A practical review of the analysis steps," *Front Neurol*, vol. 10, no. APR, 2019, doi: 10.3389/fneur.2019.00325.
- [2] M. N. Rayi A, *Electroencephalogram*. 2022.
- [3] A. Chaddad, Y. Wu, R. Kateb, and A. Bouridane, "Electroencephalography Signal Processing: A Comprehensive Review and Analysis of Methods and Techniques," Jul. 01, 2023, *Multidisciplinary Digital Publishing Institute (MDPI)*. doi: 10.3390/s23146434.
- [4] S. A. Murad and N. Rahimi, "Unveiling Thoughts: A Review of Advancements in EEG Brain Signal Decoding into Text," Apr. 2024, doi: 10.1109/TCDS.2024.3462452.
- [5] P. A. Abhang, B. W. Gawali, and S. C. Mehrotra, "Technological Basics of EEG Recording and Operation of Apparatus," in *Introduction to EEG- and Speech-Based Emotion Recognition*, Elsevier, 2016, pp. 19–50. doi: 10.1016/b978-0-12-804490-2.00002-6.
- [6] E. C. Djama, R. I. Ramadhan, M. I. Mandasari, and D. Djajasmita, "Identification of post-stroke eeg signal using wavelet and convolutional neural networks," *Bulletin of Electrical Engineering and Informatics*, vol. 9, no. 5, pp. 1890–1898, 2020, doi: 10.11591/eei.v9i5.2005.
- [7] Y. Ikeda, Y. Nishimura, N. Shin, and S. Higuchi, "A study of EEG mu neurofeedback during action observation," *Exp Brain Res*, vol. 238, no. 5, pp. 1277–1284, 2020, doi: 10.1007/s00221-020-05808-9.
- [8] M. Shafiq Ibrahim, S. Rahayu Kamat, S. Shamsuddin, and F. Kejuruteraan Pembuatan, "Malaysian Journal on Composites Science and Manufacturing The Role of Brain Wave Activity by Electroencephalogram (EEG) in Assessing Cognitive Skills as an Indicator for Driving Fatigue: A Review," *Malaysian Journal on Composites Science and Manufacturing*, vol. 11, no. 1, pp. 19–31, 2023.
- [9] R. Andrade-Machado, V. Benjumea Cuartas, and I. K. Muhammad, "Recognition of interictal and ictal discharges on EEG. Focal vs generalized epilepsy," *Epilepsy and Behavior*, vol. 117, p. 107830, 2021, doi: 10.1016/j.yebeh.2021.107830.
- [10] G. Kaur, M. Gupta, and R. Kumar, "Swarm Intelligence-Based Feature Selection Algorithm of EEG Classification for Brain Emotion Detection: A Review," *2023 IEEE 8th International Conference for Convergence in Technology, I2CT 2023*, pp. 1–7, 2023, doi: 10.1109/I2CT57861.2023.10126425.
- [11] Y. Wang, S. Wang, and M. Xu, "The function of color and structure based on eeg features in landscape recognition," *Int J Environ Res Public Health*, vol. 18, no. 9, 2021, doi: 10.3390/ijerph18094866.
- [12] K. Goyal, D. A. Borkholder, and S. W. Day, "A biomimetic skin phantom for characterizing wearable electrodes in the low-frequency regime," *Sens Actuators A Phys*, vol. 340, Jun. 2022, doi: 10.1016/j.sna.2022.113513.
- [13] C. C. Ploch, C. S. S. A. Mansi, J. Jayamohan, and E. Kuhl, "Using 3D Printing to Create Personalized Brain Models for Neurosurgical Training and Preoperative Planning," *World Neurosurg*, vol. 90, pp. 668–674, Jun. 2016, doi: 10.1016/j.wneu.2016.02.081.

- [14] T. J. Seebeck and H. Kõiv, "Developing tissue phantom materials with required electric conductivities."
- [15] D. D. Klimov, M. A. Buinov, A. A. Vorotnikov, A. M. Meleshnikov, and Y. V. Poduraev, "Production approaches of a human brain tissue phantom for robot-assisted stereotactic biopsy," in *Journal of Physics: Conference Series*, Institute of Physics Publishing, Nov. 2019. doi: 10.1088/1742-6596/1353/1/012051.
- [16] F. Cao *et al.*, "Realistic three-layer head phantom for optically pumped magnetometer-based magnetoencephalography," *Comput Biol Med*, vol. 164, Sep. 2023, doi: 10.1016/j.compbiomed.2023.107318.
- [17] A. Hossain *et al.*, "Sensor-based microwave brain imaging system (SMBIS): An experimental six-layered tissue based human head phantom model for brain tumor diagnosis using electromagnetic signals," *Engineering Science and Technology, an International Journal*, vol. 45, Sep. 2023, doi: 10.1016/j.jestch.2023.101491.
- [18] Ş. Özen and H. Köylü, "Phantom Model of Human Brain Tissue for Cellular Phone Frequencies in Electromagnetic Field Radiation Absorption Studies," *Fen Bilimleri Dergisi*, vol. 18, no. 2, pp. 193–200, 2005.
- [19] I. Ibanez Labiano, D. Arslan, E. Ozden Yenigun, A. Asadi, H. Cebeci, and A. Alomainy, "Screen Printing Carbon Nanotubes Textiles Antennas for Smart Wearables," *Sensors (Basel)*, vol. 21, no. 14, 2021, doi: 10.3390/s21144934.
- [20] D. Leonov, M. Kodenko, D. Leichenko, A. Nasibullina, and N. Kulberg, "Design and validation of a phantom for transcranial ultrasonography," *Int J Comput Assist Radiol Surg*, vol. 17, no. 9, pp. 1579–1588, Sep. 2022, doi: 10.1007/s11548-022-02614-2.
- [21] M. Navarro-Lozoya, M. S. Kennedy, D. Dean, and J. I. Rodriguez-Devora, "Development of phantom material that resembles compression properties of human brain tissue for training models," *Materialia (Oxf)*, vol. 8, Dec. 2019, doi: 10.1016/j.mtl.2019.100438.
- [22] F. O. Okoh, N. A. Kabir, M. F. M. Yusof, A. S. A. Mohammed, and R. Zaimon, "Investigation of polyvinyl alcohol (PVAL) composite gels and the outcome of variation in breast phantom densities on image quality and dose in full-field digital mammography," *Radiation Physics and Chemistry*, vol. 200, Nov. 2022, doi: 10.1016/j.radphyschem.2022.110393.
- [23] A. Varallo *et al.*, "Fabrication of 3D printed patient-derived anthropomorphic breast phantoms for mammography and digital breast tomosynthesis: Imaging assessment with clinical X-ray spectra," *Physica Medica*, vol. 98, pp. 88–97, Jun. 2022, doi: 10.1016/j.ejmp.2022.04.006.
- [24] C. Stengl, S. Ghafoory, A. Weidner, B. Murphy, and S. Wöfl, "Development of an Artificial 3D Liver Phantom for Analysis of Radiotherapeutic Effects In Vitro," *Applied Sciences (Switzerland)*, vol. 12, no. 21, Nov. 2022, doi: 10.3390/app122110867.
- [25] L. B. Christie *et al.*, "Review of imaging test phantoms," *J Biomed Opt*, vol. 28, no. 08, Aug. 2023, doi: 10.1117/1.jbo.28.8.080903.
- [26] A. Hunold, D. Strohmeier, P. Fiedler, and J. Haueisen, "Head phantoms for electroencephalography and transcranial electric stimulation: A skull material study," *Biomedizinische Technik*, vol. 63, no. 6, pp. 647–655, Dec. 2018, doi: 10.1515/bmt-2017-0069.
- [27] E. N. Selçuk and M. Reşit, "Engineering Use of The Skull Pantom As A Biomechatronic Construction Element," *Dicle*, Oct. 2022.
- [28] J. Lacik *et al.*, "Anisotropic Conductivity of Rat Head Phantom and its Influence on Electroencephalogram Source Localization," *IEEE Access*, vol. 10, pp. 9877–9888, 2022, doi: 10.1109/ACCESS.2022.3143952.
- [29] A. Bashirov and D. Balovnev, "Phantom Electroencephalogram Simulator for Automated Tests and Validation: Signals Repeatability," *Proceedings - 2021 International Russian Automation Conference, RusAutoCon 2021*, pp. 660–664, 2021, doi: 10.1109/RusAutoCon52004.2021.9537436.
- [30] M. C. Piastra, R. Oostenveld, S. Homölle, B. Han, Q. Chen, and T. Oostendorp, "How to assess the accuracy of volume conduction models? A validation study with stereotactic EEG data," *Front Hum Neurosci*, vol. 18, 2024, doi: 10.3389/fnhum.2024.1279183.
- [31] R. R. Daru, M. M. Rabby, T. Ko, Y. Shinglot, R. Raihan, and A. Adnan, "Electrically Equivalent Head Tissue Materials for Electroencephalogram Study on Head Surrogates," *Applied Sciences (Switzerland)*, vol. 14, no. 6, Mar. 2024, doi: 10.3390/app14062495.
- [32] O. V. Mikhailov, "Gelatin as It Is: History and Modernity," Feb. 01, 2023, *Multidisciplinary Digital Publishing Institute (MDPI)*. doi: 10.3390/ijms24043583.
- [33] W. E. Audette and L. V. Allen, "Design and Demonstration of a Head Phantom for Testing of Electroencephalography (EEG) Equipment", doi: 10.13140/RG.2.2.12078.25920.
- [34] J. Harries *et al.*, "A realistic phantom of the human head for PET-MRI," *EJNMMI Phys*, vol. 7, no. 1, Dec. 2020, doi: 10.1186/s40658-020-00320-z.
- [35] M. E. H. Chowdhury, A. Khandakar, B. Hossain, and K. Alzoubi, "Effects of the phantom shape on the gradient artefact of electroencephalography (EEG) data in simultaneous EEG-fMRI," *Applied Sciences (Switzerland)*, vol. 8, no. 10, Oct. 2018, doi: 10.3390/app8101969.
- [36] T. Hoffmann, F. Klink, A. Boese, K. Fischer, O. Beuing, and G. Rose, "Development of a skull phantom for the assessment of implant X-ray visibility," in *Current Directions in Biomedical Engineering*, Walter de Gruyter GmbH, Sep. 2016, pp. 351–354, doi: 10.1515/cdbme-2016-0078.
- [37] A. Hunold, R. Machts, and J. Haueisen, "Head phantoms for bioelectromagnetic applications: a material study," *Biomed Eng Online*, vol. 19, no. 1, Dec. 2020, doi: 10.1186/s12938-020-00830-y.
- [38] G. B. Tseghai, B. Malengier, K. A. Fante, and L. Van Langenhove, "A long-lasting textile-based anatomically realistic head phantom for validation of eeg electrodes," *Sensors*, vol. 21, no. 14, Jul. 2021, doi: 10.3390/s21144658.
- [39] T. J. Collier, D. B. Kynor, J. Bieszczad, W. E. Audette, E. J. Kobylarz, and S. G. Diamond, "Creation of a human head phantom for testing of electroencephalography equipment and techniques," *IEEE Trans Biomed Eng*, vol. 59, no. 9, pp. 2628–2634, 2012, doi: 10.1109/TBME.2012.2207434.
- [40] H. Magsood and R. L. Hadimani, "Development of anatomically accurate brain phantom for experimental validation of stimulation strengths during TMS," *Materials Science and Engineering C*, vol. 120, no. February 2019, p. 111705, 2021, doi: 10.1016/j.msec.2020.111705.
- [41] G. Han, X. Song, X. Chen, T. Han, M. Xu, and D. Ming, "A head phantom study of frontal lobe epilepsy localization with multi-channel acoustoelectric brain imaging," *IEEE Sens J*, vol. 24, no. 19, pp. 30244–30253, 2024, doi: 10.1109/JSEN.2024.3447912.
- [42] I. M. Saied and T. Arslan, "Wearable RF Device for Monitoring Brain Activities in the Ageing Population," *Proceedings - IEEE International Symposium on Circuits and Systems*, vol. 2023-May, pp. 1–5, 2023, doi: 10.1109/ISCAS46773.2023.10181795.
- [43] OpenBCI, "No Title." [Online]. Available: <https://openbci.com/>
- [44] LORETA, "No Title." [Online]. Available: <https://www.uzh.ch/keyinst/loreta.htm>
- [45] J. R. Hughes, "Gamma, fast, and ultrafast waves of the brain: Their relationships with epilepsy and behavior," *Epilepsy and Behavior*, vol. 13, no. 1, pp. 25–31, 2008, doi: 10.1016/j.yebeh.2008.01.011.
- [46] S. M. Redwan, M. P. Uddin, A. Ulhaq, M. I. Sharif, and G. Krishnamoorthy, "Power spectral density-based resting-state EEG classification of first-episode psychosis," *Sci Rep*, vol. 14, no. 1, pp. 1–12, 2024, doi: 10.1038/s41598-024-66110-0.
- [47] S. M. Casillo, D. D. Luy, and E. Goldschmidt, "A History of the Lobes of the Brain," *World Neurosurg*, vol. 134, pp. 353–360, 2020, doi: 10.1016/j.wneu.2019.10.155.
- [48] L. Johansson *et al.*, "Longstanding smoking associated with frontal brain lobe atrophy: a 32-year follow-up study in women," *BMJ Open*, vol. 13, no. 10, pp. 1–8, 2023, doi: 10.1136/bmjopen-2023-072803.
- [49] M. Sobstyl, M. Konopko, A. Wierzbička, T. Pietras, M. Prokopienko, and K. Sipowicz, "Deep brain stimulation of hippocampus in treatment of refractory temporal lobe epilepsy," *Neurol Neurochir Pol*, vol. 58, no. 4, pp. 393–404, 2024, doi: 10.5603/pjnns.99150.
- [50] Y. Jiang *et al.*, "Identification of four biotypes in temporal lobe epilepsy via machine learning on brain images," *Nat Commun*, vol. 15, no. 1, 2024, doi: 10.1038/s41467-024-46629-6.

-
- [51] G. Maresca *et al.*, "Traumatic Brain Injury and Related Antisocial Behavioral Outcomes: A Systematic Review," *Medicina (Lithuania)*, vol. 59, no. 8, pp. 1–12, 2023, doi: 10.3390/medicina59081377.
- [52] Z. Dary, B. Lenggenhager, S. Lagarde, S. Medina Villalon, F. Bartolomei, and C. Lopez, "Neural bases of the bodily self as revealed by electrical brain stimulation: A systematic review," *Hum Brain Mapp*, vol. 44, no. 7, pp. 2936–2959, 2023, doi: 10.1002/hbm.26253.

Detection of Surface Defects on Cold-Rolled Galvanized Steel Using AI-Driven Image Filtering Techniques

YASİN BIYIKLI¹, YUSUF BAHİRİ ÖZÇELİK², AYTAÇ ALTAN³

¹Zonguldak Bülent Ecevit University, Zonguldak/Turkey, yasinbiyikli94@gmail.com

²Zonguldak Bülent Ecevit University, Zonguldak/Turkey, ybahri.ozcelik@beun.edu.tr

³Zonguldak Bülent Ecevit University, Zonguldak/Turkey, aytacaltan@beun.edu.tr

Abstract - Steel surface defects caused by mechanical, thermal or chemical factors during production can significantly affect the structural integrity and performance of the material. These defects are generally categorized as dirty area, scratches, welding line, and clean surfaces. Early detection and accurate classification of such defects is critical to optimize production processes, improve final product quality and reduce costs. This study proposes a deep learning-based model for surface defect detection on cold-rolled galvanized steel using noise-free steel surface images. The model operates in two stages: first, noise is reduced from the images using Gaussian and median filters to improve classification accuracy. In the second stage, the denoised images are processed by a pre-trained convolutional neural network. A dataset of 3,400 surface defect images representing scratches, welds, clean and dirty surfaces was used to train the model. The model was then tested on a further 600 images and its performance evaluated using 10-fold cross-validation, achieving an accuracy of 98.30%. This approach, in particular the use of the Gaussian filter, provides a robust solution for the effective detection of surface defects on cold-rolled galvanized steel.

Keywords - Steel surface defects, Deep learning, Image denoising, Convolutional neural network, Gaussian filter.

I. INTRODUCTION

STEEL surface defects are undesirable surface defects caused by mechanical, thermal or chemical factors in the manufacturing process that adversely affect the structural integrity, aesthetics and performance of the material. Steel surface defects can occur due to factors such as external forces in the production process of the material, fatigue, steel quality and can significantly affect product quality [1]. These defects can generally be of different types such as scratches, welding defects, clean and dirty surfaces. Scratches occur on the material surface due to mechanical damage during processing or improper use of equipment, while welding defects are caused by errors in the welding process and can lead to structural weaknesses. Dirty surfaces are caused by contamination of the surface during production or the accumulation of unwanted residues on the surface. A clean surface is one with no obvious defects. Detecting such defects is critical to improving production processes and increasing the quality of the final product. Incorrectly detected or overlooked defects can

adversely affect the durability, aesthetics and performance of the product. Particularly for materials such as steel, which are used extensively in industry, the early detection and classification of defects is critical to reducing costs, increasing production efficiency and ensuring safety [2-4].

In the steel industry, surface defects are usually inspected manually, but this method has limitations and risks. The process, which poses a significant risk to the health and safety of inspectors, can result in accidents such as the breakage or fragmentation of defective steel surfaces. In addition, manual inspection is time-consuming, slows down the production process and leaves it open to human error [5]. To overcome these problems, computer vision-based techniques enable faster and safer detection of steel surface defects. Automated systems speed up production processes while reducing quality control costs and minimizing potential accident risks. These technologies both increase industrial productivity and provide a superior solution in terms of human safety.

The development of machine learning and deep learning methods using computer vision has revolutionized industrial defect detection processes and made it highly effective. Today, these techniques provide fast and accurate detection of surface defects compared to manual inspection. In this regard, Demir et al. [6] developed a new deep learning model, PAR-CNN (Parallel Attention Residual-Convolutional Neural Network), to detect and classify steel surface defects. The model improved classification performance by combining attention mechanisms and residual blocks and reduced computational cost using the NCA-ReliefF algorithm. The study, which achieved high accuracy on the Severstal: Steel Defect Detection dataset, provides a more successful solution than manual inspection methods. Li et al. [7] developed a new deep learning model incorporating MSFE (Multiscale Feature Extraction) and EFF (Efficient Feature Fusion) modules for steel surface defect detection. The model used fewer normalization layers to reduce overfitting while optimizing the multi-scale feature extraction and fusion capabilities. The proposed model achieved high accuracy with a small number of parameters. Shao et al. [8] developed a lightweight deep learning model called Multi-Scale Lightweight Neural Network to detect steel surface defects. The accuracy and efficiency of the model are increased by using Gaussian difference pyramid and multi-kernel fusion. Although

it has fewer parameters than networks such as ResNet-50 and VGG, it exhibits superior performance with 98.06% accuracy. Although it has fewer parameters than networks such as ResNet-50 and VGG, it shows superior performance with an accuracy of 98.06%. You and Kong [9] presented an improved algorithm based on YOLOv8 for steel surface defect detection. The algorithm includes improvements that increase the accuracy of detecting small targets without the attention mechanism and increase the detection range with the SPPF module. Tests on the NEU-DET dataset showed significant improvements in sensitivity, recall and mAP rates. There are numerous studies in the literature demonstrating their success in this area, particularly in critical areas such as the steel industry, and these methods have been shown to play a key role in improving production quality [10-13].

This study presents a model based on convolutional neural networks for the early and efficient detection of surface defects on cold-rolled galvanized steel using noise-cancelling filters. The performance of the models is evaluated using metrics such as accuracy (Acc), precision (Prec), recall (Rec) and F1 score. The robustness of the model is also tested using 10-fold cross-validation. The rest of the paper is organized as follows: Section II introduces the materials and methods used in the study. Section III presents and discusses the results of the proposed model and other models. Section IV highlights the conclusions of the study.

II. MATERIALS AND METHODS

This section presents information about the dataset used for the detection and classification of cold rolled galvanized steel surface defects and the framework of the proposed model. The content of the proposed model for the detection of cold rolled galvanized steel surface defects is shown in Figure 1.

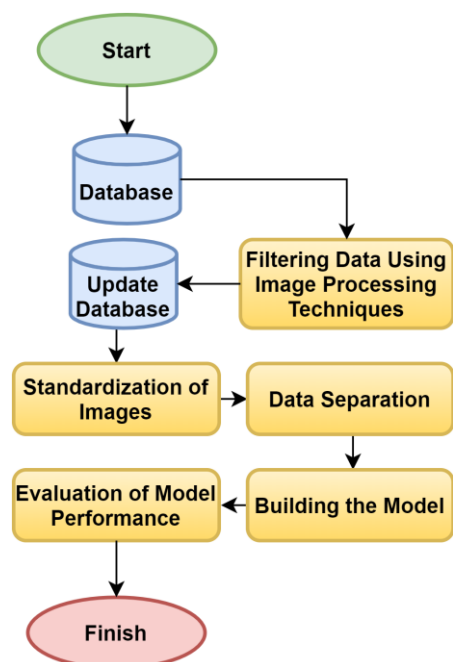


Figure 1: The framework of proposed model.

The content of the proposed model consists of the pre-processing of steel surface images, the training phase of the proposed CNN algorithm and the testing phase on the dataset of cold rolled galvanized steel surface images allocated for testing the model. In the pre-processing phase of the proposed model, a Gaussian filter is used to remove noise in the images, the images are reduced to a size of 227×227 and normalized. The training of the model is done with the CNN based EfficientNet architecture using the pre-processed images. 85% of the dataset consisting of cold rolled galvanized steel surface defects is used to train the training model and the remaining 15% is used to test the performance of the model. The validity of the model is tested using 10-fold cross-validation. The performance of the model is measured by classification performance metrics such as accuracy, precision, recall and F1 score. Additionally, the proposed model is compared with other CNN-based architectures that use median filters for denoising.

A. Cold Rolled Galvanized Steel Surface Data Set

The study uses a dataset obtained experimentally for the detection of steel surface defects. The dataset of cold-rolled galvanized steel surface images consists of a total of 4000 steel surface images collected from the production line of the company operating in the iron and steel industry. The resolutions of the steel surface images in the dataset vary between 381×256 and 4096×512 pixels. The steel surface defect dataset contains 1000 clean, 1000 scratched, 1000 dirty and 1000 welding line class images. When examining the dataset, it is observed that the number of images belonging to the classes is balanced, while it is noticeable that it is unbalanced in terms of resolution. In order to improve the performance and robustness of the model, dimensioning and normalization techniques have been applied to the dataset consisting of images of cold-rolled galvanized steel surfaces. In addition, it is important that the dataset is balanced appearance in terms of the number of images for each class to avoid overfitting of the proposed model. The images of the flawless, scratched, dirty and welded classes in the cold-rolled galvanized steel surface dataset used in the study are shown in Figure 2.

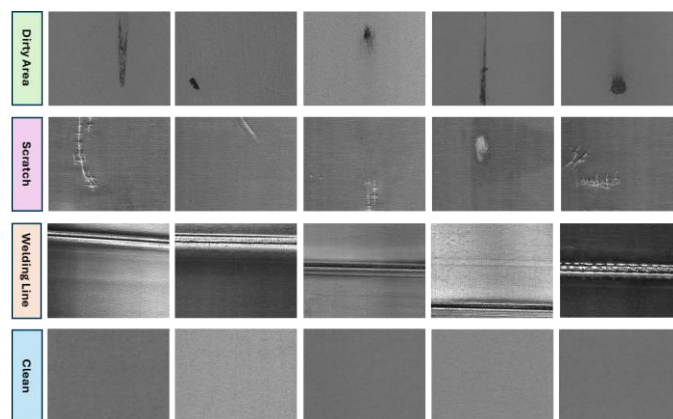


Figure 2: The sample images of all stages surface defects.

B. Image Denoising

In image processing processes, the images obtained may be subject to noise depending on the physical hardware of the camera used for shooting, lighting conditions and environmental factors. This prevents the images from being effectively analyzed. Therefore, in order to perform effective analysis, denoising should be applied to the images. Denoising improves the analysis process by sharpening the image, increasing model accuracy and providing more reliable results in applications such as object recognition. There are many techniques in the literature for removing noise that may be present in images. Among these techniques, Gaussian and median filters are commonly used. The Gaussian filter is an effective method, particularly for reducing randomly distributed noise. This filter reduces excessive differences between pixels by smoothing an image. The fact that the Gaussian filter blurs by giving higher weights to the pixels closest to the center makes the denoising process quite effective. This feature makes the Gaussian filter more successful than other low-pass filters. Gaussian filter is defined by

$$G(x, y) = \frac{1}{2\pi\sigma^2} e^{-\frac{x^2+y^2}{2\sigma^2}} \quad (1)$$

where $G(x, y)$ is the filter coefficient, σ is the standard deviation, and x and y are the horizontal and vertical distances of the pixel from the center, respectively. Each pixel in the image is calculated by multiplying it with the Gaussian function weights of the surrounding pixels. In this way, the contribution of the surrounding pixels is taken into account in a more balanced way [14]. The median filter works by taking the median of a pixel and its neighbors. The median filter is defined as

$$\text{Median}(p(i, j)) = \text{median}\{W(i, j)\} \quad (2)$$

Here, for each pixel $p(i, j)$, a neighboring window $W(i, j)$ is created for the neighboring window and the pixels in this window are sorted and their median is taken [15].

The Gaussian filter produces a natural blur by creating smoother transitions between pixels, resulting in less loss of detail. The median filter preserves sudden changes better, but can create sharp transitions. This makes the Gaussian filter superior to the median filter in preserving detail and maintaining a natural appearance. Therefore, in this study, the Gaussian filter was used as a denoiser to remove noise in images containing surface defects of cold-rolled galvanized steel and for effective classification.

C. Transfer Learning

Transfer learning is a technique often used in deep learning and offers great advantages, especially in cases where the entire model cannot be built from scratch. This approach aims to adapt the information of a large image classification model, trained on a large dataset, to a smaller dataset. Basically, the features of the small dataset are extracted using the weights of a pre-trained model, and the model parameters are optimized by fine-

tuning [16]. In this study, a robust model is proposed using the Efficient-Net network trained on the ImageNet dataset [17]. The performance of the proposed model is compared with the performance of models built using the VGG-16 and Xception architectures, which were trained on the ImageNet dataset.

D. Performance Metrics

The confusion matrix is used to evaluate the performance of classification models and consists of the terms true positive (TP), true negative (TN), false positive (FP) and false negative (FN). This matrix summarizes the types of correct and incorrect classifications and allows the calculation of important performance metrics such as Acc, Prec, Rec, and F1 score. The performance of the proposed model and other models in detecting surface defects on cold-rolled galvanized steel is evaluated by metrics such as the correct prediction rate, Acc, the correct assignment rate to the positive class, Prec, the correct classification of what should be positive, Rec, and the F1 score, which balances both precision and recall.

III. EXPERIMENTAL RESULTS AND DISCUSSION

In this section, the experimental results of the proposed model and other models are presented and discussed. In this study, the Gaussian filter was first applied to the images of cold-rolled galvanized steel surfaces to remove noise, and then the images were scaled to 227×227 pixels, since the standardized inputs of the architectures used take 227×227 pixel images. The same steps were repeated for the median filter model. During the training of the models, the Adam optimization technique was used to update the learning per epoch. In the proposed model, the learning rate, batch size and epoch values were set to 0.01, 32, and 25 respectively.

All experiments on surface defects of cold-rolled galvanized steel were performed in Google Colab environment with 13 GB CPU and 16 GB NVIDIA Tesla T4 GPU. All codes were compiled using Python scripting language. The confusion matrix showing the average performance of the proposed model for detecting surface defects of cold-rolled galvanized steel in the classes of "scratch", "welding line", "dirty area" and "clean" is shown in Figure 3.

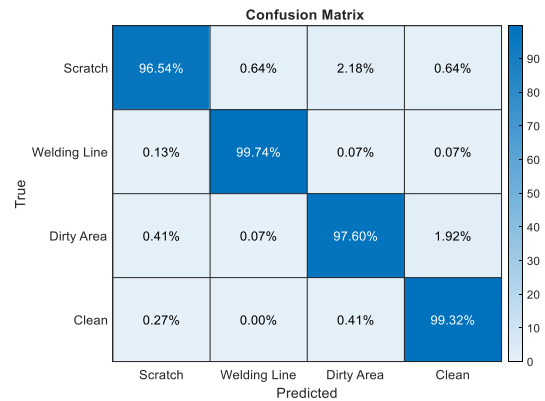


Figure 3: The confusion matrix of proposed model.

When the confusion matrix is examined, it can be seen that the proposed model has a high accuracy rate of 98.30% on average in all classes. The proposed model achieves an accuracy value of approximately 96% in all classes and the

highest accuracy rate is achieved by classifying the weld line class without any errors in all folds. In addition, the most confusion in the classification phase is observed between "scratch" and "dirty area". During the classification of the "scratch" class with an accuracy rate of 96.54%, it was confused with the "dirty area" class at a rate of 2.18%, and the "dirty area" class was classified as "clean" at a rate of 1.92%, despite having an accuracy rate of 97.60%. These small confusions may be due to visual similarities between other classes and suggest that the model has difficulty in distinguishing between these classes. However, the accuracy rates of each class are quite satisfactory, indicating that the proposed model has a superior success in detecting steel surface defects. The results obtained show that the proposed model can be used with confidence in industrial classification or quality control processes.

According to the performance criteria of Acc, Prec, Rec, and F1 score, the performance of the proposed model and other models obtained with Gaussian denoising, median denoising and no preprocessing for each class are presented in Table 1. Looking at the models produced using the EfficientNet architecture, which includes the proposed model, it can be seen that the no-preprocessing model achieves 97.33% Acc, the model produced using median denoising achieves 97.25% Acc and the proposed model achieves 98.30% Acc. Furthermore, taking into account the specified performance criteria, it is observed that while the Prec, Rec, and F1 values of the no-preprocessing model are above 95% for each class, the Rec value of the model created with median denoising drops to about 93% in the "scratch" class, and the Prec, Rec, and F1 values are above 94% in all other classes. This situation shows that median denoising in the models created with the EfficientNet architecture performs worse than no pre-processing in the detection of steel surface defects. The Acc values of the models without pre-processing, with median denoising and with Gaussian denoising created with the VGG-16 architecture were measured to be 96.55%, 96.28%, and 97.17% respectively. Looking at the performance criteria of the models created with this architecture, it can be seen that the Prec, Rec, and F1 values for each class of no pre-processing are above 94%, while the Rec criterion of the model created with median denoising drops to around 92% in the "scratch" class, the Prec criterion drops to around 93% in the "dirty area" class, and the Prec, Rec, and F1 values are above 94% in all other classes. Looking at the models created with VGG-16, the model with median denoising shows the lowest performance, similar to those created with EfficientNet. The Acc values of the models without pre-processing, with median denoising and with Gaussian denoising created with the Xception architecture were measured to be 97.00%, 97.10%, and 97.56%, respectively. Looking at the performance criteria of the models created with Xception, although the accuracy value of the model with median denoising is higher than without pre-processing, it can be observed that the Prec, Rec, and F1 values for each class of the no pre-processing are approximately above 93%, while the Rec value of the model created with median denoising drops to approximately 92% in the "scratch" class, the Prec criterion drops to approximately 93% in the "dirty area" class, and the Prec, Rec, and F1 values are above 94% in all other classes. Looking at Table 1, it can be said that all the

models created generally show lower performance in the "scratch" and "dirty area" classes than in the other classes. However, it is clear that the Gaussian filter contributes to the superior performance of the models by more effectively removing noise in the detection of the scratch and dirty area classes and all other classes and by revealing the defect lines.

Table 1: Performance of the models created for all classes.

	Detection	Prec (%)	Rec (%)	F1 Score (%)	Acc (%)
Efficient Gauss Denoising	Scratch	99.17	96.54	97.84	98.30
	Welding Line	99.29	99.73	99.51	
	Dirty Area	97.35	97.60	97.47	
	Clean	97.42	99.32	98.36	
Efficient Median Denoising	Scratch	96.96	93.85	95.38	97.25
	Welding Line	97.94	100.00	98.96	
	Dirty Area	95.23	96.58	95.90	
	Clean	98.87	98.56	98.71	
Efficient No Pre-Process	Scratch	96.43	96.16	96.29	97.33
	Welding Line	99.34	100.00	99.67	
	Dirty Area	95.44	96.16	95.80	
	Clean	98.09	96.98	97.53	
VGG-16 Gauss Denoising	Scratch	98.07	92.94	95.44	97.17
	Welding Line	99.03	99.20	99.12	
	Dirty Area	95.67	97.33	96.49	
	Clean	95.98	99.17	97.55	
VGG-16 Median Denoising	Scratch	94.48	92.50	93.48	96.28
	Welding Line	99.23	99.47	99.35	
	Dirty Area	93.49	94.46	93.97	
	Clean	97.90	98.70	98.30	
VGG-16 No Pre-Process	Scratch	94.65	94.61	94.63	96.55
	Welding Line	99.42	99.93	99.68	
	Dirty Area	94.91	95.48	95.19	
	Clean	97.20	96.16	96.68	
Xception Gauss Denoising	Scratch	97.48	94.87	96.16	97.56
	Welding Line	98.85	99.41	99.13	
	Dirty Area	96.83	96.84	96.84	
	Clean	97.07	99.11	98.08	
Xception Median Denoising	Scratch	97.06	92.69	94.82	97.10
	Welding Line	99.11	100.00	99.55	
	Dirty Area	93.93	96.51	95.20	
	Clean	98.34	99.18	98.76	
Xception No Pre-Process	Scratch	97.02	93.59	95.28	97.00
	Welding Line	99.21	99.80	99.51	
	Dirty Area	94.83	96.65	95.73	
	Clean	96.95	97.95	97.45	

The average performance metrics of 9 different models designed using the Xception, VGG-16 and EfficientNet

architectures for the detection of surface defects in cold-rolled galvanized steel are presented in Table 2 of this study. According to the results in the table, when comparing the three architectures, it is observed that the models designed with EfficientNet generally show the highest performance. In addition, the proposed model designed with EfficientNet and Gaussian denoising proved its superior performance with 98.31%, 98.30%, and 98.30% Prec, Rec, and F1 score metrics respectively. It can be seen that EfficientNet's 97.25% Prec and 98.30% Rec metrics obtained with median denoising are also higher than the best performances of other architectures. It can be seen that the Xception architecture shows its best performance with 97.56% Prec, 97.56% Rec, and 97.55% F1 with Gaussian denoising. It can be said that it showed a successful result with Prec and Rec values around 97% without pre-processing and with median denoising. However, these values could not reach the level achieved by EfficientNet with Gaussian denoising. It is observed that the VGG-16 architecture performs best with 97.19% Prec, 96.61% Rec, and 96.93% F1 with Gaussian denoising. It can be seen that in the case without pre-processing, it gave an average performance with 96.55% Prec and Rec, while median denoising gave the lowest results with 96.28% Prec.

Table 2: The average performance of the built models for all architectures and all pre-processing steps.

AI Architectures	Methods	Prec (%)	Rec (%)	F1 Score (%)
Xception	No Pre-Process	97.00	97.00	96.99
	Gauss Denoising	97.56	97.56	97.55
	Median Denoising	97.11	97.10	97.08
VGG-16	No Pre-Process	96.55	96.55	96.54
	Gauss Denoising	97.19	96.61	96.93
	Median Denoising	96.28	96.48	96.79
Efficient	No Pre-Process	97.33	97.32	97.32
	Gauss Denoising	98.31	98.30	98.30
	Median Denoising	97.25	98.30	98.30

In general, the EfficientNet architecture achieved the highest and most effective results in all pre-processing methods and showed a superior performance especially in Gaussian denoising. While the models created with the Xception architecture achieved the best results with Gaussian denoising, the models created with the VGG-16 architecture achieved the best performance with Gaussian denoising, but it was observed that it was behind EfficientNet and Xception. These results show that EfficientNet with Gaussian denoising is the most effective model for detecting surface defects on cold-rolled galvanized steel, while models built with Xception provide a flexible and powerful alternative to preprocessing methods compared to models built with EfficientNet, while VGG-16 ranks third with lower performance. The results also show that the EfficientNet architecture is the most ideal combination for industrial quality control applications in the detection of cold-rolled galvanized steel surface defects, due to its efficient model structure and Gaussian denoising process that reveals steel surface defects more clearly.

IV. CONCLUSION

Early detection of cold rolled galvanized steel surface defects caused by mechanical, thermal or chemical factors during the production process, which negatively affect the aesthetics and performance of the material, is crucial to improve the production process and increase the final quality of the product. In this study, a dataset containing steel surface defects was used for early detection by classifying cold rolled galvanized steel defects as "clean, scratch, dirty area, and welding line" and a deep learning model with CNN based EfficientNet architecture was proposed by applying Gaussian filter to the images to perform effective classification. The proposed model was tested by considering both accuracy and robustness parameters. The Acc, Prec, Rec, and F1 score values of the proposed model for detection and classification of cold rolled galvanized steel surface defects were measured to be 98.30%, 98.31%, 98.30%, and 98.30% respectively. The performance of the proposed model was compared with models built using Xception and VGG-16 architectures and median filter using performance metrics. The results obtained show that the proposed model for the detection of cold rolled galvanized steel surface defects has a superior classification performance compared to the other models mentioned. In future studies, models that deal with the fractal dimensions and complex structures of the images will be investigated in order to improve the performance of the cold rolled galvanized steel surface defect classification model. The model to be developed aims to cope with the uncertainties and non-linear dynamics in the defect situations.

REFERENCES

- [1] Q. Luo, X. Fang, L. Liu, C. Yang, and Y. Sun, "Automated visual defect detection for flat steel surface: A survey," *IEEE Transactions on Instrumentation and Measurement*, vol. 69(3), pp. 626-644, 2020.
- [2] M. Li, H. Wang, and Z. Wan, "Surface defect detection of steel strips based on improved YOLOv4," *Computers and Electrical Engineering*, vol. 102, 2022.
- [3] X. Fang, Q. Luo, B. Zhou, C. Li, and L. Tian, "Research progress of automated visual surface defect detection for industrial metal planar materials," *Sensors*, vol. 20(18), 2020.
- [4] S. Wang, X. Xia, L. Ye, and B. Yang, "Automatic detection and classification of steel surface defect using deep convolutional neural networks," *Metals*, vol. 11(3), 388, 2021.
- [5] W. Y. Lin, C. Y. Lin, G. S. Chen, and C. Y. Hsu, *Steel surface defects detection based on deep learning*. Advances in Physical Ergonomics & Human Factors: Proceedings of the AHFE 2018 International Conference on Physical Ergonomics & Human Factors, Springer International Publishing, pp. 141-149, 2019.
- [6] K. Demir, M. Ay, M. Cavas, and F. Demir, "Automated steel surface defect detection and classification using a new deep learning-based approach," *Neural Computing and Applications*, vol. 35(11), pp. 8389-8406, 2023.
- [7] Z. Li, X. Wei, M. Hassaballah, Y. Li, and X. Jiang, "A deep learning model for steel surface defect detection," *Complex & Intelligent Systems*, vol. 10(1), pp. 885-897, 2024.
- [8] Y. Shao, S. Fan, H. Sun, Z. Tan, Y. Cai, C. Zhang, and L. Zhang, "Multi-scale lightweight neural network for steel surface defect detection," *Coatings*, vol. 13(7), 2023.
- [9] H. Kong, and C. You, "Improved steel surface defect detection algorithm based on YOLOv8," *IEEE Access*, vol. 12, pp. 99570-99577 2024.
- [10] M. Li, H. Wang, and Z. Wan, "Surface defect detection of steel strips based on improved YOLOv4," *Computers and Electrical Engineering*, vol. 102, 2022.

- [11] B. Zhao, Y. Chen, X. Jia, and T. Ma, "Steel surface defect detection algorithm in complex background scenarios," *Measurement*, vol. 237, 2024.
- [12] X. Hu, J. Yang, F. Jiang, A. Hussain, K. Dashtipour, and M. Gogate, "Steel surface defect detection based on self-supervised contrastive representation learning with matching metric," *Applied Soft Computing*, vol. 145, 2023.
- [13] C. Zhao, X. Shu, X. Yan, X. Zuo, and F. Zhu, "RDD-YOLO: A modified YOLO for detection of steel surface defects," *Measurement*, vol. 214, 2023.
- [14] M. Gupta, H. Taneja, and L. Chand, "Performance enhancement and analysis of filters in ultrasound image denoising," *Procedia Computer Science*, vol. 132, pp. 643-652, 2018.
- [15] M. Mafi, H. Martin, M. Cabrerizo, J. Andrian, A. Barreto, and M. Adjouadi, "A comprehensive survey on impulse and Gaussian denoising filters for digital images," *Signal Processing*, vol. 157, pp. 236-260, 2019.
- [16] S. Khan, N. Islam, Z. Jan, I. U. Din, and J. J. C. Rodrigues, "A novel deep learning-based framework for the detection and classification of breast cancer using transfer learning," *Pattern Recognition Letters*, vol. 125, pp. 1-6, 2019.
- [17] O. Russakovsky, J. Deng, H. Su, J. Krause, S. Satheesh, S. Ma, Z. Huang, A. Karpathy, A. Khosla, M. Bernstein, A. C. Berg, and L. Fei-Fei, "Imagenet large scale visual recognition challenge," *International Journal of Computer Vision*, vol. 115(3), pp. 211-252, 2015.

Silent Mode Application for Mobile Devices with Wireless Broadcast Technology

MUHAMMED ABDÜL VAHAP İSTER¹, AHMET CEVAHIR CINAR²

¹ Selçuk University, Konya, Türkiye, 228273001002@lisansustu.selcuk.edu.tr

² Selçuk University, Konya, Türkiye, accinar@selcuk.edu.tr

Abstract - As the population continues to grow, societies are becoming more crowded. In environments where people gather collectively, the necessary silence for beneficial activities is occasionally disrupted by the effects of technological devices, particularly mobile phones. This study focuses on efforts made to automatically silence incoming call notifications on mobile phones in places where people congregate, such as places of worship, seminar rooms, cinemas, meeting rooms, libraries, and similar settings. An application has been developed using the Kotlin programming language, and a device capable of broadcasting via Wi-Fi and Bluetooth has been designed to activate this application. The Wi-Fi-Bluetooth broadcasting device is plugged into an electrical outlet and begins to broadcast over an area of approximately 70 square meters. As soon as the application on the mobile phone detects this broadcast, it silences the phone without requiring any connection. When the mobile phone moves away from the broadcast area, it returns to its previous sound mode.

Keywords - Bluetooth, call, meeting, silent mode, Wi-Fi

I. INTRODUCTION

RAPIDLY increasing population, developing technology, people's search for information, social activities, etc. have caused the interaction between people to increase and some problems to emerge along with the solutions. One of these problems is the subject of this report. There are environments where people are gathered. These are; movie theaters, places of worship, meeting rooms, libraries and similar. Since these environments are places where people need to focus or focus on a point, they are environments where silence is required. With developing technology, the phones that people use for communication have entered the pockets of every individual and become mobile phones. Unless the users turn down the volume, phones can disrupt this silence with message and call sounds even in environments where silence is preferred. Some devices called signal blockers prevent the phone from receiving any calls by disconnecting it from the base station. However, this solution has not been preferred by the majority. A partial solution has been found for this situation with some applications that are automatically installed and automatically adjusted according to the time or location from the phone settings. However, these solutions bring with them the obligation to adapt to a certain time or the requirement to be in a certain location.

A system that can silence the phone mode during the time spent in a place where there is a group of people can be developed without interrupting the signals coming to the

phone or calculating the location and time. The subject of our study is the situation where the phone, which receives the signals emitted by a Wi-Fi (Wireless Fidelity-Wireless Connection Area) or Bluetooth device in the place, silences the phone when it starts receiving these signals, and the phone remains silent as long as the Wi-Fi or Bluetooth signal continues, and when the signal is interrupted, i.e. when the environment is moved away, the phone returns to normal mode.

The hardware-software duo that is intended to be revealed as a result of this study will work as follows. The person enters an environment where silence is required. The mobile application that we have prepared is installed on the person's phone. The Wi-Fi and Bluetooth device that we have prepared is broadcasting in the environment entered. The mobile application scans the name of the Wi-Fi and Bluetooth device broadcasting in the background without the person having to run the application on their phone. In order for the application to do this, the phone's Wi-Fi-location or Bluetooth-location duo must be open. When the SSID (Service Set Identifier) that we defined earlier is found, the phone switches itself to silent mode. As long as the Wi-Fi and Bluetooth device is broadcasting, the phone that is within the coverage area continues to remain in silent mode. If the Wi-Fi and Bluetooth broadcasting is turned off or the person leaves the coverage area of the Wi-Fi and Bluetooth network, the phone switches itself back to normal mode and the ringtones return to normal.

Thanks to the hardware that mobile phones have, the way for phones to communicate with the external environment has been opened with triggers that will be caught as a result of the interactions they enter with the signals coming from outside. Some of the studies carried out in order to make the desired changes on the phone using this communication are given below.

Firdaus [1], determined a geographical boundary using the Geofencing technique. The mobile phone that enters these boundaries automatically switches itself to silent mode. In this way, the sounds of incoming calls and the phone's own warning tones are turned off. In this study, the location information must be constantly open in order for the application installed on the phone to work and therefore for the phone to understand that it has entered the specified area.

Jang and Kim [2] developed an Android application for phones to be able to switch to silent mode. This application can automatically silence the phone mode according to the planned program. The phone user prepares an agenda

program. I will be at a meeting in this building at this time on Sunday. The application that memorizes this event uses the location feature to silence the phone during those hours. Similarly, in this study, the phone's location information must be turned on in order to determine the location.

Zin and friends [3] by drawing a digital area using the geofencing technique, it has managed to silence mobile phones within the drawn border. This system, which uses GPS (Global Positioning System) hardware, detects when a mobile phone enters or leaves this area. Previously visited locations are recorded. When the person leaves the specified location area, the phone returns to its previous mode.

In the studies conducted in the literature, the reasons for automatically muting the phone mode have been for environments where people are in groups, as in our study. In these environments, the main problem has been considered as people forgetting to mute their phones and the distraction of a ringing phone in the environment. The methods used have been created by the phone owners using predetermined time or location information.

Based on the knowledge that location information will not work properly in indoor environments, some studies have accessed location information using Wi-Fi and Bluetooth waves.

Coşar [4], in the study, a person's location was determined using a Wi-Fi access point and certain messages were sent. In the study conducted in the university building, Access Points (Wi-Fi signal booster connection points) were placed on certain floors and corridors and the locations of people connected to these connection points were determined. In this study, users who wanted to benefit from this system were informed that the Wi-Fi service should be on at all times.

Bayar [5] obtained the location information of people in closed environments by using Bluetooth Beacon (signal distributors that contain multiple Bluetooth broadcasts) technology. When the person enters the closed environment and is within the coverage areas of Beacons placed in certain places, the person's location is sent to the mobile phone via the Android application. As in the Wi-Fi location determination study, in this example, the Bluetooth feature on the phone must be turned on in order for this application to communicate with the phone.

As seen in the literature examples, the studies conducted require an application that is pre-installed on the phone. This application is generally specific to the study conducted. However, features such as Wi-Fi, GPS and Bluetooth, which are hardware features of the phone, constitute the main subject of the studies given as examples above.

II. MATERIAL AND METHODS

The programmable cards used in the study, the hardware of the mobile phone and external software were brought together under suitable conditions and a system was prepared by utilizing wireless broadcast technology. A system that distributes Wi-Fi and Bluetooth signals was created with the development card, also known as Ai-WB2, which will be used in this project and has many different models. In order to access the interface of this card, the card is connected to the computer with a USB (Universal Serial Bus) cable. There

are many IDE (Integrated Development Environment) to program the card and they are very simple to use. The operating voltage is between 2.7 volts and 3.6 volts. It can be used by giving energy via the computer or via an external adapter.

The Wi-Fi-Bluetooth module comes ready on this card that we purchased. This card is quite cheap, small and useful. No other card was integrated into this card in the project. It was made to broadcast as an Access Point using only Eclipse IDE. Figure 1 shows the Ai-WB2-12F and Ai-WB2-32S cards that we purchased for use in our study. Since these cards are very small in size, they save space in many projects. These cards have BL602 chips that have low power consumption and are produced by Bouffalo Labs [6].

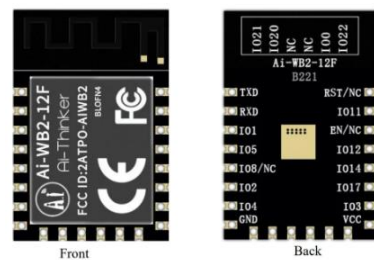


Figure 1: Ai-WB2 front and back

The Wi-Fi and Bluetooth features on the mobile phone were used to see the signals emitted by the Ai-WB2 card, which will distribute Bluetooth and Wi-Fi. In addition, the GPS feature required by the Android operating system was used so that this two ready-made hardware could see the signals.

In order for these three hardware features and the broadcasting card to interact, an application was developed to be loaded onto a mobile phone by coding via the Android Studio platform.

In addition, a domain name and a domain name were purchased and made ready to design a website for the promotion, supply and tracking of the device and application.

III. IMPLEMENTATION OF THE PROJECT

In this study, firstly, Ai_WB2 card, which is a device that will broadcast both Bluetooth and Wi-Fi, was supplied. The software required for programming this card was coded. Although Buffalo Lab's BLDevCub.exe program is both fast and easy to use, since the ready code was modified, the Eclipse IDE compiler program was used. Eclipse IDE can be downloaded from the official website <https://www.eclipse.org/> [7].

After the necessary coding for programming the card was completed, the card was made available to broadcast under the name "sessizmod" [8].

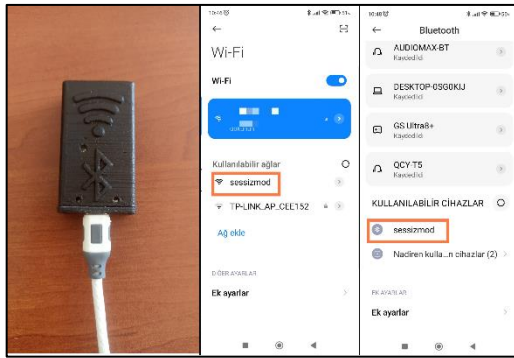


Figure 2: Ai-WB2 card's Wi-Fi and Bluetooth broadcast

As seen in Figure 2, when the phone's Wi-Fi and Bluetooth features are turned on, a connection point appears that broadcasts with the SSID "sessizmod". It continues to broadcast as long as the power is not cut off.

Then, the coding phase of the Android application that will capture the broadcasts of this card and perform mute/unmute operations was started [9].

After installing Android Studio, a new project was created and coding was done in Kotlin language. This coding will do the following; If the mobile phone catches a broadcast named "sessizmod", the phone will be automatically put into silent mode. If the mobile phone moves away from this broadcast area or the power supply of the broadcasting device is cut off, the phone will put itself back into silent mode [10]. There is no need to connect the phone to any network for all these operations.

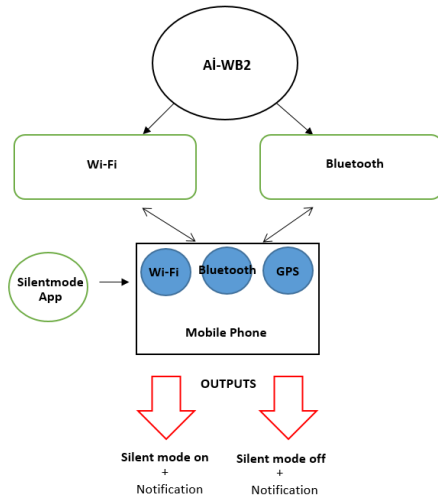


Figure 3: Block diagram of the study

A block diagram of the study is given in Figure 3. The card is powered and starts broadcasting, the mobile phone catches this broadcast, the coded application is loaded onto the phone and this application checks the broadcast names that appear in the Wi-Fi or Bluetooth list and turns the phone silent or mute.

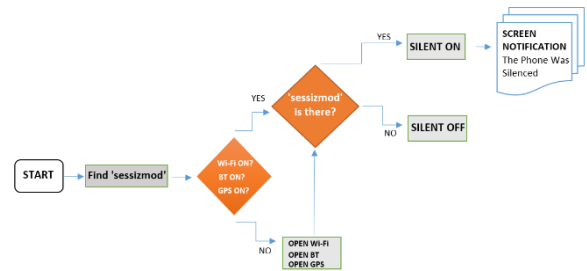


Figure 4: Flow diagram of the study

In the flow chart of the study in Figure 4, it is seen that Wi-Fi, Bluetooth and location features must be kept open at all times in order for the application to remain actively running at all times.

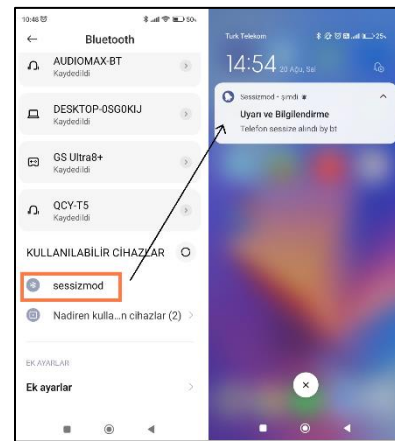


Figure 5: Testing the application via Bluetooth

Figure 5 shows how the application works over Bluetooth. The name "sessizmod" is included in the Bluetooth scan list. The phone has switched itself to silent mode without having to connect to this broadcast. The same process occurs when a Wi-Fi broadcast is detected.

IV. RESEARCH FINDINGS AND DISCUSSION

Android application was installed on mobile phones. Test operations related to the study were performed by virtual phones of many different versions and actively used physical phones. Wi-Fi, Bluetooth and location permissions, which are considered mandatory for Android operating systems, were given. Power was given to the device that will broadcast Bluetooth and Wi-Fi.



Figure 6: Test environment

An average 70 square meter hall was used for the test environment. An image of the test environment is shared in Figure 6. The findings are shown in Table 1 in a tabular form for different situations.

Table 1: Application and device inputs outputs

STATUS	1	2	3	4	5	6	7
W-Fi	ON	ON	ON	ON	OFF	OFF	ON
BLUETOOTH	ON	ON	ON	OFF	ON	ON	OFF
GPS	ON	ON	OFF	ON	ON	ON	ON
"sessizmod" Broadcast	ON	OFF	ON/ OFF	ON	ON	OFF	OFF
RESULT	Silent On	Silent Off	X	Silent On	Silent On	Silent Off	Silent Off
NOTIFICATION	ON			ON	ON		

Findings were created for 7 different situations. Apart from the Table 1, if the phone is silenced by the person, the application is closed in the background and a notification is sent to the phone for the user to open the application ("Silent mode application closed, tap here to open the application"). According to the table, the application will continue to run in the background as long as Wi-Fi/GPS or Bluetooth/GPS are open.

The device that broadcasts Wi-Fi and Bluetooth should be positioned in the center of the room where the system needs to work. It has been observed that if there is a window edge or a wall, the broadcast will also broadcast outside the room. In rooms with an average area of 50-70 square meters, two broadcast devices may be required. Since the Android operating system restricts back-to-back Wi-Fi scanning, scanning via Bluetooth works better. One of the reasons why a card that broadcasts both Bluetooth and Wi-Fi are preferred is to get rid of these Wi-Fi restrictions. For this purpose, a development card known as NodeMCU, which broadcasts only Wi-Fi, was initially programmed, but it was changed when it could not be effective due to the broadcast restriction.

V. CONCLUSIONS AND RECOMMENDATIONS

In our literature review, which we conducted to prevent phones from ringing in areas where people are gathered and where silence should prevail, it is seen that in order for phones to be able to switch themselves to silent mode, the user needs to enter some information into their phone in advance using certain applications. This information includes being in a mosque at a certain time, attending a meeting at a certain time, going to the cinema at a certain time. Alternatively, the user needs to specify the locations of the places they will go through applications to be installed on the phone. However, our main problem is that the person has forgotten to silence their phone before entering the environment. In this case, there is a possibility that daily programs can change at any time, and there are also cases where people do not comply with these programs and forget to enter this information. There may be different environments to be visited other than the places they routinely go to, in which case it may not be possible to enter location information. Unlike previous studies, our application has the advantage of saving the person from such memories,

reminders and planning. As a result, the aim of this study is to silence the phone without the person even knowing, with the information of an SSID broadcasting in the environment where the person is at that moment. The only thing that needs to be done is for the person to have installed the prepared 'Sessizmod' application on their phone once and to have the Wi-Fi/GPS or Bluetooth/GPS duo turned on. The disadvantage of the application is that the phone's Wi-Fi, GPS or Bluetooth features must be constantly on. Moreover, according to a report by MOBİSAD Association, 95.4% of the population of Turkey and 86% of the world's population use smartphones. The Bluetooth features of phones are constantly on due to the Bluetooth devices used (smart watches, headphones, etc.). The spread of Wi-Fi networks to public areas every passing day necessitates that the Wi-Fi feature is constantly on. The location feature is constantly on due to many applications that have to use location information (Google Maps, etc.). These features, which cause power consumption, are no longer disadvantages over time due to the necessity of use [11].

In this study, the phone's Wi-Fi and Bluetooth features were used to automatically switch to silent mode. It may be possible to achieve the goal of this study in a shorter way by using hardware that can continuously listen, such as the proximity sensor found in mobile phones, without the need for any application.

If these devices and applications reach more people, we will no longer have to see the familiar "Please Turn Off/Mute Your Phone" and similar messages. With the hope of becoming a more educated, more understanding, more patient and more sensitive society.

ACKNOWLEDGMENT

We thank the Selcuk University Scientific Research Coordinatorship for their support. This study was produced from Muhammed Abdül Vahap İster's MSc thesis project whose number is 24201031.

REFERENCES

- [1] Ai-Thinker Co., L. Ai-WB2-13. 2024 [cited 2024; Available from: http://www.ai-thinker.com/pro_view-111.html.
- [2] Jang, J.Y.K., Il-Min, Developing a Schedulable App for Switching to Silent Mode Using an Android phone. The Journal of The Institute of Internet Broadcasting and Communication, 2012: p. 53-58.
- [3] Zin, M., et al., Geofencing-based Auto-Silent Mode Application. Journal of Telecommunication, Electronic and Computer Engineering (JTEC), 2016. 8(10): p. 199-204.
- [4] Çoşar, M., Üniversite Yerleşkelerinde Wi-Fi Erişim Noktaları Kullanılarak Konum Belirleme Çalışması. Harita Teknolojileri Elektronik Dergisi, 2014. 6(3): p. 1-9.
- [5] Bayar, A., Kapalı Mekanlarda BLE Beacon Kullanarak Sunucu Tabanlı Konum Takibi, in Fen Bilimleri Enstitüsü Bilgisayar Mühendisliği Anabilim Dalı. 2019, Karabük Üniversitesi.
- [6] Tran, D. and R. Trokic, Mätning av tidsfördröjningar i inbygda system med extern Wi-Fi-modul. 2024.
- [7] Sayiner, B. Eclipse IDE Kurulumu-1. Java 08.03.2021 [cited 2024 08]; 06]. Available from: <https://gelecegiyazanlar.turkcell.com.tr/konu/egitim/java-101/eclipse-ide-kurulumu-1>.
- [8] Qiu, T. Ai-Thinker Ai-WB2-07S WiFi Bluetooth BLE, BL602 Chip. 2024 [cited 2024 08]; 05]. Available from: <https://medium.com/@taraquaithinker/ai-thinker-ai-wb2-07s-wifi-bluetooth-ble-bl602-chip-d1d253097473>.

- [9] Anonim. Android Studio ile Tanışın. 2024; Available from: <https://developer.android.com/studio/intro?hl=tr>.
- [10] Al Tantawy, A. Android Activity Lifecycle. 2020; Available from: <https://www.linkedin.com/pulse/android-activity-lifecycle-ahmed-al-tantawy>.
- [11] MOBISAD, Mobil İletişim Sektörü Raporu, M.İ.A.v.B.T.İ.İ. Demeği, Editor. 2023. p. 14-16.

A Study on Solar-Assisted Hydrogen Production and Reutilization in Rural Areas

S. Z. SHEKARDASHT¹, ALİ ATEŞ²

¹Selcuk University, Konya/Turkey, sajed.zendehdel@yahoo.com

²Sinop University, Sinop/Turkey, aates@sinop.edu.tr

Abstract - Hydrogen is a significant energy source and a strong candidate for energy storage. Solar energy, while clean, is not a continuous energy source. The primary aim of this study is to evaluate, through computer simulation, the feasibility of developing an integrated system for small-scale consumers in rural areas that are disconnected from the electrical grid. In this system, energy generated from solar panels is used both to charge a battery and to produce hydrogen via water electrolysis. The produced hydrogen is stored and can be utilized either as a fuel or converted back into electricity through a fuel cell when needed. A mathematical model was developed for this system, and a theoretical analysis was conducted using computer-assisted solutions. The model utilized data on Sinop City's average monthly solar radiation over the years. Based on the developed mathematical model, a two-stage solution to the problem was implemented using the MATLAB programming language and its auxiliary software package, SIMULINK. Input parameters included water inlet temperature and pressure to the electrolyzer, as well as the efficiency rates of photovoltaic panels. The overall system efficiency and effectiveness, along with the amounts of electricity and hydrogen produced, were obtained as output parameters. The energy density obtained from the fuel cell is closely related to the amount of hydrogen input, the quality of the cell membrane, and the cell pressure. It was found that the inlet temperature is a critical parameter in the amount of hydrogen produced from the electrolyzer. The proposed system can be applied in rural areas of Sinop and in standalone residential regions, such as country houses.

Keywords - PEM fuel cell, PV solar panels, Solar cells, Water electrolysis.

I. INTRODUCTION

THE importance of a clean world and environment is becoming increasingly recognized, prompting many countries worldwide to make substantial investments in developing environmentally friendly systems aimed at climate protection. However, the growing global demand for energy continues to drive the persistent and increasingly rapid use of conventional energy sources, which are major contributors to environmental pollution. Nevertheless, the emphasis on clean and renewable energy sources has also been steadily rising. Although the share of renewable energy in total energy consumption remains relatively low, investments and efforts in this field globally are significant and cannot be underestimated.

Despite being richer in solar energy potential than many European countries, our nation lags behind in effectively converting this energy into usable forms. It should also be

considered that the inability to store solar energy poses additional challenges, necessitating supplementary measures. In this study, solar energy is utilized as a renewable energy source. Hydrogen, recognized as both a renewable energy resource and an excellent energy carrier, is employed alongside photovoltaic panels and fuel cells as the primary electricity generation system.

Several studies on hydrogen production from solar energy are summarized below:

Shabani and Andrews [1] conducted a study to make a solar-hydrogen system more economical for meeting the energy needs of rural households. Their research, supported by experimental validation, involved computer simulations and employed PEM fuel cells. They demonstrated that the stoichiometry of input air and the operating temperature of the fuel cell significantly affect the performance of the Combined Heat and Power (CHP) system. Niknam and Zare [2] investigated PEM fuel cell power plants (FCPPs) and boilers in distribution networks. Their study proposed a framework for stochastic multi-objective optimal operation methods (SMOOM) and utilized the Multi-Objective Modified Firefly Algorithm (MFA). Shahsavari et al. [3] examined air-cooled proton exchange membrane fuel cells (PEMFCs), which are less complex than water-cooled fuel cells. Their findings highlighted that the thermal conductivity of the plates and air velocity significantly impact thermal performance. Najafi et al. [4] proposed a novel configuration to replace conventional PEM fuel cell-based micro-cogeneration systems. By substituting the traditional low-temperature PEM fuel cell with a high-temperature model, they analyzed the new system's behavior from various perspectives. Kahraman et al. [5] investigated the effects of system pressure on fuel cell performance. They found that high temperature and low pressure are favorable for electrolysis, whereas the opposite holds true for fuel cells. Ngoh et al. [6] designed and simulated a high-temperature solar hybrid system for hydrogen production. Dincer et al. [7] explored the effects of coating the anode electrode on the performance of a commonly used fuel cell, identifying positive impacts of the coating on fuel cell lifespan. Ural et al. [8] modeled and simulated a polymer electrolyte membrane fuel cell system using Matlab-Simulink software for mathematical modeling and problem-solving. Their model included a specific function defined for PEM fuel cells.

In this study, a simulation model was developed and

analyzed for a system where hydrogen obtained using solar energy is stored and later converted back into electrical energy using photovoltaic panels and fuel cells. The results obtained from the simulation were evaluated.

II. MATERIALS AND METHODS

The sun, as long as it shines in the sky, provides a continuous and clean source of energy. However, solar energy becomes unavailable during cloudy weather and at night. Moreover, solar energy cannot be stored directly, necessitating its conversion into other forms of energy for practical use. Hydrogen serves as both a renewable and clean energy source, with the added advantage of being storable and accessible when needed.

In this study, a simulation was developed for a hybrid structure utilizing a triple-system setup. In this system, hydrogen is produced via electrolysis using electricity generated from solar panels. The hydrogen is then stored for later use. During periods when solar energy is unavailable, the stored hydrogen is converted back into electricity through a PEM fuel cell. This system offers a viable solution for remote rural areas that are not connected to the main electricity grid.

The modeling process was conducted using MATLAB-SIMULINK™ and further supported by additional MATLAB-based software. The mathematical and theoretical models, as well as the numerical solution methods and methodology employed for the simulation experiment, are detailed below.

In the mathematical model developed, all meteorological data relevant to the environment and conditions in Sinop province were taken into consideration. Since solar energy is the primary energy source, meteorological data play a critical role. Key meteorological data for Sinop, including average annual solar irradiation values for summer and winter months, average regional radiation levels, and other relevant statistics, were obtained from the Regional Meteorological Directorate.

The schematic representation of the simulation system utilized in this study is provided in Figure 1.

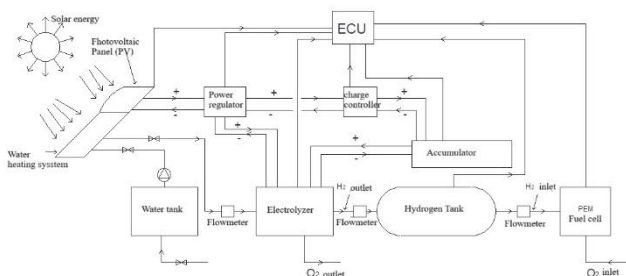


Figure 1: Schematic view of the simulation system planned to be established within the scope of this study

As shown in Figure 1, the system generates electrical energy using PV panels. A solar collector is employed in parallel with the PV panel system to heat the input water for the electrolyzer. The hot water exiting the collector is directly fed into the electrolyzer. The electrical energy generated by the PV panels passes through a power regulator. Part of this energy is supplied to the electrolyzer unit, while the remaining portion is sent to a

charge controller unit and then stored in an accumulator.

The hydrogen H_2 produced via electrolysis is collected in a storage tank, while the oxygen O_2 produced as a byproduct is released into the environment. The hydrogen tank may be pressurized, which would require a small compressor to pump the hydrogen into the tank. The hydrogen required by the PEM fuel cell for energy production is drawn from this tank, while the oxygen needed is sourced from the air.

In the second stage of the system, a PEM fuel cell is used to generate electricity. An Electronic Control Unit (ECU) is employed to monitor all the components, with each unit connected to the ECU.

Mathematical Model:

The energy entering the system in the process of separating hydrogen and oxygen from water is equal to the enthalpy change [9].

$$\Delta H = \Delta G + \Delta Q = 79 \text{ W/mol} \quad (1)$$

Here ΔG is the Gibbs free energy and ΔQ is the change in thermal energy.

Energy conversion of photovoltaic system:

In the PV system, solar energy is converted into electrical energy. The electrical energy produced can be written as follows [9].

$$E_{el} = \eta_e A q_1 R_{Cor} \quad (2)$$

Here E_{el} is the generated electrical energy, η_e is the electrical efficiency of the solar collector system, A is the area of the solar collector system, q_1 is the effective solar heat flux per unit area, R_{Cor} is the correction factor.

The produced heat energy is as follows [9];

$$E_t = \eta_t A q_1 R_{Cor} \quad (3)$$

Here E_t is the total heat energy produced, η_t is the thermal efficiency of the solar collector system.

The total energy of the collector is calculated from the relation;

$$E_{tot} = E_{el} + E_t \quad (4)$$

The energy drawn by the electrolyzer can be expressed as follows [10]:

$$E_{elec} = U/R_{elec} (6.5 \cdot 10^{-5} T_{elec} \ln(P_{elec})) \quad (5)$$

Where U is the potential difference required to separate a unit mass of water, R_{elec} is the electrolyzer resistance, T_{elec} is the temperature of the electrolyzer, P_{elec} is the pressure of the electrolyzer.

The thermal energy entering the electrolyzer through the solar collector is given as [9];

$$E_{th,elec} = T_{elec} \Delta S/t \quad (6)$$

ΔS is the entropy change for the dissociation of a unit mass of water and is $\Delta S = 116 \text{ J/K}$.

The total energy drawn by the electrolyzer is expressed as:

$$E_{tot,elec} = E_{elec} + E_{th,elec} \quad (7)$$

The electrical energy produced from the collector directly enters the power regulator. In the power regulator, a portion of the energy enters the electrolyzer machine based on the electrolyzer's needs and the remaining extra energy is stored in

the accumulator via the charge controller.

The following expression can be given for the amount of hydrogen produced in electrolysis [9]:

$$m_{H_2} = E_{tot.elec}/(9 \cdot E_{elec}) \quad (8)$$

The following relations can be given for the fuel cell [11]:

$$V_{cell} = E_{Nernst} - V_{act} - V_{ohm} - V_{conc} \quad (9)$$

Here V_{cell} is the cell voltage, E_{Nernst} is the no-load voltage, V_{act} is the activation voltage drop, V_{ohm} is the ohmic voltage, V_{conc} is the overvoltage.

The electrical energy produced by the system is calculated with the relation [11];

$$P = I \cdot V_{cell} \quad (10)$$

The Nernst equation is given by the following equation [12]:

$$E = E_0 - 0.85 \cdot 10^{-3} (T - 298.15) + \frac{RT}{2.F} \ln \left(\frac{p_{H_2} \cdot p_{O_2}^{0.5}}{p_{H_2O} \cdot p^{0.5}} \right) \quad (11)$$

The activation voltage drop can be analyzed by the Tafel connection [13]:

$$E_{act} = -0.9514 + 0.00312 \cdot T - 0.000187 \cdot T \cdot [\ln(I)] + 7.4 \cdot 10^{-5} \cdot T \cdot [\ln(C_{O_2})] \quad (12)$$

$$C_{O_2} = \frac{p_{O_2}}{5.08 \cdot 10^6 \exp(-498/T)} \quad (13)$$

$$V_{ohm} = I \cdot R_{mem} \quad (14)$$

Here R_{mem} is the membrane resistance;

$$R_{mem} = \frac{t_{mem}}{\sigma} \quad (15)$$

is given as [8]. t_m is the membrane thickness and σ is the membrane conductivity.

By assuming that all gases are ideal, the ideal gas law can be extended for dynamic analyses and the law of conservation of mass, general equations and the reactant flow model can be used (Gemmen, 2001a).

$$\frac{V}{RT} \frac{dP_g}{dt} = m_{in} - m_{out} \pm \frac{I}{n.F}$$

System Simulation:

MATLAB-SIMULINK™ software was used for the simulation of the system. The main system in the program consists of some subsystems as seen in Figure 2. Each of these subsystems represents the solutions of various components that make up the system. The subsystems that make up this system are as follows: Calculations and simulation of the electrical and thermal energy produced by solar panels, calculations and simulation of the distribution of electrical energy in the power regulator to consumers, calculations and simulation of the electrical demand of the electrolyzer and the amount of H2 produced, calculations and simulation of the charge controller, calculations and simulation of the electrical energy sent to charge the accumulator, fuel cell calculations and simulation, and finally, simulation of the operations performed by the ECU in the system for the purpose of controlling these units.

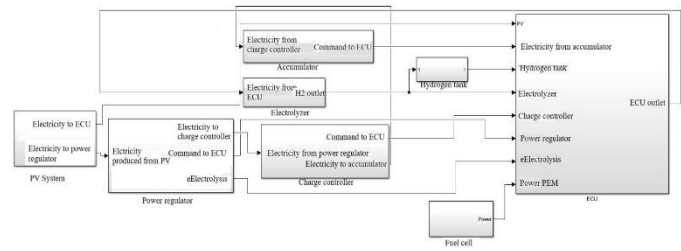


Figure 2: Block diagram of hydrogen production system

III. RESEARCH FINDINGS AND DISCUSSION

In this study, MATLAB-SIMULINK™ software was used for the simulation of the system. Various key loops were integrated to prevent issues that may arise from algebraic loops and excessively high numerical values. This study consists of two stages. The first stage involves hydrogen production supported by a solar collector and the storage of the produced hydrogen in a tank. The second stage involves utilizing the produced and stored hydrogen in a fuel cell.

In the first stage, the monthly average solar radiation and sunshine duration for the Sinop region were obtained from the General Directorate of Meteorology. Simulations were conducted for the PV system using three different panel efficiencies (11.5%, 13.5%, and 17%), two different operating temperatures (353 K and 473 K), and two different operating pressures (100 kPa and 400 kPa) as the main input parameters. The results were presented in graphical form, showing variations under constant temperature with different pressures and constant pressure with different temperatures. The results indicate that the amount of hydrogen production is more significantly influenced by temperature increases than by pressure changes.

In the second stage, simulations were carried out for a PEM fuel cell using three different hydrogen flow rates (5.5, 8, and 11.2 SLPM - standard liters per minute) and the corresponding air flow rates (81, 120, and 166 SLPM). The simulation duration was set to 1.5 seconds. The results were plotted as graphs of cell voltage and stack power over time.

Figure 3 shows the electrical energy obtained from PV systems with different efficiencies. As seen in the figure, the electrical energy produced is closely related to the efficiency of the PV system. The increase in electrical energy obtained from high-efficiency and high-quality materials is clearly observable in the figure.

In Figure 4, the amount of energy going to the electrolyzer according to the temperature of 353 K is given according to monthly averages. As can be understood from the figure, the energy going to the electrolyzer is at the lowest level in the summer months. Because while the energy produced by the PV in the summer months is at the maximum level, if the energy consumed by the electrolyzer is considered constant, the ratio decreases according to the energy produced in the PV. While very little change is observed depending on the pressures, the energy going to the electrolyzer is slightly higher at low pressures and slightly lower at high pressures.

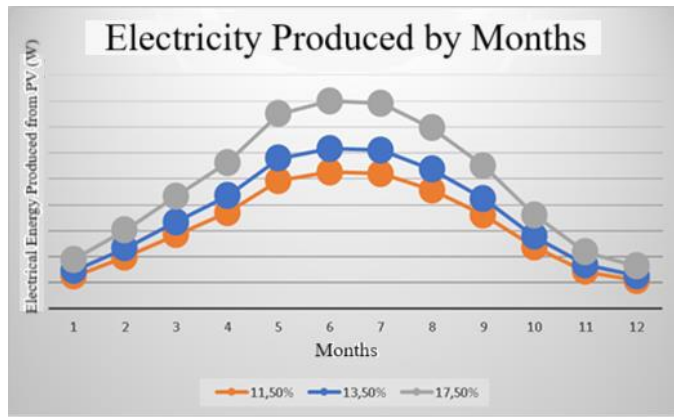


Figure 3. Electrical energy obtained from PC according to different efficiencies.

Similar interpretations can be made for these figures as for those obtained for temperature values. In other words, as evident from both figures, the energy supplied to the electrolyzer increases only slightly with temperature. Additionally, there is no significant variation in the monthly averages of both figures. Thus, the change in energy supplied to the electrolyzer is not primarily dependent on temperature or pressure.

When the graphs from Figures 4 to 7 are carefully examined, it becomes clear that the highest electrical energy consumption by the electrolyzer occurs at a pressure of 100 kPa and a temperature of 473 K. However, this difference is not substantial, and it can be confidently stated that the energy consumed by the electrolyzer is not primarily dependent on temperature or pressure.

The situation differs when considering the amount of hydrogen produced. Specifically, when Figure 8, which shows the monthly average hydrogen production for 100 kPa, is examined closely, it is evident that the amount of hydrogen produced increases noticeably with temperature. According to the figure, hydrogen production increases during the summer months. This is due to the longer duration of solar radiation during the summer.

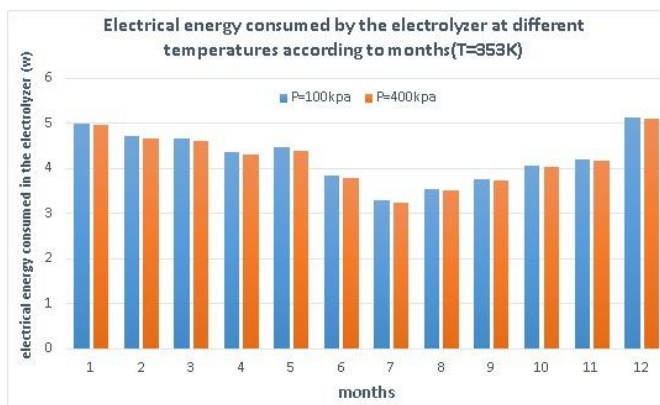


Figure 4: Monthly average electrical energy going to the electrolyzer at 353 K temperature

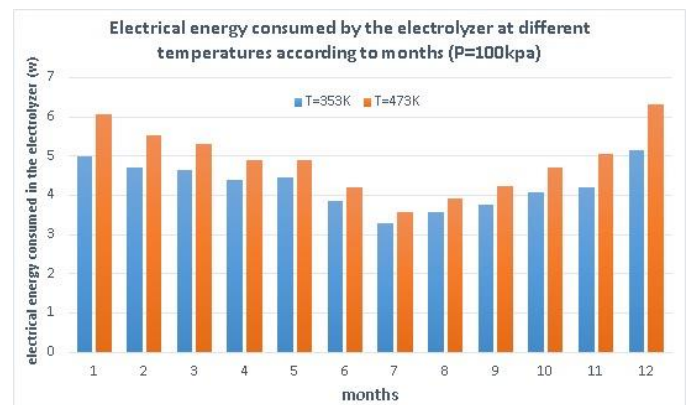


Figure 6: Monthly average electrical energy going to the electrolyzer at 100 kPa pressure

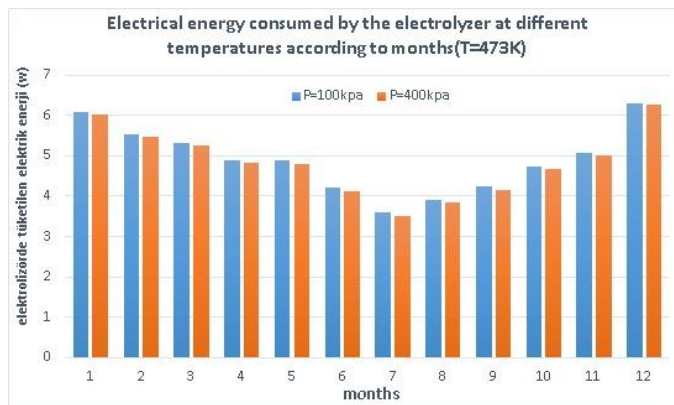


Figure 5: Monthly average electrical energy going to the electrolyzer at 473 K temperature

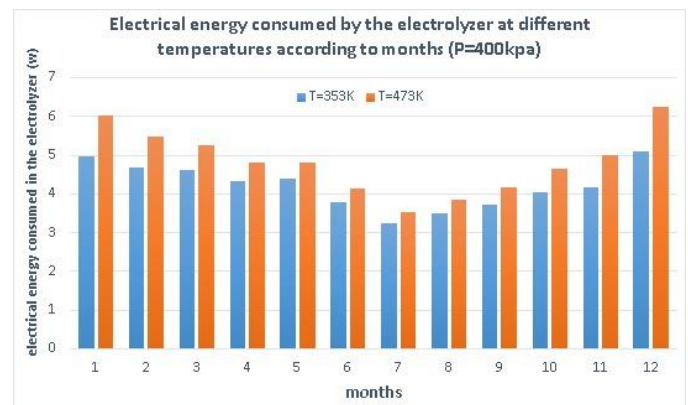


Figure 7: Monthly average electrical energy going to the electrolyzer at 400 kPa pressure

In Figure 5, the amount of energy going to the electrolyzer according to the temperature of 473 K is given according to monthly averages. Due to the similarities of this figure to Figure 4, the same comments made for Figure 4 are valid for this figure. Therefore, the energy consumed by the electrolyzer changes very little with pressure and temperature or remains the same.

Figures 6 and 7 illustrate the monthly average energy delivered to the electrolyzer for pressures of 100 and 400 kPa.

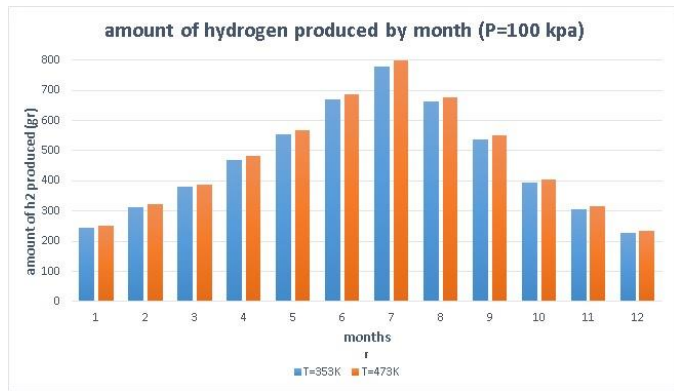


Figure 8: Monthly average amount of H₂ produced at 100 kPa pressure.

The same comments can be made in Figure 9, given for a pressure of 400 kPa. However, as can be understood from the fact that the figures are very close to each other, the effect of the pressure increase is small. Nevertheless, it can be said that the amount of hydrogen production increases very little at high pressures.

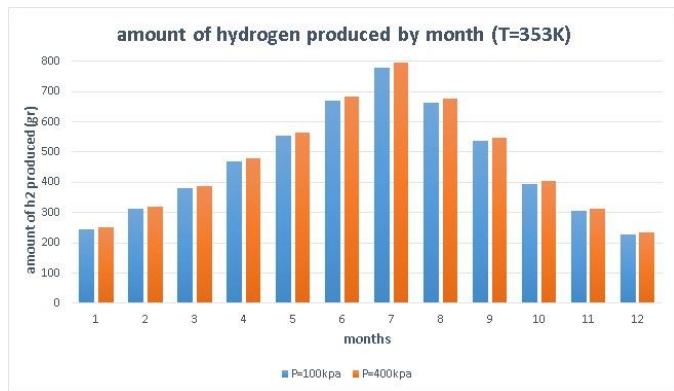


Figure 10: Monthly average H₂ amount produced at 353 K temperature

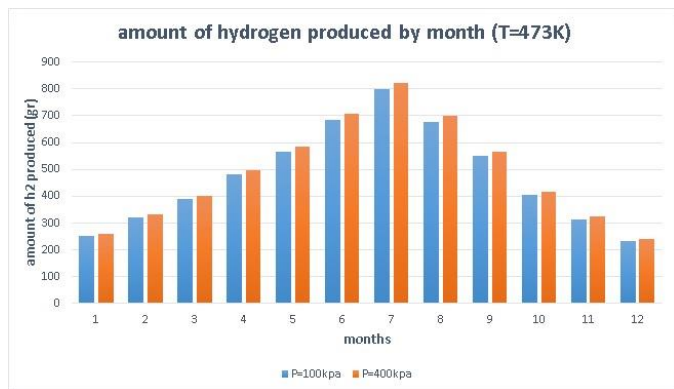


Figure 11: Monthly average H₂ amount produced at 473 K temperature

Figures 10 and 11 present the monthly average hydrogen production graphs for temperatures of 353 K and 473 K, respectively. In Figure 10, corresponding to 353 K, it can be

observed that the amount of hydrogen produced increases with rising pressure. However, the difference is not very significant. Additionally, the graph clearly shows that the hydrogen production during the summer months is higher compared to the winter months. For example, the average production in summer ranges between 600 and 800 grams, whereas in winter, it ranges between 200 and 400 grams. This difference is related to the longer solar radiation duration in summer.

Figure 11 depicts the graph obtained for 473 K. In this case, the average production during the summer months is between 700 and 900 grams, while the winter average is approximately 325 grams.

As clearly seen from these data, the amount of hydrogen production increases with temperature. This can be attributed to the weakening of atomic bonds between water molecules with increased temperature, reducing the energy required to break the bonds.

In the second stage or phase of the study, the produced hydrogen gas was used in a PEM fuel cell to generate electrical energy. The PEM fuel cell used in this study was selected from catalog specifications.

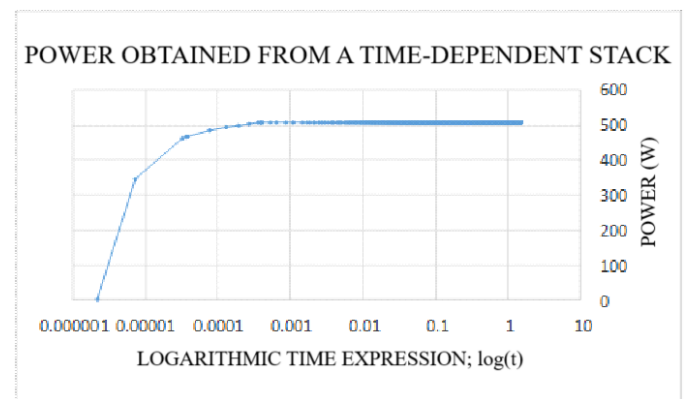


Figure 12: PEM fuel cell power curve for 5.5 SLPM H₂

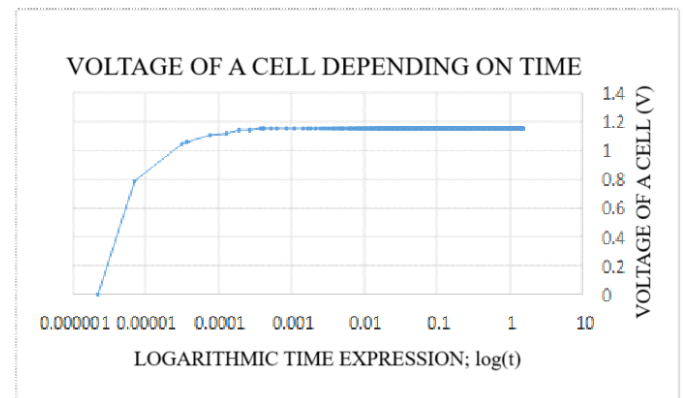


Figure 13: Cell output voltage for 5.5 SLPM H₂

The modeled PEM fuel cell has a nominal power of 500 W. When operating at this power, the DC voltage is 23 V, and the current is 22 A. Although the maximum power of the PEM fuel cell is 1100 W, due to internal resistances, the actual achievable power is around 1000 W. Under these conditions, the DC

voltage can still be considered as 23 V, while the current reaches approximately 45 A. For a power output of 500 W, the hydrogen input is 5.5 SLPM, and for a power output of 1000 W, the hydrogen input corresponds to 11.2 SLPM.

The simulation results obtained for the given input parameters are shown in the graphs below, specifically for 5.5 SLPM. In these studies, the simulation duration was set to 1.5 seconds. The graphs are plotted as power vs. time and voltage vs. time. To better visualize the results at the initial time points, the time axis in the graphs is presented using a logarithmic scale.

IV. CONCLUSION

Solar energy systems have low efficiency; however, since this energy is continuous and easily accessible, it can be utilized to generate electricity. If part of the energy obtained from the sun is used for water electrolysis, hydrogen fuel—another clean and renewable energy source—can be produced affordably and easily. Although the efficiency during energy conversions is currently low, it can be improved with the development of new technologies. Both the conversion of solar energy into electricity and the processes of hydrogen production using this energy and its utilization in fuel cells stand out as extremely clean, environmentally friendly, and renewable energy methods.

In this study, an experimental energy production setup proposed to be established in the Sinop province was simulated. For this simulation, necessary formulations for main processes, including electricity generation from PV solar panels, hydrogen production via water electrolysis, and the use of hydrogen in a PEM fuel cell, were implemented using software developed in MATLAB programming language and MATLAB-SIMULINKTM package software.

The results indicate that the energy generated from PV solar panels reaches its peak levels during summer months. A portion of this total energy is consumed by the electrolyzer. Considering that the energy consumed by the electrolyzer remains approximately constant, the portion of electrical energy from PV panels sent to the electrolyzer is at its minimum during summer.

The amount of hydrogen production increases slightly with the rise in pressure in the electrolyzer. However, this increase is not substantial. In contrast, the amount of hydrogen production rises significantly with increasing temperature compared to pressure. This is because higher temperatures weaken the atomic bonds, making it easier to separate molecules into their constituent atoms.

On the other hand, the energy consumption of the electrolyzer does not vary significantly with temperature or pressure.

Hydrogen should be supplied to the PEM fuel cell under pressure. In this study, the fuel cell pressure was set to 2 bar. Additionally, the internal resistance of the fuel cell is a critical factor in power generation. The membrane is the primary component contributing to the internal resistance. In this study, the internal resistance was set to 100 mOhm for calculations.

The simulation duration was set to 1.5 seconds, as no changes in power or cell voltage occur beyond this point.

The graphs clearly demonstrate that the power generated by the PEM fuel cell is directly related to the amount of hydrogen supplied to it.

Although the power output increases with the amount of hydrogen supplied, this should be limited to a certain value. This is because the fuel cell has a specific capacity, and excess hydrogen results in excess heat. Overheating the device is undesirable.

REFERENCES

- [1] B. Shabani, and J. Andrews, 2011, An experimental investigation of a PEM fuel cell to supply both heat and power in a solar-hydrogen RAPS system, *International Journal of Hydrogen Energy*, 36 (9), 5442-5452.
- [2] T. Niknam, and M. Zare, 2012, Probabilistic hydrogen, thermal and electrical management of PEM-fuel cell power plants in distribution networks, *International Journal of Hydrogen Energy*, 37 (23), 18243-18260.
- [3] Shahsavari, S., Desouza, A., Bahrami, M. ve Kjeang, E., 2012, Thermal analysis of air-cooled PEM fuel cells, *International Journal of Hydrogen Energy*, 37 (23), 18261-18271.
- [4] B. Najafi, A. H. Mamaghani, A. Baricci, F. Rinaldi, and A. Casalegno, 2015, Mathematical modelling and parametric study on a 30 kW el high temperature PEM fuel cell based residential micro cogeneration plant, *International Journal of Hydrogen Energy*, 40 (3), 1569-1583.
- [5] H. Kahraman, I. Çevik, and S. Coşman, 2014, Sıkıştırma Basıncının PEM Yakıt Pili Performansına Etkisi. ISITES. Karabük – TURKEY.
- [6] Ngoh, S. K., Ohandja, L. A., Kemajou, A. ve Monkam, L., 2014, Design and simulation of hybrid solar high-temperature hydrogen production system using both solar photovoltaic and thermal energy, *Sustainable Energy Technologies and Assessments*, 7, 279-293.
- [7] K. Dinçer, O. Şahin, S. Yayla, and A. Avcı, 2014, Anot tarafi elektrosin metodu ile YSZ+SDC+NaCaNiBO ile kaplanmış PEM Yakıt hücresinin performansının deneysel olarak incelenmesi, *Journal of Technical-Online*, 13, 1.
- [8] Z. Ural, 2007, Yakıt Pilleri ve Bir PEM Yakıt Pili Sisteminin Dinamik Benzetimi, M.Sc. Thesis, Institute of Science, June, Dicle University.
- [9] J. Padin, T. Veziroglu, and A. Şahin, 2000, Hybrid solar high-temperature hydrogen production system, *International Journal of Hydrogen Energy*, 25 (4), 295-317.
- [10] M. Rzaeva, O. Salamov, and M. Kerimov, 2001, Modeling to get hydrogen and oxygen by solar water electrolysis, *International Journal of Hydrogen Energy*, 26 (3), 195-201.
- [11] C. Ziogou, S. Voutetakis, S. Papadopoulou, and M. C. Georgiadis, 2011, Modeling, simulation and experimental validation of a PEM fuel cell system, *Computers & Chemical Engineering*, 35 (9), 1886-1900.
- [12] J. Larminie, A. Dicks, and M. S. McDonald, 2003, Fuel cell systems explained, Wiley New York, p.
- [13] J. C. Amphlett, R. M. Baumert, R.F. Mann, B. A. Peppley, P. R. Roberge, and T. J. Harris, 1995, Performance Modeling of the Ballard-Mark-Iv Solid Polymer Electrolyte Fuel-Cell .1. Mechanistic Model Development, *Journal of the Electrochemical Society*, 142 (1), 1-8.

Investigation of Superstrate Effects on Seljuk Star Microstrip Antenna

AYŞE ÖZGE CINAR AK¹, DİLEK UZER¹

¹ Konya Technical University, Konya/Turkey, aocinar@ktun.edu.tr

¹ Konya Technical University, Konya/Turkey, duzer@ktun.edu.tr

Abstract—In this study, the effects of using a dielectric superstrate on the microstrip antenna have been investigated such as operating frequency and gain in the Industrial Scientific Medical (ISM) band. Seljuk Star patch geometry is preferred due to its many advantages in microstrip antenna design and 4.75 mm thick RT-Duroid 5880 LZ dielectric material of is used as the substrate material. Simulations by ANSYS HFSS and measurements of the manufactured antenna are performed by stacking three different superstrate layers as woolen felt, FR-4 and RT-Duroid 5880 LZ above the patch and the results are compared. The effect of the change in the height of these different superstrate materials on the antenna performance is also investigated with simulations. The results from simulation show that with the addition of woolen felt, FR-4 and RT-Duroid 5880 LZ superstrate, the basic antenna gain is increased by 4%, 5% and 20% when it is 7.92 dB for the basic design, and the frequency is shifted down by 9%, 14% and 8% from 5.5 GHz of the basic design. In addition, when the thickness of the superstrate used increased, the frequency shifted more downward. Therefore, with the down shift of the frequency, a decrease in patch size is obtained for the same target frequency. As seen from these results, the addition of superstrates with different features on the patch is a simple and low-cost method to expand the antenna gains and can be applied in the basic design of the antenna and after manufacturing.

Keywords—Dielectric Superstrate, Gain, HFSS, Microstrip antenna, Resonant frequency, Seljuk star, Woolen felt.

I. INTRODUCTION

THE concept of the microstrip antenna was first proposed in the 1950s, and with the advancement of printed circuit technology, numerous practical applications of microstrip antennas mounted on missiles and aircraft were developed in the early 1970s. During this period, research on microstrip antennas rapidly increased, laying the foundation for the emergence of a new antenna industry [1]. Microstrip antennas are among the most popular types of antennas due to their design flexibility, lightweight, low production costs, and ease of implementation. Microstrip patch antennas have a low profile and weight. Their small size and the ability to share the same dielectric layer with circuit components enable easy integration with circuit structures, without increasing the size of portable devices [2]. However, the electrical parameters such as resonance frequency,

bandwidth, return loss, gain, and efficiency may sometimes be insufficient. Therefore, various methods are applied to enhance the gain of microstrip antennas; [3,4] adding a dielectric superstrate to the antenna is one of these methods [5-22]. In previous studies, adding a dielectric superstrate to an antenna has proven to be a simple and effective method for adjusting the operating frequency and enhancing the antenna's gain [6]. Initially, the dielectric superstrate was used as a protective cover to shield the antenna from environmental factors and for privacy purposes. Later, it was discovered that the antenna's gain and efficiency could be improved by using a superstrate with optimized parameters [7-11]. The dielectric superstrate antenna functions as a directive parasitic element to enhance the antenna's gain. Such a dielectric superstrate behaves like an aperture antenna, increasing the effective aperture size and extending the antenna's directivity beyond the original design. The use of a superstrate with high electrical permittivity results in a gain improvement; additionally, reflective layers can also be employed to further increase gain. However, if the dielectric superstrate is not designed under appropriate conditions, it can negatively affect the gain and efficiency. Therefore, the radiation characteristics of the superstrate antenna should be carefully evaluated, and necessary precautions should be taken to prevent any adverse impact, whether positive or negative [10,12]. The effectiveness of the dielectric superstrates used can be enhanced by achieving the resonance condition of a quarter-wavelength air gap on the antenna surface [9]. This addition shifts the resonance frequency downward by altering the effective permittivity of the antenna. As a result, it reduces the antenna size for the same target frequency while improving narrowband characteristics and increasing the half-power bandwidth. The bandwidth increases in direct proportion to the thickness of the superstrate. If the lower substrate is sufficiently thin, the addition of the superstrate significantly improves the antenna's efficiency [10,11,13,14,15]. This study aims to examine the scope and applicability of the superstrate as a performance enhancement tool for antennas. This technique provides improvements in antenna parameters such as bandwidth, beamwidth, gain, resonance frequency, input impedance, return loss, and

VSWR (Voltage Standing Wave Ratio) without significant cost or design complexity.

When designing a microstrip antenna, characteristics must be considered such as the patch size, substrate height, substrate width, and their relative proportions. Microstrip patch antennas consist of three layers: a conductive patch, a dielectric substrate, and a conductive ground plane. Numerous geometries can be used in the design of the conductive patch, with the most popular being rectangular and circular shapes. However, in this study, the Seljuk Star patch geometry, introduced by Uzer and shown to offer numerous advantages compared to other geometries, has been preferred [16]. Accordingly, in this study, a dielectric superstrate has been added in contact with the antenna on a Seljuk Star-shaped patch antenna, using different materials such as wool felt, FR-4, and Duroid 5880 LZ. The effects of using superstrates made from these different materials on antenna performance have been investigated. In addition, the impact of the thickness parameters of these dielectric materials on antenna performance has been examined.

II. MATERIAL AND METHOD

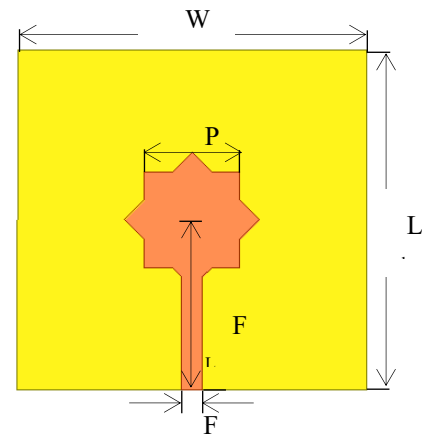
A. Design of Seljuk Star Microstrip Patch Antenna

The patch geometry has first introduced to literature in [17,18] and the initial design parameters are determined based on traditional circular patch antenna formulas. Using the trial-and-error method, the optimum results can be obtained. For the same resonant frequency, the surface area of Seljuk star patch is smaller than the circular one and this provides advantages in terms of some losses.

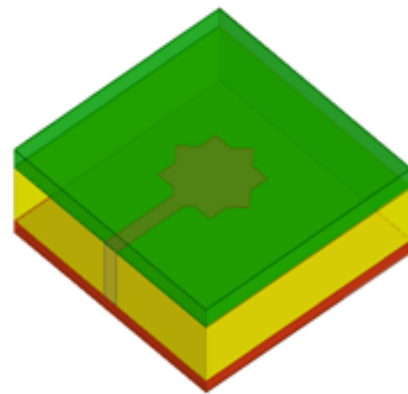
As shown in Figure 1.a, an antenna has been designed using a simple Seljuk Star patch shape. The optimal parameters for this design were determined using the HFSS program at a frequency of 5.8 GHz, and the design was implemented on a Rogers RT/Duroid 5880 LZ substrate ($h = 4.75$ mm). Figure 1.b shows an example of one of the superstrate structures added on top of the microstrip antenna. The physical parameters of the basic antenna are provided in Table 1. As a feeding method, a microstrip line feed has been chosen.

Table 1: Seljuk Star-Shaped Microstrip Antenna Parameters

Parameter	Value (mm)
P_x	18.00
L_{gnd}	64.00
W_{gnd}	66.00
F_L	32.00
F_W	4.00
h	4.75
ϵ_r	1.96



(a)



(b)

Figure 1: The designed antenna; a) Basic design, from HFSS model, b) With superstrate from HFSS model.

B. Superstrate Addition and Effects

In Figure 2, the initial microstrip antenna structure manufactured and the configurations after the addition of superstrates are shown.

Here, the characteristics of the antenna parameters change as a function of the dielectric superstrate layer. When the effective dielectric constant of the structure is known, the resonance frequency of a microstrip antenna covered with a dielectric superstrate can be determined. The change in resonance frequency with the placement of the dielectric superstrate is calculated using Equation 1 and Equation 2 [19].

$$\frac{\nabla f_r}{f_r} = \frac{\sqrt{\epsilon_e} - \sqrt{\epsilon_{e0}}}{\sqrt{\epsilon_e}} \quad (1)$$

If $\epsilon_e = \epsilon_{e0} + \nabla \epsilon_e$ and $\nabla \epsilon_e \leq 0.1 \epsilon_{e0}$, then

$$\frac{\Delta f_r}{f_r} = \frac{1}{2} \frac{\Delta \epsilon_e / \epsilon_{e0}}{1 + 1/2 \Delta \epsilon_e / \epsilon_{e0}} \quad (2)$$

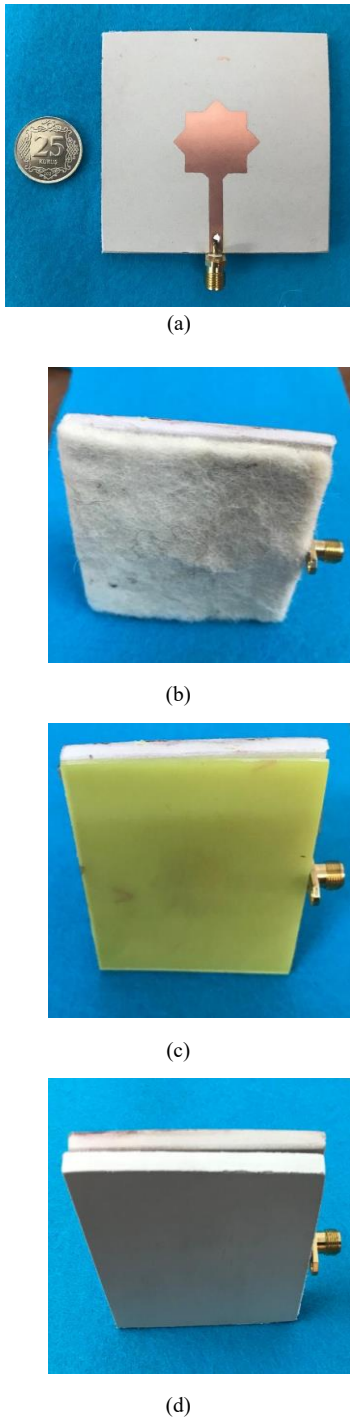


Figure 2: Superstrate-Added Antennas: a) Initial design, fabricated antenna, b) Fabricated antenna with wool felt superstrate, c) Fabricated antenna with FR-4, d) Fabricated antenna with RT-Duroid 5880 LZ.

Where,

ϵ_e = Effective dielectric constant with dielectric superstrate

ϵ_{e0} = Effective dielectric constant without dielectric superstrate

$\Delta\epsilon_e$ = Change in dielectric constant due to dielectric superstrate

Δf_r = Fractional change in resonance frequency

f_r = Resonance frequency

Due to the inability of the felt used as the superstrate to stand upright on its own, it was placed adjacent to the patch without leaving any air gap. However, due to the pin height

of the SMA connector, a very small air gap between the superstrate and the patch surface occurred around the junction point. Double-sided tape was used for fixation. Because of the tape's very thin structure, dielectric effects of it were neglected. Other superstrate materials were also evaluated using the same configuration.

Table 2: Parameters Of Used Superstrates

Material	Parameters		
	Thickness (mm)	ϵ_r	$\tan\delta$
Woolen Felt*	3.000	1.45	0.044
RT-5880LZ*	4.750	1.96	0.002
FR-4	1.600	4.17**	0.020*

* Parameters from literature

**This value is measured with TLM.

III. EXPERIMENTAL RESULTS AND DISCUSSION

The fabricated microstrip antenna was measured first in its initial form, and then with the sequential addition of woolen felt, Duroid 5880 LZ, and FR-4 superstrates. A Rohde Schwarz ZVL-13 vector network analyzer was used to measure the antenna prototypes, and the device was calibrated prior to measurements using a calibration kit. The antenna measurement setup is shown in Figure 3.

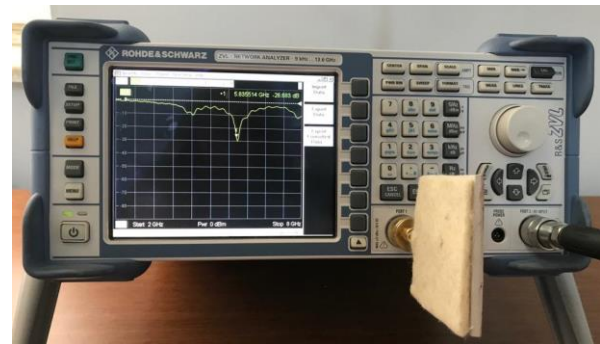
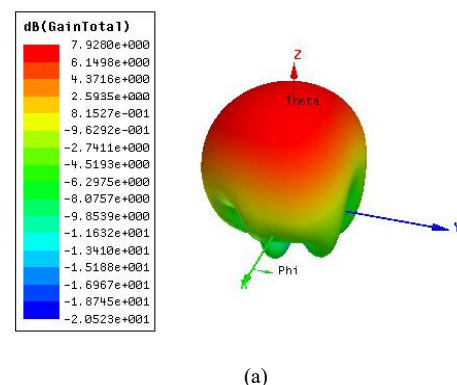


Figure 3: Measurement of the microstrip antenna with woolen felt superstrate using a network analyzer.

Figure 4 shows the 3D polar (in dB gain) plots obtained using HFSS for all the proposed antenna configurations. The gain of the initial design antenna is 7.92 dB, while with the addition of the felt superstrate ($\epsilon_r = 1.45$), FR-4 superstrate ($\epsilon_r = 4.17$), and RT-Duroid 5880 LZ superstrate ($\epsilon_r = 1.96$), the gain increases to 8.27 dB, 8.36 dB, and 9.51 dB, respectively.



(a)

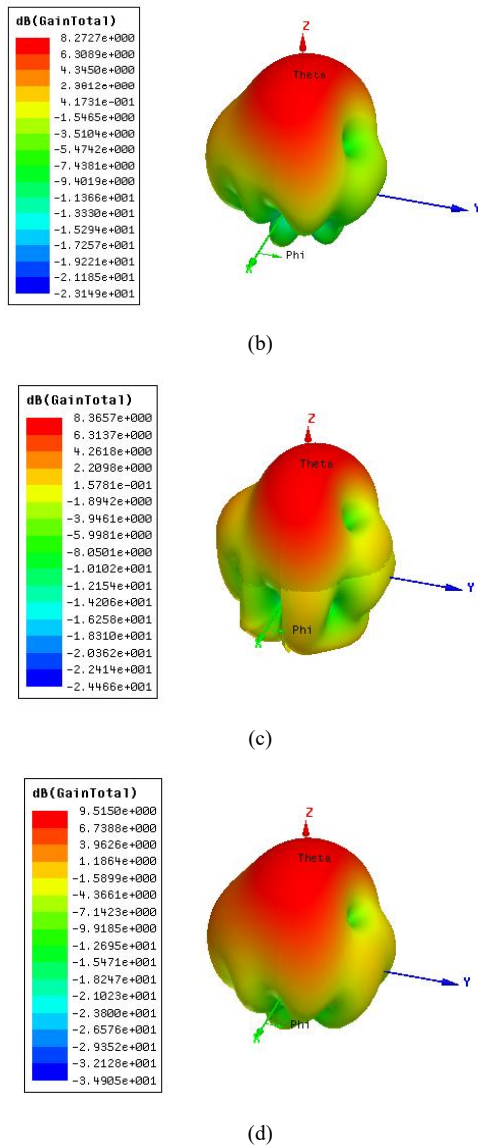
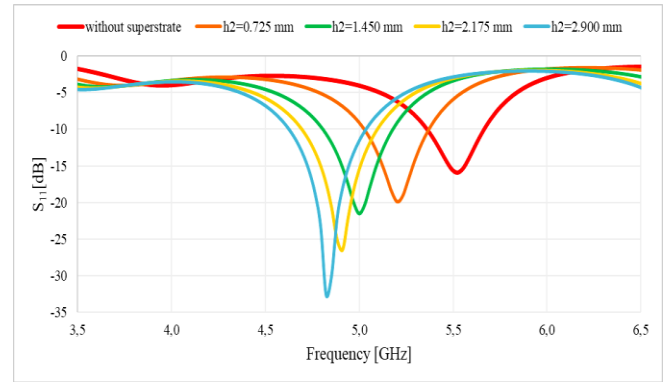


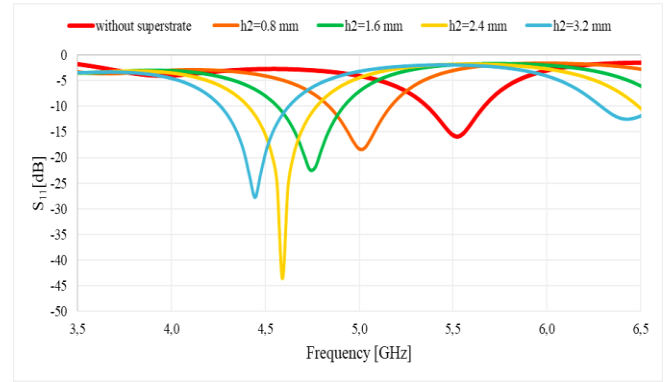
Figure 4: 3D Polar Gain Plots from HFSS; a) Initial design antenna, b) With wool felt superstrate, $h_2 = 1.45$ mm, c) With FR-4 superstrate, $h_2 = 1.60$ mm, d) With RT-Duroid 5880 LZ superstrate, $h_2 = 4.75$ mm

Figure 5 shows the effect of different dielectric superstrate thicknesses on the operating frequency of the antenna. Designs were made for wool felt at thicknesses of 0.725 mm, 1.420 mm, 2.175 mm, and 2.900 mm; for FR-4 at 0.800 mm, 1.600 mm, 2.400 mm, and 3.200 mm; and for RT-Duroid 5880 LZ at 1.187 mm, 2.375 mm, 3.562 mm, and 4.750 mm. As the thickness of the dielectric superstrate material increased, the frequency shifted downward.

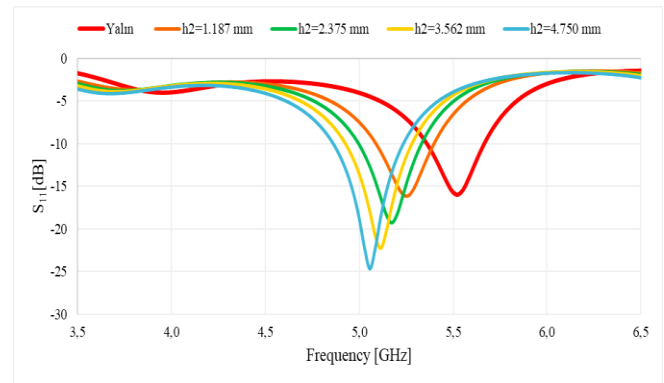
The thicknesses of the dielectric materials were selected based on commonly used values found in the literature.



(a)



(b)



(c)

Figure 5: Effect of Superstrate Thickness on the Antenna: a) Wool felt superstrate, S_{11} values, b) FR-4 superstrate, S_{11} values, c) RT-Duroid 5880 LZ superstrate, S_{11} values.

Figure 6 shows the measurement and simulation results for the fabricated antennas. Production was carried out for wool felt, FR-4, and RT-Duroid 5880 LZ dielectrics with thicknesses of 3.00 mm, 4.75 mm, and 1.60 mm, respectively. The initial antenna has a return loss of -15.94 dB at a frequency of 5.50 GHz, while the addition of the superstrates shifted the resonance frequency downward. For the FR-4 superstrate, the S_{11} value at 4.73 GHz was -22.31 dB, for the wool felt superstrate the S_{11} value at 4.99 GHz it was -21.46 dB, and for RT-Duroid 5880 LZ the S_{11} value at 5.05 GHz it was -24.63 dB. The bandwidth of the initial antenna at 5.5 GHz was 5%, whereas with the addition of wool felt, FR-4, and RT-Duroid 5880 LZ superstrates, dielectrics, the bandwidth increased to 41.2% at 4.99 GHz, 37.9% at 4.73 GHz, and 39.36% at 5.05 GHz, respectively. From the measurement results, it is observed that the addition of the

superstrate shifted the frequency downward. While the simulation and measurement graphs for the initial antenna closely match, frequency differences in the superstrate antennas are believed to arise from factors such as the air gap between the upper and lower layers and the dielectric effects of the double-sided tape used to fix the superstrate, which were neglected during the fabrication process.

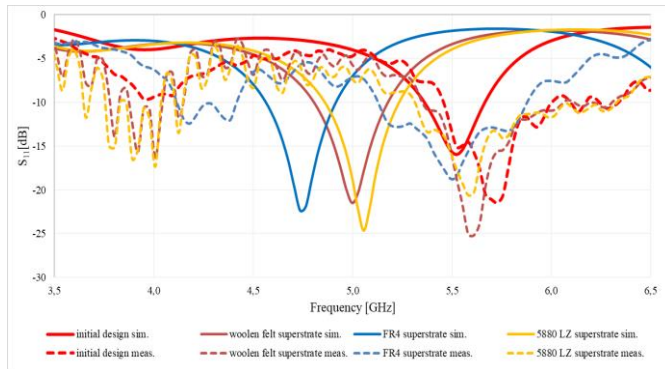


Figure 6: S_{11} Simulation and Measurement Results of the Fabricated Antennas.

IV. CONCLUSION

In this study, the effects of using different materials as superstrates on the Seljuk star strip-fed microstrip antenna were investigated. The impact of dielectric superstrates on parameters such as bandwidth, gain, resonance frequency, and return loss was experimentally examined. When a dielectric superstrate was added, changes in the antenna parameters were observed; in particular, the resonance frequency shifted to a lower value, and differences in other parameters also appeared. Maximum gain enhancement was achieved when the dielectric constant of the superstrate was the same as that of the substrate material, while the maximum increase in bandwidth was observed when the dielectric constant was lower. Additionally, the effects of superstrate thickness were investigated, and simulation and measurement results were compared. The results show that as the superstrate thickness increases, the resonance frequency shifts further downward.

ACKNOWLEDGMENT

We would like to express our gratitude to Dr. Mehmet Yerlikaya and Dr. Rabia Toprak from Selçuk University and Karamanoglu Mehmetbey University, Department of Electrical and Electronics Engineering, for their assistance in the measurements.

REFERENCES

- [1] K. L. Wong, "Design of nonplanar microstrip antennas and transmission lines," John Wiley & sons, 2004.
- [2] C. A. Balanis, Constantine A. "Antenna theory: analysis and design," John Wiley & sons, 2016.
- [3] A. Kumar, et al. "A review on gain enhancement techniques of microstrip antenna." *2021 2nd International Conference on Intelligent Engineering and Management (ICIEM)*, IEEE, 2021.
- [4] M. Pallavi, et al. "A review on gain enhancement techniques for vertically polarized mid-air collision avoidance antenna for airborne applications." *IEEE Access* 9, 2021: 30761-30792.

- [5] A. O. Cinar Ak, "Investigation of Different Manufacturing Techniques in High-Gain Microstrip Antenna Design," (*Master's Thesis*), Konya Technical University, Institute of Science, 2022.
- [6] S. M. Sayem and K. P. Esselle, "A robust, flexible and frequency reconfigurable antenna with flexible superstrate and substrate," *2021 International Symposium on Antennas and Propagation (ISAP)*, IEEE, 2021.
- [7] D. Pozar and D. Schaubert, "Microstrip antennas," *IEEE Press*, New York, 1995.
- [8] S. Farhat, et al, "Wideband patch array antenna using superstrate configuration for future 5G applications," *Turkish Journal of Electrical Engineering and Computer Sciences* 28.3, 2020: 1673-1685.
- [9] P. K. Singh, and S. Jasmine, "Effect of superstrate on a cylindrical microstrip antenna," *Progress In Electromagnetics Research Letters* 75, 2018: 83-89.
- [10] S. K. Gupta, et al. "Triple band circular patch microstrip antenna with superstrate," *Wireless personal communications* 77, 2024: 395-410.
- [11] S. Kumar, et al. "Single-feed superstrate loaded circularly polarized microstrip antenna for wireless applications," *Wireless Personal Communications* 92, 2017: 1333-1346.
- [12] V. Saidulu, "Effects of superstrate on microstrip antenna with coaxial probe feed," *International Journal Of Creative Research Thoughts (IJCRT)*, 2021.
- [13] F. Benmeddour, D. Christophe and K. Elhadi, "Effects of Superstrate Layer on the Resonant Characteristics of Annular-Ring printed Antenna," *The Eurasia Proceedings of Science Technology Engineering and Mathematics* 7, 2019: 147-154.
- [14] V. Saidulu, "Study of Superstrate Effects on Patch Antenna for WiMax/WLAN Applications," *Indian Journal Of Applied Research*, 2016.
- [15] V. Saidulu, "Design, Simulation and Experimental Analysis on Rectangular Microstrip Patch Antenna with Superstrates." *International Journal of Engineering and Advanced Technology(IJEAT)* 9.3, 2020: 3641-3645.
- [16] D. Uzer and S. S. Gultekin, "A New Seljuk Star Shape Microstrip Antenna Design," *Proceedings of Progress in Electromagnetics Research Symposium (Piers)*, 2012, 574-577.
- [17] D. Uzer, "Investigation of Suitable Methods for Wideband Microstrip Patch Antenna Designs," (*PhD Dissertation*), Selçuk University, Institute of Science, 2016.
- [18] D. Uzer, et al. "A Comparison of Different Patch Geometry Effects on Bandwidth," *International Journal of Applied Mathematics Electronics and Computers(Special Issue-1)*, 421-423, 2016.
- [19] L. J. Bahl and P. Bhartia, "Microstrip Antennas," Artech House, 1980. [2] JR James, PS Hall, C. Wood, *Microstrip Antenna Theory and Design*, Peter Peregrinus, 1981. [3] KR Carver, et al. *IEEE Trans. on AP*, AP-29, 1-182.
- [20] V. Saidulu, V., et al, "Comparison analysis of rectangular and circular patch microstrip antennas with dielectric superstrates," *International Journal of Microwaves Applications* 2.5, 2013: 125-134.
- [21] N. Hussain, et al. "A high-gain microstrip patch antenna using multiple dielectric superstrates for WLAN applications," *The Applied Computational Electromagnetics Society Journal (ACES)*, 2020, 187-193.
- [22] W. Choi, et al. "A high-gain microstrip patch array antenna using a superstrate layer," *ETRI journal* 25.5, 2003: 407-411.

Dynamic Analysis of 3D-printed ABS, PET-G and PLA Straight Beam

SİNAN MARAŞ¹

¹ Ondokuz Mayıs University, Samsun/Turkey, sinan.maras@omu.edu.tr

Abstract - In the modern industrial landscape, while conventional manufacturing techniques such as machining, casting, welding, powder metallurgy, and plastic forming are still predominantly used for metallic, polymeric, composite, and ceramic components, this trend has started to shift in recent years. Three-dimensional (3D) printing technology has emerged as one of the advanced production methods that enables the creation of intricate designs. Moreover, 3D printing offers several advantages over traditional manufacturing processes, including faster production times and reduced material consumption. Therefore, the free vibration analysis of structures made from such materials is of great significance in the design process. The aim of this study is to investigate how variations in parameters such as length, boundary conditions, and thickness influence the vibrational characteristics of 3D-printed straight beams made from PET-G, PLA, and ABS materials. The vibration parameters of the 3D straight beams were determined through modeling using the ANSYS finite element software. To validate the accuracy and feasibility of the proposed model, numerical results were compared with findings in existing literature. The results revealed that changes in material and geometric properties of 3D-printed straight beams significantly affect their natural frequencies.

Keywords - Free vibration; Straight beams; Additive manufacturing; Finite element method, Dynamics.

I. INTRODUCTION

ADDITIVE manufacturing (AM), commonly referred to as 3D printing, was originally favored for creating prototypes, but today it is widely employed to produce functional and lightweight end-use products [1-3]. An important field of research within AM is the vibration analysis of materials used in 3D printing, which aims to explore the vibrational characteristics of components made through additive manufacturing techniques. The analysis of free vibrations in 3D printed beams made from materials such as Acrylonitrile Butadiene Styrene (ABS), Polylactic Acid (PLA), and Polyethylene Terephthalate Glycol (PET-G) is critical for understanding their mechanical performance and potential applications in engineering. Various studies have investigated the vibrational characteristics of these materials, focusing on parameters such as infill density, print orientation, and material composition.

Biju et al. [4] conducted free vibration studies on composite beams, emphasizing the importance of boundary conditions in vibration analysis. Their findings highlight that the natural

frequencies of beams can significantly vary based on their structural configuration, which is also echoed in the work of Ergene et al. [3], who examined the vibration behavior of 3D printed PET-G beams. They found that the infill rate and build orientation are crucial factors affecting the natural frequencies, suggesting that careful optimization of these parameters can lead to improved vibrational performance.

In the context of PLA, Kannan [5] explored the frequency and deflection responses of 3D printed carbon fiber reinforced PLA composites. Their experimental results indicated that the addition of carbon fibers enhances the damping characteristics and natural frequencies of the material, which is vital for applications where vibration control is essential.

The influence of processing parameters on the vibrational properties of ABS has also been extensively studied. For instance, Parpală et al. [6] investigated how infill parameters affect the natural frequencies of ABS specimens, revealing that variations in infill density and print speed can lead to significant changes in vibrational characteristics. This is consistent with the findings of Kannan and Ramamoorthy [7] provided a comprehensive analysis of the mechanical and vibrational properties of 3D printed ABS, PC, and PC-ABS materials, emphasizing the role of processing conditions in determining the performance of these materials.

Moreover, the dynamic response of 3D printed functionally graded materials has been explored by Bonthu [8] noted that the layer thickness ratio and boundary conditions significantly influence the free vibration behavior of sandwich beams. This aligns with the insights from Gunasegeran and Sudhagar [9] examined bioinspired sandwich beams and found that the core material's properties play a crucial role in the overall vibrational response.

Research by Grammatikopoulos et al. [10] demonstrated that combining modal testing of 3D-printed samples with finite element analysis (FEA) can effectively predict the natural frequencies of complex thin-walled structures. This methodology provides important insights into how additive manufacturing techniques can affect the vibrational characteristics of printed components. Similarly, Boron et al. [11] conducted experiments to establish a relationship between material properties studies, field experiments, shaking table tests, and FEM modeling to accurately determine the natural frequencies of 3D-printed structures. In addition, Maidin et al. [12] investigated the mechanical properties of recycled ABS printed with an open-source FDM printer enhanced with

ultrasound vibration, revealing notable improvements in flexural, compressive, and tensile strength.

Upon reviewing existing literature on 3D-printed straight beams produced via Fused Filament Fabrication (FFF), it becomes clear that despite the limited number of studies, the mechanical behavior of such structures is generally explored through experimental methods. The analysis of free vibrations in 3D-printed straight beams, particularly in terms of identifying natural frequencies, mode shapes, and damping characteristics, is vital during the design phase. For this reason, investigating the free vibration behavior of these materials is critical for engineering applications. This study seeks to numerically examine the impact of beam length, boundary conditions, and thickness on the free vibration characteristics of 3D-printed straight beams using the ANSYS finite element software.

II. MATERIAL AND METHODS

A. Validation of the Numerical Model

In order to validate the solution method, the natural frequency values obtained in this study using the ANSYS finite element package were compared with the results provided in the study by Hu et al. [13]. Table 1 presents the material and geometric properties used in the study.

Table 1: Material and geometrical properties [13].

Mechanical and Geometrical Properties	Units
E_{11}	134 GPa
E_{22}	10.3 Gpa
$G_{12}=G_{13}$	5 Gpa
ν_{12}	0.33
ρ	$1.48 \times 10^3 \text{ kg/m}^3$
L (Beam Length)	127 mm
b (With)	12.7 mm
h (Thickness)	1.02 mm

As can be seen from Table 2, the results given in the study of Hu et al. [13] and the values found in this study are very close to each other.

Table 2: The comparison of natural frequency values obtained by various methods for an 8-layer composite straight beam with $[0^\circ/90^\circ]_2$ s stacking sequence under clamped-free boundary conditions.

Solution Methods	1. Mode (Hz)
Hu et al [13]	81.87
Hu [14]	82.00
Luo and Hanagud [15]	81.86
Shen and Grady [16]	80.09
Present study	83.36

As a second example, the natural frequency values of the laminated composite flat beam provided in the study by Topçu et al. [17] were compared with the natural frequency values obtained using the ANSYS finite element software package.

Table 3 shows the material and geometric properties used in the study.

Table 3: Material and geometrical properties [17].

Mechanical and Geometrical Properties	Units
E_{11}	26950 MPa
E_{22}	21800 Mpa
$G_{12}=G_{13}$	7540 Mpa
ν_{12}	0.15
ρ	2030 kg/m^3
L	0.320 m
b	0.036 m
h	0.008 m

As seen in Table 4, the current results are quite consistent with the findings of the study by Topçu et al. [17].

Table 4: The comparison of natural frequencies obtained by various methods for 12 layered composite straight beam with $[(0^\circ/90^\circ)_3]_s$ stacking sequence under clamped-free boundary condition [17].

Mod (n)	Analytical (Hz)	Numerical (Hz)	Experimental (Hz)	Present Study (Hz)
1	43.150	42.773	43.152	43.523
2	270.360	267.830	-	271.80
3	757.210	747.960	-	756.78

III. NUMERICAL ANALYSIS

Following the validation of the theoretical model, ANSYS software was employed to conduct a free vibration analysis on a 3D printed flat beam. The beam was assumed to be constructed from ABS, PLA, and PET-G materials. The model was developed and analyzed in ANSYS using the SHELL 281 element, representing the beam as a structural \rightarrow linear \rightarrow elastic \rightarrow isotropic material. The mechanical properties of the ABS, PLA, and PET-G materials used in this study were derived from literature data [18]. Table 5 presents the material properties of the 3D printed beam discussed in the study by Bolat et al. [18]. The model comprises 320 elements and 1050 nodes. Figure 1 illustrates an example of the ANSYS model for a 3D printed beam. The natural frequencies of the structure were numerically determined through modal analysis performed on the created finite element model.

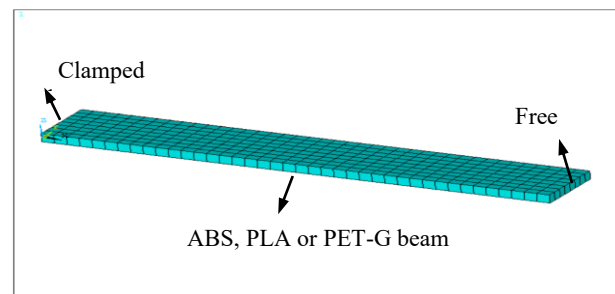


Figure 1: The ANSYS model of the 3D-printed beam.

Table 6 presents the configurations analyzed to assess how changes in geometric and material properties affect the natural frequencies of 3D-printed straight beams in this study.

Table 5: Physical and material properties of the 3D-printed beam (Bolat et al. [18]).

Property	PLA	PET-G	ABS
Colour	Black	Yellow	Grey
Diameter	1.75	1.75	1.75
Density (kg/m ³)	1240	1290	1040
Bed temperature (°C)	60-80	60-80	80-120
Printing temperature (°C)	190-210	210-250	220-250
Elasticity modulus (MPa)	1500	2100	1250
Tensile strength (MPa)	50	46	48
Elongation at break (%)	7	8	5

Table 6: The configurations of 3D-printed straight beam according to beam length, thickness (t), and boundary conditions.

Material	Beam Length	Thickness	Boundary Condition
PLA	200 mm	5 mm	Clamped-Free
PET-G	250 mm	10 mm	Clamped-Clamped
ABS	300 mm	15 mm	-

As beam materials, 3D-printed ABS, PLA, and PET-G were considered. The beam lengths of 200, 250, and 300 mm were examined. Additionally, the boundary conditions of cantilever

(clamped-free) and clamped-clamped configurations were investigated for the beams.

IV. RESULTS AND DISCUSSIONS

Figure 2 illustrates how changes in beam length influence the natural frequencies of 3D-printed straight beams. As shown in Figure 2, increasing the beam length results in reduced stiffness of the straight beams, which subsequently decreases the first, second, and third natural frequencies. Furthermore, among the materials, PET-G exhibits the highest natural frequency values, followed by PLA and then ABS. It is also evident that the natural frequencies for straight beams made from PLA and ABS are quite close to each other. This finding aligns with the data in Table 5, suggesting that materials with similar mechanical properties tend to have comparable natural frequency values.

Figure 3 explores how thickness variations impact the first, second, and third natural frequencies of 3D-printed straight beams. As shown in Figure 3, increasing the thickness of a straight beam strengthens the rigidity of the structure, which in turn raises its natural frequencies. Among the materials tested, PET-G yields the highest natural frequency values, while ABS produces the lowest. Additionally, a noteworthy observation is that the natural frequencies for beams made of PLA and ABS are very similar to each other. This conclusion is also consistent with the material properties presented in Table 5.

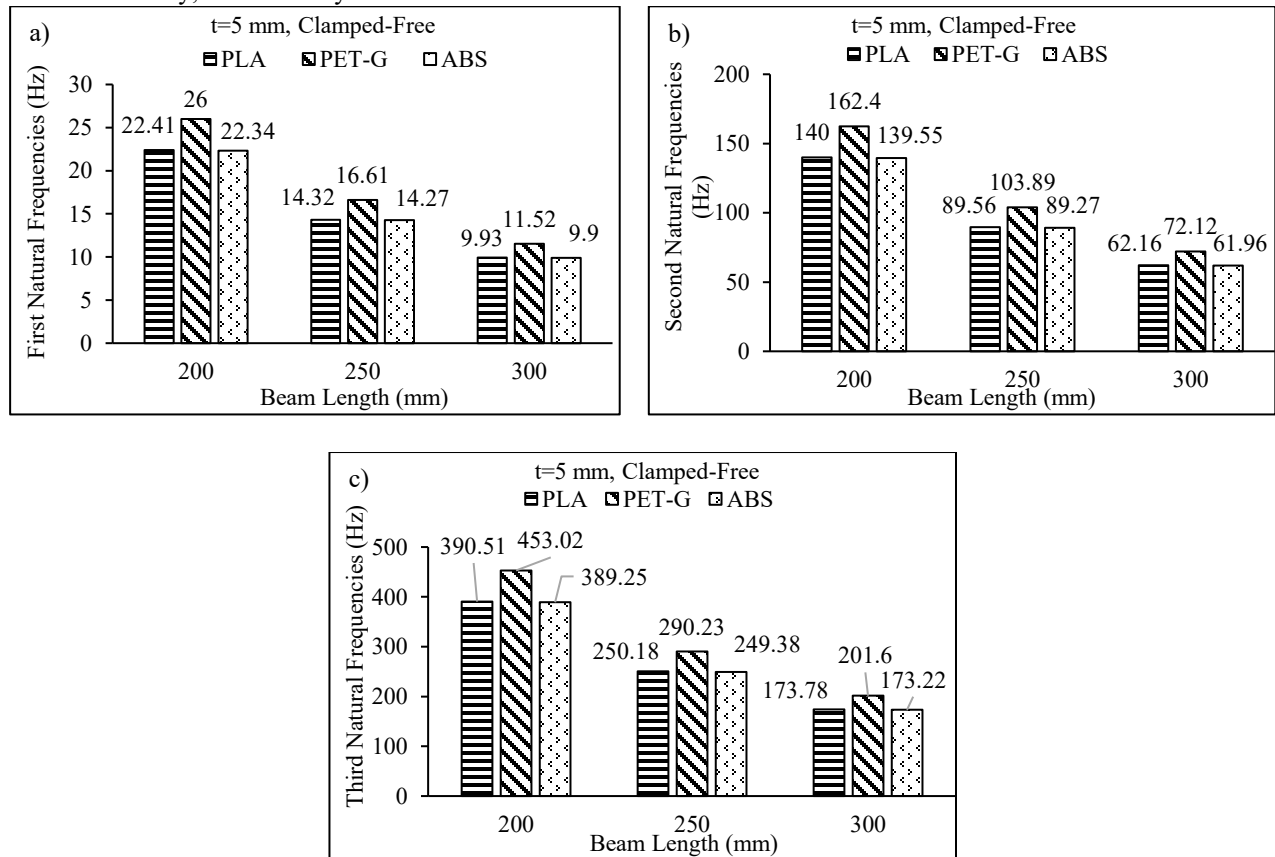


Figure 2: The effect of beam length variation on the natural frequencies of 3D-printed straight beams: a) First natural frequency b) Second natural frequency c) Third natural frequency

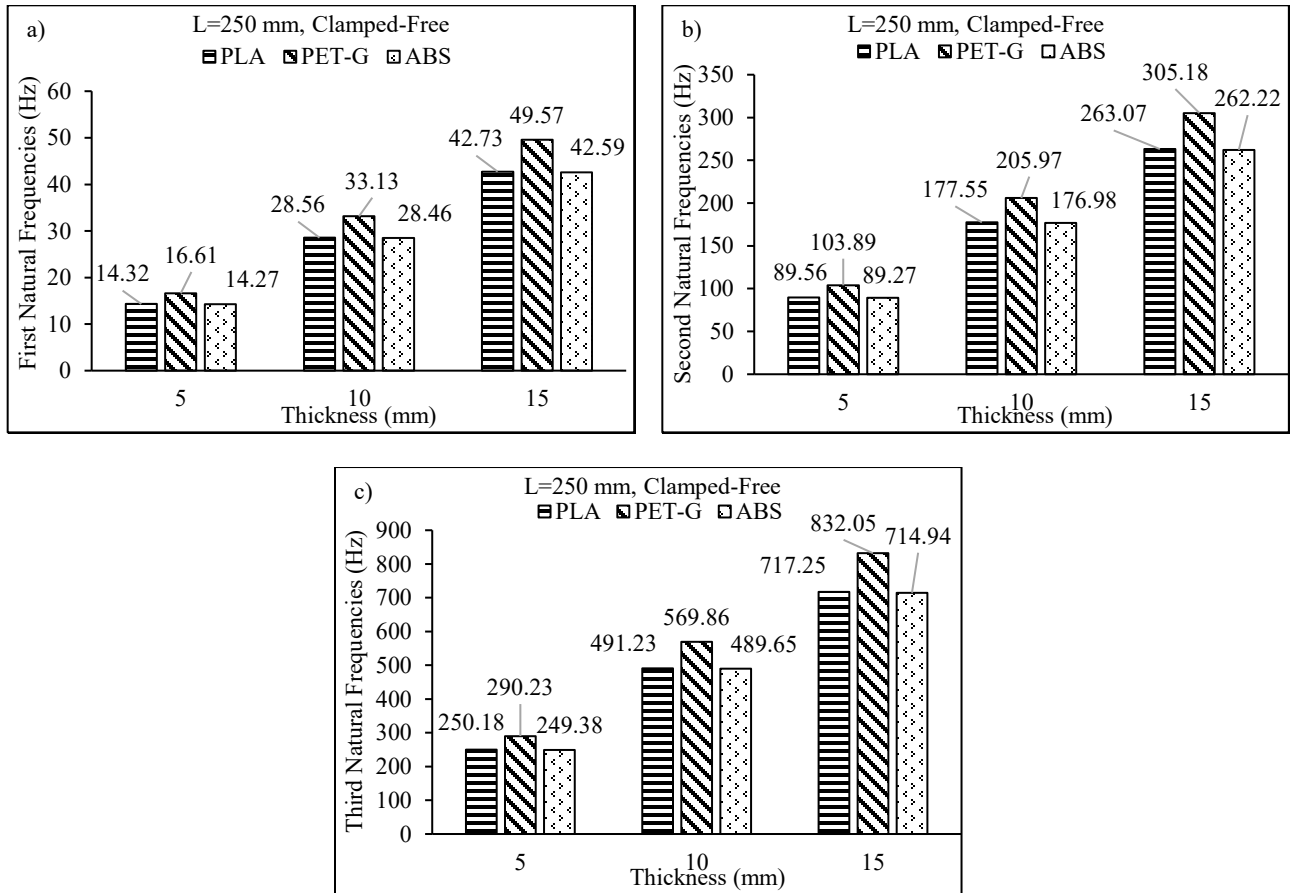


Figure 3: The effect of thickness on the natural frequencies of 3D-printed straight beams: a) First natural frequency b) Second natural frequency c) Third natural frequency

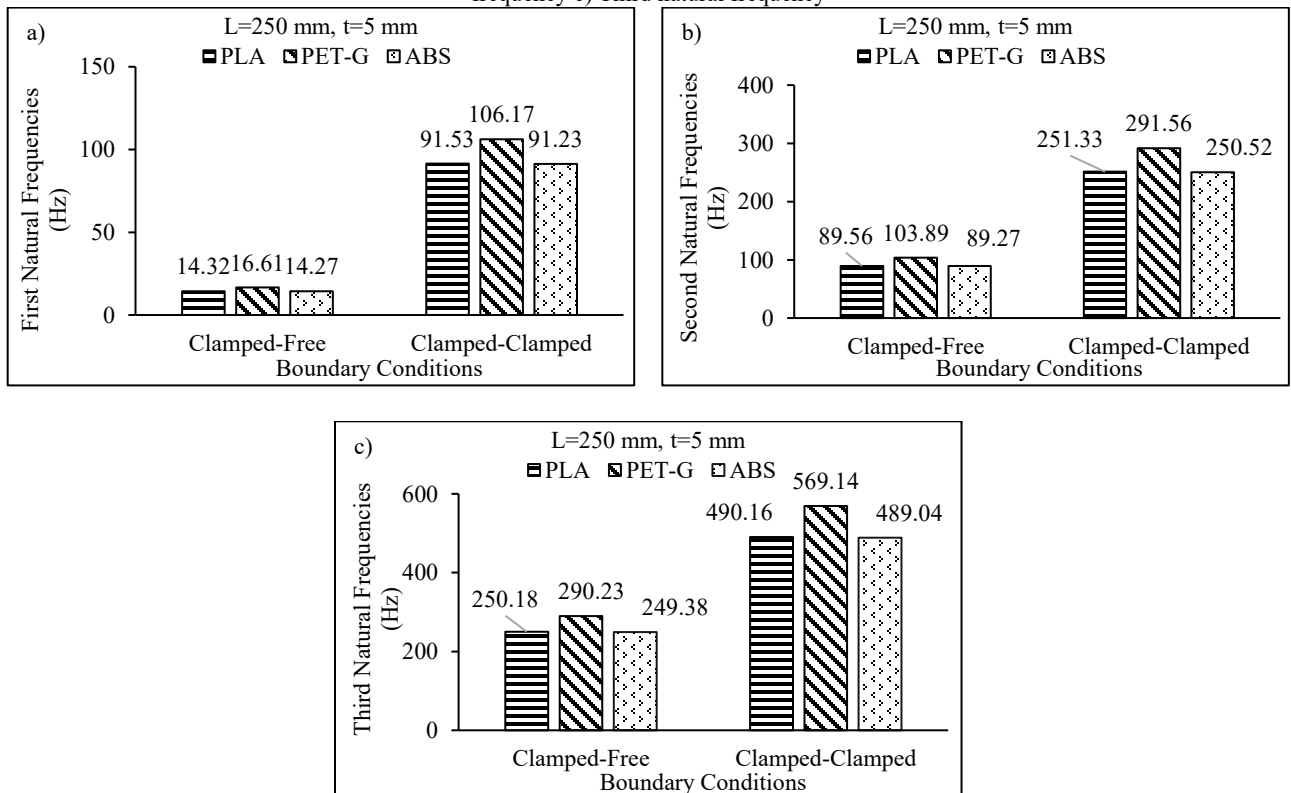


Figure 4: The effect of boundary conditions on the natural frequencies of 3D-printed straight beams: a) First natural frequency b) Second natural frequency c) Third natural frequency.

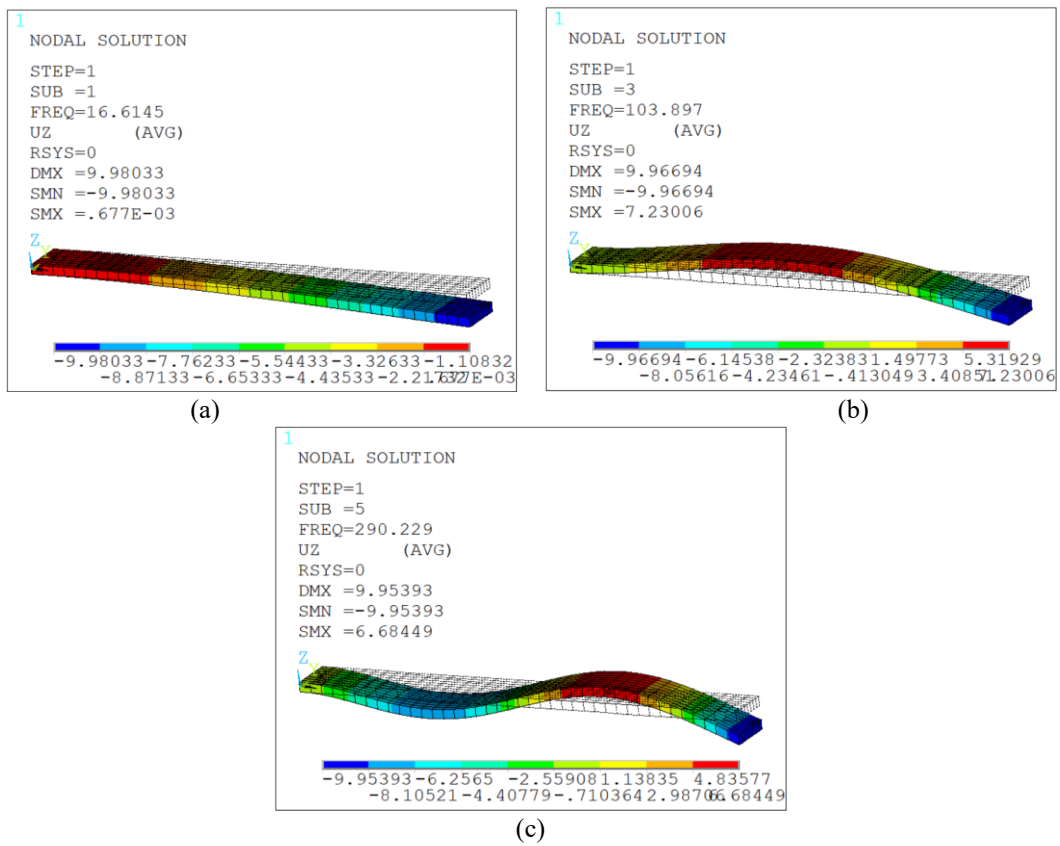


Figure 5: Mode shapes and natural frequencies of a PET-G beam with a thickness of $t=5$ mm and a length of $L=250$ mm under clamped-free boundary conditions: a) First mode b) Second mode c) Third mode.

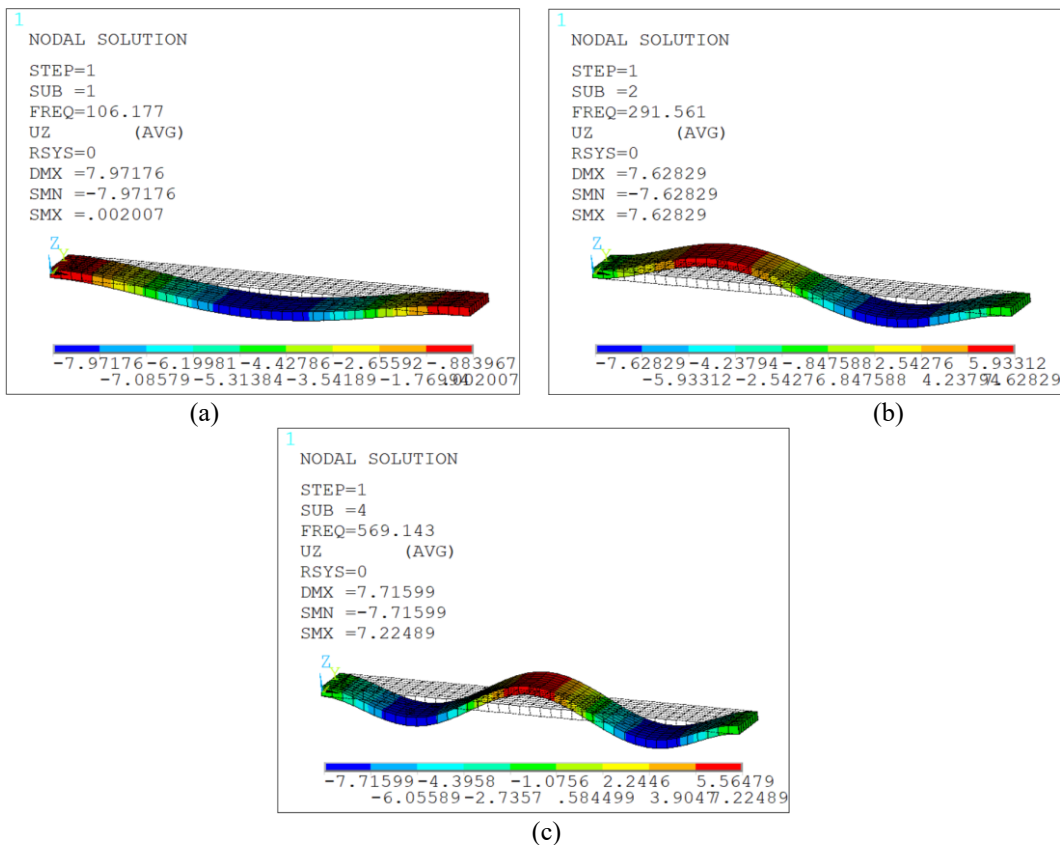


Figure 6: Mode shapes and natural frequencies of a PET-G beam with a thickness of $t=5$ mm and a length of $L=250$ mm under clamped-clamped boundary conditions: a) First mode b) Second mode c) Third mode.

The results of the free vibration analysis of 3D-printed straight beams with a length of 250 mm and a thickness of 5 mm under clamped-free and clamped-clamped boundary conditions are presented in Figure 4. As shown in Figure 4, the first, second, and third natural frequencies of beams under clamped-clamped boundary conditions are higher than those under clamped-free boundary conditions. This is due to the greater rigidity of beams with clamped-clamped boundary conditions compared to those with clamped-free boundary conditions. Moreover, the natural frequency values of PET-G beams are higher than those of ABS and PLA beams. Similar to Figures 2 and 3, Figure 4 also shows that the natural frequency values of ABS and PLA beams are very close to each other.

In Figures 5 and 6, the mode shapes and natural frequencies of a PET-G beam with a thickness of $t=5\text{mm}$ and a length of $L=250\text{mm}$ are shown under clamped-free and clamped-clamped boundary conditions, respectively.

V. CONCLUSION

In the present study, the free vibration analyses of 3D-printed straight beams were numerically investigated. This research examined the effects of variations in material properties, beam length, beam thickness, and boundary conditions on the natural frequencies of flat beams made from ABS, PLA, and PET-G materials using the finite element software ANSYS. The accuracy of the proposed method was validated by comparing the results with data obtained from previous studies.

Key findings of the study indicate that as the length of the 3D-printed beams increases, the natural frequencies decrease due to a reduction in stiffness. Additionally, among the materials examined, PET-G beams exhibited the highest natural frequency values, while the natural frequencies of ABS and PLA beams were found to be quite similar. As the beam thickness increases, the natural frequencies also increase due to the increase in stiffness. Beams with clamped-clamped boundary conditions have higher natural frequency values than those with clamped-free boundary conditions.

From these findings, it was concluded that the vibration behavior of 3D-printed beams is greatly influenced by material and geometric parameters. This characteristic can be leveraged to adapt the design of 3D-printed structures in industrial environments.

REFERENCES

- [1] G. Stano and G. Percoco, "Additive manufacturing aimed to soft robots fabrication: A review", *Extreme Mechanics Letters*, vol. 42, pp. 101079, 2021.
- [2] D. Mishra and A.K. Das, "Linear model analysis of fused deposition modeling process parameters for obtaining the maximum tensile strength in acrylonitrile butadiene styrene (ABS) and carbon fiber poly(lactic acid) (PLA) materials", *Multidiscipline Modeling in Materials and Structures*, vol. 17(5), pp. 915-930, 2021.
- [3] B. Ergene, G. Atlıhan and A.M. Pinar, "Experimental and finite element analyses on the vibration behavior of 3D-printed PET-G tapered beams with fused filament fabrication", *Multidiscipline Modeling in Materials and Structures*, vol. 19(4), pp. 634-651, 2023.
- [4] B. Biju, S. Jans, R. Mathew and F. Kiliyami, "Free vibration studies on bi-directional composite beam", *International Journal of Engineering Research & Technology*, vol. 4(3), pp. 633-636, 2015.
- [5] S. Kannan, "Frequency and deflection responses of 3d-printed carbon fiber reinforced polylactic acid composites: theoretical and experimental verification", *Polymer Composites*, vol. 44(7), pp. 4095-4108, 2023.
- [6] R. Parpală, D. Popescu, and C. Pupăză, "Infill parameters influence over the natural frequencies of abs specimens obtained by extrusion-based 3d printing", *Rapid Prototyping Journal*, vol. 27(6), pp. 1273-1285, 2021.
- [7] S. Kannan and M. Ramamoorthy, "Mechanical characterization and experimental modal analysis of 3d printed abs, pc and pc-abs materials", *Materials Research Express*, vol. 7(1), pp. 015341, 2020.
- [8] D. Bonthu, "Dynamic response of 3d printed functionally graded sandwich foams", *Rapid Prototyping Journal*, vol. 29(10), pp. 2257-2271, 2023.
- [9] M. Gunasegeran and P. Sudhagar, "Free and forced vibration analysis of 3d printed bioinspired sandwich beam using hsd: numerical and experimental study", *Polymer Composites*, vol. 43(6), pp. 3659-3677, 2022.
- [10] A. Grammatikopoulos, J. Banks and P. Temarel, "Prediction of the vibratory properties of ship models with realistic structural configurations produced using additive manufacturing", *Marine Structures*, vol. 73, pp. 102801, 2020.
- [11] P. Boron, J. Chelmecki, J.M. Dulinska, N. Jurkowska, B. Ratajczak, P. Stecz, and T. Tatara, "On the Possibility of Using 3D Printed Polymer Models for Modal Tests on Shaking Tables: Linking Material Properties Investigations, Field Experiments, Shaking Table Tests, and FEM Modeling", *Materials*, vol. 16(4), pp. 1471, 2023.
- [12] S. Maidin, K. Ting and Y. Sim, "Investigation of Mechanical Properties of Recycled ABS Printed with Open Source FDM Printer Integrated with Ultrasound Vibration", *International Journal of Integrated Engineering*, vol. 14(4), pp. 57-63, 2022.
- [13] N. Hu, H. Fukunaga, M. Kameyama, Y. Aramaki and F. K. Chang, "Vibration analysis of delaminated composite beams and plates using a higher-order finite element", *International Journal of Mechanical Sciences*, vol. 44(7), pp.1479-1503, 2002.
- [14] N. Hu, "Buckling analysis of delaminated laminates with consideration of contact in buckling mode", *International journal for numerical methods in engineering*, vol. 44(10), pp. 1457-1479, 1999.
- [15] H. Luo and S. Hanagud, "Dynamics of delaminated beams", *International Journal of Solids and Structures*, vol. 37(10), pp. 1501-1519, 2000.
- [16] M. H. Shen and J. E. Grady, "Free vibrations of delaminated beams", *AIAA journal*, vol. 30(5), pp. 1361-1370, 1992.
- [17] M. Topcu, G. Atlıhan, H. Çalloğlu and E. Ş. Çonkur, "Stacking sequence effects on natural frequency of laminated composite beams", *Advanced Composites Letters*, vol. 17(1), pp. 5-11, 2008.
- [18] Ç. Bolat, B. Ergene and H. İspartalı, "A comparative analysis of the effect of post-production treatments and layer thickness on tensile and impact properties of additively manufactured polymers", *International Polymer Processing*, vol. 38(2), pp. 244-256, 2023.

Pan-Sharpening in Satellite Imagery

DAMLANUR ALKAN¹, LÜTFİYE KARASAKA¹

¹ Konya Technical University, Konya/Türkiye, dalkan@ktun.edu.tr

¹ Konya Technical University, Konya/Türkiye, lkarasaka@ktun.edu.tr

Abstract - Image fusion combines information from images obtained by different sensors to produce a new image with more advanced information. Image fusion can also be applied to images obtained from satellites. Pan-sharpening, one of the image fusion methods, improves the multispectral image by using the features in the panchromatic image obtained from the sensors. Multispectral images have high spectral resolution and low spatial resolution. In panchromatic images, spatial resolution is high and spectral resolution is low. With pan-sharpening methods, the details in the panchromatic band with high spatial resolution are transferred to the multispectral band image with high spectral resolution to create a new image. In this new image, both spectral resolution and spatial resolution are high. Due to its advantages, pan-sharpening process is preferred by researchers. In this study, pan-sharpening process was performed using Landsat-9 satellite image. Within the scope of the study, IHS, Ehler's, HCS, HPF, wavelet, Brovey and Gram-Schmidt pan-sharpening methods were used. Pan-sharpened images with these methods were visually and statistically evaluated. RMSE, SAM, CC and ERGAS metrics were used for statistical evaluation of pan-sharpened images.

Keywords - image fusion, pan-sharpening, remote sensing.

I. INTRODUCTION

THERE are four different resolutions in remote sensing. These are radiometric resolution, temporal resolution, spectral resolution and spatial resolution. Radiometric resolution is the sensitivity of satellite sensors to variation in the radiation intensities they measure. It is related to the number of bits. Temporal resolution is the frequency with which satellites acquire imagery for a specific region of the earth. Spatial resolution is a concept related to pixel size. It is the area of the ground that a pixel in an image represents. Spectral resolution is the sensitivity of sensors to identify regions of the electromagnetic spectrum. It is related to the number of bands. Satellites need to have large-sized sensors in order to produce spectrally high-resolution images. However, in this case, the spatial resolution of the images is low. However, since the engineering practices require satellite images with both high spatial resolution and high spectral resolution, researchers have been trying to overcome this situation by using image fusion methods and they aim to produce images with high spatial and spectral resolution [1]. Image fusion provides a new image containing more advanced information by integrating information from images obtained by different sensors. Different image fusion methods result in different outcomes.

Some methods can successfully keep spatial details while distorting spectral features. Some methods keep spectral features but perform weakly in the transmission of spatial details. Therefore, the method to be used should be determined by the researchers through experimentation [2].

Remote sensing satellites are equipped with various sensors. Among these, multispectral sensors are detectors that possess multiple spectral bands, each capable of detecting radiation in different regions of the electromagnetic spectrum. In contrast, panchromatic sensors detect all radiation within the visible region, composed of red, green, and blue wavelengths, represented as a single band. Therefore, panchromatic sensors are single-band detectors and do not contain any colour information. Due to this, the spectral resolution of panchromatic sensors is lower when compared to multispectral sensors. However, a different scenario emerges when considering spatial resolution. The spatial resolution of multispectral sensors in satellite systems developed for remote sensing applications is generally lower than that of panchromatic sensors. The spatial resolution difference between multispectral and panchromatic bands varies across satellites.

Pan-sharpening is one of the image fusion techniques used in remote sensing, enabling the enhancement of a multispectral image by incorporating features from the panchromatic image. Through pan-sharpening methods, high spatial resolution details from the panchromatic band are transferred to the multispectral image, which has high spectral resolution, thereby creating a new image. This resulting image possesses both high spectral and spatial resolution.

From past to present, various satellite images, including those from Rasat [3], Göktürk-2 [4], Worldview-2 [5], Quickbird-2 [6], and Landsat-8 [7] have been used to perform pan-sharpening methods, and the results have been evaluated. In this study, pan-sharpening methods are examined using Landsat-9 satellite imagery.

II. MATERIAL AND METHODS

A. Landsat-9

Launched into space in 2021, the Landsat-9 satellite has a high imaging capacity similar to Landsat-8, along with improvements in geometric and radiometric quality compared to previous satellites [8]. Landsat-9 is equipped with the OLI-2 (Operational Land Imager 2) and TIRS-2 (Thermal Infrared Sensor 2) sensors. The OLI-2 sensor enables the detection of

the visible, near-infrared (NIR), and shortwave-infrared (SWIR) regions, while the TIRS-2 sensor detects the thermal infrared region [9]. Table 1 presents detailed information on the Landsat-9 satellite [10].

Table 1: Landsat-9 bands and information [10]

No.	Bands	Wavelengths (nm)	Spatial Resolution (m)
1	Coastal/Aerosol	433 – 453	30
2	Blue	450 – 515	30
3	Green	525 – 600	30
4	Red	630 – 680	30
5	NIR	845 – 885	30
6	SWIR-1	1560 - 1660	30
7	SWIR -2	2100 – 2300	30
8	Panchromatic	500 – 680	15
9	Cirrus	1360 – 1390	30
10	Thermal	10300 - 11300	100
11	Thermal	11500 – 12500	100

In this study, the selected Landsat-9 image was used after being cropped (Figure 1). The multispectral image used for pan-sharpening was created by combining the red, green, and blue bands, while the panchromatic image was obtained using the panchromatic band.

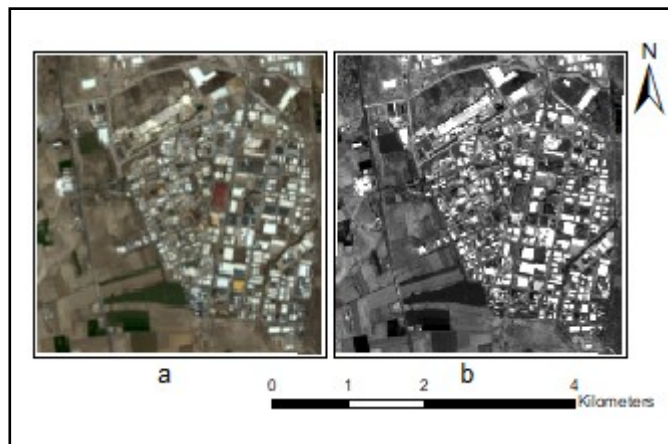


Figure 1: a) Multispectral (red, green, blue) and b) panchromatic images

B. Pan-sharpening

Pan-sharpening is the process of producing a high-resolution multispectral image by integrating the spatial details from the high-resolution panchromatic image with the spectral information from the low-resolution multispectral image [11] (Figure 2). IHS, Ehler's, HCS, HPF, wavelet, Brovey and Gram-Schmidt algorithms are among the methods developed for pan-sharpening. The choice of pan-sharpening method should be based on the needs of the application. For example, since geometric details are more important than spectral features for

urban and regional planners, methods that preserve more geometric details should be preferred for studies in this field, on the other hand, methods that preserve spectral information should generally be used in remote sensing applications [12].

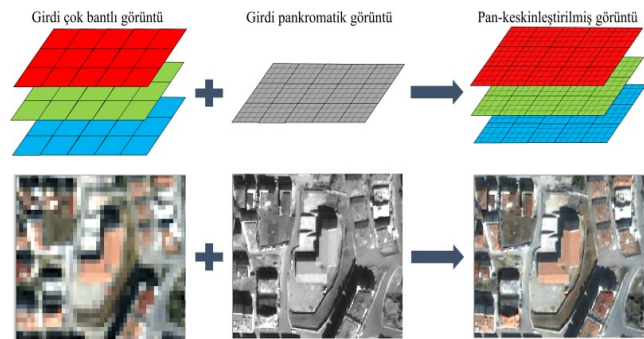


Figure 2: Pan-sharpening [1]

- **IHS (Intensity Hue Saturation):**

In the IHS method, the multispectral image is first transformed from RGB (Red Green Blue) colour space to IHS colour space. Then the intensity component and the panchromatic band are replaced [4] to improve the spatial resolution of the image. After these operations, a reverse IHS transformation is performed, this time from IHS colour space to RGB colour space [3].

- **Ehler's:**

In Ehler's method, a transformation from the RGB colour space to the IHS colour space is performed, similar to the IHS method. Then, FFT (Fast Fourier Transform) is applied to both the intensity component and the panchromatic band. [13]. A low-pass filter is applied to the intensity component with the FFT transform, while a high-pass filter is applied to the panchromatic band. The resulting images are then subjected to an inverse FFT to obtain an improved intensity component image [3]. The inverse IHS transformation is performed using the intensity component along with the H and S components [13].

- **HCS (Hyperspherical Colour Sphere):**

In the HCS method, the transformation of the multispectral image from the RGB colour space to the hyperspherical colour space is performed [4]. The intensity component in the hyperspherical colour space is replaced with its counterpart from the panchromatic band [5]. Then, the inverse transformation is performed [4].

- **HPF (High-Pass Filter):**

In the HPF method, the ratio between the spatial resolutions of the multispectral and panchromatic images is calculated to determine a high-frequency filter [4]. Applying this filter to the high spatial resolution panchromatic band yields high-frequency components [3]. The obtained components are then added to each of the low spatial resolution multispectral bands [4].

- **Wavelet:**

In the wavelet method, wavelet transformation is applied separately to the multispectral and panchromatic images [12]. This process transforms the images into the wavelet domain, yielding detail coefficients and the approximation image [14]. Then, the detail coefficients of the multispectral image are replaced with those of the panchromatic image, while aiming to preserve the approximation coefficients of the multispectral image [12]. Finally, the inverse wavelet transformation is applied [14].

- **Brovvey:**

In the Brovvey method, each of the bands in the multispectral image is multiplied by the panchromatic band. The result is divided by the sum of all bands [12].

- **Gram-Schmidt:**

In the Gram-Schmidt method, a kind of panchromatic image is obtained by calculating the weighted average of the bands in the multispectral image. Then, the main panchromatic image is selected as the first band and all bands are vertically equalized using the Gram-Schmidt orthogonalization algorithm [12].

C. Metrics

Different evaluation metrics are used in the statistical assessment of pan-sharpening results. In this study, RMSE, SAM, RASE, CC and ERGAS metrics were used.

- **RMSE (Root Mean Square Error):**

It shows how different two images are from each other. The expressions $u(m,n)$ and $v(m,n)$ correspond to two different images of size $M \times N$, and the RMSE calculation is done as follows [15]:

$$RMSE = \sqrt{\frac{1}{MN} \sum_{m=1}^M \sum_{n=1}^N |u(m,n) - v(m,n)|^2}, \quad (1)$$

- **SAM (Spectral Angle Mapper):**

It calculates the change in colours in terms of angle [16]. Using this metric, the spectral similarity between two spectral vectors is calculated angularly [17]. This angle can be expressed in degrees or radians. Let u and v be two spectral vectors, and the SAM (Spectral Angle Mapper) metric is calculated as follows [15]:

$$SAM = \arccos\left(\frac{\langle u, v \rangle}{\|u\|_2 \cdot \|v\|_2}\right), \quad (2)$$

- **CC (Correlation Coefficient):**

The expressions X and Y correspond to the original multispectral image and the pan-sharpened image, respectively, and the CC metric is calculated as follows [17]:

$$CC(x,y) = \frac{\sum_{i=1}^M \sum_{j=1}^N (x_{i,j} - x')(y_{i,j} - y')}{\sqrt{\sum_{i=1}^M \sum_{j=1}^N (x_{i,j} - x')^2 \sum_{i=1}^M \sum_{j=1}^N (y_{i,j} - y')^2}}, \quad (3)$$

- **ERGAS**

The ERGAS metric, calculated using RMSE, provides information about the distortion in the pan-sharpened image [15]. The h/r represents the geometric resolution ratio between the multispectral and panchromatic images, N denotes the number of bands, and $\mu(n)$ corresponds to the mean of the bands. The ERGAS metric is calculated as follows [17]:

$$ERGAS = 100 \frac{h}{l} \sqrt{\frac{1}{N} \sum_{n=1}^N \left(\frac{RMSE(n)}{\mu(n)}\right)^2}, \quad (4)$$

III. RESULTS

In this study, pan-sharpening was performed with IHS, Ehler's, HCS, HPF, wavelet, Brovvey and Gram-Schmidt algorithms using Landsat-9 satellite imagery and the outcome products were visually and statistically evaluated.

A. Visual Assessment

Pan-sharpened results can be visually analysed in two different ways: in terms of preserving spectral values and in terms of preserving the sharpness of objects.

With regard to the spectral aspect, the Gram-Schmidt method gave the best results in terms of preserving spectral values (Figure 3g). After this method, IHS and Brovvey methods gave better results than the other methods (Figure 3a and Figure 3f). HPF and wavelet methods, on the other hand, produced spectrally worse results. These results are dominated by pale colour tones (Figure 3d and Figure 3e). The Ehler's method produced more vivid colours (Figure 3b), while the HCS method produced darker tones (Figure 3c).

With regard to the sharpness of the objects, the Ehler's method produced more sharp results than the other methods (Figure 3b). Following this method, the IHS and Brovvey methods produced better results in terms of the details compared to the other methods (Figure 3a and Figure 3f). The Wavelet method produces the fuzziest results (Figure 3e).

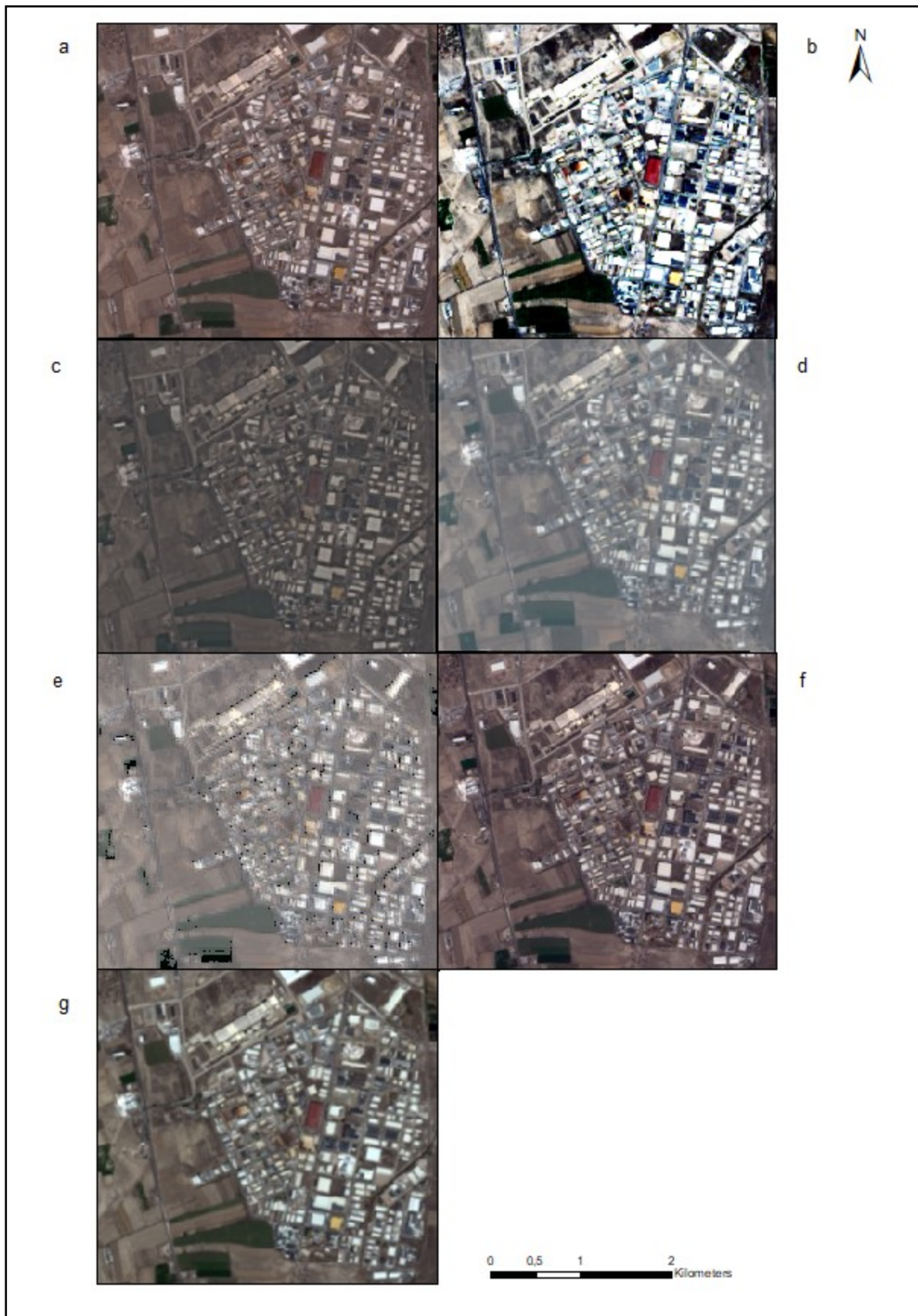


Figure 3: Pan-sharpening results for a) IHS, b) Ehler's, c) HCS, d) HPF, e) Wavelet, f) Brovey and g) Gram-Schmidt methods

A. Statistical Assessment

The statistical results obtained for the pan-sharpened images are shown in Table 2. In the table, the worst values are shown in bold, and the best values are underlined.

Table 2: Metric results of the pan sharpening methods

Method/Metric	RMSE	SAM	CC	ERGAS
IHS	2182.6572	1.9533	0.7494	0.0689
Ehler's	5316.3345	5.4744	0.8335	0.1677
HCS	3295.9512	2.3993	0.7222	0.1040
HPF	1605.0268	<u>1.7601</u>	<u>0.8878</u>	0.0506
Wavelet	2019.0206	3,1300	0.8134	0.0637
Brovvey	8417.6812	1.9532	0.7489	0.2655
Gram-Schmidt	<u>1574.3029</u>	2.1395	0.8759	<u>0.0497</u>

Table 2 shows that Gram-Schmidt and HPF methods give the best results. RMSE, ERGAS and CC values of these methods are close to each other. Then IHS and wavelet methods give better results than the other methods. The worst results are obtained with the Brovvey method. Table 2 shows that the RMSE and ERGAS values of the Brovvey method produced very large results compared to all other methods.

REFERENCES

- [1] Yılmaz, Ç.Ş., V. Yılmaz, and O. Güngör, *Çok bantlı görüntülerde pan-keskinleştirme üzerine bir inceleme*. Gümüşhane Üniversitesi Fen Bilimleri Dergisi, 2021. **11**(4): p. 1340-1357.
- [2] Yılmaz, V. and O. Gungor, *Determining the optimum image fusion method for better interpretation of the surface of the Earth*. Norsk Geografisk Tidsskrift-Norwegian Journal of Geography, 2016. **70**(2): p. 69-81.
- [3] Abdikan, S., *RASAT verisi kullanarak farklı pan-keskinleştirme yöntemlerinin istatistiksel analizi*. Türk Coğrafya Dergisi, 2017(68): p. 57-62.
- [4] Akar, Ö., *Göktürk-2 ve Worldview-2 Uydu Görüntüleri için Görüntü Keskinleştirme Yöntemlerinin Değerlendirilmesi*. Erzincan University Journal of Science and Technology, 2019. **12**(2): p. 874-885.
- [5] Ghosh, A. and P. Joshi, *Assessment of pan-sharpened very high-resolution WorldView-2 images*. International journal of remote sensing, 2013. **34**(23): p. 8336-8359.
- [6] Pushparaj, J. and A.V. Hegde, *Comparison of various pan-sharpening methods using Quickbird-2 and Landsat-8 imagery*. Arabian Journal of Geosciences, 2017. **10**: p. 1-17.
- [7] Rahaman, K.R., Q.K. Hassan, and M.R. Ahmed, *Pan-sharpening of Landsat-8 images and its application in calculating vegetation greenness and canopy water contents*. ISPRS International Journal of Geo-Information, 2017. **6**(6): p. 168.
- [8] URL-1. *Landsat 9*. [accessed on 31 October 2024]; Available from: <https://landsat.gsfc.nasa.gov/satellites/landsat-9/>.

- [9] URL-2. *Landsat 9 Overview*. [accessed on 31 October 2024]; Available from: <https://landsat.gsfc.nasa.gov/satellites/landsat-9/landsat-9-overview/>.
- [10] URL-3. *Landsat 9 Bands*. [accessed on 31 October 2024]; Available from: <https://landsat.gsfc.nasa.gov/satellites/landsat-9/landsat-9-instruments/landsat-9-spectral-specifications/>
- [11] Du, Q., et al., *On the performance evaluation of pan-sharpening techniques*. IEEE Geoscience and Remote Sensing Letters, 2007. **4**(4): p. 518-522.
- [12] Teke, M., E. San, and E. Koç. *Unsharp masking based pansharpening of high resolution satellite imagery*. in *2018 26th Signal Processing and Communications Applications Conference (SIU)*. 2018. IEEE.
- [13] Yılmaz, V. and O. Gungor. *Performance analysis on image fusion methods*. in *CaGIS/ASPRS Specialty Conference*. 2013.
- [14] DadrasJavan, F., F. Samadzadegan, and F. Fathollahi, *Spectral and spatial quality assessment of IHS and wavelet based pan-sharpening techniques for high resolution satellite imagery*. Image Video Process, 2018. **6**(1).
- [15] ÖZENDİ, M., et al., *PLÉIDAS-1A GÖRÜNTÜLERİNİN PAN-SHARPENING PERFORMANSININ İNCELENMESİ*. 2014.
- [16] Yıldırım, D. and O. Güngör, *İKONOS uydu görüntüleri ile yeni bir görüntü kaynaştırma yöntemi*. Jeodezi ve Jeoinformasyon Dergisi, 2012(105): p. 75-83.
- [17] Teke, M., E. San, and E. Koç. *Unsharp based Pansharpening of Göktürk-2 Satellite Imagery*. in *26th Signal Processing and Communications Applications Conference (SIU)*, IEEE, Izmir, Turkey. 2018.

Google Earth Engine and Its Usage in Remote Sensing: The Case Study of Sapanca Lake, Türkiye

DAMLANUR ALKAN¹, LÜTFİYE KARASAKA¹

¹ Konya Technical University, Konya/Türkiye, dalkan@ktun.edu.tr

¹ Konya Technical University, Konya/Türkiye, lkarasaka@ktun.edu.tr

Abstract - From the past to the present, various advances in technology have led to improvements in satellite sensor systems as well. These developments have enabled satellite imagery to be generally high resolution in terms of spatial, spectral, radiometric and temporal resolution. High resolution satellite imagery has a larger size compared to low resolution satellite imagery. In case of applications that require the use of multiple satellite imagery, the data amount becomes even larger. This causes problems in data downloading, storage, utilization and processing. Google Earth Engine (GEE), which was developed to overcome such problems, is a platform that provides simplicity to researchers by providing storage and processing of a large number of big data sets without the need for any downloading process. In recent years, this platform has been preferred by researchers in various remote sensing studies. Within the scope of this study, Sapanca Lake wetland change was investigated using the GEE platform. For this purpose, the annual amount of Sapanca Lake wetland area was determined by using Landsat-8 satellite images between 2014-2024 and by calculation of the Normalized Difference Water Index (NDWI).

Keywords - Google Earth Engine, Remote Sensing.

I. INTRODUCTION

REMOTE sensing is a science that aims to produce images without any physical contact with the earth and extract information about the earth through the images produced. The concept of sensing mentioned here is related to the type of sensor used in remote sensing. Remote sensing sensors are divided into two groups. These are active and passive sensors that perform active and passive sensing. Active sensors are satellites that have their own sources to provide sensing. Passive sensors, on the other hand, are satellites that do not have any sources of their own and therefore they perform sensing using the radiation from the Sun. It is possible to obtain satellite imagery for free. These free satellite images are available through USGS (<https://earthexplorer.usgs.gov/>, accessed on 09 October 2024), Copernicus (<https://browser.dataspace.copernicus.eu/>, accessed on 09

October 2024), etc. Resolution of the images obtained from satellites in such various ways depends on the types of sensors that the receivers have. There are four different resolutions in remote sensing. These are spatial resolution, spectral resolution, radiometric resolution and temporal resolution. Spatial resolution is a concept related to pixel size. It is the amount of area that a pixel in an image represents on the ground. This area, referred to as the ground resolution element, is determined by the receiver's platform altitude and the observation angle, expressed as the instantaneous field of view (IFOV). Spectral resolution is the sensitivity of satellite sensors in the ability to identify regions of the electromagnetic spectrum. It is a concept related to the number of bands and the width of the wavelength. Radiometric resolution is the sensitivity of satellite sensors to differences measured in radiation intensity. It is related to the number of bits. Temporal resolution is the frequency of satellite imagery acquisitions for a specific region of the Earth's surface.

Developments in satellite technologies affect the resolution of images obtained by satellites. Improvements in satellite technologies usually results with the acquisition of high-resolution imagery. Since high-resolution data sets have large sizes, storage and processing of these data causes problems. However, nowadays, with the advancement of cloud technologies, these processes have started to be performed online, and the unnecessary use of storage has been prevented. With the help of the online platforms, the need to download satellite images used for remote sensing applications on personal computers has been eliminated [1]. Google Earth Engine (GEE), one of the online platforms, enables to process any number of large data sets through the cloud, without any downloading process and regardless of the characteristics of the computer used [2]. GEE provides opportunities for applications in various fields such as producing land use maps [2], detecting burned areas and forest fire severity [3, 4], monitoring the regeneration process of areas destroyed by fires [5, 6], analysing forest pests [7], observing agricultural drought [8], crop mapping [9], determining water surfaces [10], creating wetland inventories [11], and determining ground surface temperature [12, 13]. In addition, it is possible to calculate various spectral indices such as NDWI (Normalized Difference Water Index), NDVI (Normalized Difference Vegetation Index), SAVI (Soil-Adjusted Vegetation Index) and NDBI (Normalized Difference Built-up Index) [2, 3, 7]; and to

perform classification methods such as Support Vector Machine and Random Forest Classification Algorithm [2, 7].

II. MATERIAL AND METHODS

Study area

Sapanca Lake is a freshwater lake formed by tectonic formations in Sakarya and Kocaeli provinces in the eastern part of the Marmara Region in Türkiye. It is located at the coordinates $40^{\circ} 43' N$, $30^{\circ} 15' E$ (Figure 1). While it has been used as drinkable water, it is also preferred in industrial and agricultural areas [7].

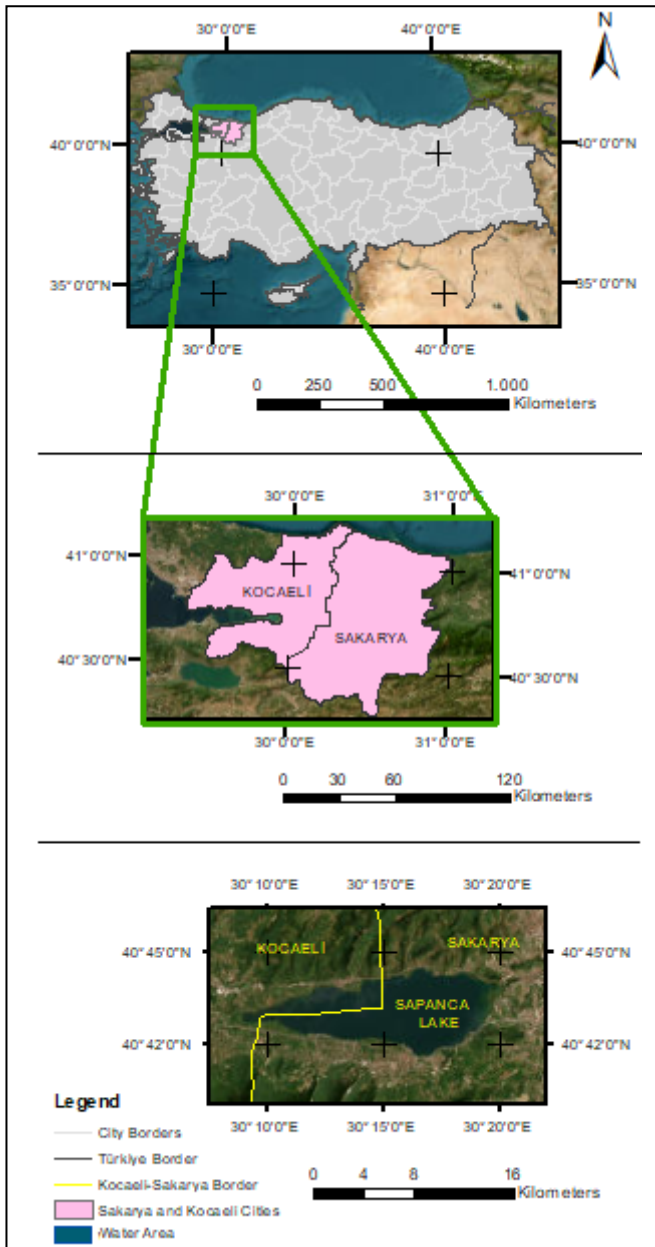


Figure 1: Study area

Google Earth Engine

GEE is a web-based remote sensing interface that is user-friendly and easily accessible [14]. It provides storage of images obtained from various receivers (Landsat, Sentinel, etc.). It also contains a large repository of publicly available data, including layers of land cover, weather and climate data, digital elevation models and GIS-based vector data [14, 15]. For such purposes, GEE enables the online processing of preferred data with a set of commands [1]. These commands can be implemented by using the ready-to-use codes available on the GEE as well as by writing new codes by the researchers [7]. Satellite images can be easily and quickly visualized and analysed by users with the help of GEE. In addition to these, it is also possible to perform image pre-processing steps that are required before image analysis through GEE. GEE enables researchers to organize their own data in the cloud and perform analysis without the need for computers that require large computing power [14]. GEE uses the JavaScript programming language and it can also work with Python and other languages [16]. To access the GEE platform, users need to register and log in via the Earth Engine Homepage (<https://earthengine.google.com/>, accessed on 09 October 2024). Afterwards, users can perform the desired operations using the code editor (<https://code.earthengine.google.com/>, accessed on 09 October 2024) (Figure 2).

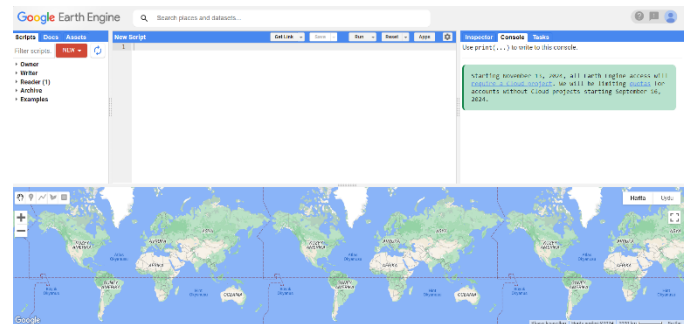


Figure 2: GEE interface.

Dataset

In this study, Landsat-8 satellite data on Level 2, Collection 2, Tier 1 was used. This collection includes atmospherically corrected surface reflectance and surface temperature values. These values are obtained by the OLI and TIRS sensors on the Landsat-8 satellite platform [17]. Table 1 shows the bands and wavelength ranges of Landsat 8 satellite [18].

Table 1: Landsat-8 bands and wavelengths

Bands	Wavelengths (μm)
Band 1 : Coastal/Aerosol	0.435 – 0.0451
Band 2: Blue	0.452 – 0.512
Band 3: Green	0.533 – 0.590
Band 4 : Red	0.636 – 0.673
Band 5: NIR (Near infrared)	0.851 – 0.879
Band 6 : SWIR-1 (Short-wave infrared-1)	1.566 - 1.651
Band 7: SWIR -2 (Short-wave infrared-2)	2.107 – 2.294
Band 8: Pan	0.503 – 0.676
Band 9: Cirrus	1.363 – 1.384
Band 10: TIR-1 (Thermal infrared-1)	10.60 - 11.19
Band 11: TIR-2 (Thermal infrared-2)	11.50 – 12.51

The Landsat-8 collection used in this study is defined as “ee.ImageCollection("LANDSAT/LC08/C02/T1_L2")” in the GEE platform [17].

NDWI

NDWI is an index for analysing the change of wetlands. Water bodies have the characteristic of absorbing radiation in the visible and infrared regions of the electromagnetic spectrum. Therefore, green and NIR bands are used for NDWI calculation. NDWI calculation for Landsat-8 satellite is given in (1).

$$NDWI = \frac{Band\ 3 - Band\ 5}{Band\ 3 + Band\ 5} \quad (1)$$

Although NDWI is an effective method for detecting water bodies, it is often affected by clouds and cloud shadows on the water surface [19]. Especially cloudy conditions between June and September make it difficult to extract wetland information [20].

Workflow

The workflow carried out within the scope of the study is shown in Figure 3.

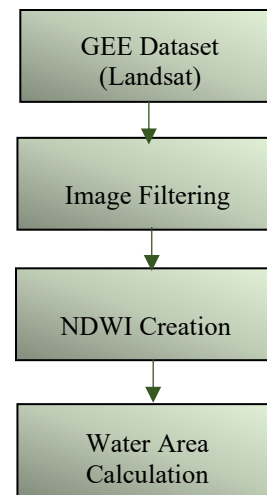


Figure 3: Workflow

In this study, first of all, a rectangular area surrounding Sapanca Lake was defined on the GEE platform. For this purpose, the drawing tool on the platform was used. The drawn area is visualized on the platform (Figure 4).

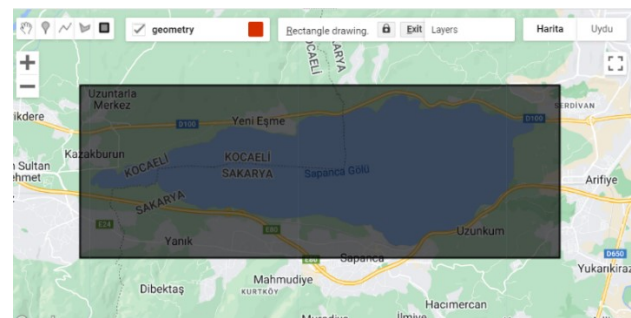


Figure 4: Definition of study area on GEE

After the study area was determined, the time period for the implementation was defined. In this study, the initial and final time periods were set as January 1, 2014 and October 31, 2024, respectively. Then, the satellite data to be used in this study was defined and the cloudiness was set to be lower than 10%. Then, NDWI calculation was performed using Landsat-8 images that satisfies the specified criteria. NDWI Threshold data was obtained by applying the thresholding method to the NDWI data. NDWI Threshold data consists of only black and white regions. Area calculation was performed in km² using the pixels within the white region corresponding to the wetland.

III. RESULTS

In this study, NDWI and NDWI Threshold results were obtained to analyse the areal change in Sapanca Lake between 2014 and 2024. In order to visually display the results, a single NDWI map was created by taking the median of the NDWI values. NDWI Threshold map was obtained by applying thresholding method to this map. With the addition of scale, legend and grid information to the NDWI and NDWI Threshold results and a white layer in the background, NDWI and NDWI

Threshold maps were obtained on the GEE platform (Figure 5 and Figure 6).

In this study, the areal change in Sapanca Lake between 2014 and 2024 was analysed through graphical representation on the

GEE platform. For this purpose, the area was calculated in km^2 through NDWI and NDWI Threshold data obtained within the specified time interval and then the annual water area graph was obtained (Figure 5).

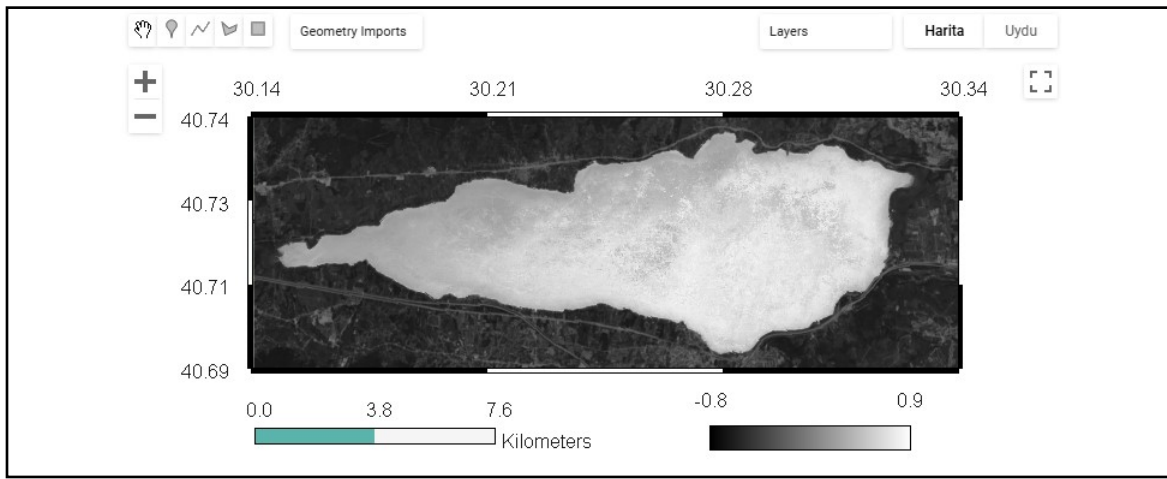


Figure 5: NDWI of Sapanca Lake

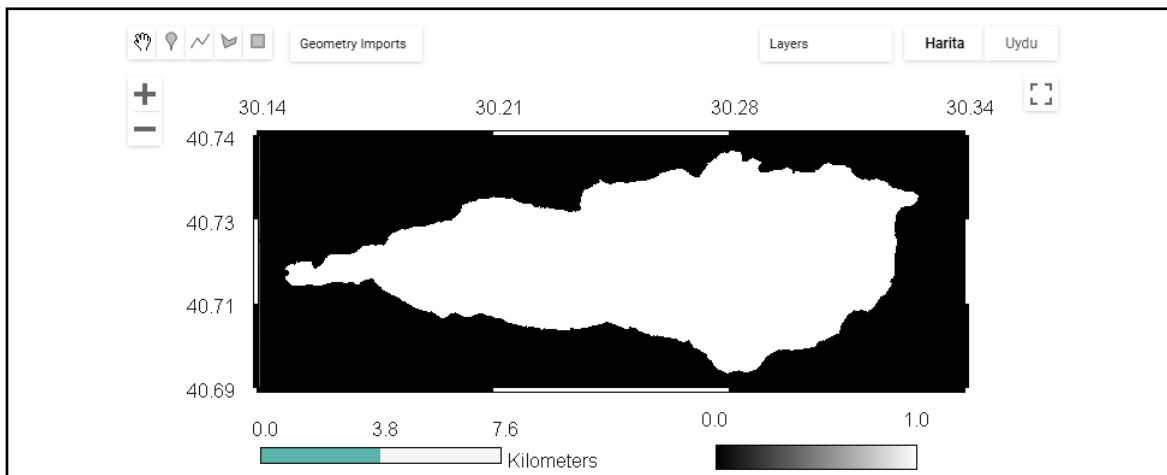


Figure 6: NDWI Threshold of Sapanca Lake

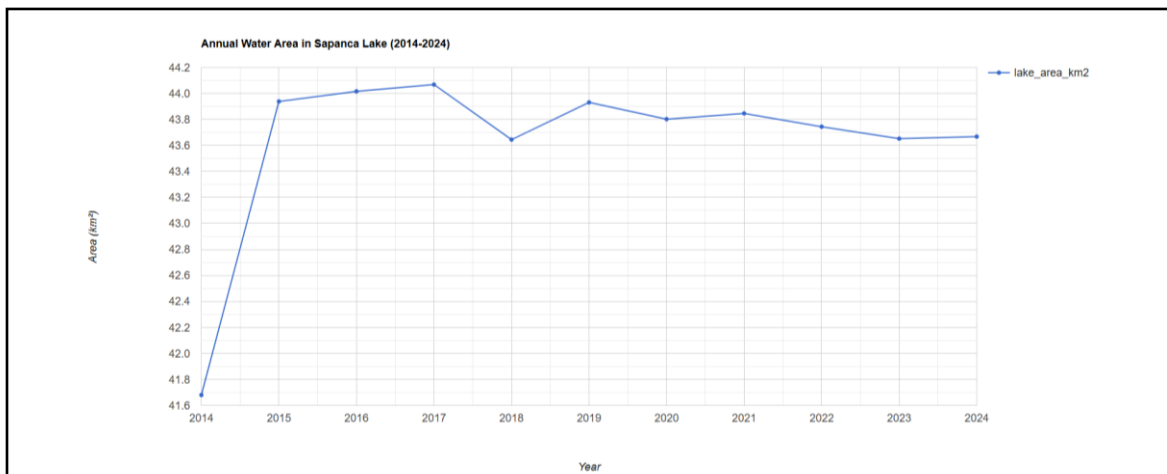


Figure 7: Wetland change in Sapanca Lake

Figure 5 shows that there are some fluctuations in the area of Sapanca Lake between 2014 and 2024. Regarding the 10-year change, it is noticeable that the Lake area in 2014 was lower than in other years. The drought season experienced in our country in 2013-2014 [21] was effective in the low Lake Area boundaries. On the other hand, other factors such as the use of streams feeding the Lake by water bottling factories and the placement of fish farms on stream paths are also effective in the changes in the Lake area over the years [22]. The Lake area was 41.68 km² in 2014 and then it increased to 43.93 km², 44.02 km² and 44.07 km² in the years 2015, 2016 and 2017, respectively. In 2018, the Lake area decreased to 43.65 km² and reached 43.67 km² by having small changes until 2024. Looking at the 10-year values, it is noted that the average area of Sapanca Lake is 43.82 km².

REFERENCES

- [1] Dereli, M. *Web Tabanlı Google Earth Engine ile NDVI Zaman Serisi Analizi: Şanlıurfa il Merkezi Örneği*. in *6th International GAP Engineering Conference-GAP2018. Proceedings*. 2018.
- [2] Aghlmand, M., et al., *Google Earth Engine ile arazi kullanımı haritalarının üretimi*. Niğde Ömer Halisdemir Üniversitesi Mühendislik Bilimleri Dergisi, 2021. **10**(1): p. 38-47.
- [3] Demir, S., *Google Earth Engine üzerinde Sentinel-2 uydu görüntüleri kullanılarak yanan alanların farklı eşik değerlerinde belirlenmesi*. Türk Uzaktan Algılama ve CBS Dergisi, 2023. **4**(2): p. 262-275.
- [4] Yılmaz, O.S., et al., *Orman yangın şiddetinin Google Earth Engine ve coğrafi bilgi sistemleri kullanarak analizi: Hatay-Belen örneği*. Journal of the Institute of Science and Technology, 2021. **11**(2): p. 1519-1532.
- [5] Güzel, A., et al., *Monitoring the regeneration process of areas destroyed by forest fires aided by Google Earth Engine*. Kastamonu University Journal of Forestry Faculty, 2021. **21**(2): p. 122-130.
- [6] GÜRBÜZ, E., *GOOGLE EARTH ENGINE İLE YANGIN TAHRİBATININ VE SONRASI İYİLEŞTİRME SÜREÇLERİNİN İZLENMESİ*. 2022.
- [7] Yaman, Ş. and E.T. Görmüş, *Orman Zararlılarının Verdiği Zararın Google Earth Engine Kullanılarak İzlenmesi*. Türk Uzaktan Algılama ve CBS Dergisi, 2022. **3**(2): p. 139-149.
- [8] Gül, G.O., *Türkiye'de tarımsal kuraklığın uzaktan algılama verileri ile Google Earth Engine üzerinden izlenmesi*. Pamukkale Üniversitesi Mühendislik Bilimleri Dergisi, 2024. **30**(1): p. 71-80.
- [9] Liu, X., et al., *Large-scale crop mapping from multisource remote sensing images in google earth engine*. IEEE Journal of Selected Topics in Applied Earth Observations and Remote Sensing, 2020. **13**: p. 414-427.
- [10] Yılmaz, O.S., *Uzaktan algılama teknikleri ile su yüzeylerinin tespit edilmesinde kullanılan su çıkarma indekslerinin performans analizi*. Türk Uzaktan Algılama ve CBS Dergisi, 2023. **4**(2): p. 242-261.
- [11] Amani, M., et al., *Canadian wetland inventory using Google Earth Engine: The first map and preliminary results*. Remote Sensing, 2019. **11**(7): p. 842.
- [12] Yıldız, M.C. and M. Yılmaz, *Yer Yüzeyi Sıcaklığının Google Earth Engine Kullanılarak Elde Edilmesi ve Değerlendirilmesi*. Afyon Kocatepe Üniversitesi Fen Ve Mühendislik Bilimleri Dergisi, 2022. **22**(6): p. 1380-1387.
- [13] Ermida, S.L., et al., *Google earth engine open-source code for land surface temperature estimation from the landsat series*. Remote Sensing, 2020. **12**(9): p. 1471.
- [14] Mutanga, O. and L. Kumar, *Google earth engine applications*. 2019, MDPI. p. 591.
- [15] Gorelick, N., et al., *Google Earth Engine: Planetary-scale geospatial analysis for everyone*. Remote sensing of Environment, 2017. **202**: p. 18-27.
- [16] Velastegui-Montoya, A., et al., *Google Earth Engine: a global analysis and future trends*. Remote Sensing, 2023. **15**(14): p. 3675.
- [17] URL-1. *USGS Landsat 8 Level 2, Collection 2, Tier 1*. [accessed on 20 October 2024]; Available from: https://developers.google.com/earth-engine/datasets/catalog/LANDSAT_LC08_C02_T1_L2.
- [18] URL-2. *Landsat 8*. [accessed on 20 October 2024]; Available from: <https://landsat.gsfc.nasa.gov/satellites/landsat-8/>.
- [19] Liuzzo, L., et al., *Parameterization of a Bayesian normalized difference water index for surface water detection*. Geosciences, 2020. **10**(7): p. 260.
- [20] Ma, F., Q. Wang, and M. Zhang, *Dynamic changes of wetland resources based on MODIS and Landsat image data fusion*. EURASIP Journal on Image and Video Processing, 2018. **2018**: p. 1-10.
- [21] Durmuş, B. and İ. Bulut, *Batı Akdeniz'deki ekstrem kuraklık şartlarının SPEI yöntemiyle belirlenmesi*. Türk Coğrafya Dergisi, 2023(84): p. 41-52.
- [22] Yılmaz, F., *Kuruhan Göller ve Dereler*. 2014.

Radiological Evaluation with Possible Accident Scenario of Sinop Nuclear Power Plant

ABDULLAH ZENGİN¹, HÜSEYİN ŞAHİNER², EKREM GÜLSEVİNÇLER³

¹ Sinop University, Sinop/Türkiye, abdullahzeng1999@gmail.com

² Sinop University, Sinop/Türkiye, hsahiner@sinop.edu.tr

³ Sinop University, Sinop/Türkiye, egulsevinctler@sinop.edu.tr

Abstract – Nuclear power plants are equipped with comprehensive safety measures to mitigate the potential risks associated with accidents during operation. Action plans are developed to address potential accidents and their aftermath, including the determination of optimal evacuation routes for the local population. To prepare for actions to be taken during and after an accident, simulations and calculations are performed annually using data from meteorological conditions, transportation infrastructure, seismic activity, and natural events in the region prior to the construction of the nuclear power plant. Based on the data obtained from these simulations and calculations, a roadmap is established for responding to an accident. This study analyzes the direction of a radioactive cloud that may form in the event of an accident at the Sinop Nuclear Power Plant, which is planned to be commissioned in Sinop province. The dispersion of radionuclides released after the accident is analyzed using the HotSpot simulation program, with data obtained from the nearest weather station to the plant. The results indicate the direction of the radioactive cloud and the radiation dose that the exposed area will receive when meteorological data and nuclear power plant data are entered into the program.

Keywords – Sinop Nuclear Power Plant, Nuclear Accident, Atmospheric Dispersion Model, Gaussian Plume Model, HotSpot

I. INTRODUCTION

THE non-zero risk of accidents in nuclear power plants always creates a concern and prevents the acceptance of these nuclear power plants by the public. Nuclear choices do not release any radioactive material in normal operating life. On the other hand, pushing the limits of the power plant design and causing a nuclear disaster in the power plant to release a large portion of the radionuclides that emerge into the atmosphere. The radionuclides carried by the radioactive cloud spread after the accident threaten both the power plant personnel and general conversations and malicious software. The life-threatening risk of nuclear radiation requires these to be done about a serious accident in the power plant. Therefore, the analysis of such data collection results and the addition of an emergency response plan for radiological emergencies based on the findings are extremely important before the commercialization of any nuclear system. [1]

In the Sinop Nuclear Power Plant project, which was developed under the international agreement signed between the Republic of Turkey and Japan on May 3, 2013, the founding status of EUAS International ICC, one of the project's founders, was terminated on January 16, 2023. For the Nuclear Power Plant project to be established in the Sinop

region, the founding status and site approval were granted to the Turkish Nuclear Energy Corporation (TÜNAŞ) on January 27, 2023, for the purpose of constructing a nuclear power plant at the İnceburun site in Abalı Village, located along Turkey's Black Sea coast within the borders of Sinop Province. [2, 3]

The nuclear power plant is being constructed approximately 22 km away from the center of Sinop. It has 4 ATMEA 1 reactors with a total power of 4560 MW. This is a modern design Gen III+ reactor that is fully capable of meeting all international safety requirements. ATMEA 1 is a reactor type resulting from the combination of Framatome's EPR and APWR technology. The most specific feature of ATMEA 1 is that it has 3 steam generators and 1 hot leg and 1 cold leg per steam generator. [3]

The atmospheric transport and distribution of radioactive clouds resulting from nuclear power plant accidents are shaped by the prevailing wind direction and other meteorological factors, which determine the range of the resulting radioactive cloud. The HotSpot atmospheric dispersion model can be used to analyze radioactivity levels, air concentration, ground contamination, and the radiation dose to the population in both real and hypothetical nuclear accident scenarios. When the radioactive cloud released from a nuclear explosion reaches equilibrium, radiological impact assessments are conducted using Gaussian models or Lagrangian particle tracking equations. [4]

This study is taking place at the Sinop NPP site. Radioactive distribution analysis for the Large Fracture Coolant Accident (LBLOCA) was performed by NARAC using the Hotspot health physics code. Cs and I activity values used in atmospheric distribution analyzes using HotSpot 3.1.2. The total possibilities of Cs and I distributed in the Fukushima Nuclear Power Plant Accident are available from the accident site of the earthquake and tsunami data in Japan in March 2011.

II. CHARACTERISTICS OF THE SINOP NGS REGION

The Sinop NGS project, which is planned to be Turkey's second nuclear power plant, is set to be located in the İnceburun area, the northernmost point of Turkey. The site of the nuclear power plant is situated 22 km away from the city center.

A. Geographic characteristics of the Sinop region

Sinop is located on the Boztepe Cape and Peninsula, which extends most prominently northward along the Black Sea coastline. The province's largest mountains are the Kure Mountains, which run parallel to the Black Sea. These mountains are characterized by a relatively gentle topography. Approximately 74.3% of the province is covered by mountains. As the İsfendiyar (Kure) Mountains approach the city center of Sinop from the west, their elevation decreases [5].



Figure 1: Sinop Physical Map [13]

B. Agriculture and livestock in the Sinop region

In the Sinop province, 174,117 hectares of land are suitable for agriculture, with 76,635 hectares currently under cultivation [6]. The total agricultural area comprises various product groups, including vegetables, fruits, cultivated fields, fallow land, meadows, and unused agricultural land. These data indicate that approximately 30% of the province is designated as agricultural land. [7]

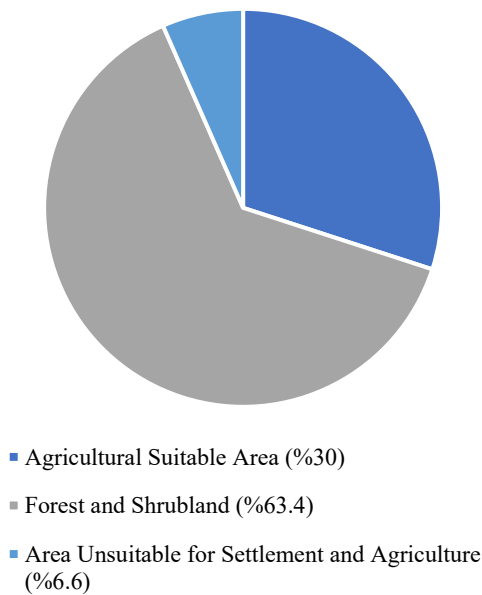


Figure 2: Land Resources of Sinop

Sinop, receiving precipitation throughout the year, boasts a rich diversity of forests and vegetation. The forest cover primarily consists of species such as Yellow Pine, Black Pine, Red Pine, Maritime Pine, Fir, Beech, Oak, Ash,

Chestnut, Poplar, and Hornbeam. The region encompasses a total of 369,466 hectares of forested land.

C. Meteorological data of the Sinop region

Sinop has a climate characterized by a mixture of Eastern and Western Black Sea climates. The northern parts of the province are heavily influenced by the Black Sea climate. However, in the southern regions, the mountains reduce the influence of the Black Sea climate and give way to the influence of the steppe climate. The province experiences relatively small temperature changes between seasons. In general, Sinop has a semiarid, humid climate with cool winters and mild summers. The region is less humid than the Eastern and Western Black Sea regions and receives precipitation throughout the year, except for a certain period in the summer months. Constant winds blow throughout the province throughout the year. [5, 8]

III. MODELS, DATA, METHODOLOGY

A. HotSpot codes

This study utilizes the HotSpot analytical model, developed by the National Atmospheric Release Advisory Center (NARAC), to conduct a safety analysis for facilities handling radioactive materials. HotSpot is employed to simulate the spread of radioactivity and estimate the potential radiation dose to the public following a nuclear detonation. [4] The HotSpot distribution models are tailored for near-surface releases, short-range dispersions (less than 10 km), open terrain, and brief release events, with straightforward meteorological conditions. The model connects radiation effects to the atmospheric release of radioactive substances through an extension of Gaussian-based mathematical modeling. [9]

B. Gaussian dispersion model

$$C(x, y, z, H) = \frac{Q}{2\pi\sigma_y(x)\sigma_z(x)\bar{u}} \exp\left[-\left(\frac{y}{2\sigma_y}\right)^2\right] \left\{ \exp\left[-\left(\frac{z-H}{2\sigma_z(x)}\right)^2\right] + \exp\left[-\left(\frac{z+H}{2\sigma_z(x)}\right)^2\right] \right\} \exp\left[-\frac{\lambda x}{\bar{u}}\right] DF(x) \quad [4]$$

These terms define several parameters used to model the distribution and concentration of pollutants in the atmosphere. C represents the time-integrated atmospheric concentration ($\text{Ci}\cdot\text{seconds}/\text{m}^3$). x is the downwind distance (meters), and y is the crosswind distance (meters). z indicates the vertical distance (meters), while H refers to the effective release height (meters). Q is the source term (Ci). σ_y and σ_z are the standard deviations of the integrated concentration distribution in the crosswind (meters) and vertical (meters) directions, respectively.

\bar{u} is the mean wind speed in the x direction (m/s). λ denotes the radioactive decay constant (s^{-1}). Lastly, $DF(x)$ is the depletion factor or dry deposition correction factor. [4, 9].

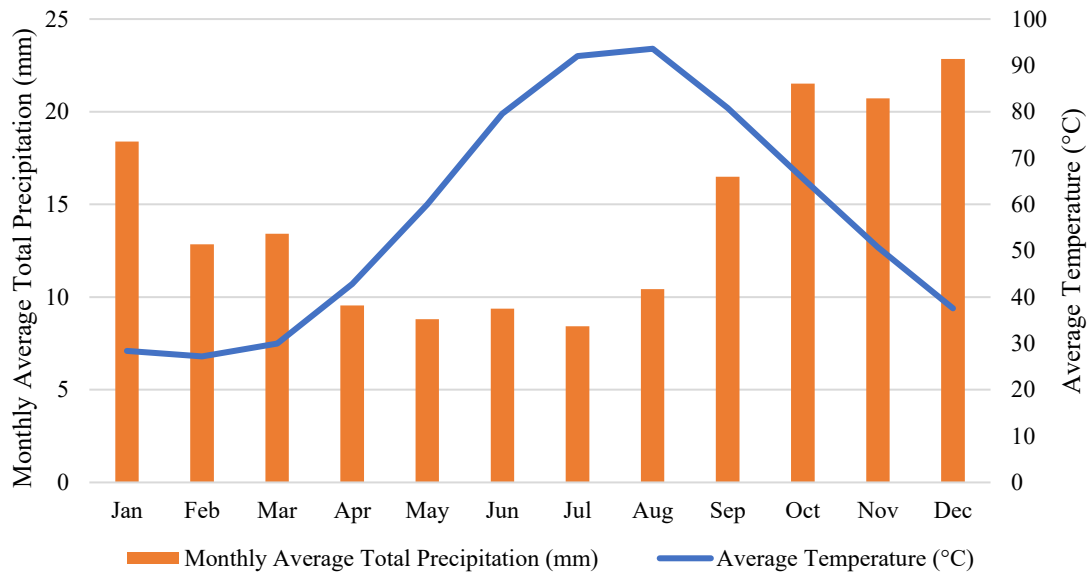


Figure 3: General Directorate of Meteorology Sinop Climate Diagram [12]

Source term refers to the amount of hazardous materials released into the environment following a nuclear power plant accident. The initial and resultant events of such accidents are significant, making risk assessment critically important. The source term also plays a crucial role in determining how hazardous materials released from accidents disperse due to various natural factors, as well as in assessing the potential impacts on the workers in the vicinity of the accident and the general population [10].

C. HotSpot Modeling

In the HotSpot program, the General Plume method was selected as the dispersion model applied in the accident scenario of Sinop NPP. Other data entered into the program are given in Table 1. I-131 and Cs-137 radioisotopes, which have the highest fission-oriented aerosol properties emitted from nuclear power plants, were selected.

Table 1: Input parameters

HotSpot codes input parameters	
Dispersion model	Gaussian
Release	Plume
Radionuclide	I-131 Cs-137
Source-term	Gama radiation
Effective release height (m)	Ground release
Stability Class	D (neutral)
Exposure (DCF)	FGR 11

D. Meteorological input data

Average wind direction and average wind speed data were obtained from Sinop NGS and Sinop Meteorological Station located close to the center of Sinop for use in the Hotspot program in light of 57 years of meteorological data. The wind roses of the regional station (Figure 4) were obtained using the Sinop Meteorological Station Average Wind Speed Data According to Directions and Sinop Meteorological Station

Total Wind Blowing Numbers According to Directions Data given in Table 2.

IV. RESULTS AND DISCUSSION

The wind rose values drawn with the data obtained from the Sinop meteorology field, which is the closest to the Sinop NGS location, are defined in HotSpot. The wind direction is defined as 315 (NW), and the wind speed is defined as 2.45 m/s. The definitions of the nuclear power plant workers, the public and the background values have been made to the HotSpot program. The annual value for the nuclear power plant workers is defined as 0.05 Sv, the annual value for the public is defined as 0.02 Sv and the annual background value is defined as 2.4E-03 Sv.

Figure 5 illustrates the cloud centerline as a function of the downwind distance. The deposition rate of the radioactive cloud is calculated using the default value of 0.3 cm/s for non-noble gases. By examining the specifics of the effective release rates, Figure 5 presents various scenarios with effective release heights of 10 m, 20 m, 30 m, and 40 m, respectively. The results show that the effective release height affects the separation between the Total Effective Dose Equivalent (TEDE) and the ground-level concentration.

The default location of Sinop NPP was obtained in the EIA report (fig 6.). When the location information Hotspot range is entered, the simulation results in Table 3 provide clear data for the values of inhalation, ground radiation and organ effect dose for each device.

Table 2: Sinop meteorological station annual wind data [3]

Directions	Yearly	
	Sinop Meteorological Station Average Wind Speed Data According to Directions (m/s)(1960-2017)	Sinop Meteorological Station Total Wind Blowing Numbers According to Directions Data (1960 - 2017)
N	2,8	29982
NNE	2,5	24564
NE	2,0	8971
ENE	2,1	13601
E	2,1	11541
ESE	2,6	40964
SE	2,6	45254
SSE	2,4	70850
S	2,0	21838
SSW	1,8	15852
SW	1,6	6675
WSW	1,7	13885
W	2,1	14423
WNW	3,5	68553
NW	3,9	53249
NNW	3,5	48019

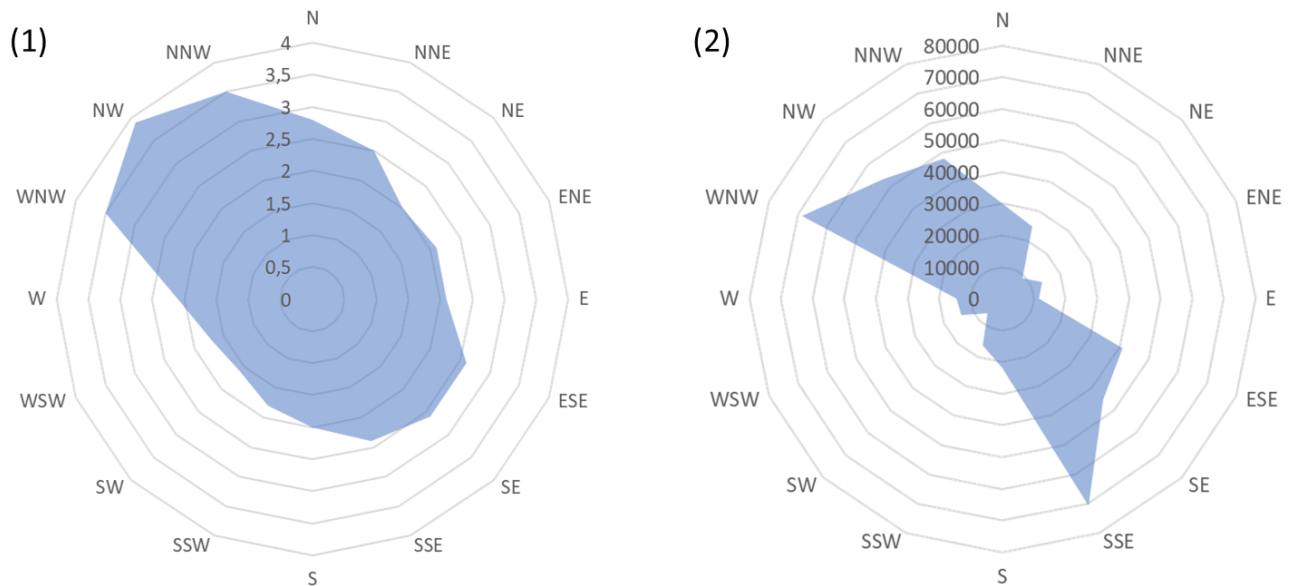


Figure 4: Sinop Meteorological Station Annual Average Wind Speed (1) and Annual Wind Diagram According to Blow Numbers (2) According to Directions (1960 - 2017)

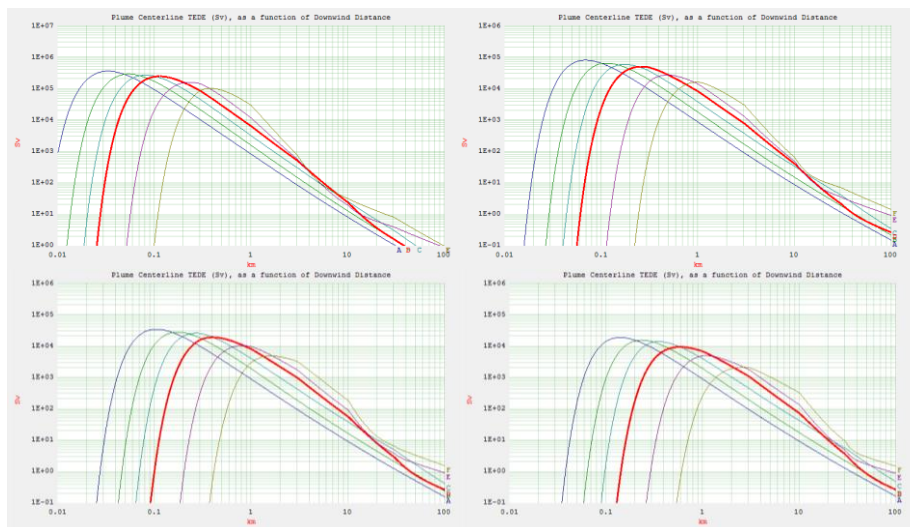


Figure 5: Plume centerline TEDE (Sv) as a function of downwind distance (In picture order 1;10 m,2;20 m,3;30 m,4;40 m)

Table 3: TEDE (Sv) values for accident scenarios at different distances from the source

Distance km	Te de (Sv)	Respirable Time- Integrated Air Concentration (Bq-Sec)/m ³	Ground Surface Deposition (kBq/m ²)	Ground Shine Dose Rate (Sv/hr)	Arrival Time (hour:min)
0,030	6,8E+01	2,5E+13	5,8E+09	9,1E+00	<00:01
0,100	2,4E+05	1,2E+15	8,3E+14	1,3E+06	<00:01
0,200	1,6E+05	2,2E+16	5,9E+14	9,2E+05	00:01
0,300	8,4E+04	5,3E+16	3,1E+14	4,9E+05	00:02
0,400	4,6E+04	3,4E+16	1,7E+14	2,7E+05	00:02
0,500	2,9E+04	2,4E+16	1,1E+14	1,7E+05	00:03
0,600	1,9E+04	1,8E+16	7,2E+13	1,1E+05	00:04
0,700	1,4E+04	1,4E+16	5,1E+13	8,0E+04	00:04
0,800	1,0E+04	1,1E+16	3,8E+13	6,0E+04	00:05
0,900	8,0E+03	9,1E+15	3,0E+13	4,6E+04	00:06
1,000	6,4E+03	7,7E+15	2,4E+13	3,7E+04	00:06
2,000	1,3E+03	2,5E+15	4,7E+12	7,3E+03	00:13
4,000	2,4E+02	8,9E+14	8,4E+11	1,3E+03	00:27
6,000	8,4E+01	5,0E+14	2,8E+11	4,4E+02	00:40
8,000	4,1E+01	3,3E+14	1,3E+11	2,0E+02	00:54
10,000	2,4E+01	2,5E+14	7,3E+10	1,1E+02	01:08
20,000	3,7E+00	9,9E+13	6,4E+09	1,0E+01	02:16
40,000	9,6E-01	4,1E+13	4,6E+08	7,1E-01	04:32
60,000	5,3E-01	2,5E+13	1,2E+08	1,8E-01	06:48
80,000	3,7E-01	1,7E+13	6,1E+07	9,6E-02	09:04



Figure 6: Google Earth view of the nominated site.

In the Sinop NPP scenario, the direction and area of the radioactive cloud released as a result of the nuclear power plant accident were obtained with the simulation results obtained from the Hotspot program. In this area, the dose to which the plant workers and people living in the vicinity of the plant will be exposed, indicated in red, is indicated.

In the area indicated in green, the dose rate to which the residents and public officials in the area where the plant will be built and its surroundings will be exposed is indicated. Finally, in the wide area indicated in blue, the background dose amount is indicated.

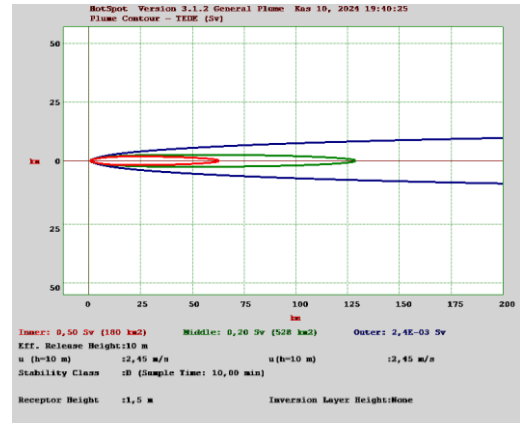


Figure 7: Contour graph resulting from Sinop NPP accident scenario results

V. CONCLUSIONS

The hypothetical accident scenario modeling performed at the D class stability level for the Sinop NPP site was evaluated. The results were run by changing the effective release height at the D class stability level and the simulation assumptions. These assumptions reveal that the increase in the effective release height causes a decrease in TEDE and ground accumulation. The TEDE values obtained from the HotSpot were estimated for different groups of people (NPP workers, public officials, Sinop residents and tourists) around the source point released after the nuclear accident. In the simulation application, it was observed that the radiation levels to which groups of people would be exposed at distances of 0.1 km, 1 km and 80 km around the NPP were 2.4E+05 Sv, 6.4E+03 Sv and 3.7E-01, respectively.

The Contour graphic obtained for the Sinop Power Plant, when opened on Google Earth based on the current planned location, shows the assumed direction of the radioactive cloud released in the accident scenario and the cities located in this area.(Fig 8.) When examined in detail, the city center where the power plant will be built and Samsun, which has a population of 1,377,546 according to TÜİK data and is the 16th most populous city in Turkey, are located in this area. In the event of a nuclear leak or major accident, the radioactive cloud that would be released would greatly affect populated areas, agricultural areas, the Black Sea coastline and livestock areas. [11]

As a result, the most appropriate means of communication must be available to warn and inform the public about the areas where the nuclear power plant will be built. The most appropriate means of transport and evacuation routes must be determined to evacuate the people in danger. The necessary shelters and houses must be built to accommodate the people who will be evacuated from the accident area or an emergency action plan must be developed. Annual censuses can be conducted in risky areas to accurately track the number of residents and the distribution of critical groups, so that the number of vehicles or other measures required can be properly estimated.

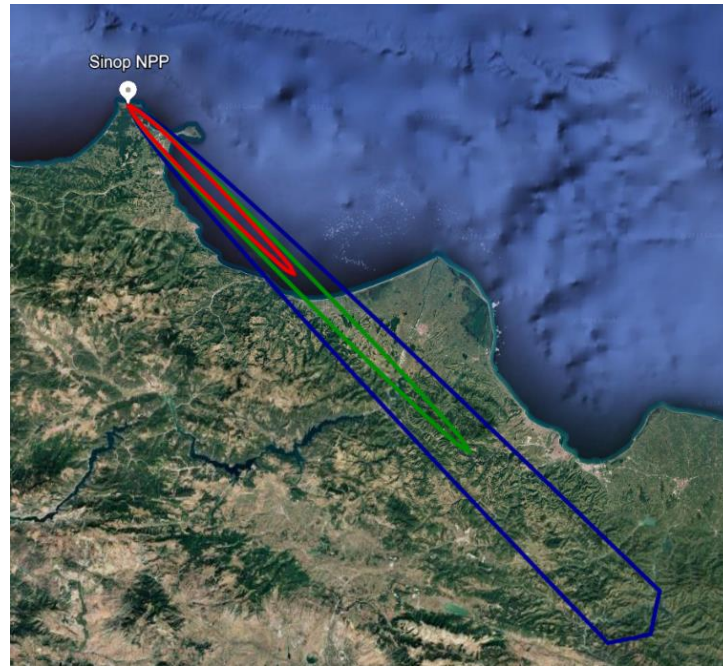


Figure 8: Sinop NPP Google earth Contour graphic

REFERENCES

- [1] A. Fairuz and H. Sahadath, "Assessment of the potential Total Effective Dose (TED) and Ground Deposition (GD) following a hypothetical accident at the proposed Rooppur Nuclear Power Plant," *Applied Radiation and Isotopes*, no. 158, 2020.
- [2] Nükleer Düzenleme Kurumu (NDK), "Sinop Nükleer Santrali Nükleer Tesislerin Yetkilendirilmesi," [Online]. Available: <https://www.ndk.gov.tr/sinop-nukleer-santrali>. [Accessed 04 11 2024].
- [3] A. A.Ş., "Sinop Nükleer Güç Santrali Projesi(ÇED raporu)," EUAS International ICC Merkezi,T.C. Çevre, Şehircilik ve İklim Değişikliği Bakanlığı., Ankara, 2020.
- [4] Dipan Kundu, C.V. Srinivas, S. Chandrasekaran and B. Venkatraman, "Radiological consequence assessment for hypothetical nuclear explosion scenario using HotSpot," *Progress in Nuclear Energy*, 2022.
- [5] T.C. Sinop Valiliği, "T.C. Sinop Valiliği," [Online]. Available: <http://www.sinop.gov.tr/cografya>. [Accessed 26 10 2024].
- [6] TÜİK, "TÜİK Bölgesel istatistikler," 2023. [Online]. Available: <https://biruni.tuik.gov.tr/bolgeselistatistik/tabloOlustur.do#>. [Accessed 24 10 2024].
- [7] T.C.Sinop Valiliği, "T.C.Sinop Valiliği," [Online]. Available: <http://www.sinop.gov.tr/tarim>. [Accessed 24 10 2024].
- [8] Samsun Meteoroloji Genel Müdürlüğü, "Sinop İklim Değerlendirmesi," [Online]. Available: <https://samsun.mgm.gov.tr/FILES/iklim/sinop.pdf>. [Accessed 29 10 2024].
- [9] Juliana de Sa Sanchez, Andressa dos Santos Nicolau, Claudio M.N.A Pereira and Cesar Marques Salgado, "Methodology to calculate doses from gamma-emitting plumes using MCNP6 Monte Carlo N-particle and HotSpot codes," *Nuclear Engineering and Design*, 2024.
- [10] R. Alam, "Modeling of atmospheric dispersion and radiological dose consequences for a hypothetical accident in the perspective of Rooppur Nuclear Power Plant (RNPP)," *Nuclear Engineering and Design*, vol. 420, 2024.
- [11] Türkiye istatistik kurumu, "Nüfus İstatistikleri Portalı," 2023. [Online]. Available: <https://nip.tuik.gov.tr/>. [Accessed 2024 11 10].
- [12] Meteoroloji Genel Müdürlüğü, "Resmi İklim İstatistikleri," Meteoroloji Genel Müdürlüğü, [Online]. Available: <https://mgm.gov.tr/veridegerlendirme/il-ve-ilceler-istatistik.aspx?m=SINOP>. [Accessed 29 10 2024].
- [13] Harita Genel Müdürlüğü, "T.C. Milli Savunma Bakanlığı Harita Genel Müdürlüğü," [Online]. Available: <https://www.harita.gov.tr/urun/sinop-fiziki-il-haritasi/334>. [Accessed 10 11 2024].

Malware and Their Remote Control in the Context of Detection and Prevention of Global Threats

NURETTİN DOĞAN¹, ZEYNEP BAKIRTEMİZLER AYDIN²

¹Selcuk University Technology Faculty Computer Engineering Department, Konya/Turkey, ndogan@ymail.com

²Selcuk University Graduate School of Natural and Applied Sciences Department of Computer Engineering , zbakirtemizler@gmail.com

Abstract - Malware are software designed to harm computer systems, steal data, or manipulate users. These malicious programs can be of various types, including viruses, worms, trojans, spyware, and ransomware. They spread through methods such as email attachments, websites, and social engineering tactics. Malware can be controlled remotely through Command and Control (C&C) servers, Remote Access Tools (RATs), and botnets. C&C servers act as central management points for malware, allowing attackers to direct their actions. RATs enable attackers to gain remote access to target systems, while botnets are used for large-scale attacks.

Malware can be detected using signature-based detection, behavioral analysis, and heuristic analysis. Signature-based detection uses known malware signatures, while behavioral analysis monitors the malware's actions within the system. Heuristic analysis predicts potential threats. To protect against malware, antivirus and antimalware software, firewalls, and regular updates are essential. User awareness and taking security measures play a critical role in mitigating the impact of malware.

Real-world examples demonstrate the dangers of malware. For instance, the WannaCry ransomware affected thousands of systems worldwide, causing significant financial losses. Similarly, in Lebanon, pagers were used to detonate explosives, showcasing another method of remote control and the potential for significant harm. Such attacks highlight the importance of detecting and preventing malware.

Keywords – Malware, Remote Control, Detection, Command and Control (C&C), Security.

I. INTRODUCTION

MALWARE has become one of the largest threats computer systems face in the modern digital world. The increasing use of the internet and network connections has enabled malware to spread rapidly and grow more complex. Malware types are typically designed to steal data from users' computers, damage systems, or take control of them for malicious purposes [1][2]. In recent years, the remote control of malware has laid the groundwork for larger and more organized cyber-attacks [3]. This paper will provide a comprehensive analysis of malware types, remote control mechanisms, detection techniques, and security measures. Furthermore, it will address methods for protection against cyber threats and explore global examples of these threats.

II. TYPES OF MALWARE AND METHODS OF SPREAD

The diversity of malware and its transmission methods have made it a serious global threat. Common types of malware include:

1. **Viruses:** Software that infects files, replicates, and spreads to other systems [2].
2. **Worms:** Malware that spreads over networks by targeting security vulnerabilities [3].
3. **Trojans:** Software that deceives users to infiltrate systems and operates covertly to cause harm [4].
4. **Ransomware:** Malware that encrypts user data, blocking access and demanding a ransom. For example, the WannaCry ransomware in 2017 impacted thousands of systems worldwide [9].
5. **Spyware and Adware:** Software that tracks users without permission, subjecting them to advertisements [5].

These types of malware often spread via email attachments, malicious websites, and social engineering tactics. Users may inadvertently expose themselves to these threats by downloading malicious files or installing fake software [6].

III. REMOTE CONTROL MECHANISMS

Remote control is a crucial element that enables malware to conduct large-scale, coordinated attacks. Malware can be controlled via remote access tools (RATs) and botnets [3]. Key mechanisms include:

- **Command and Control (C&C) Servers:** C&C servers allow centralized control over malware, enabling attackers to send commands and control malware remotely [4].

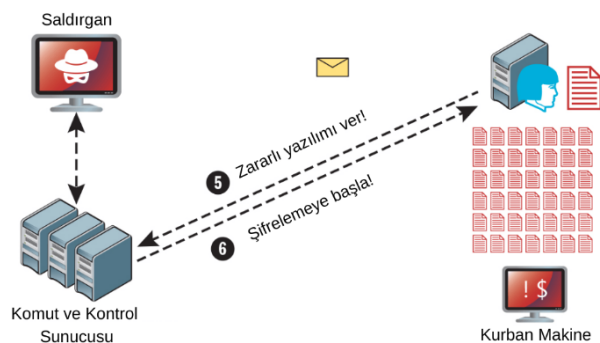


Figure 1: Command and Control Servers

In cybersecurity, human error is often the weakest link. Attackers may induce panic by sending alarming emails with malicious attachments, prompting users to act unwittingly. When malware is downloaded and executed, it bypasses security defenses, compromising networks and computers [11].

C2 attacks can originate through the following channels:

- **Phishing emails:** Containing malicious links or attachments.
- **Browser plugin vulnerabilities.**
- **Compromised software or updates:** Malicious updates posing as legitimate ones.
- **Updates from trusted platforms:** Malware can even be distributed through updates on reputable platforms like app stores.

A C2 attack proceeds through stages:

1. **Infection:** Attackers introduce malware into the target system via phishing, security exploits, or malicious ads.
2. **Establishing a C2 Channel:** The infected system communicates with the C2 server once the C2 channel is set up.
3. **Receiving Commands:** The malware remains undetected, receiving commands such as installing software, encrypting data, or extracting information.
4. **Command Propagation:** The C2 server may instruct other systems to scan for vulnerabilities, forming a botnet that could compromise an organization's IT infrastructure.

C2 servers can be structured in various configurations:

- **Star Topology:** Bots are centralized around a single server.
- **Multiple Server Topology:** Several servers are utilized.
- **Hierarchical Topology:** Multiple C2 servers arranged in a hierarchy.
- **Random Topology:** Peer-to-peer (P2P) communication enables direct interaction among bots.

An example includes the ToxicEye malware, which stole data and monitored users in 130 cases using platforms like Telegram in 2017 [11].

- **Remote Access Tools (RATs):** RATs enable attackers to access target systems remotely, allowing full system control and modification capabilities [5].

RATs often accompany other malware, such as keyloggers. Keyloggers collect keystrokes in the background, enabling attackers to obtain user credentials or corporate account information. This data can then be used for financial theft or to gain elevated privileges on other network devices for remote control [12].

RATs are often installed through malicious email attachments, downloaded files, or macros in Microsoft Word/Excel documents. These macros allow RATs to operate silently, facilitating remote control of the device. Attackers may use authenticated email accounts on remotely controlled devices to send malware to other victims, giving the impression that the email originates from a reliable source and thus convincing recipients to open malicious files. This process exploits users, often without detection, to provide attackers with a valuable channel for obtaining sensitive information [12].

- **Botnets:** Botnets are malware-controlled networks of multiple devices that attackers can use for large-scale attacks [6].

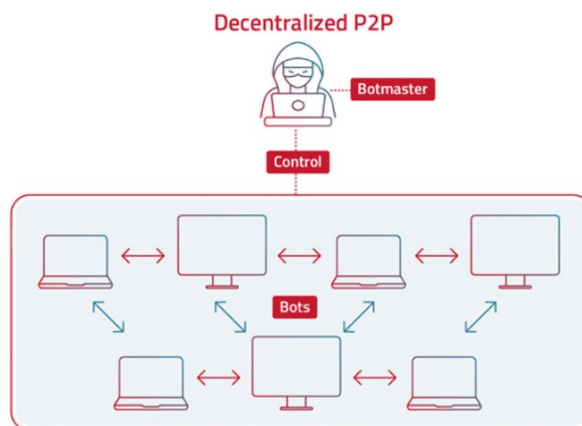


Figure 2: Botnets

Botnets consist of a network of infected devices, including computers and IoT (Internet of Things) devices, typically spread through social engineering, security vulnerabilities, or exploit kits. Botnet control may be achieved through a centralized command and control (C&C) server or a decentralized peer-to-peer (P2P) model [13].

Botnets can carry out various malicious activities on target devices, such as collecting personal data, sending files, scanning other devices for vulnerabilities, and executing remote commands. While botnets traditionally use centralized servers to manage infected devices, the P2P model has become more prevalent in recent years due to increased security measures. The P2P model is more resilient against single points of failure, enabling direct communication among devices for command execution [13].

A real-world example includes the remote bombing incident in Lebanon using call devices, highlighting the dangers and potentially harmful impact of remote control [10].

IV. MALWARE DETECTION METHODS

Detecting malware is a critical phase of security measures. Malware detection methods include:

- **Signature-Based Detection:** Identifies known malware based on digital signatures, recognizing previously documented threats [7].
- **Behavioral Analysis:** Observes system activity to detect malicious behaviors, useful for identifying previously unknown threats [6].
- **Heuristic Analysis:** Predicts potential threats by analyzing behavior patterns to identify abnormal system activity [8].

The accuracy of these detection methods depends on the algorithms employed, with each method having unique advantages and limitations [6].

V. CONCLUSION

Malware and remote control mechanisms represent some of the most dangerous cyber threats today. The complexity of malware types, control methods, and detection techniques continues to increase, underscoring the need for constantly updated cybersecurity measures and user awareness. Real-world examples demonstrate the extensive global damage that malware can cause and highlight the critical importance of addressing cybersecurity gaps [9][10].

REFERENCES

- [1] K. Kalıncıoğlu, "Zararlı Yazılımların Tespiti İçin Hibrit Sistem Tasarımı" *Bursa Uludağ University (Turkey) ProQuest Dissertations & Theses*, 2020, <https://www.proquest.com/openview/fc62928017f88cf9e8d2daf27490c3f/1?pq-origsite=gscholar&cbl=2026366&diss=y>
- [2] Ü. Köse, R. Samet, "Detection of Malware with Deep Learning Method", *2021 6th International Conference on Computer Science and Engineering*, 2021, <https://ieeexplore.ieee.org/abstract/document/9559020/metrics#metrics>
- [3] M. Yalçınkaya, "Zararlı Yazılım Yayma Aracı Olarak Mobil Uygulamaların Kullanılması: Pokemon Go Örneği", *Mehmet Akif Ersoy Üniversitesi Fen Bilimleri Enstitüsü Dergisi Özel Sayı 1*, 2017, <https://dergipark.org.tr/en/download/article-file/311953>
- [4] İ. Kara, "Truva Atı Zararlı Yazılımlarının Tespit, Teknik Analiz ve Çözüm Önerileri", *Bilgi Yönetimi Dergisi*, 2019, <https://dergipark.org.tr/en/download/article-file/726511>
- [5] Sriramachandramurthy, R., Balasubramanian, S.K. and Alexandra Hodis, M. "pyware and Adware: How Do Internet Users Defend Themselves?", *American Journal of Business*, 2009, <https://www.emerald.com/insight/content/doi/10.1108/19355181200900010/full/html>
- [6] S. Çakır, M. Kesler, "Bilgisayar Güvenliğini Tehdit Eden Virüsler Ve Antivirüs Yazılımları", *Bilecik Üniversitesi*, <https://ab.org.tr/ab12/bildiri/82.pdf>
- [7] S. Atasever, İ. Özçelik, Ş. Sağıroğlu, "An Overview of Machine Learning Based Approaches in DDoS Detection", *IEEE*, 2020, <https://ieeexplore.ieee.org/abstract/document/9302121>
- [8] Ö. Şahinaslan, "Bilgisayar Ağlarında Açık Kaynak Kodlu Güvenlik Yazılımları İle Anti-Spam Modülünün Geliştirilmesi", 2007, <https://www.proquest.com/openview/e2974883ba4284f3cd13be008d2c33be/1?pq-origsite=gscholar&cbl=2026366&diss=y>
- [9] S. Çelik, B. Çeliktaş, "Güncel Siber Güvenlik Tehditleri: Fidyeye Yazılımlar", *Cyberpolitik Journal Vol. 3*, 2018, https://www.researchgate.net/profile/Baris-Celiktas/publication/330764616_GUNCEL_SIBER_GUVENLIK_TEHDITLERI_FIDYEE_YAZILIMLAR/links/5c5342d3299bf12be3f0ffc0/GUeNCEL-SIBER-GUeVENLIK-TEHDITLERI-FIDYEE-YAZILIMLAR.pdf
- [10] A. Kiraz, "Patlayan Motorola & Gold Apollo Çağrı Cihazlarının Olay Analizi", 2024, <https://alican-kiraz1.medium.com/motorola-advisor-pager-patlama%C4%B1-incident%C4%B1-analizi-part-1-82116ee6daf>
- [11] İ. Başaran, "Komut ve Kontrol Sunucusu (Command and Control

Server/C2)

Nedir?",

2022,

<https://www.aucyberclub.org/cybercamp/intro/2022/10/30/KomutveKontrolSunucusuNedir.html>

[12] " Uzaktan Erişim Truva Atı (RAT) Nedir?",

<https://www.proofpoint.com/au/threat-reference/remote-access-trojan>

[13] " Botnet Definition: What Is a Botnet and How Does It Work?",

<https://www.radware.com/cyberpedia/bot-management/botnet/#HowDoBotnetsWork>

Design of a Maximum Power Point Tracking System Using a Switched-Capacitor with a Class E Resonant Inverter

KENAN ÜNAL¹, SALIH NACAR²

¹ Gazi University, TUSAŞ Kazan Vocational School, Department of Motor Vehicles and Transportation Technology, 06980, Ankara, Türkiye

²Bandırma Onyedü Eylül University, Engineering and Natural Sciences Faculty, Department of Electrical Engineering, 10200, Balıkesir, Türkiye

Abstract - Resonant power converters have become increasingly preferred in recent years due to their low electromagnetic interference (EMI) and low switching losses. Implementing resonant power converters in maximum power point tracking (MPPT) systems for photovoltaic panels is crucial for achieving high efficiency. In this study, an MPPT system utilizing a switched-capacitor with a Class-E resonant power converter is proposed. The simulation study was carried out at 450 W/m^2 , 250 W/m^2 and 550 W/m^2 irradiation values, respectively. The average MPPT efficiency for all three irradiance values was 99.7%.

Keywords - Class-E resonant inverter, Maximum power point tracking, Switched-capacitor, Soft-switching

I. INTRODUCTION

The power extracted from photovoltaic (PV) panels, which convert photons from the sun into DC energy, is directly dependent on irradiation and temperature level of the PV panel. Consequently, variety of weather conditions is affect the power drawn from PV panels [1]. Therefore, it makes necessary the use of converters or inverters that function as impedance matching between the PV panel and the load. MPPT systems, also known as controlled power converters or inverters, are used today to obtain electrical energy from PV panels at peak efficiency. Basically, power converter or inverter is positioned between the PV panels and the load. This converter continuously measures the PV panel current and voltage to calculate its power. As a result of these measurements, the power of the power converter is controlled with a microcontroller. In this way, maximum power point tracking is performed.

Power converters used to MPPT in PV panels can be divided into two groups: hard-switching and soft-switching power converters. Conventional hard-switching power converters cause electromagnetic interference (EMI) and high switching losses at high frequencies [2], [3]. Soft-switching power converters are available as a solution for MPPT operation as a replacement for hard-switching power converters. The Class-E resonant converter/inverter, which is the one of the single-switch soft-switching power converters, is widely used in many applications with especially low input voltage and power [4],

[5]. The primary reason for the preference of these converter/inverter is their ease of design and control, as well as their ability to achieve soft-switching at high frequencies [4], [6]. This converter/inverter, utilized in applications like LED drivers and induction heaters, is also employed as MPPT system in PV panels. There are mainly two types control techniques used in power control of Class-E resonant converter/inverter. These power control techniques are fixed frequency and variable frequency switching [7]–[9].

In this paper, a switched-capacitor controlled MPPT system by using Class-E resonant inverter proposed for in PV panels. The fundamental theoretical analysis presented. In order to validate its effectiveness, a simulation is performed in MATLAB/Simulink. The simulation result was carried out under three different PV panel irradiation levels, and the results are presented.

II. CLASS-E RESONANT INVERTER AND MPPT

The Class-E resonant inverter circuit is depicted in Figure 1. Here, L_1 represents the input coil, C_1 represents the parallel capacitor of power switch, L_2 represents the resonant coil, C_2 represents the resonant capacitor, and R represents the load.

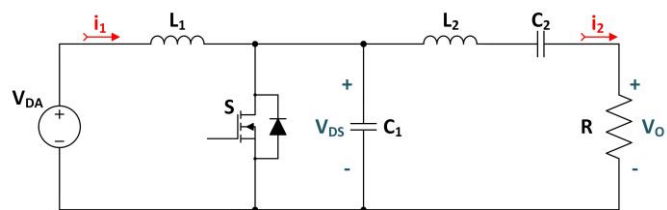


Figure 1: Class-E resonant inverter

There are two resonant frequencies in the Class-E resonant power converter [4]. These two resonant angular frequencies can be calculated by Eq. 1 and Eq. 2 [4], [10].

$$\omega_{r1} = \frac{1}{\sqrt{L_2 C_2}} \quad (1)$$

$$\omega_{r2} = \frac{1}{\sqrt{L_2 \left[\frac{C_1 C_2}{C_1 + C_2} \right]}} \quad (2)$$

If the V_{DS} voltage in a Class-E resonant power converter is zero when the MOSFET turn-on, this situation is called zero voltage switching (ZVS) and is expressed by Eq. 3 [5].

$$V_{DS}(2\pi) = 0 \quad (3)$$

In addition, if both V_{DS} and its derivative are zero when MOSFET is turn-on, this situation is called zero derivative switching (ZDS) and is expressed in Eq. 4 [6].

$$\frac{dV_{DS}(\omega t)}{d(\omega t)} \Big|_{\omega t=2\pi} = 0 \quad (4)$$

When the Class-E resonant inverter meets these two conditions, it operates under optimal conditions [6], [11]. Switching losses are also reduced in optimal operating conditions [12]. A resonant capacitor for power control in a Class-E resonant inverter can be implemented using a switched capacitor. The switched capacitor can be regulated the power via the MPPT algorithm. The flow chart of the perturb & observe (P&O) algorithm is presented in Figure 2 [13].

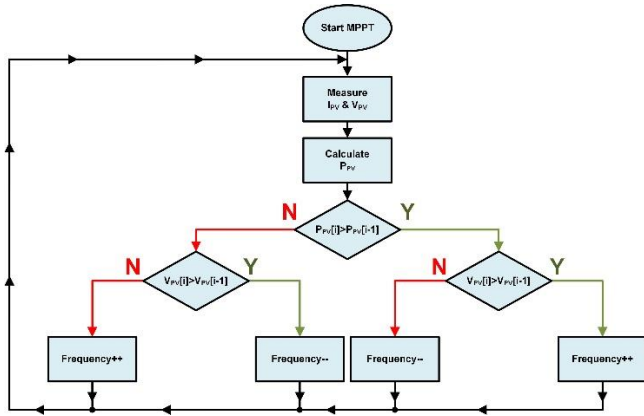


Figure 2: The flowchart of the MPPT algorithm [13]

According to this algorithm, first V_{PV} and I_{PV} are measured. Then P_{PV} is calculated of PV panel. The calculated P_{PV} is compared with the previous cycle ($P_{PV}[i-1]$). If P_{PV} is greater than $P_{PV}[i-1]$, V_{PV} comparison is started. Here, if V_{PV} is greater than $V_{PV}[i-1]$, the switched-capacitor circuit frequency is increased, if not, it is decreased. On the other hand, if $P_{PV}[i-1]$ is greater than P_{PV} , V_{PV} comparison is started as a previous. In this case, if V_{PV} is greater than $V_{PV}[i-1]$, the frequency increases and vice versa, the switched-capacitor circuit frequency decreases.

III. SWITCHED-CAPACITOR BASED MPPT SIMULATION

The simulation study performed in MATLAB/Simulink is presented in Figure 3.

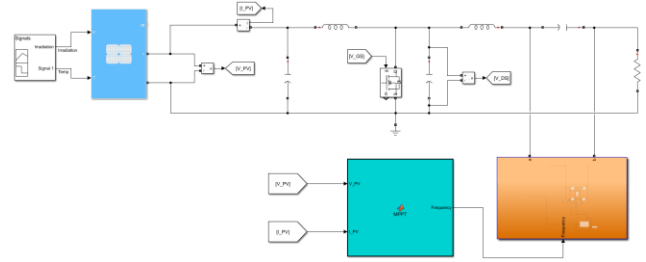


Figure 3: Switched-capacitor controlled MPPT system simulation

The circuit parameters used are given in Table 1.

Table 1: Class-E Resonant Power Converter Parameters

Parameters	Value
L_1	3 mH
L_2	52.35 μ H
C_1	4.8 nF
C_2	15 nF

In the simulation study, a 0.4 μ F capacitor (C_a) was parallel connected with the C_2 , as seen in Figure 4. The switching frequency of the circuit depicted in Figure 4 is adjusted by the MPPT algorithm to regulate the power of the Class-E resonant inverter.

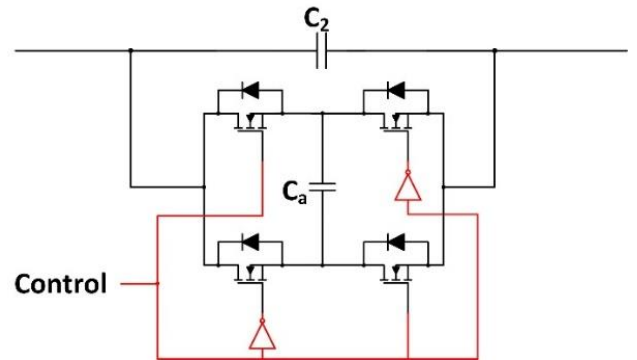


Figure 4: Switched-capacitor circuit

Simulations were performed for MPPT at three different irradiation levels as shown in Figure 5. The irradiation levels of the PV panel were determined as 450 W/m^2 , 250 W/m^2 ve 550 W/m^2 , respectively.

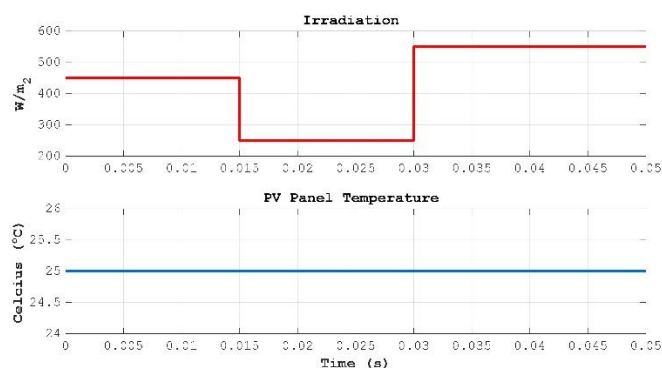


Figure 5: PV panel irradiation and temperature levels

The MPPT result using a Class-E resonant power converter with switched-capacitor operating at these irradiation levels is presented in Figure 6.

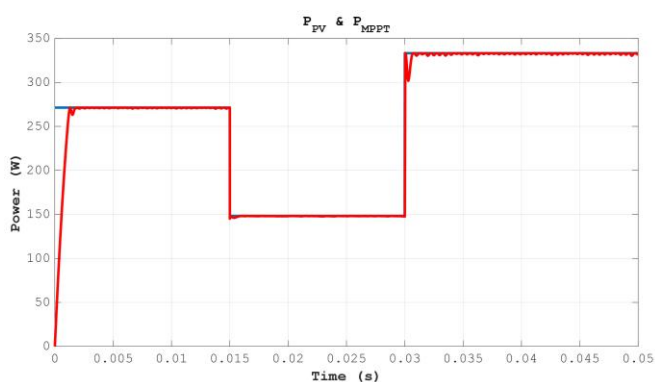


Figure 6: Simulation result

The simulation results show that the calculated MPPT efficiency (η_{MPPT}) at each irradiation level is presented in Table 2.

Table 2: Efficiency result

Irradiation Levels	η_{MPPT}
450 W/m^2	99.82%
250 W/m^2	99.71%
550 W/m^2	99.64%

The average η_{MPPT} at three irradiation levels was calculated as 99.7%. In the simulation study, in addition to MPPT efficiency of the PV panel with the Class-E resonant inverter, the fulfillment of soft-switching conditions was also evaluated. The V_{GS} and V_{DS} voltages of the MOSFET at each irradiation levels are presented in Figure 7.

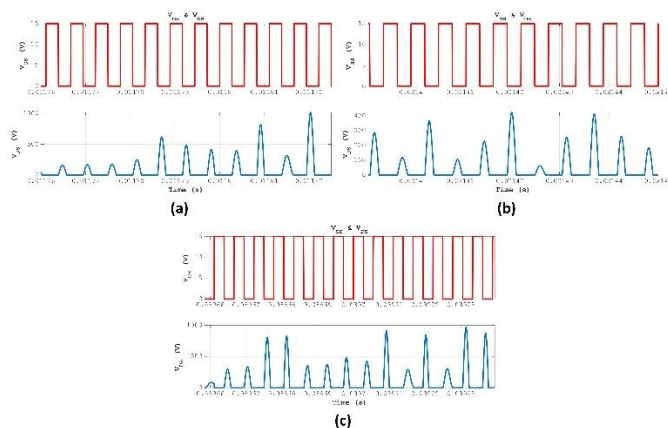


Figure 7: PV panel irradiation and temperature levels

Although occasional hard-switching was observed during MPPT operation with the proposed switched-capacitor circuit, it mostly operated under soft-switching conditions.

IV. CONCLUSIONS

In this paper, a simulation study of MPPT from PV panels using switched-capacitors in a Class-E resonant converter has been performed. MATLAB/Simulink has been used for the simulation study. The simulation study has been performed at 25 °C PV panel temperature and irradiance values of 450 W/m^2 , 250 W/m^2 ve 550 W/m^2 , respectively. MPPT efficiencies have been calculated at each irradiation value as 99.82%, 99.71% and 99.64%, respectively. The average MPPT efficiency obtained as a result of the simulation study has been calculated as 99.7%. Power control has been achieved to a high degree under soft-switching conditions, although occasional hard-switching occurs, by changing the frequency of the switched-capacitor structure. Although using a switched-capacitor in the MPPT offers an advantage in reducing switching losses, voltage spikes have been observed in the V_{DS} of the MOSFET. To prevent this issue, the quality factor should be adjusted, or a MOSFET capable of operating at higher voltages should be selected.

REFERENCES

- [1] K. Unal, G. Bal, S. Oncu, and N. Ozturk, "MPPT Design for PV-Powered WPT System with Irregular Pulse Density Modulation," *Electr. Power Components Syst.*, vol. 51, no. 1, pp. 83–91, Jan. 2023.
- [2] T. V. Kucuk and S. Oncu, "Full Bridge LLC Resonant Converter Design for Photovoltaic Applications," *10th Int. Conf. Smart Grid, icSmartGrid 2022*, pp. 333–338, 2022.
- [3] S. Deshmukh (Gore) *et al.*, "Review on classification of resonant converters for electric vehicle application," *Energy Reports*, vol. 8, pp. 1091–1113, 2022.
- [4] S. Nacar, "Hybrid-Controlled Class-E resonant converter with synchronous rectifier for LED driver applications," *Eng. Sci. Technol. an Int. J.*, vol. 56, no. November 2023, p. 101781, 2024.
- [5] R. H. Ashique *et al.*, "An Analysis and Modeling of the Class-E Inverter for ZVS/ZVDS at Any Duty Ratio with High Input Ripple Current," *Electronics*, vol. 10, no. 11, p. 1312, May 2021.
- [6] Y. Komiyama, W. Zhu, K. Nguyen, and H. Sekiya, "Class-E Inverter with Frequency Modulation Control," in *2021 10th International Conference on Renewable Energy Research and Application (ICRERA)*, Sep. 2021, pp. 94–98.

- [7] G. Liang, H. Tian, H. Wang, Y. Xia, and X. Xiao, "Constant frequency, non-isolated multichannel LED driver based on variable inductor," *IET Circuits, Devices Syst.*, vol. 15, no. 8, pp. 803–813, 2021.
- [8] S. NACAR, S. ÖNCÜ, and G. BAL, "Comparison of Control Techniques for Series Resonant Converter," *Gazi Üniversitesi Fen Bilim. Derg. Part C Tasarım ve Teknol.*, vol. 9, no. 2, pp. 283–296, Jun. 2021.
- [9] K. Unal, G. Bal, and S. Oncu, "Implementation of the irregular pulse density modulation-controlled wireless power transfer system for constant current and constant voltage output," *Int. J. Circuit Theory Appl.*, vol. 52, no. 5, pp. 2231–2248, May 2024.
- [10] M. K. Kazimierczuk and D. Czarkowski, *Resonant Power Converters*. John Wiley & Sons Inc., 2011.
- [11] F. Corti, A. Reatti, Y.-H. Wu, D. Czarkowski, and S. Musumeci, "Zero Voltage Switching Condition in Class-E Inverter for Capacitive Wireless Power Transfer Applications," *Energies*, vol. 14, no. 4, p. 911, Feb. 2021.
- [12] W. Zhu, Y. Komiyama, K. Nguyen, and H. Sekiya, "Comprehensive and Simplified Numerical Design Procedure for Class-E Switching Circuits," *IEEE Access*, vol. 9, pp. 149971–149981, 2021.
- [13] A. K. Devarakonda, N. Karuppiyah, T. Selvaraj, P. K. Balachandran, R. Shanmugasundaram, and T. Senjyu, "A Comparative Analysis of Maximum Power Point Techniques for Solar Photovoltaic Systems," *Energies*, vol. 15, no. 22, pp. 1–30, 2022.

Interface optimization of MASnI₃/FASnI₃ based perovskite solar cells

KENAN OZEL¹, ABDULLAH YILDIZ²

¹ Ankara University, Ankara/Turkey, kenanozel89@gmail.com

² Ankara Yildirim Beyazit University, Ankara/Turkey, yildizab@gmail.com

Abstract - Global paradigms have changed in the current technological era to favor the use of green energy. The most remarkable environmentally friendly energy source is solar energy, which can be captured with the aid of photovoltaic cells. Perovskite solar cells have demonstrated exceptional photovoltaic performance. However, a notable obstacle is their reduced stability under various environmental conditions. Although perovskite solar cells have shown impressive efficiency, they face challenges related to stability and toxicity, primarily due to the widespread use of lead-based and hybrid organic-inorganic materials. In this context, SCAPS-1D has performed a numerical simulation of an all-perovskite bilayer solar cell. The structure employs FASnI₃ as the top absorber, which has a reasonably large bandgap of 1.41 eV, and MASnI₃ as the bottom absorber, with a narrower bandgap of 1.3 eV. Two processes are involved in ensuring the viability of the proposed design. Firstly, two solar cells are simulated and calibrated in standalone settings to align with previously published state-of-the-art results, validating this work. To enhance performance, a bilayer configuration assembled with MASnI₃ and FASnI₃ is evaluated. It is demonstrated that utilizing bilayer structures can readily extend the absorption spectrum into the near-infrared range and significantly improve performance, which is largely determined by the interface trap density between perovskite layers and the bulk defect density of FASnI₃. The optimized all-perovskite bilayer solar cell, with thicknesses of 500 nm for MASnI₃ and 250 nm for FASnI₃, achieves a power conversion efficiency of 29.10%, a fill factor of 83.7%, an open-circuit voltage of 1.078 V, and a short-circuit current density of 32.24 mA/cm² at an interface trap density of 10¹² cm⁻². These findings provide theoretical guidance for enhancing the performance of perovskite solar cells constructed with a bilayer of MASnI₃ and FASnI₃.

Keywords - Perovskite Solar Cells, MASnI₃, FASnI₃, SCAPS 1D.

I. INTRODUCTION

OUR society and environment are negatively impacted by the depletion of energy resources and the reliance on fossil fuels like natural gas and coal [1]. Consequently, global research efforts are concentrated on developing sustainable energy sources and alternative energy supplies that minimize environmental and economic harm [2]. Solar cells have emerged as a promising renewable energy solution to address the growing demand for electricity and mitigate climate change. Perovskite solar cells, in particular, have gained significant attention since 2009 due to their remarkable progress in power conversion efficiency, increasing from 3.8% to 25.2% [3]. The need for non-toxic, lead-free perovskite solar cells (PSCs) has

spurred researchers to explore alternative materials. One approach involves substituting lead (Pb) with bivalent tin (Sn) to create lead-free perovskite compounds [4].

Device modeling is a valuable tool for gaining deeper insights into the operational mechanisms of solar cells. A range of software programs, such as SCAPS-1D and AMPS-1D, are commercially available for solar cell modeling [5]. Researchers have utilized the SCAPS-1D simulation program to model and optimize MASnI₃ and FASnI₃-based PSCs. The estimated efficiencies for these PSCs are 20.36% and 14.03%, respectively [6-7]. Heterojunction solar cells have garnered significant attention from researchers seeking to further enhance PSC efficiency. To maximize light absorption across the solar spectrum, researchers are focusing on bilayer solar cell configurations [8]. Bilayer perovskite solar cells, comprising distinct perovskite materials that absorb different spectral regions, offer an effective approach to overcome the limitations of single-junction perovskite solar cells. This strategy enables broader solar spectrum utilization and the generation of a higher density of photocarriers, leading to improved power conversion efficiency. However, studies investigating the impact of double absorber layers on solar cell performance, compared to single absorber layers, remain limited.

To investigate how bulk and interfacial defects influence photovoltaic parameters, this study aims to theoretically explore perovskite solar cells composed of a bilayer of MASnI₃ and FASnI₃, interfaced with suitable carrier transport layers. To assess the photovoltaic performance of these bilayer perovskite solar cells, SCAPS-1D simulations were employed.

II. MATERIALS AND METHODOLOGY

This study involves the creation of a theoretical model for a solar cell. The goal is to understand how various factors impact the cell's performance and to optimize its efficiency. The SCAPS-1D simulation tool, developed by Burgelman [9], is used to analyze the internal workings of the solar cell. This tool functions by solving essential equations, including the Poisson equation (Equation (1)) and the continuity equations for charge carriers (Equations (1)-(2)), while also considering recombination processes as described by the Shockley-Read-Hall model.

$$\frac{d^2}{dx^2} \psi(x) = -\frac{q}{\epsilon_0 \epsilon_r} (p(x) - n(x) + N_D - N_A + p_t(x) - n_t(x)) \quad (1)$$

$$\frac{dp}{dt} = -\frac{dJ_p}{dx} - R_p + G_p \quad (2)$$

$$\frac{dn}{dt} = -\frac{dJ_n}{dx} - R_n + G_n \quad (3)$$

where $\psi(x)$, p , n , q , ϵ_0 , ϵ_r , N_D , N_A , $p_t(x)$, $n_t(x)$, J_p , J_n , G_p (G_n), and R_p (R_n) are the electrostatic potential, holes, and electron concentration, permittivity of free space, relative permittivity, donor and acceptor charge impurity, the trapped holes and electron densities, current hole densities, current electron densities, generation, and recombination rate of hole (electron), respectively. Table 1 gives the material parameters depicted in the simulation program.

Table 1: The material parameters depicted in the simulation program.

Parameters	FTO	C60	MASnI ₃	FASnI ₃	CuI
Thickness [μm]	0.4	0.05	0.5	0.25	0.1
Band gap [eV]	3.2	1.7	1.3	1.41	2.98
Electron affinity [eV]	4.4	3.9	4.17	4	2.1
Dielectric permittivity	9	4.2	10	8.2	6.5
CB effective density of states [cm ⁻³]	2.2x10 ¹⁸	8x10 ¹⁹	1x10 ¹⁸	1x10 ¹⁸	2.8x10 ¹⁹
VB effective density of states [cm ⁻³]	1.8x10 ¹⁹	8x10 ¹⁹	1x10 ¹⁹	1x10 ¹⁸	1x10 ¹⁹
Electron thermal velocity [cm/s]	1x10 ⁷	1x10 ⁷	1x10 ⁷	1x10 ⁷	1x10 ⁷
Hole thermal velocity [cm/s]	1x10 ⁷	1x10 ⁷	1x10 ⁷	1x10 ⁷	1x10 ⁷
Electron mobility [cm ² Vs ⁻¹]	20	0.08	1.6	22	1.69x10 ⁻⁴
Hole mobility [cm ² Vs ⁻¹]	10	0.0035	1.6	22	1.69x10 ⁻⁴
Donor density [cm ⁻³]	1x10 ¹⁹	1x10 ¹⁷	0	0	0
Acceptor density [cm ⁻³]	0	0	1x10 ¹⁷	0	7x10 ¹⁶
Bulk defect density [cm ⁻³]	1x10 ¹⁴	1x10 ¹⁵	1x10 ¹³	1x10 ¹³	1x10 ¹³

As a result, SCAPS-1D can determine the performance characteristics of solar cells, such as open-circuit voltage (V_{oc}), current density (J_{sc}), fill factor (FF), power conversion efficiency (PCE), and quantum efficiency (QE). This is achieved by solving specific equations under specific conditions. The work function of the gold (Au) back electrode was set to 5.1 eV [10]. Additionally, the design configuration of the MASnI₃/FASnI₃ heterojunction perovskite solar cell is depicted in Fig. 1.

III. RESULTS AND DISCUSSION

This study investigates single and bilayer absorber layers composed of FASnI₃ and MASnI₃. Specifically, the FTO/C60/FASnI₃/CuI/Au, FTO/C60/MASnI₃/CuI/Au, and FTO/C60/FASnI₃/MASnI₃/CuI/Au perovskite solar cell structures are examined. Among the proposed materials, C60 and CuI were identified as suitable transport layers [11]. Optimal thicknesses of 50 nm and 100 nm were determined for C60 and CuI, respectively. The total thickness of the bilayer assembly, comprising MASnI₃ and FASnI₃, was set to 750 nm.

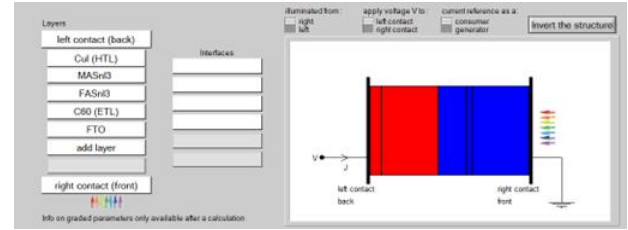


Figure 1: The design configuration of MASnI₃/FASnI₃ heterojunction-based perovskite solar cell.

To further enhance power conversion efficiency performance, the bulk defect density in FASnI₃ perovskite layer, and interfacial defect density at the perovskite/perovskite, the perovskite/ETL and HTL/perovskite interfaces were all adjusted.

As shown in Table 2, which lists the photovoltaic parameters of perovskite solar cells with single and bilayer absorber layers, the FTO/C60/FASnI₃/MASnI₃/CuI/Au perovskite solar cell with a bilayer absorber layer outperforms both the FTO/C60/FASnI₃/CuI/Au and FTO/C60/MASnI₃/CuI/Au devices with single absorber layers.

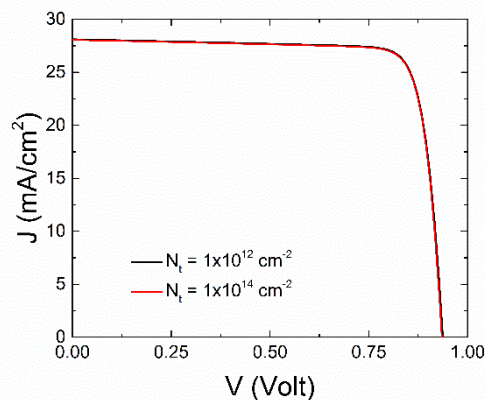
A defect-free device can achieve a power conversion efficiency of 29.46%. While MASnI₃ and FASnI₃-based devices individually exhibit either high J_{sc} or V_{oc} , the bilayer configuration effectively combines these strengths.

Table 2: Photovoltaic parameters of perovskite solar cells with single and bilayer absorber layers.

Absorption Layer	V_{oc} (V)	J_{sc} (mA/cm ²)	FF (%)	PCE (%)
MASnI ₃	0.875	32.41	0.749	21.20
FASnI ₃	1.256	25.31	0.861	27.36
MASnI ₃ /FASnI ₃	1.082	32.24	0.844	29.46

The interface defect density at the HTL/MASnI₃ and ETL/FASnI₃ perovskite layer interfaces ranged from 10¹² to 10¹⁴ cm⁻². As shown in Fig. 2, power conversion efficiency remained relatively unaffected by this variation. Typically, interface defects lead to an increase in trap states at recombination centers [12]. However, it appears that when the defect density at the interfaces falls below 10¹⁴ cm⁻², its impact on power conversion efficiency becomes negligible.

(a)



(b)

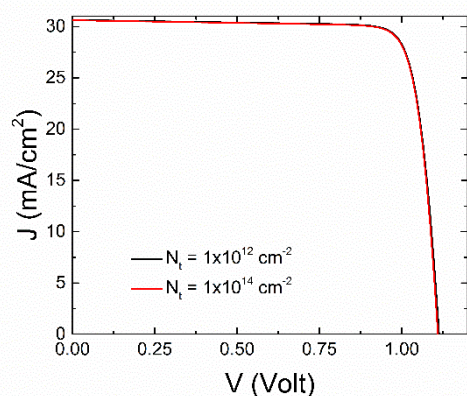


Figure 2: Effect of the interface defect density between (a) HTL and MASnI₃ (b) ETL and FASnI₃ perovskite layer on the performance parameters of the device assembled with bilayer of MASnI₃ and FASnI₃.

The interface defect density within the MASnI₃/FASnI₃ perovskite layers was also varied from 10^{12} to 10^{14} cm⁻². As illustrated in Fig. 3, a marginal decrease in power conversion efficiency, from 29.10% to 22.87%, was observed with increasing interface defect density (Table 3). Interface defects result in a significantly increased number of traps at the recombination centers. Since the interface defects in the actual device are unavoidable, it is possible to achieve high performance with a defect density of less than 10^{12} cm⁻².

The effect of interface defect density between perovskite layers on photovoltaic parameters of the device is given in Table 3. Even though J_{sc} is insensitive to this variation, especially V_{oc} is remarkably reduced to 0.966 from 1.078 V. It is associated with an increased recombination center.

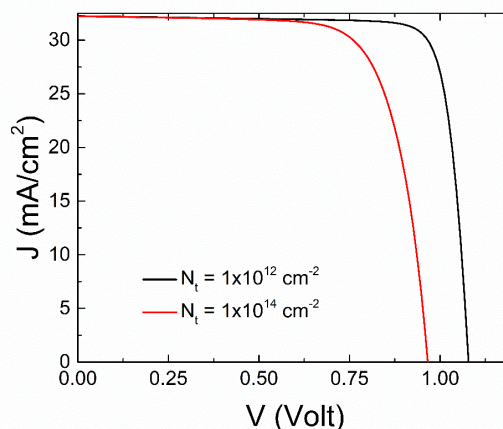


Figure 3: Effect of the interface trap density between perovskite layers on the performance parameters of the device.

Table 3: The effect of interface defect density between perovskite layers on photovoltaic parameters of the device assembled with bilayer of MASnI₃ and FASnI₃.

N_t (cm ⁻²)	V_{oc} (V)	J_{sc} (mA/cm ²)	FF (%)	PCE (%)
10^{14}	0.966	32.22	0.734	22.87
10^{12}	1.078	32.24	0.837	29.10

Fig. 4 depicts the effect of the bulk defect density of FASnI₃ perovskite layer on the performance parameters of the device assembled with bilayer of MASnI₃ and FASnI₃. To examine the performance of the cell, the bulk defect density was altered from 10^{12} to 10^{18} cm⁻³.

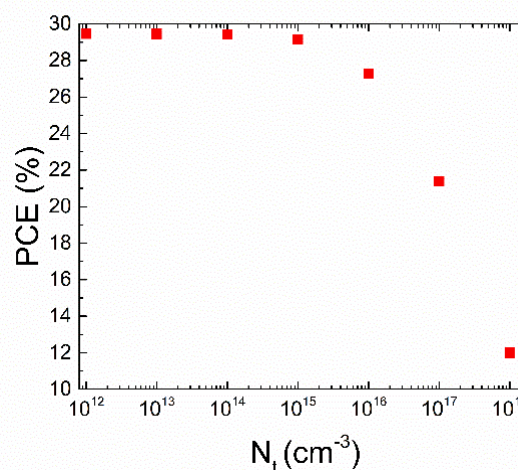


Figure 4: Effect of the interface trap density between perovskite layers on the performance parameters of the device.

Power conversion efficiency falls from 29.10 % to 12.01 % when bulk defect density rises from 10^{12} to 10^{18} cm⁻³. Cell performance is lowered by higher defect densities because they produce more recombination centers and traps [13]. Smaller defect densities are therefore advantageous for better device performance.

IV. CONCLUSION

A numerical simulation of an all-perovskite bilayer solar cell was conducted using SCAPS-1D. This study investigated a bilayer structure composed of MASnI₃ and FASnI₃ to enhance device performance. Results indicate that the bulk defect density of FASnI₃ and the interface trap density between the perovskite layers significantly influence overall performance. By employing a bilayer structure, the absorption spectrum can be effectively extended into the near-infrared region, leading to a substantial performance boost. With layer thicknesses of 500 nm for MASnI₃ and 250 nm for FASnI₃, the optimized all-perovskite bilayer solar cell exhibited a fill factor of 83.7%, an open-circuit voltage of 1.078 V, a short-circuit current density of 32.24 mA/cm², and a power conversion efficiency of 29.10% at an interface trap density of 10^{12} cm⁻² between the perovskite layers. These findings provide valuable theoretical insights for improving the efficiency of perovskite solar cells based on MASnI₃ and FASnI₃ bilayer architectures.

ACKNOWLEDGMENT

We are appreciative to Dr. Marc Burgelman and his colleagues at the University of Gent in Belgium for developing and providing the free SCAPS 1-D simulation software.

REFERENCES

- [1] J. Wang, and W. Azam, "Natural resource scarcity, fossil fuel energy consumption, and total greenhouse gas emissions in top emitting countries," *Geoscience Frontiers*, 15(2), 101757, 2024.
- [2] N. L. Panwar, S. C. Kaushik, and S. Kothari, "Role of renewable energy sources in environmental protection: A review," *Renewable and sustainable energy reviews*, 15(3), 1513-1524, 2011.
- [3] S. Yang, W. Fu, Z. Zhang, H. Chen, and C. Z. Li, "Recent advances in perovskite solar cells: efficiency, stability and lead-free perovskite," *Journal of Materials Chemistry A*, 5(23), 11462-11482, 2017.
- [4] R. Kour, S. Arya, S. Verma, J. Gupta, P. Bandhoria, V. Bharti, ..., and V. Gupta, "Potential substitutes for replacement of lead in perovskite solar cells: a review," *Global Challenges*, 3(11), 1900050, 2019.
- [5] A. Kowsar, M. Billah, S. Dey, S. C. Debnath, S. Yeakin, and S. F. U. Farhad, "Comparative study on solar cell simulators," *In 2019 2nd Int. Conf. on Innovation in Engineering and Technology (ICIET) IEEE*, pp. 1-6, December 2019.
- [6] P. Saha, S. Singh, and S. Bhattacharya, "Performance optimization of MASnI₃ perovskite solar cells: Insights into device architecture," *Micro and Nanostructures*, 191, 207827, 2024.
- [7] S. Abdelaziz, A. Zekry, A. Shaker, and M. J. O. M. Abouelatta, "Investigating the performance of formamidinium tin-based perovskite solar cell by SCAPS device simulation," *Optical materials*, 101, 109738, 2020.
- [8] S. Khatoun, S. K. Yadav, J. Singh, and R. B. Singh, "Design of a CH₃NH₃PbI₃/CsPbI₃-based bilayer solar cell using device simulation," *Heliyon*, 8(7), 2022.
- [9] J. Verschraegen, and M. Burgelman, "Numerical modeling of intra-band tunneling for heterojunction solar cells in SCAPS," *Thin Solid Films*, 515(15), 6276-6279, 2007.
- [10] G. T. Sayah, "A comprehensive simulation study of methylammonium-free perovskite solar cells," *Results in Optics*, 11, 100390, 2023.
- [11] Z. Qirong, Z. Bao, H. Yongmao, L. Liang, D. Zhuoqi, X. Zaixin, and Y. Xiaobo, "A study on numerical simulation optimization of perovskite solar cell based on CuI and C60," *Materials Research Express*, 9(3), 036401, 2022.
- [12] T. S. Sherkar, C. Momblona, L. Gil-Escrig, J. Avila, M. Sessolo, H. J. Bolink, and L. J. A. Koster, "Recombination in perovskite solar cells: significance of grain boundaries, interface traps, and defect ions," *ACS energy letters*, 2(5), 1214-1222, 2017.
- [13] J. Chen, and N. G. Park, "Causes and solutions of recombination in perovskite solar cells," *Advanced Materials*, 31(47), 1803019, 2019.

Importance of Artificial Intelligence Applications in Food Industry

RABİA SERPİL GÜNHAN¹

¹ Konya Technical University, Konya/Turkey, rsgunhan@ktun.edu.tr

Abstract - The use and utilization of the magnificent possibilities of artificial intelligence technology in many areas of the food industry provides significant advantages. AI technology includes theory and computation to perform tasks such as sensory observation and decision-making that imitate human intelligence. Experts refer to the ability of machines to perform cognitive tasks such as seeing, learning, reasoning and problem solving as artificial intelligence. It is possible to perform various activities such as determining food quality, classifying foods, making predictions, and providing control mechanisms with artificial intelligence applications in the food industry. Food preparation, processing, palletizing, packaging and serving methods can change completely with AI-enabled technologies. In addition, new products can be developed by predicting consumer preferences with artificial intelligence applications. Foods can be produced in a healthier, more efficient and less waste-generating way with artificial intelligence-supported systems. In this study, scientific studies on the use of artificial intelligence technology in the food industry are evaluated and its inevitable importance in future safe and sustainable food development and processing is emphasized.

Keywords – Food Industry, Artificial Intelligence.

I. INTRODUCTION

THE use and evaluation of artificial intelligence technology (AI) in many areas of the food industry has initiated revolutionary transformations. AI significantly affects efficiency, personalization and sustainability. The global AI market size in manufacturing was valued at \$8.14 billion in 2019 and is expected to reach \$695.16 billion by 2032 [1]. It is seen that AI technologies are increasingly being adopted in the manufacturing sector.

Artificial intelligence technology includes theory and computational systems to perform tasks such as sensory observation and decision making that mimic human intelligence. Experts refer to the ability of machines to perform cognitive tasks such as vision, learning, reasoning, and problem solving as AI.

With artificial intelligence applications in the food industry, it is possible to carry out various activities such as planning production, determining food quality, classifying foods, making predictions, and providing control mechanisms. The ways food is prepared, processed, packaged, and offered for consumption can be completely changed with artificial intelligence-supported technologies. Standard and reliable new products can be developed by predicting consumer preferences.

Food can be produced healthier, more efficiently, and less wastefully with artificial intelligence-supported systems. Detecting nutritional components and allergens in foods, optimizing food delivery routes and programs are other areas of use of artificial intelligence in the food production industry. Developments in artificial intelligence technologies improve efficiency, productivity, and decision-making processes in the sector.

Artificial intelligence saves farmers time, costs, such as field trials and food inspections. The technology helps farmers proactively detect pest infestations and plant diseases by analyzing large amounts of data to determine environmental conditions. AI technology helps better monitor food standards, test products at all levels, and ensure food hygiene installations. Production can be monitored in real time, so food contamination and other safety issues can be detected more quickly and effectively.

Food waste worldwide consists of 30% of grains (half of the world's annual grain production), 40-50% of root crops, fruits and vegetables, and 20% of oilseeds, meat and dairy products, and fish [2]. Food is wasted at different rates during harvesting, processing, storage, logistics, and consumption. The world's population is also increasing rapidly. Millions of people are starving to death and many people are malnourished. In this context, optimized production and supply chain management with the help of artificial intelligence makes a difference, especially in reducing waste. This study was prepared to pave the way for a visionary approach in the future by emphasizing the importance of artificial intelligence in the food industry in line with scientific studies using artificial intelligence.

II. AI IN FOOD INDUSTRY

There is no universal definition of artificial intelligence. Artificial intelligence definitions vary depending on the application areas. Artificial intelligence is a multidisciplinary branch of science and engineering that develops intelligent systems. Intelligent systems consist of software and hardware designed to fulfill a defined purpose [3].

As in other sectors, in the food industry, in order to meet future food demand, artificial intelligence applications are inevitable for supply chain management, food classification, production development, food quality improvement and adequate industrial hygiene [4].

Among the artificial intelligence elements that are useful and can be used in the processed food sector are supervised methods

such as fuzzy logic models, artificial neural networks, deep learning and support vector machines [31].

Artificial intelligence has roles in the food industry such as food quality management, food inspection and classification using image processing and recognition technologies, food inspection and classification, ensuring the safety of food and food warehouses using robots, and ensuring food safety using smart technologies and information sharing mechanisms. It has effects such as mathematical modeling techniques to manage food quality and machine learning techniques to increase the efficiency of high-quality food production [19].

Analyzing large-scale data and complex variables from the initial stages in the laboratory to the final stages on an industrial scale during the food production process requires both high-level technology and time. This need can only be met with the use of artificial intelligence. The Internet of Things, sensing, machine learning, computing and data analytics have led to significant developments in the food industry [5].

Artificial intelligence-supported sensing technologies, called intelligent systems, are revolutionizing the food industry. Controlling the drying process for food drying technology is one example of such AI-supported applications [4]. Intelligent models and systems in the food sector have been successfully applied to tasks such as classifying fresh products, classifying and estimating parameters, quality control, predicting consumer preferences, and developing new products with greater efficiency and cost savings. The preferred methods in the food industry include electronic nose (ES), machine learning (ML), fuzzy logic (FL), Artificial Neural Network (ANN), and adaptive neuro-fuzzy inference systems (ANFIS) [4].

Industrial automation is the best possible solution to overcome the problems of food industries. Automation is completely based on artificial intelligence (AI) or machine learning (ML) or deep learning (DL) algorithms. By using AI-based system, food production and distribution processes can be improved efficiently [19].

To improve quality systems in different contexts and at different stages of food production, relevant data and models are shared in the Internet of Food (IoF) network, thus ensuring greater efficiency and sustainability [5].

The impact of climate change on food security is complex and multidimensional because the hazards that emerge in the food system are numerous, diverse and interconnected. AI is already making a significant impact on the food system and in predicting the impacts of climate change. AI is data-driven. There is a large knowledge gap between what is known and what is not known about the impact of climate change on food security. Therefore, widespread data collection efforts are needed to quantify the individual impacts of each climate change scenario on individual components, including microorganisms that make up the food system [16].

A. AI in Dairy Products Industry

Dairy products are among the products with high potential for adulteration due to high demand and production costs. Milk fat in butter is usually mixed with vegetable oils such as palm oil or sesame oil by producers to reduce costs. Detecting

adulteration in dairy products is quite laborious and requires a well-equipped laboratory. A powerful and simple method has been proposed by [10] to identify dairy products with or without milk additives (NDA) using neural networks trained on acoustic frequency responses and also to distinguish organic food products from non-organic ones. The hypothesis was tested on butter samples. Different materials have different frequency bands that they transmit or block due to their molecular structures. It has been stated that it is possible to identify adulterated or non-organic products easily and cost-effectively without compromising the physical integrity of the product using an artificial intelligence (AI) algorithm.

Cheese production is a sector of considerable economic importance. Cheese varieties had been classified using supervised machine learning (ML) techniques. The characteristics of free volatile carboxylic acids (FVCA) were used to characterize cheese varieties. It was reported that 241 samples of 10 different cheese varieties from Switzerland were classified with 90% accuracy using ML algorithms based on FVCA profiles [11].

A prediction model using confocal Raman microscopy and ANN was developed to measure adulteration by adding different levels of whey to milk. It was stated that the use of confocal Raman microscopy together with ANN is an excellent method to measure adulteration of milk with whey due to its high speed, simplicity and efficiency. It was emphasized that a high-capacity prediction model with an R2 value of 0.9999 was obtained using ANN [20].

Researchers developed and compared Radial Base (Less Neurons) and Multiple Linear Regression (MLR) models to predict the shelf life of processed cheese. They took soluble nitrogen, pH, Standard plate count, yeast and mold count and spore count as input parameters and sensory score as output parameter. They stated that Radial Base (Less Neurons) model is superior to MLR model in predicting the shelf life of processed cheese [21].

Milk quality is determined by using machine learning algorithms. As a dataset, Milk Quality from Kaggle repository, 1059 milk data samples from the dataset and pH, Temperature, Taste, Odor, Fat, Turbidity and Color data belonging to each sample were used as features. Artificial Neural Network (NN) and Adaptive Boosting (AdaBoost: AB) algorithms were used. In the system trained using 100 samples belonging to each class, 99.9% success rate with AdaBoost algorithm and 95.4% success rate with Artificial Neural Network algorithm were concluded in the classification accuracy [24].

B. AI in Fruit and Vegetable Industry

Berry fruits are rich in a wide range of nutritional bioactive compounds such as vitamins, anthocyanins, polyphenols and organic acids. Berry fruits can be consumed as fresh food or processed after harvest and offered for consumption as frozen berry, dried berry, berry juice and berry jam. During the processing of the product, there are changes in the color, texture, structure, chemical content and biological activity of the fruits, which determine the quality of the product. Artificial intelligence-based methods have been applied for detection and

prediction during the sorting, drying, disinfection, sterilization and freezing processes of berry fruits by [6]. It has been stated that advanced detection techniques include computer vision system, near infrared, hyperspectral imaging, thermal imaging, low-field nuclear magnetic resonance, magnetic resonance imaging, electronic nose and X-ray computerized tomography. It has been stated that mathematical modeling, chemometrics, machine learning, deep learning and artificial neural networks are used among artificial intelligence methods. They suggested the use of validated computer simulation techniques such as CFD (Computational Fluid Dynamics) in the optimization and design of fruit processing systems [6].

The effect of different storage conditions on blackcurrant quality was evaluated using image analysis and artificial intelligence algorithms. As a result, an objective, non-destructive, fast and cheap evaluation was made possible. He stated that changes in blackcurrant quality during storage can be determined using image features [8].

Researchers investigated the applicability of cyclic voltammetry (CV) technique with ANN to predict changes in antioxidant activities of green tea during storage. They analyzed the electrochemical response signals of green tea products from different origins and different storage times by CV technique. They stated that the predicted values of the results showed good agreement with the measured values and the prediction models had high stability and reliability. They stated that ANN models accurately predicted changes in antioxidant activities of green tea during storage. They emphasized that compared with traditional analytical methods, the proposed intelligent method was efficient, sensitive, environmentally friendly and had high prediction accuracy [22].

Researchers predicted the drying behavior of onion in a pilot plant fluidized bed dryer using three different modeling techniques and compared the accuracy of these models. They conducted a comparative study among nonlinear regression techniques, fuzzy logic and artificial neural networks to predict the drying behavior of onion. They proved that both traditional and new modeling techniques can predict the drying kinetics of onions during fluidized bed drying [27].

C. AI in Meat industry

Processing of meat products causes changes in the composition and structure of protein. Protein degradation and quality changes were investigated by [7] during the processing of dry-cured ham. They stated that protein degradation can be used as an indicator to control the quality of hams. They proved that BP-ANN is a reliable tool for the prediction of multiple quality of dry-cured hams. They emphasized that the results provide new perspectives for predicting product quality based on protein degradation without resorting to experiments [7].

In this study a new colorimetric sensor array (CSA) produced from oxidized chitin nanocrystals (O-ChNCs) together with convolutional neural network (CNN) was developed for real-time monitoring of beef freshness. It was stated that beef freshness can be monitored rapidly and reliably with the method they developed [14].

D. AI in Other Food Industry

It was aimed to analyze the metabolome of hazelnuts to estimate the industrial quality of high-quality hazelnuts used in confectionery. Both non-volatile and volatile metabolites were mapped and analyzed using liquid chromatography coupled with comprehensive two-dimensional gas chromatography (GC×GC) and high-resolution mass spectrometry (LC-HRMS). Data fusion techniques such as low-level data fusion (LLDF) and medium-level data fusion (MLDF) were used to improve the classification performance and information capacity. The findings were stated to be promising for improving the detection of mislabeling and increasing the reliability of identifying the authenticity of plant-based products in the food industry such as hazelnuts [9].

In this study, molecular dynamics approach and artificial neural network application was used to understand the interactive effect of sugars on crystallization stability in Indian honey samples. Comparative studies were carried out to understand the interactive effects of fructose, glucose, sucrose, maltose and water on crystallization of honey samples. It was stated that all the simulations led to stable crystal formation with different interaction energies. It was suggested that Fructose-glucose ratio should be kept above 1.18 to prevent crystallization in honey samples. It was also stated that not only Fructose: Glucose ratio but also sucrose, maltose and water have a significant effect on the overall crystallization process. It was stated that application of ANN has the potential to predict stability with high efficiency while analyzing different properties of honey [29].

Evaluation of biogenic amines is one of the most commonly used methods to determine fish quality. In this study the quality of sardine (*Sardinella* sp.) was evaluated according to biogenic amine content using fuzzy logic model (FLM). Fish were stored at 0, 3 and 10 °C for fifteen days and eight biogenic amine production was monitored during this period. Based on the results, histamine, putrescine and cadaverine were selected as input variables and twelve quality grades were considered for fish quality as output variables for FLM. Input data were processed according to the rules defined in the model and then fuzzified according to defined output variables. Pearson correlation between storage periods and fish quality was reported as $r = 0.97, 0.95$ and 1 for fish stored at 0, 3 and 10 °C, respectively [28].

In this study they used an eight-sensor E-nose to evaluate the probability of adulteration in oxidized and non-oxidized oils and prepared different adulteration percentages and evaluated them. The model performance was evaluated by the official AOCS method. Cluster analysis CA, principle component analysis PCA and artificial neural network ANN methods were also applied for the qualitative discrimination of different adulteration percentages in oxidized and non-oxidized oils. The results indicated that the application of E-nose together with CA, PCA, principal component regression PCR, linear discriminant analysis LDA and ANN methods is a promising approach for the successful detection of adulteration in edible oils [30].

Machine learning is a data mining method that enables the recognition of unknown samples with high precision based on known sample information. The combination of convolutional neural network (CNN) and Low-field and Nuclear magnetic resonance (LF-NMR) is increasingly applied in food quality analysis. In this study, low-field NMR signals of different types of edible oils were analyzed by convolutional neural networks to investigate the feasibility of oil classification. It was concluded that the combination of CNN and LF-NMR could be an intelligent and automatic approach for the classification of edible oils [12].

Adulteration in sesame oil was detected by [13] using E-nose, GC-MS and chemometric methods. Chemometric methods such as Principal Component Analysis (PCA), Linear Discriminant Analysis (LDA), Support Vector Machine (SVM) and Artificial Neural Networks (ANN) were used to analyze the signals from the electronic nose.

Researchers designed and implemented a fuzzy logic control system to control the leavening process in bread making (A fuzzy logic control system). They experimented with different initial conditions and different amounts of yeast added to leaven the dough. The controller was evaluated experimentally and compared with those obtained from the proportional-integral-derivative PID controller. They stated that the fuzzy logic controller can provide significantly better control, does not require a mathematical model, and has better disturbance rejection properties [26].

Electronic noses can potentially be used as rapid, noninvasive, cost-effective and portable systems for the detection of mycotoxin contamination in cereals and can provide real-time monitoring data to facilitate the removal of contaminated batches. In a related study, the potential use of an electronic nose based on portable metal oxide sensors was investigated to detect aflatoxin contamination in Kenyan maize varieties artificially and naturally infected with *Aspergillus flavus*. It was concluded that it is a cost-effective screening method [15].

Aflatoxin is a natural toxic substance produced by fungi and molds found in certain foods. It is a strong carcinogen and is widely found in peanuts, corn, and their agricultural products. Researchers firstly constructed a hyperspectral imaging system using a lattice module, SCOMS camera, and electric displacement platform to detect aflatoxin in peanuts. They obtained 146 hyperspectral image cubes of 73 peanut samples before and after aflatoxin contamination. Then, they proposed the pixel spectral reconstructed image method for the deep convolutional neural network CNN method. They obtained results by working on random selection datasets and comparing with different recognition models. It was stated that the reconstructed image generated by the spectral at the pixel level is good enough for aflatoxin detection problems, and the overall recognition rate reached over 95% at the pixel level. At pixel level or kernel level, the deep learning method achieved high accuracy and was better than traditional recognition models, the recognition rate was higher than 96% at pixel level and 90% at kernel level [32].

Three different prediction models (random forest, artificial neural networks and support vector machines) was developed to detect fraud in wine and to guarantee the authenticity of the wine. It was stated that prediction models based on artificial neural networks, random forests and support vector machines were developed using chemical analyses of wine samples with ICPMS and ICPOES and that fewer variables were used to save time and cost. In the study, it was emphasized that three different prediction models based on RF, ANN and SVM were developed to classify wines according to 45 input variables. It was stated that the accuracy and errors obtained with the selected models (except for red wines - artificial neural network developed using reduced variables) were at acceptable levels [17].

Adulteration is frequently done in coffee, hence fast and reliable detection techniques are required. Researchers investigated the potential use of CNN models for determining the amount of adulterants in coffee and compared their performance with the standard chemometrics approach. They stated that convolutional neural networks CNN, a deep learning algorithm, showed excellent performances comparable to classical chemometrics algorithms (PLS, iPLS). They stated that the results confirmed the applicability of CNN algorithm for determining the amount of adulteration from FT-NIR spectra. It was stated that CNN, a deep learning algorithm, is a feasible and practical alternative to classical chemometrics for determining the amount of coffee adulteration [23].

A new method was evaluated to improve the identification ability of low-quality *P. notoginseng* mixed into *Panax notoginseng* (*P. notoginseng*) using spectroscopic techniques and chemometric methods. They mixed different grades of *P. notoginseng* powder at different percentages (0-100%). They obtained NIR and FT-MIR spectra of the samples and used principal component analysis (PCA) to reduce the data size of the characteristic spectra. They constructed Support vector machine (SVM) for the classification of foreign substances with different mixing ratios. They applied particle swarm optimization (PSO) to optimize the parameters of SVM. As a result, they stated that the data fusion of NIR and FT-MIR spectra combined with chemometric and PSO algorithm increased the discrimination accuracy of different grades of *P. notoginseng* powder counterfeiting. They emphasized that the identification sensitivity of counterfeiting was improved by using data fusion and PSO-SVM [33].

III. CONCLUSION

The application of AI technology in the food industry provides significant benefits such as increased productivity, reduced costs, optimized supply chain management, and improved product quality and safety. In the future, AI will transform the food processing industry because it has so much potential to create reasonable and healthier productivity for consumers and employees. The role of AI will become more vital with each passing day due to its ability to improve hygiene, food preservation, and waste management systems.

REFERENCES

- [1] Last updated October 28, 2024 <https://www.fortunebusinessinsights.com/artificial-intelligence-ai-in-manufacturing-market-102824>
- [2] Tekiner, İ. H., Mercan, N. N., Kahraman, A., & Özel, M. (2021). Dünya ve Türkiye'de gıda israfı ve kaybına genel bir bakış. *İstanbul Sabahattin Zaim Üniversitesi Fen Bilimleri Enstitüsü Dergisi*, 3(2), 123-128.
- [3] Türkiye Bilişim Derneği, Kavramsal Rapor, 2020, <https://www.tbd.org.tr/pdf/yapay-zeka-raporu.pdf>
- [4] Thapa, A., Nishad, S., Biswas, D., & Roy, S. (2023). A comprehensive review on artificial intelligence assisted technologies in food industry. *Food Bioscience*, 103231.
- [5] Esmaeily, R., Razavi, M. A., & Razavi, S. H. (2023). A step forward in food science, technology and industry using artificial intelligence. *Trends in Food Science & Technology*, 104286.
- [6] Wang, D., Zhang, M., Mujumdar, A. S., & Yu, D. (2022). Advanced detection techniques using artificial intelligence in processing of berries. *Food Engineering Reviews*, 14(1), 176-199.
- [7] Zhu, N., Wang, K., Zhang, S. L., Zhao, B., Yang, J. N., & Wang, S. W. (2021). Application of artificial neural networks to predict multiple quality of dry-cured ham based on protein degradation. *Food Chemistry*, 344, 128586.
- [8] Ropelewska, E. (2022). Application of imaging and artificial intelligence for quality monitoring of stored black currant (*Ribes nigrum* L.). *Foods*, 11(22), 3589.
- [9] Squara, S., Caratti, A., Fina, A., Libertò, E., Koljančić, N., Špánik, I., ... & Cordero, C. (2024). Artificial intelligence decision making tools in food metabolomics: Data fusion unravels synergies within the hazelnut (*Corylus avellana* L.) metabolome and improves quality prediction. *Food Research International*, 194, 114873.
- [10] Iymen, G., Tanriver, G., Hayirlioglu, Y. Z., & Ergen, O. (2020). Artificial intelligence-based identification of butter variations as a model study for detecting food adulteration. *Innovative Food Science & Emerging Technologies*, 66, 102527.
- [11] Fröhlich-Wyder, M. T., Bachmann, H. P., & Schmidt, R. S. (2023). Classification of cheese varieties from Switzerland using machine learning methods: Free volatile carboxylic acids. *LWT*, 184, 115095.
- [12] Hou, X., Wang, G., Wang, X., Ge, X., Fan, Y., & Nie, S. (2020). Convolutional neural network based approach for classification of edible oils using low-field nuclear magnetic resonance. *Journal of Food Composition and Analysis*, 92, 103566.
- [13] Aghili, N. S., Rasekh, M., Karami, H., Azizi, V., & Gancarz, M. (2022). Detection of fraud in sesame oil with the help of artificial intelligence combined with chemometrics methods and chemical compounds characterization by gas chromatography–mass spectrometry. *Lwt*, 167, 113863.
- [14] Jia, X., Ma, P., Tarwa, K., Mao, Y., & Wang, Q. (2023). Development of a novel colorimetric sensor array based on oxidized chitin nanocrystals and deep learning for monitoring beef freshness. *Sensors and Actuators B: Chemical*, 390, 133931.
- [15] Machungo, C. W., Berna, A. Z., McNeven, D., Wang, R., Harvey, J., & Trowell, S. (2023). Evaluation of performance of metal oxide electronic nose for detection of aflatoxin in artificially and naturally contaminated maize. *Sensors and Actuators B: Chemical*, 381, 133446.
- [16] Karanth, S., Benefo, E. O., Patra, D., & Pradhan, A. K. (2023). Importance of artificial intelligence in evaluating climate change and food safety risk. *Journal of Agriculture and Food Research*, 11, 100485.
- [17] Astray, G., Martinez-Castillo, C., Mejuto, J. C., & Simal-Gandara, J. (2021). Metal and metalloids profile as a fingerprint for traceability of wines under any Galician protected designation of origin. *Journal of Food Composition and Analysis*, 102, 104043.
- [18] Abekoon, T., Buthpitiya, B. L. S. K., Sajindra, H., Samarakoon, E. R. J., Jayakody, J. A. D. C. A., Kantamaneni, K., & Rathnayake, U. (2024). A comprehensive review to evaluate the synergy of intelligent food packaging with modern food technology and artificial intelligence field. *Discover Sustainability*, 5(1), 160.
- [19] Kumar, I., Rawat, J., Mohd, N., & Husain, S. (2021). Opportunities of artificial intelligence and machine learning in the food industry. *Journal of Food Quality*, 2021(1), 4535567.
- [20] da Rocha, R. A., Paiva, I. M., Anjos, V., Furtado, M. A. M., & Bell, M. J. V. (2015). Quantification of whey in fluid milk using confocal Raman microscopy and artificial neural network. *Journal of dairy science*, 98(6), 3559-3567.
- [21] Goyal, S., & Kumar Goyal, G. (2012). Shelflife prediction of processed cheese using artificial intelligence ANN technique. *Hrvatski časopis za prehrambenu tehnologiju, biotehnologiju i nutricionizam*, 7(3-4), 184-187.
- [22] Jiang, L., & Zheng, K. (2023). Towards the intelligent antioxidant activity evaluation of green tea products during storage: A joint cyclic voltammetry and machine learning study. *Food Control*, 148, 109660.
- [23] Chakravartula, S. S. N., Moschetti, R., Bedini, G., Nardella, M., & Massantini, R. (2022). Use of convolutional neural network (CNN) combined with FT-NIR spectroscopy to predict food adulteration: A case study on coffee. *Food Control*, 135, 108816.
- [24] Çelik, A. (2022). Using machine learning algorithms to detect milk quality. *Eurasian Journal of Food Science and Technology*, 6(2), 76-87.
- [25] Gutiérrez, P., Godoy, S. E., Torres, S., Oyarzún, P., Sanhueza, I., Diaz-García, V., ... & Coelho, P. (2020). Improved antibiotic detection in raw milk using machine learning tools over the absorption spectra of a problem-specific nanobiosensor. *Sensors*, 20(16), 4552.
- [26] Yousefi-Darani, A., Paquet-Durand, O., & Hitzmann, B. (2019). Application of fuzzy logic control for the dough proofing process. *Food and bioproducts processing*, 115, 36-46.
- [27] Jafari, S. M., Ganje, M., Dehnad, D., & Ghanbari, V. (2016). Mathematical, fuzzy logic and artificial neural network modeling techniques to predict drying kinetics of onion. *Journal of Food Processing and Preservation*, 40(2), 329-339.
- [28] Zare, D., & Ghazali, H. M. (2017). Assessing the quality of sardine based on biogenic amines using a fuzzy logic model. *Food Chemistry*, 221, 936-943.
- [29] Naik, R. R., Gandhi, N. S., Thakur, M., & Nanda, V. (2019). Analysis of crystallization phenomenon in Indian honey using molecular dynamics simulations and artificial neural network. *Food chemistry*, 300, 125182.
- [30] Karami, H., Rasekh, M., & Mirzaee-Ghaleh, E. (2020). Application of the E-nose machine system to detect adulterations in mixed edible oils using chemometrics methods. *Journal of Food Processing and Preservation*, 44(9), e14696.
- [31] Jadhav, H. B., Alaskar, K., Desai, V., Sane, A., Chaudhary, P., Annapure, U., ... & Nayik, G. A. (2024). Transformative impact: Artificial intelligence in the evolving landscape of processed food—a concise review focusing on some food processing sectors. *Food Control*, 110803.
- [32] Han, Z., & Gao, J. (2019). Pixel-level aflatoxin detecting based on deep learning and hyperspectral imaging. *Computers and Electronics in Agriculture*, 164, 104888.
- [33] Yang, X., Song, J., Peng, L., Gao, L., Liu, X., Xie, L., & Li, G. (2019). Improving identification ability of adulterants in powdered Panax notoginseng using particle swarm optimization and data fusion. *Infrared Physics & Technology*, 103, 103101.

Development of a Deep Learning Method Using Magnetic Resonance Images for the Diagnosis of Multiple Sclerosis

FATMA AKSU¹, AHMET CEVAHİR CINAR²

¹ Selcuk University, Konya/Turkey, fatmaksu46@gmail.com

² Selcuk University, Konya/Turkey, accinar@selcuk.edu.tr

Abstract- Multiple Sclerosis (MS) is a chronic neurological disease characterized by the formation of plaques in the white matter of the central nervous system. It is usually diagnosed by cerebrospinal fluid and brain imaging techniques. Magnetic Resonance Imaging (MRI) is a neuroimaging method commonly used to diagnose MS. In recent years, advances in deep learning (DL) techniques have been widely used in detecting and diagnosing MS. In this study, a novel DL-based artificial intelligence model is proposed to detect MS using MRI images. In the proposed model, a richer feature map is created by extracting features from the intermediate layers of pre-trained network architectures. Furthermore, attribute integration is achieved by applying deeply adjustable convolution layers to these attributes. After these attributes, Global Average Pooling was applied to vectorize the attributes and finally, these attributes were merged and transferred to the fully connected layer and SoftMax layer. Pre-trained network architectures such as VGG16, ResNet101, and DenseNet121 were used in the study. In the experimental studies, a dataset of axial and sagittal brain MRI images collected from 72 MS patients and 59 healthy individuals at Turgut Özal University Faculty of Medicine in 2021 was used. In this dataset, axial images (n = 1652) and sagittal images (n = 1775) were evaluated separately and the model produced highly effective results. The highest accuracy scores were 98.78% with DenseNet121 for axial images and 99.32% with VGG16 for sagittal images. These results show that deep learning-based systems can be used in MS diagnosis.

Keywords- Multiple Sclerosis, Magnetic resonance, Deep Learning, DenseNet121, VGG16

I. INTRODUCTION

MULTIPLE sclerosis (MS) is an autoimmune disease in which nerve fibers in the central nervous system (brain and spinal cord) are damaged due to inflammation [1]. In autoimmune diseases, the immune system's defense mechanism, which normally exists to fight against foreign organisms, attacks the body's own tissues (Lublin, 2022). The exact cause of MS is unknown, but genetic and environmental factors are thought to play a role in the development of the disease.

Treatment of MS focuses on alleviating symptoms, controlling relapses, and slowing the progression of the disease [2]. Various treatment modalities such as medications, physical

therapy, rehabilitation, supportive therapies, and lifestyle changes are used to manage the disease [3].

Many studies have been conducted in the literature on the diagnosis and follow-up of Multiple Sclerosis (MS) and monitoring changes in the disease process. When these studies are analyzed, it is observed that different methods using magnetic resonance (MR) images are prominent in the detection of MS. Various studies have been carried out using magnetic resonance (MR) images for the detection and periodic follow-up of MS [4]. The use of computer-aided automated diagnostic systems has led to significant advances in the diagnosis of MS [5]. Before the development of MR imaging technologies, important studies were carried out by physicians in the clinical field [6]. In addition, several studies using machine learning algorithms have been developed to detect MS lesions in MR images [7]. It is observed that these studies have low detection accuracy due to the need for preprocessing for use by physicians, limited data sets, and difficulties in detecting small MS lesions.

Souplet et al. (2008) used basic image processing techniques for MS detection. They identified the brain region by performing normalization and regional focusing operations on three different MR sequences. In T1w and T2w sequences, they highlighted the regions suspicious for MS by maximization with the algorithm they developed. Finally, these suspicious regions were classified in FLAIR sequences [8].

Bosc et al. (2003) created a software framework to automatically track the evolution of lesions over time using MR images of healthy and MS patients. In this framework, brain region segmentation was first performed on the images, followed by preprocessing steps such as normalization and low-pass filtering. Finally, by comparing with healthy images, changes in lesions were detected and consistent results were obtained with the evaluations of expert radiologists [9]. Roura et al. (2015) developed a software tool for white matter segmentation and automatic detection of MS lesions using multicenter patient data obtained from different imaging devices [10]. In studies for the detection of MS lesions with image processing methods, preprocessing of MR images (normalization) followed by lesion detection (segmentation) has been generally followed [11].

In a study using advanced deep learning models, Nair et al. (2020) developed a model for detecting MS lesions using 3D

CNN. In their study, they emphasized the importance of the subtraction layer in lesion detection [11]. In another study, Gabr et al. (2020) developed a fully connected deep-learning CNN model for MS lesion detection. Although they achieved a certain level of accuracy in their experimental studies on a unique dataset, the success of the system has not been evaluated on public datasets [12].

In another study, Gessert et al. (2020) used a bidirectional CNN (convolutional neural network) to detect MS lesions using the model they developed. This study was conducted on an initially prepared 3D dataset and the experimental results were found to be close to the evaluations of medical experts. However, among the limitations of the study, it was emphasized that the performance of the model should be tested on high-resolution data sets, and some difficulties were experienced in the preparation and use of the data set [13]. The applications proposed as web-based CDS have been included in several academic studies to monitor MS lesions, track analytics, and questionnaires during disease progression, and evaluate the effects of drug therapy. In one of these studies, a web-based CDS was proposed to monitor the treatment processes and disease progression of MS patients [14]. In another study, Mo et al. (2015) proposed a web-based infrastructure system that can also utilize MRI images. The proposed system can perform lesion counting and lesion detection in images obtained from MR devices [15].

II. METHODOLOGY

A. Convolutional Neural Networks (CNN)

A widely used type of artificial neural network in the field of deep learning is the Convolutional Neural Network (CNN). It is used to achieve successful results in various fields such as image processing, audio processing, and natural language processing. One of the important advantages of CNN models is that feature extraction and training processes are performed together [16].

There are important CNN architectures used for automatic segmentation and classification with MRI neuroimaging methods for MS diagnosis [17]. In this study, the CNN architectures with the best results are DenseNet121 and VGG16.

DenseNet 121: One of the popular convolutional neural networks model is DenseNets where each layer in the network is connected to every other subsequent layer in a feed-forward form. The inputs of each layer are the concatenation of the feature maps of all the previous layers. The network has a total of $(L \times (L+1))/2$ connections between the layers. In this network, the dense connection reduces the effect of the vanishing gradient problem.

A DenseNet consists of L layers. At each layer implements a non-linear transformation $H_i(\cdot)$ where i is the index of the layer, $H_i(\cdot)$ is a composite function of batch normalization (BN), followed by a rectified linear unit (ReLU) and a convolution (Conv). The dense connectivity of the input of layer i in the network can be expressed by Eq. 1.

$$x_i = H_i([x_0, x_1, \dots, x_{i-1}]) \quad (1)$$

where x_i is the input of the layer and $[x_0, x_1, \dots, x_{i-1}]$ is the concatenation of feature maps from 0 to $i - 1$ layers. A sample of DenseNet121 architecture is shown in Fig. 1.

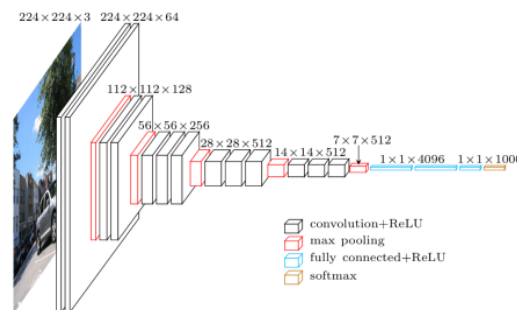


Figure 1: Sample DenseNet121 Architecture[18]

VGG16: The VGG-16 model is a convolutional neural network (CNN) architecture that was proposed by the Visual Geometry Group (VGG) at the University of Oxford. It is characterized by its depth, consisting of 16 layers, including 13 convolutional layers and 3 fully connected layers. Sample VGG16 architecture is shown in Fig. 2.



Figure 2: VGG16 Architecture [18]

III. PROPOSED MODEL

In this study, a convolutional Neural Network model based on feature integration is proposed for the detection of MS disease from MR images. The proposed method is tested with the most widely used deep learning models such as VGG16, InceptionV3, ResNet101, and DenseNet121. With the feature integration method, more features are extracted from the pre-trained network architectures. In this way, a more comprehensive feature map was obtained than traditional CNN architectures. Low- and high-level features are combined to obtain the final feature map. These feature maps contain both spatial and semantic details. The proposed model is given in Fig. 3.

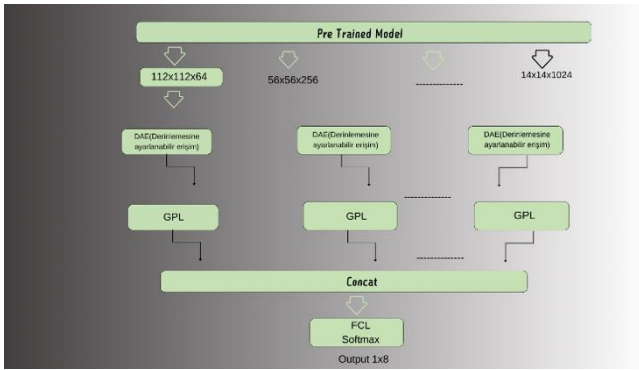


Figure 3: Proposed model

As can be seen in Fig. 3, a 224x224x3 input image is given to the input of the pre-trained network architectures. VGG16, InceptionV3, ResNet101, and DenseNet121 network architectures were used as network architectures. In each trial, 4 different feature maps were taken. These feature maps were obtained from the middle layers of the pre-trained network architectures. The height and width of these feature maps are 112x112, 56x56, 28x28, and 14x14 for a 224x224 dimensional input, respectively.

To combine the attributes, Global pooling Layer (GPL) was applied to convert the attribute maps into vectors. These feature vectors are then combined to obtain the final feature vector used for classification. Softmax classifier is applied to the final feature vector (F) obtained in the last layer of the proposed model to obtain the classification output. This process is shown in Equation (1).

$$P = \text{softmax}(PB^n(F))$$

$$\text{softmax}(x_i) = \frac{e^{x_i}}{\sum_{j=1}^n e^{x_j}} \quad (1)$$

IV. EXPERIMENTAL STUDIES AND RESULTS

Many experiments have been conducted to calculate the performance of the proposed method. The performance parameters used in these experiments are explained. The parameter values calculated because of the experiments are given.

Experimental studies were carried out on a computer with an Intel i9 processor, 64GB RAM, and an RTX 3080 Ti graphics card. Python programming language and Keras-Tensorflow library were used in the design of the deep learning model. The hyperparameters used were a batch size of 16, an image size of 224x224x3, and a training-test-validation data set split of 80%-10%-10%. The model was trained for 100 epochs. Adam optimizer is used to minimize the loss function and optimize the model. The performance of the proposed method is evaluated by using F1-score and classification accuracy. The calculation of the accuracy value is as in Equation (2).

$$\text{Acc} = \frac{TP+FP}{TP+TN+FP+FN} \quad (2)$$

The F1 score is an indispensable metric for balancing precision and sensitivity, especially when classes are unbalanced. It provides a single score that captures both precision and sensitivity, making it a powerful measure for overall model performance evaluation (Havd., 2022; Naseri et al., 2021; Shahin et al., 2019). The F1 score is calculated as in Equation (3).

$$\text{Doğruluk} = \frac{TP + TN}{TP + FP + TN + FN}$$

$$\text{Kesinlik} = \frac{TP}{TP + FP}$$

$$\text{Duyarlılık} = \frac{TP}{TP + FN}$$

$$F1 - \text{puanı} = 2 * \frac{\text{Kesinlik} * \text{Duyarlılık}}{\text{Kesinlik} + \text{Duyarlılık}} \quad (3)$$

VGG16, InceptionV3, ResNet101, and DenseNet121 architectures were used in this study. The results obtained using axial images are given in Table 1.

Table 1. Performance values calculated for axial images

Model	accuracy	f1 score	recall	precision	TP	TN	FN	FP
resnet101	96.36%	97.08%	99.20%	95.04%	249	2	13	149
vgg16	97.82%	98.23%	99.60%	96.90%	250	1	8	154
densenet121	98.78%	99.01%	100.00%	98.05%	251	0	5	157
inceptionv3	98.54%	98.82%	100.00%	97.67%	251	0	6	156

Table 2. Performance values calculated for rightittal images.

Model	accuracy	f1 score	recall	precision	TP	TN	FN	FP
resnet101	98.64%	98.83%	100.00%	97.69%	254	0	6	184
vgg16	99.32%	99.41%	100.00%	98.83%	254	0	3	187
densenet121	99.09%	99.22%	100.00%	98.45%	254	0	4	186
inceptionv3	99.09%	99.22%	100.00%	98.45%	254	0	4	186

Table 1 shows 98.78% accuracy with DenseNet121 in axial images, when Table 2 is examined, an accuracy of 99.32% was calculated with VGG16 in sagittal images. The complexity matrix values are also given in Tables 1-2.

Instead of extracting features from the last layers of traditionally pre-trained network architectures, the proposed model generates a comprehensive feature map by extracting richer features from the intermediate layers of these architectures. This approach allows the model to learn deep and meaningful features more effectively. Furthermore, attribute integration is achieved by adding deeply adjustable convolution layers to the extracted attributes. This process optimizes the combination of different features to create a more effective learning process. After the attributes, these attributes are vectorized with the Global Average Pooling method and then transferred to the SoftMax classifier with a fully connected layer. At this stage, it creates customized vectors that support the final decision-making process of the model. In the development of the model, pre-trained network architectures such as VGG16, ResNet101 and DenseNet121 were used.

These architectures offer diversity by incorporating features of network structures at different depths. The experimental studies were conducted at Turgut Özal University Faculty of Medicine in 2021 with 72 MS patients and 59 healthy individuals on a dataset of axial and sagittal brain MRI images. In this dataset, axial images (n = 1652) and sagittal images (n = 1775) are analyzed separately. The experimental results show that the model performs effectively with these images.

The highest accuracy scores obtained were 98.78% with DenseNet121 for axial images and 99.32% with VGG16 for sagittal images. These results show that sagittal images provide higher accuracy in MS diagnosis and that this image type provides more information in the decision-making process of the model. These findings emphasize the importance of image types in MS diagnosis and open new areas for future research.

REFERENCES

- [1] Shoeibi, A., et al., *Applications of deep learning techniques for automated multiple sclerosis detection using magnetic resonance imaging: A review*. Computers in Biology and Medicine, 2021. **136**: p. 104697.
- [2] DeSousa, E.A., R.H. Albert, and B. Kalman, *Cognitive impairments in multiple sclerosis: a review*. American Journal of Alzheimer's Disease & Other Dementias®, 2002. **17**(1): p. 23-29.
- [3] Murray, T.J., *Multiple sclerosis: the history of a disease*. 2004: Demos medical publishing.
- [4] Bakshi, R., *Fatigue associated with multiple sclerosis: diagnosis, impact and management*. Multiple Sclerosis Journal, 2003. **9**(3): p. 219-227.
- [5] Solari, A., et al., *Computer-aided retraining of memory and attention in people with multiple sclerosis: a randomized, double-blind controlled trial*. Journal of the neurological sciences, 2004. **222**(1-2): p. 99-104.
- [6] McDonald, W.I., et al., *Recommended diagnostic criteria for multiple sclerosis: guidelines from the International Panel on the diagnosis of multiple sclerosis*. Annals of Neurology: Official Journal of the American Neurological Association and the Child Neurology Society, 2001. **50**(1): p. 121-127.
- [7] Ghahazi, M.A., et al. *Fuzzy rule based expert system for diagnosis of multiple sclerosis*. in *2014 IEEE Conference on Norbert Wiener in the 21st Century (21CW)*. 2014. IEEE.
- [8] Souplet, J.-C., et al. *An automatic segmentation of T2-FLAIR multiple sclerosis lesions*. in *MICCAI-Multiple sclerosis lesion segmentation challenge workshop*. 2008.
- [9] Bosc, M., et al., *Automatic change detection in multimodal serial MRI: application to multiple sclerosis lesion evolution*. NeuroImage, 2003. **20**(2): p. 643-656.
- [10] Roura, E., et al., *A toolbox for multiple sclerosis lesion segmentation*. Neuroradiology, 2015. **57**: p. 1031-1043.
- [11] Nair, T., et al., *Exploring uncertainty measures in deep networks for multiple sclerosis lesion detection and segmentation*. Medical image analysis, 2020. **59**: p. 101557.
- [12] Gabr, R.E., et al., *Brain and lesion segmentation in multiple sclerosis using fully convolutional neural networks: a large-scale study*. Multiple Sclerosis Journal, 2020. **26**(10): p. 1217-1226.
- [13] Gessert, N., et al., *Multiple sclerosis lesion activity segmentation with attention-guided two-path CNNs*. Computerized Medical Imaging and Graphics, 2020. **84**: p. 101772.
- [14] Daumer, M., et al., *Prognosis of the individual course of disease-steps in developing a decision support tool for Multiple Sclerosis*. BMC medical informatics and decision making, 2007. **7**: p. 1-6.
- [15] Mortazavi, D., A.Z. Kouzani, and H. Soltanian-Zadeh, *Segmentation of multiple sclerosis lesions in MR images: a review*. Neuroradiology, 2012. **54**: p. 299-320.
- [16] Hauser, S.L. and B.A. Cree, *Treatment of multiple sclerosis: a review*. The American journal of medicine, 2020. **133**(12): p. 1380-1390. e2.
- [17] Siegert, R.J. and D.A. Abernethy, *Depression in multiple sclerosis: a review*. Journal of Neurology, Neurosurgery & Psychiatry, 2005. **76**(4): p. 469-475.
- [18] <https://amaarora.github.io/posts/2020-08-02-densenets.html>
- [19] <https://www.geeksforgeeks.org/vgg-16-cnn-model/>

A Four-way Stripline Power Divider Design with Increased Isolation in the 500-1000 MHz Frequency Band

BETÜL ÖZEN GÜLER^{1,2}, MESUT KARTAL¹

¹ Istanbul Technical University, Istanbul/Turkey, kartalme@itu.edu.tr

² Aselsan Inc., Ankara/Turkey, ozenb16@itu.edu.tr

Abstract - In this work, a four-way stripline power divider with improved isolation between ports is presented. The main power divider and isolation circuits designed for this purpose are connected to each other using vias on a multi-layered structure. The isolation circuit is formed by the combination of broadside coupled lines used as baluns to ensure high isolation for each output port. The proposed power divider covers the frequency range of 500–1000 MHz. EM simulation results highlight that the insertion loss is less than 0.68 dB, while the return loss is greater than 14.7 dB. It has also been observed that the designed power divider exhibits a good performance with more than 14 dB of isolation between output ports, less than 0.56 dB of amplitude imbalance and less than 4° of phase imbalance.

Keywords - four-way power divider, isolation, stripline, balun, coupled lines

I. INTRODUCTION

POWER dividers are essential components for various RF engineering areas, such as spacecraft communication, radar systems, telecommunications and other applications [1]. A power divider is a device that splits an input signal into two or more output signals. Insertion loss, amplitude balance, phase balance, frequency range, dimensions, and isolation are common design issues for power dividers. Reduced insertion loss is essential because it preserves more signal power, which improves efficiency and system performance. Applications like phased array systems that demand constant level of signal over several channels require maintaining amplitude balance. Proper phase balancing assures coherent signal dividing for applications like beamforming in radar and communication systems, where phase alignment directly affects the performance. In order to ensure compatibility with specific purposes and performance over the whole frequency band, it is critical that the divider is able to operate over the required frequency range. Compact dividers are necessary for integration into systems with limited space, including satellite communication equipment and mobile devices. The divider's ability to minimize crosstalk or leakage between its output ports is identified as isolation. High isolation reduces crosstalk, ensuring that signals from one output port do not interfere with signals from closest neighboring port [2]. Moreover, strong

isolation prevents distortion caused by the interaction of output signals with other signals, thus preserving their original characteristics, and is vital for systems that must transmit signals with extreme accuracy and quality, such as radar and communication networks [3, 4]. These advantages are essential for power amplifier systems to operate as reliably and efficiently as possible in a variety of applications. Moreover, signals from one amplifier cannot leak into the inputs of other amplifiers when there is high isolation. This is necessary to make sure that every amplifier runs effectively and independently without interfering with one another and lowering performance. Insufficient isolation, which puts other amplifiers at risk if one amplifier fails, also makes it difficult to reduce the effects of amplitude and phase imbalance that may be present across several amplifiers, even if all of them are operational [5]. Since the stability and reliability of the power amplifier depend on this protection, the stripline structure, which can give good isolation performance, is selected in our proposed design.

Stripline is a kind of transmission line that is covered with a dielectric substance and positioned between two ground planes [6]. The ground planes and the dielectric entirely encapsulate the signal conductor. Maintaining signal integrity requires consistent impedance, which is ensured by the enclosed construction. The ground planes reduce loss and boost performance by efficiently preventing signal radiation. Additionally, stripline's symmetric topology lowers crosstalk, enhances isolation and overall electromagnetic performance. Its low radiation loss and regulated impedance make it a viable choice for high frequency applications [1]. Stripline, however, has drawbacks in terms of accessibility and manufacture. Because stripline circuits need exact alignment and have a multilayer structure, producing them is more expensive and difficult. Since the signal conductor is encased, it is also difficult to access for probing and alteration, in comparison to microstrip, the multilayer architecture may lead to a thicker and heavier design.

In this paper, a new four-way high isolation divider design in the 500 MHz to 1000 MHz operating frequency range is presented, by using the stripline structure, considering its high isolation and other advantages discussed here.

II. RELATED WORK

When designing power dividers, there are important design parameters as mentioned in the previous section and many studies have been conducted in the past to optimize these parameters; just like in this study.

Guo et al. proposed a four-way suspended stripline power divider, with the suspended stripline structure playing a significant part in reducing insertion loss while preserving a compact design [1]. The isolation circuit, created using microstrip lines and connected by vias, provided high isolation, with the isolation measured at the X-band (7.82-9.86 GHz) being over 20 dB. The combination of suspended stripline for power division and microstrip for isolation produced an insertion loss less than 0.37 dB. Suspended striplines are particularly important because they provide low loss transmission, which is required for high efficiency power dividing applications.

Furgal et al. demonstrated a broadband four-way power divider that uses a multilayer structure with stripline and microstrip technologies to improve isolation and bandwidth performance [7]. The stripline architecture improves heat dissipation and integration, solving the constraints of traditional designs like as the Wilkinson divider, which has difficulty handling high power due to insufficient isolation and thermal management. Because the resistor in the Wilkinson power divider is located between transmission lines, heat cannot be properly dissipated from the circuit to the ground plane. The ungrounded resistor greatly limits the possibility of operating at high power. By strategically arranging isolation resistors in the stripline layers, the design improves the circuit's power handling capacity while maintaining isolation without compromising bandwidth.

Momenzadeh et al. demonstrated isolation strategies by adding coaxial baluns and quarter-wave transformers into a broadband high-power combiner for digital video broadcasting-terrestrial applications [8]. Although power combiners can be used as power dividers, this design and simulation studies in this paper focus on power combiner characteristics. This study describes two power combiners that are extensions of the ordinary Wilkinson power divider. These combiners use a 100 Ω floating resistor to convert 50 Ω terminating resistors. The first power combiner uses coaxial cable baluns to convert 50 Ω terminating resistors into floating 100 Ω resistors, the second power combiner makes use of 3 dB quadrature hybrids. The quadrature coupler which is short-circuited with one port converts the impedance of normal 50 Ω terminating resistors into floating 100 Ω resistors, ensuring effective isolation throughout a wide frequency range 470-860 MHz. This technique not only increases bandwidth but also enhances port isolation by utilizing the quarter-wave structure's intrinsic features.

Beside the related researches, the aim is to increase isolation while also eliminating the difficulties of inserting isolation resistors with the design of four-way divider and four pairs of broadside coupled lines that used as baluns in this study. As it

discussed in the related studies, the stripline design ensures low insertion loss which is also implemented in the study.

III. DESIGN AND SIMULATION

In this section, the designed power divider circuit, stack-up details of this circuit and simulation results are depicted. The designed power divider consists of two circuits: The main power divider circuit and the isolation circuit.

A. Main Power Divider Circuit

Figure 1 shows the schematic of the divider circuit, which has a symmetrical construction. In Figure 1, a 50 Ω microstrip line at Port 1 is separated into two parallel lines, each with a 50 Ω impedance, using a T-junction design. The parallel lines of two 50 Ω lines yields a total impedance of 25 Ω . Figure 2 highlighted the transition from 25 Ω to 50 Ω using a quarter-wave transmission line. As it is well known that the impedance of a quarter-wavelength ($\lambda / 4$) transmission line is equal to the square root of the product of Z_1 and Z_2 [9]. Consequently, a quarter-wavelength 35 Ω transmission line is inserted between the two lines.

The 50 Ω transmission lines are further split by T-junctions again. In order to ensure that the output of each 50 Ω line will again have a 50 Ω line impedance, the two line segments separated by a T-junction must now have a characteristic impedance of 100 Ω . Since the output ports must terminate with 50 Ω impedance, other quarter-wave transmission lines are also included in the circuit to transform this impedance to 100 Ω . To accomplish adequate impedance matching, a $\lambda / 4$ length of line with an impedance of around 70 Ω is utilized. The wavelength required to determine the line lengths was obtained using Equation (1). In the equation, the value of the frequency (f) is 750 MHz and dielectric constant (ϵ_r) is 3.55 [10]. As a result, a four-way, symmetric power divider without isolation is designed.

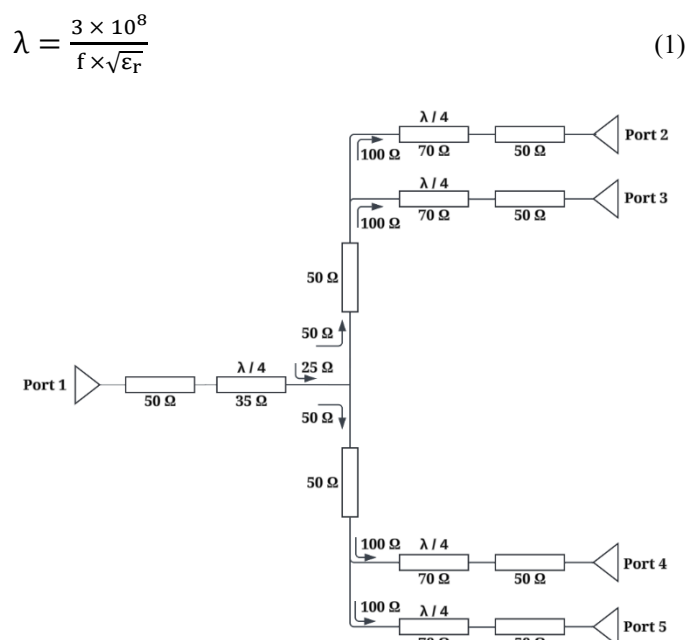


Figure 1: The schematic of power divider circuit

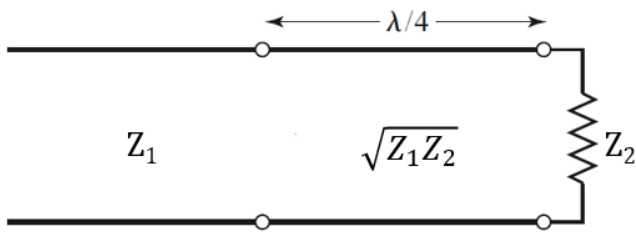


Figure 2: Quarter-wavelength impedance transformation

B. Isolation Circuit

The main power divider circuit lacks adequate isolation when it is used alone. The isolation parameters of the main power divider circuit are highlighted in Figure 3. An isolation circuit is necessary because low isolation promotes crosstalk, which results in signal interference between the output ports. To achieve this isolation, an isolation circuit is established. In this circuit, each output port includes a quarter-wavelength broadside coupled lines that functions as a balun.

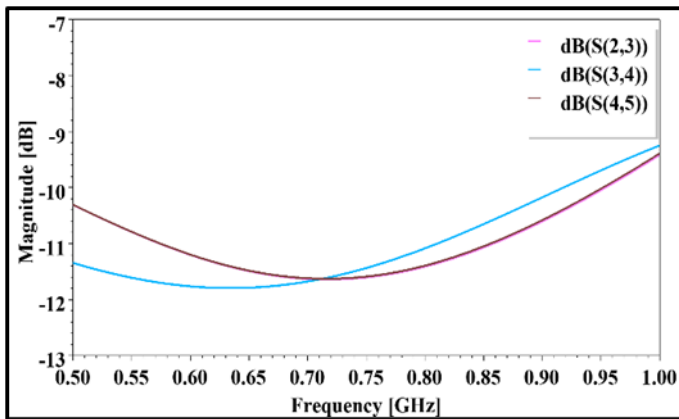


Figure 3: The isolation parameters of the main power divider

In order to explain the isolation circuit, the quarter-wavelength broadside coupled lines model is first presented in Figure 4. Ideal lossless coupled lines at 750 MHz are used. It is important to note that when the quarter-wavelength coupled lines are utilized as a balun and specific criteria are met, it yields considerably good performance. For the modeling of the balun, related parameters are specified in Equations (2-5). It is also significant to indicate an ideal balun is obtained when the line lengths are $\lambda / 4$ and Z_{even} equals $Z_{\text{unbalanced}}$ and Z_{odd} equals Z_{balanced} at the center frequency as depicted in (2-5) [11]. As shown in the graph in Figure 5, the return loss is particularly good at the center frequency of 750 MHz. In this design, the goal is to achieve isolation for each output port of the divider by using a $\lambda / 4$ length broadside coupled line balun.

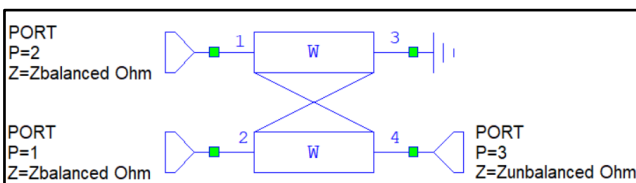


Figure 4: Balanced to unbalanced model

$$Z_{\text{unbalanced}} = Z_{\text{even}} = 50 \Omega \tag{2}$$

$$Z_{\text{balanced}} = Z_{\text{odd}} = 35 \Omega \tag{3}$$

$$Z_{\text{differential}} = 2Z_{\text{balanced}} = 70 \Omega \tag{4}$$

$$\text{Impedance ratio} = \frac{Z_{\text{differential}}}{Z_{\text{unbalanced}}} = \frac{70}{50} = 1.4 \tag{5}$$

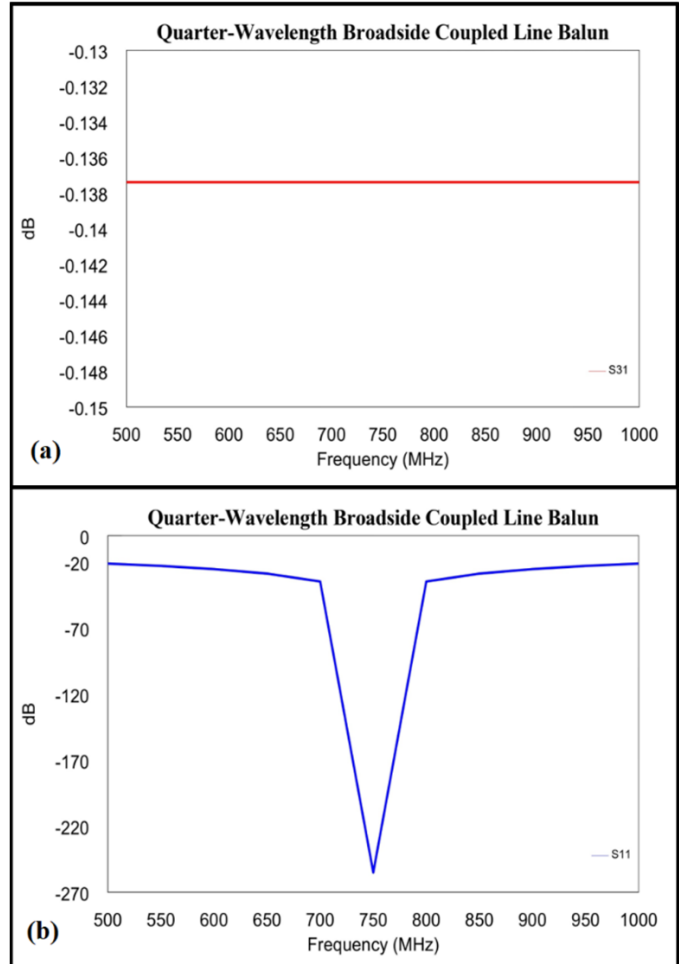


Figure 5: Graph of a quarter-wavelength broadside coupled line balun for (a) Insertion loss (b) Return loss

In Figure 6, it is demonstrated a circuit structure which matches the balance ports to 35Ω for all adjacent ports which use quarter-wavelength broadside couple line. It is important to mention that to ensure upper lines also 35Ω and $Z_{\text{diff}} 70 \Omega$, upper lines connected each other. The lower lines terminated with 50Ω and upper lines are grounded. The coupled lines which used in Figure 6 are not ideal and lossless components. Substrate of the components is modelled according to stack-up by considering the loss tangent of the material. In Figure 7, given graph shows the return loss for each port. The values of $S_{11}, S_{22}, S_{33}, S_{44}$ are equal for each frequency and all of them are around 20 dB.

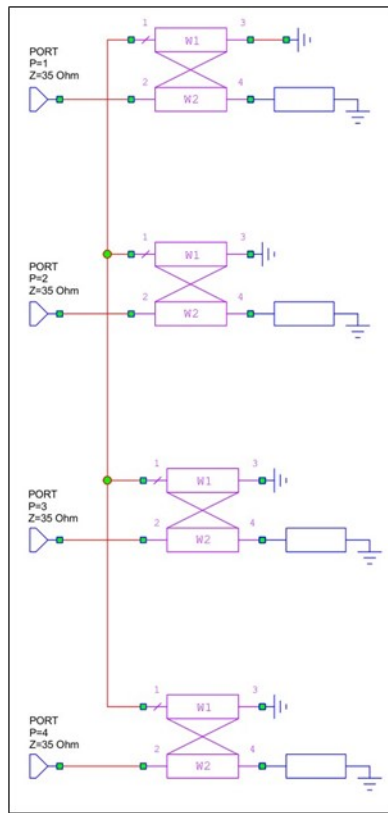


Figure 6: Schematic of isolation circuit

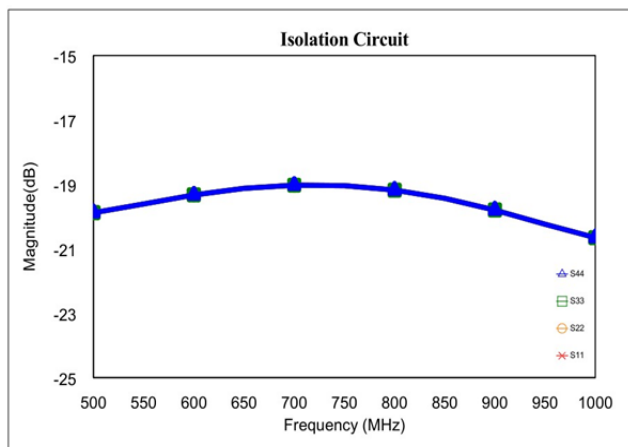


Figure 7: Return loss of isolation circuit for each port

C. Stack-up

The stack-up has eight layers total of 149.2 mil in thickness. As seen in Figure 8, the main power divider circuit has a stripline structure and it is at the center of the stack-up and situated on Signal Layer 1. Quarter-wavelength broadside coupled lines placed on Signal Layer 2 and Signal Layer 3 to function as baluns. To ground the upper coupled lines, conductive shapes are implemented which placed on Signal Layer 4. The purpose of using conductive shape in Signal Layer 4 is to strengthen the connection between Via-Type 2 and Via-Type 3 and to connect the upper coupled lines, which is placed in Signal Layer 3, to the ground layer. Otherwise, if the

alignment of Substrate 7 and Substrate 8 is disrupted, the upper coupled lines cannot be reached Ground Plane properly since Via-Type 2 and Via-Type 3 does not overlap. The connection between Via-Type 2 and Via-Type 3 is provided through the conductive shape.

The broadside coupled lines are connected to Signal Layer 1 by blind vias which referred to as Via-Type 1 in Figure 8. Via-Type 1 are placed on Signal Layers 2 and 3 across Substrate 5 from the end of the quarter-wavelength 70 Ω lines in the main power divider circuit. The distance between the broadside coupled lines are 4 mil, corresponding to height of the Substrate 6 in Figure 8. Through vias, labeled as Via-Type 4, are also used for grounding.

Rogers 4003C is used in two layers of the eight layers, while Rogers 4350B is used in the remaining six layers. It is used Rogers RO4003C 60 mil for Substrate 1 and 8 with a dielectric constant of 3.55 and a dissipation factor of 0.0021. It is used Rogers RO4350B 4 mil for Substrate 2, 3, 6 and 7 and RO4350B 6.6 mil for Substrate 4 and 5 layers with a dielectric constant of 3.66 and a dissipation factor of 0.0031 [10].

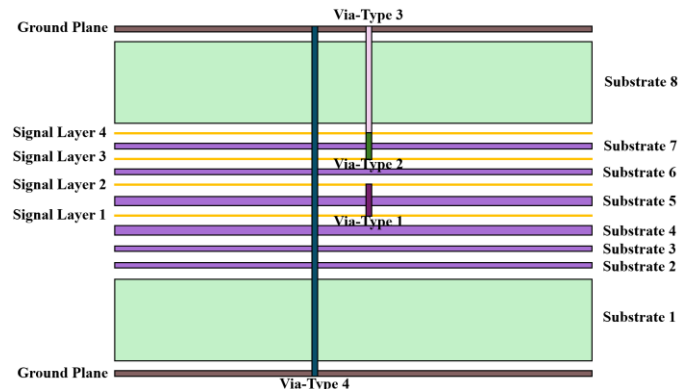


Figure 8: Stack-up of the model

D. Simulation and Results

A 3D model is simulated in ANSYS HFSS simulation tool that is highlighted in Figure 9 and Figure 10. Line widths and lengths are calculated using the impedances that obtained from main power divider circuit schematic. The board dimensions are 122.1 mm by 107.1 mm.

The EM model is simulated from 500 MHz to 1000 MHz. The simulated results are given in Figure 11. As can be seen in Figure 11-a, the variation range of insertion loss (S_{21} , S_{31} , S_{41} , S_{51}) is from 0.07 to 0.68 dB and amplitude imbalance is less than 0.56 dB. Return loss (S_{11}) varies between 14.7 dB and 22 dB as shown in Figure 11-b. The isolation parameters (S_{23} , S_{34} , S_{45}) vary between 14 dB and 20 dB as demonstrated in Figure 11-c. As seen in Figure 3, the isolation parameters of the main power divider are greater than 9 dB. Therefore, the isolation circuit has positively affected the isolation parameter values. On the other hand, the phase imbalance between the outputs is less than $\pm 4^\circ$ as shown in Figure 11-d.

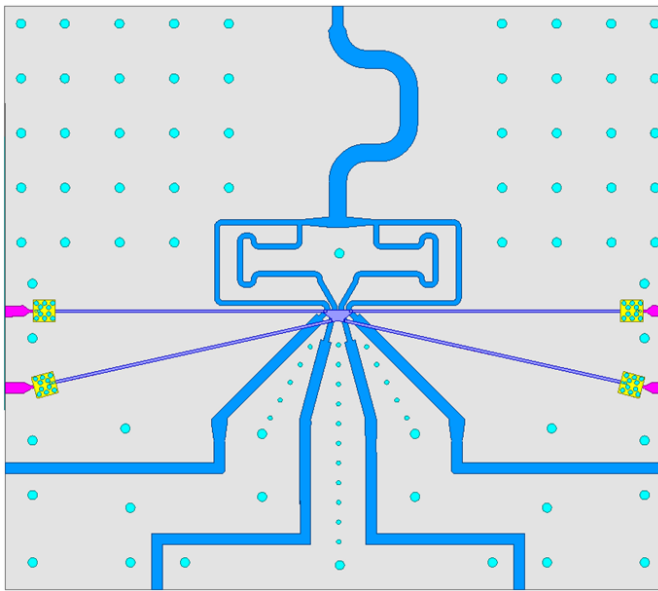


Figure 9: View of the EM model

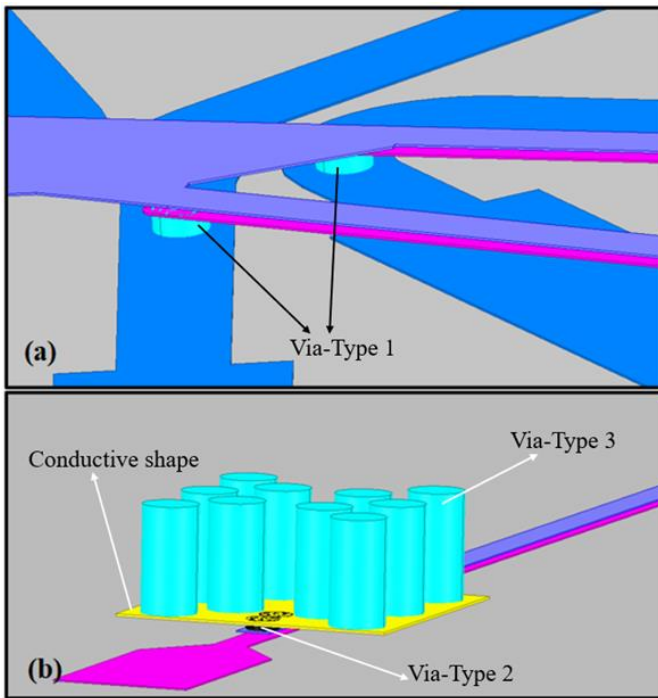


Figure 10: The via types: (a) Via-Type 1 which connects main power divider circuit and lower coupled lines, (b) Via-Type 2 that is used for connecting upper coupled lines and conductive shapes and Via-Type 3 from conductive shapes to upper ground

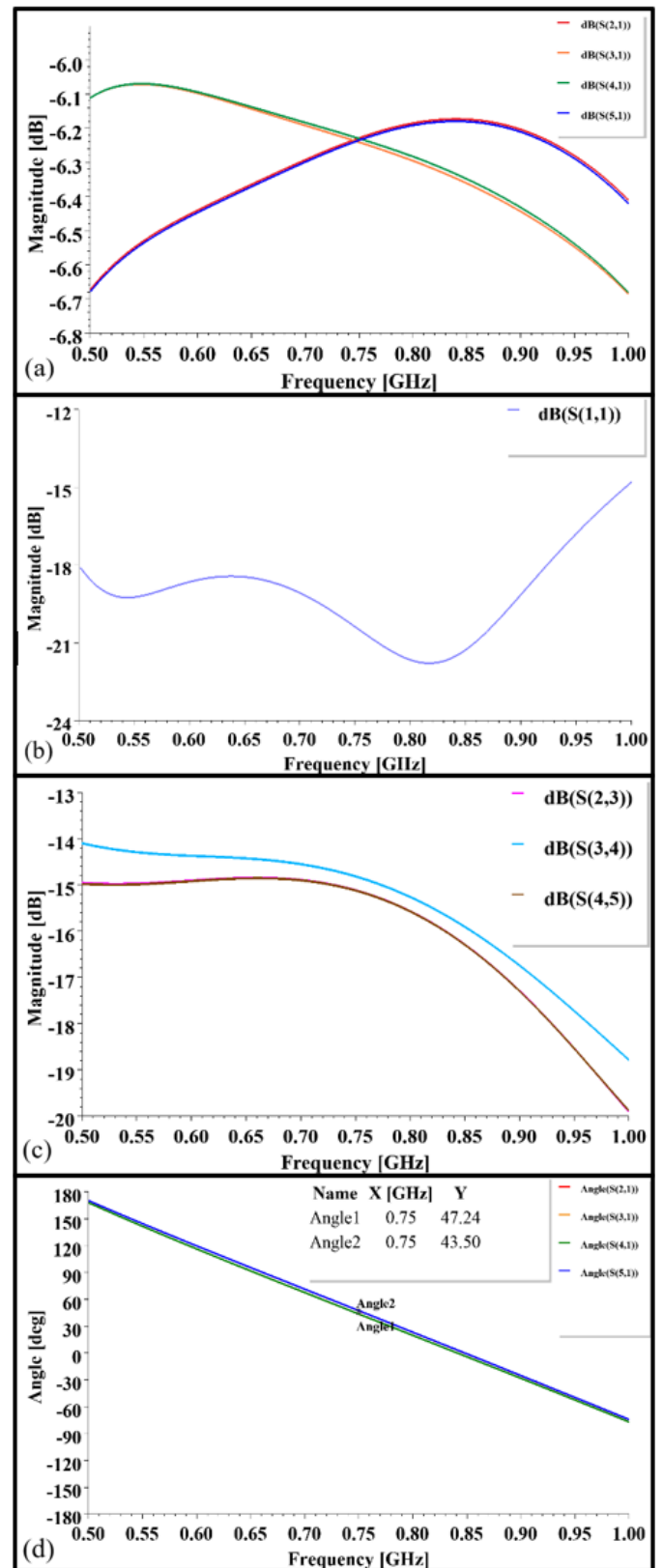


Figure 11: The simulated results: (a) Insertion loss, (b) Return loss, (c) Isolation, (d) Phase

IV. CONCLUSION

In this study, a new four-way stripline power divider with increased port isolation that will operate in the 500-1000 MHz band was designed as an alternative to the power dividers commonly used in RF/Microwave applications. The isolation of each adjacent port is provided by broadside coupled lines that act as baluns and the unbalanced ports are terminated with 50 Ω .

According to EM simulation results, the insertion loss (S_{21} , S_{31} , S_{41} , S_{51}) values vary between 0.07 and 0.68 dB. Furthermore, the return loss across the band is between 14.7 and 22 dB, while the isolation parameters vary between 14 and 20 dB which shows significant improvement compared to the results without isolation. In addition, the phase imbalance between the outputs is less than 4° and amplitude imbalance is less than 0.56 dB.

EM simulation results show that the four-way power divider performs promising results with low insertion and return loss, high isolation, low amplitude and phase imbalance. The next study will cover the manufacturing of the power divider and, after obtaining the measurement output, checking how well the simulation results can be provided and, if necessary, improvement studies on the prototype circuit.

REFERENCES

- [1] S. Guo, K. Song, and Y. Fan, "Compact four-way suspended-stripline power divider with low loss and high isolation," *International Journal of Microwave and Wireless Technologies*, vol. 12, no. 8, pp. 749–753, Feb. 2020, doi: <https://doi.org/10.1017/s1759078720000082>.
- [2] M. Jamil and N. N. M. Yusof, "A review of Wilkinson power divider as a splitter/combiner based on method, design and technology," 2020.
- [3] M. Atasoyu, S. Ozoguz, S. Paker and O. Palamutcuogullari, "Wideband hybrid power combiner using double-sided-parallel-strip lines," *2016 39th International Conference on Telecommunications and Signal Processing (TSP)*, Vienna, Austria, 2016, pp. 227-230, doi: 10.1109/TSP.2016.7760866. J. Williams, "Narrow-band analyzer (Thesis or Dissertation style)," Ph.D. dissertation, Dept. Elect. Eng., Harvard Univ., Cambridge, MA, 1993.
- [4] J. C. Kao, Z. M. Tsai, K. Y. Lin, and H. Wang, "A modified Wilkinson power divider with isolation bandwidth improvement," *IEEE Transactions on Microwave Theory and Techniques*, vol. 60, no. 9, pp. 2768-2780, Sep. 2012.
- [5] S. H. Javid-Hosseini, P. Toofanzadeh, and V. Nayyeri, "Planar N-way power combiner with high isolation between input ports," in *2021 51st European Microwave Conference (EuMC)*, London, UK, Apr. 2022, pp. 83-86.
- [6] D. M. Pozar, *Microwave Engineering*, 4th ed. New Delhi, India: Wiley India, 2017.
- [7] J. Furgal, K. Xu, J. H. Choi, and J. K. Lee, "Broadband equal-split planar 4-way power divider/combiner suitable for high power applications," in *2020 50th European Microwave Conference (EuMC)*, Utrecht, Netherlands, Jan. 2021, pp. 840-843. doi: 10.23919/EuMC48046.2021.9337968.
- [8] M. Momenzadeh and A. Ahmadi, "High-power combiners with terminating resistors for DTV applications in the frequency range of 470–860 MHz," *IET Microwaves Antennas & Propagation*, vol. 14, no. 3, pp. 174–182, Nov. 2019, doi: <https://doi.org/10.1049/iet-map.2019.0244>.
- [9] M. B. Steer, *Microwave and RF Design. Volume 3, Networks*, Raleigh, NC: NC State University, 2019.
- [10] Rogers Corporation, *Rogers 4003C, 4350B Datasheet*.
- [11] X. Shi, Y. Xue, Y. -J. Yang and J. -X. Chen, "A Wideband DRWG Balun With Low Loss and Compact Size," in *IEEE Microwave and Wireless Technology Letters*, vol. 34, no. 4, pp. 379-382, April 2024, doi: 10.1109/LMWT.2024.3364667.
- [12] S. Itapu, M. Almalkawi, and V. Devabhaktuni, "A 0.8–8 GHz multi-section coupled line balun," *Electronics*, vol. 4, no. 2, pp. 274–282, 2015. doi: 10.3390/electronics4020274

Enhancing Automated and Early Detection of Alzheimer's Disease Using Image Processing and Machine Learning

FURKAN ŞENOL¹, HÜSEYİN ESAD ÖNER², MAHMUT BÜYÜKBAŞ³

¹Abdullah Gül University, Kayseri/Turkey, furkan.senol@agu.edu.tr

²Abdullah Gül University, Kayseri/Turkey, huseyinesad.oner@agu.edu.tr

³Abdullah Gül University, Kayseri/Turkey, mahmut.buyukbas@agu.edu.tr

Abstract - Alzheimer's disease is a common type of dementia and progressive neurological disorder that causes the brain atrophy and brain cells to disappear. Early diagnosis is very important in the treatment of the disease and controlling it. Technological developments such as image processing and machine learning have a very important place in the medical industry, as they eliminate the difficulties experienced by doctors in diagnosing Alzheimer's disease using MRI and contribute to the early diagnosis and classification of this disease. The goal of this research is to apply feature extraction and classification techniques to build a system for the early diagnosis of Alzheimer's disease. In 4 classes, the brain tissue region was segmented after applying the necessary filter and pre-processing steps to the MR images. Then, different features related to the segmented images were extracted using various feature extraction methods. These features were reduced with different feature selection techniques. Different classification techniques were applied to the selected features. An accuracy value of 95.97% was obtained with the K-Nearest Neighbors technique, which is one of these classification methods.

Keywords - Alzheimer's disease, MRI, machine learning, image processing, biomedical imaging.

I. INTRODUCTION

ALZHEIMER'S disease (AD) is a common type of dementia and a neurological disease that increases with time and causes the death of brain cells. An estimated 24 million people worldwide have dementia, the majority of whom are thought to have Alzheimer's disease [1]. This illness causes problems with thinking, learning, and remembering in addition to memory loss and cognitive decline. The condition worsens slowly. As the disease worsens and shrinkage becomes more pronounced, the brain eventually shrinks to about 60% of its normal size. Shrinking of brain tissue due to AD can be diagnosed using brain imaging techniques such as MRI scans. Several years prior to the beginning of clinical symptoms, MRI can identify primarily left atrophic alterations in the amygdala, anterior hippocampus, and entorhinal cortex [2].

The brain MRI scans from the OASIS [3] dataset utilized in this study are divided into various phases of Alzheimer's

disease. Non-demented, very mild dementia, mild dementia, and moderate dementia are among these stages. The loss of brain tissue, which worsens with the progress of the disease, is the main area of interest (ROI) in these pictures. Since most patients are unaware of their condition until serious brain volume loss occurs, early diagnosis and therapy are essential.

This project's main objective is to use machine learning techniques to develop a model that can correctly identify different Alzheimer's disease stages from MRI scans. To reduce incorrect diagnosis, this requires putting the required preprocessing procedures, feature extraction, and classification techniques into practice.

II. PRE-PROCESSING AND SEGMENTATION

Pre-processing is an essential step in preparing MRI images for further analysis and feature extraction. The pre-processing of the image is essential for the importance gap of the latent feature in the precise diagnosis and classification of Alzheimer's disease. Below are the series of pre-processing steps carried out on the MRI images in the sequence given above.

A. Thresholding

In thresholding, the technique applied to the MRI images transforms the grayscale image into a binary image, where pixel values are 0 for black and 255 for white above a specified cutoff value. Classically in such threshold image segmentation, an image is segmented and then objects, and background are usually distinguished by a threshold only [4]. This process helps to enhance the contrast of essential brain features so that they can stand out from the background and other non-brain elements. Therefore, the effect of carrying out this process will provide an image showing essential brain features made more distinctive.

B. Median Filtering and Masking

After thresholding, the next step is applying a median filter to the binary image. The median filter is a nonlinear filter that is one of the most effective and common filters used for removing impulse noise and their edge preservation, and as a result, this work deals with this filter for better filtration [5]. It performs noise reduction, and its result is the substitution of the

value of each pixel with the median result of the pixel's neighborhood. This will help in removing noise but preserve the edges. Masking is then applied to the median filtering process. Masking by binary masks isolates ROIs and retains only the critical brain structures, losing all other parts.

C. Application of Mask

The mask obtained previously is superimposed on the original MRI. During this process, only such elements are retained in the entire process that reflect the brain structures and have been recognized by thresholding and filtering. All the non-brain tissues and the background elements are thus effectively eliminated, providing an image only of the brain and effectively masking away all the irrelevant regions.

D. Cropping

The resultant masked image is finally cropped. Cropping means trimming the image to the region of interest as it eliminates the rest of the content and retains only what the image is interested in analyzing. This ensures only the relevant portion will be analyzed in the further steps of feature extraction and classification, reducing the computational load and improving the accuracy of the results.

Such pre-processing steps prepare these MRI images for correct feature extraction and classification, which ultimately helps in enabling the early and automatic detection of Alzheimer's disease. The importance of these steps is manifested in the subsequent analysis and model training processes.

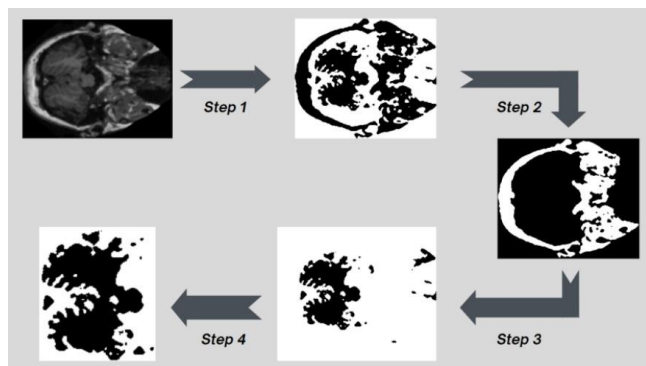


Figure 2.1: Pre-Processing & Segmentation

To enable more precise feature extraction, image segmentation separates regions of interest, such as certain brain regions impacted by Alzheimer's disease.

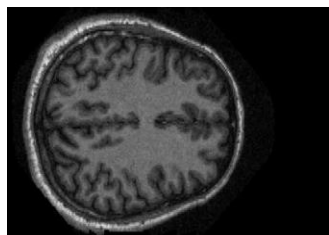


Figure 1.2: Original MRI Image

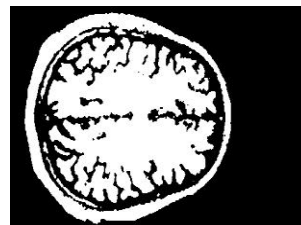


Figure 2.3: Pre-processing & Threshold

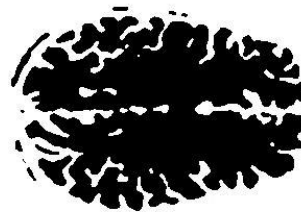


Figure 2.4: Segmentation

III. FEATURE EXTRACTION

A. Shape Features and Pixel-Intensity Based Features

Regarding the problem of classifying a pattern, feature extraction refers to a procedure or a formalism for describing the shape information present useful for classification in the layout of the pattern [6]. To extract important properties from MRI images, feature extraction is performed. Shape features provide information about the geometry of brain structures, and pixel-intensity features reveal the grayscale values of the image. Shape features are critical in capturing the geometrical properties of brain structures. These features include:

- Edge length
- Mean area
- Minimum area
- Maximum area
- Number of regions
- Mean perimeter
- Minimum perimeter
- Maximum perimeter

Pixel-intensity features provide information about the grayscale values within the MRI images. Key features include:

- Total brain area
- Brain percentage
- Mean intensity
- Median intensity
- Minimum intensity
- Maximum intensity
- Variance
- Entropy
- Skewness

B. Principal Component Analysis (PCA)

Using PCA, the dataset's dimensionality is decreased while maintaining a high degree of variance. PCA assists in producing more relevant and lower-dimensional features by converting the original features into a new set of orthogonal components,

which helps to handle the data better for machine learning algorithms.

C. Scale-Invariant Feature Transform (SIFT)

SIFT is a powerful tool for detecting critical locations in MRI images because it finds and describes local characteristics in images that are invariant to scale and rotation. SIFT is an algorithm that detects and describes local features in images. These features are invariant to changes in illumination, rotation, and scale. The steps involved in SIFT are:

1. Applying a Gaussian filter to the image.
2. Calculating the difference of Gaussian (DoG) to highlight key points.
3. Identifying local maxima and minima in the filtered images to detect key points.
4. Using gradient information around these key points to describe them.

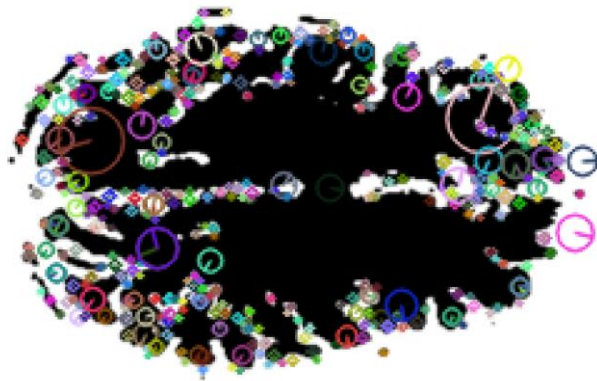


Figure 3.1: SIFT on Processed Image

IV. FEATURE SELECTION

A. CfsSubsetEval Method

A feature selection technique that is based on correlation is CfsSubsetEval. It works by evaluating how features correlate both among themselves and with the class label. The objective is to generate a subset of characteristics with minimal inter-correlation among them and high correlation with the class label. For datasets with a lot of features, this approach is helpful. To ensure that the features chosen to offer substantial and independent information for categorization, the "Best First" search approach is employed to identify the best feature combinations.

```
csf_area
max_area
num_keypoints
cropped_height
cropped_width
gabor_feature_0
mean_descriptor_1
mean_descriptor_8
mean_descriptor_9
mean_descriptor_11
mean_descriptor_12
mean_descriptor_16
mean_descriptor_24
mean_descriptor_26
mean_descriptor_28
mean_descriptor_29
mean_descriptor_31
mean_descriptor_41
mean_descriptor_47
mean_descriptor_50
mean_descriptor_51
mean_descriptor_55
mean_descriptor_58
mean_descriptor_59
mean_descriptor_61
mean_descriptor_68
mean_descriptor_71
mean_descriptor_81
mean_descriptor_88
mean_descriptor_89
```

Figure 4.1: Selected Features of CfsSubsetEval

Search Method:

```
Best first.
Start set: no attributes
Search direction: forward
Stale search after 5 node expansions
Total number of subsets evaluated: 7309
Merit of best subset found: 0.445
```

Figure 4.2: Summary of Selection

B. InfoGainAttributeEval Method

InfoGainAttributeEval measures a feature's information gain relative to the class to determine its value. According to how much they contribute to lowering class uncertainty, the features are ranked using this approach. To make sure that the most important and relevant features are included in the classification model, the features with the largest information gain are chosen for additional examination.

```

Ranked attributes:
0.5299      4 csf_percentage
0.5299      3 csf_area
0.4871     28 cropped_height
0.4795    105 mean_descriptor_59
0.4619      90 mean_descriptor_44
0.4597    107 mean_descriptor_61
0.4495    171 mean_descriptor_125
0.4463    137 mean_descriptor_91
0.4442    139 mean_descriptor_93
0.4413    104 mean_descriptor_58
0.434       73 mean_descriptor_27
0.4267    169 mean_descriptor_123
0.426      140 mean_descriptor_94
0.4233     29 cropped_width
0.4231    126 mean_descriptor_80
0.4219     23 max_area
    
```

Figure 4.3: Selected Features of InfoGainAttributeEval

V. CLASSIFICATION METHODS

A. Random Forest

During training, Random Forest builds several decision trees and then combines them to create a forecast that is more reliable and accurate. It is a group learning technique. A separate subset of the data is used to train each tree, and the majority vote of the trees determines the final classification. This technique works well with big datasets and efficiently manages overfitting. [7]

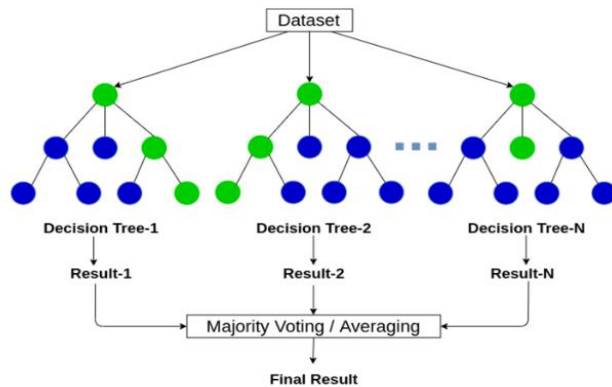


Figure 5.1: Working Principle of Random Forest

Correctly Classified Instances	1972	92.2789 %
Kappa statistic	0.8967	
Mean absolute error	0.1192	
Root mean squared error	0.2048	
Relative absolute error	31.878 %	
Root relative squared error	47.3562 %	
Total Number of Instances	2137	

Figure 5.2: Summary of Random Forest Model

a	b	c	d	<-- classified as
421	43	28	14	a = 1_Non Demented
28	416	12	22	b = 2_Very mild Dementia
6	9	588	6	c = 3_Mild Dementia
0	1	1	542	d = 4_Moderate Dementia

Figure 5.3: Confusion Matrix of Random Forest Model

B. Random Committee

Using a range of base classifiers in place of decision trees, the Random Committee approach has similarities to Random Forest. To lower variance and increase stability, it integrates the predictions made by various classifiers. It uses various samples for training instead of using random subsets of characteristics like Random Forest does. This method improves the accuracy of predictions by combining the strengths of various classifiers. [8]

Correctly Classified Instances	2012	94.1507 %
Kappa statistic	0.9217	
Mean absolute error	0.1103	
Root mean squared error	0.1928	
Relative absolute error	29.4945 %	
Root relative squared error	44.5812 %	
Total Number of Instances	2137	

Figure 5.4: Summary of Random Committee

a	b	c	d	<-- classified as
443	32	20	11	a = 1_Non Demented
18	435	5	20	b = 2_Very mild Dementia
6	5	592	6	c = 3_Mild Dementia
0	1	1	542	d = 4_Moderate Dementia

Figure 5.5: Confusion Matrix of Random Committee

C. K-Nearest Neighbors (KNN)

K-Nearest Neighbors (KNN) is simple, but an effective algorithm widely used for classification and regression problems. The majority vote of a new instance's k-nearest neighbors determines its classification, according to the instance-based learning algorithm K-Nearest Neighbors (KNN). The method measures the distance between instances using a variety of metrics. KNN provides effective results, especially on low-dimensional datasets. [9] The underlying theory is simple: given the data point to be classified (such as point P in Fig. 5.6), calculate the distances between it and the other data points, and then decide on basis of its closest neighbors. To assign a point to the class of the unknown class point, it is looked at the classes of the nearest neighbors of the point and classified them to the class having the most neighbors.

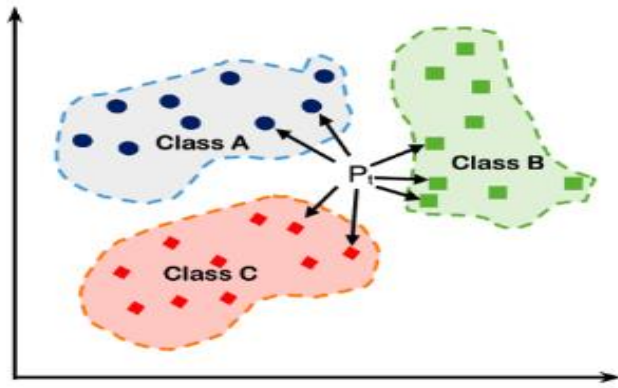


Figure 5.6: Working Principle of K-Nearest Neighbors

Correctly Classified Instances	2051	95.9757 %
Kappa statistic	0.9462	
Mean absolute error	0.0194	
Root mean squared error	0.1357	
Relative absolute error	5.2003 %	
Root relative squared error	31.386 %	
Total Number of Instances	2137	

Figure 5.7: Summary of K-Nearest Neighbors

```

a  b  c  d  <-- classified as
471 22  7  6 | a = 1_Non Demented
  7 452 15  4 | b = 2_Very mild Dementia
  0 17 589  3 | c = 3_Mild Dementia
  0  4  1 539 | d = 4_Moderate Dementia
    
```

Figure 5.8: Confusion Matrix of K-Nearest Neighbors

D. K-Star

Based on an entropy-based distance function, K-Star is an instance-based classifier. Unlike KNN, it is robust to various data distribution types since it considers the likelihood of converting one instance into another. K-Star is more robust to different data distributions by taking data transformation possibilities into account. [10]

Correctly Classified Instances	2047	95.7
Kappa statistic	0.9437	
Mean absolute error	0.0217	
Root mean squared error	0.145	
Relative absolute error	5.7908 %	
Root relative squared error	33.5251 %	
Total Number of Instances	2137	

Figure 5.9: Summary of K-Star

```

a  b  c  d  <-- classified as
466 27 10  3 | a = 1_Non Demented
  7 449 13  9 | b = 2_Very mild Dementia
  5 11 593  0 | c = 3_Mild Dementia
  0  4  1 539 | d = 4_Moderate Dementia
    
```

Figure 5.10: Confusion Matrix of K-Star

CLASSIFICATION METHOD	VALIDATION TECHNIQUES			
	Folds=7	Folds=14	Perc. Split=33%	Perc. Split=66%
Random Forest	0,9115	0,9227	0,8344	0,8927
K-Nearest Neighb.	0,9564	0,9597	0,8994	0,9504
K-Star	0,9550	0,9578	0,8854	0,9559
Random Committee	0,8951	0,9415	0,7974	0,8693

Figure 5.11: Accuracy of Classification Methods with Validation Techniques

VI. PERFORMANCE EVALUATION

Evaluation Metrics: The performance of each classification model is evaluated using several metrics:

- True Positive Rate (TP Rate)
- False Positive Rate (FP Rate)
- Precision
- Recall
- F-Measure
- Matthews Correlation Coefficient (MCC)
- Area Under the ROC Curve (ROC Area)

A. Random Forest Model Performance:

The Random Forest model achieved high accuracy, with a precision of 0.930 and a recall of 0.923 for the non-demented class. The model's overall performance demonstrates its effectiveness in early Alzheimer's detection.

B. Random Committee Model Performance

The Random Committee model showed slightly better results, particularly in the non-demented and mild dementia classes, indicating its robustness in handling diverse data.

C. K-Nearest Neighbors (KNN) Performance

KNN exhibited excellent accuracy, especially in the non-demented class, with a precision of 0.975 and a recall of 0.921.

D. K-Star Performance

K-Star also performed well, particularly in the moderate dementia class, with high precision and recall values, indicating its suitability for this classification task.

CLASSIFICATION METHOD	EVALUATION								
	TP RATE	FP RATE	PRECISION	RECALL	F-MEASURE	MCC	ROC AREA	PRC AREA	ACCURACY
Random Forest	0,917	0,027	0,917	0,917	0,916	0,890	0,989	0,970	92.27%
K-Nearest Neighbors	0,960	0,013	0,960	0,960	0,960	0,947	0,996	0,988	95.97%
K-Star	0,958	0,014	0,958	0,958	0,958	0,944	0,978	0,943	95.78%
Random Committee	0,900	0,032	0,902	0,900	0,900	0,868	0,982	0,947	94.15%

Figure 6.1: Evaluation Table of Classification Methods

VII. DISCUSSION

The current study attempted to exploit the potential applicability of state-of-the-art machine learning techniques to improve the early detection and diagnosis problem of Alzheimer's disease. The focus of this study is on the significant features of these images and the classification of the stages of AD.

The introduction of preprocessing steps in MRI image processing, such as threshold, median filtering, masking, and cropping, has played a significant role in improving the quality of the MRI images used for feature extraction. These steps isolated most effectively the regions of interest that are very critical for accurate classification. PCA is applied as a preprocessing step to reduce dimensionality, while SIFT detects critical points.

We have tried various machine learning models for classification that Random Forest and Random Committee used to compare the results. Also, KNN and K-Star have helped in the classification. Of all, K-Nearest was one of the best models to differentiate between each AD stage. Random Committee and KNN also performed well in dealing with diverse data, giving higher precision and recall values for classes 'non-demented' and 'mild dementia.' K-Star had moderate efficiency in class 'moderate dementia' due to its entropy-based distance function and, therefore, the potential for use in targeted classification.

The findings underscore the need to use comprehensive preprocessing and feature extraction techniques that enhance the performance of classification models used for AD detection. High accuracies and precisions from the models indicate that machine learning would be a crucial aid toward the early diagnosis of Alzheimer's disease, so it is critical for timely intervention and management of the condition. The findings further show that different models may be more appropriate for various stages of AD, thus leaving room for hybrid approaches that could containerize more strengths of the several algorithms.

Expanding the dataset to include a more diverse set of MRI scans that may increase the generalizability of the models. Moreover, deep learning techniques in the image analysis domain, which have shown promising results, need to be researched further to make the detection of AD more accurate and credible. Additionally, clinical data, when integrated with features obtained from imaging, may also be more detailed in developing a diagnosis and understanding of Alzheimer's disease.

VIII. CONCLUSION

In summary, our study clearly illustrated that machine learning models could have great value in the initial detection and diagnosis of Alzheimer's disease with MRI technique. Pre-processing: we used several intense pre-processing and features extraction techniques that would isolate the gray matter structures and filter out the noisy data. Our classification models, notably Random Forest, while not perfect in accuracy, delivered a surprisingly accurate and robust solution to the problem of early AD detection. The potential impact of this study is significant and could lead to better diagnosis and an increased chance of survival of the patient. With this progression, the addition of advanced methods and varied datasets will undoubtedly make these diagnostic aids more effective as the landscape of machine learning expands, thus progressing in the management and treatment of Alzheimer's disease.

REFERENCES

- [1] Ballard, C., Gauthier, S., Corbett, A., Brayne, C., Aarsland, D., & Jones, E. (2011). Alzheimer's disease. *Lancet* (London, England), 377(9770), 1019–1031. [https://doi.org/10.1016/S0140-6736\(10\)61349-9](https://doi.org/10.1016/S0140-6736(10)61349-9).
- [2] Henry-Feugeas, M. C. (2007). MRI of 'Alzheimer syndrome'. *Journal of Neuroradiology*, 34(4), 220-227.
- [3] <https://www.kaggle.com/datasets/ninadaihal/imagesoasis>
- [4] Zhu, S., Xia, X., Zhang, Q., & Belloulata, K. (2007, December). An image segmentation algorithm in image processing based on threshold segmentation. In 2007 third international IEEE conference on signal-image technologies and internet-based system (pp. 673-678). IEEE. H. V./9153027
- [5] Zhu, Y., & Huang, C. (2012). An improved median filtering algorithm for image noise reduction. *Physics Procedia*, 25, 609-616.
- [6] Kumar, G., & Bhatia, P. K. (2014, February). A detailed review of feature extraction in image processing systems. In 2014 Fourth international conference on advanced computing & communication technologies (pp. 5-12). IEEE.
- [7] Henry-Feugeas, M. C. (2007). MRI of 'Alzheimer syndrome'. *Journal of Neuroradiology*, 34(4), 220-227.
- [8] Ho, T. K. (1998). The random subspace method for constructing decision forests. *IEEE Transactions on Pattern Analysis and Machine Intelligence*, 20(8), 832-844. <https://doi.org/10.1109/34.709601>
- [9] Cover, T. M., & Hart, P. E. (1967). Nearest neighbor pattern classification. *IEEE Transactions on Information Theory*, 13(1), 21-27. <https://doi.org/10.1109/TIT.1967.1053964>
- [10] Cleary, J. G., & Trigg, L. E. (1995). K*: An instance-based learner using an entropic distance measure. *Proceedings of the 12th International Conference on Machine Learning* (pp. 108-114).

Industry 4.0 Based Customer-Oriented Unmanned Production System

AHMET SAİT MÜLAYİM¹, YUSUF KEREM TÜRKMEN¹, MERAL ÖZARSLAN YATAK¹

¹ Gazi University, Ankara/Türkiye, asmulayim@gmail.com

¹ Gazi University, Ankara/Türkiye, yusufkeremtrkmen@gmail.com

¹ Gazi University, Ankara/Türkiye, ozarlanm@gazi.edu.tr

Abstract - This study presents an Industry 4.0-based unmanned, customer-oriented automated production system that connects to the Internet thanks to the Internet of Things (IoT). Automation systems are manufacturer-managed systems initially set once in mass production manufacturing processes and continue production by meeting only maintenance requirements. Product design and ordering systems can be unmanned like automation systems to increase production speed and product efficiency. Customized manufacturing can also be added to this system to reduce waste. In this study, as a case prototype, an automatic nuts-filling machine (ANFM) design and implementation was realized. This prototype produces unmanned products based on the order received from the customer. It lists the order received with Google Forms in Google Sheets and creates a data bank. Each order has a unique number so the machine knows when to work. In the prepared ordering interface, the customer is given the required information thanks to a simplified order form that serves a certain range. The design for ANFM is a linear conveyor belt with six units at one station. Each unit has its own hardware for each nuts. As a result, the Industry-4.0-based production automation system increased the potential to provide customized solutions for customer demands. The developed system made production processes more flexible and scalable by increasing customer engagement.

Keywords - Industry 4.0, Internet of Things, automatic production system, customer-oriented system, conveyor

I. INTRODUCTION

NOWADAYS, the design and implementation of customer-oriented production systems get easier with Industry 4.0 by using Internet of Things (IoT) and these systems increase the fast and effective reply to the customer's requests. The industrial automation system in the production phase is composed of sensors, robotic components, control systems, and collecting and analyzing data processes. This system is digitalized with Industry 4.0 and the Internet of Things (IoT) to be efficient, reliable, and flexible. Using an industrial automation system decreases the cost, increases production quality, and optimizes the ability to make fast decisions with real-time data analysis. Firms can adapt to changing marketing requests and global competition conditions thanks to the flexibility and scalability of these systems.

Industrial automation systems become a flexible, autonomous, and increasing productivity a new generation cyber-physical system (CPS) with the Industry 4.0 integration.

The machines and the systems connect to each other on the Internet with Industry 4.0 and optimize themselves by sharing real-time data.

Industry 4.0 enables to form of smart factories and manufacturing plants with data analysis and real-time monitoring by integrating IoT technologies. The basic IoT components include hardware such as sensors, actuators, and embedded devices, as well as middleware and visualization and analytics tools accessible on various platforms [1]. IoT technologies enable remote monitoring and control of physical objects via network connectivity. This pervasive interconnection of diverse devices facilitates innovative applications across various domains, from small-scale embedded electronics to large-scale systems like automated buildings and vehicles [2].

Customer-oriented production systems gain flexibility with reconfigurability to the customer needs, production uncertainties, and market changes by using Industry 4.0 technology [3]. Industry 4.0 is intricately linked to a subset of IoT, the Industrial Internet of Things (IIoT) paradigm, characterized by robust and exploratory interactions in the industrial area [2, 4, 5]. This integration supplies a data-driven production process by supplying smart production systems.

IoT solutions feed enterprise decision-making systems with real-time status data from the factory floors, including information about people, materials, vehicles, machinery, and environments. Design and manufacturing systems can be maintained and optimized without human intervention by using those data to automate workflows and procedures [6]. The core technology for IoT applications is embedded systems, which allow devices to be seamlessly integrated for real-time data processing and communication [7].

The rapid evolution of industrial processes has been driven by advancements in high-speed, cost-effective electronic circuits, accelerated signal processing techniques, and cutting-edge manufacturing technologies [8]. The advancement of IoT has been greatly influenced by innovations in sensor technologies [9, 10]. These improvements direct people to study revealing on using IoT for production and manufacturing lines. Nissanka et al. proposed the IoT framework for monitoring and managing an automatic storage and retrieval system within a manufacturing line. [11]. Lu and Ju proposed a Service-Oriented Architecture method for incorporating business applications into the design of smart manufacturing

system based on the concept of cyber-physical manufacturing services [3]. Wan et al. designed a load-balancing mechanism that concentrates on intelligent equipment in the smart factory. They also proposed the ontology modeling and the Jena tool. They implemented a case study to verify their proposal. The results showed that the scheduling method based on Jena reasoning and CNP technology impacted the load-balance of intelligent equipment. [12]. Shah et al. presented the design of an IoT testbed using a multi-stage centrifugal pumping system outfitted with noninvasive IoT vibration sensors emphasizing data integrity. They examined the properties of the data gathered from these IoT devices [13].

In this study, an implementation of an industry 4.0-based IoT application of an automatic custom-made production system is presented. An automatic nuts-filling machine (ANFM) design and implementation are done. Depending on the customer's order, this prototype generates unmanned products and a data bank and lists the order obtained via Google Forms in Google Sheets. This study aims to make significant contributions to the literature in this field by targeting the use of IoT Systems, Industry 4.0, unmanned production systems, and customer-oriented production systems. While IoT enables this machine to work connected to the internet, Industry 4.0 enables this machine to be involved in a smart, flexible and automated production process. Just as automation systems is unmanned, the product design and ordering systems are also unmanned to increase production speed and efficiency in this system. This approach also reduces waste through customized manufacturing.

For the presentation of the study, in the "Introduction" section, general information about Industry 4.0 and the IoT concept and their usage for production and manufacturing systems with the literature are given. In the second section, "Material and Method", the system architecture, design steps, and hardware components are explained. Additionally, the software and flowchart are given in this section. The third section is Discussion section. The outputs and evaluations are done in this section. The last section is "Conclusion" section and it contains the general acquisition and future studies.

II. HARDWARE DESIGN AND IMPLEMENTATION

Customer-oriented in other words order-based production systems are automated, requiring no human involvement from the manufacturing order to the finished product, in contrast to the different production methods. These systems initiate and finish the process by directly accepting the production order from the customer. The manufacturer provides the raw materials, completes the operations, and delivers the finished product once the consumer demands a certain product.

Orders are created by the customer and sent directly to the production system in order-based automated production systems. The production system automatically follows the order. Raw materials are always available since each machine produces in its area of expertise, which speeds up and improves production efficiency. The production quality is improved and the error rate is decreased when human assistance is not present.

The proposed ANFM in this study and built to be an example of an order-based production system, produces unmanned production according to the order received from the customer. The implemented ANFM system is formed of four units:

1. Linear Conveyor Band Unit
2. Cup Silo Unit
3. Main Chamber
4. Material Silo Unit

The main system diagram with the numbered sections can be seen in Figure 1. The system begins to work by taking an order from the customer. In the first step, a cup is put on the conveyor band from the cup silo unit when an order is taken. The conveyor band moves. The cup sensed by an infrared sensor is stopped under the main chamber. Each material silo unit begins to fill the cup according to the customer's order. When all the units finish the filling process, the conveyor band moves again and the cup reaches the delivery point.

A. Mechanic System Design

In this section, the sub-units are explained separately. The first unit is the Linear Conveyor Band Unit as seen in Figure 2. This unit consists of an iron frame (1) made from two plates, a tensioning mechanism (2) for the conveyer band, a plastic conveyer band (3), an opposing dual bearing assembly (4), a 12 V DC wiper motor (5) for the drive system, an infrared sensor (6) for sensing the cup, and an LCD screen (7) for showing the customer and order information. Additionally, an electronic card design (8) is implemented with ESP32 to control the main conveyor and to send/receive data to/from the material silo unit.

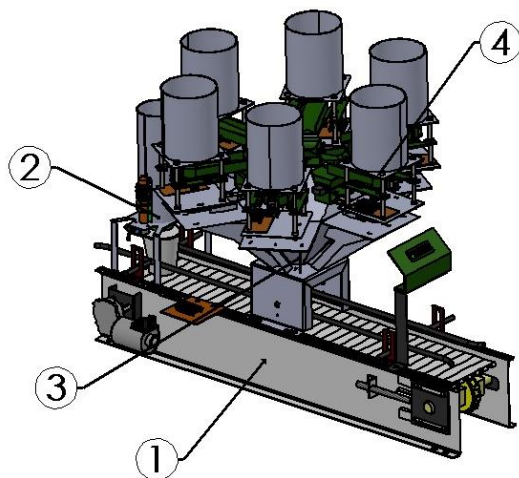


Figure 1: The main system diagram

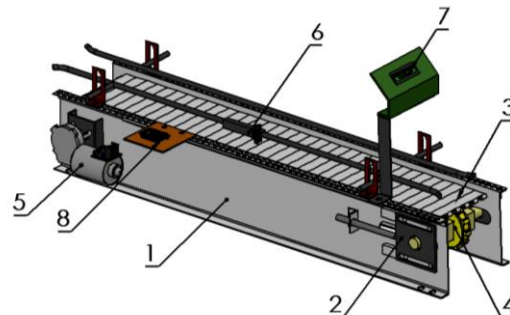


Figure 2: The linear conveyor band unit

The second unit is the Cup Silo Unit as seen in Figure 3. This unit consists of a silo (1) that holds the cups, a helosonic assembly (2) that separates the cups from each other and puts it on the conveyor band, a 5V step motor (3) to actuate the helosonic assembly. The step motor turns once every time an order comes. The system puts a cup on the conveyor.

The third unit is the main chamber as seen in Figure 4. This unit is a hexagonal funnel-shaped structure. Each side of this unit has a material silo unit. Thanks to the funnel structure, the material of each unit is transferred to the cup below the main chamber.

The fourth and last unit is the material silo unit as seen in Figure 5. This unit is composed of two parts. The first part is the silo section. There is a silo (1) that holds the material, a vibratory carrier (2) that transfers the material to the dosage chamber, and a vibration motor (3) that provides the vibration. The second section is a mechanic transfer section of the material. The second part consists of a load cell (4) that senses the weight of the material, a dosage chamber (5), a servo motor (6) that provides the movement of the dosage chamber, and an ESP32 control card (7) that controls these units. This unit starts to run when the cup reaches the main chamber unit. The vibration motor fills the dosage chamber. When the weight data from the load cell is equal to the weight of the customer's order, the vibration motor stops and the servo motor empties the material into the main chamber.

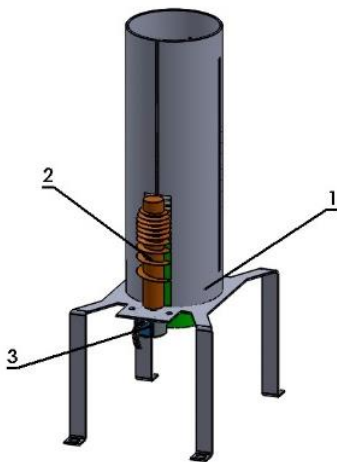


Figure 3: The cup silo unit

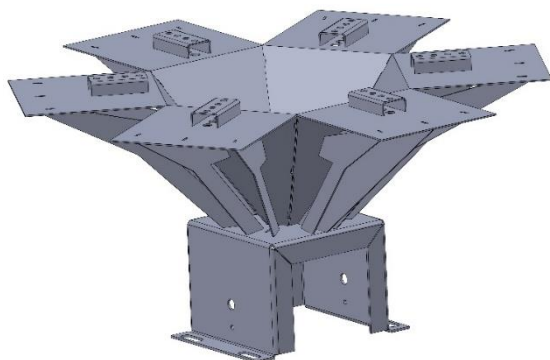


Figure 4: The main chamber

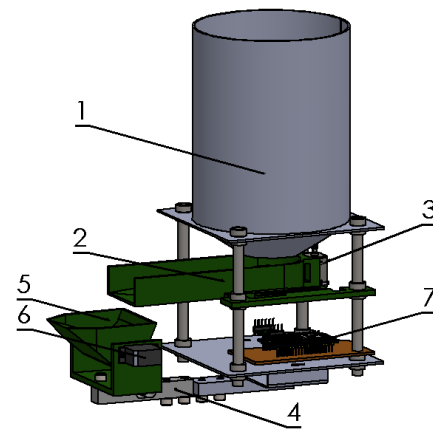


Figure 5: The material silo unit

B. Electronic System Design

There are seven control cards in the system; one control and communication card in each silo unit, and a main control card that provides conveyor control and communication by controlling these cards. The main control with the communication card is seen in Figure 6. As considered easy implementation, easy usage, low cost, and low power consumption, the Esp32-WROOM microcontroller module with Wi-Fi + Bluetooth integration was preferred in this study. Esp32 connects to the Internet via a Wi-Fi module for data transfer and receives data from Google Sheets.

Customer data and order date are displayed on the LCD screen in the system. ULN2003 step motor driver and step motor, which is a low-cost motor with an adjustable number of rotation turns, was preferred for the dropping process of the cup on the conveyor when the order arrived. Considering the cost and robustness, a 12 V wiper motor with an L298N driver was preferred for the band movement. The TCRT5000 infrared sensor in the system provided the data that the glass had reached the main chamber.

In the silo control unit shown in Figure 7, Esp32-WROOM microcontroller module is used as microcontroller board. The materials are transported from the silo to the dosage chamber by vibratory carrier. This transportation process is done by vibration. This vibration is provided by the vibration motor. The vibration motor is driven by a transistor.

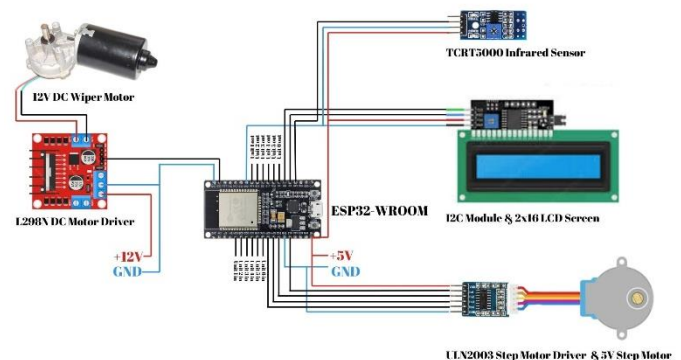


Figure 6: Main control card (Linear conveyor band unit control and communication card)

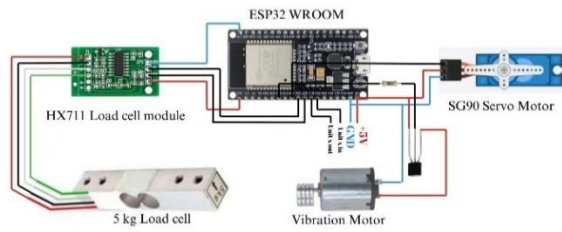


Figure 7: Material silo unit control and communication card

The weight of the material is sensed by a load cell with a capacity of 5 kg. The resistance value in the load cell is processed with the HX711 load cell module and made suitable for the controller. The SG90 servo motor used in the system was preferred because it is cheap and easily accessible.

III. SOFTWARE DESIGN

ANFM has been designed to facilitate a fast and sensitive filling process. This machine supplies reducing waste and increasing efficiency. The system software determines the system's performance and accuracy. The software is compulsory for optimizing and tracking the filling amount, speed, and quality. This section presents the software properties and their contributions to system performance.

In the ANFM system, Google Forms are used to receive the order from the customer. This form sample is shown in Figure 8. Each order entered from Google Forms is registered to Google Drive. It saves all entered data in Google Sheets. Thanks to this system, it is possible to examine and access the order.

The software was created in two parts. The first part ensures the main tasks and communication with each silo unit. The flowchart for the central part is seen in Figure 9. The central unit first adjusts the LCD settings, makes the necessary pinadjustments, and connects to Wi-Fi. Through the Wi-Fi connection, it downloads the table with the order list. It checks the new data in the downloaded table. If there is no new order, it downloads the order list again. If there is new data, it checks

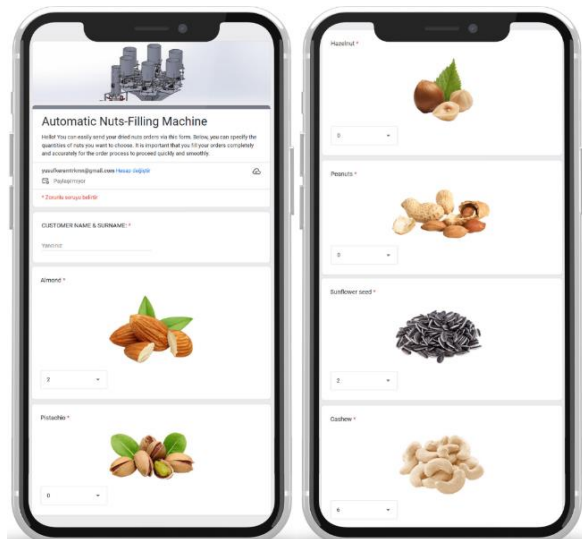


Figure 8: The Google Form Interface

if the order is correct. If the order is incorrect, it stops the software. If the order is accurate, it prints the customer name and date on the LCD screen. After writing, the cup to be filled is placed on the conveyor band unit. When the cup is placed, the band is moved. The band is moved until the glass is under the main chamber. With the help of the sensor, the band is stopped when the glass is under the chamber. A message is sent to the silo cards. The silo waits until it receives data from the silo cards. The stopped band moves the system again and the software returns to the beginning.

The second software part is the silo control software and is seen in figure 10. First of all, pin adjustments are made. The initial settings of the load cell and Wi-Fi connection are made after the pin adjustments made. The material silo unit software waits for data from the central software after the connection is made. The order list is downloaded via Wi-Fi connection. In the downloaded table, it checks that the order comes without errors. If the order is incorrect, it stops the software. If the order is correct, it fills a dosage chamber until it reaches the weight in the order. When it reaches the desired weight, it fills the nuts

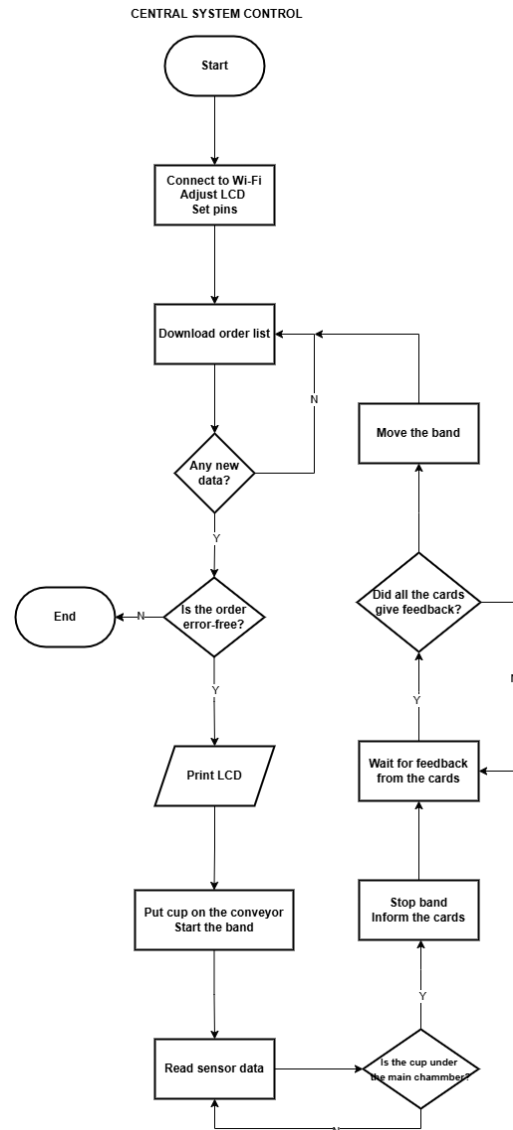


Figure 9: The flowchart of the central system

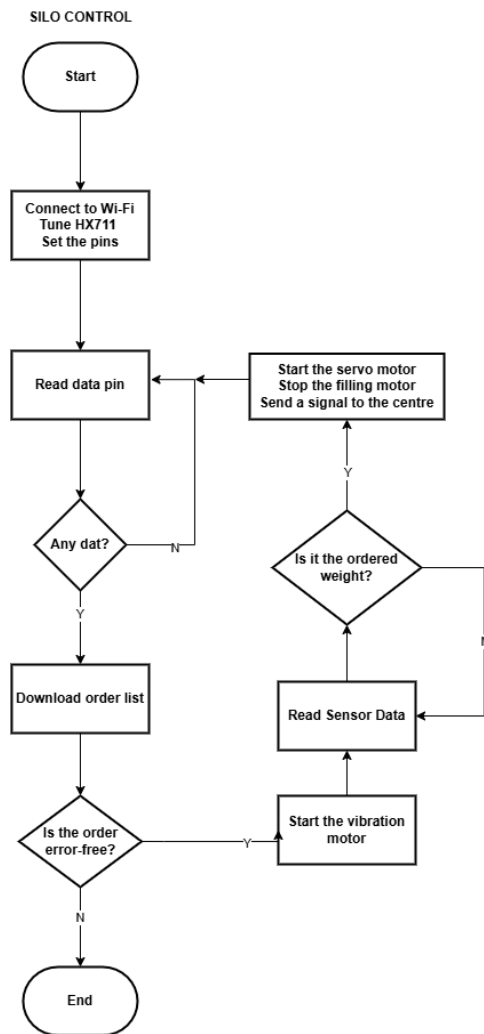


Figure 10: The flowchart of the silo control

from the chamber into the cup. When the filling into the cup is completed, it sends a notification to the central part and returns to the beginning.

The ANFM was implemented to be a sample for an order-based unmanned industrial production system according to the design and software criteria. The implemented system is shown in Figure 11. This system consists of mechanic parts, electronic assemblies, and wireless communication. IoT enables this system to connect to the Internet and Industry 4.0 enables the system as an automatic production system.

IV. CONCLUSION

This study has been realized as an automatic and efficient filling system for nuts sector. The implemented ANFM is capable of filling various types of nuts precisely and quickly. The system has an ability to fill the nuts ordered types and weight accurately.

The machine minimizes human errors encountered in manual filling processes and increases production capacity. In addition, the software and hardware infrastructure used can be easily updated and expanded according to future requirements. This makes it possible to adapt to changing nut types and different filling requirements.



Figure 11: The implemented ANFM

In conclusion, this study presents an effective automation solution that meets the criteria of speed, accuracy and efficiency in the nuts filling process and has the potential to be applied on an industrial scale.

ACKNOWLEDGMENT

This study was conducted as a project of bachelor's thesis at Gazi University, Technology Faculty.

REFERENCES

- [1] C. Alexakos, C. Anagnostopoulos, and A. P. Kalogeras, "Integrating IoT to manufacturing processes utilizing semantics," in *Conf. Rec. 2016 IEEE 14th Int. Conf. on Industrial Informatics*, pp. 154-159. Available: <https://dx.doi.org/10.1109/indin.2016.7819150>
- [2] R. Badarinath and V. V. Prabhu, "Advances in Internet of Things (IoT) in Manufacturing", in *Conf. 2017 IFIP Int. Conf. on Advances in Production Management Systems*, pp. 111-118. Available: https://doi.org/10.1007/978-3-319-66923-6_13
- [3] Y. Lu and F. Ju, "Smart manufacturing systems based on cyber-physical manufacturing services (CPMS)," *IFAC-PapersOnLine*, vol.50, no. 1, pp. 15883-15889, 2017. <https://doi.org/10.1016/j.ifacol.2017.08.2349>
- [4] C. Alexakos, C. Anagnostopoulos, A. Fournaris, C. Koulamas, and A. Kalogeras, "IoT Integration for Adaptive Manufacturing," in *Conf. 2018 IEEE Int. Symp. on Object-Oriented Real-Time Distributed Computing* [Online]. Available: <https://dx.doi.org/10.1109/isorc.2018.00030>
- [5] G. Saravanan, S. S. Parkhe, C. M. Thakar, V. V. Kulkarni, H. G. Mishra, and G. Gulothungan, "Implementation of IoT in production and manufacturing: An Industry 4.0 approach," *Materials Today: Proceedings*, vol. 51, pp. 2427-2430, 2022. Available: <https://doi.org/10.1016/j.matpr.2021.11.604>
- [6] C. Yang, W. Shen, and X. Wang, "The Internet of Things in Manufacturing: Key Issues and Potential Applications," *IEEE Systems, Man, and Cybernetics Magazine*, vol. 4, no. 1, pp. 6-15, 2018, doi: [10.1109/msmc.2017.2702391](https://doi.org/10.1109/msmc.2017.2702391).
- [7] F. Duran and M. Teke, "Akıllı Yol Durum Sensörü Tasarımı," *Uluslararası Mühendislik Araştırma ve Geliştirme Dergisi*, pp. 396-401, 2019, doi: [10.29137/umagd.510777](https://doi.org/10.29137/umagd.510777).
- [8] T. Kalsoom *et al.*, "Impact of IoT on Manufacturing Industry 4.0: A New Triangular Systematic Review," *Sustainability*, vol. 13, no. 22, p. 12506, 2021, doi: [10.3390/su132212506](https://doi.org/10.3390/su132212506).
- [9] T. Ercan and M. Kutay, "Endüstriye nesnelerin interneti (IoT) uygulamaları," *Afyon Kocatepe Üniversitesi Fen ve Mühendislik Bilimleri Dergisi*, vol. 16, no. 3, pp. 599-607, 2016, doi: [10.5578/fmbd.43411](https://doi.org/10.5578/fmbd.43411).

-
- [10] H. Mamur, Z. Dicle, and S. Erdener, "IoT Based Smart Embedded System Design for Indoor Plants Tracking," *Uluslararası Muhendislik Arastirma ve Gelistirme Dergisi*, vol. 14, no. 2, pp. 611-618, 2022, doi: [10.29137/umagd.1078968](https://doi.org/10.29137/umagd.1078968).
- [11] S. Nissanka, M. Senevirathna, and M. Dharmawardana, "IoT based automatic storing and retrieval system," in *2016 Manufacturing & Industrial Engineering Symposium (MIES)*, 2016: IEEE, pp. 1-5. doi: [10.1109/MIES.2016.7780259](https://doi.org/10.1109/MIES.2016.7780259)
- [12] J. Wan *et al.*, "Toward Dynamic Resources Management for IoT-Based Manufacturing," *IEEE Communications Magazine*, vol. 56, no. 2, pp. 52-59, 2018, doi: [10.1109/mcom.2018.1700629](https://doi.org/10.1109/mcom.2018.1700629).
- [13] D. Shah, J. Wang, and Q. P. He, "An internet-of-things enabled smart manufacturing testbed," *IFAC-PapersOnLine*, vol. 52, no. 1, pp. 562-567, 2019. <https://doi.org/10.1016/j.ifacol.2019.06.122>

Four Years Update of LPG Conversion Field Status of a Spark Ignition Internal Combustion Engine Passenger Vehicle

EYUB CANLI¹

¹ Selcuk University, Konya/Turkey, ecanli@selcuk.edu.tr

Abstract - Previously, a report on four years field operation of a LPG converted gasoline spark ignition internal combustion engine passenger vehicle was published. The report lays out four years data of gasoline and LPG fuel consumption, alongside price data of the fuels and some periodic maintenances. The present paper updates the previously presented data by adding another four years by the period between 2020 and 2024. This latter period includes a specific heavy maintenance incidence that sheds light to long term benefits assessment of the LPG conversion via a solid example from real-world operation. This work utilizes net present value and net future value approaches to evaluate LPG conversion investment whether it is beneficial in terms of economic terms. Also, the gross exhaust emissions by LPG combustion are approximated and compared to gasoline combustion emissions in order to evaluate environmental impacts. Future maintenance issues are laid down and general literature on LPG conversion and other fuel conversion types are evaluated.

Keywords - Economic analysis, Fuel conversion, Liquid petroleum gas, Net present value.

I. INTRODUCTION

LONG term evaluation of Liquid Petroleum Gas (LPG) conversion of gasoline Spark Ignition (SI) Internal Combustion Engine (ICE) by means of practical real world data is somehow absent. The short-term benefit of LPG conversion is less fuel cost per travelled distance. Also, it is known that the hydrogen to carbon ratio in LPG fuel is higher than gasoline, by considering octane for gasoline and a mixture of propane and butane for LPG. However, converting an engine from its design fuel to another alternative fuel that has differences in its fuel properties may create earlier depreciation cost issues even though some precautions in terms of engine and fuel systems operational parameters are applied. Accordingly, field data is very important. This work provides the field data by an eight years period of a passenger vehicle.

Previously two earlier documents were published that provide half of the data of the present report [1,2]. In the previous reports, fuel consumption per kilometer was stated, basic payback period and net present value of the LPG conversion investment were calculated and given. The fuel prices were monitored by two-dimensional line charts using nominal and relative values based on gold and USD values. Since LPG has a higher hydrogen to carbon ratio compared to gasoline, positive environmental impact was approximated in

terms of emitted carbon dioxide amount. For that first four years period, LPG conversion investment was found beneficial both in terms of economics and in terms of exhaust emissions. However, in the conclusion parts of the reports, long term depreciation cost was mentioned as it should be monitored and reported in the future. Last but not least, the earlier documents indicated a slight fuel consumption reduction of the engine, which was also noted as a point to be tracked in the future.

In the present document, field data of four additional years is presented alongside a major rectification cost due to the LPG conversion related effects. The rectification is about engine valves. This latter four years period also contains information about global high inflation and changes in commodity prices relative to fiat currencies. Accordingly, the present paper improves and matures conclusions of the previous four years period examination by an additional four-year field data.

II. METHODOLOGY

The field data has been being obtained by recording travelled kilometer every time a fuel purchase is realized, together with the fuel amount and price value information, for a SI ICE passenger vehicle, which's engine and fuel system is converted to LPG compatible one. The LPG conversion kit necessitates partial gasoline usage at the minimum level together with LPG usage as the major source of fuel and hence the energy. So, one can mention about a dual fuel operation where gasoline plays a role about 20% of the total fuel consumption of the dual operation. When above mentioned data is gathered as unprocessed raw data, data reduction can be done for deriving new parameters either by using or not using additional market data that is available in the open literature.

Un processed data is visualized via two-dimensional line plots and then a simple filtering is applied to clear outliers, by applying a basic but nested "if – else" logic test where upper and lower limits are set for LPG and gasoline consumption per kilometer, based on the experience from the previous works. Also, linear regression is employed in order to mark and show the general trend of the fuel consumption per kilometer for the whole eight-year period and in the sub-periods of the total.

The net present value of the possible benefits of the LPG conversion is obtained by a different approach compared to the previous papers. The eight-year period total fuel amounts and travelled kilometers amount is used together with the present-day fuel prices.

The carbon dioxide emission calculation and accordingly the evaluation of the LPG conversion of the gasoline SI ICE in terms of environmental impact, based on the field data is done by the ratios provided in the previous papers, where stoichiometric combustion and chemical composition and formulas were assumed.

The most critical part in the present report is that a major rectification cost was realized in July 2024 and the cost was due to the LPG conversion. The intake and exhaust valves were

renewed, and the engine cap was grinded. This cost is the only major cost throughout the lifetime of the LPG converted SI ICE.

III. RESULTS

In the following, Figure 1 shows eight years period of LPG and gasoline dual fuel operation fuel consumption per kilometer via several versions of the same plot, in order to discuss the behavior of the LPG converted vehicle in different time frames.

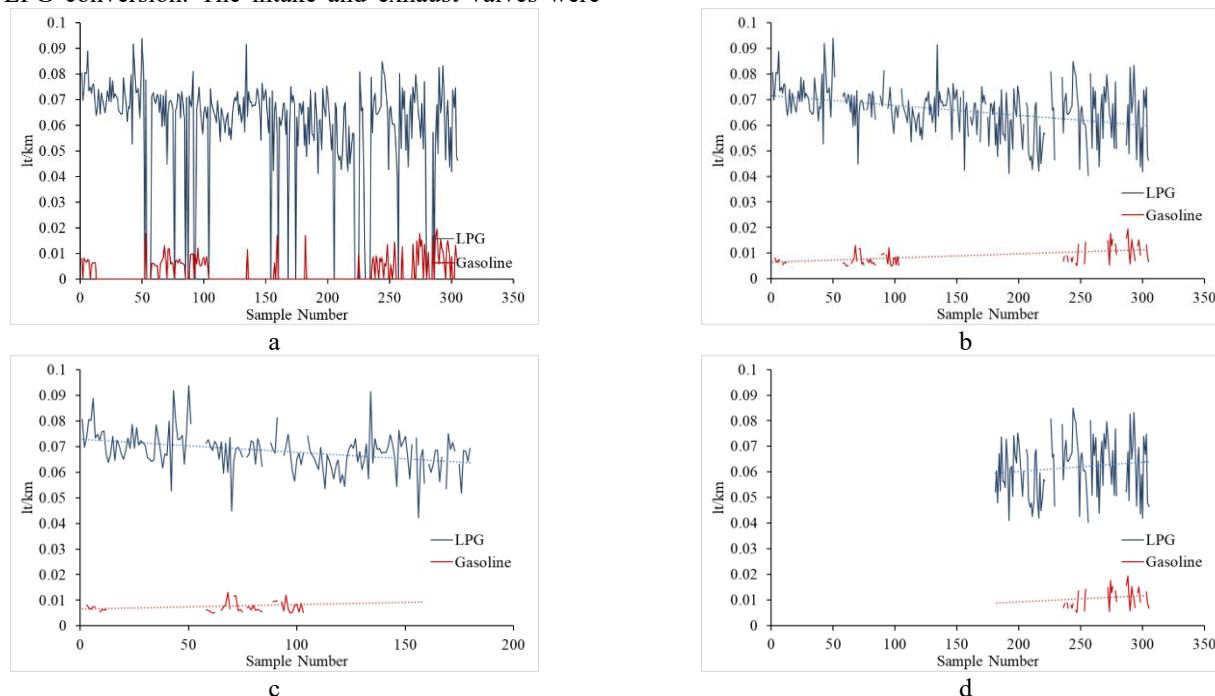


Figure 1: Two dimensional line plots of the LPG and gasoline fuel consumption per kilometer data in the eight years period by 305 sample points. a – Unfiltered and unprocessed data, b – filtered data, c – first four years, last four years.

Figure 1 shows that slightly decreasing fuel consumption of the system in the first four years period should be due to the gradual deformation of the intake and exhaust port valves of the engine. After the rectification of the valves and related equipment and parts, we see that the fuel consumption amount is restored to its initial values.

The average fuel consumption results from the eight years period, from two four years periods, and from two different segmentation of the total time are shown in Table 1. The table supports the evaluations that are given for Figure 1. In general, fuel consumption slightly decreases towards the end of the first four-year period. However, after the rectification, the fuel consumption restores to its initial values. The table shows total consumed LPG, total consumed gasoline and total travelled kilometers for different periods of time. The eight-year period has 305 sample points. Therefore, the whole period is also divided into three, yielding 100 samples periods, and also divided to six that gives 50 samples periods. The logic here is to show the effect of the engine deformation due to the LPG utilization.

Table 1: Average fuel consumption values for different time segmentations of the eight years period.

Time segmentation	LPG (lt)	Gasoline (lt)	km	LPG (lt/km)	Gasoline (lt/km)	LPG + Gasoline (lt/km)
8 years	8932.15	2111.64	150155.12	0.0595	0.0141	0.0735
First four years	5453.53	1012.29	87861.82	0.0621	0.0115	0.0736
Last four years	3478.62	1099.35	62293.30	0.0558	0.0176	0.0735

First 100 samples	2968.78	568.50	46832.92	0.0634	0.0121	0.0755
Second 100 samples	3145.43	586.59	52168.00	0.0603	0.0112	0.0715
Third 100 samples	2675.84	916.16	48730.50	0.0549	0.0188	0.0737
First 50 samples	1503.97	128.63	21068.92	0.0714	0.0061	0.0775
Second 50 samples	1464.81	439.87	25764.00	0.0569	0.0171	0.0739
Third 50 samples	1550.04	185.12	24571.80	0.0631	0.0075	0.0706
Fourth 50 samples	1595.39	401.47	27596.20	0.0578	0.0145	0.0724
Fifth 50 samples	1269.28	538.26	24599.00	0.0516	0.0219	0.0735
Sixth 50 samples	1406.56	377.90	24131.50	0.0583	0.0157	0.0739

The price changes during the eight years period are tried to be illustrated by Figure 2. The figure emphasizes the domestic price instability periods and changing price ratio between the gasoline and the LPG. Since petroleum and its derivatives have globally bounding prices, one may evaluate that Figure 2 also gives an idea about the global inflation. This may have affected the commodity prices including petroleum and its derivatives. Accordingly, the net present value calculation in the present document may not be regarded as definitive and should contain some sort of uncertainty. A better approach, as a future goal, is calculating net present value of the investment by using the past inflation data to adjust the prices.

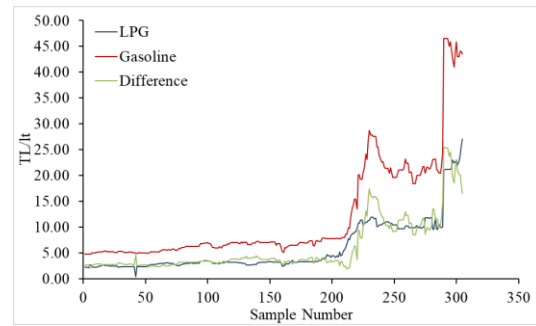


Figure 2: Two-dimensional line plots of the prices of the fuels for the eight years period by 305 sample points.

According to the obtained data and the net present value approach in the present work, the savings or economical benefits by the LPG conversion is about between 60,000.00 ₺ and 85,000.00 ₺. These numbers are about two to three times the major rectification cost that is realized in July 2024. Accordingly, unlike the previous reports, the LPG conversion now seems like an application that should be carefully thought and decided. Decision makers should consider several different scenarios and make their decisions.

By the consumed LPG fuel, a total of 14,390 kg CO₂ was emitted. On the other hand, 4,800 kg CO₂ was emitted due to the burned gasoline fuel. One may expect higher CO₂ emission values if only gasoline was used since hydrogen to total weight of the gasoline is 16% while that ratio for LPG is 19%.

IV. CONCLUSION

According to the eight years period of utilization of a LPG converted gasoline SI ICE, it can be asserted that long term early depreciation costs and other implicit/subtle costs such as the necessity for chasing additional maintenance and documentation due to LPG conversion can barely compensated by the benefits, i.e., savings between each refilling period by the low LPG fuel price. Accordingly, decision makers should either decide to utilize LPG conversion based on below conditions/circumstances or avoid LPG conversion:

- Short term operation period and in the following, transferring the system to an alien part.
- Higher price difference ratios of the gasoline and LPG fuel couple compared to the ratios in this eight years period.
- Exhaust emission regulations or aims for less carbon dioxide emissions...
- An intermediate investment with the savings since major depreciation costs occur after significantly long times

The finding of the reports about the first four years period, which implies a decreasing fuel consumption amount per kilometer as time passes and as the system is getting older, seems to be changed by the rectification. This may imply that different LPG conversion applications may create similar or adverse effects.

Global inflation and commodity prices should also be monitored by the decision makers on whether LPG conversion is logical.

REFERENCES

- [1] E. Canli, "Technical and Economical Assessment of Liquid Petroleum Gas Modification/Conversion on a Gasoline Engine in Turkey for Time Interval between 2016-2020," International Conference on Engineering Technologies (ICENTE'20), pp. 310-316, November 2020.
- [2] E. Canli, "Technical and economic assessment of liquid petroleum gas modification/conversion on a gasoline engine in Turkey for time interval between 2016-2020," *Selcuk University Journal of Engineering Sciences*, vol. 20, iss. 2, pp. 38-45, September 2021.

An experimental study on the effect of colemanite concentrator waste on gamma-ray beams, setting time, and compressive strength properties in cement-based mortars

ŞEVKİ EREN¹, DOĞAN YAŞAR², SELAHATTİN GÜZELKÜÇÜK³, GÖKHAN EKİNCİOĞLU⁴,
YUNUS KARATAŞ⁵

¹Kırşehir Ahi Evran University, Kırşehir/Türkiye, seren@ahievran.edu.tr

²Kırşehir Ahi Evran University, Kırşehir/Türkiye, dogan.yasar@ahievran.edu.tr

³Ankara University, Ankara/Türkiye, sguzelkucuk@ankara.edu.tr

⁴Kırşehir Ahi Evran University, Kırşehir/Türkiye, gekincioglu@ahievran.edu.tr

⁵Kırşehir Ahi Evran University, Kırşehir/Türkiye, ykaratas@ahievran.edu.tr

Abstract - The current study presents the effects of colemanite concentrator waste (CW) substitution in cement-based mortars on the gamma-ray shielding performance, setting time, compressive strength, and pulse velocity properties. Cement mortars were prepared to substitute different proportions of CW particles, up to 4-weight percent of cement. The gamma-ray (Cs-137-662 keV) shielding performance was investigated with an experimental study. Increasing CW substitution causes a decrease in compressive strength and an increase in setting time. It was found that the lead equivalent levels of materials with CW added and control specimens with a similar thickness differ significantly from one another. The incorporation of CW contributed to the attenuation of ionizing radiation including gamma rays.

Keywords - Colemanite concentrator waste, radiation shielding, gamma-ray shielding, compressive strength, cement-based mortar.

I. INTRODUCTION

IONIZING radiation is recognized to be harmful to human health, and shielding methods, time, and distance can provide protection from these radiation sources [1]. The attenuation characteristics of shielding materials are influenced by various factors, including atomic mass number, density, thickness, cross-section, and photon energy [2]. Numerous materials, each with unique properties, can be used as radiation shields, such as iron, water, lead, compacted soil, ordinary and heavyweight concrete, and iron [3-5]. High-density concrete known as "radiation shielding concrete" stops potential X-ray, gamma, and fast-moving neutron leaks in a variety of settings, including hospital nuclear power plants and X-ray or radiology department rooms [6]. It is the most commonly utilized shielding material due to its affordability, ease of molding, and suitability for neutron shielding [7]. In recent years, the growing interest in radiation-shielding concrete mixtures has coincided with an increased focus on creating different concrete mixtures and using different additives [8-10]. Because of its accessibility and affordability, colemanite has been investigated for use as

an aggregate or binder in geopolymers, lightweight concretes, bricks, and regular cements and mortars. The authors are also still investigating its potential for use in radiation-shielding concrete [11]. Below are the findings of studies on the gamma-ray attenuation capabilities of colemanite concentrator wastes in cement-based composites that have been published in the literature (Table 1).

Upon analyzing the aforementioned literature studies, it is observed that certain concretes containing colemanite improve attenuating gamma rays [15, 17, 19], while other studies report no discernible improvement [12, 13, 16, 18]. In this context, there are differences in the literature results. The objective of this research is to evaluate the compressive strength, pulse velocity, and setting time and to investigate the attenuating effects of gamma rays against the ionizing radiation of colemanite concentrator wastes experimentally and through an interdisciplinary study. The present study provides important technical support for the use of CW in cement-based mortars.

II. MATERIALS AND METHODS

A. Materials

The cement mortars were produced by Portland cement (CEM I 42.5 R), CW powders, standard sand (conforming to TS EN 197-1), and tap water. CW was supplied by Emet Boron Operations Directorate Emet/Kütahya/Türkiye. The chemical composition of the Portland cement is given in Table 2. SEM and EDX images of the CW powders are presented in Figure 1 and the particle size distribution of CW powders obtained by the laser diffraction technique is presented in Figure 2. As seen in Figure 2, the particle size of CW powders varies between 1.65 μm and 1260 μm and the d10, d50, and d90 grain diameter values of CW are 72,6 μm , 157 μm , and 366 μm , respectively.

Table 1: Published results in the literature.

Authors	Testings and results				
	Composite type/specification	Colemanite ratios/specification (wt-%)	Setting time	Compressive strength	Gamma-ray shielding/specification
Öztürk et al. (2020) [12]	Alkali-activated cement mortar mixtures (AAC), Boron-containing waste clay material (WCB), Granular blast furnace slag (GGBFS), Ordinary Portland Cement (OPC)	AAC2: WCB 100% AAC3: 50% GGBFS and 50% WCB WCB was calcined at 800 °C for 2 h CEM I 42.5 R	-	AAC2 and AAC3 mixtures were lower than the OPC.	NaI (Tl) detection system, Cs 137 (662 keV), Co 60 (1173 and 1332 keV), In the AAC composition, the gamma attenuation coefficient of mortars decreased with the increase of WCB content.
Oto et al. (2019) [13]	Concretes with colemanite aggregate, CEM I 42.5 N	up to 20% as an aggregate	-	Compressive strength increased up to 10% colemanite ratio, but decreased after a 10% colemanite ratio.	NaI(Tl) detector, 59.5 and 81 keV energies, Concretes with colemanite minerals are not very effective in gamma radiation shielding.
Yadollahi et al. (2016) [14]	Concrete containing colemanite aggregate, CEM II	up to 50% as an aggregate	Boron additives delay the setting time	Boron additives reduce the compressive strength	-
Yaltay et al. (2015) [15]	Lightweight concrete containing different proportions of pumice aggregate	up to 2%	Increasing the colemanite rate (between 2 and 6%) caused delayed setting times.	-	PTW™ Ion chamber. Co 60 (1250 keV) By replacing cement with 0.4% to 2% colemanite, 28-day lightweight concrete's radiation shielding qualities can be enhanced.
Binici et al. (2014) [16]	Cement-based mortars CEM I	0.25, 0.5, and 0.75%	-	The increase in colemanite content decreased the compressive strength. However, the reference group's compressive strengths are lower than those of all the samples with 0.75% colemanite ratios.	The shielding of gamma-rays is lower than those of the reference samples.
Oto et al. (2013) [17]	Concretes containing barite and colemanite aggregates	up to 20% as an aggregate	-	-	NaI(Tl) detector, Ba 133 (80.99 and 303 keV) and Am 241 (59.54 keV), Concretes containing barite and colemanite are more effective at attenuating gamma rays than the ordinary concretes.
Demir et al. (2011) [18]	Concrete produced with barite, colemanite, and normal aggregate. CEM I 42.5	up to 15% as an aggregate	-	-	NaI(Tl) scintillation detector, Cs ¹³⁷ (663 keV), The linear attenuation coefficient decreased with the colemanite concentration.
Demir and Keleş (2006) [19]	Cement-based mortars containing borogypsum and colemanite concentration waste CEM I 42.5	up to 15% in to clinker	-	-	Narrow collimated beam transmission method for 59.54 and 80.99 keV gamma energy with a Si(Li) detector. The colemanite concentration waste are useful in stopping the spread of radiation.

Table 2: Chemical composition of Portland cement, wt-%

Material	CaO	SiO ₂	Al ₂ O ₃	Fe ₂ O ₃	MgO	Na ₂ O	K ₂ O	SO ₃	Loss on ignition
CEM I 42.5 R	62.02	17.46	3.56	3.31	1.43	0.29	1.07	3.96	5.52

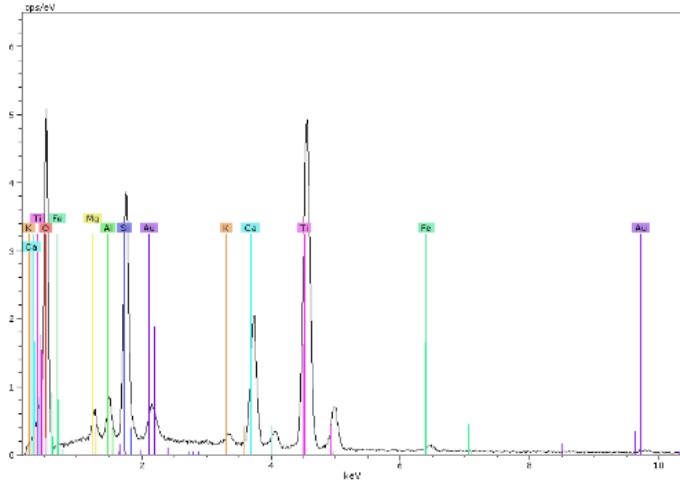
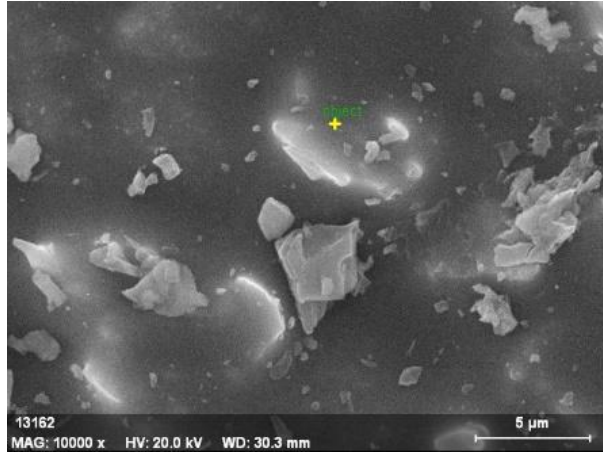


Figure 1: SEM (left) and EDX (right) images of CW powders

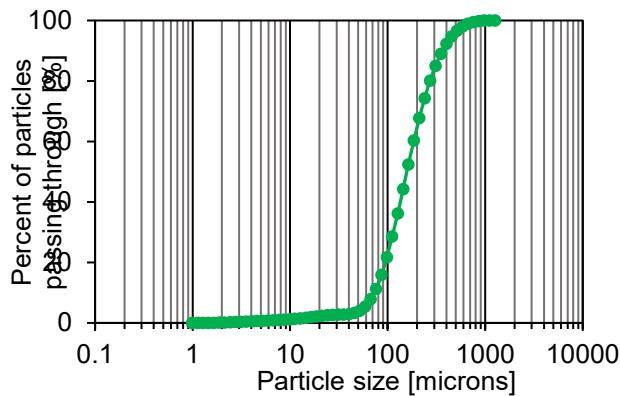


Figure 2: Particle size distribution of CW powders

Table 3: Cement mortar mixture design.

Mortar mixtures	Sand [g]	Cement [g]	Water [g]	CW		water/binder
				[wt-%]	[g]	
C0	1350	491	238	-	-	0.485
CW1	1350	486.1	238	1	4.91	0.485
CW2	1350	481.2	238	2	9.82	0.485
CW3	1350	476.3	238	3	14.73	0.485
CW4	1350	471.4	238	4	19.64	0.485

C. Mixing procedure and testing methods

The test standards, equations, and specifications performed in the current study are given in Table 4.

B. Mixture compositions

The cement mortars (conforming to ASTM C 109) were produced with a water-to-binder fixed ratio of 0.485 and a sand-to-binder fixed ratio of 2.75. In total, five series of mortars were produced, including a control cement mortar (C0). Four series of mortars containing 1, 2, 3, and 4, wt-% CW as cement replacement were produced, and these parts were designated as CW1, CW2, CW3, and CW4, respectively. To provide the transition from a crystalline structure to an amorphous one, CW was calcined at 800 degrees for two hours and grounded. The number next to the letter indicates the percentage of CW powders used as a cement substitute by weight. The mixture composition of the cement mortars is presented in Table 3.

Table 4: Test standards, equations, and specifications.

Tests	Standards	Equation/Specifications
Preparing mortar mixtures	ASTM C 305-06	
Compressive strength (7th and 28th days curing); 50mm cube molds	ASTM C 109	$f_m = P/A,$ where f_m is compressive strength (MPa), P is the total maximum load (N) and A is the area of loaded surface (mm ²). $V=L/T,$
Pulse velocity	ASTM C 597-09	where V is the pulse velocity (m/s), L is the distance between centers of transducer faces (m),

and T is the transit time (s).

Setting time TS EN 196-3 -

D. Measurement of lead equivalent thickness of cement-based mortars in gamma radiation.

For the mortar samples to be used in radiation attenuation experiments, molds with 100 mm diameter and 5, 10, 20 and 30mm thickness were prepared and the mortars were compressed into the molds in two layers. The exact thickness of each concrete mixture sample was determined and noted using a micrometer. Radiation attenuation experiments were carried out in the standard calibration laboratory at Ankara University Institute of Nuclear Sciences in accordance with the TS EN ISO 61331-1 standard [20], in Cs-137 (662 keV) gamma radiation beam. The radiation attenuation curve in the lead filter was obtained at the energy quality specified above using lead filters with 99.9% purity and different thicknesses between 0.15 mmPb and 1.5 mmPb. The radiation transmittance of the produced mortar samples was measured at the radiation energy and irradiation geometries specified above. The attenuation amounts and lead equivalent thicknesses of the mortar samples were determined using the equation of standard lead exponential curves. Cs-137 gamma irradiation system; In the radiation attenuation tests of mortar samples, Hopewell Design Gamma irradiation unit G10 model, a system containing 2 Cs-137 sources with nominal activities of 50 mCi and 10 Ci was used. Mortar samples and standard filters were placed on a bench that provided 3-dimensional movement between the radiation source and the detector and measurements were performed. In the radiation measurements, PTW trademark 30 cm³ spherical ion chamber and a PTW Unidose Webline dose rate reading system calibrated in the secondary standard dosimetry laboratory were used. The irradiation system and test measurement setup are shown in Figure 3.



Figure 3: Cs-137 gamma irradiation system and geometry.

III. RESULTS AND DISCUSSION

The findings of all tests conducted within the scope of the study are explained in detail below.

A. Setting time

All mixtures' setting time tests were determined using the Vicat apparatus. The setting time results of the mortar mixtures are shown in Figure 4.

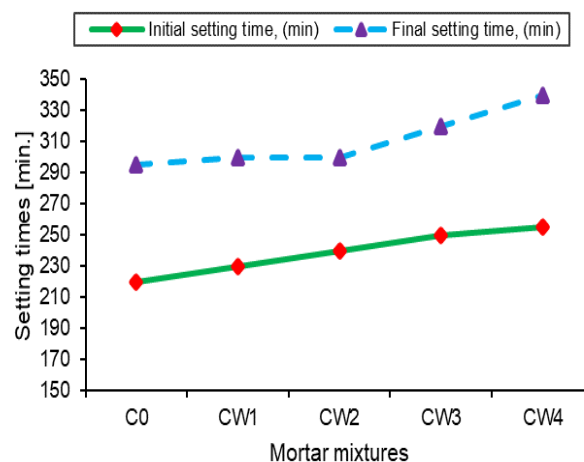


Figure 4: Setting time results of the mixtures.

The TS EN 196-3 standard requires that the initial setting time should not start before 55 minutes and the final setting time should be completed before 10 hours. In addition, ASTM C150 (2011) requires that the setting time begin no earlier than 45 minutes and last no longer than 375 minutes. As seen in Figure 4, the control mortar mixture's initial setting time is 220 minutes, and the final setting time is 295 minutes. CW1 mixtures' setting times are almost the same as the setting times of C0. C0, CW1, CW2, CW3, and CW4 mixtures' setting times are within the limit values specified in the TS EN 196-3 and ASTM C150 (2011) standard. It is observed that the setting times gradually increase with increasing CW substitution. The CW4 mixture's initial setting time increases by 15.9% when compared to C0. These gradual increases appear to be consistent with the works of Yadollahi et al. [14] and Yaltay et al. [15]. Factors such as the decrease in the amount of cement in the mixture with increasing CW replacement and colemanite's tendency to slow down hydration cause the initial and final setting times of CW-replaced mixtures to extend.

B. Compressive strength and pulse velocity

The compressive strengths and pulse velocities of the specimens on the 28 days are presented in Figure 5.

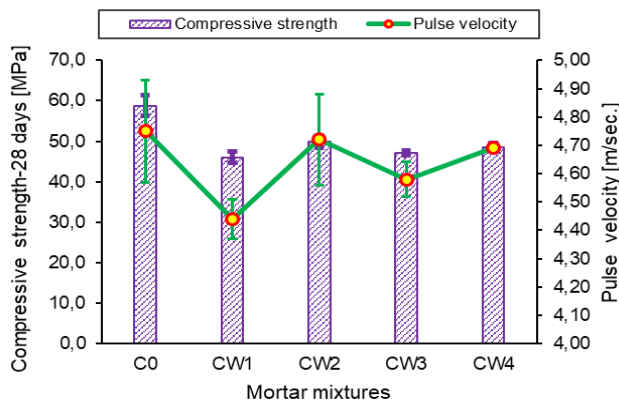


Figure 5: Compressive strengths and pulse velocity values of the specimens on the 28th days.

Table 5: Lead equivalent thickness values of the specimens at Cs-137 (662keV) gamma-ray energy.

Serial number	C0		CW1		CW2	
	Material thickness (mm)	Gamma-ray energies	Material thickness (mm)	Gamma-ray energies	Material thickness (mm)	Gamma-ray energies
		Cs-137 (mmPb)		Cs-137 (mmPb)		Cs-137 (mmPb)
1	7.3	0.62	6,1	0,62	6,3	0,66
2	11.3	1.26	11	1,2	11	1,12
3	21.4	1.74	21	1,725	22	1,742
4	31.2	1.9	32,1	1,91	30,8	1,9

Serial number	CW3		CW4	
	Material thickness (mm)	Gamma-ray energies	Material thickness (mm)	Gamma-ray energies
		Cs-137 (mmPb)		Cs-137 (mmPb)
1	6,2	0,67	7	0,75
2	10,9	1,2	11,1	1,2
3	21,3	1,72	21,3	1,754
4	30	1,9	31,2	1,9

As seen in Figure 5, with increasing substitution of CW, both compressive strengths and pulse velocity values decrease compared to C0. In this context, compressive strengths and pulse velocity values are compatible. However, no significant change occurs in the strengths of CW-substituted mixtures. CW1-CW4 mixtures' 28-day compressive strength loss is in the range 15.1-21.7%.

In the present study, strength loss in CW-substituted mixtures seems to agree with the works by Öztürk et al. [12], Yadollahi et al. [14], and Binici et al. [16]. However, Oto et al. [13] determined that the compressive strength increased up to 10% colemanite ratio, but decreased after a 10% colemanite ratio. In the present study, the substitution of colemanite for cement resulted in a decrease in the mixture's cement content as well as a decrease in strength due to colemanite's tendency to slow down hydration.

C. Radiation attenuation

Radiation attenuation tests were carried out in a standard calibration laboratory. For this purpose, relatively high energy Cs-137 (662 keV) gamma radiation was used [20, 21]. To determine the effect of CW on radiation attenuation, C0 coded

samples without CW were tested first, followed by CW coded samples containing 1, 2, 3, and 4 wt%. Gamma radiation attenuation curves of mortar mixtures exposed to Cs-137 (662 keV) gamma radiation are given in Figure 6, and lead equivalent thickness values are given in Table 5.

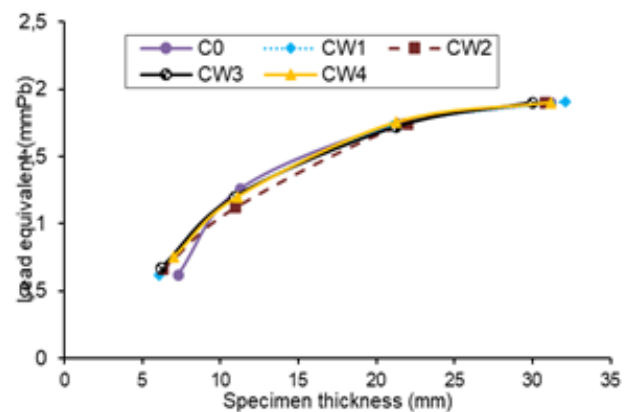


Figure 6: Lead equivalent thickness values of mortar mixtures under Cs-137 (662keV) gamma radiation.

In the study, although the materials with and without colemonite additives were tried to be produced in the same thickness, there are some differences, but the obtained data are at a comparable level. The data obtained at the lowest thickness clearly reveals the radiation attenuation of colemonite additive. Lead equivalent levels increase linearly with increasing mortar thickness. However, the fact that the colemonite ratio remains low with increasing mortar thickness masks the radiation attenuation effect of colemonite additive.

The lead equivalent thicknesses are 0.62 mmPb for the 7.3 mm thick undoped material C0 and 0.62 mmPb for CW1 with a thickness of 6.1 mm and the radiation attenuation change is 1.00. Considering that the material thicknesses are not equal, it is seen that equality is achieved with a thickness difference of 1.2 mm. For CW2 with a thickness of 6.3 mm, the change with the 0.66 mmPb lead equivalent thickness and the undoped material C0 is 1.065. For CW3 with a thickness of 6.2 mm, the change with the 0.67 mmPb lead equivalent thickness and the undoped material C0 is 1.081. For CW4 with a thickness of 7 mm, the change with the 0.75 mmPb lead equivalent thickness and the undoped material C0 is 1.210. It is seen that the radiation attenuation effect increases linearly even at close thicknesses with the increase in colemonite additive ratios.

IV. CONCLUSIONS

The current study evaluates the possible advantages of substituting CW to cement-based mortars to develop a lead-free shielding material against gamma-ray beams. The performance of mortar mixtures with and without CW replacement is compared in terms of radiation shielding, compressive strength, and setting time. The following conclusions can be drawn from the experimental results given above:

1. It is observed that the setting times gradually increase with increasing CW substitution. CW1 mixtures' setting times are almost the same as the setting times of C0. All CW-substituted specimens' setting times are within the limits specified in the standard.

2. Compared with C0, all CW-substituted mortars' compressive strength decreases. In addition, no significant change occurs in the strengths of CW-substituted mixtures.

3. The present study reports that the lead equivalent levels of CW added materials and control samples with similar thickness are significantly different from each other. At Cs-137 gamma energy, the lead equivalent levels of the lowest thickness mortars to which CW was added at 4 different rates were found to be 0.62 mmPb, 0.66 mmPb, 0.67 mmPb and 0.75 mmPb, respectively. The study showed that the lead equivalent values increased linearly depending on the mortar thickness. We can say that CW contributes significantly to radiation retention in low thickness mortar mixtures.

ACKNOWLEDGMENT

This work was supported by the Scientific Research Projects Coordination Unit of Kırşehir Ahi Evran University (Grant number: MMF.A3.22.011). The authors appreciate the Scientific Research Projects Coordination Unit of Kırşehir Ahi

Evran University that supported this study.

REFERENCES

- [1] H.E. Hassan, et al., "Studying the effect of nano lead compounds additives on the concrete shielding properties for γ -rays," *Nuclear Instruments and Methods in Physics Research Section B: Beam Interactions with Materials and Atoms*, vol. 360, pp.81-89, 2015. <https://doi.org/10.1016/j.nimb.2015.07.126>
- [2] A.E. Ersundu, et al., "The heavy metal oxide glasses within the WO₃-MoO₃-TeO₂ system to investigate the shielding properties of radiation applications," *Prog. Nucl. Energy*, vol. 104 pp. 280–287, 2018. <https://doi.org/10.1016/j.pnucene.2017.10.008>.
- [3] A.S. Ouda, "Development of high-performance heavy density concrete using different aggregates for gamma-ray shielding," *Progress in Nuclear Energy*, vol.79, pp. 48-55, 2015. <https://doi.org/10.1016/j.pnucene.2014.11.009>
- [4] A.E.S. Abdo, "Calculation of the cross-sections for fast neutrons and gamma-rays in concrete shields," *Annals of Nuclear Energy*, vol.29(16), pp. 1977-1988, 2002. [https://doi.org/10.1016/S0306-4549\(02\)00019-1](https://doi.org/10.1016/S0306-4549(02)00019-1)
- [5] D. Rezaei-Ochbelagh and S. Azimkhani, "Investigation of gamma-ray shielding properties of concrete containing different percentages of lead," *Applied Radiation and Isotopes*, vol. 70(10), pp. 2282-2286, 2012. <https://doi.org/10.1016/j.apradiso.2012.06.020>
- [6] G. Tyagi, et al., "A review on sustainable utilization of industrial wastes in radiation shielding Concrete," *Materials Today: Proceedings*. 2020.
- [7] B. Han, L. Zhang, and J. Ou, *Smart and multifunctional concrete toward sustainable infrastructures*. 1st ed., Berlin, Heidelberg, Springer, 2017.
- [8] A.J. Al-Saadi and A.K. Saadon, "Gamma ray attenuation coefficients for lead oxide and iron oxide reinforced in silicate glasses as radiation shielding windows," *Ibn AL-Haitham Journal For Pure and Applied Science*, vol. 27(3), pp. 201-214, 2017. <https://jih.uobaghdad.edu.iq/index.php/j/article/view/282>
- [9] H.A. Saudi, "Lead phosphate glass containing boron and lithium oxides as a shielding material for neutron and gamma radiation," *Applied Mathematics and Physics*, vol. 1 (4), pp. 143-146, 2013. <https://doi.org/10.12691/amp-1-4-7>
- [10] E. Kavaz, et al., "Estimation of gamma radiation shielding qualification of newly developed glasses by using WinXCOM and MCNPX code," *Progress in nuclear energy*, vol.115, pp. 12-20, 2019. <https://doi.org/10.1016/j.pnucene.2019.03.029>
- [11] P. Lotti, et al., "Thermal stability and high-temperature behavior of the natural borate colemanite: an aggregate in radiation-shielding concretes," *Construction and Building Materials*, vol. 203, pp.679-686,2019.
- [12] B.C. Öztürk, et al., "Gamma and neutron attenuation properties of alkali-activated cement mortars," *Radiation Physics and Chemistry*, vol. 166:108478, 2020.
- [13] B. Oto, et al., "Nuclear radiation shielding and mechanical properties of colemanite mineral doped concretes," *Radiation Effects and Defects in Solids*, vol. 174(9-10), pp. 899-914, 2019.
- [14] A. Yadollahi, et al., "Optimization of thermal neutron shield concrete mixture using artificial neural network," *Nuclear Engineering and Design*, vol. 305, pp. 146-155, 2016.
- [15] N. Yaltay, et al., "Photon attenuation properties of concrete produced with pumice aggregate and colemanite addition in different rates and the effect of curing age to these properties," *Progress in Nuclear Energy*, vol. 78, pp. 25-35, 2015.
- [16] H. Binici, et al., "Mechanical and radioactivity shielding performances of mortars made with colemanite, barite, ground basaltic pumice and ground blast furnace slag," *Construction and Building Materials*, vol. 50, pp. 177-183, 2014.
- [17] B. Oto, et al., "Photon attenuation properties of some concretes containing barite and colemanite in different rates," *Annals of Nuclear Energy*, vol. 51, pp. 120-124, 2013.
- [18] F. Demir, et al., "Determination of radiation attenuation coefficients of heavyweight-and normal-weight concretes containing colemanite and barite for 0.663 MeV γ -rays," *Annals of Nuclear Energy*, vol. 38(6), pp. 1274-1278, 2011.
- [19] D. Demir and G. Keleş, "Radiation transmission of concrete including boron waste for 59.54 and 80.99 keV gamma rays," *Nuclear Instruments and Methods in Physics Research Section B: Beam Interactions with Materials and Atoms*, vol. 245(2), pp. 501-504, 2006.
- [20] IEC 61331-1 2014 - 05, Protective devices against diagnostic medical X-radiation – Part 1: Determination of attenuation properties of materials.

- [21] ISO 4037-1, X and gamma reference radiation for calibrating doseimeters and doserate meters and for determining their response as a function of photon energy – Part 1: Radiation characteristics and production methods.

Detection of Plant Diseases with Deep Learning for Productivity and Sustainability in Agriculture

SEYMA TAS¹, AHMET GUREL², MEHMET EREN³, OZLEM DILEK ACAR⁴, SEMA SERVI⁵, ONUR INAN⁶

¹Selcuk University, Konya-Türkiye, 213311058@ogr.selcuk.edu.tr,

²Selcuk University, Konya-Türkiye, 213311064@ogr.selcuk.edu.tr,

³Selcuk University, Konya-Türkiye, 213311067@ogr.selcuk.edu.tr,

⁴Selcuk University, Konya-Türkiye, 213311016@ogr.selcuk.edu.tr,

⁵Selcuk University, Konya-Türkiye, semaservi@selcuk.edu.tr,

⁶Selcuk University, Konya-Türkiye, onan@selcuk.edu.tr,

Abstract -This study aims to develop a plant disease detection system based on deep learning to address the critical problem of early detection and prevention of plant diseases in the agricultural sector. Recent literature reviews show that traditional machine learning algorithms are widely used; however, there is an increasing interest in deep learning models that show superior performance compared to conventional methods. While developing the application of this study, Betel Leaf Image Dataset, which contains one healthy and three unhealthy plant classes obtained from Bangladesh, was used. VGG, MobileNet, CNN deep learning models, widely used for image analysis and classification, were selected and trained. The developed models analyze plant images with 89%, 83%, and 87% accuracy rates respectively, and distinguish healthy and diseased plants with a high success rate. Thus, diseases will be detected more quickly and the necessary reactions will be provided. This project has the potential to contribute positively to national income and employment by improving automation and productivity in the agricultural sector.

Keywords: Deep Learning, CNN, VGG, MobileNet.

I. INTRODUCTION

PLANT health is very important in agricultural production and plant diseases are a serious problem in agricultural production. Early diagnosis of the disease/problem by analyzing the health of the plant is important for the treatment and prevention of the spread of the disease over a wide area. Prevention of plant diseases and problems by traditional methods is time consuming and costly. Image pre-processing and deep learning based plant health analysis systems can help farmers for the recognition and early detection of

plant diseases [1].

Deep learning models have become more widely used in the literature for plant disease recognition in recent years.

L. Minh Dang et al. achieved success rates of 95.7%, 93.1%, 96.4%, respectively with Inception-V3, VGG-16 and the RadRGB model they developed for the detection of “fusarium wilt” on radish plants [2].

Waleed Albattah et al., in their study on PlantVillage, a large dataset for an AI-based drone system proved that it is quite possible and successful to detect with 99% accuracy using the EfficientNetV2 model and integrate the model they trained into a drone [3].

Pearline et al. achieved 99.41% accuracy for Swedish leaf clusters using VGG19 artificial neural network architecture with logistic regression in their study. [4]

When we review the studies in the literature, we can see that many different methods are used for the detection of plant diseases. In this study, by focusing on CNN model, the models that give the highest accuracy results are determined and the healthy/unhealthy classification of the plant is created with the determined models. Then, disease detection was performed for plants in the unhealthy class.

As a result of the literature review, it has been seen that 'Deep learning algorithms/artificial intelligence provide a faster, more effective approach for early detection of plant diseases in agricultural areas compared to traditional methods, providing more sustainable and more efficient results at less cost.

II. RESOURCE RESEARCH

In recent years, it is seen from the following literature studies that the use of deep learning models in plant disease recognition has become increasingly widespread.

L. Minh Dang et al. achieved success rates of 95.7%, 93.1%, 96.4%, respectively with Inception-V3, VGG-16 and the RadRGB model they developed for the detection of “fusarium wilt” on radish plants [2].

Waleed Albattah et al., in their study on PlantVillage, a large

dataset for an AI-based drone system, proved that it is quite possible and successful to detect with 99% accuracy using the EfficientNetV2 model and integrate the model they trained into a drone [3].

In their study on a large dataset, Mohanty et al. showed that it is 99% possible to detect diseases on any plant using well-known pre-trained deep learning models such as AlexNet and GoogleNet [3,6].

Ferantinos et al. used not only images taken in the lab, but also lower quality images taken with mobile phones. When they tried to detect plant diseases with VGG on the dataset they obtained, the accuracy rate dropped to 65%. [3, 7]

Pearline et al. achieved 99.41% accuracy for Swedish leaf clusters using VGG19 artificial neural network architecture with logistic regression in their study. [4]

Shivali Amit Wagle and Harikrishnan R. obtained an accuracy rate of 99.17% with the VGG16 model in their study on the classification of tomato plant leaf images as sick and healthy. [5]

Furkan Alp Esen and Aytuğ Onan achieved 94.88% accuracy with VGG16, 92.89% with Resnet18 and 92.48% with EfficientNetB7, which are models that provide services for the classification of plant diseases. Here you see that the most successful model is VGG16. [6]

As a result of the studies conducted by İrem Nur Ecemiş for the detection of plant diseases, ResNet50V2 for 2-stage training and DenseNet169 for single-stage training are the two models that achieved the highest accuracy rates. The accuracy rates, respectively, are as follows: 96.2% and 94.55%. [7]

A review of the literature shows that many different methods have been used to detect plant diseases.

III. MATERIAL METHOD

In the study, the dataset named Betel Leaf Image Dataset from Bangladesh, which we obtained from Mendeley, was used. The data contains healthy and unhealthy images of plants. For the classification of plant images and detection of plant diseases, CNN, VGG, MobileNet, which are deep learning models, were used. Deep learning is a machine learning method consisting of multiple layers that predicts results with a given data set. It has the ability to learn with a high number of data. CNN, VGG, MobileNet, which is a deep learning model, were preferred because they perform better than traditionally known machine learning methods in many areas.

A. Dataset

We chose the Betel Leaf Image dataset from Mendeley[8]. There are two folders in this dataset: original images and augmented images. We combined this augmented images folder and the original images folder and divided them into 80% training, 10% testing and 10% validation. Each of the testing, training and validation folders contains 4 different categories: healthy, dry, bacterial and brown fungal disease. In there are around 1200 images in the dataset. Figure 1 and Figure 2 show examples of healthy, diseased and dry plant images.



Figure 1.1

Figure 1.1: The Betel Leaf Image dataset includes diseased, dead, healthy and brown fungal disease image samples.

In this study, modeling was performed using Python, one of the most common and preferred programming languages in deep learning modeling. Python is a popular programming language, especially in areas such as data science, machine learning and deep learning.

B. VGG-16

VGG-16 is a deep learning-based convolutional neural network developed by Karen Simonyan and Andrew Zisserman of Oxford University in 2014.

The VGG-16 model consists of 16 weighted layers, using more layers to increase depth and complexity. VGG-16 is particularly known for its results in the ImageNet competition. It has achieved high performances in image classification tasks. The model provides an efficient structure for deep feature extraction by successively using a 3x3 convolutional layer and a 2x2 maximum pooling layer [9].

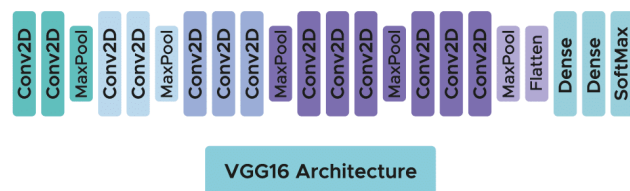


Figure 1.2: VGG-16 Architecture [12]

The depth of VGG-16 allows it to learn more complex object features better than other models, improving its overall performance in image recognition. The model achieves better classification results by extracting deeper and more abstract features from the input images. Adding more layers allows the model to learn more complex structures. VGG-16 is widely used in image analysis, object recognition and many other applications and has become an important model and reference in the deep learning community. The development of VGG-16 has contributed significantly to deep learning research and laid the foundation for many subsequent models.

C. MobilNet-V2

MobileNetV2 is a deep learning-based convolutional neural network developed in 2018 by Google Research team members Mark Sandler, Andrew Howard, Menglong Zhu, Andrey Zhmoginov and Liang-Chieh Chen. Optimized to work on systems with limited resources, such as mobile devices, one of the main goals of this model is to strike a good balance between efficiency and accuracy. The major innovation that MobileNetV2 brings to deep learning models is the use of 'inverted residual connections' and 'linear bottleneck layers', which reduce computational requirements without reducing high accuracy. [10].

MobileNetV2 optimizes and reduces the number of parameters and processing time by using deeply separable convolutions in addition to 1x1 and 3x3 convolution layers. This allows the model to run much more efficiently and effectively on mobile devices and embedded systems than other models. MobileNetV2 is mostly used for image classification, object detection and segmentation, making it an optimal solution for applications with limited hardware resources. The development of MobileNetV2 is recognized by most developers as a significant advancement in mobile AI applications.

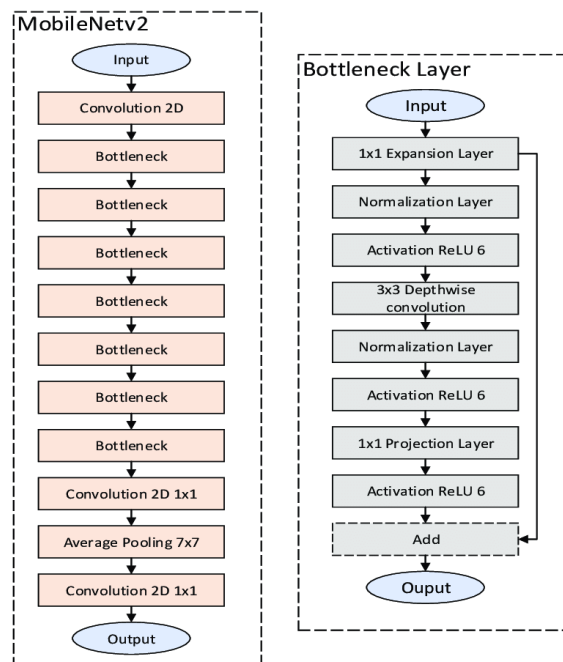


Figure 1.3: The architecture of MobileNetV2. [13]

D. CNN

Convolutional Neural Network (CNN) is a deep learning architecture developed by Yann LeCun and his team in the 1980s that literally revolutionized image processing and computer vision and related fields. CNNs learn local features of an image through layers such as convolutional, pooling and fully connected layers, enabling classification, object recognition, segmentation and similar tasks. In 1998, the basic LeNet-5 model for handwritten digit recognition introduced the core components of CNNs and was presented in the paper Gradient-Based Learning Applied to Document Recognition. This model has had a major impact on the development of the deep learning field by forming the basis of modern CNN architectures. [11].

In this study, a CNN-based model is used. The model consists of three convolutional layers, each containing 3x3 filters, and a 2x2 maximum pooling layer after each convolutional layer. This structure gradually learns the basic features of the image. The features from the convolutional layers are smoothed and transferred to a fully connected layer of 512 neurons, where dropout is applied to prevent overlearning. In the final stage, the model includes an output layer with the number of neurons equal to the number of classes and completes the classification using the softmax activation function to generate probability values for each class.

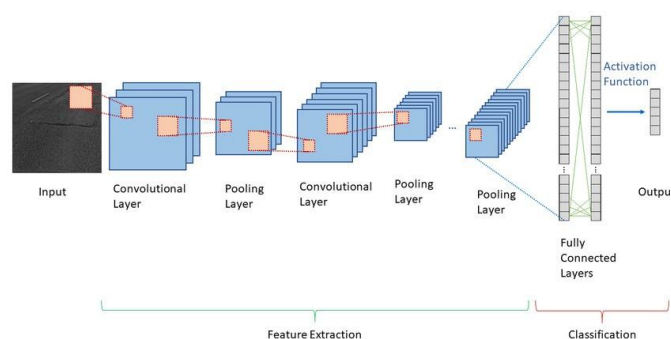


Figure 1.4: CNN Model Layers [14]

IV. METHODS

A. Dataset

In this study, Betal Leaf Image dataset from Mendeley was used, which consists of two folders, original and enriched images. After merging these datasets, they were divided into 3 parts, 80% for training, 10% for testing and 10% for validation. Here, the dataset consists of approximately 1200 images and contains four categories, namely healthy, dry, bacterial and brown fungus disease. Examples of healthy, diseased and dry plant images are presented in Figures 1 and 2. This is explained in detail in the 'Dataset' section under the 'Material Methods' heading.

B. Data Preprocessing

The images in the dataset were resized to (224, 224) to match the input size of our deep learning models, allowing the model to process the data more efficiently. Additionally, the ImageDataGenerator class in Keras was used to dynamically load the images and make them easily accessible during the training process. ImageDataGenerator speeds up the training process by appropriately processing each image in the dataset and facilitating the model's training integration.

C. Model Architecture

C.1) VGG-16

In this study, the VGG-16 model was trained with ImageNet. The model was initially preprocessed to receive input images of size (224, 224, 3) and the upper layers were removed, allowing the use of convolutional layers and thus allowing more general features to be learned. Several new layers were added instead of the removed layers to customize the model. In the first part of the model, BatchNormalization was used to further reduce instabilities and help the model learn more efficiently and faster. Then, the extracted features were made one-dimensional with the Flatten layer and these outputs were processed with the Dense layer. 'ReLU' was used as the activation function. In addition, 50% Dropout and then 10% Dropout were added between the Dense layers to reduce the risk of overfitting. The output of the model was directed to the softmax layer and allowed to classify four different

plant disease categories that can detect healthy, dry, bacterial and brown fungus disease. The model was trained using Adadelta optimization and the accuracy of the model was monitored with the accuracy metric.

C.2) MobileNetV2

In our study, we used the pre-trained MobileNetV2 model. The outputs of the model were set to be accepted as inputs in the size of (224, 224, 3). General features were extracted using the pre-trained convolutional layers of the MobileNetV2 model and the classification of plant diseases was performed by removing and reconstructing the upper layers.

To adapt our model to our dataset, new layers were added on top of the basic MobileNetV2 model. Finally, 'softmax' was used to divide the output of the model into four classes.

C.3) CNN (Convolutional Neural Networks)

In this method used in the study, unlike other methods, a pre-trained model was not used. Therefore, although the validation results were slightly lower than pre-trained models such as MobileNetV2 and VGG-16, plant diseases were successfully classified. In this model, a solution specific to the plant disease classification task was produced with basic convolution layers, feature extraction and classification steps.

D) Training

In our training phase, categorical cross-entropy loss function was used in all our models. For optimization, it was preferred to use different algorithms due to differences in the models. In each model, early stopping was applied if the model was overfitting to prevent overfitting.

E) Evaluation Metrics

'Accuracy' was used to evaluate model performance. After the training was completed, the accuracy of each model on the test dataset was calculated and then the accuracy values were compared with each other. The highest accuracy rate was obtained with the VGG-16 model with 94.8%. Accuracy rates of 91.5% and 90% were obtained from the MobileNetV2 and CNN models, respectively. In addition, the CNN model showed promising performance despite being trained without using a previously trained model, unlike other models.

F) Computational Environment

This study was carried out using the Python programming language in the Google Colab environment, which offers the opportunity to work together with GPU support; TensorFlow and Keras libraries were used in the development of the model.

V. RESEARCH RESULTS AND DISCUSSION

VGG-16	94.8
CNN	90
MobileNetV2	91.5

Figure 1.5: Model Performances

Figure 1.5 shows the accuracy rates of VGG-16, MobileNetV2 and CNN deep learning models that we trained with our dataset used in plant disease detection. The VGG-16 model gave us the best performance with the highest accuracy rate of 94.8%. The deeper structure and more parameters of VGG-16 compared to other models further strengthen the feature extraction ability of the model. Thus, more accurate results can be obtained by performing more detailed feature extraction. This accuracy rate obtained has shown that VGG-16 is quite successful in classifying plant diseases. In particular, the hyperparameters we optimized helped our model to achieve higher results in our dataset and to extract better features. However, since this model is large, its computational cost is high.

The other model we used, MobileNetV2, provided an accuracy of 91.5%. Although it performed lower than VGG-16, MobileNetV2 is a smaller model compared to VGG-16. The MobileNetV2 model requires less computational power and memory, so it can be used in portable or simpler systems. This small difference in accuracy compared to large models such as VGG-16 is negligible for applications that require speed and efficiency.

The CNN model, which is a model that we both developed and trained, ranks third with 90% accuracy. Our CNN model was not used as a pre-trained model like the other models we used. Since it is not a deep model like the other models we used, it has a lower accuracy rate. Although it is a model without pre-training, it gave an approximate result to the other models. It is a model that can be used as an alternative in simple classification tasks where computational resources are limited.

As a result of our study, it has been observed that the deep learning models used have an important potential in terms of disease diagnosis in the field of agriculture. The dataset used in the training process consists of images of healthy and diseased plants and provides a unique evaluation as it is a dataset that has not been studied before. Compared to traditional machine learning algorithms, deep learning models were found to achieve higher accuracy rates. This result shows that deep learning and image processing techniques can quickly and effectively analyze plant health. However, studies with larger datasets can increase the generalizability of the method.

VI. CONCLUSION

In this study, a deep learning-based analysis system was developed for disease diagnosis in agriculture, and the results were positive. The developed system aims to reduce product

losses through early diagnosis and provides faster and more cost-effective solutions than traditional methods. For future studies, it is recommended to use more comprehensive data sets for different plant species and disease variants. In addition, testing the system in different climatic conditions and agricultural areas will allow us to better evaluate its performance. Such extended studies can not only increase the reliability of the system, but also contribute to its widespread adoption.

REFERENCES

- [1] Demir, Kubilay & Tümen, Vedat. (2021). Drone-assisted Automated Plant Diseases Identification using Spiking Deep Conventional Neural Learning. *Ai Communications*. 34. 1. 10.3233/AIC-210009.
- [2] Dang LM, Wang H, Li Y, Min K, Kwak JT, Lee ON, Park H, Moon H. Fusarium Wilt of Radish Detection Using RGB and Near Infrared Images from Unmanned Aerial Vehicles. *Remote Sensing*. 2020; 12(17):2863. <https://doi.org/10.3390/rs12172863>
- [3] Albattah W, Javed A, Nawaz M, Masood M and Albahli S (2022) Artificial Intelligence-Based Drone System for Multiclass Plant Disease Detection Using an Improved Efficient Convolutional Neural Network. *Front. Plant Sci*. 13:808380. doi: 10.3389/fpls.2022.808380
- [4] Anubha Pearline, S., Sathiesh Kumar, V., and Harini, S. 'A Study on Plant Recognition Using Conventional Image Processing and Deep Learning Approaches'. 1 Jan. 2019 : 1997 – 2004. doi: 10.3233/JIFS-169911
- [5] Wagle, S.A., R. H. (2021). A deep learning-based approach in classification and validation of tomato leaf disease. *Traitement du Signal*, Vol. 38, No. 3, pp. 699-709. <https://doi.org/10.18280/ts.380317>
- [6] Esen, F. A., & Onan, A. (2022). Derin Öğrenme Yöntemleri ile Bitki Yaprakları Üzerindeki Hastalıkların Sınıflandırılması. *Avrupa Bilim Ve Teknoloji Dergisi*(40), 151-155. <https://doi.org/10.31590/ejosat.1181081>
- [7] Ecemiş İ.N (2022). Derin Öğrenme Teknikleri Kullılarak Bitki Yaprak Görüntüleri Üzerinden Tür ve Olası Hastalık Tespiti. Yüksek Lisans Tezi, Yıldız Teknik Üniversitesi Fen Bilimleri Enstitüsü. https://scholar.google.com/citations?view_op=view_citation&hl=tr&user=Bui3JDEAAAAJ&citation_for_view=Bui3JDEAAAAJ:9yKSN-GCBOIC
- [8] Dataset: <https://data.mendeley.com/datasets/g7fpgj57wc/1>
- [9] Simonyan, K., & Zisserman, A. (2015). Very deep convolutional networks for large-scale image recognition. 3rd International Conference on Learning Representations (ICLR 2015), 1–14.
- [10] Sandler, Mark & Howard, Andrew & Zhu, Menglong & Zhmoginov, Andrey & Chen, Liang-Chieh. (2018). MobileNetV2: Inverted Residuals and Linear Bottlenecks. 4510-4520. 10.1109/CVPR.2018.00474.
- [11] Y. Lecun, L. Bottou, Y. Bengio and P. Haffner, "Gradient-based learning applied to document recognition," in Proceedings of the IEEE, vol. 86, no. 11, pp. 2278-2324, Nov. 1998, doi: 10.1109/5.726791.
- [12] [https:// datascientest.com/en/unveiling-the-secrets-of-the-vgg-model-a-deep-dive-with-daniel](https://datascientest.com/en/unveiling-the-secrets-of-the-vgg-model-a-deep-dive-with-daniel) [accessed 2 Nov 2024]
- [13] Design Space Exploration of a Sparse MobileNetV2 Using High-Level Synthesis and Sparse Matrix Techniques on FPGAs - Scientific Figure on ResearchGate. Available from: https://www.researchgate.net/figure/The-architecture-of-MobileNetV2-DNN_fig1_361260658 [accessed 2 Nov 2024]
- [12] <https://www.linkedin.com/pulse/decoding-cnn-architecture-unveiling-power-precision-neural-moustafa/> [accessed 2 Nov 2024]

Characterization of AA2024/CNT Nanocomposites as a Function of Milling Time and CNT Content

HAYRUNNİSA ÖZER¹, ÖZLEM CANPOLAT², TEMEL VAROL^{3,4,5}

¹Bursa Technical University, Bursa/Turkey, hayrunnisa7@gmail.com

²Karadeniz Technical University, Abdullah Kanca Vocational School of Higher Education, Trabzon/Turkey, ozlemcanpolat@ktu.edu.tr

³Karadeniz Tehcnical University, Medical Device Design and Production Application and Research Center (METAM), Trabzon/Turkey

⁴Karadeniz Tehcnical University, Department of Metallurgical and Materials Engineering, Trabzon, Turkey

⁵Karadeniz Tehcnical University, Advanced Engineering Materials Research Group tvarol@ktu.edu.tr

Abstract - The properties of particle-reinforced composites depend on the type of matrix and reinforcement. In this study, the production of AA2024 matrix CNT (carbon nanotube)-reinforced nanocomposite materials was performed by a hot pressing process. The ultrasonic dispersion method was applied for the uniform distribution of CNT particles (15 min). CNT powder concentrations of 0.125%, 0.25%, 0.5%, and 1.0% by weight were chosen for the AA2024 matrix. The ball milling process was carried out in three different time periods: 0.5, 1.5, and 3.0 hours. The density, hardness, and tensile strength of the generated composites were quantified, and their morphologies were examined using SEM. The investigations revealed a decrease in density values with the increasing concentrations of CNT. The hardness and tensile properties enhanced with higher concentrations of CNT and increased milling times, attaining maximum values for 0.5% CNT-reinforced AA2024 alloy matrix composites. At 1% CNT concentration, CNT poroeration and distribution inhomogeneity resulted in a reduction in mechanical properties.

Keywords – Ultrasonic Dispersion, Carbon Nanotube, Nanocomposite, Ball Milling, AA2024.

I. INTRODUCTION

ALUMINUM (Al) matrix composites' low density, high strength, toughness, and wear and corrosion resistance make them hopeful engineering materials for automotive, aerospace, defense, and structural applications [1-3]. It is believed that reinforcing Carbon nanotubes (CNTs) is an effective way to improve the mechanical and thermal properties of metal matrix composites. However, poor wettability, interface bond, and non-homogeneous dispersion of CNT particles in metal matrix limit its application as reinforcement material [4]. Numerous researches are being conducted by the researchers in order to find a solution to the problems caused by the negative properties such as semi-wet and slurry based

methods [5], mechanical alloying [6], ultrasonic, low energy ball-milling, medium energy ball-milling and high energy ball-milling [7].

The aforementioned literature review shows that researchers have studied the homogeneous distribution of CNT particles within the Al matrix by ball milling and different mixing methods, as well as the synthesis and characterization of Al-CNT metal matrix composites by powder metallurgy, hot pressing, hot extrusion, and different casting methods. However, this study investigates the effect of ball milling time and CNT ratio on the morphology and mechanical properties of AA2024/CNT composites. CNT particles were first dispersed by ultrasonic mixing, and then they were ball milled with AA2024 alloy powder at different milling times and CNT ratios. Additionally, the physical and mechanical properties of hot-pressed composites were examined.

II. EXPERIMENTAL PROCEDURE

AA2024 powders with an average particle size of 115 μm , provided by Gundogdu Exoterm Industry, was utilized as the matrix material. The CNTs with an average diameter of 9.5 nm, provided by Graphen Future, were utilized as a reinforcing material. After the CNT powders were ultrasonically mixed in 1000 liters of ethyl alcohol for 15 minutes, they were added to AA2024 powder in four ratios (0.125, 0.25, 0.5, and 1 wt. %) and milled at different milled times of 0.5, 1.5 and 3 hours. AA2024/CNT composite powders were hot pressed into a steel die at 500°C for 2 hours and 500 MPa. Figure 1 and Table 1 show the schematic representations of the production processes and the experimental codes of the composites, respectively.

Scanning electron microscopy (SEM, Zeiss Evo LS10) was used to investigate the morphology of AA2024/CNT composites. The PANalytical brand X'Pert3 Powder XRD device (45 kv) was employed to record the XRD patterns of composite samples in the 20-90o range using Cu Ka radiation ($k: 1,54059 \text{ \AA}$). The theoretical densities of hot-pressed

samples were calculated using the mixing rule, whereas experimental densities were determined using the Archimedes principle. Innovatest Nemesis 9000 hardness tester (31.25 kgf load, 10 s dwell time, 2.54 mm diameter penetrating tip) was used to measure hardness using the Brinell hardness measuring method. Tensile testing was performed at room temperature with an MTS 45 tensile testing machine at a crosshead speed of 0.5 mm min^{-1} .

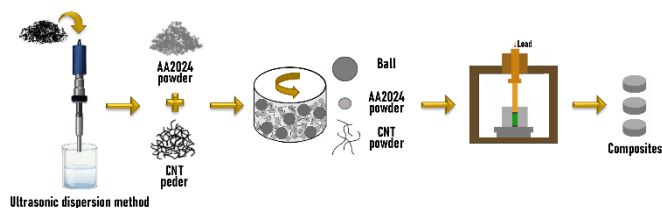


Figure 1: The production process of AA2024/CNT composites.

Table 1: Sample codes of AA2024/CNT composites

Sample Code	AA2024 Alloy (wt.%)	CNT (wt.%)
A/C0.125	99.875	0.125
A/C0.25	99.75	0.25
A/C0.5	99.5	0.5
A/C1	99	1

III. RESULT AND DISCUSSION

A. XRD Analysis

The XRD patterns of the composites is shown in Figure 2. Similar phases in the composites' XRD patterns point to an existence of Al, Al_2Cu , and MgCuAl_2 phases. At diffraction angles of 38.45, 44.74, 65.09, 78.21, and 82.45, respectively, the major peaks associated with the (111), (200), (220), (311), and (222) planes of Al were seen. The Al_2Cu and MgCuAl_2 phases can precipitate in a homogeneous Al-Cu-Mg solid solution that is formed by hot pressing at a temperature of 500°C . Solid state diffusion causes Cu atoms to diffuse into Al atoms and then settle in the locations.

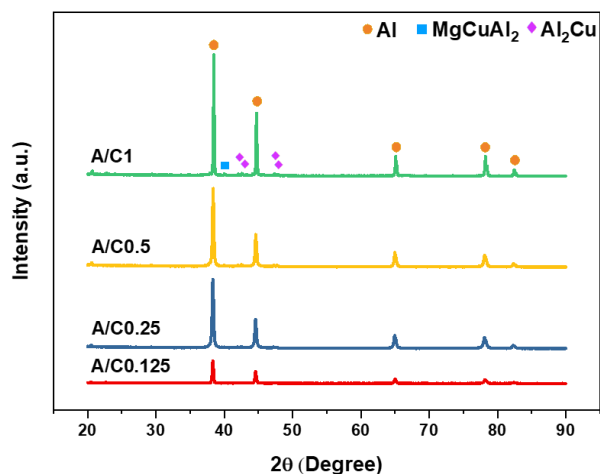


Figure 2: XRD patterns of the composites

B. Density and Hardness

The Figure 3 shows density and porosity of AA2024/CNT composites depending on CNT concentration and milling time after hot pressing at 500°C . The density of the composites lowered as the CNT concentration increases. This can be attributed to the low density and clustering of CNTs. The aggregation of CNTs inhibits their adhesion to the AA2024 alloy matrix [8]. With constant CNTs content, an increase in milling time enhances density; for instance, A/C0.125 milled for 3 hours reaches a maximum density of 2.684 g/cm^3 , but A/C1 milled for 0.5 hours exhibits the lowest density of 2.549 g/cm^3 . Longer milling times enhance density by increasing the amount of smaller particles, which can be explained by the small particles entering between the larger matrix powders and filling the pores [9].

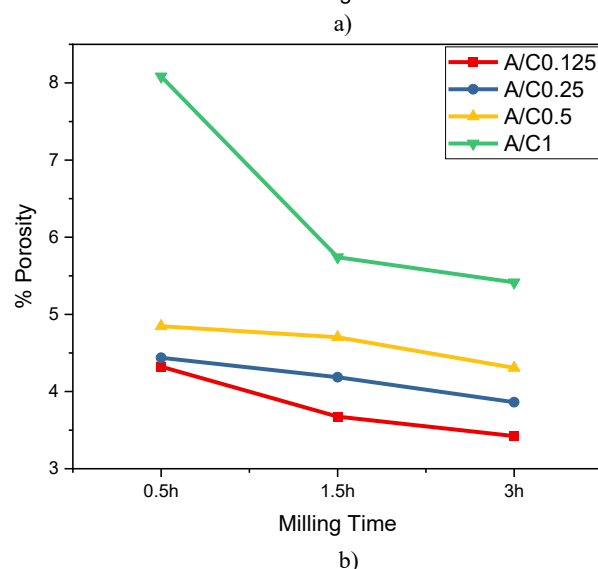
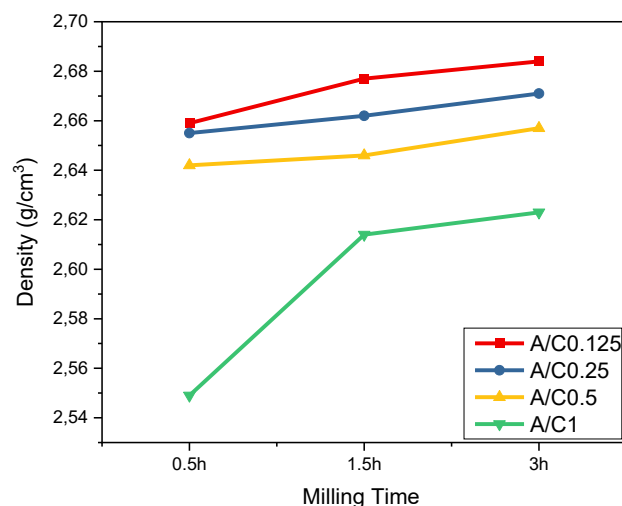


Figure 3: The (a) density and (b) porosity of composites

The effect of CNT concentration and milling time on the hardness of AA2024/CNT composites is shown in Figure 4. While the highest hardness values were obtained at 0.5% CNT content, the increase in hardness values can be attributed to grain refinement due to increasing milling time and higher CNT

concentration [10]. However, the A/C1 composites with the highest concentration of CNT have the lowest hardness values, attributed to CNTs agglomeration, poor sintering, and high porosity. After 3 hours of milling, the A/C0.5 composite attained a hardness value of 150.19 HB.

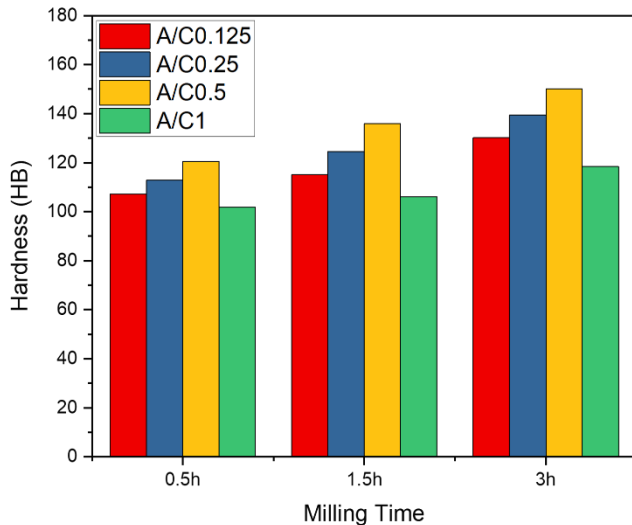


Figure 4: Hardness of composites

C. Microstructure Analysis

Figure 5 illustrates the morphology of AA2024/CNT composites produced with different CNT concentrations and milling times. The addition of CNTs results in an increase in the distance between the matrix grains, leading to a higher pore amount and a decrease in mechanical strength. The bright regions indicate intermetallic phases, whereas the dark regions mostly consist of AA2024.

A smaller amount of CNT reinforcement increases the probability of achieving homogenous dispersion within the matrix alloy. This is due to the large surface area, strong van der Waals forces, and nanoscale properties of CNTs, all of which contribute greatly to the aggregation of CNTs [11]. As the CNT ratio increased, an increase in porosity was observed. The increase in porosity can be attributed to the challenges in dispersing higher CNT concentrations, which decrease the product's compressibility during consolidation, slow down the densification process, and ultimately lower the relative density of the composites.

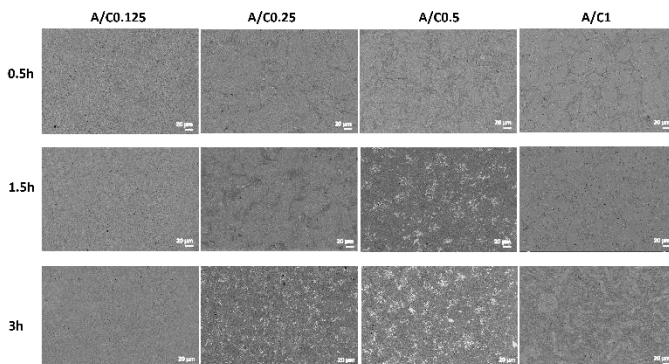


Figure 5: The microstructure of composites

D. Tensile Strength

The tensile strengths of the composites are shown in Figure 6. Increasing the amount of CNT in the samples has been demonstrated to have a positive effect on the tensile strength of the samples. Adding more CNTs (A/C1) results in a decrease in strength, which is maximum at A/C0.5 and then decreases further. According to the results, the strength of the AA2024 alloy matrix can be improved by using small quantities of CNT. It is possible that this is the result of the dispersion strength that is caused by the introduction of a tiny amount of CNT. After three hours of milling, the tensile strength of A/C0.5 sample reached a maximum value of 173.9 MPa.

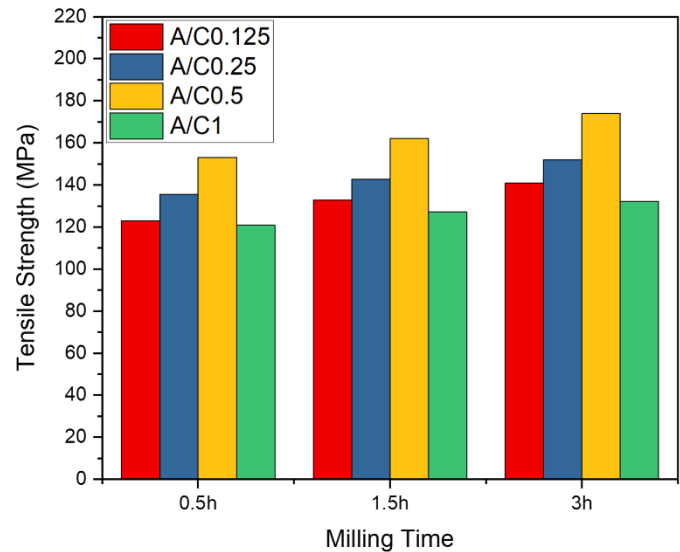


Figure 6: Tensile Strength of composites

IV. CONCLUSION

In this study, AA2024-CNT composites were produced by hot pressing method from AA2024 alloy powders and CNT supported by ultrasonic dispersion method to evaluate the effects of CNT content and milling time on the density, hardness and tensile strength of AA2024-CNT composites.

The following results were derived:

- The diffraction peaks indicated the presence of Al, Al₂Cu, and MgCuAl₂ phases in accordance with the XRD analyses conducted to identify the crystal phases of CNT-reinforced AA2024 composites. The main peaks for the Al planes (111), (200), (220), (311), and (222) were observed at 38.45, 44.74, 65.9, 78.21, and 82. It was observed at 45 diffraction angles. However, the peaks of the Al₂Cu and MgCuAl₂ intermetallic compounds were observed in the XRD patterns of the bulk composites.

- As the concentration of CNT increased, a decrease in composite density was observed due to CNT agglomeration, but an increase in density showed up with prolong milling time at a constant CNT content. While the maximum density value of A/C0.125 milled for 3 hours was 2.684 g/cm³, the minimum density value of A/C1 milled for 0.5 hour was 2.549 g/cm³.

- An increase in hardness values occurred with a 0.5% increase in CNT content. The AC/0.5 composite had a highest hardness value of 150.19 HB after three hours of milling. The lowest hardness value was observed in A/C1 composites with the highest CNT concentration.
- Tensile strength gradually enhanced with an increase in CNT content (by 0.5%). The maximum tensile strength recorded was 173.9 MPa in A/C0.5 composites. The lowest tensile strength was observed in AC/1 composites with the highest concentration of CNT. This reduction can be attributed to CNT agglomeration.

REFERENCES

- [1] L. A. Batista, M. D. V. Felisberto, L. S. Silva, T. H. R. da Cunha, and E. M. Mazzer, "Influence of multi-walled carbon nanotubes reinforcements on hardness and abrasion behaviour of porous Al-matrix composite processed by cold pressing and sintering," *J. Alloys Compd.*, vol. 791, pp. 96–99, 2019, doi: 10.1016/j.jallcom.2019.03.265.
- [2] H. Karakoç, Ş. Karabulut, and R. Çıtak, "Study on mechanical and ballistic performances of boron carbide reinforced Al 6061 aluminum alloy produced by powder metallurgy," *Compos. Part B Eng.*, vol. 148, no. May 2017, pp. 68–80, 2018, doi: 10.1016/j.compositesb.2018.04.043.
- [3] S. Kumar, A. Sharma, R. Arora, and O. P. Pandey, "The microstructure and wear behaviour of garnet particle reinforced Al matrix composites," *J. Mater. Res. Technol.*, vol. 8, no. 6, pp. 5443–5455, 2019, doi: 10.1016/j.jmrt.2019.09.012.
- [4] H. Zare, M. Jahedi, M. R. Toroghinejad, M. Meratian, and M. Knezevic, "Compressive, shear, and fracture behavior of CNT reinforced Al matrix composites manufactured by severe plastic deformation," *Mater. Des.*, vol. 106, pp. 112–119, 2016, doi: 10.1016/j.matdes.2016.05.109.
- [5] F. Rikhtegar, S. G. Shabestari, and H. Saghafian, "Microstructural evaluation and mechanical properties of Al-CNT nanocomposites produced by different processing methods," *J. Alloys Compd.*, vol. 723, pp. 633–641, 2017, doi: 10.1016/j.jallcom.2017.06.222.
- [6] R. Pérez-Bustamante, F. Pérez-Bustamante, M. C. Maldonado-Orozco, and R. Martínez-Sánchez, "The effect of heat treatment on microstructure evolution in artificially aged carbon nanotube/Al2024 composites synthesized by mechanical alloying," *Mater. Charact.*, vol. 126, pp. 28–34, 2017, doi: 10.1016/j.matchar.2017.01.006.
- [7] J. Stein, B. Lenczowski, N. Fréty, and E. Anglaret, "Mechanical reinforcement of a high-performance aluminium alloy AA5083 with homogeneously dispersed multi-walled carbon nanotubes," *Carbon N. Y.*, vol. 50, no. 6, pp. 2264–2272, 2012, doi: 10.1016/j.carbon.2012.01.044.
- [8] M. R. Akbarpour and A. Poursmaeil, "The influence of CNTs on the microstructure and strength of Al-CNT composites produced by flake powder metallurgy and hot pressing method," *Diam. Relat. Mater.*, vol. 88, pp. 6–11, 2018, doi: 10.1016/j.diamond.2018.06.021.
- [9] A. M. K. Esawi, K. Morsi, A. Sayed, M. Taher, and S. Lanka, "The influence of carbon nanotube (CNT) morphology and diameter on the processing and properties of CNT-reinforced aluminium composites," *Compos. Part A Appl. Sci. Manuf.*, vol. 42, no. 3, pp. 234–243, 2011, doi: 10.1016/j.compositesa.2010.11.008.
- [10] R. Zheng, X. Hao, Y. Yuan, Z. Wang, K. Ameyama, and C. Ma, "Effect of high volume fraction of B4C particles on the microstructure and mechanical properties of aluminum alloy based composites," *J. Alloys Compd.*, vol. 576, no. 2013, pp. 291–298, 2013, doi: 10.1016/j.jallcom.2013.04.141.
- [11] K. S. Munir, Y. Li, D. Liang, M. Qian, W. Xu, and C. Wen, "Effect of dispersion method on the deterioration, interfacial interactions and re-agglomeration of carbon nanotubes in titanium metal matrix composites," *Mater. Des.*, vol. 88, pp. 138–148, 2015, doi: 10.1016/j.matdes.2015.08.112.

Agrivoltaic Technology Implementation on Soybean Farms in Nigeria

HAMZE MOHAMED ABDULLAHI^{1*} ÖMER ÖNDER ERAT², BÜLENT YEŞİLATA³

^{1*} Ankara Yıldırım Beyazıt University, Ankara/Turkey, hiirey.official@gmail.com

² Ankara Yıldırım Beyazıt University, Ankara/Turkey, omerondermak@gmail.com

³ Ankara Yıldırım Beyazıt University, Ankara/Turkey, byesilata@gmail.com

Abstract - Agrivoltaic (AV) technology has become popular in the last decade since it efficiently allows both crop production and PV electricity generation on the same land. While AV technologies have made significant advances in Europe and North America, their implementation in Africa, despite the continent's great potential for solar energy, has been limited due to a lack of comprehensive research and pilot studies. This study investigates the feasibility of implementing agrivoltaic (AV) technology on existing soybean farms in Nigeria by assessing its potential. The methodology involves simulating an AV pilot system using Revit software to analyze how PV panel shading affects the crop surface area. The simulation results show that the shaded area under PV panels ranges from 25.67% to 31.29% of the total area. Additionally, we developed an empirical model for soybean crop yield based on the percentage of available light, indicating that yields decrease as shading increases. Nevertheless, our proposed system design ensures that 70% of the yield remains unaffected at all levels of shading. The advantages of the system were assessed using the land equivalent ratio (LER), which consistently equaled one, showing that the dual-purpose system is just as effective as single-purpose land in terms of productivity.

Keywords - Agrivoltaic, AV system, Simulation, Soybean, Africa, Shading, LER

I. INTRODUCTION

SOLAR photovoltaics (PV) are the emerging powerful solution for large-scale, low-carbon electricity generation, playing a key role in the transition toward cleaner energy. In fact, the International Energy Agency (IEA) predicts that by 2050, around 6000 TWh of electricity will come from PV, making up about 16% of the world's total energy production [1]. However, to achieve this, large areas of land will be required for PV installations, which raises the challenge of competing with other land uses (agriculture) [2,3].

This is where the concept of agrivoltaics comes in. It involves using the same land for both solar energy generation and farming, allowing us to meet energy needs without sacrificing food production. The idea was first introduced back in the early 1980s by Goetzberger and Zastrow [4], suggested planting crops in the space between solar panels. Since then, agrivoltaics has proven successful in different contexts, from growing Aloe

vera in semi-arid regions [5] lettuce [6] and cherry tomatoes [7] under solar panels. In addition to increasing land-use efficiency, research shows that crops grown beneath solar panels can help cool the panels, improving their efficiency by up to 3.2% [8]. A recent model by Sar et al. [9] even suggests that smaller PV panel sizes can enhance agricultural productivity, while slightly reducing energy output. Similarly, Warman et al. [10] highlighted the potential for solar PV systems to reduce water use while simultaneously increasing crop productivity.

Agrivoltaic systems also have strong financial potential by can increase operational income by as much as 210% [11]. In densely populated regions where land is scarce, agrivoltaics offers an exciting way to address the dual challenges of food and energy security because of its economic and environmental advantages [12]. Despite significant progress in Europe and North America, Africa has only seen limited adoption of agrivoltaic systems, even though the continent holds higher potential for solar energy [13]. This limited implementation in Africa, particularly in addressing food and energy insecurity, highlights the need for more research and pilot projects to fully understand the potential of agrivoltaics in this context.

In this study we focus on exploring how agrivoltaics could be applied to existing soybean farms in Nigeria. Our goal is to investigate how we can generate solar power without negatively impacting agricultural output. Specifically, we'll look at the feasibility of installing solar panels 4 meters above the ground, with 6.4 meters of space between the rows on soybean farms. From there, we'll assess how much electricity can be generated per unit area. A sensitivity analysis will also be conducted, exploring factors such as geographical location, module and inverter selection, row spacing, and the orientation of the panels. The findings will provide valuable insights and help shape best practices for implementing agrivoltaic systems in Nigeria and beyond.

II. MATERIALS AND METHOD

We developed a simulation module for designing an agrivoltaic system integrated within agricultural lands in Nigeria. The simulations were conducted in the Makurdi region of Benue State, situated at coordinates {7.7411 N, 8.5125 E} within the Southern Guinea Savanna of Nigeria. The annual average solar energy potential for this location is 18.9 MJ/m²

per day [14]. The methodological framework used in this thesis is represented in a schematic block diagram, as shown in Figure 1.

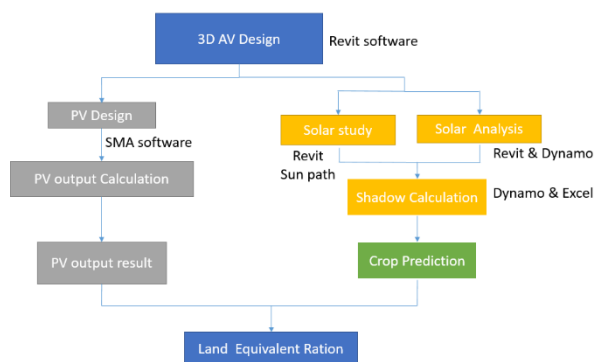


Figure 1: Block Diagram

A. Creation of a 3D Model

A plot dimension was established for an area of 313 square meters, precisely measuring 18.89 by 16.57 meters. This designated plot was developed for yield production. A 3D photovoltaic (PV) panel was meticulously designed to cast shadows on the site, facilitating an in-depth examination of solar exposure. Finally, a structural design for the agrivoltaic system was incorporated, featuring a clear height of 4 meters from the ground. The model spacing and structural parameters shown in Figure 2 depicts the 2D and 3D schematic arrangement of the structure.

The entire 3D modeling process was executed using Revit software. Revit is a commercial Building Information Modeling (BIM) program developed by Autodesk (version 2023) and is widely used by structural engineers and architects to create 3D models and site plans.

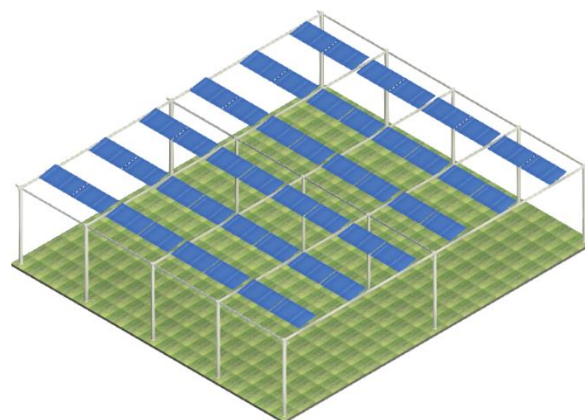
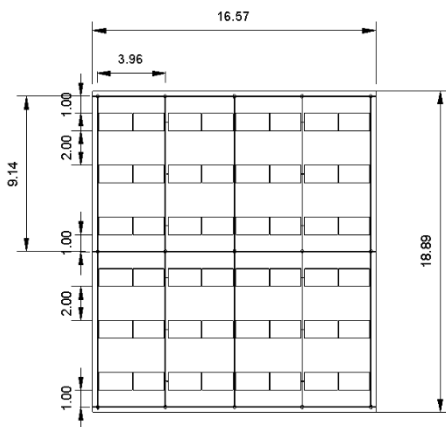


Figure 2: Full 2D and 3D View of the AV Design

B. Solar Irradiation Model

To capture the dynamic nature of sunlight, a 30-minute time-lapse was set within Revit to simulate the progression of the sun. The solar analysis tool in Revit's Insight module is based on the Perez solar model [15]. To perform accurate solar analysis, the tool relies on weather data specific to the location, sourced from Revit's location file, which includes information from a weather station (ID: 1584265) in Makurdi, Benue State, Nigeria. The data spans a typical meteorological year (TMY) from 2006 to 2021, with an elevation of 123 degrees.

As shown in Figure 3, the final design, created with Dynamo, presented a visual representation of the system's operation, demonstrating how each component interacts under various conditions. The full dataset was analyzed by the solar analysis node (see Figure 4), which calculated solar insolation for both the monoculture (MC) and agrivoltaic (AV) systems. This research provided valuable insights into the effectiveness of each system configuration, guiding decisions on optimal solar panel deployment and overall system design.

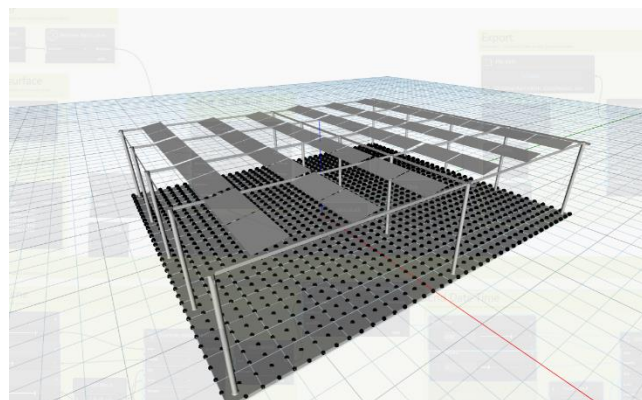


Figure 3: AV System Uploaded to Dynamo



Figure 4. All AV System Components Connected to the Solar Node

The SAM was used to simulate the energy production of the photovoltaic (PV) system. The PV modules used in the design are JKM400M types, with a nominal power output of 400 W and an efficiency of 20.17%. The modules measure 1.807 meters by 1.063 meters, and their high efficiency ensures significant energy output. The row spacing between PV panels was set at 2 meters to minimize shading between rows while maintaining optimal spacing.

C. Crop Model

Crop yield is calculated based on several parameters, including weather and soil conditions, crop variety, irrigation availability, drought stress, shade sensitivity, and collective physiological and morphological responses of crops. Shade has been shown to be an important factor affecting crop physiology and morphology, reducing overall biomass production [16]. Several models have been developed to evaluate soybean performance in an agrivoltaic (AV) system [17-21]. We developed an empirical model to quantify the impact of varying light levels on soybean production, specifically focusing on seed mass in grams (g). Data for this model was sourced from a research paper by Ephrath et al. [22], which investigated the impact of shade on soybean attributes under controlled conditions (see Figure 5).

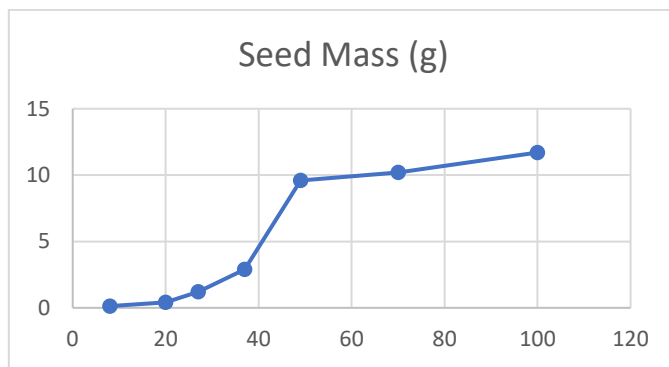


Figure 5: Influence of Available Light on Soybean Yield

The following empirical model was then derived from the data to estimate yield (Y) of soybean based on light percentage (L):

$$Y(L) = a * e^{bL} + c \quad (1)$$

where Y is the yield (either seed mass or pod mass), L is the percentage of available light, and a, b, and c are parameters to be estimated from the data. The yield sensitivity factor (YSF) for soybeans was determined by analyzing empirical data related to light percentage. This factor estimates soybean yield based on varying light levels relative to full-light conditions. Essentially, the YSF quantifies how soybean yield changes as light availability decreases from optimal levels.

D. Land Saving Model

Land Equivalent Ratios (LERs) are used to assess the value of mixed cropping systems [23,24]. We propose applying this concept to agrivoltaic systems. The LER of an agrivoltaic system is defined as:

$$LER = \frac{\text{Annual Electricity AV}}{\text{Annual Electricity Mono}} + \frac{\text{Yield AV}}{\text{Yield Mono}} \quad (2)$$

III. RESULTS

A. Solar Irradiation Yield and Shade Effects

As shown in Figure 7, solar irradiance was significantly reduced during shaded hours. Notably, during midday, when shading is at its maximum, solar irradiance is reduced by around 30% compared to unshaded conditions. This reduction is primarily due to the system design, which directs the PV panels' shade over the plot area. Solar irradiance gradually decreases in the morning and evening.

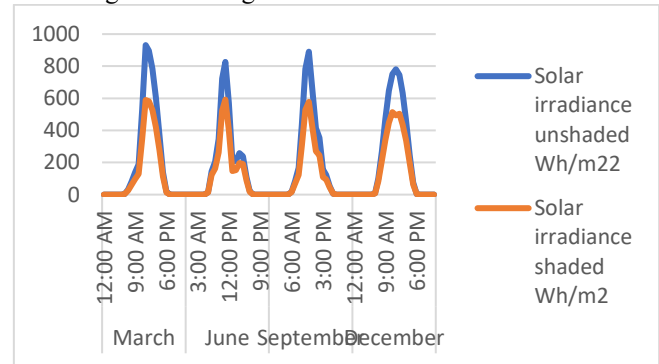


Figure 7: Monthly Solar Irradiation Variation

We show in Figure 8 the shadow effects of photovoltaic (PV) panels during noon time, indicatively and especially for the months of March and September, when the Sun is at its highest point in the sky (zenith), shading from the photovoltaic panels is considerable. It is clear from the figure that the shadows are extensive, covering almost one-third of the pilot area, confirming the obtained significantly lower irradiances given in Fig. 7 above.

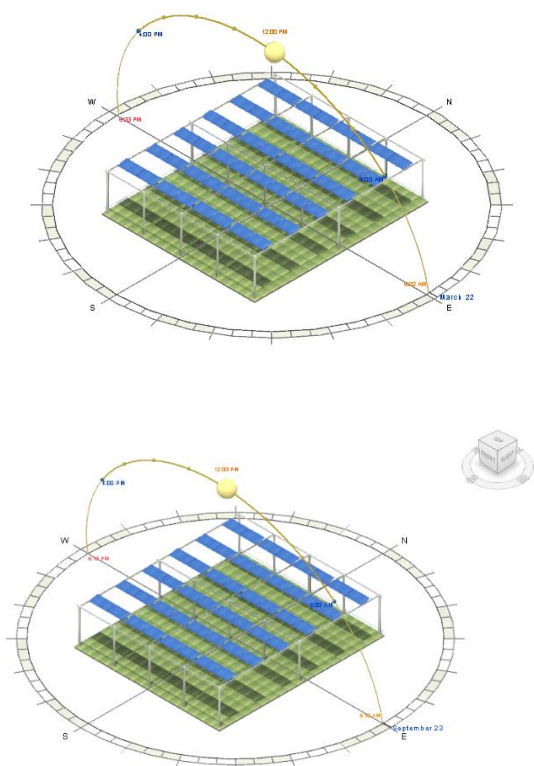


Figure 8: Variation in shadow of PV at noon over the crop surface during March and September

B. Energy Yield

The system's electricity generation potential was analyzed using SAM simulation software, resulting in important performance metrics for the first year of operation. The PV system of AV produced a total of 26,952 kWh in the first year, reflecting the aggregate energy output after accounting for fluctuations in solar irradiation and shading patterns. Then, a "Mono-cultural System" (MS) of PV was designed solely for electricity generation, covering the entire 313 m² plot area and resulting in an annual AC power output of 92,932 kWh. The purpose of this system was to evaluate the energy output of a PV-only setup and to calculate the Land Equivalent Ratio (LER), as presented in Table 1.

Table 1: LER Calculation for the PV System

Months	MS (kW)	AV (kW)	LER
March	12	3.6	0.29
Jun	8	2.4	0.30
Sep	9	2.6	0.30
Dec	13	3.9	0.30

C. Crop Yield

Soybean production in Nigeria was estimated to be between 0.9 and 1.4 tons per hectare. The yield was calculated in kilograms per square meter (kg/m²) based on the plot area. The monocultural (MS) system utilized the entire 313 m² plot for soybean cultivation. The agrivoltaics (AV) system, with an

active cropping area of 313 m², was then examined. The Land Equivalent Ratio (LER) was calculated to compare the yields of both systems, as shown in Table 2.

Table 2: LER calculation of crop system

Months	MS Yield (Kg)	AV Yield (Kg)	LER
March	28.17	21.77	0.77
Jun	28.17	22.97	0.82
Sep	28.17	21.90	0.78
Dec	28.17	22.30	0.79

IV. CONCLUSION

We developed an innovative model that integrates agrivoltaic systems into Nigeria's agricultural landscape, focusing on the dual use of land for both solar energy production and crop cultivation. Our findings revealed distinct seasonal variations in shading, with significant differences observed during the solstices and equinoxes. These patterns had a notable impact on both solar energy efficiency and crop development, particularly in our case study of soybean production. The projected soybean yield is approximately 28.17 to 43.82 kg under monocropping conditions. This provides an accurate assessment of production potential in the context of localized agricultural practices. Despite the shading, the agrivoltaic system produced 26,952 kWh of power in its first year, achieving a capacity factor of 16% while maintaining effective land usage. The Land Equivalent Ratio (LER) for both crop and photovoltaic (PV) systems in monocultural and AV Systems was combined to assess overall performance. The results showed that the total LER consistently achieved a value of 1, indicating ideal land use efficiency with no substantial reduction in overall production. This balance demonstrates how the system effectively supports both agricultural and energy output while maintaining crop yield. Overall, this study demonstrates the potential of agrivoltaic systems to increase energy generation while preserving agricultural productivity, providing a feasible framework for future application in similar settings.

ACKNOWLEDGMENT

The first author would like to thank the Revit BIM software development team for offering a student license and express his special thanks to ChatGPT software for providing user-friendly assistance during the linguistic revision of this work.

REFERENCES

- [1] IEA (2014), Technology Roadmap - Solar Photovoltaic Energy 2014, IEA, Paris <https://www.iea.org/reports/technology-roadmap-solar-photovoltaic-energy-2014>, Licence: CC BY 4.0
- [2] Sacchelli S, Garegnani G, Geri F, Grilli G, Paletto A, Zambelli P, et al. Trade-off between photovoltaic systems installation and agricultural practices on arable lands: an environmental and socio-economic impact analysis for Italy. *Land Use Policy* 2016;56:90–6.
- [3] Fthenakis V, Kim CK. Land use and electricity generation: a life-cycle analysis. *Renew Sustain Energy Rev* 2009;13:1465–74. <http://dx.doi.org/10.1016/j.rser>.

- [4] Goetzberger, A.; Zastrow, A. On the Coexistence of Solar-Energy Conversion and Plant Cultivation. *Int. J. Sol. Energy* 1981, 1, 55–69
- [5] Ravi S, Macknick J, Lobell D, Field C, Ganesan K, Jain R, et al. Colocation opportunities for large solar infrastructures and agriculture in drylands. *Appl Energy* 2016;165:383–92.
- [6] Marrou H, Wery J, Dufour L, Dupraz C. Productivity and radiation use efficiency of lettuces grown in the partial shade of photovoltaic panels. *Eur J Agron* 2013;44:54–66.
- [7] Cossu Marco, Murgia Lelia, Ledda Luigi, Deligios Paola A, Sirigu Antonella, Chessa Franseco, Pazzona Antonio. Solar radiation distribution inside a greenhouse with south-oriented photovoltaic roofs and effects on crop productivity. *Appl Energy* 2014;133:89–100.
- [8] Teng, Jerome & Soh, Chew & Devihosur, Shiddalingeshwar & Tay, Ryan & Jusuf, Steve. (2022). Effects of Agrivoltaic Systems on the Surrounding Rooftop Microclimate. *Sustainability*. 14. 7089. 10.3390/su14127089.
- [9] Aminata Sarr, Y.M. Soro, Alain K. Tossa, Lamine Diop, A new approach for modelling photovoltaic panel configuration maximizing crop yield and photovoltaic array outputs in agrivoltaics systems, *Energy Conversion and Management*, Volume 309, 2024, 118436, ISSN 0196-8904,
- [10] Warmann, Emily & Jenerette, G & Barron-Gafford, Greg. (2024). Agrivoltaic system design tools for managing trade-offs between energy production, crop productivity and water consumption. *Environmental Research Letters*. 19. 10.1088/1748-9326/ad2ab8.
- [11] Garrod, Aydan & Hussain, Shanza & Ghosh, Aritra. (2024). The technical and economic potential for crop based agrivoltaics in the United Kingdom. *Solar Energy*. 277. 112744. 10.1016/j.solener.2024.112744.
- [12] Wagner, Moritz & Lask, Jan & Kiesel, Andreas & Lewandowski, Iris & Weselek, Axel & Högy, Petra & Trommsdorff, Max & Schnaiker, Marc-André & Bauerle, Andrea. (2023). Agrivoltaics: The Environmental Impacts of Combining Food Crop Cultivation and Solar Energy Generation. *Agronomy*. 13. 299. 10.3390/agronomy13020299.
- [13] Ebhota, Williams & Tabakov, Pavel. (2024). Vol. 43, No. 2, June 2024. LEVERAGING AGRIVOLTAICS TO INCREASE FOOD, ENERGY, AND WATER ACCESS IN THE GLOBAL SOUTH: A CASE STUDY SUB-SAHARAN AFRICA. *Nigerian Journal of Technology*. 43. 364 - 380. 10.4314/njt.v43i2.20.
- [14] Abur, Benjamin & Ayubaduvuna, Gideon. (2014). Renewable Energy Resources in Benue State-Nigeria: Estimation and Mapping of Solar Energy Potentials.
- [15] Perez, R., F. P. N. K. L. A., & M. A. (1990). "Modeling daylight availability and irradiance data." *Solar Energy*, 44(5), 271-289.
- [16] Gommers, C.M.; Visser, E.J.; Onge, K.R.S.; Voesenek, L.A.; Pierik, R. Shade tolerance: When growing tall is not an option. *Trends Plant. Sci.* 2013, 18, 65–71.
- [17] Croci, Michele & Colauzzi, Michele & Amaducci, Stefano & Potenza, Eleonora. (2022). Agrivoltaic System and Modelling Simulation: A Case Study of Soybean (*Glycine max L.*) in Italy. *Horticulturae*. 8. 10.3390/horticulturae8121160.
- [18] Ningning Wang, Qinjun Huang, Jingru Sun, Suli Yan, Changjun Ding, Xindi Mei, Dan Li, Xianjun Zeng, Xiaohua Su, Yingbai Shen, Shade tolerance plays an important role in biomass production of different poplar genotypes in a high-density plantation, *Forest Ecology and Management*, Volume 331, 2014, Pages 40-49, ISSN 0378-1127
- [19] Ko, J.; Cho, J.; Choi, J.; Yoon, C.Y.; An, K.N.; Ban, J.O.; Kim, D.K. Simulation of Crop Yields Grown under Agro-Photovoltaic Panels: A Case Study in Chonnam Province, South Korea. *Energies* 2021, 14, 8463
- [20] Cuppari, R.I.; Higgins, C.W.; Characklis, G.W. Agrivoltaics and weather risk: A diversification strategy for landowners. *Appl. Energy* 2021, 291, 116809.
- [21] Kim, S.; Kim, S.; Yoon, C.Y. An efficient structure of an agrophotovoltaic system in a temperate climate region. *Agronomy* 2021, 11, 1584\
- [22] Ephrath, Jhonathan & Wang, R. & Terashima, K. & Hesketh, J. & Huck, M. & Hummel, J. & テラシマ, (1993). Shading effects on soybean and corn. 22.
- [23] Nimay Chandra Giri, Ramesh Chandra Mohanty, Agrivoltaic system: Experimental analysis for enhancing land productivity and revenue of farmers, *Energy for Sustainable Development*, Volume 70, 2022, Pages 54-61,
- [24] S. Sacchelli, G. Garegnani, F. Geri, G. Grilli, A. Paletto, P. Zambelli, M. Ciolli, D. Vettorato, Trade-off between photovoltaic systems installation and agricultural practices on arable lands: An environmental and socio-economic impact analysis for Italy, *Land Use Policy*, Volume 56, 2016, Pages 90-99, ISSN 0264-8377,

Lyapunov-based Deep Neural Network Robust Trajectory Control for Robotic System

FIRAT CAN YILMAZ¹, RECEP ONLER¹

¹ Gebze Technical University, Kocaeli/Turkey, fcyilmaz@gtu.edu.tr

¹ Gebze Technical University, Kocaeli/Turkey, ronler@gtu.edu.tr

Abstract - In this study, trajectory tracking of a robotic system was investigated. A Lyapunov-based robust deep neural network algorithm was designed to obtain the control aim. The proposed control algorithm design involves a neural network algorithm and robust disturbance rejection for the unknown system under disturbance signals. The Neural network algorithm has 3 hidden layers, and the activation function of the network is a rectified linear unit. The system's trajectory tracking performance was investigated under the variable unknown parameters and unknown disturbance signals. The proposed approach has shown a remarkable performance in trajectory control.

Keywords - Neural Networks, Robotic, Learning Algorithm, Robust Control, Trajectory Control

I. INTRODUCTION

THE control algorithm design to find some engineering problems has been investigated for some decades. A set of researchers in the control algorithm methodology interested the vibration analysis in systems like trains, trucks, or cars. The vibration suppression analysis can be done for the increment of the comfort parameters or for the prevention of the vibration's negative effects. Other researchers of the methodology are attracted to trajectory tracking control. In the tracking control, how the system state term is driven to the desired state term is examined.

In the development of the control algorithm theory, different methodologies were studied by researchers from all around the world. Some milestones of the evolution of theory are Linear Matrix Inequalities (LMI)-based linear control algorithms [1], adaptive control [2], and Model Predictive Control [3]. The interaction between methodologies helps to improve themselves such as image processing and control theory. The interaction between machine learning and control theory allows us to expand the borders of approaches such as adaptive control. In the [4], a real-time Deep Neural Network(DNN) architecture was developed for trajectory control. The performance of the proposed controller was investigated for the Van der Pol oscillator. Also, similar approach examples can be found between [5:6]. The real-world system has also some imperfections such as external effects. These disturbance signals can affect the performance of the controller performance. For example, in the vibration suppression analysis, the road surface is the important variable. One of the works was studied by Metin [7]. In the study, the fuzzy logic control algorithm and PID control algorithm were investigated for 11 degree-of-freedom rail vehicle models. The performance

of the proposed controller algorithms was shown in time and frequency domains. Another work [8] proposed a control algorithm design for a two-degree-of-freedom (dof) robot manipulator model under external variations.

In this work, we present a control algorithm model that includes a DNN algorithm and compression of the external variations. By the designed control algorithm, the uncertain robot manipulator's state term can be driven to the desired state term. While disturbance signals affect the robot manipulator, the control algorithm shows superior performance and guarantees the stability of the system through the disturbance rejection part in the algorithm. Also, the manipulator system's mass parameter can be variable during the process. The proposed control ability was investigated at the variable unknown parameters.

This paper was organized as follows. In Section 2, Mathematical Model, we present the general mechanical model of an n-degree fully connected robot manipulator system. In Section 3, Error System Development, we present the main control objective and design the adaptation law for the outer layer of the DNN and show the proposed control algorithm. In Section 4, Analysis, the stability analysis of the designed control algorithm was done. In Section 5, Numerical Study, the simulation of the developed algorithm was presented. Finally, Section 6, Conclusion, is the closure of the study.

II. MATHEMATICAL MODEL

The general mechanical model representation of an n-degree fully actuated robot manipulator system is given as (1) [9].

$$M(q)\ddot{q} + C(q, \dot{q})\dot{q} + G(q) + F_d\dot{q} + \tau_d = \tau \quad (1)$$

where $q(t)$, $\dot{q}(t)$, $\ddot{q}(t) \in R^n$ denote the position, velocity, and acceleration vectors, respectively. $M(q) \in R^{n \times n}$ is the inertia matrix, $C(q, \dot{q}) \in R^{n \times n}$ is the centripetal Coriolis matrix, $G(q) \in R^n$ represents the gravitational effects, $F_d \in R^{n \times n}$ is the viscous frictional effects, $\tau_d \in R^n$ is the external disturbance effects, and $\tau \in R^n$ is the control input torques.

III. ERROR SYSTEM DEVELOPMENT

The main control objective is for the robot manipulator system states to drive the desired signals. While the control algorithm theory at the manipulator has been designed, the signals of the states should be held in a bound. The control signals drive the position vector $q(t)$ to the desired position signals $q_d(t)$ smoothly despite the existence of uncertainties in the investigated dynamic system. To design the control

algorithm signals, firstly, the error signal vector, $e(t) \in R^n$ and the filtered tracking term $r(t) \in R^n$ are define as

$$e(t) \triangleq q_d - q \quad (2)$$

$$r(t) \triangleq \dot{e} + e \quad (3)$$

DNN algorithm design will be used to estimate the effects of the uncertain dynamic system. The system representation over DNN algorithm is given in (4)

$$M(q)(\ddot{q}_d + \dot{e}) + C(q, \dot{q})(\dot{q}_d + \dot{e}) + G(q) + F_d \dot{q} = W\sigma(I(x)) + \epsilon(x) \quad (3)$$

where the input vector to DNN, $x \in R^{5n}$ is defined as $x = [q^T, \dot{q}^T, q_d^T, \dot{q}_d^T, \ddot{q}_d^T]^T$, $W \in R^{L \times n}$ is the ideal output-layer weight matrix, $\sigma(\cdot): R^p \rightarrow R^L$ is the vector of the ideal activation functions, $I(x)$ represents the ideal DNN inner layers.

To obtain the open-loop error dynamics of the system, the time derivation of the (3) after it was multiplied by the inertia matrix is done

$$M(q)\dot{r} = M(q)(\ddot{q}_d + \dot{e}) + C(q, \dot{q})(\dot{q}_d + \dot{e}) + G(q) + F_d \dot{q} + \tau_d - \tau - C(q, \dot{q})r \quad (4)$$

The DNN representation of the system in (3) was substituted into (4).

$$M(q)\dot{r} = W\sigma(I(x)) + \epsilon(x) + \tau_d - \tau - C(q, \dot{q})r \quad (5)$$

The proposed control algorithm and the outer layer adaptation law of the DNN were designed as

$$\tau = \hat{W}\hat{\sigma}(\hat{I}(x)) + k_1 r + k_2 \text{sgn}(r) + k_3 \text{sgn}(\dot{r}) \quad (6)$$

$$\dot{\hat{W}} = \Gamma_w \hat{\sigma}(\hat{I}(x)) r^T \quad (7)$$

where k_1, k_2, k_3 are positive definite control gains with proper sizes, $\text{sgn}(\cdot)$ represents the signum function and $\Gamma_w = R^{L \times L}$ is the diagonal, positive valued adaptation gain matrix.

IV. ANALYSIS

In the analysis of the proposed control algorithm, a non-negative function, a candidate Lyapunov function, is defined as

$$V = \frac{1}{2} r^T M(q) r + \frac{1}{2} \text{tr}(\tilde{W}^T \Gamma_w \tilde{W}) \quad (7)$$

where $\text{tr}(\cdot)$ is used to trace of a matrix. After taking the derivation of the candidate Lyapunov function, the proposed controller algorithm in (6) and system mathematical representation in (5) will be inserted while using the skew-symmetric relationship (i. e. $r^T \left(\frac{1}{2} \dot{M}(q) - C(q, \dot{q}) \right) r = 0$).

$$\dot{V} = r^T \left(W \left(\sigma(I(x)) - \hat{\sigma}(\hat{I}(x)) \right) + \epsilon(x) + \tau_d - k_1 r - k_2 \text{sgn}(r) - k_3 \text{sgn}(\dot{r}) \right) \quad (8)$$

The controller gain, k_1, k_2, k_3 is selected to satisfy the stability

$$k_2 \geq \overline{W \left(\sigma(I(x)) - \hat{\sigma}(\hat{I}(x)) \right)} + \bar{\epsilon} \quad (9)$$

$$k_3 \geq \overline{\tau_d} \quad (10)$$

The upper bound for the time derivation of $V(t)$ as

$$\dot{V} \leq -\lambda_{\min}\{k_1\} \|r\|^2 \quad (11)$$

where $\overline{(\cdot)}$ is used to represent the upper bound of the function (\cdot) . From the design of $V(t)$ in (7) and the time derivation of $V(t)$ in (11), $V(t)$ is found to a bounded. Therefore, the signals $e(t)$, and $r(t)$ and are also found as bounded. From the boundedness of $e(t)$, and $r(t)$ the time

derivation of the error term, $\dot{e}(t)$, is also bounded. From the direct application of Barablat's Lemma[10].

$$\lim_{t \rightarrow \infty} e(t) = 0 \quad (12)$$

which concludes the analysis section.

V. NUMERICAL STUDY

In this section, the proposed control algorithm was investigated. In the performance investigation of the control algorithm, the system was affected by external disturbances. Also, the trajectory tracking performance was shown under the variable unknown parameters. In the studies, a 2 dof robot manipulator system was used. The viscous friction effects, F_d , in the system were ignored in the simulations. The disturbance signals to the system

$$\begin{aligned} d_1 &= 10 \sin(1.4\pi t) + 7 \cos(\pi t) \\ d_2 &= 4 \sin(1.4\pi t) + 12 \cos(1\pi t) \\ \tau_d &= [d_1^T, d_2^T]^T \end{aligned} \quad (13)$$

The reference term in the studies

$$\begin{aligned} q_{d1} &= 0.2 \sin(0.5\pi t) (1 - e^{-0.1t^2}) \\ q_{d2} &= 1.2 \sin(t) (1 - e^{-0.1t^2}) \\ q_d &= [q_{d1}^T, q_{d2}^T]^T \end{aligned} \quad (14)$$

The DNN algorithm that was used in the proposed control algorithm was shown in Figure 1.

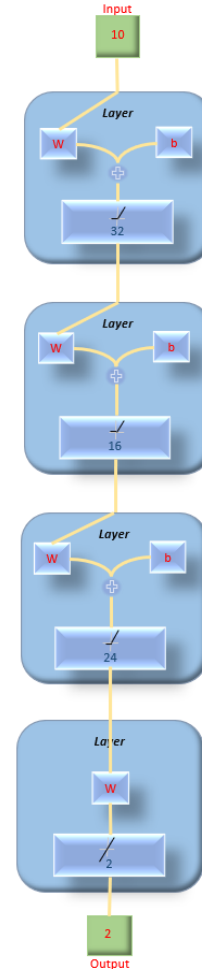


Figure 1: The neural network design.

In the DNN algorithm, the input size is 10, and the output size is 2. The activation function in the network was selected as Rectified Linear Units (ReLU). By the usage of this activation function, if the input to the activation function is lower than 0, the output from the ReLU becomes 0. The outer layer of the network is updated with the adaptation law in (7). The weights and biases of the inner layer of the network design were randomly assigned within the range of $[-1, 1]$. The beginning weights of the outer layer of the network were also assigned randomly with the same range. The hidden layers of the network are 32, 16, and 24, respectively.

In numerical studies, the mass term of the robot manipulator links was used as $m = m_n + \Delta m$. m_n is the unknown nominal mass term, and the Δm is the variable term of the mass term. In Figure 2, the performance of the proposed control algorithm was shown for q_1 .

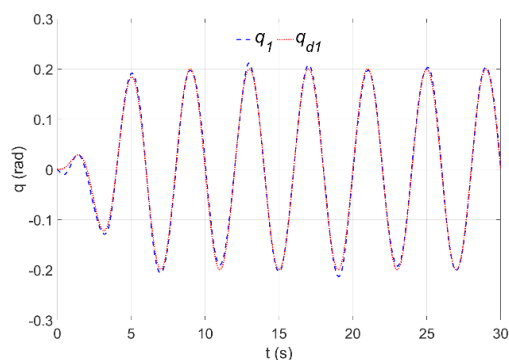


Figure 2: The reference and system angular displacements - 1

The proposed control approach has shown a remarkable performance in trajectory control. Under the variation of the mass term and the disturbance effects at the system, the trajectory tracking was effectively good. This performance by the approach shows the ability of the proposed control signal to deal with external effects and variations. In Figure 2, the control algorithm performance for q_2 was shown.

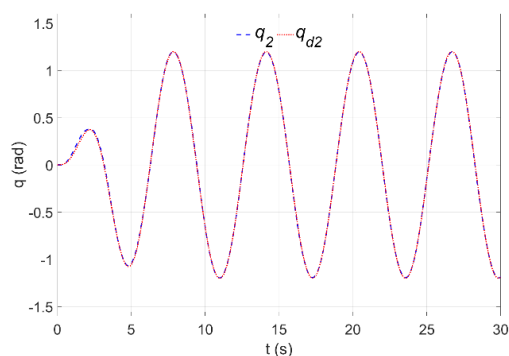


Figure 3: The reference and system angular displacements - 2

The tracking performance of the proposed control algorithm in q_2 is also superior as the performance at q_1 . The q , angular displacement term of the system, was driven to q_d , desired angular signals, by τ , the designed control algorithm term. In Figure 4, the control algorithm term under the simulation was shown.

The proposed control algorithm signals need to provide the

trajectory tracking performance of approximately 60 Nm. The torque values have high chattering due to the existence of the signum function.

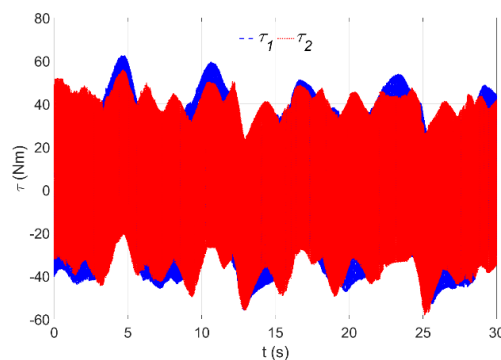


Figure 4: The control algorithm signals

VI. CONCLUSION

In this study, a control algorithm approach was developed using DNN and disturbance rejection. The DNN algorithm has 3 hidden layers and ReLU activation functions. The weights and biases of the network were randomly assigned. Also, the initial weights of the outer layer of the network are randomly assigned. The outer layer's weights of the network were updated online. The designed DNN algorithm has been used for the estimation of the system, and the disturbance rejection has been used for the external disturbance effects. Under the numerical study, the performance of the proposed approach was investigated for the system which has unknown variable parameters. The results exhibit the DNN integrated control algorithm design has shown a superior performance under these conditions.

REFERENCES

- [1] S. Boyd, L. El Ghaoui, E. Feron, and V. Balakrishnan, *Linear Matrix Inequalities in System and Control Theory*. Society for industrial and applied mathematics, 1994.
- [2] K. J. Åström, and B. Wittenmark, *Adaptive Control*. Courier Corporation, 2013.
- [3] J. A. Rossiter, *Model-Based Predictive Control: A Practical Approach*. CRC press, 2017.
- [4] R. Sun, M. L. Greene, D. M. Le, Z. I. Bell, G. Chowdhary, and W. E. Dixon, "Lyapunov-based real-time and iterative adjustment of deep neural networks," *IEEE Control Systems Letters*, vol. 6, pp. 193-198, 2021.
- [5] O. S. Patil, D. M. Le, M. L. Greene, and W. E. Dixon, "Lyapunov-derived control and adaptive update laws for inner and outer layer weights of a deep neural network," *IEEE Control Systems Letters*, vol. 6, pp. 1855-1860, 2021.
- [6] O. S. Patil, D. M. Le, E. J. Griffis, and W. E. Dixon, "Deep residual neural network (ResNet)-based adaptive control: A Lyapunov-based approach," In *2022 IEEE 61st Conference on Decision and Control (CDC)*, pp. 3487-3492.
- [7] M. Metin, and R. Guclu, "Active vibration control with comparative algorithms of half rail vehicle model under various track irregularities," *Journal of Vibration and Control*, vol. 17(10), pp. 1525-1539, 2011.
- [8] F. Massaoudi, D. Elleuch, and T. Damak, "Robust control for a two DOF robot manipulator," *Journal of Electrical and Computer Engineering*, vol. 2019(1) pp. 1-11, 2019.
- [9] F. L. Lewis, D. M. Dawson, and C. T. Abdallah, *Robot Manipulator Control: Theory and Practice*. CRC Press, 2003.
- [10] J. J. E. Slotine, W. Li, *Applied Nonlinear Control*. Englewood Cliffs, NJ: Prentice hall, 1991.

Controlled Morphology Transformation in NiCo₂O₄ via Hydrothermal Synthesis

BURAK KIVRAK¹, İ. BALCI¹, İ.C. KAYA¹, M. AKYOL², H. AKYILDIZ¹

¹ Konya Technical University, Konya/Turkey, bkivrak@ktun.edu.tr, f231219012@ktun.edu.tr, ickaya@ktun.edu.tr, hakyildiz@ktun.edu.tr

²Adana Alparslan Türkeş Science and Technology University, Adana/Turkey, makyol@atu.edu.tr

Abstract - In this study, we synthesized NiCo₂O₄ particles with distinctive urchin-like and hollow urchin-like morphologies using hydrothermal method with varying reaction times, followed by heat treatment. X-ray diffraction (XRD) analysis confirmed the high crystallinity and cubic spinel structure of all samples, consistent with NiCo₂O₄ reference data (JCPDS: 01-073-1702). Electron microscopy analyses revealed that morphology evolved from urchin-like particles to hollow urchin-like structures as reaction time increased, a transformation attributed to dissolution-recrystallization mechanisms. Images further showed an increase in particle and needle sizes with reaction time, with average particle diameters of 3.17 μm, 3.95 μm, and 6.04 μm, and needle lengths of 0.832 μm, 1.22 μm, and 1.53 μm for 90, 150, and 210 min, respectively. These findings demonstrate the effectiveness of time-dependent hydrothermal synthesis in tailoring NiCo₂O₄ structures, providing insight into controlled morphological evolution for potential applications in catalysis, energy storage, and environmental remediation.

Keywords – Nickel cobaltite, cubic spinel, hydrothermal synthesis.

I. INTRODUCTION

NiCo₂O₄ ternary spinel transition metal oxide, have gained huge interest due to its exceptional properties such as high specific capacity, electrical conductivity, high electrochemical response, controllable morphology, low cost and environmentally friendly nature [1-3]. In connection with its properties, it has been widely used in electrochemical reactions, supercapacitor applications, Li-ion batteries, microwave absorption applications, and photocatalysis [2-6]. In crystal structure of cubic NiCo₂O₄ with *Fd3m* space group symmetry, Ni ions occupy the octahedral sites while the Co ions occupy both octahedral and tetrahedral sites which efficiently influences its electrochemical performance [7].

Due to its anisotropic shape factor, NiCo₂O₄ can be synthesized in various morphologies like 1D nanowires (NWs), nanosheets (NSs), plate-like nanoparticles, flower-like particles (FLWs) and urchin-like structures which are beneficial in various applications [8-12]. For example, Su et al., have manufactured flower-like structures using hydrothermal synthesis and investigated its microwave absorption characteristics depending on morphology. Their results showed that the control of morphology have significant impact on the

optimizing the electromagnetic performance of the absorber resulting in the minimum reflection loss of -50.3 dB with an effective absorption bandwidth of 4 GHz at 2 mm thickness [5]. On the other hand, Sasmal et al., have synthesized nano-flower, nanorod and nanosheet like NiCo₂O₄ using solvothermal method and investigated impact of morphology on the supercapacitor properties. According to this study, among all the morphologies, NiCo₂O₄ nanoflowers showed the best performance due to its large surface area, high number of active sites and lower charge transfer resistance [13]. In addition, Bai et al., synthesized 1D rod and 2D sheet morphologies of NiCo₂O₄ and displayed their electrochemical sensing performance for glucose. The study's findings demonstrated that the magnitude of oxidation peak current of rod-like morphology is nearly two times higher than that of sheet-like NiCo₂O₄ and exhibited higher electrocatalytic activity. Considering the above studies, the morphological features and diversities of NiCo₂O₄ are highly important and have great impact on the final device properties.

In this study, urchin-like and hollow urchin-like NiCo₂O₄ particles were synthesized via the hydrothermal method under varying reaction times, followed by heat treatment. X-ray diffraction (XRD) analysis confirmed that all samples are crystalline, with peaks well corresponding to the cubic spinel structure of NiCo₂O₄. Scanning electron microscopy (SEM) images further revealed the morphological transition from urchin-like to hollow urchin-like shapes with increasing reaction time.

II. EXPERIMENTAL PROCEDURE

NiCo₂O₄ (NCO) particles were synthesized using mild hydrothermal conditions as illustrated in Figure 1. In synthesis, the reaction temperature was kept at 120 °C and the reaction time varied as 90, 150 and 210 min. Initially, 0.809 g nickel nitrate hexahydrate (Ni(NO₃)₂·6H₂O, Ni-source, ≥99% purity, Merck) was weighed and dissolved in 85 mL de-ionized (DI) water using a magnetic stirrer at 1200 rpm for 15 min at room temperature. Then, 1.621 g of cobalt nitrate hexahydrate (Co(NO₃)₂·6H₂O, Co-source, ≥99% purity, Sigma Aldrich) was weighed and added to the above solution for 15 min. In the last step of solution preparation, 2.50 g of urea (CH₄N₂O, alkali source, reducing and hydrolyzing component, 100% purity, VWR Chemicals) was added to the solution for further mixing

at room temperature for 1 h. After complete dissolution of the starting components, the transparent solution was transferred into a polytetrafluoroethylene (PTFE, Teflon) container and the hydrothermal synthesis step was started.

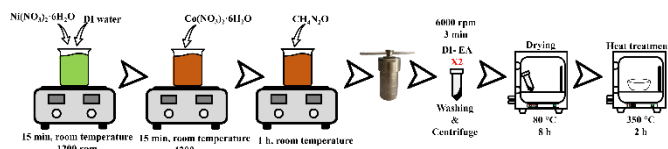


Figure 1: Schematic illustration of the synthesis procedure.

Upon completion of the hydrothermal process, the synthesized powders were rinsed twice with deionized water and ethanol (96% purity). Following the washing step, the powders were dried at 80 °C for 8 h. To enhance crystallization, the powders were subsequently heated to 350 °C at a rate of 3 °C/min in a muffle furnace in air for 2 h. After naturally cooling to room temperature, the powders were prepared for subsequent characterization without further treatment.

III. RESULTS AND DISCUSSION

The structural properties of the samples were examined using XRD within a 2θ range of 20–80°. Lattice parameters and crystallite sizes were calculated using the formula $1/d^2 = (h^2 + k^2 + l^2)/a^2$ and Debye-Scherrer equation, respectively. Additionally, these results were confirmed using the X-Pert Highscore Plus software.

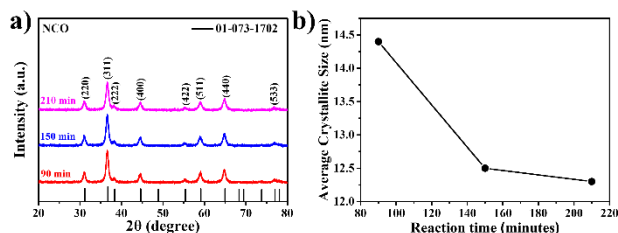


Figure 2: Structural properties of manufactured samples a) diffraction patterns and b) average crystallite size graph with respect to the reaction time.

The diffraction patterns of the samples are presented in Figure 2a, with vertical black lines indicating the theoretical peak positions for cubic NiCo_2O_4 (JCPDS: 01-073-1702). The patterns show no evidence of impurities or secondary phases, with all peaks aligning well with the $Fd\bar{3}m$ space group of the cubic structure. It can be seen from these patterns that the peak intensities gradually decrease with the increasing reaction time. This can be explained by the growth mechanisms of the NiCo_2O_4 through dissolving-recrystallization reaction (will be discussed in the morphological examination section). The lattice parameter for NCO particles synthesized at 120°C was calculated to be $a = 8.12 \text{ \AA}$, consistent with literature values. Figure 2b and Table 1 present the calculated average crystallite sizes of the samples, which were found to be 14.4 nm, 12.5 nm, and 12.3 nm for reaction time of 90, 150 and 210 min, respectively. The reduction in crystallite size correlates with the observed decrease in peak intensities.

Table 1: Average crystallite, particle and needle sizes as a function of hydrothermal reaction time.

Sample Code	Average Crystallite Size (nm)	Average Particle size (diameter, μm)	Average Needle size (μm)
NCO-90 min	14.4	3.17	0.83
NCO-120 min	12.5	3.95	1.22
NCO-150 min	12.3	6.04	1.53

The morphological features of the synthesized samples were investigated using SEM with magnification of 10 kX and 20 kX besides resulting images were displayed in Figure 3. According to Figs 3a-b, particles formed in spherical shapes and prone to agglomeration. Images recorded at higher magnifications show that these spherical particles are actually composed of needles extending outward from the center, similar to the appearance of a sea urchin.

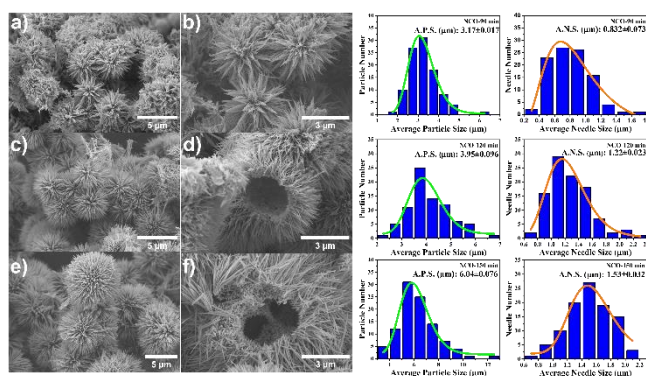
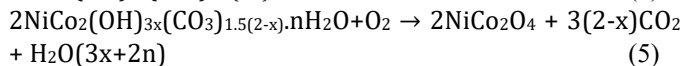
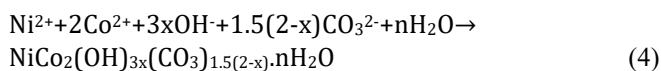


Figure 3. Representative SEM images of samples along with average particle size and needle size distribution graphs, a-b) NCO-90 min, c-d) NCO-120 min and e-f) NCO-150 min. The size distribution graphs are given on the right side of SEM images.

The morphology observed here for the collected NCO particles was also reported in some previous studies [14-16]. Furthermore, Panja et al. presented a SEM image of a fractured microsphere and claimed that in fact the centers of all microspheres are hollow and around this hollow core, bundles of spikes come together to form these microspheres. They attributed the formation of such a hierarchical morphology to the self-template organizer and precipitant roles of urea [17]. The first three reactions given below shows the reactants resulting from the decomposition of urea with water [18]. Among these components, CO_3^{2-} has been reported to be important for the sea urchin-like NiCo_2O_4 morphology formed by the assembly of nano-needle bundles. When urea is used as an alkaline hydrolysis agent, it is mentioned that Ni^{2+} and Co^{2+} react with CO_3^{2-} and OH^- to form the bi-metallic (Ni, Co) carbonate hydroxide phase seen in equation 4, which is composed of these aggregated nano-needles, and this phase is transformed into the NiCo_2O_4 given in the last step by annealing without undergoing much morphological transformation [18, 19].





With extended synthesis time, the particle morphology evolves into a hollow, urchin-like structure, first emerging at 150 min and becoming more pronounced after 210 min. This transformation aligns with observations reported by Luo et al.[15]. Initially, during the solvothermal process, the Ni–Co precursor is seen as solid microspheres with smooth surfaces, likely due to minimized surface tension effects. The surface energy difference between the inner and outer grains leads to the dissolution of the grains inside the microsphere as the reaction progresses. This dissolution process, followed by recrystallization, supports secondary crystal growth along the microsphere's outer shell. As time progresses, the microspheres develop core–shell configurations, with nanoneedles growing vertically on their surfaces. This kind of reaction sequence looks valid for the samples synthesized in the current study.

The average particle and needle dimensions are shown on the right side of Fig. 3 and summarized in Table 1. According to the data, the mean diameter of the spherical particles is approximately 3.17 μm , 3.95 μm , and 6.04 μm for samples synthesized over 90, 150, and 210 minutes, respectively. Similarly, the average length of the needles increases with reaction time, measured as 0.832 μm , 1.22 μm , and 1.53 μm . It may be worth emphasizing here that the needle shape turned into rod-like for extended reaction times. These findings suggest that NCO particles increase in size with longer synthesis times, adopting a hollow, urchin-like morphology as illustrated in Fig 4. Such a controlled morphological evolution is highly desirable for a variety of applications where the shape, the amount of surface area as well as the surface energy is important.

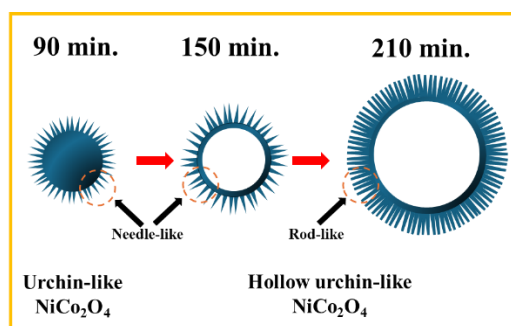


Figure 4. Schematic illustration of morphological evolution in hydrothermally synthesized NiCo_2O_4 as a function of reaction time.

ACKNOWLEDGMENT

This study was supported by Konya Technical University Scientific Research Projects under project number 232219041.

REFERENCES

- [1] Liu, S., et al., *Nickel Cobaltite Nanostructures for Photoelectric and Catalytic Applications*. *Small*, 2015. **11**(34): p. 4267-4283.

- [2] Li, Y., et al., *Review and prospect of NiCo_2O_4 -based composite materials for supercapacitor electrodes*. *Journal of Energy Chemistry*, 2019. **31**: p. 54-78.
- [3] Han, X., et al., *Recent progress of NiCo_2O_4 -based anodes for high-performance lithium-ion batteries*. *Current Opinion in Solid State and Materials Science*, 2018. **22**(4): p. 109-126.
- [4] Pathak, M., S.M. Jeong, and C.S. Rout, *Spinel NiCo_2O_4 based hybrid materials for supercapacitors: Recent developments and future perspectives*. *Journal of Energy Storage*, 2023. **73**: p. 108881.
- [5] Su, X., et al., *Design of controlled-morphology NiCo_2O_4 with tunable and excellent microwave absorption performance*. *Ceramics International*, 2020. **46**(6): p. 7833-7841.
- [6] Lal, S., et al., *Enhancing photocatalytic, photoelectrochemical hydrogen evolution, and dye degradation using p-type NiCo_2O_4 spinel photocatalyst synthesized via tapioca leaf extract mediated process*. *Colloids and Surfaces A: Physicochemical and Engineering Aspects*, 2023. **676**: p. 132262.
- [7] Wang, C., et al., *NiCo_2O_4 -Based Supercapacitor Nanomaterials*. *Nanomaterials*, 2017. **7**(2): p. 41.
- [8] Xu, Z., et al., *Facile Hierarchical Growth of N-Doped Carbon-Coated NiCo_2O_4 Nanowire Arrays on Ni Foam for Advanced Supercapacitor Electrodes*. *ACS Sustainable Chemistry & Engineering*, 2019. **7**(14): p. 12447-12456.
- [9] Lee, D.U., B.J. Kim, and Z. Chen, *One-pot synthesis of a mesoporous NiCo_2O_4 nanoplatelet and graphene hybrid and its oxygen reduction and evolution activities as an efficient bifunctional electrocatalyst*. *Journal of Materials Chemistry A*, 2013. **1**(15): p. 4754-4762.
- [10] Liu, Z.-Q., et al., *Fabrication of hierarchical flower-like superstructures consisting of porous NiCo_2O_4 nanosheets and their electrochemical and magnetic properties*. *RSC Advances*, 2013. **3**(13): p. 4372-4380.
- [11] Dong, J.Y. and X.T. Zhang, *The preparation and electrochemical characterization of urchin-like NiCo_2O_4 nanostructures*. *Applied Surface Science*, 2015. **332**: p. 247-252.
- [12] Dubal, D.P., et al., *Nickel cobaltite as an emerging material for supercapacitors: An overview*. *Nano Energy*, 2015. **11**: p. 377-399.
- [13] Sasmal, A. and A.K. Nayak, *Morphology-dependent solvothermal synthesis of spinel NiCo_2O_4 nanostructures for enhanced energy storage device application*. *Journal of Energy Storage*, 2023. **58**: p. 106342.
- [14] Liu, Z.-Q., et al., *Facile hydrothermal synthesis of urchin-like NiCo_2O_4 spheres as efficient electrocatalysts for oxygen reduction reaction*. *International Journal of Hydrogen Energy*, 2013. **38**(16): p. 6657-6662.
- [15] Luo, Z., et al., *Urchin-like NiCo_2O_4 hollow microspheres with oxygen vacancies synthesized by self-template for supercapacitor*. *New Journal of Chemistry*, 2021. **45**(48): p. 22748-22757.
- [16] Nayak, P., M. Sahoo, and S.K. Nayak, *Urchin-like NiCo_2O_4 microsphere by hydrothermal route: Structural, electrochemical, optical and magnetic properties*. *Ceramics International*, 2020. **46**(3): p. 3818-3826.
- [17] Panja, T., et al., *Robust NiCo_2O_4 /Superactivated Carbon Aqueous Supercapacitor with High Power Density and Stable Cyclability*. *ChemElectroChem*, 2019. **6**(9): p. 2536-2545.
- [18] Wang, J., et al., *Facile synthesis of three-dimensional NiCo_2O_4 with different morphology for supercapacitors*. *RSC Advances*, 2016. **6**(74): p. 70077-70084.
- [19] Guragain, D., et al., *Influence of Urea on the Synthesis of NiCo_2O_4 Nanostructure: Morphological and Electrochemical Studies*. *J Nanosci Nanotechnol*, 2020. **20**(4): p. 2526-2537.

Offline Signature Verification of Genuine Signatures: A Siamese CNN-based Majority Voting Method

ERCE ÖZTÜRK¹, ÖNSEN TOYGAR^{2*}

¹Department of Computer Engineering, Faculty of Engineering, Eastern Mediterranean University, 99628 Gazimağusa, North Cyprus, Mersin 10, Turkey, erce.ozturk@emu.edu.tr, ORCID: 0009-0003-9969-0688

²Department of Computer Engineering, Faculty of Engineering, Eastern Mediterranean University, 99628 Gazimağusa, North Cyprus, Mersin 10, Turkey, onsen.toygar@emu.edu.tr, ORCID: 0000-0001-7402-9058

Abstract - Signatures are used in various fields including banking, government services, and e-commerce to indicate approval, obligation, or knowledge. The use of signatures in digital environments has led the research in signature verification and forged signature detection. Signature verification is a type of biometric verification, which has many advantages over password-based verification techniques. Signature verification can be mainly categorized into offline signature verification or online signature verification. Forged signatures are imitations of another person's handwritten signature, typically forged for criminal purposes. Detection of forged signatures is crucial for preventing security breaches and illegal activities in signature verification systems. Therefore, the objective of this paper is to propose a novel method for writer-independent offline signature verification. The proposed method uses deep learning architecture Siamese Neural Network (SNN) along with three different Convolutional Neural Network (CNN) architectures. The SNN uses two identical CNN subnetworks with a contrastive loss function for training. The proposed method utilizes CNN architectures AlexNet, VGG19, and ResNet50 individually in the SNN subnetworks. The individually trained methods are combined at the decision level with the Majority Voting method, aiming to utilize the individual strengths of each architecture. The proposed method is tested on BHSig260 (Bengali), BHSig260 (Hindi), and CEDAR datasets. The experimental results achieved an accuracy of 86.42% on the Bengali dataset, 88.11% on the Hindi dataset, and 100% on the CEDAR dataset. The proposed method generally indicates stronger performance than individual methods and it is also competitive with some state-of-the-art methods. In addition, FAR and FRR values indicate that the proposed method is good at recognizing genuine signatures. These instructions give you guidelines for preparing papers for ICENTE 2024. Use this document as a template if you are using Microsoft Word 6.0 or later. Otherwise, use this document as an instruction set. The electronic file of your paper must be in this format. Define all symbols used in the abstract. Do not cite references in the abstract.

Keywords - Offline signature verification, deep learning, writer-independent verification, majority voting.

I. INTRODUCTION

SIGNATURES are widely used on documents to indicate obligation, approval, or acknowledgment. They are now also used digitally for authentication in banking, government, and e-commerce, driving research in signature verification and forgery detection. Signature verification is a behavioral biometric verification used to verify an individual's identity [1].

Forged signatures mimic another person's handwriting, often for criminal purposes, and can be categorized as simple, random, or skilled. Skilled forgeries are made by experts achieving a high degree of similarity that signature verification systems must detect to prevent security breaches [1]. Examples of genuine and forged Hindi signatures are shown in Figure 1.



Figure 1: Hindi signatures from the Hindi database. Signatures are genuine, genuine, and forged respectively.

Offline (static) signature verification and online (dynamic) signature verification are the main categories of signature verification. Online verification captures dynamic, real-time user input, like pen pressure and writing speed, whereas offline verification analyzes static images of signatures, which must be scanned and compared. Offline verification can be writer-dependent, requiring a separate model per user, or writer-independent, using a single model for all users. Offline signature verification is more challenging than online because of the static visual features of the signature, which vary with writing styles [1] [4]. Writer-independent signature verification makes the task even harder as models must generalize the differences between forged and genuine signatures for all users [1].

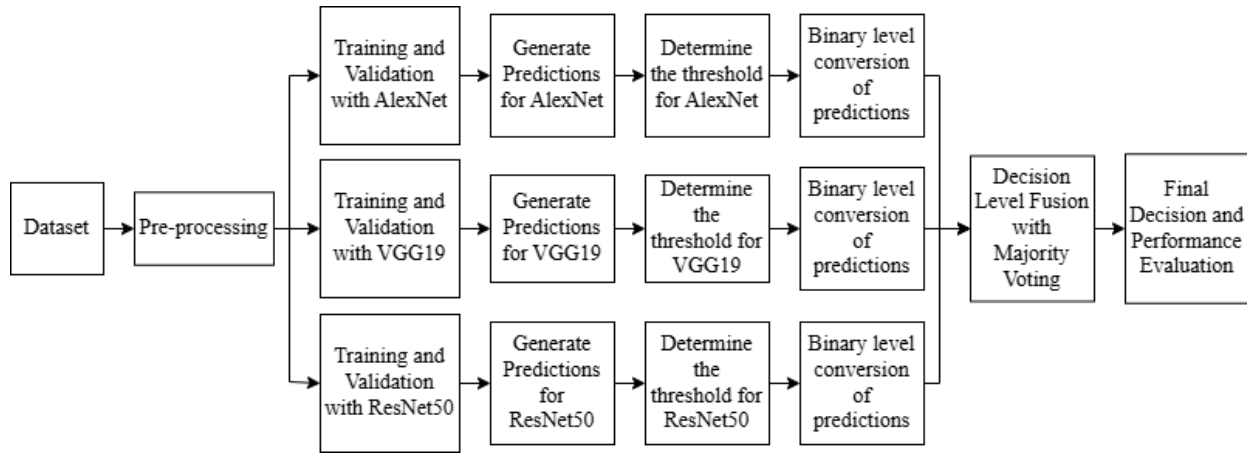


Figure 2: Block diagram of the proposed method.

The manual verification of signatures is often challenged with human errors, making the automated verification a key area in machine learning and pattern recognition [1]. Accurate detection of forgeries in automated systems can prevent fraud, protect assets, and ensure document integrity.

This paper proposes a novel writer-independent offline signature verification method using Siamese Neural Networks (SNN) based on three CNN architectures VGG19, ResNet50, and AlexNet [6] [7] [8]. Each model is trained independently to predict whether a given signature is forged or genuine. The final decision is made using Majority Voting which combines the predictions of the three models. This approach aims to use each individual model's strengths to improve the verification system's overall accuracy. Our method includes data collection, preprocessing, training with Siamese CNN architectures, and final classification using Majority Voting. By combining the strengths of multiple deep learning architectures with Majority Voting, the proposed method aims to advance writer-independent offline signature verification.

II. LITERATURE REVIEW

In this paper, mainly deep learning techniques such as Siamese Neural Networks (SNN) and types of Convolutional Neural Network (CNN) architectures that proved to be superior for image recognition are studied for signature verification [5]. After validating SNN's effectiveness in offline signature verification [1] [2] [3] [4], we decided to implement the SNN in our proposed method. Given that different CNN architectures perform better across different signature datasets [5], our method proposes combining multiple Siamese CNN architectures through Majority Voting, utilizing the individual strengths of each.

III. DATASETS AND PREPROCESSING

The datasets used are the Hindi and Bengali Signature Datasets (BHSig260), and CEDAR Signature Dataset. These datasets contain genuine and forged signatures from multiple individuals. The preprocessing is done to ensure consistency across samples.

The Hindi Signature Dataset (BHSig260) includes signatures

from 160 individuals where each person has 54 signatures, out of which 30 are forged and 24 are genuine. Therefore, there are a total of 8,640 signatures. This dataset is the biggest dataset used in this paper and has a diverse and variable set of Hindi signatures, offering a lot of samples for training and testing. Similarly, the Bengali Signature Dataset (BHSig260) comprises signatures from 100 individuals where each person has 54 signatures, 30 being forged and 24 being genuine. Therefore, the dataset is comprised of 5,400 signatures in total. The CEDAR Signature Dataset consists of signatures from 55 writers, where each writer provided 48 signatures, 24 being forged and 24 genuine. Therefore, there are 1,320 forged signatures and 1,320 genuine signatures, making a total of 2,640 signatures.

During pre-processing, signature images were prepared for deep learning phases by standardizing their format and organization. For all datasets, signature images are divided into groups for each person. Genuine signatures are stored in the "orig groups" list and forged signatures in the "forged groups" list. Each person has a separate group in both lists, ensuring that the order in one list corresponds to the same person in the other. After the segregation, image sizes are normalized to 155 pixels in height to 220 pixels in width. The image input size is set to 155x220x1, which indicates grayscale images as signatures are only black and white. Finally, before training, validation, and testing, batches of signature pairs are created from the genuine and forged groups. Each person has 24 genuine signatures, and we pair each with every other genuine signature to form $\binom{24}{2} = 276$ unique genuine-genuine pairs. For genuine-forged pairs, each genuine signature is paired with 12 randomly selected forged signatures, resulting in $24 * 12 = 288$ genuine-forged pairs per person.

IV. PROPOSED METHOD

The proposed method includes data acquisition and pre-processing as initial steps. After the data acquisition and pre-processing, each of the architecture models AlexNet, VGG19, and ResNet50 are trained and validated separately using the training and validation batches that consist of genuine-forged and genuine-genuine signature pairs on the

Siamese Neural Network. Predictions are generated individually using the trained models and then converted into binary classifications. These classifications are then combined at the decision level using Majority Voting. The block diagram of the proposed method can be seen in Figure 2.

A. Convolutional Neural Networks (CNN) & Siamese Neural Network (SNN)

Convolutional Neural Networks (CNNs) are a class of deep learning networks designed to learn from grid-type data, making them ideal for images.

CNNs consist of series of layers where each output is the input for the next one. These layers include input, convolutional (conv), pooling, and fully connected (FC) layers [2]. Feature extractors in CNNs are convolutional layers, producing feature maps that capture features such as edges and patterns. Pooling layers reduce spatial dimensions and fully connected layers use these learned features to create vectors [2]. A Siamese Neural Network (SNN) is a powerful tool for verification tasks like signature verification, as it consists of twin subnetworks with shared weights that learn feature spaces in a way that similar samples (genuine-genuine) are close and dissimilar samples (genuine-forged) are distant [4]. In our proposed method, each subnetwork uses the given CNN architecture AlexNet, VGG19, or ResNet50, where each subnetwork uses the same set of parameters. A contrastive loss function minimizes the distance between genuine-genuine pairs and maximizes it for genuine-forged pairs [4] [10].

AlexNet consists of 8 layers, 5 being conv layers (convolutional layers) and 3 being FC layers (fully connected layers) [6]. VGG19 is a 19-layer deep CNN architecture, and its main contribution is through the use of small convolution filters (3x3 size) with a deep network [7]. ResNet50 is a 50 layer deep CNN, and it is known for its residual learning framework [8]. The residual learning framework allows the training of very deep networks.

B. Training, validation & classification

For each dataset (Bengali, Hindi, and CEDAR), three separate models are trained on the AlexNet, VGG19, and ResNet50 architectures, resulting in nine training processes. Each model is trained with the training set and the best-performing model among multiple epochs is saved based on the lowest validation loss for each of 9 training process. These best models are then tested on a single batch from the test data. For each model, a threshold is calculated to convert prediction scores into binary labels where scores below the threshold are labeled as genuine (1), and scores above as forged (0). This binary labeling is based on contrastive loss, where smaller scores indicate higher similarity. At the decision level, classifications from all models are combined using Majority Voting where the final label (genuine or forged) is determined by the majority of votes. Lastly, the proposed model's performance is evaluated based on this combined decision.

V. EXPERIMENTS AND RESULTS

Experiments are conducted on Bengali, Hindi, and CEDAR datasets to evaluate the effectiveness of the proposed method. The experimental setup includes the libraries and environment used, the process of splitting the datasets, and the selection of key hyperparameters for model training. Evaluation metrics such as accuracy, validation loss, and error rates are utilized to evaluate performance. The process of validating the trained models is also explained, focusing on the best-performing models. Finally, experimental results are presented, offering a comprehensive comparison of the models' and the proposed method's performance across different datasets and state-of-the-art methods.

The proposed model is implemented, trained, and tested on Google Colab with an NVIDIA Tesla T4 GPU. The setup uses Linux, Python 3 and Tensorflow version 2.12.0, Keras and CUDA version 11.8. The Python notebooks used are a highly modified version of the SigNet implementation by /hlamba28 [9]. Each dataset is split into 80% for training, 10% for validation, and 10% for testing. There are 276 genuine-genuine image pairs, and 288 genuine-forged pairs for each person in all datasets. Batch sizes For AlexNet, VGG19, and ResNet50 were set as follows: 128 for all datasets in AlexNet; 32 for Hindi and 64 for Bengali and CEDAR in VGG19; and 32 for Hindi and Bengali, with 64 for CEDAR in ResNet50. The ResNet50 model was the most computationally demanding. In addition, the learning rate was adjusted to $1e-5$ to stabilize training. All methods use the same parameters: RMSprop optimizer with rho 0.9, epsilon $1e-8$, clip value 1.0 with the contrastive loss function. Models are saved after each epoch, with early stopping after 12 epochs and a learning rate reduction by 0.1 if validation loss fails to improve over 5 epochs.

Several evaluation metrics including accuracy, false accept rate (FAR), and false reject rate (FRR) were used to evaluate the models and allow the effective comparison with state-of-the-art methods. Accuracy is the number of correctly classified signatures both as forged and genuine (correct predictions) divided by the number of all predictions made. As accuracy only provides a general measure of the performance but does not provide the types of errors, we also need to calculate FAR and FRR. FAR measures the rate of forged signatures that are classified as genuine signatures.

A lower FAR value indicates the verification system is more secure against signature forgeries. FRR measures the rate of genuine signatures that are classified as forged signatures. A lower FRR value indicates the verification system is accurately verifying authentic users.

In our proposed model, each dataset's validation set is used to validate the trained models, helping us to select the best model based on the lowest validation loss (highest validation accuracy). SigNet and ResNet50 show the lowest validation losses on the Bengali dataset, while ResNet50 performs best for Hindi with a 0.09 validation loss. For the CEDAR dataset, both AlexNet and ResNet50 show almost perfect validation losses. Overall, ResNet50 achieved the best performance across datasets with the lowest average validation loss.

Table 1: Results on Bengali, Hindi, and CEDAR datasets.

Dataset	Method	Accuracy	Threshold	FAR	FRR
Bengali	SigNet	88.28%	0.42	5.36%	18.08%
	AlexNet	80.81%	0.42	11.66%	26.71%
	VGG19	79.07%	0.47	9.73%	32.13%
	ResNet50	80.81%	0.43	17.00%	21.39%
	Majority Voting	86.42%	-	22.84%	3.90%
Hindi	SigNet	84.74%	0.56	10.94%	19.57%
	AlexNet	72.93%	0.60	18.42%	35.73%
	VGG19	86.32%	0.63	8.44%	18.91%
	ResNet50	90.05%	0.45	7.92%	11.97%
	Majority Voting	88.11%	-	16.49%	7.07%
CEDAR	SigNet	100.0%	0.39	0.00%	0.00%
	AlexNet	100.0%	0.02	0.00%	0.00%
	VGG19	78.87%	0.06	34.53%	7.73%
	ResNet50	100.0%	0.08	0.00%	0.00%
	Majority Voting	100.0%	-	0.00%	0.00%

Table 2: Comparison of the proposed method metrics with state-of-the-art methods across Hindi, Bengali, and CEDAR datasets.

Dataset	Method	Accuracy	FAR	FRR
Hindi	Arisoy et al. [1]	92.35	8.92	7.65
	Xiao and Ding [3]	88.98	9.6	12.29
	Dey et al. [4]	85.90	13.10	15.09
	Proposed Method	88.11	16.49	7.07
Bengali	Arisoy et al. [1]	91.17	9.83	8.27
	Xiao and Ding [3]	90.64	6.41	14.25
	Dey et al. [4]	86.11	13.89	13.89
	Proposed Method	86.42	22.84	3.90
CEDAR	Jagtap et al. [2]	100	0	0
	Xiao and Ding [3]	95.66	4.20	6.78
	Dey et al. [4]	100	0	0
	Chokshi et al. [11]	99.91	-	-
	Proposed Method	100	0	0

A. Experimental results

The experimental results of each implemented model and the proposed Majority Voting method are given for the Bengali, Hindi, and CEDAR datasets in Table 1. The experimental results are calculated using the testing set of each dataset. For each method, the accuracy, best threshold, FAR, and FRR metrics are given. For each method, the best threshold that gives the best accuracy was calculated to determine whether the difference score corresponds to a genuine or forged signature. Scores smaller than the threshold are considered genuine and scores bigger are forged. Therefore, the forged signatures below the threshold contribute to FAR, and the genuine ones above the threshold contribute to FRR. Even though it is expected for a lower threshold to raise FAR, AlexNet (0.02) and ResNet50 (0.08) achieved 0% FAR with the CEDAR dataset, while VGG19 (0.06) struggled with a 34.53% FAR. As seen in Table 1, the proposed Majority Voting method generally performed better or comparably to the individual model performances. For Bengali, our model reached 86.42% accuracy, just behind SigNet, and higher than the individual models in Majority

Voting. However, the FAR was higher as well, suggesting less effective forgery detection. In the Hindi dataset, the proposed method performed close to the highest accuracy model, ResNet50. The FAR (16.49%) of the proposed method is relatively higher than individual methods but the FFR (7.07%) is significantly lower, implying strong performance in identifying authentic users in the Hindi dataset. In the CEDAR dataset, the proposed method performed 100% accuracy, along with some other individual models, indicating excellent performance with no errors in classification. Overall, the proposed method generally improved the individual model performance, except for the ResNet50 in the Hindi dataset. While the overall accuracy increased, there is a trade-off between the FAR and FRR.

B. Comparison of experimental results

The proposed method is compared with some state-of-the-art methods that are also evaluated on the Hindi, Bengali, and CEDAR datasets. The results can be seen in Table 2.

With the Hindi dataset, the proposed method has similar accuracy to Arisoy et al. [1], which has the highest accuracy,

but the FAR value of the proposed model is higher than other methods. This indicates that our proposed method is worse at detecting forged signatures, but the lower FRR value shows it is better at identifying genuine signatures. For the Bengali dataset, the proposed method performed worse than Arisoy et al. [1] and Xiao and Ding [3], and again has the highest FAR and lowest FRR among the methods. FAR in this dataset is the highest among all methods, indicating poor performance in forged signature detection in the Bengali dataset. This time FRR is as low as 3.9%, indicating brilliant performance in identifying genuine signatures. For the CEDAR dataset, the proposed method performed equally with most of the other methods, giving 100% accuracy with 0% error rates. These results suggest that the proposed method made progress in identifying genuine signatures by trading off the forged signature detection. This can be preferred in systems that prioritize reducing the risk of falsely rejecting authentic users.

VI. CONCLUSION

In this paper, a new method for writer-independent offline signature verification is proposed, enhancing the effectiveness of individual models AlexNet, VGG19, and ResNet50 by combining them at the decision level using Majority Voting. The proposed method is evaluated on Hindi, Bengali, and CEDAR datasets, achieving 88.11%, 86.42%, and 100% accuracies, respectively. When the proposed method is compared to individual models, the proposed method achieves higher accuracy, but it lags behind some state-of-the-art methods. The FAR of the proposed method is generally higher, indicating the forged signature detection performance is low. However, the proposed method consistently shows the best FRR, performing better in terms of identifying genuine signatures and indicating that false rejections are significantly decreased in this study. This indicates that the proposed method combines the strengths of individual models through Majority Voting, and prioritizes minimizing the rejection of genuine signatures. Therefore, the proposed method is suitable for systems where the accurate acceptance of genuine signatures is essential or as an enhancement to systems already effective in detecting forged signatures, contributing to a more reliable and comprehensive signature verification system. Future work can focus on minimizing the FAR and increasing the performance of the forged signature detection. This can be achieved by using more CNN architectures and combining them through Majority Voting, using more datasets, or implementing data augmentation techniques.

REFERENCES

- [1] Arisoy, M. V., Signature verification using siamese neural network one-shot learning, *International Journal of Engineering and Innovative 174 Research*, 3(3), 2021, 248–260. <https://doi.org/10.47933/ijeir.972796>
- [2] Jagtap, A. B., Sawat, D. D., Hegadi, R. S., & Hegadi, R. S., Verification of genuine and forged offline signatures using Siamese Neural Network (SNN), *Multimedia Tools and Applications*, 79(47), 2020, 35109–35123.
- [3] Xiao, W., & Ding, Y., A two-stage siamese network model for offline handwritten signature verification, *Symmetry*, 14(6), 2022, 1216.
- [4] Dey, S., Dutta, A., Toledo, J. I., Ghosh, S. K., Llado's, J., & Pal, U., Signet: Convolutional siamese network for writer independent offline signature verification, arXiv preprint arXiv:1707.02131, 2017.
- [5] Yarıcı, M. M., Tekerek, A., & Topaloglu, N., Deep learning-based data augmentation method and signature verification system for offline handwritten signature, *Pattern Analysis and Applications*, 24(1), 2021, 165–179.
- [6] Krizhevsky, A., Sutskever, I., & Hinton, G. E., Imagenet classification with deep convolutional neural networks, *Advances in Neural Information Processing Systems*, 25, 2012.
- [7] Simonyan, K., & Zisserman, A., Very deep convolutional networks for large-scale image recognition, arXiv preprint arXiv:1409.1556, 2014.
- [8] He, K., Zhang, X., Ren, S., & Sun, J., Deep residual learning for image recognition, In *Proceedings of the IEEE Conference on Computer Vision and Pattern Recognition*, 2016, pp. 770–778.
- [9] hlamba28, Hlamba28/offline-signature-verification-using-siamese-network: Identifying forged signatures using convolutional siamese networks implemented in Keras, GitHub, 2019. Available at: <https://github.com/hlamba28/Offline-Signature-Verification-using-Siamese-Network> (Accessed: 07 August 2024).
- [10] Hadsell, R., Chopra, S., & LeCun, Y., Dimensionality reduction by learning an invariant mapping, In *2006 IEEE Computer Society Conference on Computer Vision and Pattern Recognition (CVPR'06)*, Vol. 2, 2006, pp. 1735–1742, IEEE.
- [11] Chokshi, A., Jain, V., Bhope, R., & Dhage, S., SigScatNet: A Siamese+ Scattering based Deep Learning Approach for Signature Forgery Detection and Similarity Assessment, In *2023 International Conference on Modeling, Simulation & Intelligent Computing (MoSICom)*, 2023, 194pp. 480–485, IEEE.

A Lie Detection: Via Spectral Features Using “Bag of Lies”

SEMİYE DEMİRCAN¹ and S. KUMRU²

¹ Konya Technical University, Konya/Turkiye, sdemircan@ktun.edu.tr

² Konya Technical University, Konya/Turkiye, kumrusertug@gmail.com

Abstract - In the last decade, the major development of technology has made information sharing easier, but it has also facilitated the spread of misleading information and lies. Lie detection plays an important role in preventing fraud, protecting security, ensuring justice and in daily communications. Traditional lie detection methods are typically time-consuming and based on personal assessments, whereas machine learning techniques have the potential to automate this process. Speech is a rich data source that reflects human behavior and emotional states. Elements such as tone, speed, and pitch of speech can provide information about whether an individual is lying.

In this application, a lie detection system is developed based on spectral features using the "Bag of Lies" dataset. This dataset contains a wide collection of video recordings from various scenarios, including both lying and non-lying situations. In the application, features are extracted from speech recordings, and Artificial Neural Network (ANN) are applied. The goal of this study is to develop a model that can effectively and accurately detect lies through speech analysis. This model aims to speed up the process.

The methods used in this project cover the entire process, from data processing to model training and testing, and the model's performance has been evaluated using various metrics.

Keywords - Lie Detection, Feature Extraction, Spectral Features, Bag of Lies, ANN.

I. INTRODUCTION

IN recent years, the speed and accessibility of information flow has increased with the distribution of digital communication tools. This situation covers the way for the rapid spread of misleading or false information. Especially in communication through social media platforms and other digital channels, the detection of false information and access to accurate information is of major importance. Lie detection plays a critical role not only in maintaining trust between individuals, but also in protecting the overall information health of society. Speech analysis technology has played an important role in advances in lie detection. Elements such as intonation, speed and emphasis in the human voice provide valuable clues as to whether a person is telling the truth or not. Analyzing signals has great potential to reveal lying tendencies by analyzing these fine details in nonverbal communication.

Talaat proposes an improved recurrent neural network (ERNN) model for lie detection. This model aims to detect

stress patterns in individuals' voices using voice stress analysis. The ERNN is based on the long short-term memory (LSTM) architecture and its hyperparameters are optimized using fuzzy logic. The model is trained using audio recordings of interviews from a randomly selected group. The proposed ERNN achieved a statistically significant accuracy rate of 97.3% on the voice stress analysis problem.[1]

Sehrawat et al. propose a multimodal stacked Bi-LSTM model for lie detection using real trial data and videos from other datasets. By combining visual features from text transcriptions, audio spectrograms and videos, this model has achieved accuracy rates of up to 96% in distinguishing between false and true statements. [2]

Fathima Bareeda et al. aims to design an efficient lie detector that can detect lies in spoken sentences. The study performs lie detection using only the subject's voice recordings, rather than invasive methods such as EEG. The researchers extracted meaningful features (such as MFCC) from the audio signal and developed support vector machine (SVM) based classifiers using these features. With this method, 81% accuracy rate was achieved by using features extracted from audio recordings to distinguish between true and false statements. The study aims to perform lie detection using psychological and neural aspects of audio signals. [3]

Kubis, J. F. evaluated the effectiveness of voice analysis techniques as lie detection and compared the efficiency of two voice analyzers with a polygraph. 174 subjects were used in a simulated burglary experiment. The results showed that voice analysis techniques were not effective in the simulated burglary, whereas the polygraph achieved 73% accuracy. The findings of the study reveal the inadequacy of existing sound analyzers.[4]

Lloyd et al. present a new dataset called the Miami University Deception Detection Database (MU3D). This dataset consists of 320 videos of 80 different target individuals telling truths and lies about their social relationships. There are 20 Black females, 20 Black males, 20 White females and 20 White males in the dataset. Each target produced four different videos: positive truth, negative truth, positive lie, and negative lie. The videos were transcribed by trained research assistants and evaluated by naive raters. [5]

In their work, Xiu et al. report that acoustic lie detection has received increasing attention due to its covert nature and remote processing capability. The aim of this study is to develop an acoustic polygraph based on various phonetic and acoustic

features instead of electro waves, cardiovascular and respiratory values. The study included 62 participants aged between 18-30 years. Participants were randomly assigned to innocent and guilty groups and 31 false and true voice recordings were collected. The results revealed that voice onset time (VOT) performed well in lie detection. The mean sensitivity and specificity of the area under the curve were 0.888, and the lower and upper confidence limits at the 95% confidence level were 0.803 and 0.973, respectively. Although the other acoustic features had lower reference values, they provided a trend in overall lie detection. The results of the study suggest that some acoustic features can be effectively utilized to aid in lie detection. [6]

Sondhi et al. in their study, examine the ability of the human voice to signal the psychological state of an individual. The aim of the study is to determine which voice parameter can be used as a reliable indicator of stress caused by deception. In the study, voice recordings of criminals during police interrogation were made and analyzed using PRAAT software. The results revealed a significant increase in fundamental frequency (F0) and formant frequencies (F1, F2) and a marginal decrease in jitter. Shimmer was not found to be associated with deception-induced stress. The pitch curves show that offenders have a significantly rising pitch when responding to certain direct questions. In this context, it was concluded that mean F0 and formant frequencies F1, F2 are strongly related to stress. [7]

Gupta et al. present a new multimodal dataset called Bag of Lies, which includes video, audio, EEG and eye-tracking data. This dataset is the first multimodal dataset to investigate the use of various methods (such as video, audio, EEG, and eye-tracking data) for deception detection, providing 325 annotated data points containing 162 lies and 163 truths from 35 unique participants. [8]

As summarized in the literature, the importance of voice analysis in lie detection is clear. In this study, the "Bag of Lies" dataset [8] was used. The MP4 format videos in this dataset, which contain 325 videos in total, were converted to WAV format via "FFmpeg" software and the audio files were prepared for analysis. In the feature extraction phase, various spectral features were extracted from the audio signals using the openSMILE tool. The resulting data set was classified using Artificial Neural Networks (ANN) algorithm.

This study is planned as follows: The materials and methods are presented in the second section; the application and discussions are presented in the third section and the conclusion is presented in the fourth section.

II. MATERIALS AND METHODS

A. Materials

In this study, the Bag-of-Lies dataset was used [8]. This dataset is a multimodal deception database consisting of video, audio, eye movements and EEG recordings from 35 participants (25 males and 10 females). EEG signals are only available for 22 users. At the request of the database authors, data from one female participant (user 12) were not used. Thus, there are 315 records in total, of which 157 are false statements and 158 are

true statements. The database was collected under realistic conditions. Participants were shown 6-10 pictures and asked to freely identify them by lying or telling the truth. Video and audio recordings were made with a conventional smartphone and therefore the audio recordings contain a significant amount of noise. Eye data were recorded using a Gazepoint GP3 Eye Tracker (Gazepoint, Vancouver, BC, Canada). In addition, EEG signals were recorded with a 14 Channel Emotiv EPOC+EEG headset (Emotiv, San Francisco, CA, USA). Only audio (Voice) modes were used in the study. Audio was extracted from the video recordings using "FFmpeg" software. The required audio files were edited using "Audacity" software so that only the speaker's voice was present. audio features were extracted using openSmile.[8]

B. Preprocessing and feature extraction Materials

OpenSMILE (Munich open-Source Media Interpretation by Large feature-space Extraction) :openSMILE is a modular and flexible feature extraction tool for signal processing and machine learning applications [9]. It focuses primarily on audio signal features, but through its high degree of abstraction, it can also analyze physiological signals, visual signals and signals from other physical sensors, given the appropriate input components [9].

In this study, MFCC features were extracted from the dataset. Some statistical measurements were extracted from these spectral features. In the study, feature of minimum of the MFCC attributes were defined the as "mfcc_min". the mean (amean) of the MFCC attributes were defined as "mfcc_amean". "mfcc_skewness" was represents the skewness of the mfcc features. "mfcc_maxPos" was represent the maximum position of a given MFCC attribute, and "mfcc_stddev", which represents its standard deviation (stddev).

Line Spectral Pairs (LSP) attributes were also extracted. The "lspFreq_min" feature was defined by taking the minimum of the LSP attributes. By taking the mean (amean) of the LSP attributes, the features "lspFreq_amean" and "lspFreq_linregc2" representing the linear regression coefficient were also obtained.

Among the features related to F0 (fundamental frequency), "F0env_maxPos" represents the highest position, while "F0_sma_de_linregc2" represents the linear regression coefficient. Furthermore, "F0_sma_de_quartile1" represents the first quartile of the fundamental frequency attributes.

Finally, the mean and maximum value of the 9th and 11th components of the "mfcc_sma_de" series derived from the MFCC attributes are defined as "mfcc_sma_de[9]_amean" and "mfcc_sma_de[11]_max". "lspFreq_sma_de[3]_skewness", which expresses the skewness of LSP features, was also obtained as an important feature.

In this way, various features were extracted from the audio data with different statistical measurements and a feature set was created to be used in the lie detection model.

C. Classifiers

Artificial Neural Networks: In the study, an Artificial Neural

Network (ANN) classifier is used for lie detection. ANNs are parallel and distributed information-processing structures, inspired by the working logic of the human brain, consisting of processing elements connected to each other through weighted connections, each with its own memory [10]. Artificial neural networks (ANNs) are biologically inspired computer programs designed to mimic the way the human brain processes information. These networks learn by detecting patterns and relationships in data and gather information through experience.[10]

ANNs are composed of neurons, which are simple interconnected processing units. The connections between neurons are characterized by weights that can be adjusted throughout the learning process. ANNs have been successfully applied to a variety of tasks such as pattern recognition, classification, regression and time series prediction (Haykin, 1999) [11].

Artificial neural networks work by combining supervised, reinforcement and unsupervised learning rules in simple networks and using various algorithms such as back propagation and back propagation variants. ANNs are composed of hundreds of artificial neurons or processing elements (PEs), which are organized in layers. Each PE has weighted inputs, a transfer function and an output. The behavior of the network is determined by the transfer functions, learning rules and architecture of the neurons. [12, 13]

ANNs are characterized by parameters such as number of nodes, number of hidden layers, learning rules and activation functions. These parameters are tuned to optimize the performance and accuracy of the network [14]. ANNs are trained using supervised, reinforcement and unsupervised learning rules. In supervised learning, the network uses labeled data to learn the correct outputs. In unsupervised learning, the network discovers patterns and structures in the data [13][14].

The back propagation algorithm is a widely used learning method for multilayer perceptrons (MLPs) and back propagation algorithm is a widely used learning method of ANNs. This algorithm adjusts the weights to minimize the error function. [15, 16]

III. APPLICATION AND DISCUSSION

In this study, an Artificial Neural Network (ANN) model for lie detection is developed using audio features extracted from the 'Bag of Lies' dataset. Feature selection is performed using Recursive Feature Elimination (RFE) method to improve the performance of the model. RFE is a method based on the principle of determining the importance of all features using a given model and systematically eliminating the least important features. In this process, the model is first trained with all features and then the least influential features are identified and removed from the set. This process is repeated until a certain stopping criterion is met. The features selected include statistical metrics such as MFCC and Line Spectral Pairs (LSP). Use the Microsoft Equation Editor for equations in your paper (Insert | Object | Create New | Microsoft Equation). "Float over text" should *not* be selected. The extracted features are shown

in Table1.

Table 1: Extracted features

Feaures	Definition
mfcc_linregc1	Linear regression coefficient of MFCC coefficient in time series 1
mfcc_min	Minimum value of MFCC coefficient
mfcc_amean	Arithmetic mean of MFCC coefficient
mfcc_skewness	Skewness value of MFCC coefficient
mfcc_linregerrA	Linear regression error term A of MFCC coefficient
mfcc_quartile3	Third quartile value of MFCC coefficient
mfcc_iqr23	Difference between second and third quartiles of MFCC coefficient
mfcc_maxPos	Position of maximum value of MFCC coefficient
mfcc_stddev	Standard deviation of MFCC coefficient
mfcc_quartile3	Third quartile value of MFCC coefficient
lspFreq_linregc2	Linear regression coefficient of LSP frequency in time series 2
lspFreq_min	Minimum value of LSP frequency
lspFreq_amean	Arithmetic mean of LSP frequency
lspFreq_linregc2	Linear regression coefficient of LSP frequency
F0env_maxPos	Position of maximum value of envelope of fundamental frequency (F0)
mfcc_de_amean	Arithmetic average
mfcc_de_max	11. Maximum value of the derivative of the MFCC coefficient
lspFreq_de_skewness	3. Skewness value of the derivative of the LSP frequency
F0_de_linregc2	Linear regression coefficient of the derivative of the fundamental frequency (F0) 2
F0_de_quartile1	First quartile value of the derivative of the fundamental frequency (F0)

In Figure 1 the process of classification is shown. The target variables are the categories 'Truthful' and 'Deceptive' and are coded in binary format to values "1" and "0" respectively. The features are scaled using "StandardScaler" for data standardization.

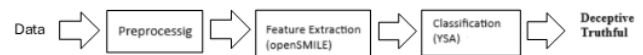


Figure 1: Process of the classification

The model architecture includes an input layer with 128 neurons and a ReLU activation function, and two hidden layers (with 64 and 32 neurons, respectively) are equipped with both ReLU activation functions. L1 and L2 regularizations are applied in the first hidden layer. The output layer of the model is single-neuron and has a sigmoid activation function. Both hidden layers contain Dropout and BatchNormalization layers with a ratio of 30%. The model is optimized using the Adam optimizer and a binary_crossentropy loss function with a learning rate of 0.0005. Training was performed for 100 epochs and a batch size of 16, and training was stopped if there was no improvement for a certain period with the EarlyStopping callback (patience=15). The model achieved 77.78% accuracy

rate and 0.5802 loss value on the test set. The performance of the model is detailed in the classification shown in Table2.

Table 2: Performance metrics obtained with ANN classifier

	Recall	F1-Score	Accuracy%	Support
Deceptive	0.67	0.72	0.78	27
Truthful	0.86	0.82	0.78	36
Macro Avg	0.76	0.77	0.78	63
Weighted Avg	0.78	0.77	0.78	63

IV. CONCLUSIONS

In this study, the analysis performed on the audio files obtained from the 'Bag of Lies' dataset showed that the Artificial Neural Network (ANN) model can be an effective tool in lie detection. The results obtained successfully demonstrated the potential of audio features in lie detection by reaching a high accuracy rate of 77.78%. Among the spectral features used in the project, features such as MFCC and Linear Spectral Coupled Frequencies (LSP) came to the fore, and it was observed that these features had decisive effects on the classification performance of the model. In addition, the techniques applied in the model's configuration and training processes played a critical role in improving the overall performance of the model. This study offers a contact-free, fast and cost-effective alternative compared to traditional methods used for lie detection. Rapid detection of lies is of great importance in protecting information health and preventing the spread of misleading information. The findings obtained show that lie detection using audio analysis and Artificial Neural Networks is promising for both theoretical and practical applications.

REFERENCES

- [1] F. M. Talaat, "Explainable Enhanced Recurrent Neural Network for lie detection using voice stress analysis," *Multimedia Tools and Applications*, vol. 83, pp. 32277-32299, 2024/03/01 2024.
- [2] P. K. Sehrawat, R. Kumar, N. Kumar, and D. K. Vishwakarma, "Deception Detection using a Multimodal Stacked Bi-LSTM Model," in *2023 International Conference on Innovative Data Communication Technologies and Application (ICIDCA)*, 2023, pp. 318-326.
- [3] E. P. Fathima Bareeda, B. S. Shajee Mohan, and K. V. Ahammed Muneer, "Lie Detection using Speech Processing Techniques," *Journal of Physics: Conference Series*, vol. 1921, p. 012028, 2021/05/01 2021.
- [4] J. F. KUBIS. Comparison of Voice Analysis and Polygraph as Lie Detection Procedures
- [5] E. P. Lloyd, J. C. Deska, K. Hugenberg, A. R. McConnell, B. T. Humphrey, and J. W. Kunstman, "Miami University deception detection database," *Behavior Research Methods*, vol. 51, pp. 429-439, 2019/02/01 2019.
- [6] N. Xiu, W. Li, Z. Liu, B. Vaxelaire, R. Sock, and Z. Ling, "Lie Detection Based on Acoustic Analysis," *Journal of Voice*, 2024/08/06/ 2024.
- [7] S. Sondhi, R. Vijay, M. Khan, and A. K. Salhan, "Voice analysis for detection of deception," in *2016 11th International Conference on*

- Knowledge, Information and Creativity Support Systems (KICSS)*, 2016, pp. 1-6.
- [8] V. Gupta, M. Agarwal, M. Arora, T. Chakraborty, R. Singh, and M. Vatsa, "Bag-of-Lies: A Multimodal Dataset for Deception Detection," in *2019 IEEE/CVF Conference on Computer Vision and Pattern Recognition Workshops (CVPRW)*, 2019, pp. 83-90. (October). <https://audeering.github.io/opensmile/about.html#what-is-opensmile>.
- [9] Ç. Elmas, *Yapay Sinir Ağları: Seçkin Yayıncılık*, 2003.
- [10] S. S. Haykin, *Neural Networks: A Comprehensive Foundation*: Prentice Hall, 1999.
- [11] S. Agatonovic-Kustrin and R. Beresford, "Basic concepts of artificial neural network (ANN) modeling and its application in pharmaceutical research," *Journal of Pharmaceutical and Biomedical Analysis*, vol. 22, pp. 717-727, 2000/06/01/ 2000.
- [12] J. Zou, Y. Han, and S.-S. So, "Overview of Artificial Neural Networks," in *Artificial Neural Networks: Methods and Applications*, D. J. Livingstone, Ed., ed Totowa, NJ: Humana Press, 2009, pp. 14-22.
- [13] A. Wesam Salah and Q. Abdul Hannan, "Data Processing Using Artificial Neural Networks," in *Dynamic Data Assimilation*, G. H. Dinesh, Ed., ed Rijeka: IntechOpen, 2020, p. Ch. 6.
- [14] F. Günther and S. Fritsch, "neuralnet: Training of Neural Networks," *The R Journal*, vol. 2, pp. 30-38, 2010.
- [15] M. Tkáč and R. Verner, "Artificial neural networks in business: Two decades of research," *Applied Soft Computing*, vol. 38, pp. 788-804, 2016/01/01/ 2016.

Application of Deep Learning-Based Transfer Learning Models in Monkeypox Diagnosis

MUSTAFA KEMAL TOPÇU¹, ONUR İNAN²

¹ Selcuk University, Konya/Turkey, mktopcu@msn.com

² Selcuk University, Konya/Turkey, oinan@selcuk.edu.tr

Abstract- In recent years, the potential for monkeypox to spread again worldwide has increased the need for early diagnosis methods. In this context, deep learning-based artificial intelligence methods stand out as an important tool in the diagnosis of infectious diseases. The aim of this study is to perform automatic diagnosis of the disease using different transfer learning models on images of monkeypox-specific skin lesions.

In the study, five different transfer learning models were evaluated, namely DarkNet19, AlexNet, NASNetMobile, SqueezeNet and InceptionV3. The accuracy performances of the models were compared and the average success rates of 78.00%, 78.44%, 81.11%, 81.77% and 83.33% were achieved, respectively. The results show that the InceptionV3 model offers a higher accuracy rate compared to the other models.

The findings of this study highlight the potential to assist specialist doctors in early diagnosis of infectious diseases, especially monkeypox. In addition, this technology can contribute to diagnostic processes in regions where specialist doctors are not available. The study is considered an important step in preventing a potential pandemic by demonstrating the effectiveness of AI-based deep learning methods in the field of medical imaging.

In conclusion, strong evidence has been provided that deep learning methods can be used as a reliable diagnostic tool in measures to be taken against the risk of a wider spread of monkeypox on a global scale.

Keywords - Monkeypox, Virus, Deep Learning, Transfer Learning

I. INTRODUCTION

In recent decades, we have been faced with new epidemics such as Covid-19 and Monkeypox around the world. Covid-19 is a virus that targets the respiratory tract and spreads rapidly [1], while Monkeypox is a viral disease that is usually transmitted from animals to humans and has symptoms similar to smallpox [2,3]. Any disease that has a high rate of transmission and can cross geographical boundaries is defined as an epidemic [4].

Monkeypox virus can be transmitted through contact with infected animals, contact with skin lesions or inhalation [5]. Although the exact reservoir of the virus is unknown, it is thought that it can be transmitted to other animals via rodents [6].

As a result, epidemics pose a significant threat to humanity. Studies on the causes of the emergence of these diseases, their transmission routes and their effects will help to treat and prevent them in a short time.

The monkeypox virus is a zoonotic disease that is usually transmitted from animals to humans. However, according to the reports of the World Health Organization [7], it has been observed that human-to-human transmission through sexual contact has increased especially in 2022. This situation is associated with factors such as the decrease in immunity levels against smallpox and the fact that people come together more frequently and are in close contact with each other due to globalization [8].

One of the most important factors that increase the speed of the spread of epidemics is the increase in people's freedom of movement and the expansion of communication networks with the development of technology. The ease of transportation and communication causes diseases to spread rapidly across geographical borders [4].

In this context, technology has both negative and positive effects in the fight against epidemics. On the one hand, it paves the way for the rapid spread of epidemics, and on the other hand, it plays an important role in the planning, monitoring and control of health services. Artificial intelligence methods, especially deep learning, offer great potential in the field of medical imaging.

Deep learning algorithms have the ability to detect complex patterns by analyzing large amounts of data. In this way, they can distinguish subtle differences in medical images such as skin lesions and help diagnose diseases earlier and more accurately.

The use of deep learning methods in the diagnosis of infectious diseases such as monkeypox is considered a promising approach to slow the spread of the disease and improve treatment processes. With this method, faster and more accurate diagnoses can be made by supporting specialist physicians, thus improving the quality of life of patients.

The study is structured as follows. Information about monkeypox disease is given in Section II, Deep learning and transfer learning are included in Section III. Research method and findings are included in Section IV, and finally, the conclusion of the study is included in Section V.

II. MONKEYPOX DISEASE

Monkeypox is a zoonotic infection caused by the Monkeypox virus, a DNA virus belonging to the Orthopoxviridae family [3].

Monkeypox is a zoonotic viral infection that manifests itself

in humans with characteristic rashes and flu-like symptoms similar to smallpox. The virus is endemic among various mammalian species, such as rodents and primates, in its natural habitat. Monkeypox is usually transmitted through close contact with infected animals or infected individuals. It is especially common in the tropical rainforests of the African continent [6]. Although monkeypox is usually seen in a limited number of cases, it can spread rapidly, especially through travel and large social events. Therefore, early diagnosis of the disease and isolation of infected individuals are of great importance [9].

Monkeypox usually begins with flu-like symptoms. After a short time, raised, red lesions appear on the body, especially on the face, palms, and soles. These lesions heal over time by turning into fluid-filled blisters, then crusts. The disease is usually mild, but in some cases it can lead to serious complications. Vaccines are effective in protecting against this disease [7]. Monkeypox is usually mild and heals on its own. However, in people with weak immune systems, children, pregnant women and in cases of sexual transmission, the disease can be more severe and cause serious complications. Therefore, it is important for people at risk to be informed about the disease and take the necessary precautions [9].

III. DEEP LEARNING

Deep learning is a more advanced method of machine learning, a sub-branch of artificial intelligence. Inspired by the neural networks in the human brain, this method provides computers with large amounts of data and allows them to learn complex patterns in this data on their own.

Machine learning is a general concept that allows computers to make decisions by learning from data. For example, you can teach a machine learning algorithm the characteristics of an apple (such as color, shape, size) and have it guess that it is an apple when it sees a new object with these characteristics.

Deep learning takes this process one step further. For example, when you give a deep learning algorithm pictures of different fruits, this algorithm learns the characteristics of fruits such as apples, pears, and grapes on its own and can then correctly guess which type a new fruit it encounters belongs to.

In short, deep learning is a more advanced version of machine learning and allows computers to gain human-like learning abilities. It is used in many areas such as image recognition, natural language processing, and autonomous vehicles.

For example, if a deep learning algorithm is trained on millions of photographs, it can become so advanced that it can distinguish a cat from a dog or a car from a motorcycle. The main purpose of this study is to achieve successful results in the diagnosis of monkeypox by using transfer learning methods, a deep learning method, for the classification of monkeypox [10].

3.1. Transfer Learning

Transfer learning is an artificial intelligence technique that uses knowledge from a previously solved problem to tackle a

new, related problem more quickly. This approach mimics how people learn by applying previously learned information to novel contexts, enabling you to learn more quickly and efficiently. An illustration of this would be applying grammatical principles from a language you have already learned to another language you are learning.

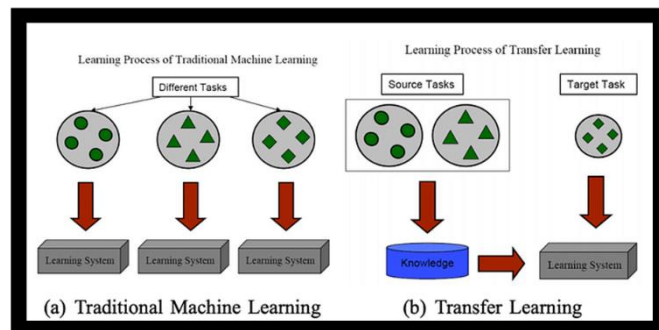


Figure 1: Transfer Learning [10].

Transfer learning offers a significant benefit, particularly when computational resources or data volumes are restricted. Models for new tasks can be created faster and with less data by utilizing the strength of huge pre-trained models. [10].

3.1.1. DarkNet19 Model

Darknet-19 architecture is a lightweight and efficient convolutional neural network specifically designed for the YOLO (You Only Look Once) object detection system. This deep learning model, consisting of 19 layers, extracts meaningful features from visual data by using 3x3 convolution filters and max pooling operations. The architecture of the model is optimized to show high performance in both image classification and object detection tasks [11]

3.1.2. AlexNet Model

AlexNet is a convolutional neural network (CNN) architecture that broke new ground in the field of deep learning with its success in the ImageNet visual recognition competition in 2012. Developed by Krizhevsky and his colleagues, AlexNet has achieved high accuracy rates in object recognition and classification tasks by learning the hierarchical features of visual data. By using regularization techniques such as ReLU activation functions and dropout, AlexNet has gained the ability to learn and generalize faster than previous models [12].

3.1.3. NASNetMobile Model

NASNetMobile is a high-performance convolutional neural network designed by Google considering the limited computational capacity of mobile devices. This model, which is automatically generated by the Neural Architecture Search (NAS) method, is equipped with max pooling layers and variable-size convolutional filters; in addition, information loss is minimized by improving the gradient flow through skip

connections. NASNetMobile, which stands out with its computational efficiency, is pre-trained on large visual datasets such as ImageNet and provides high success in visual recognition tasks such as object recognition and image classification [13].

3.1.4. InceptionV3 Model

InceptionV3 is an advanced deep learning model used in image classification tasks. It combines filters of different sizes, increasing the learning capacity of the model and reducing the computational cost. In this way, faster and more accurate results are obtained on large and complex visual data. The model consists of 42 layers and is designed to classify images of 299x299 pixels [14].

3.1.5. SqueezeNet Model

SqueezeNet is a lightweight and efficient convolutional neural network designed for use in resource-limited devices such as mobile devices and embedded systems. Although it has much fewer parameters compared to AlexNet, it achieves similar accuracy rates. It achieves this success with a special module structure called "compression" and "expansion". With these features, it is widely preferred in mobile applications, offering both high accuracy and low computational cost [15].

IV. RESEARCH AND FINDINGS

In the study, Matlab r2024a program was used to run the model and obtain the results in the detection of monkeypox disease. The dataset used in the training of deep learning models was obtained from Kaggle [16]. In this study, the MSLD dataset, published under the name Monkeypox Skin Lesion Dataset, consisting of 224x224 pixel images, was used. The dataset contains a total of 228 Monkeypox and Others, monkeypox disease / other (chickenpox and measles) skin lesion images, 102 Monkeypox, 126 Others (Chickenpox and Measles). The workflow diagram used in the study is shown in Figure 2.

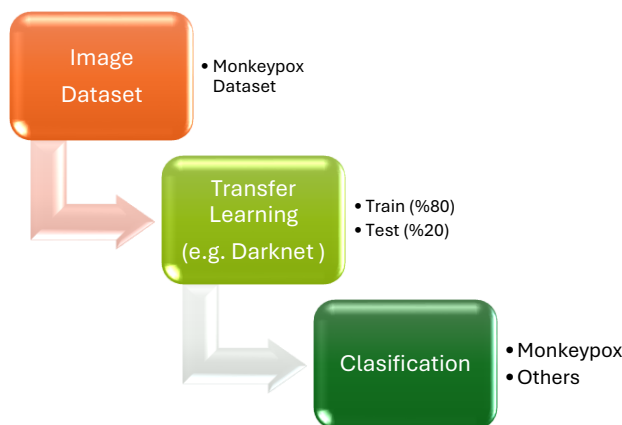


Figure 2: Workflow Diagram

When we look at the data distribution, approximately 80% of the images were used for training and 20% for testing. The images were randomly distributed according to the determined ratios. The aim of using image augmentation techniques was to diversify the existing dataset, make the model more generalizable and prevent overfitting. Our deep learning models use certain parameters to perform classification correctly. These parameters include the values used during the training of the models we use. These parameters are listed in Table 1.

Table 1: Parameters Used in Transfer Learning Models

Parameters	Values
Learning Rate	0.0001
Epochs	10
Batch Size	8
Activation	adam

When the values in Table 1 are examined, as a result of the study, 5 different transfer learning models were trained and tested using the same parameters using the learning rate 0.0001, epoch number 10 and mini batch size 8. The performance metrics of the results are compared in Table 2. In this study, 5 different transfer learning models were used, namely DarkNet19, AlexNet, NASNetMobile, SqueezeNet and InceptionV3 model. Among these, InceptionV3 model achieved the highest accuracy rate. In the test result after the training performed with InceptionV3 model in MSLD dataset, it reached 83.33% average success rate. The complexity matrix of a run as a result of the test performed with InceptionV3 model is given in Figure 3.

Confusion Matrix: inceptionv3(adam) mb:8 e:10 r:7

Output Class	Monkey Pox	Others	
Monkey Pox	15 33.3%	3 6.7%	83.3% 16.7%
Others	5 11.1%	22 48.9%	81.5% 18.5%
	75.0% 25.0%	88.0% 12.0%	82.2% 17.8%
	Monkey Pox	Others	
	Target Class		

Figure 3: InceptionV3 Model Confusion Matrix

Performance metrics obtained as a result of training with other transfer learning methods are given in Table 2.

Table 2: Transfer Learning Performance Metrics

Model	Mean Accuracy	Mean Sensitivity	Mean Specificity	Mean Precision	Mean Fscore
DarkNet19	78,00%	80,37%	77,72%	69,00%	0,7352
AlexNet	78,44%	80,98%	78,47%	69,00%	0,7308
NASNetMobile	81,11%	82,93%	80,67%	73,50%	0,7753
SqueezeNet	81,77%	81,44%	83,32%	78,50%	0,7941
InceptionV3	83,33%	83,24%	83,90%	79,00%	0,8084

V. CONCLUSION

In this study, it was aimed to test the success of Transfer Learning models in diagnosing monkeypox disease by using image datasets obtained from Kaggle website. 5 different transfer learning models were used to detect monkeypox disease from the models used in the literature. The parameters given in Table 1 were used in all models. The performance metrics of each transfer learning model are given in Table 2. Among the models, InceptionV3 had the highest success rate with an average accuracy of 83.33%. More successful results can be obtained with different and more image datasets and different parameters.

REFERENCES

- [1] Güngör, S., Kaya, M., & Alhaji, R. (2021). A Deep Learning-Based Method for Covid-19 Detection from Colorized CT Images. *Computer Science, 5th International Artificial Intelligence and Data Processing symposium*, 391-399.
- [2] Nalca A, Rimoin AW, Bavari S, Whitehouse CA. Reemergence of monkeypox: prevalence, diagnostics, and countermeasures. *Clin Infect Dis.* 2005;41(12):1765-71.
- [3] Bunge EM, Hoet B, Chen L, Lienert F, Weidenthaler H, Baer LR et al. The changing epidemiology of human monkeypox—a potential threat? A systematic review. *PLoS 52 Negl Trop Dis.* 2022;16(2):e0010141.
- [4] Tütüncü, D., & Esen, M. F. (2021). The use of Internet of Things (IoT) in the management of epidemics: COVID-19 example. *Journal of Health Academicians*, 8 (2) , 169- 177.
- [5] Reynolds MG, Yorita KL, Kuehnert MJ, Davidson WB, Huhn GD, Holman RC et al. Clinical manifestations of human monkeypox influenced by route of infection. *J Infect Dis.* 2006;194 (6):773- 80.
- [6] Centers for Disease Control and Prevention (CDC). Multistate outbreak of monkeypox-- Illinois, Indiana, and Wisconsin, 2003. *MMWR.* 2003;52:537-40.
- [7] World Health Organization. Multi-country monkeypox outbreak in non-endemic countries. Access Date 20 September 2024: <https://www.who.int/emergencies/disease-outbreak-news/item/2022-DON385>
- [8] Aslan, S. (2021). The Impact of the Covid-19 Pandemic on Globalization and Nation States. *Electronic Journal of Social Sciences*, 20 (80), 1735-1752.
- [9] Engin, M. T. (2023). Detection of monkeypox from skin lesion images using deep learning methods (Unpublished Master's Thesis) Aksaray University Institute of Social Sciences.
- [10] Şener, M. (2023). Transfer learning approach in machine learning. Access Date 20 September 2024: <https://blog.architect.com/blog/2468/makine-ogrenmesinde-aktarimli-ogrenme-yaklasimi-ve-aktarimli-ogrenme-modelleri/>
- [11] Redmon, J., & Farhadi, A. (2017). YOLO9000: better, faster, stronger. In *Proceedings of the IEEE conference on computer vision and pattern recognition* (pp. 7263-7271).
- [12] Usta, E. (2023). AlexNet. Medium. Access Date 20 September 2024: <https://medium.com/@e.usta/alexnet-f44a4a54be8a>
- [13] Ameer, A. W. A., Salehpour, P., & Asadpour, M. (2024). Deep Transfer Learning for Lip Reading Based on NASNetMobile Pretrained Model in Wild Dataset. *IEEE Access*.
- [14] Uçar, M. (2021). Detection of Glaucoma Disease with Convolutional Neural Network Architectures. *Dokuz Eylul University Faculty of Engineering Journal of Science and Engineering*, 23(68), 521-529.
- [15] Iandola, F. N. (2016). SqueezeNet: AlexNet-level accuracy with 50x fewer parameters and < 0.5 MB model size. *arXiv preprint arXiv:1602.07360*.
- [16] TensorKitty, Joydip P., Md Tazuddin A., Tasnim J.P. (2022) <https://www.kaggle.com/datasets/nafin59/monkeypox-skin-lesion-dataset/data>

A Performance Comparison of Different Machine Learning Algorithms to Forecast Wind Energy in Türkiye

SEMA SERVİ¹, ONUR İNAN², FATİH YILMAZ³, İSMAİL ARSEL⁴, AHMET PEKGÖR⁵, AŞIR GENÇ⁶, GALİP OTURANÇ⁷

¹Selcuk University, Konya/Türkiye, semaservi@selcuk.edu.tr

²Selcuk University, Konya/Türkiye, oinan@selcuk.edu.tr

³Ministry of National Education, Konya/Türkiye, yilmazoglu@gmail.com

⁴Karamanoğlu Mehmetbey University, Karaman/Türkiye, ismail.arsel@gmail.com

⁵Necmettin Erbakan University, Konya/Türkiye, istatistik@hotmail.com

⁶Necmettin Erbakan University, Konya/Türkiye, agenc@erbakan.edu.tr

Abstract - Wind energy is a prominent alternative among sustainable energy sources and it is highly important to determine the energy production potential employing accurate measurement and analysis techniques. In this paper, the researchers developed a model utilizing decision trees, k-Nearest Neighbor (KNN), and Random Forest (Random Forest) algorithms using wind data from Konya Airport, Sinop, Batman, Antakya, and Çanakkale wind measurement stations in Turkey, between 1995-2000 and tested on 2001 data. They evaluated the model taking Mean Square Error (MSE) values into account, and the Random Forest algorithm was the one with the lowest MSE value. The results evaluate the accuracy and applicability of wind forecasting models by comparing the performance of different algorithms. This paper is expected to contribute to the determination of the most efficient algorithm for wind forecasting and provides valuable information for sustainable energy investments.

Keywords - Green energy investments, Machine learning, Metaheuristic algorithms, Sustainable energy, Wind forecasting

I. INTRODUCTION

THE growing importance of renewable energy sources requires the development of highly accurate statistical models for energy production forecasts, and wind energy, in particular, has an increasingly critical role in the global energy portfolio due to the increasing need for renewable energy sources [1]. Wind energy has great potential for energy production due to its low environmental negative impacts, and accurate prediction of wind speed, direction, and persistence are critical for its effective use. Therefore, forecasting future wind data by considering earlier meteorological data has become one of the fundamental requirements for renewable investments.

The literature has several studies on the effectiveness of machine learning and deep learning techniques in forecasting wind data. Recently, the use of machine learning techniques on wind data has gained significant momentum, especially in the course of forecasting and predictive modeling. Accurate forecasting of wind is important for a variety of reasons

including renewable energy production, meteorology, and environmental management, as well.

Accordingly, the purpose of this paper, employing advanced machine learning algorithms such as K-Nearest Neighbors (KNN) [2], Random Forest [3] and Decision Trees [4], is to predict wind data for 2001 using wind data between the years 1995-2000. The methods utilized in this paper, which are especially suitable for handling complex and non-linear relationships in meteorological data, have also been frequently used in similar studies.

To illustrate, Hart et al., in their research on modeling wind damage in forests, have shown the effectiveness of the Random Forest method and have proven that it outperforms traditional logistic regression models with complex interactions between the variables [5]. Similarly, Araujo et al., in their study on wind power prediction in a semi-arid region, have come up with good results using the KNN algorithm with a normalized root mean square error (NRMSE) of 17.8% for short-term predictions [6]. At the same time, their research also reveals the potential of the KNN algorithm for wind data prediction with multidimensional meteorological inputs.

In the research by Muralidharan et al., the use of the abovementioned algorithms in wind data analysis has been demonstrated by comparing different machine learning techniques in wind turbine performance prediction [7]. In the article which is about the prediction of wind power production using tree-based regression models by Fitipaldi et al., the effectiveness of the Random Forest algorithm in revealing the dynamics of wind power production has been indicated [8]. Gholamrezaie et al., using comparative evaluations of machine learning models for wind speed prediction, showed that Random Forest provides higher accuracy compared to traditional statistical methods [9]. In addition, Akinci and Noğay studied how decision trees predict wind speed and showed how well they work in categorizing and predicting renewable energy factors [10].

Consequently, the examples from the literature indicate the sensitivity and effectiveness of machine learning algorithms in

predicting wind data. Therefore, the use of KNN, Random Forest and Decision Tree approaches used in this article provides a powerful set of methods for complex and nonlinear wind data prediction. By providing new perspectives on how well these algorithms work in wind data forecasting, this article aims to contribute to the literature in the fields of meteorology and renewable energy.

II. MATERIAL AND METHOD

A. KNN Regression Method

A popular non-parametric machine learning technique for predictive modeling in several fields is k-nearest neighbors (KNN) regression. It estimates the output for a given input by taking the average of the outputs of the k-nearest neighbors of the training dataset (where "k" is a user-defined parameter determining how many neighbors to consider). Since it does not require a specific functional default format for data distribution, this strategy works especially when the relationship between input and output values is complex and nonlinear [2], [11].

Several factors including the choice of the distance metric, the value of k, and the preprocessing of the input data may affect the performance of the KNN regression algorithm. For example, normalization techniques such as min-max have a significant impact on the regression performance of KNN models, as they help to reduce the impact of outliers and ensure that all features contribute equally to distance calculations [12]. Furthermore, the choice of an appropriate distance metric (e.g., Euclidean, Manhattan) is crucial as it directly affects the identification of nearest neighbors and thus the accuracy of predictions [13], [14].

In practical, the KNN regression method has shown its effectiveness in several fields. For instance, it has been successfully used to predict tooth age based on dental metrics, where it outperforms other regression models by achieving low mean absolute error (MAE) values [15]. Similarly, it is also widely used in redshift prediction in astrophysics due to its versatility and robustness in processing diverse datasets [16].

Moreover, studies show that the KNN regression method can provide competitive results compared to some other machine learning algorithms such as support vector regression and random forests, especially with high dimensional data [17], [18]. However, the choice of "k" in KNN regression is critical. Empirical studies indicate that optimal values are usually in a small range and can be determined by techniques such as cross-validation [19].

In addition, the simplicity and ease of implementation of the KNN method make it a useful option for researchers as it requires minimal parameter tuning compared to more complex models [2], [20]. However, it is important to note that the KNN algorithm can be computationally intensive, especially with large datasets, as it requires the calculation of distances to all training samples for each prediction [21].

In brief, KNN regression is a powerful and flexible tool for predictive modeling, particularly suitable for nonlinear relationships and high-dimensional datasets. Its performance can be improved through careful preprocessing, selection of

distance metrics, and optimization of the parameter "k". Several studies indicate that KNN regression has proven effective in multiple fields, which makes it a valuable addition to the machine learning toolkit.

B. Decision Tree Regression Method

"Decision tree regression" is an effective machine learning method, widely used to predict continuous outcomes based on input characteristics. This method involves creating a tree-like structure with a model that estimates the value of the target variable by dividing the data into subsets based on property values. The decision tree regression model is an important method both because of its easy interpretation and because of its ability to process numerical and categorical data. Thus, the Decision tree makes regression a versatile choice for various applications. One of the basic algorithms in decision tree regression is the Classification and Regression Tree (CART), which is known for its simplicity and effectiveness in modeling complex relationships. CART works by iteratively dividing the data into subsets according to the property that causes the most significant decrease in the variance of the target variable [4] which makes it very easy to interpret the results and understand the basic patterns in the data by providing a clear visualization of the decision-making process [22]. In addition, the decision tree method can manage large data sets [23].

These characteristics refer to the ongoing development of decision tree techniques and their adaptability to various types of data and structures. Several studies show that the performance of the decision tree regression method also outperforms traditional linear regression models. For example, decision tree models usually produce higher determination coefficients (R^2) and lower mean squared errors (MSE), which indicates superior prediction capabilities [24]. Also, the decision tree algorithm is especially effective when the relationship between the estimators and the target variable is nonlinear, because they can capture complex patterns that linear models can miss [25].

As a result, decision tree regression is a robust and interpretable modeling method that excels at predicting continuous results from complex data sets. The ability to process various types of data, combined with innovations in tree-based methods, reveals that this method is a powerful and valuable tool for machine learning. As studies in this area continue to develop, it is likely that decision tree regression will become an important option for researchers.

C. Random Forest Regression Method

The Random Forest regression algorithm, a powerful ensemble learning technique, works by generating multiple decision trees during training and outputs the average prediction of these trees for regression. This methodology is particularly helpful due to its ability to reduce overlearning and increase predictive accuracy compared to the Decision Trees method. The principle of the Random Forest algorithm is bagging (bootstrap aggregation), in which subsets of the training data are sampled with replacement to build each tree,

thus improving the robustness and generalization capabilities of the model [3].

One strength of the Random Forest regression method is its flexibility in various types of data and its minimal assumptions about the underlying data distribution. Unlike traditional linear regression models, which often require strict assumptions about linearity and normality, Random Forest algorithm can effectively model complex nonlinear relationships without the need for extensive data preprocessing [26], [27]. This characteristic makes it particularly suitable in various fields, including finance, health, and environmental science, where the relationships between variables may be complex and multifaceted [28], [29].

The Random Forest method has outstanding performance in terms of accuracy and predictive power. For example, research has shown that the Random Forest algorithm outperforms other machine learning algorithms such as Logistic Regression and Support Vector Machines in various predictive tasks, including crop yield prediction and fraud detection in mobile transactions [26], [30], [31]. Its ability to capture interactions between features and its inherent mechanism for feature importance evaluation further enhance its utility in model interpretation and refinement [29], [32].

Furthermore, the Random Forest algorithm is particularly effective with high-dimensional data in which the number of features exceeds the number of observations. The Random Forest method offers high accuracy and reliability in applications such as predicting drug-target interactions and analyzing clinical data for disease prediction [33], [34]. The robustness of the model against over-learning, especially when working with noisy data, is an important reason for its preference in research and industrial applications [35], [36].

In general, Random Forest regression stands out as a versatile and effective tool in machine learning. With its ability to process complex data sets, its robustness, and high prediction accuracy, it is an indispensable method for regression tasks in various fields. In today's world where machine learning continues to develop, the Random Forest algorithm continues to be an important reference for researchers.

III. PRACTICE

A. Data Set and Preparation

In this paper, the researchers made a wind speed forecast using year, month, and day data as input, and wind speed data as the output. First, they normalized the daily wind speed input data for Konya Airport, Sinop, Batman, Antakya, and Çanakkale measurement stations in Turkey between 1995 and 2000. Normalization ensured that all input features were on the same scale so that certain features did not stand out over others during the learning process of the model. They used 2001 data from the same stations as test data.

The researchers trained each algorithm (Decision Trees, K-Nearest Neighbor - KNN, and Random Forest) using the normalized data in the modeling stage. While the Decision Trees algorithm evaluates the data as a hierarchical structure and predicts by creating decision points, the KNN algorithm

predicts wind speed according to the similarities between neighboring data. On the other hand, the Random Forest algorithm used more than one decision tree to increase the accuracy of the prediction.

Consequently, each model was trained to predict wind speed based on year, month, and day as input data, and the researchers tested the predictions on 2001 data. In the end, the outputs allowed the researchers to evaluate the wind speed forecasting performance of different algorithms. The abovementioned steps, in short, can be visualized with a flow chart, as below.

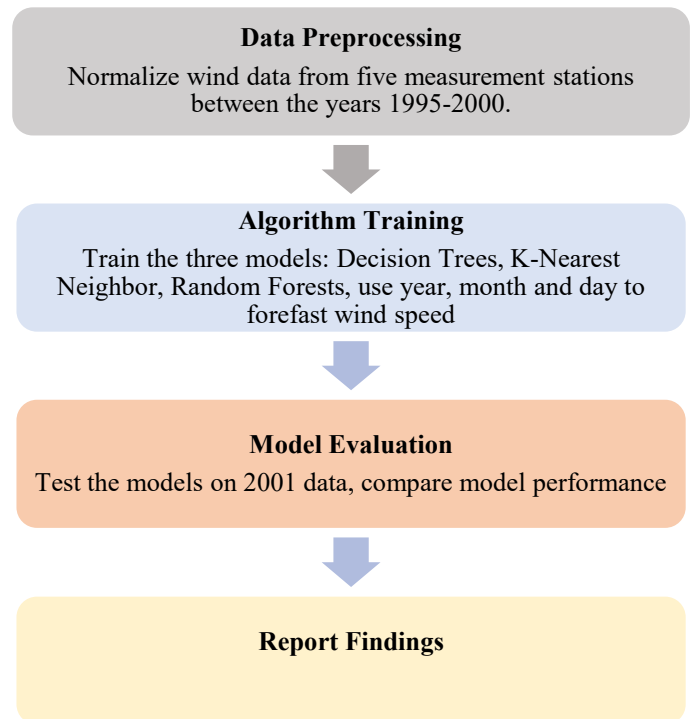


Fig.1: Wind Speed Forecasting Model Flow Diagram

IV. THE RESULTS

Table 1 has the error values (MSE) of the performance of the Decision Trees, KNN and Random Forest algorithms according to, month and year. MSE is calculated by taking the average of the squared prediction errors and is often used to evaluate model performance in regression models. Accordingly, for each month and year, the error values are compared.

Table 1: Wind Speed Forecast for Antakya

Month&Year	Decision Trees	KNN	Random Forest
1	0,682	1,205	0,459
2	0,254	0,195	0,154
3	0,692	1,465	0,725
4	0,854	1,161	0,622
5	1,998	1,809	1,502
6	2,070	3,048	1,391

7	0,477	1,152	0,264
8	0,842	1,661	0,357
9	0,984	1,688	0,783
10	0,612	1,210	0,571
11	0,357	0,458	0,277
12	0,279	0,299	0,203
Annual	0,840	1,103	0,719

Table 1 indicates that the Random Forest is the most successful model for wind speed forecasting in Antakya and gives more accurate results compared to other algorithms. Although the Decision Trees method gives good results for some months, its overall performance is not as consistent as the Random Forest. The KNN method, on the other hand, generally has the highest error values and shows the lowest performance. Considering the errors on a yearly basis, the Decision Trees, KNN, and Random Forest algorithms have error values of 0.840; 1.103; and 0.719, respectively. The results show that the Random Forest algorithm has the lowest error for the whole year and gives the most accurate results on a yearly basis.

Table 2: Wind Speed Forecast for Batman

Month&Year	Decision Trees	KNN	Random Forest
1	1,515	2,684	0,353
2	0,910	1,519	0,770
3	0,592	0,709	0,258
4	0,667	1,032	0,432
5	0,852	1,110	0,605
6	0,500	0,664	0,309
7	0,185	0,383	0,125
8	0,087	0,118	0,044
9	0,106	0,096	0,073
10	0,117	0,215	0,068
11	0,773	0,775	0,608
12	0,420	0,530	0,447
Annual	0,557	0,744	0,314

Taking Table 2 into consideration, the Random Forest algorithm has the lowest error values for Batman. Considering the values on a monthly basis, the Random Forest outperformed other algorithms, giving the lowest error values for several months. For the whole year, the Random Forest method gives the best result with the lowest error value of 0.314. The Decision Trees algorithm has higher error rates with an error value of 0.557 and the KNN algorithm has an error value of 0.744. The results show that the Random Forest approach provides the most accurate and consistent wind speed prediction for Batman.

Table 3: Wind Speed Forecast for Konya Airport

Month&Year	Decision Trees	KNN	Random Forest
1	0,669	0,319	0,398
2	0,953	1,164	0,770
3	1,242	0,772	0,654
4	0,999	1,057	0,753
5	0,561	0,889	0,490
6	0,613	0,879	0,364
7	0,305	0,354	0,253
8	0,673	0,650	0,433
9	0,300	0,495	0,250
10	0,638	0,669	0,356
11	0,805	1,127	0,767
12	0,920	1,281	0,790
Annual	0,711	0,868	0,500

Table 3 indicates that the Random Forest method, in general, has the lowest error rates for wind speed forecast for Konya Airport measurement station. Considering the monthly error values, the Random Forest algorithm performed the best for several months having lower error values than Decision Trees and KNN algorithms. Though the error rates of the KNN method appear to be lower in some months, in general, the Random Forest method gives more consistent and lower error values.

For the whole year, the Random Forest algorithm has the lowest error rate with an error value of 0.500, while the Decision Trees method has an error value of 0.711 and the KNN method has an error value of 0.868. The results show that the Random Forest method gives the most accurate and consistent results for wind speed prediction at Konya Airport throughout the year.

Table 4: Wind Speed Forecast for Sinop

Month&Year	Decision Trees	KNN	Random Forest
1	7,221	5,115	4,206
2	6,585	9,943	7,026
3	12,780	15,351	8,156
4	7,289	8,457	4,108
5	6,481	6,688	4,862
6	4,980	8,432	2,451
7	7,735	7,139	2,477
8	8,817	5,773	2,835
9	2,439	3,645	1,850
10	4,352	7,678	2,618
11	7,976	14,875	7,949

12	10,015	15,455	7,980
Annual	7,245	8,393	4,166

Table 4 indicates that the Random Forest algorithm has lower error values compared to other algorithms for Sinop. Considering monthly error values, the Random Forest method gives lower errors than Decision Trees and KNN methods for several months. In general, error values for the Random Forest method are lower and consistent, even in months that give particularly high error values. For the whole year, the Random Forest algorithm has the lowest errors with an error value of 4.166, while KNN and Decision Trees methods give higher errors with error values of 8.393 and 7.245, respectively. The results show that the Random Forest method gives the most accurate and reliable wind speed forecasts for Sinop.

Table 5: Wind Speed Forecast for Çanakkale

Month&Year	Decision Trees	KNN	Random Forest
1	8,273	10,281	6,381
2	10,318	11,111	7,201
3	8,641	14,977	8,128
4	16,916	19,546	13,905
5	5,306	7,482	3,764
6	5,782	7,402	4,640
7	2,064	4,944	1,987
8	3,743	4,234	2,826
9	3,944	5,488	3,881
10	7,794	9,790	5,575
11	16,186	18,263	13,287
12	21,096	24,934	13,848
Annual	9,0491	11,538	6,446

Considering the results for Çanakkale in Table 5, it is clear that the Random Forest has lower error values than the other algorithms. For monthly error values, the Random Forest algorithm is usually more accurate than Decision Trees and KNN methods. For the whole year, Random Forest algorithm has the lowest errors with an error value of 6.446, while KNN and Decision Trees algorithms have higher errors with error values of 11.538 and 9.049, respectively. The results show that the Random Forest gives more accurate and reliable wind speed forecasts for Çanakkale than the other two algorithms.

Taking the above tables into consideration, it is obvious that the Random Forest algorithm gives better results for wind speed forecast compared to Decision Trees and KNN algorithms. For monthly and annual forecasts for each province, Random Forest, in general, has the lowest error values, making it the most accurate algorithm.

V. CONCLUSION

The analysis results indicate that the Random Forest algorithm, considering the MSE criterion, stands out as the best-performing algorithm for wind speed prediction in this paper.

Although Decision Trees and KNN methods give better outputs in some cases, their overall performance is lower compared to the Random Forests algorithm. Thus, the researchers recommend the Random Forest method when studying wind speed forecasting and similar time series data to get more consistent and accurate results.

Considering the analyses, it is recommended to test deep learning-based or hybrid models in the future to get higher accuracy. Furthermore, studying with a larger dataset and additional features may further improve the prediction performance.

REFERENCES

- [1] International Energy Agency, *European Union 2020*. OECD, 2020. doi: 10.1787/29733c64-en.
- [2] A. Naimi, J. Deng, S. R. Shimjith, and A. J. Arul, "Fault detection and isolation of a pressurized water reactor based on neural network and k-nearest neighbor," *IEEE Access*, vol. 10, pp. 17113–17121, 2022, doi: 10.1109/ACCESS.2022.3149772.
- [3] S. V. Hutagalung, Y. Yennimar, E. R. Rumaepa, M. J. G. Hia, T. Sembiring, and D. R. Manday, "Comparison of support vector regression and random forest regression algorithms on gold price predictions," *Jurnal Sistem Informasi dan Ilmu Komputer Prima (JUSIKOM PRIMA)*, vol. 7, no. 1, pp. 255–262, Sep. 2023, doi: 10.34012/jurnalsisteminformasidanilmukomputer.v7i1.4125.
- [4] J. M. Klusowski, "Analyzing CART," Jun. 2019.
- [5] S. N. Hart *et al.*, "Comprehensive annotation of BRCA1 and BRCA2 missense variants by functionally validated sequence-based computational prediction models," *Genetics in Medicine*, vol. 21, no. 1, pp. 71–80, Jan. 2019, doi: 10.1038/s41436-018-0018-4.
- [6] M. L. S. Araujo *et al.*, "Wind power forecasting in a semi-arid region based on machine learning error correction," *Wind*, vol. 3, no. 4, pp. 496–512, Oct. 2023, doi: 10.3390/wind3040028.
- [7] S. Muralidharan, S. Parthasarathy, D. A., and J. Jersha, "A comparative study of machine learning techniques for wind turbine performance prediction," *E3S Web of Conferences*, vol. 387, p. 04011, May 2023, doi: 10.1051/e3sconf/202338704011.
- [8] C. Fitipaldi, R. Monteiro, D. Pinheiro, W. Ferreira, L. Fonseca, and A. M. Ribeiro, "Forecasting of wind power generation Cristalândia wind farm using tree-based machine learning approaches," in *Anais do XVI Congresso Brasileiro de Inteligência Computacional, SBIC*, Dec. 2023, pp. 1–7. doi: 10.21528/CBIC2023-028.
- [9] F. Gholamrezaie, A. Hosseini, and N. Ismayilova, "A comparative assessment of machine learning models for predicting wind speed," *Azerbaijan Journal of High Performance Computing*, vol. 5, no. 2, pp. 57–71, Jul. 2022, doi: 10.32010/26166127.2022.5.1.57.71.
- [10] T. Ç. Akıncı and H. S. Noğay, "Application of decision tree methods for wind speed estimation," *European Journal of Technic*, vol. 9, no. 1, pp. 74–83, Jun. 2019, doi: 10.36222/ejt.558914.
- [11] M. Sitienei, A. Otieno, and A. Anapapa, "An application of k-nearest-neighbor regression in maize yield prediction," *Asian Journal of Probability and Statistics*, vol. 24, no. 4, pp. 1–10, Sep. 2023, doi: 10.9734/ajpas/2023/v24i4529.
- [12] P. J. Muhammad Ali, "Investigating the impact of min-max data normalization on the regression performance of k-nearest neighbor with different similarity measurements," *ARO-The Scientific Journal of Koya University*, vol. 10, no. 1, pp. 85–91, Jun. 2022, doi: 10.14500/aro.10955.
- [13] A. Heena, N. Biradar, N. M. Maroof, S. Bhatia, R. Agarwal, and K. Prasad, "Machine learning based biomedical image processing for echocardiographic images," *Multimed Tools Appl*, vol. 82, no. 25, pp. 39601–39616, Oct. 2023, doi: 10.1007/s11042-022-13516-5.
- [14] M. Moeini, A. Shojaeizadeh, and M. Geza, "Supervised machine learning for estimation of total suspended solids in urban watersheds," *Water (Basel)*, vol. 13, no. 2, p. 147, Jan. 2021, doi: 10.3390/w13020147.

- [15] S. Shen, X. Yuan, J. Wang, L. Fan, J. Zhao, and J. Tao, "Evaluation of a machine learning algorithms for predicting the dental age of adolescent based on different preprocessing methods," *Front Public Health*, vol. 10, Dec. 2022, doi: 10.3389/fpubh.2022.1068253.
- [16] K. J. Luken, R. P. Norris, and L. A. F. Park, "Preliminary results of using k -nearest-neighbor regression to estimate the redshift of radio-selected data sets," *Publications of the Astronomical Society of the Pacific*, vol. 131, no. 1004, p. 108003, Oct. 2019, doi: 10.1088/1538-3873/aaea17.
- [17] M. K. Elmezughi, O. Salih, T. J. Afullo, and K. J. Duffy, "Comparative analysis of major machine-learning-based path loss models for enclosed indoor channels," *Sensors*, vol. 22, no. 13, p. 4967, Jun. 2022, doi: 10.3390/s22134967.
- [18] P. Ranjan, A. Maurya, H. Gupta, S. Yadav, and A. Sharma, "Ultra-wideband cpw fed band-notched monopole antenna optimization using machine learning," *Progress In Electromagnetics Research M*, vol. 108, pp. 27–38, 2022, doi: 10.2528/PIERM21122802.
- [19] Y. Zhou, "Comparison the effects of KNN and linear regression models in lung cancer prediction," *Applied and Computational Engineering*, vol. 15, no. 1, pp. 194–198, Oct. 2023, doi: 10.54254/2755-2721/15/20230833.
- [20] F. Aldi, I. Nozomi, and S. Soeheri, "Comparison of drug type classification performance using KNN algorithm," *Sinkron*, vol. 7, no. 3, pp. 1028–1034, Jul. 2022, doi: 10.33395/sinkron.v7i3.11487.
- [21] X.-N. Bui, P. Jaroonpattanon, H. Nguyen, Q.-H. Tran, and N. Q. Long, "A novel hybrid model for predicting blast-induced ground vibration based on k -nearest neighbors and particle swarm optimization," *Sci Rep*, vol. 9, no. 1, p. 13971, Sep. 2019, doi: 10.1038/s41598-019-50262-5.
- [22] M. R. Heldner *et al.*, "Cognitive status predicts return to functional independence after minor stroke: A decision tree analysis," *Front Neurol*, vol. 13, Feb. 2022, doi: 10.3389/fneur.2022.833020.
- [23] P. Gulati, A. Sharma, and M. Gupta, "Theoretical study of decision tree algorithms to identify pivotal factors for performance improvement: A review," *Int J Comput Appl*, vol. 141, no. 14, pp. 19–25, May 2016, doi: 10.5120/ijca2016909926.
- [24] J. Moumouh, S. Benjelloun, A. Latifi, and L. Khamar, "Data-driven modeling and optimization of an industrial phosphoric acid production unit," *MATEC Web of Conferences*, vol. 379, p. 07008, May 2023, doi: 10.1051/mateconf/202337907008.
- [25] A. Kaur, "Weather forecasting using decision tree regression," *International Journal of Scientific Research in Engineering and Management*, vol. 06, no. 05, Jun. 2022, doi: 10.55041/IJSREM16084.
- [26] G. M. Kumar, "Accuracy analysis for logistic regression algorithm and random forest algorithm to detect frauds in mobile money transaction," *Revista Gestão Inovação e Tecnologias*, vol. 11, no. 4, pp. 1228–1240, Jul. 2021, doi: 10.47059/revistageintec.v11i4.2182.
- [27] F. Xing, R. Luo, M. Liu, Z. Zhou, Z. Xiang, and X. Duan, "A new random forest algorithm-based prediction model of post-operative mortality in geriatric patients with hip fractures," *Front Med (Lausanne)*, vol. 9, May 2022, doi: 10.3389/fmed.2022.829977.
- [28] M. Ghosh and R. Gor, "Health insurance premium prediction using blockchain technology and random forest regression algorithm," *International Journal of Engineering Science Technologies*, vol. 6, no. 3, pp. 74–82, Jun. 2022, doi: 10.29121/ijoes.v6.i3.2022.346.
- [29] G. Venkat Sai Tarun and P. Sriramya, "Analyzing Ola data for predicting price based trip distance using random forest and linear regression analysis," 2022. doi: 10.3233/APC220086.
- [30] L. Su *et al.*, "Early prediction of mortality, severity, and length of stay in the intensive care unit of sepsis patients based on sepsis 3.0 by machine learning models," *Front Med (Lausanne)*, vol. 8, Jun. 2021, doi: 10.3389/fmed.2021.664966.
- [31] K. S. M. Anbananthen *et al.*, "An intelligent decision support system for crop yield prediction using hybrid machine learning algorithms," *F1000Res*, vol. 10, p. 1143, Nov. 2021, doi: 10.12688/f1000research.73009.1.
- [32] Ch. V. Sandeep and T. Deep, "A novel approach for bank loan approval by verifying background information of customers through credit score and analyze the prediction accuracy using random forest over linear regression algorithm," *J Pharm Negat Results*, vol. 13, no. S04, Jan. 2022, doi: 10.47750/pnr.2022.13.S04.211.
- [33] A. Fadli, A. Annisa, and W. A. Kusuma, "Prediction of drug-target interaction using random forest in Coronavirus disease 2019 case," *Bioinformatics and Biomedical Research Journal*, vol. 4, no. 1, pp. 1–7, Nov. 2021, doi: 10.11594/bbrj.04.01.01.
- [34] X. Mei *et al.*, "Predicting malignancy of pulmonary ground-glass nodules and their invasiveness by random forest," *J Thorac Dis*, vol. 10, no. 1, pp. 458–463, Jan. 2018, doi: 10.21037/jtd.2018.01.88.
- [35] R. Genuer, "Variance reduction in purely random forests," *J Nonparametr Stat*, vol. 24, no. 3, pp. 543–562, Sep. 2012, doi: 10.1080/10485252.2012.677843.
- [36] Z. Wang and D. Chi, "Research on wind power prediction model based on random forest and SVR," *EAI Endorsed Transactions on Energy Web*, vol. 11, Apr. 2024, doi: 10.4108/ew.5758.

Experimental Investigation of Thrust and Flow Characteristics in Terms of Ground-Body Interaction of Reusable Vertical Take-off/Landing Rocket

MAİDENUR YÜKSEL¹, ÜMMÜ SELEME ÖZLEN¹, HÜRREM AKBIYIK¹

¹Adana Alparslan Türkeş Science and Technology University, Adana/Turkey, maidenur44190@gmail.com

¹Adana Alparslan Türkeş Science and Technology University, Adana/Turkey, uselemeozlen@gmail.com

¹Adana Alparslan Türkeş Science and Technology University, Adana/Turkey, hakbiyik@atu.edu.tr

Abstract - This experimental study investigates the effect of a fixed nozzle geometry on the ground-body interaction of vertical take-off and landing rockets on the changes in flow field and thrust due to varying distance from ground and yaw angles under constant pressure. In this context, the effects of nozzle geometry on flow dynamics are studied in detail. Axial thrust measurements in the downstream direction were carried out with 10 kg capacity load cells used in the experimental setup. Velocity distributions in the radial direction were analyzed by means of flow visualization using TiO₂ surface oil technique. The obtained measurements were performed using the H/D ratio (i.e. the ratio between the axial distance (H) and the diameter (D) of the body). Among the parameters investigated, a comprehensive analysis of the relationship between ground effect, altitude and yaw angle for vertical take-off and landing rockets was carried out. The core region thrust obtained at H/D = 0.5 mm is more pronounced compared to the thrust data obtained at higher H/D ratios. Under constant pressure, at H/D = 11, it is observed that the geometry no longer interacts with the ground effect and similar results were obtained in the visualization and thrust data. After a certain distance, air-air interaction starts up to a certain level of H/D ratios enter and the effects of the geometric shape are lost. When the flow visualization and thrust results are examined, it is observed that H/D = 0.5 and 0-degree angles show better performance and that the rocket nozzle geometry plays an important role in determining the thrust performance in the ground-body interaction for various yaw angles. In conclusion, the findings of this study suggest that reusable rocket systems used in space exploration can be useful in terms of making them more efficient and potentially contributing to other sectors outside the space industry.

Keywords - Reusable vertical takeoff/landing rocket, Thrust measurement, Flow characteristics, Rocket design, Surface oil imaging

I. INTRODUCTION

WITH the advances in technology and space challenge, studies on aerospace subsystems have been increasing in recent years, with a focus on cost reduction in space research

and for situations requiring continuity. The main focus of these studies is on reusable rocket systems that can contribute the most to cost reduction. At this point, one of the biggest challenges in rocket science is to maintain nominal rocket engine performance during take-off and for the rest of the flight. The phases of rocket flight are of great importance in maintaining this performance and reducing cost. Basically, the flight phases for a reusable rocket system can be classified as follows: starting from the lift-off phase, stage separation, tumble/reverse engine ignition and positioning (boostback burn), descending phase (descending), followed by reentry burn and landing burn to complete the flight [1]. Afterwards, it completes this flight with soft touchdown. In this context, especially lift-off and soft touchdown are the phases of the flight that need to be extensively researched in terms of the rocket's stable landing and reuse. In this context, it is necessary to conduct detailed research on the performance of side force generators [2], grided fins [3] and rocket engines [4] for reusable rockets in order to ensure this precise and safe landing. Studies in areas ranging from military and commercial applications have shown that rockets cannot meet certain requirements and that improvements in rocket propulsion efficiency are critical [5]. Measurement of rocket thrust and characterization of flow properties are of great importance in terms of propulsion efficiency [6]. In this context, the development of dynamic systems used in thrust measurements and the characterization of flow properties have the potential to provide important information on how this efficiency can be improved. The thrust-time graph, which affects not only measurement but also rocket design, constitutes one of the most important parts of rocket systems to be used in design and space studies [7]. In this context, experiments conducted to determine the effects of rocket developmental tests, nozzle design, fuel/propellant mixtures, additives and engine-engine subsystem changes on performance have critical value. When rocket propulsion is currently classified as hot thrust [8] and cold thrust [9], it is seen from the literature that studies have been carried out in both areas. In this study, a cold thrust study was

carried out and, in this context, studies on the experimental process were carried out by revealing the flow characteristics and thrust-time graph. As discussed by [10] and [11], many interesting thrust measurement studies involve aerodynamic applications on ground effects and rocket smoke. One of the early examples where rocket plume mimicked the properties of nature was the design of machines for space exploration. [12] compiled a review on engineering-related applications of the systems by generating data on ground effects and stability. Another flow field analysis was performed by [13]. Thrust values were determined using flow field data. In the study, the thrust values obtained using the load cell were compared and validated with PIV (Particle Imaging Velocimetry) data. Focusing on flow field analysis for normal flight, this study shows that the thrust value can be accurately determined by considering the smoke structure under different conditions. [14] measured velocity distributions around the model using the PIV (Particle Imaging Velocimetry) measurement technique to better understand the flow structure. The measurements were performed at various angles of attack ranging from 0° to 20° . These studies aim to understand jet flow phenomena and measure changes in thrust-time plots during ground-body interactions. In many studies on propulsion system design [15], the same method has been widely used for propulsion system performance evaluation. In these studies, hydraulic, piezoelectric or load cell based thrust measurements were performed. [16] focused on the relationship between the shape design and aerodynamic characteristics of vertical landing vehicles and investigated design considerations related to approach flight capabilities and low speed performance. These studies analyze the interaction of the nozzle jet with the main flow field during the vertical landing phase and show how this interaction affects the aerodynamic forces acting on the vehicle. [17] measured thrust values for different flow rates, gas pressure levels and masses. In the study conducted by [18], thrust measurements as well as torque measurements were performed using a load cell with six degrees of freedom. This system was used to measure both thrust values and rotational moments. In their experiments, [19] observed that during 0.5 seconds of continuous thrust ignition, the vertical effective thrust of the module varied from -13.2% to +11.8% at heights between 152 cm and 15.2 cm. They showed that ground effects increase the optimum firing height and firing height margin for a rocket with a given maximum descent rate. [20] focused on the interaction of a supersonic nozzle jet with the ground surface. The proximity of the ground to the vehicle floor reduces the ground pressure, creating a downward force. This undesirable effect can be mitigated by ground modifications or roughening of the ground surface. [21] applied different turbulence models and evaluated the results obtained by comparing with available experimental data on static wall pressure and shock position. He showed that as the nozzle pressure ratio increases, the shock position moves downstream and reaches a certain maximum value. [22] aimed to minimize ground support equipment and turn time by adopting a vertical takeoff and vertical landing (VTVL) system. For this purpose, an integrated propulsion system consisting of four 2-ton

LH2/LOX expansion loop engines, a GH2/GOX reaction control system (RCS) and an auxiliary power unit (APU) was used. [23] investigated the problem of optimal landing in the vertical plane in terms of fuel consumption by considering control inputs such as the rocket's angle of attack, thrust magnitude and thrust direction. It has been observed that maximizing the application of friction is preferred to reduce fuel consumption and optimal thrust control exhibits "bang-bang" behavior [24], presented a numerical study of the smoke flow and infrared radiation characteristics of a solid propellant rocket engine. They investigated the interaction of Al_2O_3 particles with the flow and gas phase. High-temperature Al_2O_3 particles can increase the radiation effect by up to 30%, while the glow effect caused different levels of brightness near the ground. While hydraulic-based thrust measurement is used in large propulsion engines, it is insufficient for precise measurement requirements. Load cell systems have been favored in recent years as they provide more accurate measurements than both hydraulic and piezoelectric systems. In this study, based on a review of the relevant literature, the use of a load cell system for thrust measurements is proposed. [15] stated that the thrust of a hybrid rocket engine was measured to be 41 lbf and that nozzle design is an important factor to achieve the maximum measured thrust of 50 lbf. Similarly, [25] measured thrust using a load cell. The thrust-time curve, which also affects rocket design, is one of the most important factors in design and space exploration studies. [10] investigated the dust dispersion and regolith erosion caused by the rocket exhaust gases of a vehicle landing on the lunar surface. Smoke and surface interaction is analyzed with the Roberts erosion model. The analysis was performed using a quasi-equilibrium model and it was found that ground effects change the thrust in vertical rockets. The closest study in the literature [26] stated that under altitude descent conditions, the yaw angle between the landing axis of the rocket and the local gravity vector includes the angular velocity of the rocket body in three directions and is controlled by the rocket motor as a whole. It was emphasized that the yaw angle significantly affects the landing performance during landing. Also, considering the flow visualizations, it is noteworthy that the jet exhaust structures of rocket engines have been studied for normal flight, but there is a lack of research on ground effect. In this study, the fact that the ground effect interaction will be examined for both landing and take-off, and that the side-force effects will be examined by revealing the flow characteristics by studying cold thrust and determining the thrust-time curve in an experimental way makes this study different from the studies in the literature.

II. MATERIAL AND METHODS

In order to simulate the ground-air interaction in vertical take-off and landing rockets, a scaled M2020 rocket motor is used as an engine. This engine provides the jet flow necessary to evaluate the performance of the system and ground effects. The mechanism designed for this study is shown in Figure 1. The system has a motion mechanism using sigma profiles to adjust the ground-body distance according to take-off and

landing heights. The centering ring between the sigma profiles is specially designed for secure fixation of the system. A jet flow was created based on the M2020 engine. This jet flow is used to support the motion in the system and provide thrust in the desired direction. The jet flow plays an important role in the study of ground-body interaction and is particularly important for evaluating the aerodynamic effects that may occur during landing and take-off phases. A loadcell is used to measure the thrust generated by the engine at different heights and the system utilizes 2 loadcells that can carry a load of 10N. These force gauges precisely detect and measure the thrust generated by the engine. It is particularly important to identify and analyze differences in the thrust generated by the engine under the influence of varying atmospheric conditions and altitudes throughout the engine's operating range. The flow is surrounded by the M2020 engine, scaled to form a closed volume, and exhausted through a divergent nozzle. The air flow from the compressor is transferred to the M2020 engine structure. The engine geometry and the engine structure were 3D printed by using PLA (Polylactic Acid) material. In addition, the flow was visualized with TiO_2 on the surface of a 40x40 cm Plexiglas layer. This visualization allows to analyze the behavior of the jet flow and provides its interactions with ground in more detail. In this study, the change in thrust due to the variation of different heights and deflection angles was investigated. The applied height and the different deflection angles used are presented in Table 1. In order to examine the effects of the change in thrust value depending on the height, 14 different heights and 5 different yaw angles were selected. It is noteworthy that the jet exit structures of rocket engines have been studied, especially for normal flight, but ground effect studies have not been conducted in detail.



Figure 1: Photographic description of experimental setup

A. General Description of Experimental Setup

2D schematic view of the experimental setup and the equipment used for the tests shown in Figure 2. The sigma profiles on the vertical axis of the model are 1500 mm, the short sigma profiles on the x-axis are 500 mm and those on the y-axis are 1200 mm based on the coordinate system. The model has a nozzle in the center of the base region. The nozzle outlet diameter is 4 mm. The gas for the jet flow is supplied by the

compressor and then sprayed into the free stream through the nozzle outlet. Force measurements were made using an inertial balance capable of measuring six components of the aerodynamic forces. For thrust measurement, load cells with a capacity of 10 N were placed on both sides of the fuselage. Arduino was used to collect thrust data produced by engine structure.

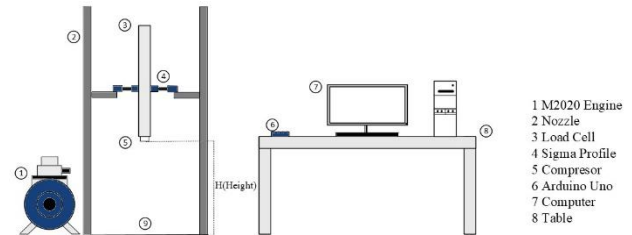


Figure 2: Schematic view of the experimental setup

B. Design of the Rocket Propulsion System

The thrust forces measured by the two load cells are averaged to determine the net thrust force. Calibrations were performed to obtain the coefficient matrix to calculate the interaction between the load cells. In addition, calibrations performed at different heights during assembly minimize deviations due to alignment errors, resulting in more accurate and reliable test results.

As the different angles between the vectors change, the flow distributions on the ground will be observed and the thrust will be measured. Table 1 shows the comparison of different deflection angles of the rocket. In order to observe the thrust variation at the nozzle exit, eight deflection angles at 2 degree intervals in the range of $0 < \theta < 8$ degrees were analyzed at specified heights. It provides a wide spectrum of observations to show how the system performs at different altitudes. The rationale for this approach is that flow distributions at different deflection angles can significantly affect the interaction of the flow with the ground. These variations therefore also affect the thrust force. Therefore, observations in this range of angles were aimed to provide a detailed and comprehensive investigation. The range of angles used in the literature provides a consistent approach to the present research method. For these reasons, the range of angles between 0 and 8 degrees provides the necessary scope for a detailed study of the effects on thrust and flow.

Table 1: The specifications of the designed systems

No	Parameter	Definition	Values to be examined
1	H (mm)	Height	2, 4, 8, 12, 16, 20, 24, 28, 32, 36, 40, 44, 48, 52, 56
2	θ°	Deflection angle	0,2,4,6,8
3	P (Pa)	Pressure value	Constant
4	R(mm)	Nozzle diameter	4

C. Flow Visualization Setup

In [27], the ratio of the fluid mixture used for flow visualization was 1:1:4. This ratio refers to a specific mixing ratio of titanium dioxide (TiO_2), oleic acid and kerosene/SAE 60 engine oil. On the other hand, in [28] and [29], this mixing ratio was determined differently and was obtained by mixing titanium dioxide, oleic acid and kerosene/SAE 60 motor oil in a ratio of 1:5:7. In this study, the ratio of the fluid mixture used for flow visualization was 1:5:7. The process of making titanium dioxide used for flow visualization is shown in Figure 3. In Figure 3, titanium dioxide (TiO_2), oleic acid, and kerosene/SAE 60 engine oil are mixed to form titanium dioxide-based visualization, which is used to clearly examine flow structure.

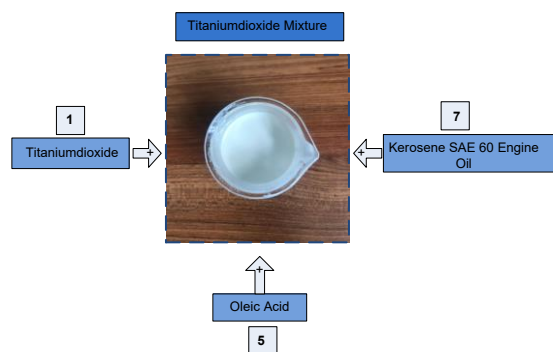


Figure 3: Visualization of titanium dioxide mixture formation

As shown in Figure 4, this mixture was applied on a TiO_2 coated plexiglass sheet placed downstream of the engine. This sheet consists of a square plexiglass sheet with dimensions of 40 cm x 40 cm and a thickness of 3 mm. The sheet was painted with black spray paint so that the flow on the surface could be seen more clearly. The air obtained by thrust from the nozzle is sprayed onto this TiO_2 coated sheet. The applied mixture is sprayed onto the black painted plexiglass sheet, allowing the flow structures generated by the thrust force at different parameters to be observed and photographed. As a result of the visualization, the effects of the flow on the plexiglass sheet, flow structures can be visually analyzed.



Figure 4: Schematic description of experimental setup for flow visualization

III. RESULT AND DISCUSSION

The interactions of a nozzle jet with the underlying flow field affect the aerodynamic forces acting on the vehicle during the vertical landing and take-off phases. In some cases, these interactions can cause changes in jet thrust and angle of attack. In this study, thrust measurement and flow visualization were performed in the vertical axial direction using different height ratios. Details on the parameters are given in the following sections.

A. Thrust experiment result

When a vehicle enters the vertical descent phase, the engine is restarted to decelerate and ensure a soft descent towards the ground surface. During this process, the supersonic nozzle jet affects the flow field in the lower region of the vehicle [30]. This causes an unexpected change in the aerodynamic forces acting on the vehicle. In order to investigate this interaction, the relationship between jet thrust and angle of attack was measured in experiments. The results are presented in Figures 5, 6 and 7. In these figures, it is possible to understand the effects of changes in the angle of attack on the thrust and the dynamics of these effects. The measurements were performed using the H/D ratio, i.e. the ratio between the axial distance (H) and the aperture diameter (D). This ratio is used for performance evaluations in rocket design. This ratio value expresses the response of the rocket under applied loads, the forces on the ground surface.

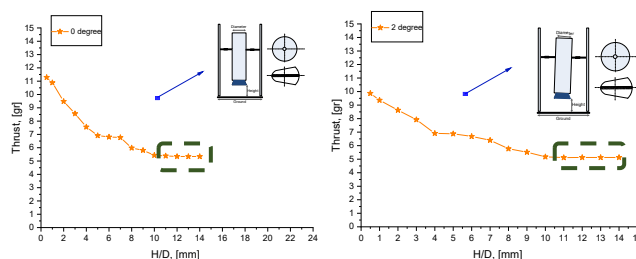


Figure 5: Thrust measurement results in the vertical axis for different heights at 0° and 2° deflection angle

Figure 5 shows that for the deflection angles of 0 and 2 degrees, the thrust value decreases with the increase in the H/D ratio. At 0 degree angle, the thrust is maximum because the jet stream exits directly from the center. In this case, the jet flow exerts an intense pressure on the bottom surface, which leads to high thrust. As the H/D ratio increases, the thrust value decreases. This decrease shows that a higher H/D ratio causes a wider distribution of force over a larger area on the ground. It also indicates that the base pressure is lower. Considering the minimum values of the H/D ratio, when the base is close to the ground surface, significant reductions in the base pressure near the center of the base are noticeable compared to a free state. The core region (i.e., the thrust generation region) obtained at $H/D = 0.5$ mm is more pronounced than the impulse data obtained at higher H/D ratios, and also varies with the change in angle with increasing H/D ratio. Higher pressure in the core can improve performance by increasing thrust. At $H/D = 11$ mm

and above, the core region effect decreases and the net thrust stabilizes. This indicates that where the jet flow is more widely distributed, significant thrust is not achieved.

At a 2-degree angle, the jet flow is directed by the slope, causing the jet flow to spread over a larger area on the bottom surface. This spreading leads to a dispersion of the jet flow. The results of this measurement, monitored in Figure 5, show that even a small change in angle can cause a significant reduction in thrust.

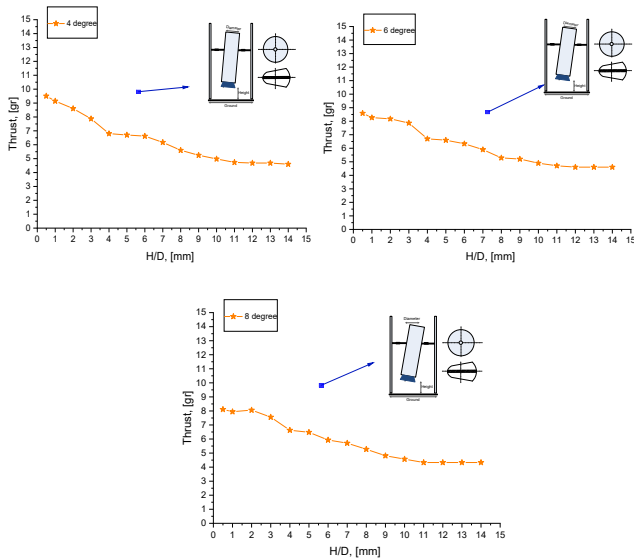


Figure 6: Thrust measurement results in the vertical axis for different heights at 4°, 6° and 8° deflection angle

In the graphs given in Figure 6, the thrust force is analyzed at 4, 6 and 8 degree angles in order to better show the effects of these angles on the jet flow. When the graph at 4 and 6 degree angles is analyzed, it is seen that by directing the jet flow, it causes the jet flow to spread over a wider area. As the yaw angle increases, the jet flow becomes more dispersed, resulting in a more pronounced reduction in thrust. At these angles, the pressure distribution of the jet flow on the bottom surface decreases, resulting in a decrease in thrust. At 8 degrees, the jet flow generates the lowest pressure at the bottom surface. In this case, the jet flow is spread the farthest from the center, resulting in the greatest reduction in thrust.

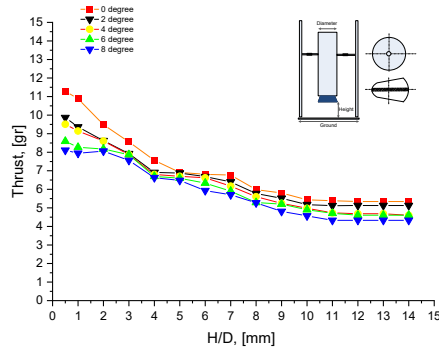


Figure 7: Comparison of thrust measurement results for different heights at different yaw angles

The comparison of the thrust measurement results at different deflection angles in Figure 7 clearly shows how the height changes depending on the thrust performance. Especially at $H/D = 11$ and above, it is observed that the geometry now interacts with the ground effect and similar results are obtained in the visualization and thrust data. This indicates that after a certain height, H/D ratios enter into air-air interaction and the effects of the geometric shape are lost. When the flow visualization and thrust results were examined, it was observed that the rocket engine may perform better at $H/D = 0.5$ and 0 degrees and that the rocket nozzle geometry plays an important role in determining the performance of the thrust force in the ground-body interaction for various deflection angles.

B. Flow Visualization Experiment Result

This study demonstrates the interaction between the nozzle jet and free flow. The effects of the jet flow on the bottom surface provide important findings, especially in terms of vortex formation and pressure drop. Experimental tests were conducted to understand the nature of these interactions and evaluate their effects. The flow visualization has contributed to depending design parameters, identification of features and analysis of fluid behavior.

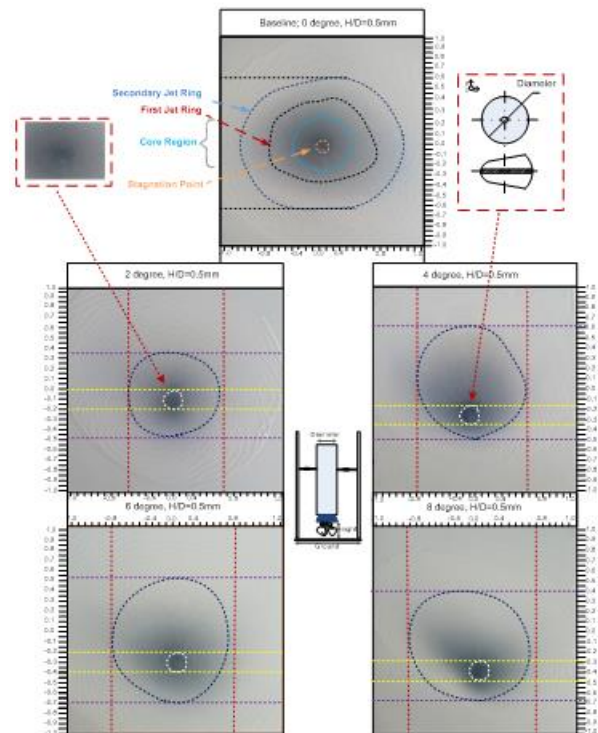


Figure 8: Flow visualization and comparison of models with H/D ratio of 0.5 mm for different deflection angles

Figure 8 compares the results of flow visualization performed at different deflection angles (0°, 2°, 4°, 6°, 8°) for a model with an H/D ratio of 0.5 mm. This graph contains data obtained using the surface oil visualization method and clearly shows the distribution of the jet flow on the bottom surface.

When looking at the increase in deflection angles, there is a significant shift in the y-axis in the fully developed region. The 4 mm outer diameter divergent nozzle used in these experiments significantly changes the effect of the jet flow. With increasing deflection angle, the prominence in the core regions decreases. The flow visualization results show how the jet flow expands depending on the divergence angles and the pressure distribution at the bottom surface to understand how they are affected. Figure 9 compares the flow visualization results for different H/D ratios (0.5, 1, 2, 4, 8, 10, 11) and deflection angles (0° , 2° , 4° , 6° , 8°). According to the visualization results, the velocities and the jet flow patterns in the radial direction show significant changes depending on the varied H/D ratios and deflection angles. Regarding the geometrical distribution of the flow, the visualization at 0° deflection angle and low H/D ratio (0.5) shows that the developing region has a rounded geometry. With low H/D ratios, the impact of the jet flow is concentrated in a small area on the bottom surface. The flow is strongly and distinctly centralized and spread over a narrow area. As the deflection angles increase, the round geometry of the developing region changes to an oval shape. This change affects the propagation and distribution of the impact of the jet flow on the bottom surface. Especially with high deflection angles, the jet flow covers a larger area and the pressure distribution at the bottom surface is spread over a larger area. This increment allows the distribution of the fluid to spread over a larger area.

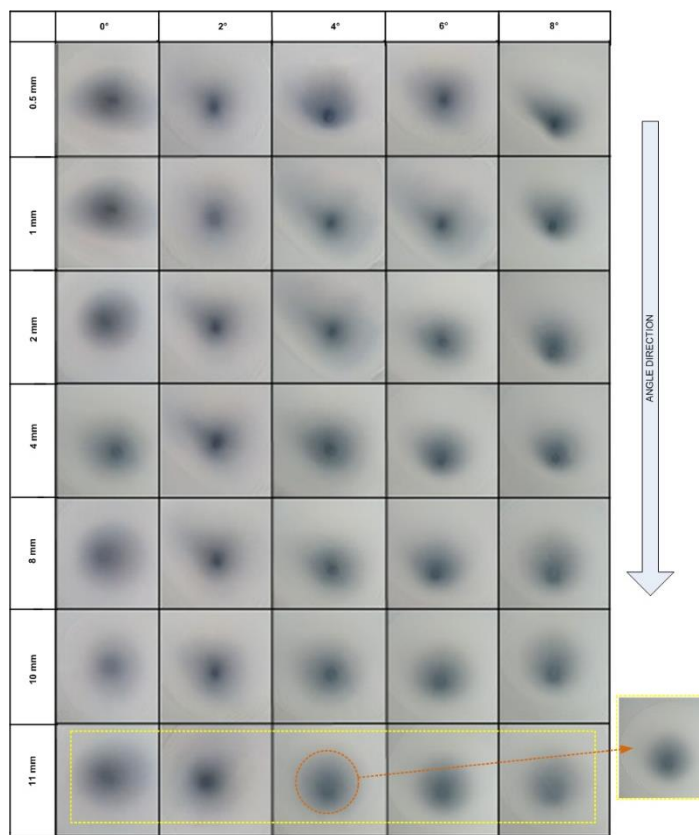


Figure 9. Flow visualization and comparison of models with different H/D ratios at different deflection angles

With a low H/D Ratio (0.5 - 2), the distance of the jet flow around the hole is more restricted. This causes the flow to concentrate in a narrow area and its effect is more pronounced. At medium and high H/D Ratios (4 - 11), the area of jet flow spread becomes wider. Figure 9 shows that as the H/D ratios increase, the area over which the titanium dioxide mixture spreads wider area. At high H/D ratios, the effect of the jet flow spreads over a larger area on the bottom surface, while the thrust force decreases significantly.

When analyzing performance at low H/D and low yaw angles, low H/D ratios and low yaw angles provide more efficient thrust. This combination allows the flow to spread more uniformly and the nozzle or rocket geometry to perform more efficiently. When high H/D ratios and ground effect are analyzed, it is observed in Figure 9 that when the H/D ratio reaches values of 11 and above, the jet flow interacts with the ground effect and the effects of the geometric shape disappear. These high ratios indicate that the jet flow interacts with the air-air and the effect of the jet flow is spread over a wider area and its effect is minimized. This is clearly visible in the image.

IV. CONCLUSION

In this study, the thrust variation of the ground-body interaction in vertical take-off and landing rockets due to different heights and yaw angles were researched. Also, the flow field properties were investigated by a surface oil visualization method. Two 10N loadcells were used for axial thrust measurements. Plexiglas square plate and oleic acid, titanium dioxide and kerosene SAE 30 Engine oil were used for surface oil visualization. A ratio of 1:5:7 was used to make this mixture and velocity distributions in the radial direction were analyzed. Surface oil visualization techniques with titanium dioxide were used to determine the flow field regimes. The resulting measurements were performed using the H/D ratio (i.e. the ratio between the axial distance (H) and the aperture diameter (D)).

- In the surface oil visualization imaging, it was observed that the best images were obtained at H/D=0.5 mm and 0° deflection angle of the rocket engine positioned at 90 degrees. It was determined that jet structure was formed at all levels.

- When the thrust measurements were analyzed, it was revealed that the core region obtained when H/D = 0.5 mm was more pronounced compared to the thrust data obtained at higher H/D ratios, and that it also differed depending on the change in angle with the increase in this ratio.

- The flow visualization at 90 degrees shows a rounded geometry of the enhanced region, while the visualizations at deviation angles show a more oval geometry.

- At H/D = 11, it is observed that the geometry is provides air-air interaction and similar results are obtained in the visualization and thrust data.

- It is observed that the jet thrust due to the changing yaw angle and height causes a significant shift in the y-axis.

- Looking at geometries with high H/D ratios, the titanium dioxide visualization shows that the thrust force decreases while the flow field expands.

• The lower H/D and the smaller yaw angle, the smaller the flow field and the stronger the flow field.

This study clarifies the flow characteristics of the jet formation depending on the altitude and yaw angle of the ground-effect interaction of vertical take-off and landing rockets. It also reveals the effects on the flow field. The obtained results contribute to a better understanding of the flow dynamics in jet applications for vertical take-off and landing rockets.

ACKNOWLEDGMENTS

This study was supported by the University Students Research Projects Support 2209-A Program conducted by TÜBİTAK with the project number 1919B012216370.

REFERENCES

- [1] Ferrante, R. (2017). A robust control approach for rocket landing. Theses Univ. Edinburgh.
- [2] Zheng, Y., Lei, J., & Yin, J. (2024). The Generation Mechanism of the Side Force and Yawing Moment of a Rotating Missile with Wrap-Around Fins. *Aerospace*, 11(9), 765.
- [3] Krammer, A., Blecha, L., & Lichtenberger, M. (2022). Fin actuation, thrust vector control and landing leg mechanisms design for the RETALT VTVL launcher. *CEAS Space Journal*, 14(3), 577-591.
- [4] SAMUR, A. E., Okulu, H. H., & KARABEYOĞLU, A. (2016). HİBRİT YAKITLI ROKET MOTORU ATEŞLEME/TEST DÜZENEGİ TASARIMI. *Journal of Aeronautics & Space Technologies/Havacılık ve Uzay Teknolojileri Dergisi*, 9(1).
- [5] YAMAN, H., & KORKMAZ, S. (2018). Sıvı Yakıtlı Çalışan Bir Roketin Farklı Yakıt Kullanımında Özgül İtki Davranışının İncelenmesi.
- [6] Vemula, R. C., Gustavsson, J., & Kumar, R. (2018). Rocket nozzle thrust and flow field measurements using particle image velocimetry. *New Space*, 6(1), 37-47.
- [7] Açık, S. (2010). Internal ballistic design optimization of a solid rocket motor (Master's thesis, Middle East Technical University).
- [8] YAMAN, H., & KORKMAZ, S. (2018). Sıvı Yakıtlı Çalışan Bir Roketin Farklı Yakıt Kullanımında Özgül İtki Davranışının İncelenmesi.
- [9] Silik, Y., Tanıker, S., & Yaman, U. (2017). Soğuk Gaz İtki Kontrol Sisteminin Pnömatik Akış Kontrolünün Benzetimi.
- [10] Rahimi A., Ejtehadi O., Lee K.H. Myong R.S., Near-field plume-surface interaction and regolith erosion and dispersal during the lunar landing. *Acta Astronautica*.308-326.
- [11] Nonaka S., Nishida H., Kato H., Ogawa H., Inatani Y. Vertical landing aerodynamics of reusable rocket vehicle. *Trans. JSASS Aerospace Tech. Japan*, 10, 1-4. (2012).
- [12] Jack F.Lands JR. Development of a Terminal Landing Rocket System for Apollo-Type Vehicles, Manned Spacecraft Center, Houston, Texas,4,3,333-338. (1967).
- [13] Vemula R., Gustaussan J., Kumar R. Rocket nozzle thrust and flow field measurements using Particle Image Velocimetry. *Mary Ann Liebert*, 6, 1, 37-46. (2018).
- [14] Suzuki T., Nonaka S., and Inatani Y. Computations of Opposing Jet from Vertical Landing Rocket Vehicle. *Japan Aerospace Exploration Agency*, 24, 1-10. (2006).
- [15] Desrochers M.F., Olsen G.W., Hudson M.K. A ground test rocket thrust measurement system, *Journal of Pyrotechnics*. 14, 50-55. (2001).
- [16] Nonaka S.,Ogawa H., and Inatani Y. Aerodynamic Design Considerations in Vertical Landing Rocket Vehicle. *The Institute of Space and Astronautical Science Sagamihara, Japan*, 10, 1-10. (2001).
- [17] Endo T., Daiman Y., Matsuo A., Hirana M., Kasahara J. Thrust measurement of a multicycle partially filled pulse detonation rocket engine. *Propulsion and Power*, 25, 1033-1041. (2009).
- [18] Wright A.A., Wright A.B., Bom T., Strickland R. A six degree -of-freedom thrust sensor for a lab scale hybrid rocket, *Meas. Sci. Technol.*, 24, 125104, 1-10. (2013).
- [19] Wirz R.E., and Shariff S S. Ground Effects for CEV Vertical Retrorockets *Metacomp Technologies Inc., Agoura Hills, CA 43*, 1-8. (2007).
- [20] Akita D., Yamada K., and Suzuki K. Experimental Study on Control of Supersonic Aerodynamic Characteristics of a Vertical Landing Rocket by Using Opposing Jet. *25,604,220-226*. (2004).
- [21] Balabel, A., Hegab, A.M., Wilson, S., Nasr, M., El-Behery, S. Numerical Simulation of Turbulent Gas Flow in a Solid Rocket Motor Nozzle. *Aerospace Sciences & Aviation Technology*, ASAT- 13-PP-13. (2009).
- [22] Ogawa H., Nonaka S., and Inatani Y. A Concept and Its Aerodynamic Design of a Sub-Orbital Reusable Rocket. *Japan Aerospace Exploration Agency, Sagamihara, Kanagawa*, 34, 1-3. (2004).
- [23] Liu X. Fuel-Optimal Rocket Landing with Aerodynamic Controls. *Beijing Institute of Technology*, 1-15. (2017).
- [24] BAO X., YU X.,WANG Z.,MAO H., LIU D. Numerical Investigation on Flow and Radiation Characteristics of Solid Rocket Motor Plume Near the Ground. *International Conference on Identification*,645-650. (2019).
- [25] Kasahara J., Hirano M., Matsuo H., Daimon Y., Endo T. Measurement of a Multicycle partially filled pulse detonation rocket engine. *Journal of Propulsion and Power*, 25, 1-6. (2019).
- [26] Zupp G.A. An Analysis and a historical review of the Apollo Program Lunar Module Touchdown Dynamics. *Technical Report NASA Johnson Space Center, Houston, USA*. (2013).
- [27] Wei Z., Lian L., Zhong Y. Enhancing the hydrodynamics performance of a tapered swept-back wing through leading edge tubercles. *Experiments in Fluids*, 59, 103. (2018).
- [28] Seyhan M., Sarioglu M. Investigation of drag reduction performance of half NACA0009 and 0012 airfoils place over a trailer on the flow around truck-trailer. *J. Mech. Sci. Technol.* 35, 2971-2979. (2021).
- [29] Sudhakar S., Kathikeriyan N., Suriyanarayanan P. Experimental studies of the leading-edge tubercles on laminar separation bubble. *AIAA Journal*, 57, 5197-5207. (2019).
- [30] Emelyanov, V. N., Pustovalov, A. V., & Volkov, K. N. (2019). Supersonic jet and nozzle flows in uniform-flow and free-vortex aerodynamic windows of gas lasers. *Acta Astronautica*, 163, 232-243.
- [30] Emelyanov, V. N., Pustovalov, A. V., & Volkov, K. N. (2019). Supersonic jet and nozzle flows in uniform-flow and free-vortex aerodynamic windows of gas lasers. *Acta Astronautica*, 163, 232-243.

Modeling and SoC Estimation of Lithium-Ion Batteries Used in Electric Vehicles

BERFİN YAĞCI¹, MURAT ÜNLÜ²

¹ Kocaeli University, Kocaeli/Turkey, berfinyagci103@gmail.com

² Kocaeli University, Kocaeli/Turkey, muratunlu@kocaeli.edu.tr

Abstract - With advancing technologies, energy demand is increasing worldwide. However, it is impossible to find enough fossil fuels to meet this energy demand. For this reason, studies on energy storage technologies have increased. Along with these studies, battery technology has also developed. In this way, electric vehicles have increased their popularity. Modeling is very important to define the battery correctly in electric vehicles. In this study, the thevenin model is taken as a reference for the lithium-ion battery. A lithium-ion battery is charged under constant current. Voltage values were taken as a function of time. A time dependent voltage graph was created using Excel. The thevenin equivalent circuit of the battery was extracted from the charge graph. Using the obtained thevenin model, the charge curve was extracted in MATLAB/Simulink. Finally, an exponential curve connected to the SoC was created using the least squares method from the numerical analysis methods

Keywords - Energy Storage, Electric Vehicles, Lithium-Ion Batteries, Battery Modeling.

I. INTRODUCTION

Rapid population growth and economic growth around the world are causing energy demand to rise continuously [1]. However, since this demand is met from fossil fuels such as coal and natural gas, which have limited reserves, there is concern about the depletion of energy fuels. This situation has further increased the need to turn to alternative and renewable energy sources. Renewable energy technologies and the use of alternative energy sources play an important role for sustainable energy.

Today, the widespread use of gasoline-fueled vehicles has led to a gradual decrease in fossil fuels. As an alternative to these vehicles, environmentally friendly and energy-saving electric vehicles have entered our lives. Electric vehicles cause less carbon emissions than internal combustion engines and thus reduce gas emissions in the atmosphere [2]. With the proliferation of these vehicles, technological advances in energy storage and battery management are also taking place. In order to accurately determine the battery parameters used in electric vehicles, the battery should be modeled in the closest way to reality. This model will facilitate the determination of battery parameters such as charge state estimation and health state estimation. Lithium-ion batteries are widely used in electric vehicles and energy storage. Lithium batteries have high energy density. In this way, it can store more energy than other batteries of the same size. They are also preferred because

they are lightweight, can be charged quickly and have a long battery life [3].

II. BATTERY MODELS

In order to accurately determine battery parameters in electric vehicles, it is necessary to model the battery as close to reality as possible. Battery Models are used to describe the battery characteristics under possible operating conditions such as temperature, voltage, discharge rate and SoH. Battery models are physical models, experimental models and abstract models [4].

Physical Model: Also known as white boxes, the model is associated with the internal structure of the battery. It expresses the complex electrochemical phenomena that occur inside the cell. It is a very difficult approach, although it gives results close to reality [1].

Experimental Model: In this model, which is defined as black boxes, only experimental data is considered, regardless of the physical characteristics of the battery. Mathematical approaches to define the black box facilitate the system, but this model alone is insufficient [1]. It gives relatively better results when used together with the physical model.

Abstract Model: Known as grey boxes. It shows different equivalent circuits of the battery [1]. Although the number of parameters is not high, it needs a data table that requires a lot of effort to configure the model. Although they have an acceptable accuracy, their usefulness is limited as some reductions are made analytically [5]. There are different forms, the most popular being the electrical equivalent circuit model. In this study, the electrical model is taken as reference.

III. BATTERY EQUIVALENT CIRCUIT MODELS

Batteries used in electric vehicles can be described by different models. These are Rint, RC, PNGV Model, Thevenin, double polarization (DP) circuit with extra RC [6]. Although the most complex and realistic model among these models is the DP model, the complexity of mathematical expressions makes it difficult to reach the result. Therefore, other models are widely used.

A. Zero Order Equivalent Circuit Model (Rint Model)

This model, which consists of a simple internal resistor, has been tested at the National Renewable Energy Laboratory and implemented in an advanced vehicle simulator. Although the voltage prediction rate of the model is between 3% and 12%, it

has been widely used due to its simplicity. However, this model can only be valid under steady-state load conditions [7]. The circuit diagram of the model is as shown in figure 1. The model consists of the battery voltage V_b and a resistor R_i connected in series with it. V_t is the voltage at the terminal terminals. I_b is the battery current. The terminal equation of the model is given in equation (1).

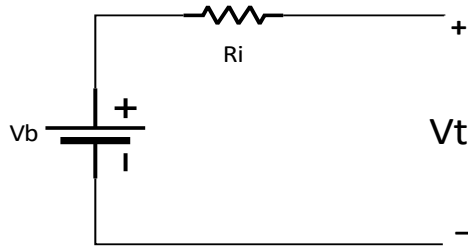


Figure 1: Rint Model

$$V_t = V_b - R_i \cdot I_b \quad (1)$$

B. First Order Equivalent Circuit Model (Thevenin Model)

The Thevenin model has an RC arm connected in series with the resistor. This model can be improved by adding additional RC arms. The study [7] found that the Thevenin model cannot explain all the behavior of batteries. A basic Thevenin model was developed [7], which aims to differentiate their values in charge and discharge processes by adding ideal diodes in series with resistors. V_b and I_b in the circuit diagram are battery voltage and battery current respectively. I_{R_1} and I_{C_1} are the currents flowing through R_1 and C_1 . $V_{R_1C_1}$ is the voltage across the the R_1C_1 branch; V_t is the voltage at the terminal ends and the terminal equations of the model are given in equations (2), (3), (4). The model taken as reference in this study is the Thevenin model.

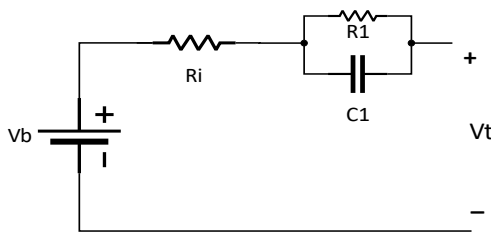


Figure 2: Thevenin Model

$$I_b = I_{R_1} + I_{C_1} \quad (2)$$

$$I_b = c_1 \cdot \frac{d}{dt}(v_{R_1C_1}) + \frac{v_{R_1C_1}}{R_1} \quad (3)$$

$$V_t = V_b - R_i \cdot I_b - V_{R_1C_1} \quad (4)$$

C. Second Order Equivalent Circuit Modeling (DP Model)

The characteristics of batteries can be simulated in a limited

way with the thevenin model. Because it is too different from the findings of the electrochemical model to be taken for granted. An inaccurate simulation occurs during charge-discharge. A dual polarization (DP) model is obtained by adding another RC arm in series to this model. In the DP model, the open circuit voltage is represented by internal resistors and two RC arms connected in series. The resistances in the parallel arm characterize the electrochemical polarization while the capacitances characterize the transient response during power transfer [4]. $V_{R_1C_1}$ and $V_{R_2C_2}$ are the voltages of the R_1C_1 and R_2C_2 branches, respectively. The terminal equations of the model are given in equation (5) and equation (6).

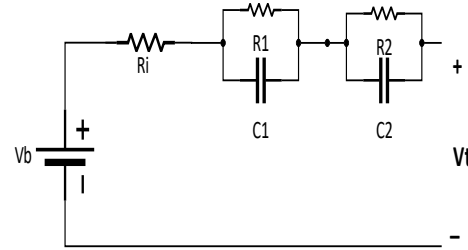


Figure 3: DP Model

$$I_b = C_1 \cdot \frac{d}{dt}(v_{R_1C_1}) + \frac{v_{R_1C_1}}{R_1} = C_2 \cdot \frac{d}{dt}(v_{R_2C_2}) + \frac{v_{R_2C_2}}{R_2} \quad (5)$$

$$V_t = V_b - R_i \cdot I_b - V_{R_1C_1} - V_{R_2C_2} \quad (6)$$

IV. BATTERY STATE OF CHARGE ESTIMATION METHODS

In general, the SoC of a battery is defined as the ratio of the current capacity of the battery to the nominal capacity [9]. Charge state estimation is one of the most important parameters in battery applications. It is also important for energy management as it shows the remaining energy. Thus, it enables more efficient use of the battery. There are many different methods for SoC estimation in batteries [8]. The general time-dependent expression of SoC is given in equation (7).

$$SoC(t) = \frac{Q(t)}{Q_n} \quad (7)$$

A. Direct Measurement Method

The direct measurement method is based on a repeatable and significant relationship between the measured battery variable and the SoC. These variables should be physically measurable, such as battery voltage (V), battery impedance (Z) and voltage relaxation time (τ). Another variable that constitutes the SoC function in this method is the battery temperature [11]. The function of SoC obtained depending on these variables is given in equation (8).

$$SoC = f_T^d(V, Z, \tau) \quad (8)$$

The advantage of this method is that it is not continuously connected to the battery. Measurements are taken when the battery is connected and the SoC is subtracted from the f_T^d function. The disadvantage is that the parameters that make up

the f_T^d function are very variable and differences in the environment can affect the battery behavior. It is therefore very difficult to construct the function correctly [10].

B. Coulomb Counting Method

This method, referred to as Book-Kepping in the literature, is based on measurement and integration. In the system, the amount of currents flowing in and out of the battery is taken into account, so it is also known as the Coulomb Counting Method [10]. The Coulomb counting method measures the discharge current of a battery and records the discharge current over time to estimate the SoC. This method requires the discharge current $I(t)$ and the previous estimate $SoC(t-1)$ to calculate the instantaneous state of charge $SoC(t)$. The equation is expressed as (9) [9].

$$SOC(t) = SOC(t-1) + \frac{I(t)}{Q_n} \Delta t \quad (9)$$

As with other methods, this method also has shortcomings. Because factors such as temperature, discharge current and cycle life of the battery cause different results in the method. This reduces the accuracy of the method [12].

C. Extended Kalman Filter (EKF)

It is possible to determine the battery parameters by direct measurement and coulomb method. However, since batteries do not have linear behavior, the values found by these methods will be reduced values. In the literature, there are different iteration methods for nonlinear equations such as Kalman filter and neural network method. With the Kalman filter, the difference between the actual and estimated values in a system can be minimized and a result that is not affected by measurement noise is obtained. In this method, non-linear prediction and measurement functions are used. These functions are transformed into linear equations by Taylor series method. The extended Kalman filter method is applied to the obtained state space equations. Although it gives results closer to reality than other methods, it has a margin of error. Because the equations and matrices used are quite complex and it is difficult to make accurate analysis predictions [5,13].

V. BATTERY CHARGING EXPERIMENTAL APPLICATION

In order to determine the battery parameters, a reference model is first considered. In this study, the thevenin model is used for its applicability and accuracy. Although there are models that give more convergent results than the Thevenin model, the complexity of the resulting mathematical expressions will make it difficult to determine the parameters correctly. The circuit diagram is as shown in Figure 2 and the terminal equations of the circuit are given below the figure. In the experiment, a lithium polymer battery model SLPB526495 was used. The battery has a capacity of 3.3 Ah and its nominal voltage is 3.7 Volts. The charging voltage is given as 4.2 V. Since 4 batteries were connected in series in the experiment, the total capacity reached 13.2 Ah. In other words, this battery can be charged in 1 hour with a constant current of 13.2 A for 1 C. The battery was first completely discharged and then charged

at 0.5 C for 2 hours with 6.6 A. An experimental setup was created to take and record voltage measurements from the battery terminals while the battery was being charged. The setup is as shown in Figure 4; 4 SLPB526495 lithium batteries connected in series, DC power supply and GL220 data logger were used.

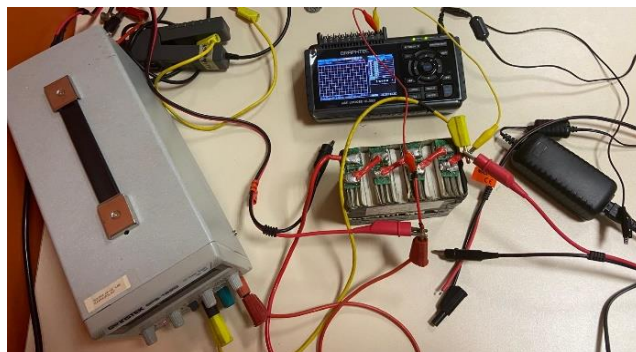


Figure 4: Charging Experiment Setup

A. Determination of Battery Parameters

After the battery charging process was completed in about 2 hours, data was taken from the GL220. A graph of battery voltage and time axis was obtained. The graph is as shown in Figure 5. The curve formed in the graph is approximately like an RC curve. Using the values in the curve, the parameters of the reference model can be found. The internal resistance can be calculated with the battery voltage and constant charging current (6.6A) that the curve shows at the first moment, $t=0$ s. The battery voltage, which is 3.2 V before charging, shows 3.412 V at the start of charging. Based on these data, $R_i = 0.0321 \Omega$ as shown in equation (10). V_0 is the voltage of the battery at open circuit. V_1 is the voltage value at $t=0$ s.

$$R_i = \frac{V_1 - V_0}{I} = \frac{3,412 - 3,2}{6,6} = 0,0321 \Omega \quad (10)$$

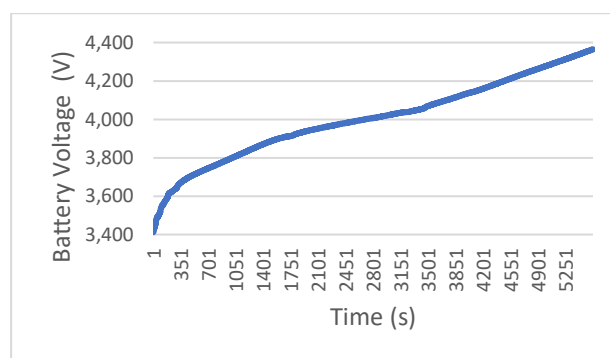


Figure 5: Battery Charging Curve (V-t)

After finding R_i , the RC values that enable the formation of the characteristic curve are calculated. First of all, the point where the curve reaches equilibrium is determined from the graph. For this curve, the equilibrium point was found to be $t=5619$ s $V_b=4.369$ V. Based on these values, R_1 was found as 0.145Ω in equation (11) using the same method, that is, using the voltage difference. V_t in the equation refers to the voltage at the terminal ends.

$$R_1 = \frac{V_t - V_1}{I} = \frac{4,369 - 3,412}{6,6} = 0.145\Omega \quad (11)$$

After finding R_1 , the capacity of C_1 can be calculated from the equation $\tau = R_1 C_1$. In the literature, the time for the charge-discharge curves to reach equilibrium is accepted as 5τ . Based on this information, $C_1 = 7750.345F$ obtained from equation (12).

$$\tau = R_1 C_1 \quad C_1 = \frac{5619}{0,145} = 7750.345 F \quad (12)$$

B. SoC Estimation

Position In batteries, the charge estimate is shown as a percentage. In other words, it is 100% at maximum voltage and 0% at minimum battery voltage. The SoC value shown as a percentage is related to time. For this battery, the entire charging process took 5600 seconds. Thus the 5600th second can be considered the moment when the battery reaches 100% charge. However, SoC changes in direct proportion to time. The percentage SoC and voltage graph is given in Figure 6.

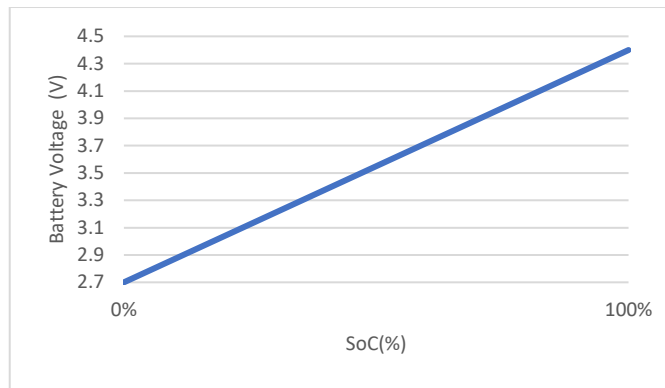


Figure 6: % SoC-Battery Voltage

Thevenin model was created with the values taken from the battery test application. And the model parameters were determined. At the same time, with this data, it is possible to create a curve equation that predicts the voltage depending on time or percent charge. The least squares method, one of the numerical analysis methods, is used to create this equation. The general matrix expression of this method is given in (13). The "x" variable in the matrix is replaced by the time values in the data and the "y" variable is replaced by the voltage values. The unknowns in the matrix are found and replaced in the general equation expression. The time dependent voltage expression for this model is found as in equation (14).

$$\begin{bmatrix} n & \sum_{i=1}^n x_i \\ \sum_{i=1}^n x_i & \sum_{i=1}^n x_i^2 \end{bmatrix} \cdot \begin{bmatrix} \ln(a_0) \\ a_1 \end{bmatrix} = \begin{bmatrix} \sum_{i=1}^n \ln(y) \\ \sum_{i=1}^n x_i \ln(y_i) \end{bmatrix} \quad (13)$$

The matrix is solved mathematically, the coefficients a_0 and a_1 are found and the expression (14) is obtained.

$$y = a_0 \cdot e^{x a_1} \quad (14)$$

The matrix shown in (15) is created using the data.

$$\begin{bmatrix} 5620 & 15795010 \\ 15795010 & 59183902470 \end{bmatrix} \cdot \begin{bmatrix} \ln(a_0) \\ a_1 \end{bmatrix} = \begin{bmatrix} 7788.99 \\ 22358437 \end{bmatrix} \quad (15)$$

Equation (16) is obtained by finding the unknowns in the matrix and replacing them in the general expression.

$$V(t) = 3.658 \cdot e^{3,16 \cdot 10^{-5} \cdot t} \quad (16)$$

With this equation, a time dependent voltage expression is obtained which is indirectly dependent on the SoC.

C. Modeling and Simulation with Simulink

In this study based on the Thevenin model, the parameters of the model were determined by using the electrical end equations. However, this model cannot explain the internal structure and behavior of the battery precisely. The model obtained is the simulation model that will be used to describe the battery. The battery is set up in simulink as shown in Figure 7. The open circuit voltage of the battery is modeled using a DC voltage source and the constant charging current is modeled using a DC current source. Other parameters are added to the thevenin model as calculated. The time dependent charging curve of the model is given in Figure 8.

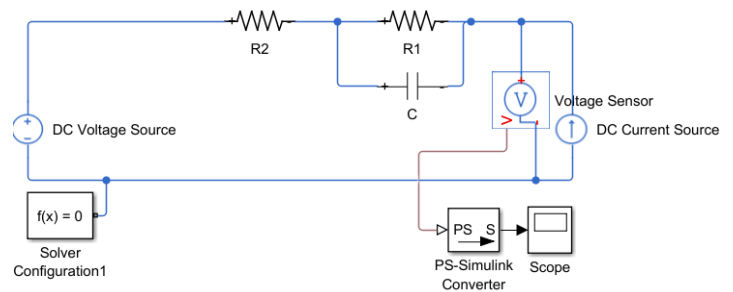


Figure 7: Thevenin Model Equivalent Circuit Simulation

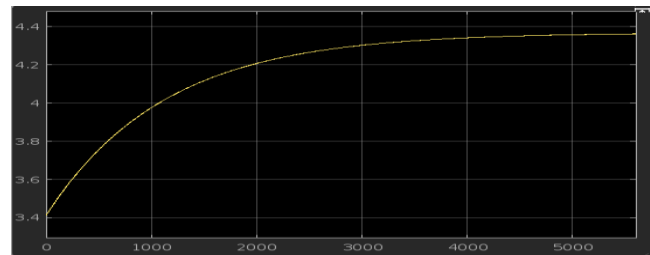


Figure 8: Thevenin Model Charging Curve Simulation

VI. CONCLUSION

With today's technologies, it is possible to say that electric vehicles will become increasingly widespread. However, batteries are of critical importance in this regard. Modeling is very important for the effective use of the battery. In this study, 4 SLPB526495 lithium-ion batteries connected in parallel were used. The battery was charged under constant current and the

battery end voltage was measured. The battery charging curve was created with the data obtained. Battery parameters were found based on the charging curve. The charge curve of the model obtained was extracted using MATLAB/Simulink.

When comparing the two models, there is a margin of error, although there are similarities. However, the fact that the battery used is old and has not been operated for a long time will make this error acceptable. In addition, charging state estimation was also performed by correlating the SoC with the battery charging time. For this purpose, the time-dependent voltage equation was created by fitting the curve with the least squares method, which is one of the numerical analysis methods, using time-dependent voltage values.

This study can be improved by using a new battery and more complex circuit models. In the following processes, it is aimed to improve the study by considering a new lithium battery group and battery health status.

REFERENCES

- [1] Fida Saidani, Franz X. Hutter, Rares-George Scurtu, J.N. Burghartz, Lithium-ion battery models: A comparative study and a model-based powerline communication, *Advances in Radio Science*, vol. 15, no. 83, 2017.
- [2] Murat Ceylan, Türev SARIKURT, Abdulkadir Balıkcı, "Model Development for Lithium-ion Batteries Used in Electric Vehicles", *Energy Efficiency and Quality Symposium*, 2013.
- [3] Muhammed Sefa Çetin, Barış Karakaya, Muhsin Tunay Gençoğlu, Modeling of Lithium-ion Batteries for Electric Vehicles, *Firat University, Eng. Science Journal*, 2021, vol.33, no.2, 755 – 763.
- [4] Efe İsa Tezde, Halil İbrahim Okumuş, Battery Models and State of Charge (SoC) Identification, *Volume*, vol.8 no.1, 21-25, 2018.
- [5] Ravishankar Rao, Sarma VrudhulaSarma Vrudhula,Daler N. Rakhmatov, Battery Modeling for Energy-Aware System Design, *IEEE Xplore*, vol.36, no.12, 77-87,2004.
- [6] Hongwen He, Rui Xiong, Jinxin Fan, Evaluation of Lithium-Ion Battery Equivalent Circuit Models for State of Charge Estimation by an Experimental Approach, *Electric and Hybrid Vehicles, Energies* 2011, vol.4, no.4, 582-59829.
- [7] Samarendra Pratap Singh, Praveen Prakash Singh, Sri Niwas Singh, Prabhakar Tiwari, State of Charge and Health Estimation of Batteries for Electric Vehicles Applications: key issues and challenges, *Global Energy Interconnection*, vol.4, no.2,145-157, 2021.
- [8] Kong-Soon Ng; Chin-Sien Moo; Yi-Ping Chen; Yao-Ching Hsieh, State-of-Charge Estimation for Lead-acid Batteries Based on Dynamic Open-Circuit Voltage, 2008 *IEEE 2nd International Power and Energy Conference*, 2009.
- [9] Wen-Yeou Chang, The State of Charge Estimating Methods for Battery: A Review, *ISRN Applied Mathematics*, 2013
- [10] H. J. Bergveld, *Battery Management Systems: Design by Modelling*, 2001.
- [11] Gökhan SEVİM, Necmi ALTIN, State of Charge (SoC) and State of Health (SoH) Estimation in Lithium Batteries, vol.5, no.1, 33 – 51, 2023.
- [12] Hiroyuki Miyamoto; Masayuki Morimoto; Katsuaki Morita, Online SOC Estimation of Battery for Wireless Tramcar, 2007 7th International Conference on Power Electronics and Drive Systems, 2008.
- [13] Anıl Ege Bostan, Charge State Estimation for Lithium-ion Batteries in Electric Vehicles Master's Thesis, no.88, 2019.

Local Anomaly Detection with Machine Learning in Embedded Systems: High Frequency Data Processing

ABDULKADIR SADAY¹, SULEYMAN CANAN², ENES ERDOGAN³

¹ Selcuk University, Konya/Turkey, asaday@selcuk.edu.tr

² Elfatek Elektronik Ltd Sti, Konya/Turkey, suleyman@elfatek.com.tr

³ Elfatek Elektronik Ltd Sti, Konya/Turkey, eerdogan660@gmail.com

Abstract - Embedded systems today play critical roles in a wide range of applications, from the Internet of Things (IoT) devices to industrial automation. Their use in applications that require real-time and high-frequency data processing directly affects the efficiency of tasks such as anomaly detection, which has an important place in the operation of systems. Considering the limited processing capacity and energy requirements of embedded systems, the need to develop efficient solutions for such data-intensive applications has emerged. In this study, an optimized method for high-frequency data processing and anomaly detection is proposed for data simplification on embedded systems. High-density data collected from various sensors are analyzed by an artificial intelligence model running on the embedded system; only data evaluated as abnormal or important are transmitted to the central system. This approach reduces the central processing load and increases energy efficiency by optimizing the amount of data transmitted over the network. The methods used for anomaly detection include the K-Means Clustering algorithm to determine data groups and the Local Outlier Factor (LOF) algorithm for local anomaly detection. The accuracy, processing speed and data reduction performances of these two algorithms are compared experimentally. The results show that the proposed method effectively reduces the data density, improves the data management of embedded systems and optimizes the system performance by reducing energy consumption.

Keywords – embedded systems, machine learning, anomaly detection, data reduction, real-time analysis, data management.

I. INTRODUCTION

WITH the increasing frequency and variety of data collection in modern embedded systems, data storage, processing and transmission processes have become increasingly complex. Especially in applications such as industrial automation, the Internet of Things (IoT) and smart cities, the high-frequency data stream continuously obtained from many sensors (e.g. weight, temperature, pressure, angle, etc.) creates a serious burden for embedded systems with limited processing power and storage capacity (Citation: Studies on IoT data density and limitations of embedded systems). With the continuous data stream, the data received from each sensor per second turns into high-volume data stacks over time, which makes data management and energy

efficiency difficult. [1, 2].

Considering the limited processing power, memory capacity and energy requirements of embedded systems, efficient solutions need to be developed to overcome continuous data processing and storage problems in such systems [3, 4]. In the literature, the use of techniques such as data compression, sampling and local anomaly detection to reduce data density in embedded systems is widely investigated [5]. It is stated that these methods provide successful results in reducing data storage costs, reducing network traffic and increasing system efficiency [6].

In this study, machine learning algorithms are used for local anomaly detection to manage high-frequency data flow in embedded systems. Managing high-frequency data flow in the most efficient way and transmitting only abnormal or important data to the central server is critical to reducing energy consumption and optimizing processing power in embedded systems [7, 8]. Transmitting only anomalous data to the center with local anomaly detection provides both energy efficiency and more efficient use of system resources by reducing the amount of data sent over the network [9].

In this study, two machine learning algorithms were preferred for anomaly detection in embedded systems: K-Means Clustering and Local Outlier Factor (LOF). K-Means is a simple and fast classification algorithm that allows distinguishing between normal and abnormal data sets by dividing data points into a certain number of clusters. [10]. This algorithm provides advantages in embedded systems due to its low processing load and fast result generation capacity in high-frequency data sets. Local Outlier Factor (LOF) performs anomaly detection by calculating the local density of each data point relative to its neighbors and can determine abnormal data points more precisely by taking into account the local density differences of the data [10, 11].

These two algorithms are compared in terms of accuracy, speed and data reduction performance for anomaly detection in embedded systems. The study provides a significant contribution in terms of optimizing high-frequency data flow and efficient use of system resources in embedded systems with limited processing resources. It is shown that the proposed method increases both energy efficiency and data transmission performance by optimizing data management of

embedded systems.

II. MATERIAL AND METHOD

In this section, data collection, data processing, model training and anomaly detection processes performed on the embedded system are detailed. The system and methods used within the scope of the study are structured in accordance with the high-frequency data processing requirements.

A. Data Collection

The embedded system used in the study collects data from two different types of sensors. The weight sensor provides data in kilograms, while the angle sensor produces angular values in the x and y axes. Data is received from both sensors once a second, producing a total of 86,400 data points per day. The data is temporarily stored in the main memory of the system and is retrieved in bulk or in real time for processing. Summary values of the sensor data are given in Table 1.

Table 1: Load and angle dataset summary

Timestamp	Load (unit)	Angle (x)	Angle (y)
2024-11-08 08:32:11	15	-3	0
2024-11-08 08:32:16	16	-1	0
2024-11-08 08:32:21	16	-2	0
2024-11-08 08:32:26	17	-3	0
2024-11-08 08:32:31	17	-3	0

The collected data is preprocessed in the system memory. This process is structured as data filtering, normalization of timestamps and scaling. In the data filtering stage, corrupt or missing data points are detected and cleaned. In the normalization stage of timestamps, the data is arranged in accordance with the time order. The X-Y time graph for the angle values is given in Figure 1 and the summary of the angle dataset is given in Table 2.

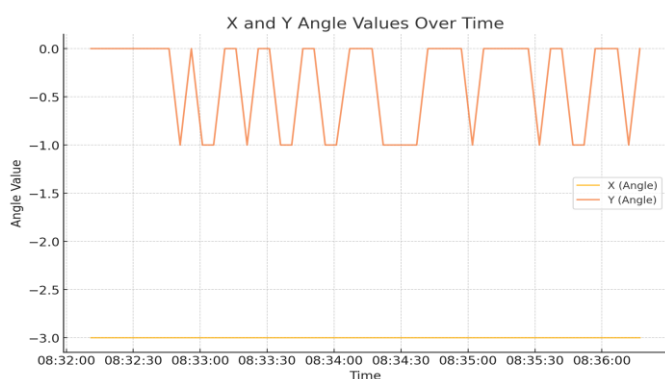


Figure 1: X-Y angle change with time

Table 2: Angle dataset summary

	X	Y
count	50	50
mean	-3.0	-0.34
std	0.0	-0.47851
min	-3.0	-1.0
max	-3.0	0

The unit time graph for load values is given in Figure 2 and the load dataset summary is given in Table 3.

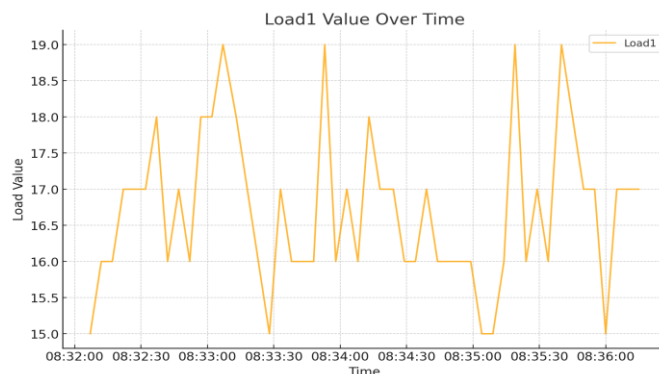


Figure 2: Unit-load change with respect to time

Table 3: Load dataset summary

	load
count	50
mean	16.7
std	1.07380
min	15
max	19.0

In the scaling phase, sensor data is scaled with min-max normalization method to improve the performance of K-means and LOF algorithms.

B. Model Selection for Anomaly Detection

Lightweight machine learning models are used for performance gain in anomaly detection. The selection of models used in this process is made by considering the processing power and memory limitations of the embedded system. The ideal model should provide a balance of low processing load, high speed and accuracy. Two models were examined in this study:

K-Means Clustering: Classifies data points according to a predetermined number of clusters (k) and marks data that show significant deviations from the cluster centers as anomalies.

Parameter Selection: The number of clusters (k) is determined experimentally according to the general distribution of sensor data. It was observed that the best results were obtained in the tests performed with 5 clusters.

Anomaly Detection: Each data point is classified according to its distance from the cluster center. Points that are significantly away from the cluster centers are considered anomalies.

Local Outlier Factor (LOF): Analyzes local density differences in the data to identify data points that have an abnormal density compared to their surrounding neighbors.

Parameter Selection: The minPts parameter of LOF is adjusted according to the number of nearest neighbors of the data to control sensitivity. High accuracy rates were obtained in tests performed with 20 neighbors (minPts=20).

Density Calculation: In the LOF algorithm, a local density

score is calculated for each data point, the density of the surrounding data is calculated, and local deviations are marked as abnormal.

C. Local Anomaly Detection and Data Reduction

Data were processed in real time on the embedded system and only data points classified as abnormal were transmitted to the center. Data classified as normal were deleted from the system memory.

In local anomaly detection, data is processed through the determined model (k-means or LOF) and the data marked as normal are immediately eliminated. Only the data detected as abnormal is transmitted to the center. Thanks to this approach, a 60% reduction in the amount of data transmitted to the center has been achieved. Preventing unnecessary data transmission has significantly reduced the energy consumption of the embedded system. The determined abnormal data is compressed with a time stamp and transmitted to the central server. This process minimizes the data traffic and storage requirements on the network.

D. Performance Criteria and Evaluation

The performances of the selected models were evaluated according to the accuracy, processing speed and data reduction criteria. While accuracy indicates the rate of correct detection of anomalies, processing speed indicates the data processing time of the model, and data reduction indicates the rate of reduction in the amount of data transmitted to the center. While the K-Means model provides an advantage with its low processing load in operations, the LOF model provided higher accuracy, especially in cases requiring precision. The results obtained show that the method proposed by the study is effective in terms of data management and energy efficiency in embedded systems.

III. RESULTS

In this section, the performance of K-Means Clustering and Local Outlier Factor (LOF) algorithms on embedded systems is analyzed. The analysis is done by considering the basic criteria such as accuracy, speed, data reduction and energy efficiency.

A. Data Reduction and Performance Gains

Data Reduction: With local anomaly detection, the data density of the embedded system has been reduced by 60%. This has significantly reduced the data transmission load and storage costs, especially in systems that collect high-frequency data. Local elimination of data classified as normal has ensured that only abnormal data is stored in the center, thus enabling efficient use of system resources.

For example, in a system that generates 86,400 data points per day, if only 40% of the data is transmitted to the center, the annual data volume is reduced from 31.5 million to 12.6 million data points. This reduction provides significant savings in data storage and transmission costs.

Accuracy and Speed Comparison:

K-Means Clustering: It provided 85% accuracy. When

evaluated together with the fast processing time, it is suitable for applications that prioritize accuracy-speed balance. The average processing time was measured as 0.5 seconds. This speed is especially advantageous in systems that require real-time processing. A data sample generated with randomly selected data for the application of the K-Means Clustering method is given in Figure 3.

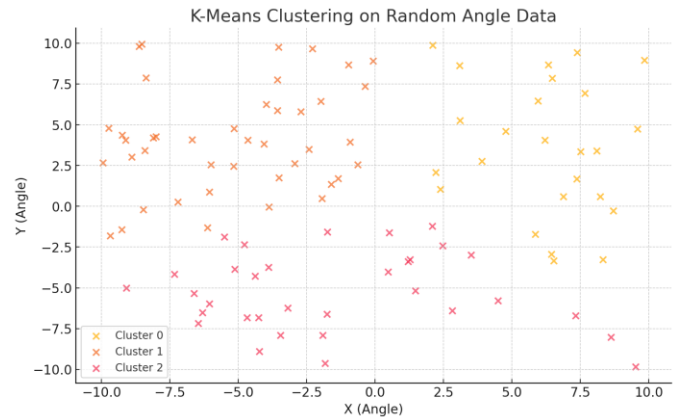


Figure 3: K-Means clustering on random data

Local Outlier Factor (LOF): It provided more precise results with 95% accuracy. This shows that it can be preferred in critical applications that require high accuracy. The average processing time was measured as 0.8 seconds. Although the processing time of LOF is longer, it balances this disadvantage with its high accuracy rate. A data sample created with randomly selected data for the application of the LOF method is given in Figure 4.

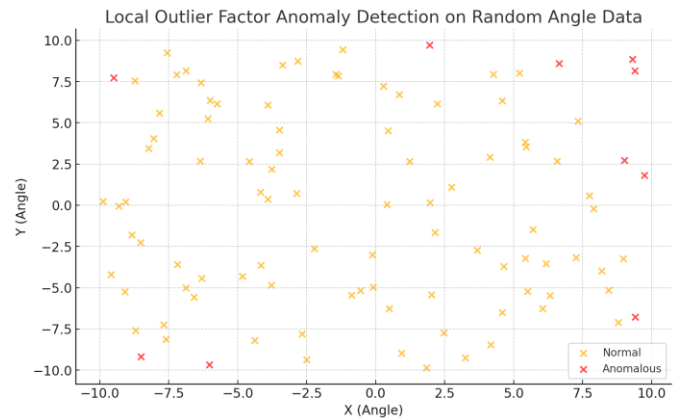


Figure 4: LOF anomaly detection on random data

Table 2: Comparison of algorithms in terms of accuracy and speed

Algorithm	Accuracy %	Processing Time	Data Reduction %
K-Means	85	0.5sn	60
LOF	95	0.8sn	60

Data reduction has been beneficial in reducing storage requirements and network traffic. Transmitting only abnormal data significantly reduces system memory and central server storage requirements. Compressing data and transmitting only

in abnormal situations optimizes network bandwidth usage.

B. Performance and Energy Efficiency

In embedded systems, local processing of data provides a significant advantage in terms of energy efficiency. Local elimination of normal data and transmission of only anomalous situations to the center significantly reduces communication costs. This offers a great advantage, especially for battery-powered embedded systems.

With the K-Means algorithm, energy consumption is minimized thanks to its fast processing time and low processing load. The K-means algorithm stands out in applications that require continuous processing in systems with high data density.

In LOF algorithm, energy consumption is higher compared to K-means due to higher processing time. However, this disadvantage is acceptable in applications requiring precision.

Considering the limited processing power and memory capacities in embedded systems, resource utilization has been optimized by implementing data reduction and local processing strategies. This optimization has not only reduced energy consumption but also increased the system lifetime and stability.

C. Evaluation

The performance results of both models reveal their strengths and weaknesses that are suitable for different usage scenarios. K-Means Clustering is a model that can be preferred in real-time applications of embedded systems due to its low processing power requirement and fast result production. However, its accuracy rate may be limited in critical applications. Local Outlier Factor addresses the need for precise anomaly detection with higher accuracy. The longer processing time does not constitute a disadvantage for scenarios where energy consumption and speed are not critical. These results show that both algorithms are applicable in different scenarios and provide a flexible solution for anomaly detection in embedded systems.

The proposed local processing method stands out as an effective method for reducing data density, increasing energy efficiency and optimizing system resources.

IV. CONCLUSION

In this study, a review was made on high-frequency data processing and local anomaly detection methods in embedded systems. By using machine learning techniques, only important data was transmitted to the center, thus significantly reducing data traffic and storage requirements. This approach optimized the overall performance of the system, while also providing benefits in terms of energy efficiency and resource management. In particular, local anomaly detection provided significant data reduction during data processing and transmission, while also reducing network bandwidth and storage costs. In this way, a more efficient system design with less resource usage was possible.

The K-Means Clustering algorithm stands out with its fast processing time and low processing power requirements. With

these features, it offers a suitable solution for embedded systems with limited resources. However, this algorithm is only effective in detecting significant deviations and may cause smaller deviations to be ignored. On the other hand, the Local Outlier Factor (LOF) algorithm has the ability to detect even small density changes thanks to its density-based structure. In this way, it provides higher accuracy and offers a more sensitive approach to small deviations. However, LOF requires more resources in terms of processing time and energy consumption since it requires a more complex process.

The choice of algorithm should be made depending on the factors such as accuracy, speed and energy efficiency required by the application. If speed and energy efficiency are at the forefront of the system, K-Means can be preferred because it can effectively process data density with lower processing time and resource requirements. However, in applications where accuracy is more important and small deviations are critical, the LOF algorithm will be a more suitable option. This algorithm, although providing high accuracy, can be more efficient in systems where critical data analysis is performed because it requires more processing time and energy consumption.

In future studies, combining these methods with more complex artificial intelligence solutions, using hybrid models and supporting them with more powerful processors can be investigated. In this way, the applicability of more sophisticated anomaly detection and data processing methods in embedded systems can increase. In addition, further optimization of data collection and processing processes can increase the performance and efficiency of embedded systems. Such developments can make significant contributions, especially in data-intensive systems such as IoT and industrial automation.

REFERENCES

- [1] W. Roth *et al.*, "Resource-efficient neural networks for embedded systems," *arXiv preprint arXiv:2001.03048*, 2020.
- [2] S. D. Hamshaw, M. M. Dewoolkar, A. W. Schroth, B. C. Wemple, and D. M. Rizzo, "A new machine-learning approach for classifying hysteresis in suspended-sediment discharge relationships using high-frequency monitoring data," *Water Resources Research*, vol. 54, no. 6, pp. 4040-4058, 2018.
- [3] H. Wu, C. Chen, and K. Weng, "Two Designs of Automatic Embedded System Energy Consumption Measuring Platforms Using GPIO," *Applied Sciences*, vol. 10, no. 14, p. 4866, 2020.
- [4] S. Kalya, M. Kulkarni, and K. Shivaprakasha, *Advances in communication, signal processing, VLSI, and embedded systems: Select proceedings of VSPICE 2019*. Springer Nature, 2019.
- [5] G. Nicolescu and P. J. Mosterman, *Model-based design for embedded systems*. Crc Press, 2018.
- [6] S. Lu and R. Lysecky, "Data-driven anomaly detection with timing features for embedded systems," *ACM Transactions on Design Automation of Electronic Systems (TODAES)*, vol. 24, no. 3, pp. 1-27, 2019.
- [7] L. Erhan *et al.*, "Smart anomaly detection in sensor systems: A multi-perspective review," *Information Fusion*, vol. 67, pp. 64-79, 2021.
- [8] A. Chatterjee and B. S. Ahmed, "IoT anomaly detection methods and applications: A survey," *Internet of Things*, vol. 19, p. 100568, 2022.
- [9] Y. Liu *et al.*, "Deep anomaly detection for time-series data in industrial IoT: A communication-efficient on-device federated learning approach," *IEEE Internet of Things Journal*, vol. 8, no. 8, pp. 6348-6358, 2020.

- [10]A. B. Nassif, M. A. Talib, Q. Nasir, and F. M. Dakalbab, "Machine learning for anomaly detection: A systematic review," *Ieee Access*, vol. 9, pp. 78658-78700, 2021.
- [11]J. Li, H. Izakian, W. Pedrycz, and I. Jamal, "Clustering-based anomaly detection in multivariate time series data," *Applied Soft Computing*, vol. 100, p. 106919, 2021.

Digital Twin Implementation Opportunities for Civil Engineering Applications

MERVE KAYA¹, ÖNDER HALİS BETTEMİR¹, MEHMET FATİH ACAR¹

¹ İnönü University, Malatya/Turkey, kya.mrw@gmail.com

¹ İnönü University, Malatya/Turkey, onder.bettemir@inonu.edu.tr

¹ İnönü University, Malatya/Turkey, mehmetfatihacr@gmail.com

Abstract – Digital Twin offers important opportunities to the construction sector. Decreasing the operating and maintenance costs of the facilities and prolonging the useful and economic life of the assets can be given as the most important two benefits. However, construction sector is reluctant to revolutionary changes within its working habits. Therefore, Digital Twin developments and implementations are condensed. In this study, a scoping literature review is conducted on digital twin in order to address the literature gap and to raise awareness on the construction sector. The concept of digital twin is presented and important contributions are briefly mentioned. Barriers on the digital twin including the cost of implementation, technical knowledge, and complexity are discussed. Then a framework for the construction of digital twin of buildings that are exposed to earthquake tremor is proposed. The proposed framework can provide important savings in heating costs and maintenance costs.

Keywords – Digital twin, IT in construction, Internet of Things, cyber-physical systems.

I. INTRODUCTION

CONSTRUCTION sector being one of the cornerstones of modern economies is of great importance for economic development. It contributes to economic growth by providing infrastructure for other industries and creating jobs, and is also characterized by its social and environmental impacts. However, traditional construction methods pose serious limitations on the productivity and quality. Employees of the construction sector can only devote 30% of their time to their main tasks, while the remaining 70% is spent on ancillary tasks such as material handling, arranging and organizing the construction site [1]. Worldwide, the construction industry loses around 1.6 trillion dollars annually due to low productivity [2]. Errors in cost calculations and lack of continuous monitoring, difficulties on the tracking of physical documents, and complex management of materials, equipment and labor force limit the efficiency of the industry, making the change imperative. In addition, the sector is project-based by nature and each project is planned and managed in line with its specific needs, conditions and objectives. As a result of this specialized structure, already complex planning, quantity take-off calculations and material procurement processes have to be created from scratch for each new project. These repetitive

and complex processes can reduce the effectiveness of project management by making time and resource management difficult. Especially in projects with intense competition and tight schedules, such challenges can make compromises in quality standards inevitable. Therefore, in construction projects, effective project management, detailed planning and efficient supply chain management are vital for the success of projects and the maintenance of quality standards. In this context, adopting a flexible yet systematic approach, taking into account the unique requirements of each project, is essential for sustainable success in the construction industry.

Digitalization involves changing socio-technical structures using digital technology and affects social and technical aspects of structures. Digital transformation, digitalization and digital innovation are interconnected and enable organizations or industries to make major changes in the way they do business [3]. With the recent developments in sensor, software and robotics technologies, data from the production process is combined with operational data from systems such as supply chain, customer service, enterprise resource planning, etc. to create high-value data for companies. These data provides benefits such as minimizing personnel errors, achieving high-speed and safe production, production tracking, and instant error detection. Considering all these, the construction industry needs to adapt to these technological changes in order to achieve efficiency in project management processes. The adaptation of Industry 4.0 and digital transformation to the construction sector aims to ensure the optimum use of cost, time and quality elements, which are defined as the triangle of success in construction projects, together with time and cost savings, quality and service standards. Digitalization in the sector will also provide benefits such as reduced reaction times in response to instant problems, improved cooperation and communication, high security, and the development of a sustainability approach [4]. Industry 4.0 is a term accepted as the fourth of the industrial revolutions and refers to digital transformation in production processes. Industry 4.0 represents the combination of the physical and digital worlds in production systems and aims to make production processes more intelligent, efficient and flexible. This new industrial era has components such as cyber-physical systems (CPS), the Internet of Things (IoT) and smart technologies, and aims for a more efficient, economical and safe output in construction processes. With the contribution of Industry 4.0, the concept

of Digital Twin (DT), which is seen as another development branch, has emerged [5]. A digital twin is a virtual model that is a digital copy of a physical building, updated with real-time data and capable of simulating building performance. Technologies such as digital twin, augmented reality, unmanned aerial vehicles and 3D printing enable more accurate and informed decisions to be made throughout the project life cycle. These technologies also contribute to solving current challenges in the industry by increasing collaboration, optimizing resource utilization and improving quality. Digital twin technology also offers significant advantages in the management of breakdown, maintenance and repair processes that may occur throughout the building lifecycle. By analyzing data from buildings equipped with sensors and other data collection tools, this technology has the capacity to detect potential failures in advance and predict maintenance needs. Thus, unexpected failures can be prevented and maintenance processes can be managed proactively. As a result, it becomes possible to both reduce the costs that may be incurred during building operations and to optimize performance throughout the service life of the building. Predictability and data-driven maintenance planning provided by the digital twin increases the efficiency of building management and keeps user satisfaction and safety at the highest level.

Digital transformation promises significant developments in the construction industry in four main areas: digital data, digital access, automation and connectivity. The mentioned phases encompass data collection and processing; self-organizing technologies; mobile communication capabilities and the integration of tasks, respectively. These four components positively affect time and cost savings, quality improvement and sustainability in construction projects. Another concept that has come to the forefront with digitalization. The use of IoT has added value to the construction industry as well as many other sectors. The Internet of Things (IoT) is a technology and computing paradigm that enables physical objects and devices to connect to each other over the internet to exchange data and perform autonomous interactions. IoT establishes an interactive and data-driven connection between the physical and digital worlds through the integration of technologies such as sensors, embedded systems and network connections. It enables real-time data collection and sharing in the areas where it is used. In the construction industry, IoT can be used in various applications such as smart healthcare facilities, transportation systems, energy efficiency, waste management and smart buildings. In the construction industry, IoT can save 22%-29% of the total costs of the Internet of Things, resulting in an annual cost improvement of 75-96 billion dollars in the construction context [2]. IoT offers advantages such as fast reporting, reduced communication costs, reduction of human errors and process control. In addition, the data collected enables better accountability, transparency and monitoring. The application of IoT can create new economic opportunities and provide big data-driven insights that can be used to solve problems in the construction industry, such as compensation

claims, disputes and low productivity. IoT can also be used in areas such as facility management and demolition waste management in the built environment [2]. All home appliances such as doors, windows, air conditioners, heating/cooling systems that can be controlled by remote controls have become IoT devices [6]. The smart building concept is based on the Internet of Things (IoT) technology and provides information to the user by communicating wirelessly with various electronic devices. This technology, which works together with the building management and information system (BMIS), is called Building Internet of Things (BIOt) and enables buildings to be smart, energy efficient, green and sustainable. IoT devices are used in various applications in smart buildings such as heating, cooling, load control, air quality, ventilation, lighting and water management [7].

II. THE CONCEPT OF DIGITAL TWIN

In the context of the digital twin, the earliest mention of the 'twin' concept is in aerospace. Its general philosophy dates back to NASA's Apollo project in the 1960s when the 'twin' was a physical system. The digital side was not included in the title of 'twin' during this period. The term digital twin was first coined by Grievens in 2003 during a lecture on product lifecycle management (PLM) [8]. The concept of DT has subsequently been developed from different perspectives by various authors. A Digital Twin is a virtual copy of a physical object, device or system created using real-time data. This concept is used to collect and analyze data that occurs throughout the life cycle of an object. Creating a Digital Twin requires three main components: a real object in the physical world, a digital representation of that object in the virtual world, and a data link between the physical object and the digital representation. The interaction between the physical entity and the virtual model is supported by highly efficient communication platforms that use real-time updates. This communication channel is a viable platform that works on a combination of Internet of Things (IoT), sensors, cloud computing and big data analytics [9]. A Digital Twin can represent parts of an object, a system or a whole facility. This virtual model contains data on the structure of the physical object and provides users with the ability to visually represent, analyze and simulate it. Furthermore, the Digital Twin has features such as measurement and reporting and can enable continuous learning and improvement by monitoring the performance of the real object [10]. The data obtained from the real object includes electrical, mechanical and environmental data that can affect the operation of the system. In addition, this data includes time-varying parameters such as temperature, vibration, pressure, torsion, etc., as well as video and photography, which are editable images. Data sources can be sensors, transducers, cameras, drones, etc. [5]. The purpose of creating and using a Digital Twin is to respond to needs such as monitoring and controlling the real object throughout its life, ensuring that it works correctly, tracking its work, and testing a possible change in a virtual environment before applying it to the object. Digital Twin offers a dynamic

interaction between the user and the object by providing easy access to the information of the structure at every stage in construction projects. It can monitor the changes of a constructed structure on a daily or hourly basis, detect inconsistencies early, and perform detailed analysis by storing historical data with dates. It also provides the opportunity to compare costs and propose alternative solutions by creating simulations in a digital environment for any design change, maintenance or repair plan. Digital Twin can monitor the structure in terms of material life and strength to create forward-looking scenarios against environmental factors and optimize the construction process with different courses of action and probability calculations.

Building Information Modeling (BIM) provides an important support for the data model underlying the Digital Twin. The more accurate the BIM model is about the structure, the better the quality of the Digital Twin [10]. BIM is a digital representation of the physical and functional characteristics of a building, which is used for decision making throughout the lifecycle of the building. Digital Twin is directly related to the object in the physical world, while BIM can exist as a virtual model. Regular monitoring and updating of a dense set of information over a long period of time is difficult for a static BIM model [10]. The following items should be considered when creating a digital twin;

- Digital twins should be an exact and complete representation of the real-world entity.
- It should be able to be used to gain valuable insights and to fully understand physical existence.
- Various datasets should be available to the twin to feed the process.
- It should be enhanced with tools such as Augmented Reality (AR) and Virtual Reality (VR) to deepen understanding in its ecosystem.

Digital twins are created by using conceptual models (ICM, CAD or GIS) to analyze and visualize enterprise and Internet of Things (IoT) data, or by scanning physical entities to extract the most up-to-date representation of the target object [11]. The collection of data used in the creation of digital twin models is realized through advanced data collection techniques and multi-source information integration. The first step is to collect accurate and complete structural and operational data of the buildings. For this purpose, three-dimensional models of buildings and infrastructure are obtained using advanced measurement technologies such as laser scanners and photogrammetry [12]. Furthermore, data from IoT sensors and smart devices are integrated to provide dynamic information such as temperature, humidity, energy consumption, movement and other environmental factors in and around the building [13]. These data constitutes the key data sources for creating the static and dynamic components of the digital twin. In addition, existing BIM data and past project records provide important reference points during the creation of the model [14]. This allows digital twins to include not only their current state, but also the changes and performance history of the building throughout its life cycle.

Keeping the collected data in cloud-based storage and processing systems allows the model to be updated in real time and more accurate simulations to be performed [15]. Thus, digital twin models can both be created with high accuracy and contribute to sustainable building management by adapting to dynamic conditions.

Despite the benefits and opportunities provided by the digital twin, the construction sector lags behind other sectors in using technology and adapting to digital transformation, following the hunting and agriculture sectors [4]. One of the main reasons for this delay is the lack of awareness and bias towards the opportunities that digital transformation will bring. In this context, it is of great importance to examine, elaborate and clarify the digital transformation adaptation processes of the construction industry and the impacts of these processes.

A. Characteristics of a Digital Twin

Madni et al. (2019) [16] stated that a Digital Twin (DT) should be capable of digitally representing a specific instance of a physical structure, its performance, maintenance and repair history, health status and other attributes. It should create preventive maintenance strategies by analyzing historical data and predict future performance and maintenance requirements through the virtual model. The DT should enable the optimization of operational processes by enabling the monitoring of physical assets throughout their lifecycle through digital links and combining IoT data with physical asset data. It should also be able to reflect the age of the system and predict its future performance by simulating the operational and maintenance data of the physical system while enabling remote troubleshooting and maintenance operations.

B. How to Create a Digital Twin

The implementation process consists of six stages. First, in the opportunity identification phase, potential opportunities are identified and scenarios are evaluated. The second stage is to select the appropriate process that will deliver the highest value and chance of success. Then, in the piloting phase, a pilot program is run in iterative and agile cycles to manage risks and increase return on investment. The process is standardized using the tools and techniques necessary to develop the pilot. Next, the data from the pilot is shared with the larger business and stakeholders to ensure that the DT scenario meets the needs of the business. Finally, the values of the results obtained are accurately measured to check whether they are at an optimal level [8].

The Digital Twin (DT) system architecture is based on engineering data such as CAD, product specifications, geometry models, material properties, validation results, IoT sensor readings and relevant simulation information. Cyber-physical systems provide a seamless integration between virtual and physical models, while sensors connect with the physical system to collect data from the virtual model to identify the behavior of physical objects and provide solutions. The information from these sensors is updated in the cloud via

IoT, synchronizing the most up-to-date data of the physical system with the virtual system. DT takes advantage of IoT to enable high-level information flow from raw data. Data mining and processing are the interaction and convergence features of DT, which requires synchronization of historical and real-time data to enable data flow between both domains [8].

C. Digital Twin Application Areas

DT applications have entered various industrial sectors and made significant contributions to industrial processes. Some examples of applications from these fields are listed below.

Digital Twin (DT) applications are being observed at the Structural Sciences Center at the US Air Force Research Laboratory. The center focuses on developing a high-safety flight model by combining virtual and physical data to generate an accurate fatigue life prediction. Significant progress in predicting the location, size and direction of damage in aircraft structural health management is obtained by proposing a DT-based damage characterization method. In another study, they used Airframe Digital Twin (ADT) to help identify damages in real time. In other studies, they have successfully applied DT to monitor damage to airplanes. Today, DT is also used in aerospace and astronautics to predict failures during product service and maintenance [8].

In the automotive sector, Tesla adopts the Digital Twin (DT) approach for its vehicles with advanced automation systems and utilizes technologies such as the Internet of Things (IoT), Artificial Intelligence (AI) and Machine Learning (ML). DT plays an important role in the long-term success of autonomous vehicles. Digital models of vehicles are simulated using real driving data; these simulations include vehicle data such as aerodynamic, engine and material data. Tesla has developed mobile apps that track the status and location of vehicles. It also releases updates by collecting data from vehicles to add safety improvements and new features. The studies aim to monitor the privacy-related behavior of smart cars with a DT-based system.

Sivalingam et al. (2018) [17] identified difficulties for technicians to access turbines and inability to perform maintenance due to unfavorable weather conditions among the factors causing cost increases in offshore power generation. These issues have made the condition-based maintenance (CBM) approach a preferred option over time-based preventive maintenance. CBM helps diagnose the health status of equipment by predicting abnormalities in the system and is integrated with DT for real-time monitoring. In Europe, a CBM DT approach has been adopted to obtain information on the status of turbines, utilizing the SCADA platform in the process. General Electric (GE) is developing Predix software, which includes virtual versions of wind, gas and steam turbines and is called a "digital twin farm". This platform monitors temperature data and helps predict the performance of physical turbines by adding sensors to turbines created in the cloud.

Laaki et al. (2019) [18] developed a DT prototype for real-time remote control using mobile networks and created a

remote surgery application which aims to improve the efficiency of the healthcare supply chain with Robotic Process Automation (RPA). Another study identified the need to increase operational efficiency to treat more patients without increasing cost and complexity. To meet these needs, DT was implemented using a Cross Technology Communication (CTC) platform that improves communication between industrial IoT and smart connected devices. CTC facilitates the exchange of information between heterogeneous devices, quickly meeting the requirements of industrial IoT [8].

Digitalization of the manufacturing industry enables real-time automated collection of manufacturing data via IoT which needs DT to improve supply chain efficiency and optimize production processes. DT is integrated with inspection databases to provide geometry assurance and includes kinematic relationships and material properties on the assembly line. In the production phase, DT develops optimized designs that meet the needs of designers and validates the functionality of products in a virtual environment. The validated product designs are managed and optimized in virtual workshops. Furthermore, DT provides proactive maintenance by monitoring the health status of products in real time, and identifies and reports failures [8]. This increases the production efficiency and reduces the downtime.

III. DT APPLICATIONS IN CONSTRUCTION INDUSTRY

Keen [19] noted that in the context of design and the built environment, DT include a variety of elements such as BIM, 3D and 2D models, schedules, contracts, construction documents including submittals, change orders, RFIs as well as operational data collected by embedded sensors and data from artificial intelligence and machine learning. Synchronizing this data allows smart building operators to manage systems, detect faults and make decisions. DT technology provides a dynamic model that is better created in the initial phase before the actual product is built [20]. This model is updated based on data from the physical model, making it easier to control and monitor the product. Geometric digital modeling, the first step in DT creation, requires a digital model linked to the physical asset. In new projects, BIM provides a critical resource for DT, especially in terms of geometric data. Laser scanning or photogrammetry plays an important role in geometric DT development by facilitating the automated data collection process for existing structures for which digital models are not available. Once the digital model is created, sensors are added to collect relevant data simulated on the IoT cloud platform to get real-time information about the state of the bridge between it and the physical model. The physical data is simulated and analyzed on this platform with the help of AI and machine learning, and continuous updates are provided with bidirectional data flow [21].

An example of the application of DT in the built environment is the Frasers Tower project in Singapore, which provides a connected workplace for DT purposes. In this

project, Bentley Systems and Schneider Electric collected data using 179 Bluetooth beacons and 900 sensors for monitoring lighting, air quality and temperature [8]. Environmental conditions, physical assets and building management systems data were collected through sensors and combined into a digital platform in a construction site project at the University of Cambridge's West Campus [12]. The collected data was used to monitor the performance of the building, optimize energy consumption and predict maintenance needs. In this way, efficient monitoring and management is achieved both during the construction phase of the building and throughout its lifetime. Singapore is creating digital twins of infrastructure systems across the city and using this data for real-time monitoring and analysis [22]. DT optimizes city life in areas such as traffic management, water treatment systems and energy consumption. This application makes it possible to make more efficient decisions in urban planning, detect problems at an early stage and achieve sustainability goals.

While the adoption of DT in the construction sector is relatively low, the increase in the construction of smart buildings provides a good foundation for DT adoption. These buildings are equipped with automated sensors, actuators and other technologies that act as a bridge to monitor and control physical assets. This provides a basis for DT implementation.

A. Benefits of DT Implementation

Although digital twins (DT) are still in their infancy in the construction industry, they have great potential and provide significant benefits in their various applications. One of the key advantages of DT is the ability to monitor and analyze the performance and operations of a facility. DT can improve automated data collection and analysis processes in the building and construction industry. This technology simulates and improves processes in areas such as visualization of plans, prefabricated production and material logistics. It also provides real-time status updates, monitoring and evaluation of buildings and structures during the operation and maintenance phases of construction projects and facilities. Data analytics and decision support systems enable advanced applications such as energy savings, predictive maintenance and optimization of maintenance schedules. Resource planning and logistics can support the construction process by providing various contributions such as safety monitoring, quality assessment, optimization of equipment usage, monitoring and tracking of workers. [21]. Although DT requires a high initial investment, it has the potential to deliver operational efficiency and return on investment in the long term. For example, applications of DT in the construction industry were reported to have led to improvements in areas such as quality, operational costs, new product introduction times, and revenue growth. Moreover, thanks to virtual simulations with DT, the future state of buildings can be predicted and analyzed through various scenarios [23]. The potential of this technology in the construction industry is becoming more evident with the increasing construction of smart buildings and solutions powered by big data. DT is a

powerful tool with the potential to improve operational efficiency, sustainable development and decision-making in the construction industry. These contributions increase operational and cost efficiency throughout the entire lifecycle of construction projects.

B. Barriers to DT Implementation

The complexities involved in developing a Digital Twin model and the volatile nature of the construction industry make the adoption of DT in the construction industry a challenging task [21]. The information management system required to build the model and manage the data involves complex and multifaceted processes. DT requires the collection and utilization of large amounts of data from a large number of points, each representing specific domains. One of the main challenges in DT applications in the construction industry is the integration of data from multiple technology sources in different formats. The heterogeneity of data sources and the need for synchronization complicate the process of ensuring continuous feedback loops. A continuous flow of data is needed for DT models to perform real-time monitoring, but this process is costly and time-consuming to manage effectively. There is also the risk of data quality degradation during data extraction or transformation. While the connections between IoT and DT are increasing, challenges remain in linking IoT data with digital models. BIM formats and semantic web data of IoT devices need to be standardized and integrated. Security is also a major concern; failure to protect data can lead to trust issues. There are also concerns about the installation and maintenance of sensors on construction sites and the risk of damage and theft. According to the Identity Management Institute, specific security protocols such as data encryption, clear definition of user roles, least privilege access, device vulnerability remediation and regular security audits are seen as key challenges in implementing DT. On the other hand, employees' lack of interest in the issue for fear of losing their jobs is another challenge. Lack of sufficient competent personnel and lack of integration for all stakeholders are major obstacles affecting the digital transformation of the construction industry [4]. The challenges of the data collection environment and complex equipment in the construction industry make it difficult to create a virtual model accurately and efficiently, and the high initial costs of digital twin applications are seen as other constraints to the adoption of DT in the construction industry. The successful development of DT requires the use of state-of-the-art technologies that require large funds, experts with the right skills and advanced computational power. Moreover, construction of a robust model which can infer results require construction of semantic relationships within building elements which cannot be done successfully by the state-of-the-art BIM software [24].

IV. POTENTIAL APPLICATION

Significant changes in energy and water consumption of buildings can occur after earthquakes or other natural disasters. Such disasters can affect the physical structure and

infrastructure of buildings, leading to failures and interruptions in energy and water distribution systems and changes in consumption patterns. While energy and water consumption may suddenly drop in damaged buildings, it may increase in undamaged buildings or those providing temporary shelter. In addition, post-disaster population movements can cause imbalances in energy and water systems by changing the intensity of demand in certain areas. For example, population shifts in a disaster-affected area to neighboring areas can place unexpected burdens on the infrastructure in those areas and lead to a sudden increase in consumption levels. Monitoring and managing such changes is crucial for rapid infrastructure recovery and sustainable resource management post-crisis. A digital twin model, the flowchart of which is shown in Figure 1, can be very effective in this regard.

First, technologies such as laser scanning, photogrammetry and unmanned aerial vehicles (UAVs) can be used to create 3D models of buildings, which can be used to visually support energy consumption analyses. Once the model is created, the twin is continuously fed by collecting real-time data from smart meters and sensors integrated into buildings.

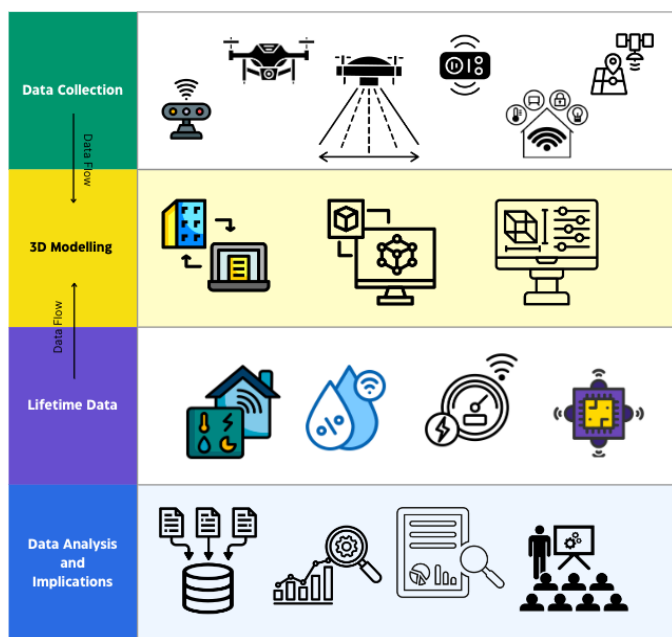


Figure 1: Flowchart of digital twin implementation.

With these collected data, time series analyses will be conducted and changes and sudden deviations in consumption trends can be analyzed in detail. Sub-regional analyses, especially as mentioned above, are also important in terms of revealing the effects of post-disaster population movements on energy and water consumption. Such analyses will enable important inferences to be made in terms of optimizing resource management and detecting infrastructural failures in advance. As a result, digital twin technology can serve as a powerful tool for the sustainable management of critical infrastructure after a disaster, for responders to manage resources efficiently, and for securing energy supply,

maintaining the balance of energy and water consumption, and meeting social needs more efficiently.

ACKNOWLEDGMENT

This study is supported by the Scientific Research Projects Coordination of İnönü University by the Grant Number FYL-2024-3668.

REFERENCES

- [1] Alaloul, W. S., Liew, M. S., Zawawi, N. A. W. A., Mohammed, B. S. (2018), Industry Revolution IR 4.0: Future Opportunities and Challenges in Construction Industry, MATEC Web of Conferences 203, 02010.
- [2] Ghosh, A., Edwards, D. J., & Hosseini, M. R. (2021). Patterns and trends in Internet of Things (IoT) research: future applications in the construction industry. *Engineering, Construction and Architectural Management*, 28(2), 457-481.
- [3] Osmundsen, K., Iden, J., & Bygstad, B. (2018). Digital transformation: Drivers, success factors, and implications, MCIS 2018 Proceedings. 37.
- [4] Aladağ, H. (2022). Türk İnşaat Sektöründe Dijital Dönüşüm Uygulamaları Üzerine Bir Araştırma, *Mühendislik Bilimleri ve Tasarım Dergisi*, 10(3), 973- 986.
- [5] Gökkuş, G. (2021). Digital Twin Concept for Renewable Energy Sources, *Konya Mühendislik Bilimleri Dergisi*, 9(3), 836-844.
- [6] Uygunoğlu T., Topçu İ. B. "The Role of Internet of Things (IoT) In Civil Engineering: RFID Applications" *Int. J. Of 3D Printing Tech. Dig. Ind.*, 4(3): 270-277, (2020).
- [7] Verma, A., Prakash, S., Srivastava, V., Kumar, A., & Mukhopadhyay, S. C. (2019). Sensing, controlling, and IoT infrastructure in smart building: A review. *IEEE Sensors Journal*, 19(20), 9036-9046.
- [8] Madubuike, O. C., Anumba, C. J., & Khallaf, R. (2022). A review of digital twin applications in construction. *Journal of Information Technology in Construction*, 27.
- [9] Liu, Z., Meyendorf, N., & Mrad, N. (2018, April). The role of data fusion in predictive maintenance using digital twin. In AIP conference proceedings (Vol. 1949, No. 1). AIP Publishing.
- [10] Ceylan, E. Z. (2019). Dijital ikizler ve inşaat sektöründeki yeri. *Yapı Bilgi Modelleme*, 1(2), 53-61.
- [11] Yiğit, A. Y., & Uysal, M. (2023). Dijital ikizlerin geliştirilmesinde fotogrametrinin kullanımı ve artırılmış gerçeklik ile görselleştirilmesi. *Niğde Ömer Halisdemir Üniversitesi Mühendislik Bilimleri Dergisi*, 12(4), 1372-1384.
- [12] Lu, Q., Parlikad, A. K., Woodall, P., Don Ranasinghe, G., Xie, X., Liang, Z., ... & Schooling, J. (2020). Developing a digital twin at building and city levels: Case study of West Cambridge campus. *Journal of Management in Engineering*, 36(3), 05020004.
- [13] Tao, F., Zhang, H., Liu, A., & Nee, A. Y. (2018). Digital twin in industry: State-of-the-art. *IEEE Transactions on industrial informatics*, 15(4), 2405-2415.
- [14] Succar, B. (2009). Building information modelling framework: A research and delivery foundation for industry stakeholders. *Automation in Construction*, 18(3), 357-375.
- [15] Qi, Q., & Tao, F. (2019). Digital twin and big data towards smart manufacturing and industry 4.0: 360-degree comparison. *IEEE Access*, 6, 3585-3593.
- [16] Madni, A. M., Madni, C. C., & Lucero, S. D. (2019). Leveraging digital twin technology in model-based systems engineering. *Systems*, 7(1), 7.
- [17] Sivalingam, K., Spring, M., Sepulveda, M. and Davies, P. (2018). A Review and methodology development for remaining useful life prediction of offshore fixed and floating wind turbine power converter with digital twin technology perspective. *2nd International Conference on Green Energy and Application*, pp. 197- 204.
- [18] Laaki, H., Miche, Y. and Tammi, K. (2019). Prototyping a digital twin for real-time remote control over mobile networks: Application of remote surgery. *IEEE*, 7, 20325-20336. Digital Object Identifier 10.1109/ACCESS.2019.2897018
- [19] Keen, M. (2019). Construction technology defined. What is Digital Twin? Autodesk Construction Cloud.

- [20] Grieves M., Vickers J. (2017). Digital Twin: Mitigating Unpredictable, Undesirable Emergent Behavior in Complex Systems. In: Kahlen F. J., Flumerfelt S., Alves A. (eds) Transdisciplinary Perspectives on Complex Systems. Springer, Cham.
- [21] Brilakis, I., Pan, Y., Borrman, A., Mayer, H. G., Rhein, F., Von, C., Pettinato, E., and Wagner, S. (2019). Built environment digital twinning. Report of the International Workshop on Built Environment Digital Twinning presented by TUM Institute for Advanced Study and Siemens AG.
- [22] Saback, V., Popescu, C., Blanksvärd, T., & Täljsten, B. (2024). Analysis of Digital Twins in the Construction Industry: Practical Applications, Purpose, and Parallel with other Industries. *Buildings*, 14(5), 1361.
- [23] Deloitte (2017). Industry 4.0 and the digital twin – Manufacturing meets its match. A Deloitte series on Industry 4.0, Deloitte University Press.
- [24] Ergen F., Bettemir Ö. H. (2024). Development of ontological algorithms for exact QTO of reinforced concrete construction items. In *Structures*, 60, 105907. <https://doi.org/10.1016/j.istruc.2024.105907>.

Development of a Battery Management System with IoT-Enabled Data Tracking for Autonomous Load Robot

İBRAHİM ETHEM DERE^{1,3}, DAVUT ERTEKİN¹, TALHA TELLİ^{2,3}, SÜLEYMAN CANAN³

¹Bursa Technical University, Bursa/Türkiye, ethemdere34@gmail.com, davut.ertekin@btu.edu.tr

²Selcuk University, Konya/ Türkiye, talhatelli427@gmail.com

³Elfatek Electronic, Konya/ Türkiye, suleyman.canan@elfatek.com.tr

Abstract - Battery Management System (BMS) with Internet of Things (IoT) monitoring capability for an autonomous payload robot. The popularity of autonomous vehicles in industrial and commercial areas increases the importance of battery systems. Balancing of cells is one of the critical parameters that must be monitored in such systems and, being able to access battery data at any time is important to increase the security level. This developed Battery Management System (BMS) aims to provide the user with access to battery system data at any time. In the design of this Battery Management System, the BQ76952 integrated circuit from Texas Instruments was used to measure voltage, current, and temperature accurately and quickly. After the necessary balancing calculations, an STM32G431 microcontroller was used to keep the battery cells balanced and to run security protocols. This microcontroller is also responsible for transmitting data to the ESP32 controller, which enables the data to work with the Internet of Things (IoT) technology. In other words, an ESP32 module was used to communicate with Firebase, which allows cloud-based data transmission. In this way, users will be able to view the necessary data of the batteries remotely, both from mobile devices such as phones and from their computers. The advantage here is that the entire decision structure allows monitoring of the data, when necessary, without being connected to the controller. In addition to using Visual Studio in the desktop interface for easy user follow-up, MIT App Inventor was used in the development of the mobile application. These interface programs aim to provide user-friendly formats for reading battery data using graphical indicators such as progress bars and line charts to monitor the State of Charge (SoC), cell voltages, temperature values, and more.

Keywords - Battery Management System (BMS), Internet of Things (IoT), Real-Time Monitoring, Smart Battery Systems

I. INTRODUCTION

IN recent years, the rapid development of autonomous vehicle technologies has led to the widespread use of these systems in industrial and commercial applications. The fact that autonomous vehicles are generally produced as electric vehicles means that these smart devices are largely dependent on the performance of the battery systems used [1-3].

As a result, battery management systems (BMS) have become a critical component for ensuring the efficient and safe operation of autonomous vehicles. In particular, the widespread use of lithium-ion batteries requires accurate monitoring of

charge-discharge cycles and the accuracy and traceability of balancing between cells. Battery management systems increase the safety and life of batteries by monitoring critical parameters such as voltage, temperature, and current of the cells [1, 4].

The widespread use of products such as autonomous vehicles, the development of battery management systems, which are directly affected, is also increasing. In addition to the efficient use of batteries and the minimization of energy losses, these systems also control many safety measures. These systems include warning mechanisms to detect dangerous situations such as excessive temperature and excessive voltage in advance and to take the necessary protective measures. In this way, the safety of autonomous vehicles is increased, while the battery life is extended, and costs are reduced [1].

This study aims to develop an innovative Battery Management System for autonomous load-carrying robots. The main goal of the study is to increase security and improve performance by providing instant data to the user with IoT technology on the necessary and important information about batteries. In this way, the aim is to increase the user's trust in this autonomous vehicle. In the designed system, Texas Instruments' BQ76952 integrated circuit is used to perform voltage, current, and temperature measurements of the battery accurately and quickly, thus preventing a direct controller from getting tired with battery reading operations and aiming to perform the main operations. The STM32G431 microcontroller, a product of STM, manages cell balancing operations and executes security protocols. This controller and the battery management system integrated circuit work in harmony with each other and provide communication between ESP32, which is used as an additional controller for IoT operations. The data read by the controller from the battery management system integrated circuit is transferred to the cloud via the ESP32 module and users can remotely monitor the battery data via mobile devices or computers [5-7].

IoT technology integration enables cloud-based tracking of battery data and thanks to this, users can get information about the battery status from anywhere in the world. Thanks to user-focused interface software, it provides easy and understandable information about the battery status for users with both desktop and mobile devices. It can also send instant notifications via e-

mail in cases of critical levels determined by the user in advance. The Battery Management System proposed in this study provides the user with flexible and comprehensive traceability with its IoT-based data monitoring feature while ensuring safe and efficient management of batteries [1-2,4].

Developed within Elfatek Electronic, AKİBA is an autonomous transportation system defined as an autonomous load-carrying robot. It can work fully integrated with humans in industrial environments such as closed areas, factories, and warehouses. AKİBA's battery systems are critical for the reliable and uninterrupted operation of the device. This study aims to develop a Battery Management System to be used in the AKİBA autonomous vehicle and equip this system with data monitoring capabilities [8].



Figure 1: AKİBA Autonomous Vehicle [8]

II. LITERATURE REVIEW

Lithium-based batteries are widely used today, from the smallest electronic devices to vehicles. The reasons for this are, in order, their high cycle life, compact size, high energy density, and ability to deliver the required current for high-current applications [9].

Battery Management Systems are the electronic circuits necessary to ensure the correct use and safety of batteries, with complexity varying according to the number of cells and the design structure of the battery pack. A well-designed BMS allows batteries to be used in a long-lasting, safe, and efficient manner. BMSs have certain key features: cell voltage measurement, stack voltage measurement, temperature measurement, current measurement, various protection circuits according to the usage scenario, and finally, cell voltage balancing [10-11,16].

Battery Management Systems are very important for protecting the safety as well as the functioning of battery operations. In this sense, the BMS is the lifeline of the battery when it cuts the load or charger in the situations listed above that are classified as overcharging, over discharging, excessive temperature, and short circuits [12,19].

Due to production differences among series-connected cells, the cells may reach different voltage levels when charging, which can prevent optimal battery usage. Some cells remain at lower voltages while others stay at higher voltages. To address this, BMSs apply a balancing method to cells. The balancing methods are generally divided into two categories: passive balancing and active balancing. In passive balancing, excess energy in a cell is dissipated, while in active balancing, energy is transferred from higher-energy cells to lower-energy cells

through various methods. Using one of these two main methods, the cell voltages are equalized [11, 13, 15-16, 18].

The State of Charge (SOC) indicates how much capacity the battery can currently store compared to its full charge. Numerous SOC estimation methods, categorized into four main groups, exist: open-circuit voltage (OCV) measurements, ampere-hour counting, model-based, and data-driven methods [14,16-17].

Battery management systems, when combined with the extensive connectivity of the digital era, have significantly transformed the monitoring and optimization of batteries, particularly through the integration of IoT technologies. IoT-enabled BMS solutions continuously collect data on critical parameters such as voltage, current, and temperature, ensuring seamless interaction with global networks. This integration facilitates real-time monitoring, adjustments, and the utilization of up-to-date information to enable proactive maintenance. By leveraging wireless communication modules and cloud-connected sensors, data is transmitted to centralized platforms for comprehensive analysis [1,3-4,20].

III. MATERIAL AND METHODS

The main objective of this study is to continuously monitor the battery data of an autonomous cargo transport vehicle, activate warning systems in critical situations and provide remote monitoring of this data with IoT technology. The developed system consists of three main sections:

- Battery Management System
- Microcontroller and Control Unit
- IoT and Warning System

Before the hardware and software components were used, a block diagram of the study was prepared. In this way, the general structure of the System was planned. The general structure of this plan is summarized in the designed diagram in Figure 2.

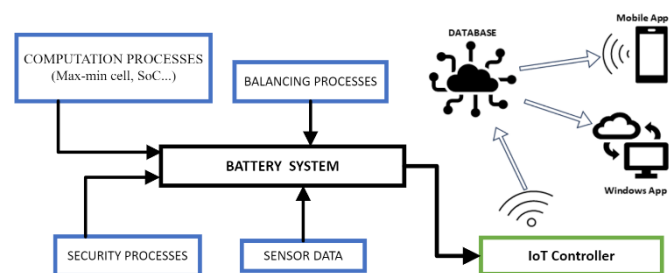


Figure 2: Working Block Diagram

After the necessary planning, research was conducted on the battery topology and balancing system. Examples of battery management system topologies include central topology, master-slave topology, and modular topology. When the battery structure and affordable costs of the autonomous vehicle were evaluated, the central topology was decided to use, as it provided the most effective results.

The balancing methods used in battery systems are of great importance in terms of system performance. There are two main balancing methods in these systems. These are active balancing

and passive balancing. Passive balancing was decided as the balancing system that will be effective for an autonomous vehicle provides appropriate cost and safety targets, and the design was planned to proceed with this balancing method.

After the basic structure was created, a diagram was first created for the product ecosystem to be used, and product selections began to be made in the light of this diagram.

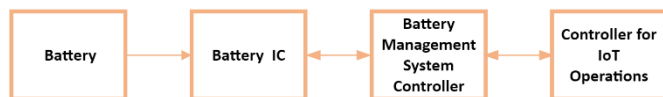


Figure 3: Product Ecosystem Diagram

A. BMS IC Selection

Selecting the appropriate integrated circuit for the battery management system is one of the important steps of the design. At this stage, integrated circuits widely used in the market were investigated. In the research conducted, it was seen that Analog Devices and Texas Instruments companies' battery management system integrated circuits were frequently preferred. Integrated circuits of these companies are often preferred in terms of reliability and performance.

Research results indicate that Texas Instruments' BQ76952 integrated circuit is planned to be preferred due to its wide cell count support and advanced protection features. It also provides easy communication with the supporting microcontroller by making an I2C protocol [5].

B. IoT Controller Selection

In the battery management system design, another controller that would provide IoT-based monitoring and data transfer was planned. An IoT module was chosen that would allow battery data to be transmitted wirelessly to a server. The ESP32 module was chosen because it was a low-cost, fast, and very popular option. In addition, the large user community and rich software support made the ESP32 more advantageous than the other options and supported the reason for its selection [7].

C. Main Controller Selection

BQ76952, which is selected as the battery management system integrated circuit, can perform many functions to ensure the safe and balanced operation of the batteries. However, an external microcontroller is required to fully control the functions of this integrated circuit and make the necessary settings. Additionally, a main controller will be needed to act as a bridge to send the data obtained from the BQ76952 integrated circuit to the cloud environment.

Planning has been done considering that these operations can be carried out safely with the communication protocols that have been used for years. The main controller will use the I2C communication protocol with BQ76952, and the ESP32 will use the UART communication protocol. STM32G431, which is a STMicroelectronics product that can perform these operations, will be preferred [6].

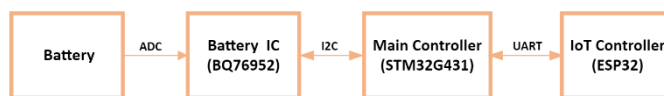


Figure 4: Selected Product Diagram

D. Software Platform Selection

In the software development process, various platforms were evaluated because of the research conducted for data storage and user interface design. Firebase was selected for real-time monitoring and analysis of IoT data, and the free use wide community support and real-time database features provided by this platform provide easy integration with the ESP32 microcontroller. Visual Studio was preferred for computer interface design. This platform meets the project requirements by offering user-friendly GUI design and development tools. On the mobile application development side, MIT App Inventor was planned to be used for simple and fast monitoring of data. These choices aim to facilitate the software process present data to the user instantly and monitor system performance.

IV. EXPERIMENTAL WORK

Before starting the battery management system design, the BQ76952 integrated circuit and controller to be used were examined in detail. The documents and sample designs of the integrated circuit used in the design process were reviewed first. As a result of these examinations, the schematic design of the system and after that PCB designs. In the schematic design performed via KiCad software, basic balancing structures and connection points were created, and all components needed by the prototype circuit were planned. For example, a header was added to simulate the communication interruption between the BQ76952 integrated circuit and the controller. In this way, it will be sufficient to remove the header to interrupt the communication, and then the necessary experiments can be easily performed.

In the designed schematic, the communication between the BQ76952 and the STM32G431 microcontroller was provided with the I2C protocol. It was planned that the ESP32 controller would be connected externally to the system, not on the PCB, and would manage IoT operations. The necessary ESP32 connection points were added to the design with a header connector. After the PCB design was completed, the PCB production process was started, and the necessary components were ordered. While the production process was ongoing, the software required for the communication protocols in the software part of the system was developed and made ready for testing. At the same time the conditions required for connecting ESP32 with Firebase after the internet connection were investigated for data transfer to the server environment.

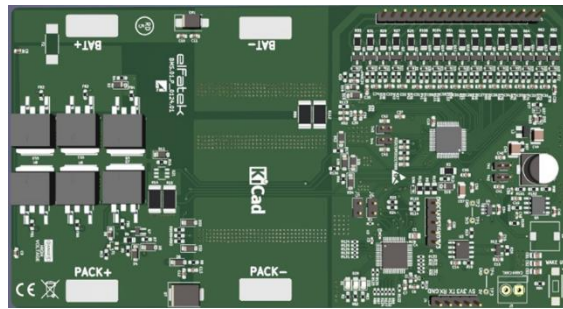


Figure 5: PCB Design 3D Screenshot

For IOT, firstly the connection of Esp32 to the internet was established. Then, the necessary software was made for the connection of data to Firebase, which will be used as a database via the internet with Esp32. Then, the necessary permissions for access of Esp32 to Firebase were given in a controlled manner and the connection of Esp32 to Firebase was ensured.

To test the communication compatibility between Firebase and ESP32, random data was generated via ESP32 and checked whether it was sent to the Firebase environment. After observing that data was transmitted from ESP32 to the Firebase platform without any problems, work began on a software that could monitor these sent data from computers.

As a preliminary study for the design in the computer program, data reading was done via firebase. Later, when designing the computer program interface, it was investigated which add-ons could be used to create the visual structure. As a result of the research, battery levels were visualized using a progress bar. A battery icon was added to the background of these progress bars and a design was made to show each battery cell separately. In addition to all this battery visual data, the mV value was added numerically to the battery icon to provide detailed monitoring.

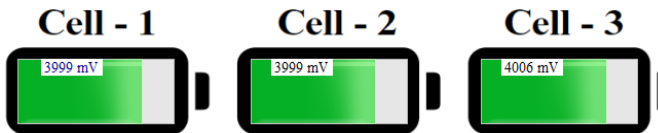


Figure 6: Cell Designs

This process was repeated for each battery cell. Since it was planned to test on a 12S battery in the collection, a design was made to add 12 battery images and data.

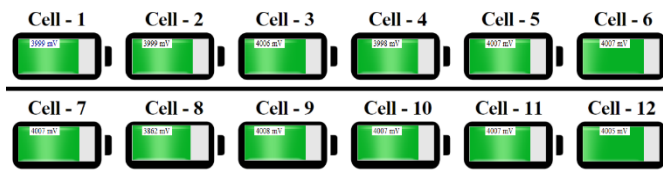


Figure 7: All Cells Design

After that an additional structure was designed to show Soc, temperature, and important battery levels. With this design, a summary of the most important data in a battery could be shown on a single screen.

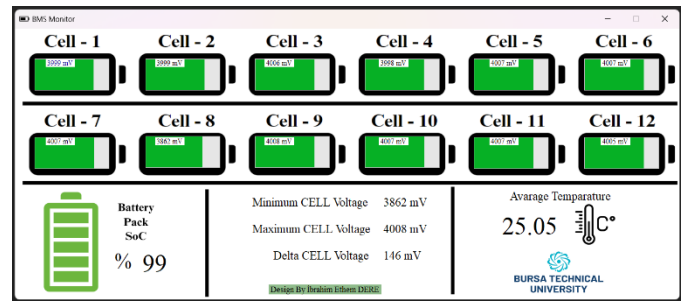


Figure 8: Windows App Screenshot

This structure designed in the computer program was followed step by step in the mobile application design and access to battery monitoring was provided at any time. First, a single data reading was made via firebase as in the computer environment, then data reading of all battery cells was performed.

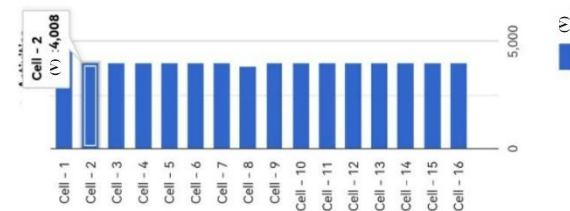


Figure 9: Mobile App Screenshot

After the orders for the PCBs required for the battery management system were completed, the cards were delivered, and the testing process began. In the first stage, the power converter the correctness of the 5V and 3.3V output voltages was checked. Then, basic tests of the STM32 microcontroller used as the main controller of the BMS were performed. In this process, the smooth operation of the controller circuit was verified with a simple test performed via LED blinking, and the necessary tests were performed for the debugging operations to be used in the future.

Communication was established with the BQ76952 selected as the BMS integrated circuit, and the voltage values of the battery cells, data received from the temperature sensors and other parameters were checked. Battery simulation was performed, and the data of all cells was displayed live on the STMCubeIDE platform. These stages proved that the system worked successfully, and a solid foundation was established for the next development steps.

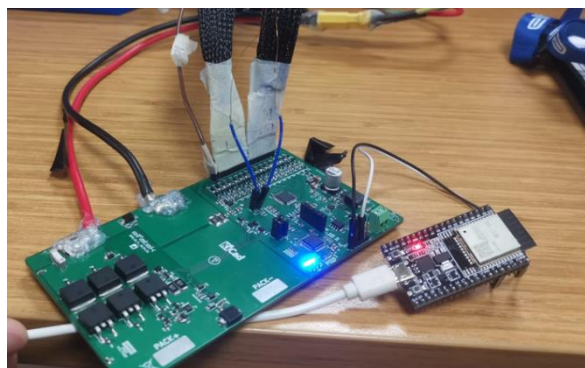


Figure 10: BMS and IOT System

In the continuation of the design, UART communication was established between STM32 and ESP32 to monitor the battery data via an IoT-based system. ESP32 took over the process of collecting battery data and sending it to a database, and this data was displayed on a computer. In the tests, it was observed that the battery management system could be monitored simultaneously on multiple devices and that the system worked reliably. In this way, the targeted IoT-supported battery management system was successfully implemented.

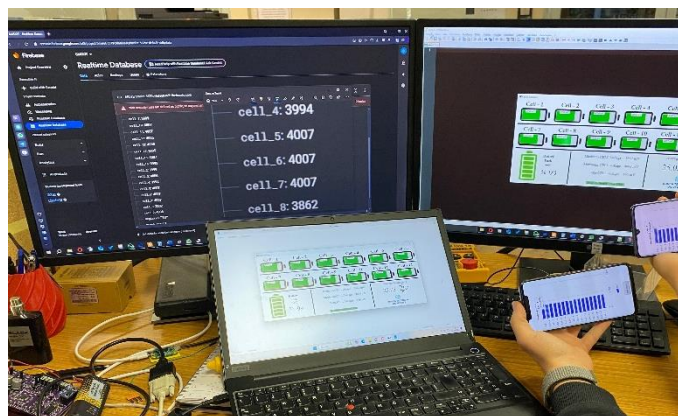


Figure 11: IOT System Interface

An email notification structure was also implemented in the experimental study. This setup allows users to receive real-time updates via email alerts when certain critical conditions or thresholds are met in the battery management system. When enabled, this feature enables timely interventions by providing instant information to the user when needed.

V. CONCLUSION

This study successfully developed an IoT-enabled Battery Management System (BMS) designed for an autonomous payload robot. The BMS uses a Texas Instruments BQ76952 integrated circuit to monitor voltage, current, and temperature precisely. It is complemented by an STM32G431 microcontroller that manages cell balancing and executes security protocols. To increase data accessibility, an ESP32 module is integrated to transmit real-time battery information to Firebase, enabling remote monitoring via cloud technology.

The design of the system prioritizes security and performance, allowing users to monitor battery status from anywhere via both desktop (Visual Studio) and mobile (MIT App Inventor) applications. These user interfaces present critical battery data such as State of Charge, cell voltages, and temperature values in a clear and graphical format enhancing usability and user confidence.

Experimental studies have validated the system's battery data monitoring and demonstrated its ability to deliver reliable data and monitor across multiple devices. This innovative approach enhances battery safety, making it a valuable solution for industrial applications.

ACKNOWLEDGMENT

This study was supported by Elfatek Electronics and supervised by Assoc. Prof. Dr. Davut ERTEKİN. It is part of İbrahim Ethem DERE's master's thesis. Special thanks to Talha TELLİ for his significant contributions to the Battery Management System design, and to Süleyman CANAN for his valuable support during the implementation phase.

REFERENCES

- [1] S. Krishnakumar et al., "IoT-based Battery Management System for E-Vehicles," 2022 3rd International Conference on Smart Electronics and Communication (ICOSEC), Trichy, India, 2022, pp. 428-434, doi: 10.1109/ICOSEC54921.2022.9952052.
- [2] K. I. V. V., A. B. K. and L. ST, "Smart Battery Management System for Electric Vehicles Using IoT," 2024 5th International Conference on Intelligent Communication Technologies and Virtual Mobile Networks (ICICV), Tirunelveli, India, 2024, pp. 720-725, doi: 10.1109/ICICV62344.2024.00120.
- [3] K. Kumari.K.S, L. Chitra, J. M. Abraham, N. Joseph and Y. K. T.K, "The Role of IOT & AI in Battery Management of Electric Vehicles," 2023 International Conference on Signal Processing, Computation, Electronics, Power and Telecommunication (IconSCEPT), Karaikal, India, 2023, pp. 1-7, doi: 10.1109/IconSCEPT57958.2023.10170275.
- [4] L. S. B, A. Sangari, E. K, K. V, J. A. Sheeba and D. Sivamani, "IoT-Based Battery Monitoring System for Electric Vehicle," 2022 IEEE International Conference on Current Development in Engineering and Technology (CCET), Bhopal, India, 2022, pp. 1-5, doi: 10.1109/CCET56606.2022.10080389.
- [5] Texas Instruments, 2021. BQ76952 3-Series to 16-Series High Accuracy Battery Monitor and Protector for Li-Ion, Li-Polymer, and LiFePO4 Battery Packs datasheet (Rev. A). Texas Instruments company <https://www.ti.com/lit/gpn/bq76952> (accessed Nov 2024).
- [6] STMicroelectronics, 2021. STM32G431x6 STM32G431x8 STM32G431xB datasheet. <https://www.st.com/resource/en/datasheet/stm32g431c6.pdf> (accessed Nov 2024).
- [7] Espressif Systems, 2024. ESP32 Series Datasheet v4.7 https://www.espressif.com/sites/default/files/documentation/esp32_datasheet_en.pdf (accessed Nov 2024).
- [8] <https://akiba.com.tr/tr>
- [9] S. M. A. S. Bukhari, J. Maqsood, M. Q. Baig, S. Ashraf and T. A. Khan, "Comparison of Characteristics -- Lead Acid, Nickel Based, Lead Crystal and Lithium Based Batteries," 2015 17th UKSim-AMSS International Conference on Modelling and Simulation (UKSim), Cambridge, UK, 2015, pp. 444-450, doi: 10.1109/UKSim.2015.69.
- [10] Lelie M, Braun T, Knips M, Nordmann H, Ringbeck F, Zappen H, Sauer DU. Battery Management System Hardware Concepts: An Overview. Applied Sciences. 2018; 8(4):534. <https://doi.org/10.3390/app8040534>
- [11] M. Darwish, S. Ioannou, A. Janbey, H. Amreiz and C. C. Marouchos, "Review of Battery Management Systems," 2021 International Conference on Electrical, Computer, Communications and Mechatronics

- Engineering (ICECCME), Mauritius, Mauritius, 2021, pp. 1-6, doi: 10.1109/ICECCME52200.2021.9590884.
- [12] A. Chinnusamy, D. Dsa and S. N. Banavath, "Intelligent Battery Protection System for Electric Vehicle Applications," 2024 IEEE 18th International Conference on Compatibility, Power Electronics and Power Engineering (CPE-POWERENG), Gdynia, Poland, 2024, pp. 1-5, doi: 10.1109/CPE-POWERENG60842.2024.10604351.
- [13] M. Kumar, V. K. Yadav, K. Mathuriya and A. K. Verma, "A Brief Review on Cell Balancing for Li-ion Battery Pack (BMS)," 2022 IEEE 10th Power India International Conference (PIICON), New Delhi, India, 2022, pp. 1-6, doi: 10.1109/PIICON56320.2022.10045109.
- [14] R. R. Kumar, C. Bharatiraja, K. Udhayakumar, S. Devakirubakaran, K. S. Sekar and L. Mihet-Popa, "Advances in Batteries, Battery Modeling, Battery Management System, Battery Thermal Management, SOC, SOH, and Charge/Discharge Characteristics in EV Applications," in IEEE Access, vol. 11, pp. 105761-105809, 2023, doi: 10.1109/ACCESS.2023.3318121.
- [15] M. Naguib, P. Kollmeyer and A. Emadi, "Lithium-Ion Battery Pack Robust State of Charge Estimation, Cell Inconsistency, and Balancing: Review," in IEEE Access, vol. 9, pp. 50570-50582, 2021, doi: 10.1109/ACCESS.2021.3068776.
- [16] Munish Manas, Ravish Yadav, Rajesh Kumar Dubey, Designing a battery Management system for electric vehicles: A congregated approach, Journal of Energy Storage, Volume 74, Part A, 2023, 109439, ISSN 2352-152X, <https://doi.org/10.1016/j.est.2023.109439>.
- [17] Osman Demirci, Sezai Taskin, Erik Schaltz, Burcu Acar Demirci, Review of battery state estimation methods for electric vehicles - Part I: SOC estimation, Journal of Energy Storage, Volume 87, 2024, 111435, ISSN 2352-152X, <https://doi.org/10.1016/j.est.2024.111435>.
- [18] Z. B. Omariba, L. Zhang and D. Sun, "Review of Battery Cell Balancing Methodologies for Optimizing Battery Pack Performance in Electric Vehicles," in IEEE Access, vol. 7, pp. 129335-129352, 2019, doi: 10.1109/ACCESS.2019.2940090.
- [19] B. Li, Y. Fu, S. Shang, Z. Li, J. Zhao and B. Wang, "Research on Functional Safety of Battery Management System (BMS) for Electric Vehicles," 2021 International Conference on Intelligent Computing, Automation and Applications (ICAA), Nanjing, China, 2021, pp. 267-270, doi: 10.1109/ICAA53760.2021.00055.
- [20] M. Helmy Abd Wahab, "IoT-Based Battery Monitoring System for Electric Vehicle", IJET, vol. 7, no. 4.31, pp. 505–510, Dec. 2018, doi: 10.14419/ijet.v8i1.4.25472.

Android Permission Analysis and Malware Detection using Machine Learning Methods

MUHAMMED TALHA ÇALIŞ¹, ZÜLEYHA YILMAZ ACAR²

¹ Selcuk University, Institute of Science, Department of Computer Engineering, Konya/Turkey,
muhammedtalhacalis@gmail.com

² Selcuk University, Faculty of Technology, Department of Computer Technology, Konya/Turkey,
zuleyhayilmaz@selcuk.edu.tr

Abstract - The Android operating system, being one of the most widely used mobile platforms globally, has also become a primary target for malware. This study analyzes various types of Android malware and the machine learning methods used to detect them. By employing a large dataset, we examine the characteristics of malware application and develop effective detection techniques. The dataset includes permissions used by malware applications, aiding in classification for malware detection. The findings provide significant insights into enhancing the security of Android devices and suggest security strategies to be developed. This study aims to offer valuable information to researchers and software developers working in mobile security through data analysis and machine learning methods applied to the dataset.

Keywords – Android, Malware Detection, Data Preprocessing, Machine Learning.

I. INTRODUCTION

THE widespread adoption of mobile devices as integral parts of daily life has led to a rapid increase in malware threats targeting the Android operating system. The open nature of the Android platform and its extensive user base make it an attractive target for malware actors, emphasizing the need for efficient malware detection and prevention. Among the methods developed for malware detection, permission-based analysis of applications has gained attention [1]. Application permissions indicate the types of data and hardware resources an application requests access to, making them a critical factor in identifying malware behavior.

This study investigates the detection of malware applications using a dataset based on Android application permissions. The dataset includes permission requests and labels indicating whether the applications are malware or benign. By analyzing these permissions, we evaluate the effectiveness of using such data for malware detection and develop detection methods using machine learning algorithms. Our research demonstrates how application permissions can be utilized to detect malware, contributing to the development of novel approaches and strategies in mobile security.

The dataset used in this project consists of permissions from over 29,000 Android applications. Data manipulation and analysis were conducted using the Python programming

language. Permissions examined include those that might indicate suspicious behavior when misaligned with the intended purpose of an application.

This study establishes a foundation for analyzing the reliability of mobile applications based on permissions. Relevant literature highlights similar observations regarding how permissions can guide malware detection efforts.

The studies in the literature on the subject of this study have been examined. In study [2], Akbar et al. focused on permission-based malware detection, introducing the PerDRaML strategy to enhance detection accuracy while minimizing the number of required permissions using Random Forest and Naive Bayes classifiers. In the study [3], Zhu et al. proposed DroidDet, a method combining multiple feature types and the Rotation Forest model to detect Android malware using static analysis. In study [4], Nawshin et al. conducted a comprehensive survey on secure and privacy-preserving machine learning approaches for malware detection, comparing Android and iOS security mechanisms and discussing traditional and deep learning models.

II. MATERIAL AND METHOD

A. Dataset

The NATICUSdroid dataset comprises permissions 29,332 Android applications, both benign and malware, released between 2010 and 2019. It was prepared to develop an Android malware detection system using the latest applications. Each row of the dataset represents an Android application. Permissions used by these applications are spread across 86 columns.

B. Platform, Libraries and Tools

To facilitate data manipulation, analysis, and modeling, several libraries and tools were utilized in this study. Python served as the primary programming language, offering robust capabilities for data manipulation, analysis, and visualization. Pandas was employed for efficient data manipulation and analysis, enabling operations such as data cleaning, aggregation, and transformation. Matplotlib and Seaborn were used for data visualization, allowing the creation of both basic and advanced plots to explore and present the dataset effectively. Scikit-learn provided tools for building and

analyzing machine learning models, offering a comprehensive suite of algorithms and utilities for preprocessing, training, and evaluation.

C. Data Preprocessing Steps

The preprocessing phase involved several steps to prepare the dataset for analysis and modeling.

- Data Import and Labeling: The dataset was read into the workspace, and a new column labeled Label was added. This column categorized each application as either Malware or Benign, improving the dataset's interpretability.
- Data Segmentation: The dataset was divided into two groups based on the Label column. Applications identified as malware were grouped separately from benign applications, facilitating targeted analyses.
- Feature Engineering: To refine the dataset, unnecessary columns were removed. Additionally, statistical metrics were computed, providing initial insights into the data and enabling a better understanding of its structure.

These steps ensured that the dataset was well-organized and suitable for further exploratory analyses and machine learning tasks.

Through preprocessing, applications were categorized, statistical summaries were computed, and machine learning models were employed to assess the relationships between permissions and malware likelihood. Visualizations and exploratory analyses were performed to identify suspicious permissions and patterns.

This methodology provides a foundation for understanding the role of application permissions in detecting malware Android applications and contributes to the advancement of mobile security strategies. Some statistical values of the data are below as in Table 1.

Table 1: Statistical analyses of the dataset

Application Type	Min value	Max value	Mean value	Median value	Standard deviation
Benign	0	1	0.126044	0.0	0.331899
Malware	0	1	0.093718	0.0	0.291436

D. Analysis of permissions used in Android applications

The 10 most used permissions in benign and malware applications are obtained separately and the numbers and rates of these permissions are analyzed. The same data is then displayed graphically. Figure 1 and Figure 2 show the most commonly used 10 permissions for Benign applications. Figure 3 and Figure 4 show the most commonly used 10 permissions for malware (malicious) applications.

Permission	Count	Ratio
android.permission.INTERNET	14230	0.970271
android.permission.ACCESS_NETWORK_STATE	14072	0.959498
android.permission.READ_PHONE_STATE	13831	0.943066
android.permission.WRITE_EXTERNAL_STORAGE	10755	0.733329
android.permission.RECEIVE_BOOT_COMPLETED	10311	0.703055
android.permission.ACCESS_COARSE_LOCATION	9973	0.680008
android.permission.ACCESS_FINE_LOCATION	9526	0.649530
android.permission.ACCESS_WIFI_STATE	9255	0.631051
android.permission.WAKE_LOCK	6692	0.456293
com.android.launcher.permission.INSTALL_SHORTCUT	5859	0.399495

Figure 1: The 10 most commonly used permissions for benign applications

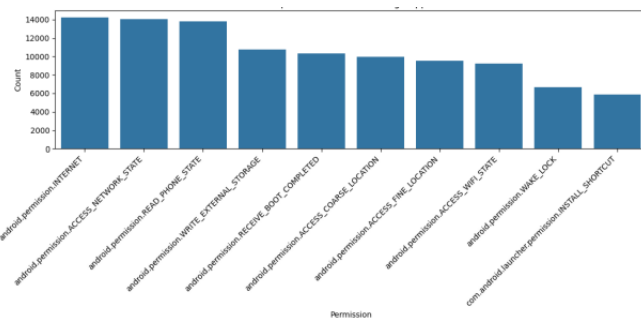


Figure 2: The visual graph of used permissions for benign applications

Permission	Count	Ratio
android.permission.INTERNET	14378	0.980363
android.permission.ACCESS_NETWORK_STATE	13765	0.938565
android.permission.WRITE_EXTERNAL_STORAGE	8874	0.605073
android.permission.WAKE_LOCK	7413	0.505455
android.permission.ACCESS_WIFI_STATE	6146	0.419065
com.google.android.c2dm.permission.RECEIVE	6024	0.410746
android.permission.VIBRATE	4700	0.320469
android.permission.READ_EXTERNAL_STORAGE	3734	0.254602
android.permission.ACCESS_COARSE_LOCATION	3634	0.247784
android.permission.ACCESS_FINE_LOCATION	3542	0.241511

Figure 3: The 10 most commonly used permissions for malware applications

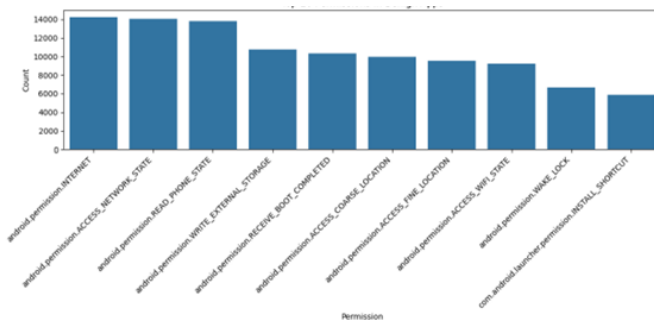


Figure 4: The visual graph of used permissions for malware applications

Then, the usage rates of these most commonly used permissions in Benign and Malware applications are shown in a table and visually for comparison.

Permission	Malicious Usage Ratio	Benign Usage Ratio	Total Usage Ratio
android.permission.INTERNET	0.980363	0.970271	1.950634
android.permission.ACCESS_NETWORK_STATE	0.938565	0.959498	1.898064
android.permission.WRITE_EXTERNAL_STORAGE	0.605073	0.733329	1.338402
android.permission.READ_PHONE_STATE	0.231692	0.943066	1.174758
android.permission.ACCESS_WIFI_STATE	0.419065	0.631051	1.050116
android.permission.WAKE_LOCK	0.505455	0.456293	0.961748
android.permission.ACCESS_COARSE_LOCATION	0.247784	0.680008	0.927792
android.permission.RECEIVE_BOOT_COMPLETED	0.206668	0.703055	0.909723
android.permission.ACCESS_FINE_LOCATION	0.241511	0.649530	0.891041
android.permission.VIBRATE	0.320469	0.377608	0.698077

Figure 5: Permission comparisons for malicious (malware) and benign Applications

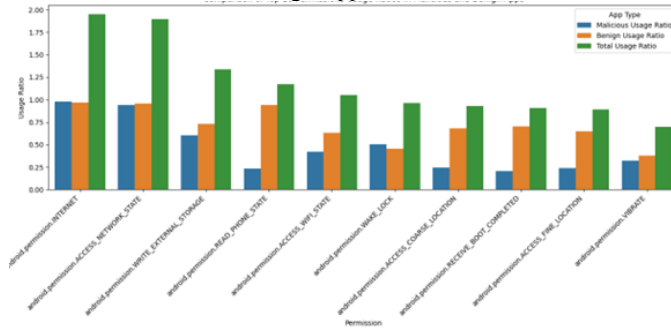


Figure 6: The visual comparison graph for benign and malware applications

III. EXPERIMENTAL ANALYSIS AND RESULTS

To evaluate the effectiveness of different machine learning models in detecting malware applications, the dataset was split into training and testing sets. The following algorithms were applied: Support Vector Machine (SVM) [5], Rotation Forest [6], Random Forest [7], Naive Bayes [8].

The performance of each model was assessed using standard metrics such as accuracy, precision, recall, and F1-score. The results obtained from these analyses are summarized as in Figure 7.

Model	Precision (Benign)	Recall (Benign)	F1-score (Benign)	Precision (Malware)	Recall (Malware)	F1-score (Malware)	Accuracy
SVM	0.95	0.96	0.96	0.96	0.95	0.96	0.96
Rotation Forest	0.97	0.96	0.96	0.96	0.97	0.96	0.96
Random Forest	0.98	0.97	0.97	0.97	0.98	0.97	0.97
Naive Bayes	0.55	1.00	0.71	0.98	0.20	0.34	0.60

Figure 7: The performance metric results for detection benign and malware applications.

The results provide valuable insights into the performance of different machine learning models in classifying Malware and Benign applications. Observations from the confusion matrices and classification reports for each model are summarized below:

- Support Vector Machine (SVM): Achieved a balanced performance with high precision and recall for both classes. Demonstrated robustness in distinguishing between Malware and Benign

applications but slightly underperformed compared to tree-based models.

- Rotation Forest: Delivered the highest performance across all metrics, including precision, recall, and F1-score. Its ability to handle complex data relationships contributed to its superior accuracy, particularly in classifying the Malware class effectively.
- Random Forest: Exhibited the highest overall accuracy. Achieved high precision, recall, and F1-score for both Malware and Benign classes, showcasing its reliability and versatility. Outperformed other models in scenarios with a balanced dataset.
- Naive Bayes: Demonstrated a strong recall for the Benign class, indicating its sensitivity to identifying benign applications. However, it struggled with the Malware class, resulting in lower recall and F1-score for this category. This highlights its limitations in capturing complex patterns and dependencies in permission data.

These findings underline the importance of selecting appropriate machine learning models based on the specific requirements of the classification task. While Random Forest emerged as the top-performing model with the highest accuracy and balanced metrics, the strengths and weaknesses of other models, such as Naive Bayes' high sensitivity to the Benign class, can be leveraged in specialized scenarios.

The analysis emphasizes that no single model is universally superior, and the choice of a model should be informed by the dataset characteristics, target performance metrics, and computational constraints.

IV. DISCUSSION

This study focuses on a permission-based analysis for detecting Android malware. It utilizes a dataset containing permissions from over 29,000 benign and malware Android applications released between 2010 and 2019. The dataset is used to explore how permissions can be employed to detect malware applications and to identify commonly utilized permissions.

At the outset, an analytical method based on Android application permissions is introduced. This method leverages a dataset comprising permission requests and corresponding labels indicating whether an application is malware or benign. The dataset is analyzed using various machine learning algorithms, and effective detection methods are developed.

The findings provide critical insights into measures that can enhance the security of Android devices and strategies that need to be developed. Moreover, the study offers valuable information for researchers and software developers working in the field of mobile security.

V. CONCLUSION

This study presents a permission-based analysis method for Android malware detection, aiming to contribute to the development of novel approaches and strategies in the mobile

security domain. By leveraging the dataset, various machine learning models were employed to identify malware applications with high accuracy. The results highlight the potential of permissions as key indicators for malware detection and underscore the importance of selecting appropriate models, such as Random Forest, for optimal performance. Acknowledging the limitations of this study, it is suggested that future research could employ larger datasets and diverse analytical methods to yield more comprehensive results.

Future studies could focus on the dynamics of user behavior and permission requests, contributing to the earlier and more accurate detection of malware. Furthermore, advancements in machine learning models and the application of new detection methods can lead to significant progress in malware prevention.

REFERENCES

- [1] Ö. Kiraz and İ. A. Doğru, "Visualising Static Features and Classifying Android Malware Using a Convolutional Neural Network Approach," *Applied Sciences*, vol. 14, p. 4772, 2024.
- [2] F. Akbar, M. Hussain, R. Mumtaz, Q. Riaz, A. W. A. Wahab, and K.-H. Jung, "Permissions-Based Detection of Android Malware Using Machine Learning," *Symmetry*, vol. 14, p. 718, 2022.
- [3] H.-J. Zhu, Z.-H. You, Z.-X. Zhu, W.-L. Shi, X. Chen, and L. Cheng, "DroidDet: Effective and robust detection of android malware using static analysis along with rotation forest model," *Neurocomputing*, vol. 272, pp. 638-646, 2018/01/10/ 2018.
- [4] F. Nawshin, R. Gad, D. Unal, A. K. Al-Ali, and P. N. Suganthan, "Malware detection for mobile computing using secure and privacy-preserving machine learning approaches: A comprehensive survey," *Computers and Electrical Engineering*, vol. 117, p. 109233, 2024/07/01/ 2024.
- [5] W. Zhou, L. Zhang, L. Jiao, and J. Pan, "Support Vector Regression Based on Unconstrained Convex Quadratic Programming," Berlin, Heidelberg, 2006, pp. 167-174.
- [6] M. Juez-Gil, Á. Arnaiz-González, J. J. Rodríguez, C. López-Nozal, and C. García-Osorio, "Rotation Forest for Big Data," *Information Fusion*, vol. 74, pp. 39-49, 2021/10/01/ 2021.
- [7] L. Breiman, "Random Forests," *Machine Learning*, vol. 45, pp. 5-32, 2001/10/01 2001.
- [8] F. J. Yang, "An Implementation of Naive Bayes Classifier," in *2018 International Conference on Computational Science and Computational Intelligence (CSCI)*, 2018, pp. 301-306.

Selection and Application of Robotics Process Automation in A Medium Sized Manufacturing Company

Mehmet Tevfik Çobanoğlu¹

¹ İstanbul Okan University/Turkey, mehmet.cobanoglu@okan.edu.tr

Abstract - Digitalization has been on the agenda of many companies in Europe and the US. In recent years, the digitalization topic has shown itself in the company agendas in Turkey as well. Generally, in large companies that mass produce, the digital implementations move rapidly however, in medium and small sized companies these applications come to life only partially. The digitalization of software technologies that are being used more and more with industry 4.0 and their application areas will be shown, and the applications, examples and classification of RPA applications in the production process. As a case study purchasing will be about replacement of repetitive processes by Robotics Process Automation (RPA) and its pre-requisite of needed digitalization of purchasing applications in a medium sized company, developing the methodology to be used and showing the implementation steps, yields and costs of a sample project. Based on the need of RPA in the purchasing department of medium-sized company, RPA software and its application area at production will be discussed.

Keywords - Robotic Process Automation, Industry 4.0, Production Department, Business Process Management.

I. INTRODUCTION

ROUTINE human actions, which were used only in solving practical needs, have led to the development of economic and commercial relations over time and created routine processes that led to production in return for labor. These processes, like the previous ones, developed slowly and led to the emergence of small-scale hand-made productions, followed by the emergence and widespread production of factories producing steam power. These production processes, which are the first steps of factory-scale production, are called Fordist tape system, where Taylorism has laid the foundations of Taylorism, in which mass production can be realized faster, and it has turned into piecemeal production processes that can use more primitive motor skills for the person. The changes in the production and the processes used in production go hand in hand with the motor skills and mental capacities of the person. Especially with the industrial revolutions increasingly equipped with technology, and thus, unmanned, more computer-controlled machines are included in production, production processes have now been purified from the labor force of the person and turned to the power of the machines. This transformation is inevitably looking for ways to become more featured, multifunctional and less costly than human labor, by prioritizing progress and development. The first of these ways

is the development of existing computer technologies, the further digitization and the use of autonomous software and smart machines. However, for a technology to be useful, it is expected to be effective, efficient, low cost and facilitate human life in every respect. It is aimed to make human life easier by becoming one of these features, which are also developing and making the machines more self-learning. In this context, more efficient and less costly use of human labor in the production process is among these features. It is especially important that there are structures that are time-consuming, repetitive, which do not contribute to the personal development of the individual, and that they can perform some routine works digitally that cause unnecessary wear. The first of these is software called robotic process automation (RPA). These tools have been developed to perform routine work done by people in the production and consumption processes, instead of existing physical robots. Its main feature is to imitate human behavior and to save the labor force in the time-consuming work processes, and to use this power where it can be more efficient. Thus, both labor power, time and costs can be saved.

RPA was developed as a technology that has been on the rise in the early 2000s to replace the time-consuming routine work performed by the human workforce. In 2012, it has passed certain levels according to the usage processes as a technology that has reached its current form. It has become a technological software that has a complex decision-making mechanism by replacing the human workforce rather than carrying out simple operations in the process from basic to advanced level and using it as an assistant to the human workforce. It should be noted, however, that RPA is not a physical helper robot, but a purely software mechanism.

II. DEVELOPMENT OF RPA

Thus, significant and profitable developments have occurred in the sectors involved in the production processes. RPA software takes an important place in the telecommunications sector, which is one of the leading sectors. Using the SIM swaps and a pre-calculated loan application system, as in the case of Telefonica O2, primarily call center operators, virtual assistants, has made significant gains with RPA. In addition, another important sector network includes banking, finance and insurance companies.

It is especially used in many workloads such as recruitment, dismissal, retirement and procedures for keeping the data of

employees, entering new data and performing transactions. According to these practices, the CVs sent for recruitment processes are transferred to the relevant pools, and the necessary people can be contacted for the position sought, and as a result, information is provided through the automation-based message application. Coca Cola, which is a global brand at first, has benefited with RPA, productivity has increased with robots running 24 hours a day instead of 8 hours. RPA applications also play an important role in reducing the existing workload in the field of health services, where technological progress is experienced, and it is important to take fast action and to undertake more workload with less workforce

Finally, the issue that should be mentioned is the implementation of RPA in production processes. Although the use of physical robots and automatic machines is quite common, RPA applications in the production process have remained in the background. It is possible to see the RPA here in the presence of processes such as product management, quality assurance, data migration, revenue estimation, order receipt and payment in order to handle back office work. However, in this paper, it is planned to analyze that RPA can yield significant rates by using small-medium volume industrial production companies in the tape system production process, and make an analysis by making an account analysis according to the priority order brought by the RPA-specific scoring system.

III. RPA APPLICATION IN PRODUCTION

The most need attention RPA using field is in production. Already there are manufacturer companies that use physical robots in many areas such as production, packaging, quality control and logistic support of products. While physical industry robots help organize the assembly line, the manufacturing industry does not want to be bogged down in managing its back office and operational processes. Manufacturer companies must achieve a time-intensive order such as labor and customer communication, procurement, inventory management and payment processing. Likewise, they should pursue cost reduction and innovative business practices. To overcome these situations, many manufacturing companies prefer RPA to achieve more rapid and practical operations in the value chain, which saves 20% in various application areas. As an example of different processes, tasks or applications in different areas used as it can be applied, although we cannot see the production line very often in the RPA area, we can just give these following samples:

Firstly, product management, it helps to bridge the gap between IT systems and related product management platforms by automated updating of both systems. Quality assurance, regression testing and customer experience can be useful for QA processes. Data migration, it allows automatic data migration through systems that are not possible using traditional tools such as documents, spreadsheets or other source data files. After that, gap solutions are robotic automatic fills gaps in process lacks with simple tasks such as password resets, system resets, etc. The using of revenue forecasting, it

performs automatic updating of the financial statements required to estimate the forecasting of income data. Order processing and payments are the order fulfillment and processing section of a supply chain consists of three stages, which includes the product selection, payment processing, order confirmation. Finally, inventory management automation, by running processes at inventory levels, RPA notifies managers when product inventory levels are low and can automatically reorder products below a certain threshold level to facilitate inventory management.” These application areas, which include the use of RPA, are used by some industrial production companies for various purposes. For this purpose, “Audi wants to relieve its employees of such work so that they can concentrate on complex and value-adding tasks. The company built up development expertise in the area of robotic process automation (RPA) last year. In mid-2019, Audi IT founded a center of excellence that provides the central platform for RPA. In the premium manufacturer’s production plants, man and machine have been working hand in hand for some years. Now, employees with PC workstations are also receiving help from robots in the form of a digital assistant called ‘Audi myMate’.”

With Industry 4.0, the concept of collective privatization primarily provides flexible production and increases production speed. These systems, which create low error rates together with more product quality, provide ease and accuracy in production processes by optimizing efficiency, especially with data-based decision making. In this way, the relations with the customer are improved and new methods of creating value are developed, and thanks to the advantages it provides, it also improves the working practices of the employees, thereby ensuring employee happiness. Therefore, RPA software, which comes out in parallel with the digitalization of the production processes, is an important technological development thanks to the increase in productivity and facilitating the work of the employees.

On the other hand, there are some criteria and sub-criteria in the implementation of RPA. In determining these criteria, AHP method will be used within the scope of this study According to this method; it is a decision making mechanism used by scoring and weight calculations based on determined criteria and processes. Thus, the questions to be answered in this section will be as follows: What are the benefits of using RPA applications and their production processes? How should the processes in production be determined to comply with RPA? Which method should be used to determine the suitability? How should the criteria and sub-criteria be determined when using the AHP method? Accordingly, how can these applications be applied in line with the production processes of medium-size Company? In this context, the results section includes the definitions obtained from the previous sections and the literature review, the RPA, which is explained in the context of these questions, to investigate the usage and criteria of the production processes and to reveal the conclusion reached on how this research was carried out for the medium-sized company.

IV. CASE STUDY

XX Company is a medium-sized company forging and hot forging, high and low pressure die casting, CNC machining and bar turning in a wide range of products in various sizes. As a metal forming company that does its job, it has a wide production line. XX Company, which wants to improve itself in the field of Industry 4.0, asked us to present a project about whether it can apply for RPA at the production department at this point.

The objective of this project is to automate routine operations done in XX Company purchasing department and free up resources which in turn will be relocated in more strategic positions. Thanks to the Robotics Process Automation (RPA) software, we take routine purchasing activities from humans and give it to the software robot. As a result of this process, the project aims to save time and money and decrease human error. At the same time, the purchasing department will be lean and by depending on it, productivity and efficiency will be increased. Also with the reduction of paper documentation, the purchasing department will become more environmentally friendly. Finally with the help of RPA, analyses will be done in much faster ways which in turn will increase quality and speed. This project, which will be made in the XXX Purchasing Department, will play a role in the implementation of RPA processes by examining the routine works of the XX Company. It will be ensured that the project is a guide by researching the terms and software's in the production

V. CONCLUSION

When the benefits of the RPA which are taken into consideration, the researches have shown that robotic solutions will increase by 77%, especially in the next 5 years. These increases and technological developments show that RPA will spread to many parts of the production area in the future. Regardless of the size of the companies, RPA is planned to be a software used in each company. In this case, companies are gradually increasing their investment in this technology. Considering all these discussions, the purpose of this paper is to analyze in which areas the RPA-based software can be used in the production processes for the XX Company, a medium-sized metal forming company. In order to make this analysis, the compliance of RPA processes and criteria with RPA should be determined. After the information we provided about how this conformity could be made, the production processes of XX Company would be analyzed within the scope of AHP method with on-site observation.

REFERENCES

- [1] Aguirre, S., & Rodriguez, A., Automation of a Business Process Using Robotic Process Automation (RPA): A Case Study. In J. C. Figueroa-García, E. R. López-Santana, J. L. Villa-Ramírez, & R. Ferro- Escobar (Eds.), *Communications in Computer and Information Science. Applied Computer Sciences in Engineering* (pp. 65–71). Cham, Switzerland: Springer International Publishing, 2017.
- [2] Aguirre, S., Automation of a Business Process Using Robotic Process Automation (RPA): A Case Study, *Applied Computer Sciences in Engineering*, Springer International Publishing AG, p. 2.
- [3] Anagnoste, S.: Robotic Automation Process - The next major revolution in terms of back office operations improvement. In: *Proceedings of the International Conference on Business Excellence*. pp. 676–686. De Gruyter, Bucharest, 2017.
- [4] Asatiani, A., & Penttinen, E., Turning robotic process automation into commercial success – Case OpusCapita, *Journal of Information Technology Teaching Cases*, 1–8, 2016, p. 4.
- [5] Asatiani, Aleksandre, Penttinen, Esko., Turning robotic process automation into commercial success – Case OpusCapita, *Journal of Information Technology Teaching Cases*, 2016, p. 2.
- [6] Asquith, A., Horsman, G., Let the robots do it!, *Taking a look at Robotic Process Automation and its potential application in digital forensics*, Forensic Science International Reports, Reports 1, 2019.
- [7] Bhatnagar, N., Role of Robotic Process Automation in Pharmaceutical Industries, A. E. Hassanien et al. (Eds.): *AMLTA 2019, AISC 921*, pp. 497–504, 2020, p. 499.
- [8] Bucak, U. Evaluation of the Maritime 4.0 Using the AHP Method, III. *Global Conference on Innovation in Marine Technology and the Future of Maritime Transportation*, 18th-19th of April 2019, Selçuk, İzmir. p. 128.
- [9] Dias, M., (et all), Knowledge Embodiment of Human and Machine Interactions: Robotic Process Automation at the Finland Government, *Twenty-Seventh European Conference on Information Systems (ECIS2019)*, Stockholm-Uppsala, Sweden, 2019.
- [10] Fernandez, D., Aman, A.: Impacts of Robotic Process Automation on Global Accounting Services. *Asian Journal of Accounting and Governance*. 9, 123–132, 2018.
- [11] Fersht, P., Slaby, J.R., Robotic automation emerges as a threat to traditional low-cost outsourcing, *HfS Research, Ltd.*, pp: 1–18., 2012.

The International Conference on Engineering Technologies (ICENTE 24) was successfully held online from November 21-23, 2024, in collaboration with Selcuk University Faculty of Technology and Sinop University Faculty of Engineering and Architecture. The conference brought together leading international and interdisciplinary research communities, developers, and practitioners of advanced technologies to discuss both theoretical and practical issues across various technological domains. It served as a platform to present research findings, share developments, and highlight significant activities from around the globe.

ICENTE'24

**INTERNATIONAL CONFERENCE
ON ENGINEERING TECHNOLOGIES**

**November 21-23, 2024
Konya/TURKEY**

icente.selcuk.edu.tr